Frank Sabath
D.V. Giri
Farhad Rachidi
Armin Kaelin

Editors

Ultra-Wideband,
Short Pulse
Electromagnetics 9

Springer

Ultra-Wideband, Short Pulse Electromagnetics 9

Frank Sabath · D.V. Giri · Farhad Rachidi · Armin Kaelin
Editors

Ultra-Wideband, Short Pulse Electromagnetics 9

Springer

Editors
Frank Sabath
Federal Ministry of Defence
Armaments Directorate IV 6
Fontainengraben 150
53123 Bonn
Germany
frank.sabath@ieee.org

Farhad Rachidi
EPFL-STI-ISE
Labo. Réseaux Électriques (LRE)
1015 Lausanne
Station 11
Switzerland

D.V. Giri
Pro-Tech
11-C Orchard Court
Alamo CA 94507
USA

Armin Kaelin
Meteolabor AG
Hofstrasse 92
8620 Wetzikon
Switzerland

Printed on acid-free paper
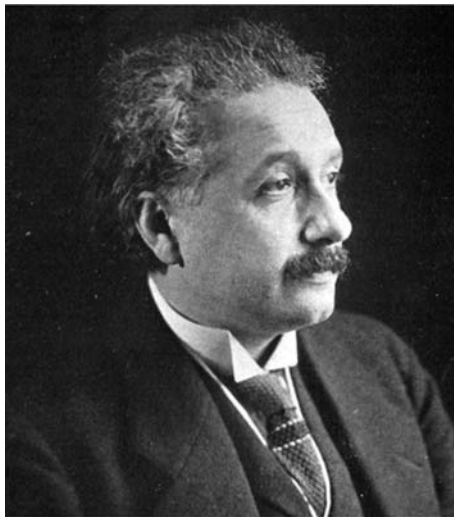
You do not really understand something unless you can explain it to your grandmother.

The important thing is not to stop questioning.

A theory is something nobody believes, except the person who made it. An experiment is something everybody believes, except the person who made it.

Albert Einstein
Nobel Prize Laureate (Physics)

Preface

When the first volume of the *Ultra-Wideband, Short Pulse Electromagnetics* book series was published in 1993, the terms ultra-wideband (UWB) and short-pulse (SP) were acronyms for challenging technologies. In 1992, the DARPA Ultra-wideband Radar Review Panel defined UWB by the need for special techniques to overcome challenging problems facing conventional systems and technologies when attempting to operate over a broad range of frequencies.

Since then notable progress in UWB and SP technologies has been achieved. As a result, wideband systems are now being used for an increasingly wide variety of applications. UWB radar systems are used for collision avoidance, concealed object detection, mine detection, and oil pipeline inspections. In the communication area, the need for increasing bandwidth boosted the development of UWB communication systems such as the impulse radio. Many high-power electromagnetic (HPEM) environments are generated employing short-pulse technology. With the advent of HPEM sources capable of interrupting and/or damaging sensitive electronics, there has been an increasing interest in protecting critical infrastructure and systems. Recently, the literature has reported the usage of SP techniques in microwave tomography systems for biomedical applications.

Through the whole development of UWB and SP technologies, *Ultra-Wideband, Short Pulse Electromagnetic* books provided new and state-of-the-art information on the tendencies and current achievements in UWB- and SP-related technologies, analyzing methodologies, theoretical models, and time domain data processing. The objectives of the *Ultra-Wideband, Short Pulse Electromagnetics* book series are as follows:

- To focus on advanced technologies for the generation, radiation, and detection of UWB and SP signals
- To report on developments in supporting mathematical and numerical methods, which are capable of analyzing the propagation of UWB and SP signals, as well as their scattering from and coupling to targets and media of interest
- To describe current and potential future applications of the UWB and SP technology

"*Ultra-Wideband, Short Pulse Electromagnetics 9*" (UWB SP 9) presents recent developments in the areas of UWB and SP technology, components, application, numerical analysis, modeling, and electromagnetic theory. The editorial board selected the initial set of contributions from presentations at the UWB-SP 9 conference that was held in conjunction with EUROEM 2008 in Lausanne, Switzerland. The editorial board's goal was to cover the complete range of aforementioned topics with articles of deep technical content and high scientific quality. Wherever we felt that something was missing, we invited selected authors to contribute additional articles to complete the overall picture. Therefore we hope that this book contains something of interest for every scientist and engineer working in the area of UWB and SP electromagnetics.

Following the tradition in the odd-numbered volumes of *Ultra-Wideband, Short Pulse Electromagnetics* (UWB SP) books, which are related to EUROEM conferences, the cover displays the picture of a renowned scientist. This ninth volume honors Albert Einstein, who is well known for his various achievements in theoretical physics. From the view point of the editorial board, Einstein is eminently well qualified for the cover picture from multiple aspects. First, Einstein started his professional life at the Swiss Patent Office in Bern and later in life was professor at the ETH Zurich. He introduced the theory of special relativity in 1905 in a paper entitled "The electrodynamics of moving bodies." The editorial board liked the idea of honoring this contribution to physics, as well as showing the link to electromagnetics. Second, there is a special relation among Maxwell, Hertz, and Einstein. A cover picture showing Einstein completes the series started with the *UWB SP 5* book. The cover of the *UWP SP 5* book shows a picture of James Clerk Maxwell, the Scottish theoretical physicist and mathematician, who developed the classical electromagnetic theory. The well known set of Maxwell's equations is the physical foundation of the research presented in the *UWB SP* books. The next odd-numbered volume, *UWB SP 7*, showed a picture of Heinrich Rudolf Herz, a German physicist, who was the first scientist to demonstrate electromagnetic waves by building an apparatus that produced radio waves. Therefore the cover of the *UWB SP 7* book continued the series by featuring the scientist who clarified Maxwell's theory. The next, and for the moment final, improvement of Maxwell's theory was Einstein's development into the special theory of relativity. Einstein noted that the special theory of relativity owes its origins to Maxwell's equations of electromagnetic fields.

Finally, I would like to express my gratitude to all persons who contributed to this book. In particular, I thank the authors for writing articles of deep technical content and high scientific quality, and the members of the editorial board, Farhad Rachidi, D.V. Giri, and Armin Kaelin, for reviewing all articles and numerous discussions, which helped improve the quality of this book.

Last but not least, I thank my family, particularly my wife Martina, for her great patience and for granting me the time to work on this book.

Bonn, Germany   Frank Sabath

Contents

Contributors

S. Abbaspour Department of Electrical and Computer Engineering, Ilam Azad University, Ilam, Iran

V.I. Afonin Russian Federal Nuclear Centre – Institute of Technical Physics, Snezhinsk, Russia

A. Alshehri EXPEC Advanced Research Center, Saudi Aramco, Dhahran, Saudi Arabia

S. Altunc Department of Electrical and Computer Engineering, University of New Mexico Albuquerque, NM 87131, USA

S. Anza Aurora Software and Testing S.L., Universidad Politecnica de Valencia, 46022, Ed. D. Empresarial 9B, Valencia, Spain

J. Armendariz Aurora Software and Testing S.L., Universidad Politecnica de Valencia, 46022, Ed. D. Empresarial 9B, Valencia, Spain

A. Balalem Chair of Microwave and Communication Engineering, University of Magdeburg, Magdeburg, Germany

E.V. Balzovsky Institute of High Current Electronics, SB RAS, 2/3 Akademichesky Ave., Tomsk 634055, Russia

W. Bandurski Poznań University of Technology, Poznań, Poland

A. Batmanov Chair of Semiconductor Technology, University of Magdeburg, Magdeburg, Germany

C.E. Baum Department of Electrical and Computer Engineering, The University of New Mexico, Albuquerque, NM, USA

P. Bechet Land Forces Academy, Sibiu, Romania

V.S. Belolipetskiy Institute of Optical-Physical Measurements, Moscow, Russia

E.H. Bleszynski Monopole Research, Thousand Oaks, CA 91360, USA

M.K. Bleszynski Monopole Research, Thousand Oaks, CA 91360, USA

J. Bonney Institut für Hochfrequenztechnik, Technische Universität Braunschweig, Schleinitzstraße 22, D-38106 Braunschweig, Germany

V.E. Boria Departamento de Comunicaciones, Universidad Politecnica de Valencia, 46022 Valencia, Spain

C. Boularak Instrumentation Laboratory, Faculty of Electronics and Informatics, USTHB University, El-Alia, Bab Ezzouar, 16111 Algiers, Algeria

I. Bouleanu Training Center for Communications and Information Systems, Sibiu, Romania

A. Boutejdar Chair of Microwave and Communication Engineering, University of Magdeburg, Magdeburg, Germany

L.H. Bowen Farr Research, Inc., Albuquerque, NM 87123, USA

G.I. Brukhnevich Institute of Optical-Physical Measurements, Moscow, Russia

E. Burte Chair of Semiconductor Technology, University of Magdeburg, Magdeburg, Germany

Y.I. Buyanov Institute of High Current Electronics, Siberian Branch of Russian Academy of Sciences, 2/3 Akademichesky Ave., Tomsk 634055, Russia

D. Caratelli IRCTR, Delft University of Technology, Delft, The Netherlands

R. Caspary Institut für Hochfrequenztechnik, Technische Universität Braunschweig, Schleinitzstraße 22, D-38106 Braunschweig, Germany

A. Chamarti Corning Incorporated, Corning, NY 14831, USA

Y. Chaolong Northwest Institute of Nuclear Technology, Xian 710024, China

C.G. Christodoulou Department of Electrical and Computer Engineering, University of New Mexico, Albuquerque, NM 87131, USA

C. Christopoulos George Green Institute for Electromagnetics Research, The University of Nottingham, University Park, Nottingham NG7 2RD, UK

G.I. Churyumov Microwave & Optoelectronics Lab., Kharkov National University of Radio Electronics, 14, Lenin Ave., Kharkov, 61166, Ukraine

R. Cicchetti Sapienza Department of Electronic Engineering, University of Rome, Rome, Italy

Annick F. Dégardin SUPELEC/Laboratoire de Génie Électrique de Paris (LGEP), CNRS UMR 8507, UPMC Univ Paris 06, Univ Paris Sud 11, Gif-sur-Yvette, France

G.Y. Delisle Technopôle Defence & Security, Quebec City, QC, Canada

P. Delmote French-German Research Institute of Saint-Louis, High Power Microwave Group, Saint-Louis, France

T.A. Denidni Institut National de la Recherche Scientifique (INRS), Montreal, QC, Canada

J.-M. Dienot Tarbes University Institute of Technology, Tarbes, France

D.J. Edwards Department of Engineering Science, University of Oxford, Parks Road, Oxford OX1 3PJ, UK

M.V. Efanov FID GmbH, Burbach, Germany

V.M. Efanov FID GmbH, Burbach, Germany

E.G. Farr Farr Research, Inc., Albuquerque, NM 87123, USA

M.S. Fealy Azad University, Kermanshah Branch, 69311-33145 Kermanshah, Iran

I. Fedotov Computer Engineering Department, Tomsk Polytechnic University, Russia

D. Firsov Department of Electrical and Computer Engineering, University of Manitoba, Winnipeg, MB, Canada

A. Gaugue Laboratoire Informatique Image Interaction (L3i), Université de La Rochelle, Avenue Michel Crépeau, 17042 La Rochelle Cedex 1, France

X. Gaztelu SUPELEC/Laboratoire de Génie Électrique de Paris (LGEP), CNRS UMR 8507, UPMC Univ Paris 06, Univ Paris Sud 11, Gif-sur-Yvette, France

J. George Corning Incorporated, Corning, NY 14831, USA

F. Ghanem Prince Mohammad Bin Fahd University, Al-Khobar, Saudi Arabia

K. Ghanem Prince Mohammad Bin Fahd University, Al-Khobar, Saudi Arabia

J. Gil Aurora Software and Testing S. L., Universidad Politecnica de Valencia, 46022, Ed. D. Empresarial 9B, Valencia, Spain

C. Gilmore Department of Electrical and Computer Engineering, University of Manitoba, Winnipeg, MB, Canada

B. Gimeno Departamento de Fisica Aplicada y Electromagnestimo, Universitat de Valencia, 46100 Valencia, Spain

P. Górniak Poznań University of Technology, Poznań, Poland

Kaoru Gotoh National Institute of Information and Communications Technology, Tokyo, Japan

M.P. Gribskii Radiophysics Department, Taurida National Vernadsky University, 4, Vernadsky Ave., Simferopol', 95007, Ukraine

L. Guozhi Northwest Institute of Nuclear Technology, Xian 710024, China

A. Hangan Land Forces Academy, Sibiu, Romania

R. Helbet Training Center for Communications and Information Systems, Sibiu, Romania

I. Immoreev Moscow Aviation Institute, Gospitalny val, Moscow 105094, Russia

Shinobu Ishigami National Institute of Information and Communications Technology, Tokyo, Japan

A.A. Jamshidifar Iran Research Organization for Science and Technology, Tehran, Iran

T. Jaroszewicz Monopole Research, Thousand Oaks, CA 91360, USA

M. Jung Rheinmetall Waffe Munition GmbH, Heinrich-Erhardt-Straße 2, D-29345 Unterlüß, Germany

M. Kamyab Department of Electrical Engineering, K. N. Toosi University of Technology, Tehran, Iran

A. Kavatjikidis Department of Engineering Science, University of Oxford, Parks Road, Oxford OX1 3PJ, UK

C. Kaye Department of Electrical and Computer Engineering, University of Manitoba, Winnipeg, MB, Canada

J. Khamlichi Laboratoire Informatique Image Interaction (L3i), Université de La Rochelle, Avenue Michel Crépeau, 17042 La Rochelle Cedex 1, France

A. Khodja Instrumentation Laboratory, Faculty of Electronics and Informatics, USTHB University, El-Alia, Bab Ezzouar, 16111 Algiers, Algeria

Y. Kim Department of Electrical Information, Inha Technical College, Incheon 402 752, Korea

M. Kmec Technische Universität Ilmenau, Ilmenau, Germany

T. Kobayashi Tokyo Denki University, Tokyo, Japan

A. Kohmura Electronic Navigation Research Institute, Tokyo, Japan

A.V. Komashko FID GmbH, Burbach, Germany

V.I. Koshelev Institute of High Current Electronics, SB RAS, 2/3 Akademichesky Ave., Tomsk 634055, Russia

Alain J. Kreisler SUPELEC/Laboratoire de Génie Électrique de Paris (LGEP), CNRS UMR 8507, UPMC Univ Paris 06, Univ Paris Sud 11, Gif-sur-Yvette, France

A.V. Kriklenko FID GmbH, Burbach, Germany

N.V. Kupyrin Russian Federal Nuclear Centre – Institute of Technical Physics, Snezhinsk, Russia

D.-H. Kwon Department of Electrical and Computer Engineering, University of Massachusetts, Amherst, MA 01003, USA

Y.N. Lazarev Russian Federal Nuclear Centre – Institute of Technical Physics, Snezhinsk, Russia

S. Lei Northwest Institute of Nuclear Technology, Xian 710024, China

B. Levitas GeoZondas Ltd., Vilnius, Lithuania

C. Liebe Laboratoire Informatique Image Interaction (L3i), Université de La Rochelle, Avenue Michel Crépeau, 17042 La Rochelle Cedex 1, France

L.P. Ligthart International Research Centre for Telecommunication and Radar, Delft University of Technology, Mekelweg 4, 2628CD Delft, The Netherlands

J. LoVetri Department of Electrical and Computer Engineering, University of Manitoba, Winnipeg, MB, Canada

J. MacGillivray Air Force Research Laboratory, Kirtland AFB, Albuquerque, NM 87117, USA

B. Martin French-German Research Institute of Saint-Louis, High Power Microwave Group, Saint-Louis, France

Yasushi Matsumoto National Institute of Information and Communications Technology, Tokyo, Japan

M. Mattes Laboratoire d'Electromagnétisme et d'Acoustique, Ecole Polytechnique Fédérale de Lausanne, 1015 Lausanne, Switzerland

J. Matuzas GeoZondas Ltd., Vilnius, Lithuania

J.S. McLean TDK R&D Corp., Cedar Park, TX, USA

M.-A. Mellah ENSTA (Ecole Nationale Supérieure de Techniques Avancées), ParisTech. 32, Boulevard Victor, 75738 Paris, France

M. Menard Laboratoire Informatique Image Interaction (L3i), Université de La Rochelle, Avenue Michel Crépeau, 17042 La Rochelle Cedex 1, France

A. Mohamed Department of Electrical and Computer Engineering, The University of Manitoba, Winnipeg, MB, Canada R3T 5V6

P. Mojabi Department of Electrical and Computer Engineering, University of Manitoba, Winnipeg, MB, Canada R3T 5V6

J. Müller Technische Universität Ilmenau, Ilmenau, Germany

A. Najafi Department of Electrical and Computer Engineering, Ilam Azad University, Ilam, Iran

Y.R. Naumar Wireless Communication Centre, Faculty of Electrical Engineering, Universiti Teknologi Malaysia, Johor Bahru, Malaysia

A. Neagu Land Forces Academy, Sibiu, Romania

S.M. Nematollahzadeh Iran Telecommunication Research Center, Tehran, Iran

R. Ngah Wireless Communication Centre, Faculty of Electrical Engineering, Universiti Teknologi Malaysia, Johor Bahru, Malaysia

A. Ng'oma Corning Incorporated, Corning, NY 14831, USA

M. Nosrati Department of Electrical and Computer Engineering, Ilam Azad University, Kermanshah Branch, 69311-33145 Kermanshah, Iran

J.-M. Ogier Laboratoire Informatique Image Interaction (L3i), Université de La Rochelle, Avenue Michel Crépeau, 17042 La Rochelle Cedex 1, France

A. Omar Chair of Microwave and Communication Engineering, University of Magdeburg, Magdeburg, Germany

E. Pancera Institut fuer Hoechstfrequenztechnik und Elektronik, Universitaet Karlsruhe, Kaiserstr. 12, 76131 Karlsruhe, Germany

Devendra Chandra Pande Electronics & Radar Development Establishment, Bangalore, India

S.B. Panin Department of Mathematics, Macquarie University, Sydney 2109, Australia

J.D. Paul George Green Institute for Electromagnetics Research, The University of Nottingham, University Park, Nottingham NG7 2RD, UK

L.Z. Pekarskaya Institute of Optical-Physical Measurements, Moscow, Russia

P.V. Petrov Russian Federal Nuclear Centre – Institute of Technical Physics, Snezhinsk, Russia

J. Picard Ecole Nationale de l'Aviation Civile, Toulouse Cedex 4, France

V.V. Plisko Institute of High Current Electronics, SB RAS, 2/3 Akademichesky Ave., Tomsk 634055, Russia

A. Podgorski Air Force Research Laboratory, Kirtland AFB, Albuquerque, NM 87117, USA

W. Prather Air Force Research Laboratory, Kirtland AFB, Albuquerque, NM 87117, USA

W.D. Prather Air Force Research Laboratory, Directed Energy Directorate, Kirtland AFB, Albuquerque, NM 87117, USA

G. Quintero Laboratoire d'Electromagnétisme et d'Acoustique (LEMA), Ecole Polytechnique Fédérale de Lausanne (EPFL), CH-1015 Lausanne, Switzerland

D. Raboso ESA-ESTEC, Keplerlaan 1, 2200 AG Noordwijk, The Netherlands

T.A. Rahman Wireless Communication Centre, Faculty of Electrical Engineering, Universiti Teknologi Malaysia, Johor Bahru, Malaysia

P. Rauschenbach Meodat GmbH, Ilmenau, Germany

S. Rentsch Technische Universität Ilmenau, Ilmenau, Germany

Nicolas Ribière-Tharaud SUPELEC/DRE, Gif-sur-Yvette, France

C. Roblin ENSTA (Ecole Nationale Supérieure de Techniques Avancées), ParisTech. 32, Boulevard Victor, 75738 Paris, France

Y.O. Romanov Russian Federal Nuclear Centre – Institute of Technical Physics, Snezhinsk, Russia

F. Sabath Federal Ministry of Defence, Bonn, Germany; Armaments Directorate IV 6, Fontainengraben 150, 53123 Bonn, Germany

J. Sachs Technische Universität Ilmenau, Ilmenau, Germany

M. Sauer Corning Incorporated, Corning, NY 14831, USA

T. Savelyev International Research Centre for Telecommunications and Radar, Delft University of Technology, Delft, The Netherlands

T.G. Savelyev International Research Centre for Telecommunication and Radar, Delft University of Technology, Mekelweg 4, 2628CD Delft, The Netherlands

E. Schamiloglu Department of Electrical and Computer Engineering, University of New Mexico, Albuquerque, NM 87131, USA

Alexander Scheuring SUPELEC/Laboratoire de Génie Électrique de Paris (LGEP), CNRS UMR 8507, UPMC Univ Paris 06, Univ Paris Sud 11, Gif-sur-Yvette, France

J. Schmitz Rheinmetall Waffe Munition GmbH, Heinrich-Erhardt-Straße 2, D-29345 Unterlüß, Germany

J. Schöbel Institut für Hochfrequenztechnik, Technische Universität Braunschweig, Schleinitzstraße 22, D-38106 Braunschweig, Germany

J. Schüür Institut für Elektromagnetische Verträglichkeit, Technische Universität Braunschweig, Schleinitzstraße 23, D-38106 Braunschweig, Germany

A.R. Sebak Electrical and Computer Engineering Department, Concordia University, Montreal, QC, Canada

A. Semnani Department of Electrical Engineering, K. N. Toosi University of Technology, Tehran, Iran

L. Shafai Department of Electrical and Computer Engineering, The University of Manitoba, Winnipeg, MB, Canada R3T 5V6

A. Sibille ENSTA (Ecole Nationale Supérieure de Techniques Avancées), ParisTech. 32, Boulevard Victor, 75738 Paris, France

M. Simeoni Delft University of Technology, IRCTR, Delft, The Netherlands

Dhiraj Kumar Singh Electronics & Radar Development Establishment, Bangalore, India

Z. Sitao Northwest Institute of Nuclear Technology, Xian 710024, China

A.K. Skrivervik Laboratoire d'Electromagnétisme et d'Acoustique (LEMA), Ecole Polytechnique Fédérale de Lausanne (EPFL), CH-1015 Lausanne, Switzerland

P.D. Smith Department of Mathematics, Macquarie University, Sydney 2109, Australia

I.A. Sorokin Russian Federal Nuclear Centre – Institute of Technical Physics, Snezhinsk, Russia

V. Spitsyn Computer Engineering Department, Tomsk Polytechnic University, Russia

V.V. Starostenko Radiophysics Department, Taurida National Vernadsky University, 4, Vernadsky Ave., Simferopol', 95007, Ukraine

C.J. Stevens Department of Engineering Science, University of Oxford, Parks Road, Oxford OX1 3PJ, UK

K.N. Sukhushin Institute of High Current Electronics, SB RAS, 2/3 Akademichesky Ave., Tomsk 634055, Russia

R. Sutton TDK R&D Corp., Cedar Park, TX, USA

Y.G. Syrtsova Russian Federal Nuclear Centre – Institute of Technical Physics, Snezhinsk, Russia

F.L. Teixeira ElectroScience Laboratory, Department of Electrical and Computer Engineering, The Ohio State University, 1320 Kinnear Road, Columbus, OH 43212, USA

V.Yr. Tereshenko Radiophysics Department, Taurida National Vernadsky University, 4, Vernadsky Ave., Simferopol', 95007, Ukraine

D. Thelen Corning Incorporated, Corning, NY 14831, USA

R.S. Thomä Electronic Measurement Research Lab, Ilmenau University of Technology, Ilmenau, Germany

D.W.P. Thomas George Green Institute for Electromagnetics Research, The University of Nottingham, University Park, Nottingham NG7 2RD, UK

J. Timmermann Institut fuer Hoechstfrequenztechnik und Elektronik, Universitaet Karlsruhe, Kaiserstr. 12, 76131 Karlsruhe, Germany

A.S. Tischenko Russian Federal Nuclear Centre – Institute of Technical Physics, Snezhinsk, Russia

Masamitsu Tokuda Musashi Institute of Technology, Tokyo, Japan

R. Touhami Instrumentation Laboratory, Faculty of Electronics and Informatics, USTHB University, El-Alia, Bab Ezzouar, 16111 Algiers, Algeria

M.L. Tounsi Instrumentation Laboratory, Faculty of Electronics and Informatics, USTHB University, El-Alia, Bab Ezzouar, 16111 Algiers, Algeria

Y.A. Tuchkin Electronics Department, Gebze Institute of Technology, Gebze-Kocaeli, Turkey

Ibrahim Türer SUPELEC/Laboratoire de Génie Électrique de Paris (LGEP), CNRS UMR 8507, UPMC Univ Paris 06, Univ Paris Sud 11, Gif-sur-Yvette, France

D.A. Unzhakov Radiophysics Department, Taurida National Vernadsky University, 4, Vernadsky Ave., Simferopol', 95007, Ukraine

N.T. van Tol International Research Centre for Telecommunication and Radar, Delft University of Technology, Mekelweg 4, 2628CD Delft, The Netherlands

C. Vicente Aurora Software and Testing S.L., Universidad Politecnica de Valencia, 46022, Ed. D. Empresarial 9B, Valencia, Spain

E.D. Vinogradova Department of Mathematics, Macquarie University, Sydney 2109, Australia

S.V. Vinogradov ICT Centre, CSIRO, Epping, NSW 1710, Australia

N.P. Voronkova Institute of Optical-Physical Measurements, Moscow, Russia

P. Walk Technische Universitaet Berlin, Lehrstuhl fuer Mobilkommunikation, Einsteinufer 25, 10587 Berlin, Germany

X. Wenfeng Northwest Institute of Nuclear Technology, Xian 710024, China

W. Wiesbeck Institut fuer Hoechstfrequenztechnik und Elektronik, Universitaet Karlsruhe, Kaiserstr. 12, 76131 Karlsruhe, Germany

X. Wu School of Electronic Engineering and Computer Science, Peking University, Beijing, P.R. China

S. Xiaoxin Northwest Institute of Nuclear Technology, Xian 710024, China

M.C.E. Yagoub SITE, 800 King Edward, University of Ottawa, Ottawa, ON, Canada K1N 6N5

F. Yajun Northwest Institute of Nuclear Technology, Xian 710024, China

S. Yakura Air Force Research Laboratory, Kirtland AFB, Albuquerque, NM 87117, USA

Masashi Yamada Musashi Institute of Technology, Tokyo, Japan

H. Yamamoto National Institute of Information and Communications Technology, Yokosuka, Japan; Tokyo Denki University, 2-2 Kanda-nishiki-cho, Chiyoda-ku, Tokyo 101-8457, Japan

K. Yamamoto Electronic Navigation Research Institute, Tokyo, Japan

B. Yang Delft University of Technology, Delft, The Netherlands

P.M. Yarin FID GmbH, Burbach, Germany

A. Yarovoy Delft University of Technology, IRCTR, Delft, The Netherlands

A.G. Yarovoy International Research Centre for Telecommunication and Radar, Delft University of Technology, Mekelweg 4, 2628CD Delft, The Netherlands

M.E. Yavuz Sensor Physics Group, Halliburton Energy Services, Houston, TX 77032, USA

N. Yonemoto Electronic Navigation Research Institute, Tokyo, Japan

Z. Yufeng Northwest Institute of Nuclear Technology, Xian 710024, China

D.O. Zamuraev Russian Federal Nuclear Centre – Institute of Technical Physics, Snezhinsk, Russia

E.V. Zavolokov Russian Federal Nuclear Centre – Institute of Technical Physics, Snezhinsk, Russia

S.V. Zazoulin FID GmbH, Burbach, Germany

R. Zetik Electronic Measurement Research Lab, Ilmenau University of Technology, Ilmenau, Germany

L. Zhou School of Electronic Engineering and Computer Science, Peking University, Beijing, P.R. China

X. Zhuge International Research Centre for Telecommunications and Radar, Delft University of Technology, Delft, The Netherlands

S.A. Zuev Radiophysics Department, Taurida National Vernadsky University, 4, Vernadsky Ave., Simferopol', 95007, Ukraine

J.F. Zürcher Laboratoire d'Electromagnétisme et d'Acoustique (LEMA), Ecole Polytechnique Fédérale de Lausanne (EPFL), CH-1015 Lausanne, Switzerland

T. Zwick Institut fuer Hoechstfrequenztechnik und Elektronik, Universitaet Karlsruhe, Kaiserstr. 12, 76131 Karlsruhe, Germany

Modeling of Electromagnetic Wave Propagation in Flows of Turbulent Plasma Inhomogeneities

V. Spitsyn and I. Fedotov

Abstract The subjects of this chapter are analytical and numerical models of electromagnetic wave propagation in flows of a slightly ionized plasma. The different shapes of a flow (cone, paraboloid, and a surface created by rotation of fourth-order curves) are addressed in this chapter. The indicatrices of turbulence reradiation (isotropic, Lambert, and quasi-mirror types) are considered. Calculations are used to determine the angular and frequency spectra of singly and multiply scattered signals. The calculated frequency spectrum of each scattering signal is compared with well-known experimental data from radio sounding of an exhaust plume of a spacecraft.

Keywords Wave propagation · Radio wave · Scattering · Turbulent plasma · Spacecraft

1 Introduction

Analytical and numerical models of interactions of electromagnetic waves with moving turbulent inhomogeneities in the flows of slightly ionized plasma are considered. The authors assume that turbulent inhomogeneities in a flow of a slightly ionized plasma correspond to statistically independent discrete scatterers [1–3].

Single and multiple scatterings of electromagnetic waves from turbulent plasma inhomogeneities near a body-of-rotation surface are investigated. Radio wave scattering from a cone, a paraboloid, and a surface created by rotating a fourth-order curve is analyzed under the assumption that the size of a body of rotation is on the order of the ratio of the wavelength of the incident field over the average size of the turbulent inhomogeneities.

Section 2 is devoted to radio wave scattering from the outer surface of the expanding turbulent flow of a plasma. The results of investigations of multiple radio wave scattering from the inner surface of a turbulent body of rotation are presented in Section 3. Conclusions are given in Section 4.

V. Spitsyn (✉)
Computer Engineering Department, Tomsk Polytechnic University, Tomsk, Russia
e-mail: spvg@tpu.ru

2 Radio Wave Scattering from the Outer Surface of Expanding Turbulent Flow of a Plasma

Electromagnetic plane wave scattering from turbulent plasma inhomogeneities near the surface of a body of rotation in the form of a cone and a paraboloid is considered in this section. The geometry of the task is presented in Fig. 1. The radio wave frequency f is governed by the inequality $f \leq [N_i/N_{0i}]^{1/2} f_p$, where f_p is the plasma frequency and N_{0i} and N_i are the equilibrium and disturbed ionic concentrations, respectively, at the height of a spacecraft's motion.

It is supposed that the turbulent inhomogeneities are distributed evenly on the surface of a body of rotation. Further, the inhomogeneities are assumed to have an equally directed velocity oriented along the generatrix of the body and a stochastic isotropic velocity distributed by the normal law. Three types of over-radiation diagrams of the turbulent inhomogeneities are studied: isotropic, Lambert, and quasi-mirror. Radiation transport theory is applied for solving this problem [4].

The solving of the task is implemented in a spherical coordinate system (θ, ϕ, r) that is shown in Fig. 2. The origin of the coordination system is located at the tip of the body of rotation. The polar angle θ is measured from the rotation axis of the body (positive z-axis). The azimuthal angle ϕ is calculated in a plane perpendicular to the rotation axis (z-axis) and with regard to the direction of propagation of the incident field $\vec{e}_i$. The index u corresponds to the coordinates of the surface of the body of rotation, and the indices i and s correspond to the parameters of the incident and scattered waves, respectively. The angle between the incident and scattered fields is φ_s, and $\vec{e}_s$ is the unit vector in the direction of propagation of the scattered wave.

The diagram of reradiation of the turbulent inhomogeneities does not depend on the direction of propagation of the incident wave $\vec{e}_i$ and can be represented by
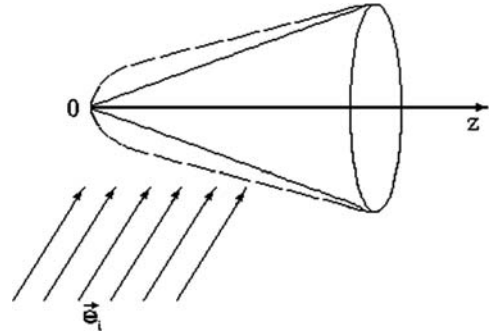
Fig. 1 Geometry for radio sounding on the outer surface of a turbulent plasma formation
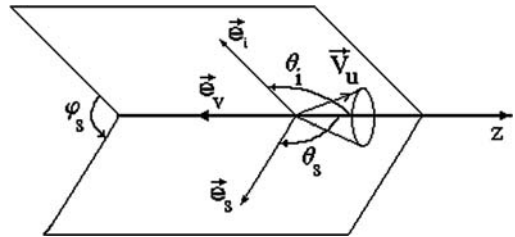
Fig. 2 Coordinate system for calculating radio wave scattering from a turbulent body of rotation

$$P(\vec{e}_s) = A_j (\vec{e}_s \vec{n})^j,$$

where $\vec{n}$ is a normal to the surface, A_j is a coefficient determined from the condition of normalization $\int P(\vec{e}_s)\, d\Omega = 1$, and $d\Omega$ is an element of the spatial angle in which the scattering occurred. The normalization implies that $A_j = (j + 1)/2\pi$. The cases $j = 0$ and $j = 1$ correspond to the isotropic diagram of turbulence reradiation and the Lambert diagram, respectively.

The diagram of reradiation of quasi-mirror type, considering the direction of propagation of the incident wave $\vec{e}_i$, can be given as

$$P(\vec{e}_s) = A \left(\Delta e_m^2 - \Delta e^2 \right), \tag{1}$$

where

$$\Delta \vec{e} = \vec{e}_s - \vec{e}_{s0}, \ \vec{e}_{s0} = \vec{e}_i - 2\vec{n}(\vec{n}\vec{e}_i).$$

In this case, the diagram of reradiation is asymmetrical, and most of the energy of the scattered signal is concentrated in the vicinity of vector e_{s0}, which corresponds to the direction of a mirror reflection of the wave from the surface. The formulas for Δe^2, Δe_m^2, and A in (1) are

$$\Delta e^2 = 2 \left(1 - \vec{e}_i \vec{e}_s + 2 (\vec{n}\vec{e}_i)(\vec{n}\vec{e}_s) \right),$$

$$\Delta e_m^2 = 2 \left(1 + \left(1 - (\vec{n}\vec{e}_i)^2 \right)^{1/2} \right),$$

$$A = 1 \left/ \left[4\pi \left(\sqrt{1 - (\vec{n}\vec{e}_i)^2} - \vec{n}\vec{e}_i \right) \right] \right.$$

The formula for the spectral density of the energy scattered from a turbulent plasma body of rotation is [1]

$$dI_s/I_0 = -(\vec{e}_i \vec{n}) P(\vec{e}_s)\, dS d\Omega/2\pi, \tag{2}$$

where dI_s is the energy scattered in a fixed direction, I_0 is the energy of the incident wave, and dS is an areal element of the scattering surface.

The magnitude of the non-dimensional Doppler shift of frequency is defined by

$$f_* = (\Delta f c) / (f_0 V_u) = (\vec{e}_s - \vec{e}_i)(\vec{e}_u (1 + \delta V/V_u) - \vec{e}_i V_0/V_u), \tag{3}$$

where c is the propagation speed of an electromagnetic wave in the plasma, f_0 is the frequency of the incident wave, V_0 is the speed of the spacecraft, V_u is the directed speed, and δV is the speed of the stochastic motion of the turbulences along the generatrix.

In spherical coordinates, formula (3) has the form

$$
\begin{aligned}
f_* = (\sin\,\theta_s \cos\,\varphi_s - \sin\,\theta_i) \sin\,\theta_u \cos\,\varphi_u + \sin\,\theta_s \sin\,\varphi_s \sin\,\theta_u \sin\,\varphi_u + \\
+ (\cos\,\theta_s - \cos\,\theta_i)(\cos\,\theta_i - V_0/V_u)
\end{aligned}
\tag{4}
$$

Solving (4) relative to the azimuthal angle φ_u and substituting the received dependence $\varphi_u(f_*)$ into (2) yields an expression for the frequency spectrum of the wave scattered from the plasma formation

$$S_n(f_*) = \frac{dI_s 4\pi}{I_0 z_m^2 d\Omega df_*} = \frac{\tan\,\theta_u}{\cos\,\theta_u} P(\vec{e}_s) \frac{d\varphi_u(f_*)}{df_*}, \tag{5}$$

where $S_n(f_*)$ is the normalized magnitude of the spectral density of energy scattered in the unit spatial angle and z_m is the size of a body of rotation along the z-axis.

In the case of backscattering, (4) and (5) lead to the frequency spectrum

$$S(f_*) = D\frac{\tan\,\theta_u}{\cos\,\theta_u} (\vec{e}_i\vec{n}) P(\vec{e}_s) \left(1 - (f_*D + B)^2\right)^{-1/2}, \tag{6}$$

where

$$D = -\frac{1}{2(1 + \delta V/V_u)\sin\,\theta_i \sin\theta_u},$$

$$B = \frac{V_0}{V_u \sin\theta_i \tan\theta_i (1 + \delta V/V_u)} - \frac{1}{\tan\theta_i \tan\theta_u},$$

$$\vec{e}_i\vec{n} = \sin\,\theta_i \cos\,\theta_u (Df_* + B) - \cos\theta_i \sin\theta_u.$$

The results of calculating the frequency spectrum of a scattered signal from a cone of turbulent flow are illustrated in Fig. 3 for several angles of incidence. The solid curves in Fig. 3 are calculated according to formula (6) with $V_0/V_u = 2$, $\theta_0 = 26.6°$, and $\delta V/V_u = 0$. The histograms correspond to frequency spectrum averaging over the frequency interval. The results of these calculations show that for inverse scattering the frequency spectrum of a signal is characterized by monotonically increasing energy with an increasing Doppler shift.

3 Multiple Radio Wave Scattering from the Inner Surface of a Turbulent Body of Rotation

In this section, suppose that the plane electromagnetic wave is reduced along the negative z direction (Fig. 4). Turbulent inhomogeneities are chaotically disposed on the surface of a body of rotation (cone, paraboloid, surface created by rotation of the fourth-order curve). These inhomogeneities have velocities that are equally distributed between the directed velocity $\vec{V}_u$, oriented along the generatrix of the body of rotation, and the stochastic isotropic velocity δV, distributed according to the normal law. Recall that the size of a body of rotation is assumed to be on the order of the ratio of the wavelength of the incident field over the average size of the turbulent inhomogeneities.

In this case, the field of the scattered wave is the result of multiple wave reflections from the dynamic rough surface. Because of the presence of chaotically disposed moving turbulent inhomogeneities on the surface of a body of rotation, the wave phases after reflections from the surface are stochastic. The energy of the scattered signal is proportional to the number of photons scattered in the defined element of a spatial angle.
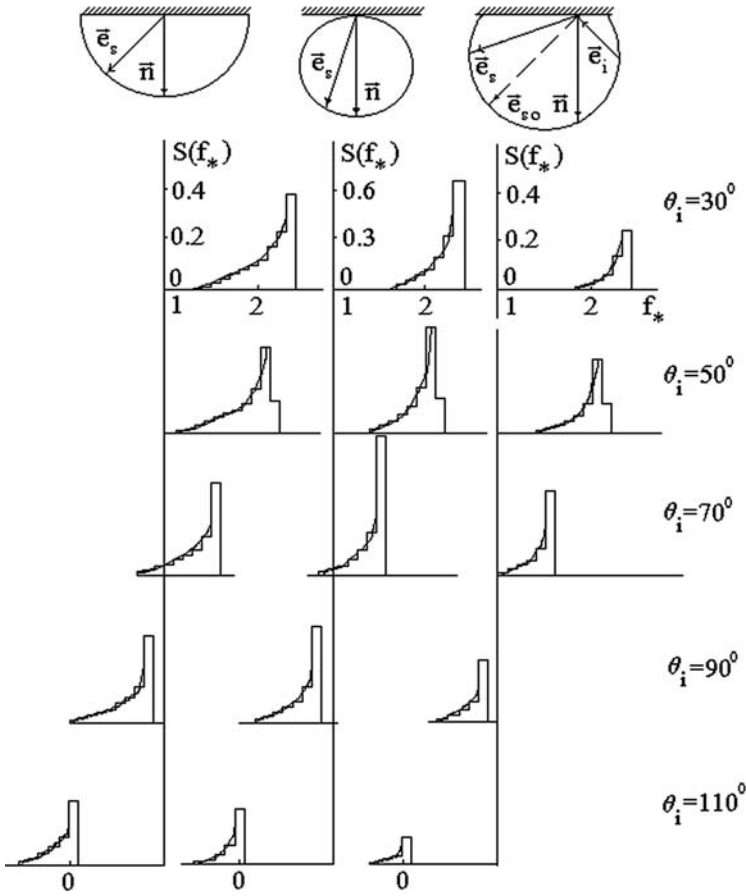
Fig. 3 Frequency spectrum of a radio signal scattered from the outer surface of a turbulent plasma formation for different angles of incidence
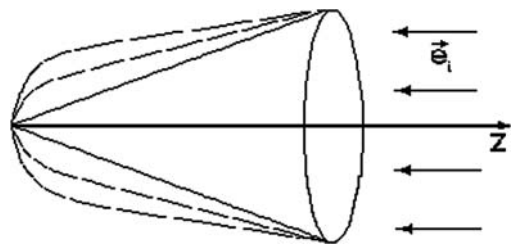
Fig. 4 The geometry for radio sounding of the inner surface of a turbulent body of rotation

The method of Monte Carlo is applied for determining the energy. The incident electromagnetic wave is simulated by non-commuted photons, uniformly distributed in the plane of the wave front [1]. Figure 5 displays the frequency spectrum of a signal that is incoherently scattered from the dynamic rough surface of a body of rotation for different ranges of the polar angle θ, in the form of an isotropic diagram of reradiation of the turbulent inhomogeneities. The magnitude
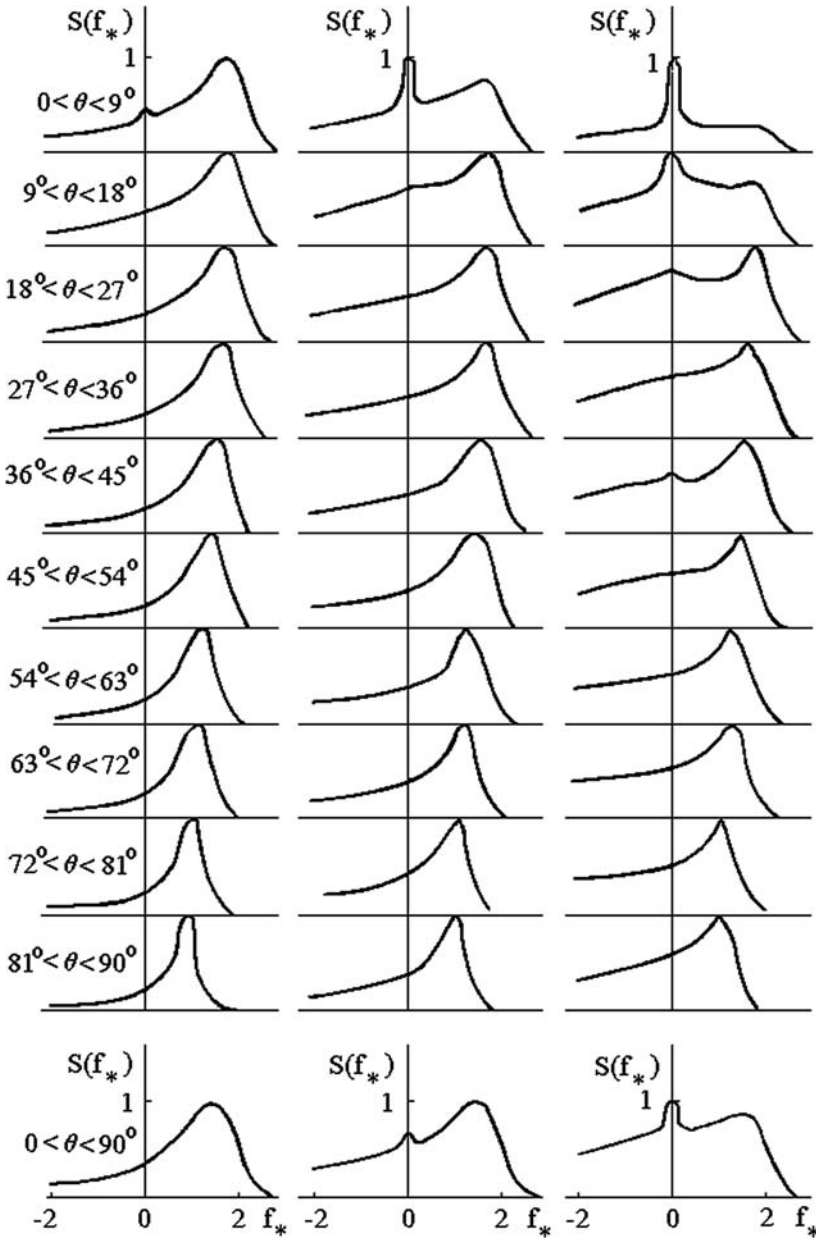
Fig. 5 The frequency spectrum of signal scattered from the inner surface of the turbulent plasma body of rotation for different ranges of θ

$f_* = (c\Delta f)/(f_0 V_u)$ is calculated on the horizontal axis. The energy of the signal, normalized by maximum spectral energy, is calculated on the vertical axis of every spectral frame.

The first, second, and third columns of frequency spectra correspond to scattering from the cone, the paraboloid of rotation, and the surface created by rotating a fourth-order curve, respectively. In each column, the frequency spectra differ by the value of the polar angle θ. The bottom frames

represent the integral frequency spectrum for all photons emanating from plasma formation in the angular range of $0 < \theta < \pi/2$.

As the reader can observe, the spectra typically have two components for small θ and the integrated spectrum: a discrete contribution at $f_* = 0$ that is caused by the mirror reflection of the radio wave from the plasma surface and a continuous component that is the aggregate of multiple scattering from the moving inhomogeneities. On the basis of these calculations, we arrive at the next conclusion: increasing the order of the equation describing the scattering surface leads to increasing the energy of a spectral component with a negative frequency shift and to focusing the signal energy near the axis of a body of rotation.

As Fig. 6 illustrates, the calculated frequency spectra of a scattered signal (dashed and dotted curves) and the experimental data (solid curve) from radio sounding of an exhaust plume of a launched rocket [5] are in good agreement. The dashed curve corresponds to the paraboloidal surface, and the dotted curve corresponds to the surface created by rotating the fourth-order curve. On the basis of this comparison, the authors conclude that indeed multiple scattering of a radio wave from the inner surface of a turbulent plasma body of rotation was realized. The form of a scattering surface was enclosed between the paraboloid and the surface created by rotation of the fourth-order curve.

Fig. 6 Comparison of calculated frequency spectra of a scattering signal with experimental data
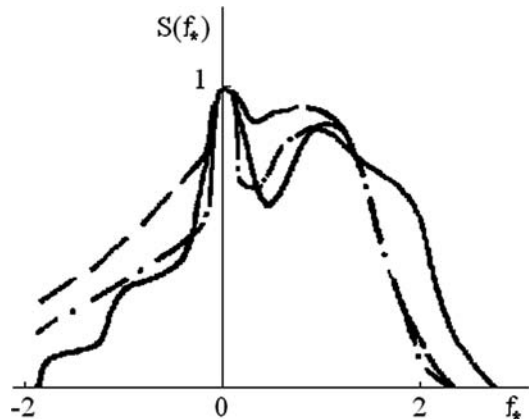
4 Conclusions

The results of this analysis demonstrate that, for backward radio sounding of the outer surface of a turbulent body of rotation, the frequency spectra of such scattered signals are characterized by a monotonic increase of energy with the growth of the Doppler frequency shift. In addition, two other phenomena were observed when the order of the equation governing the surface of the body is increased: (1) the energy of a spectral component with a negative frequency shift is increased and (2) the scattered energy from the inner surface of the turbulent plasma formation is focused along the axis of the body of rotation.

Comparisons of calculations and known experimental data from radio sounding of an exhaust plume of a rocket during the launch phase show good agreement. Thus the authors conclude that in the experiment the scattered field is formed as a result of multiple scattering from the inner surface of a turbulent body of rotation.

References

1. V. G. Spitsyn, Modelling of radio wave scattering on the ionospheric plasma disturbances created of spacecraft. Physmatlit, Moscow, 2003.
2. V. G. Spitsyn, Development of a numerical model concerning electromagnetic wave propagation in turbulent flows, Journal of Applied Electromagnetism, vol. 1, pp. 67–78, 1997.
3. V. G. Spitsyn and I. V. Fedotov, Stochastic model of electromagnetic wave propagation in stratified media including the semitransparent object and inhomogeneous flow of scatterers, Proceedings of SPIE, vol. 6522, pp. 65220F-1-65220F-8, 2006.
4. A. Ishimaru, Wave propagation and scattering in random media. IEEE Press-Oxford University Press Classic Reissue, 1997.
5. J. S. Draper, P. O. Jarvinen, and T. D. Conley, Analysis of radar return from turbulent high–altitude rocket exhaust plumes, AIAA Journal, vol. 8, pp. 1568–73, 1970.

Ultra-wideband Propagation Loss Around a Human Body in Various Surrounding Environments

H. Yamamoto and T. Kobayashi

Abstract Ultra-wideband (UWB) technologies have been anticipated for use in wireless body area networks (WBAN) because of their low power consumption and anti-multipath capabilities. This chapter presents the UWB (3.1–10.6 GHz) propagation loss in WBAN scenarios between on-body antennas in three different surrounding environments. The measurements were performed in a 3-m radio anechoic chamber, a classroom, and a small room. The propagation paths were roughly divided into line-of-sight (LOS) and non-LOS (NLOS) ones. Small rooms, particularly NLOS, yielded higher reception power than larger rooms. This was attributed to the ample multipath from the nearby floor, walls, and ceiling. The UWB maximum propagation losses in three surrounding environments were smaller than ones of CW (6.85 GHz). This is because nulls caused by interference were cancelled out by the ultra-wide bandwidth. The propagation losses of low-band (3.4–4.8 GHz) and high-band (7.25–10.25 GHz) UWB were also evaluated. In WBAN scenarios, the low-band yielded lower propagation loss than the high-band and approximately the same loss as the full-band UWB (3.1–10.6 GHz).

Keywords Ultra-wideband (UWB) · Wireless body area networks · Radio propagation · Propagation loss · Multipath propagation

1 Introduction

Wireless body area networks (WBAN) have been discussed for medical and non-medical applications [1]. For medical applications, wireless electroencephalography (EEG), electrocardiography (ECG), electromyography (EMG), and other health-care monitoring are proposed applications. Ultra-wideband (UWB) technologies were anticipated for use in WBAN because of their low power consumption and anti-multipath capabilities. In the last few years, researchers investigated UWB indoor and outdoor radio propagation modeling and characterization [2, 3]. A number of measurements were also carried out to characterize on-body UWB propagation in the WBAN scenarios [4]. However, previous WBAN studies treated mainly the cases when propagation was measured in either a radio anechoic chamber or a particular room [5–7]. It is necessary to evaluate the variation of propagation losses in various surrounding environments from the viewpoint of WBAN device design.

H. Yamamoto (✉)
Tokyo Denki University, Tokyo, Japan
e-mail: h.yamamoto@grace.c.dendai.ac.jp

This chapter presents the UWB (3.1–10.6 GHz) propagation loss in WBAN scenarios between on-body antennas in three surrounding environments: a 3-m radio anechoic chamber, a classroom, and a small room. The propagation losses of continuous wave (CW), low-band UWB (3.4–4.8 GHz), and high-band UWB (7.25–10.25 GHz) were evaluated in comparison with that of full-band UWB (3.1–10.6 GHz).

2 Experimental Setup

The measurements were carried out in the following rooms:

	Width (m)	Depth (m)	Height (m)	Volume (m^3)
Anechoic chamber	5.5	7.0	5.0	193
Classroom	6.6	4.3	2.5	71
Small room	2.6	2.7	2.3	16

The 3-m radio anechoic chamber can be considered as a room extending with an infinite volume in terms of radio propagation. The classroom and the small room were made of reinforced concrete, and their floors, walls, and ceilings were covered with linoleum, wall paper, and plaster board, respectively. A volunteer (an adult male, 1.77 m tall and 57 kg) stood upright with legs close together in either a quiet zone of the radio anechoic chamber or the center of the rooms. The UWB

Fig. 1 Placement of the transmitting and receiving antennas on the body.

(from 3.1 to 10.6 GHz) frequency- and time-domain propagations losses were measured with a vector network analyzer. Commercially available meanderline antennas [8] were used for transmission and reception. The voltage standing wave ratio of the meanderline antenna was less than 2.5 from 3.1 to 10.6 GHz and the omnidirectionality in the horizontal plane was within 3 dB in a free space. The transmitting antenna was fixed on the center back waist of the volunteer placed at a height of 1 m from the floor, as shown in Fig. 1 (also indicated by * in Fig. 2). The receiving antenna was placed at 100-mm intervals on the body. Both antennas were vertically polarized and separated 10 mm apart from the body surface. When the receiving antenna was placed on the back of the body, the path was roughly line-of-sight (LOS); when in the front, it was non-LOS (NLOS). In total 153 receiving points around the human body were employed. The transmitting and receiving antennas were fed by 2 and 3-m long coaxial cables and these cables were perpendicular in configuration without crossing to reduce unwanted cable coupling [9].

3 Measurement Results

The UWB propagation losses were calculated by integrating the power of the losses between the feeding points of the antennas over the occupied bandwidth. The calibration was conducted between the feeding points with a coaxial through adaptor. These propagation losses embraced the antenna
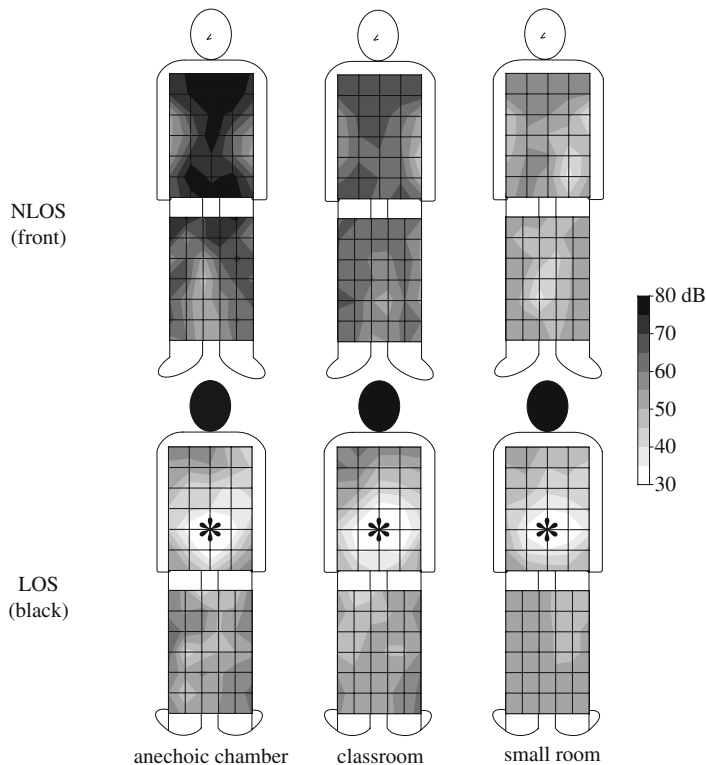
Fig. 2 The distributions of UWB propagation losses in three environments (the transmitting antenna was placed at a point denoted by *)
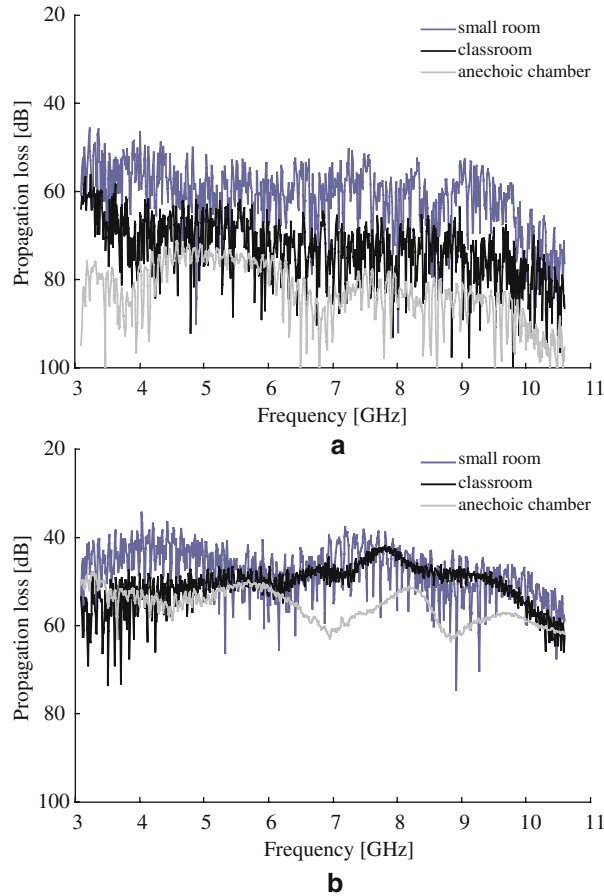
Fig. 3 Frequency-domain propagation losses at (**a**) the center of the chest (NLOS) and (**b**) the center of the back (LOS)

gains (typically −10 to 3 dBi), which were affected by the human body and depended on the radiation direction and the frequency [10]. The distributions of UWB propagation losses are shown in Fig. 2. The small room yielded higher reception power than larger rooms, particularly for NLOS. Examples of the frequency- and time-domain propagation losses on the front side of the center chest and the back side of one (receiving antenna was placed at a height of 1300 mm from the floor) are shown in Figs. 3 and 4. The propagation losses in the radio anechoic chamber and the small room were the highest and the lowest, respectively, whereas the classroom was in between, as shown in Fig. 3. This was attributed to the ample multipath from the nearby floor, walls, and ceiling in the classroom and small room, as shown in Fig. 4. The propagation path of the radio anechoic chamber was either direct or diffract wave, and thus the reception power is low. Multipath in the small room resulted in the lowest path loss because the propagation lengths were shorter than in the classroom, and therefore the total received power was the highest.

The propagation losses of the CW (6.85 GHz), low-band UWB, and high-band UWB were evaluated in comparison with full-band UWB. The maximums, minimums, and medians of UWB, CW, low-band UWB, and high-band UWB propagation losses measured in the three environments were derived, as shown in Fig. 5. The variation ranges (between the minimums and the maximums) in
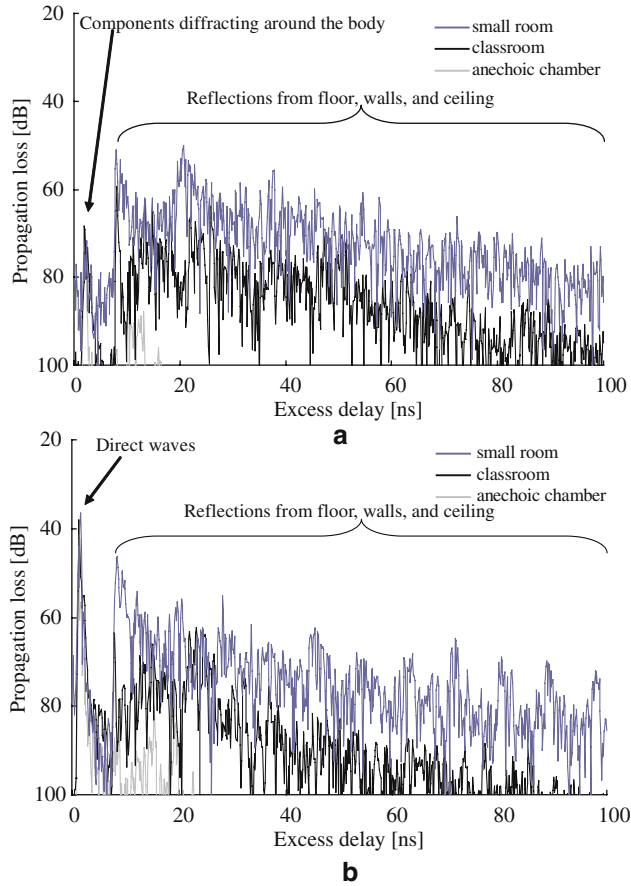
Fig. 4 Time-domain propagation losses at (**a**) the center of the chest (NLOS) and (**b**) the center of the back (LOS)

UWB were smaller than ones in CW (in particular, more than 10 dB smaller in NLOS). This is because nulls caused by interference were cancelled out by the ultra-wide bandwidth. The results indicate that UWB technologies are more advantageous than narrowband ones from the viewpoint of reducing fading margins, although frequency-selective fading inevitably takes place. The variation ranges in full- and low-band UWB were similar for both NLOS and LOS. The maximum propagation losses of the high-band UWB, in particular radio anechoic chamber, yield 17 dB (at LOS) and 11 dB (at NLOS) higher than that of full-band UWB. The low-band UWB is hence more advantageous than high-band UWB in terms of receiving high reception power, if the full-band UWB is not legalized (e. g., in Japan and Europe at present).

4 Conclusions

The UWB propagation losses were measured between on-body antennas in three different surrounding environments envisioned for WBAN scenarios. Small rooms yielded higher reception power than larger rooms. This was attributed to the ample multipath from the nearby floor, walls, and
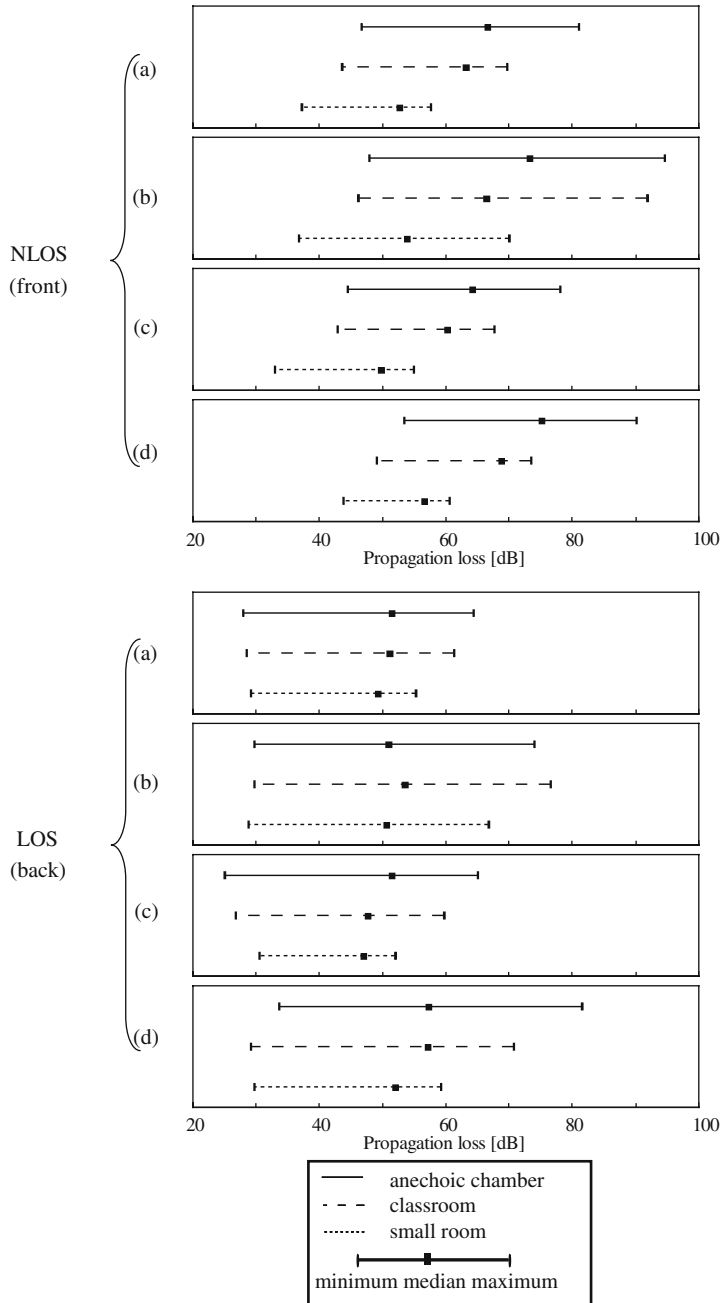
Fig. 5 The maximums, minimums, and medians of propagation losses in three environments for (**a**) UWB (3.1–10.6 GHz), (**b**) CW (6.85 GHz), (**c**) low-band UWB (3.4–4.8 GHz), and (**d**) high-band UWB (7.25–10.25 GHz)

ceiling. The UWB maximum propagation losses in three environments were smaller than that of CW. This is because nulls caused by interference were cancelled out by the ultra-wide bandwidth. The propagation losses of low-band UWB and high-band UWB were also evaluated. In WBAN scenarios, low-band UWB is more advantageous than high-band UWB from the viewpoint of reducing propagation losses, if the usage of the full-band UWB is legally banned.

References

1. J. Ryckaert, B. V. Poucke, B. Gyselinckx, and S. Donnay, Wireless body area networks, ftp://ieee:wireless@ftp.802wirelessworld.com/15/03/15-03-0484-00-004a-sg4a-cfa-response-wireless-body-area-networks.ppt, 7 November , 2003.
2. C. Chang, Y. Kim, and S. Lee, UWB indoor propagation channel measurements and data analysis in various types of high-rise apartments, in Proceedings 2004 IEEE 60th Vehicular Technology Conference (VTC2004-Fall), Los Angeles, California, USA, vol. 1, pp. 150–4, 26–29 September 2004.
3. S. S. Ghassemzadeh, R. Jana, C. W. Rice, W. Turin, and V. Tarokh, A statistical path loss model for in-home UWB channels, in Proceedings 2002 IEEE Conference on Ultra Wideband Systems and Technologies (UWBST 2002), Baltimore, USA, pp. 59–64, 21–23 May 2002.
4. P. S. Hall and Y. Hao (eds.), Antennas and Propagation for Body-Centric Wireless Communications, Artech House, Boston, MA, 2006.
5. A. Alomainy, Y. Hao, X. Hu, C. G. Parini, and P. S. Hall, UWB on-body radio propagation and system modeling for wireless body-centric networks, IEE Proceedings Communications, vol. 153, no. 1, pp. 107–14, February 2006.
6. T. Zasowski, F. Althaus, M. Stager, A. Wittneben, and G. Troster, UWB for noninvasive wireless body area networks: channel measurements and results, in Proceedings 2003 IEEE Conference on Ultra Wideband Systems and Technologies (UWBST 2003), Reston, Virginia, USA, pp. 285–9, 16–19 November 2003.
7. A. Fort, J. Ryckaert, C. Desset, P. D. Doncker, P. Wambacq, and L. V. Biesen, Ultra-wideband channel model for communication around the human body, IEEE Journal on Selected Areas in Communications, vol. 24, no. 4, pp. 927–933, April 2006.
8. Skycross, Inc., Antenna Products, 3.1–10 GHz ultra-wideband antenna, http://www.skycross.com/Products/PDFs/SMT-3TO10M-A.pdf.
9. H. Yamamoto and T. Kobayashi, Effects of feeding cable configurations on propagation measurements between small ultra wideband antennas for WBAN applications, in International Workshop on Future Wellness and Medical ICT Systems (FEELIT2008), Lapland, Finland, 9 September 2008, to be published.
10. H. Yamamoto and T. Kobayashi, Measurements and characterization of ultra wideband propagation channels between a base station and on-body antennas, in Second International Symposium on Medical Information and Communication Technology (ISMICT2007), Oulu, Finland, 11–13 December 2007.

Optimizing the Positioning of MIMO and SISO Systems in Indoor Environments

P. Bechet, I. Bouleanu, A. Neagu, R. Helbet, and A. Hangan

Abstract The adoption of multiple-input multiple-output (MIMO) technologies for the air interface of new wireless communication systems promises to meet the increasing data rate demands of future applications within a reasonable radio bandwidth. MIMO can provide increased spectrum efficiency by exploiting the spatial dimension of the radio wave propagation. The aim of this chapter is to analyze the data transfer capacity in an indoor environment which is relevant for MIMO technology due to its pronounced dispersive character. The performances of individual single-input single-output (SISO), single-input multiple-output (SIMO), multiple-input single-output (MISO), and MIMO communication channels in various scenarios are emphasized in order to identify the optimum positioning of the system components.

Keywords Indoor environments · MIMO and SISO · Optimum positioning · Propagation

1 Background, Materials, and Method

During the last years, wireless local area networks (WLANs) were widely used and succeeded to offer alternative solutions to wired networks. The IEEE 802.11 (a, b, g, n) series of standards imposed itself among the standards proposed for local area networks (LANs). Obtaining a higher data transfer capacity (necessary for wideband applications) was possible due to the adoption of spectral efficient modulation schemes, adaptive techniques for estimating the radio channel, and the implementation of diversity techniques to increase the signal strength of the transmitted symbols. The first variants of the 802.11 standard are 802.11a and 802.11b, the main differences between them being the frequency range and the modulation technique used. Presently, the most popular wireless standard is 802.11 g, which when used with the single-input single-output (SISO) technology can attain a data transfer capacity up to 54 Mbps (108 Mbps in its improved variant). The 802.11n variant is based on the multiple-input multiple-output (MIMO) technology and sums up the performances of the former standards of this series. MIMO systems increase spectral efficiency by multiplexing data on parallel independent channels without incurring any cost in terms of bandwidth or power. As a result of this multiplexing gain, the data transfer capacity of these systems increases linearly with the number

P. Bechet (✉)
Land Forces Academy, Sibiu, Romania
e-mail: pbechet@gmail.com

of antennas [1–3]. The substantial improvement of MIMO systems is possible due to the diversity techniques that are used to increase the signal strength of the transmitted symbols. Regarding spatial diversity, the MIMO system becomes more efficient than the SISO system when the environment displays a strong dispersive character. In such an environment, the ratio of line-of-sight (LOS) to non line-of-sight (NLOS) components differs significantly according to distance and the reflexive characteristics of the environment (walls, objects, etc.) [4–6]. Therefore, it is expected that, in an indoor environment, the LOS component to be stronger in the near vicinity of the radio access point (AP), thus favoring the use of SISO systems, while at a certain distance from the AP, beyond walls and different objects, the NLOS component is supposed to be stronger, thus favoring MIMO systems. In this context, not only the positions of the wireless system elements relative to the environment characteristics but also the diversity models become important. This chapter presents a comparative analysis of the data transfer capacity of SISO and MIMO systems in an indoor environment containing seven rooms (R1…R7 as in Fig. 1).

In order to get an optimum coverage of the chosen environment, measurements were performed for evaluating the electromagnetic field (EMF) emitted by an 802.11 g-type SISO AP, successively positioned in four different positions (P1, P2, P3, and P4). For the AP position displaying the best coverage, there have been performed measurements in order to measure the data transfer capacity according to the angular positioning of the multiple antenna wireless elements (MIMO AP, MIMO Wireless Adapter – WA) in three points of the indoor environment (A, B, and C). Further on, comparative measurements of the transfer data capacity variation versus distance were performed in three directions (D1, D2, and D3) for the SISO system and the MIMO system. The APs were positioned such as to grant the best coverage and the best angular position, which were previously established. For the first two positions of the SISO AP, chosen according to their coverage performance, the
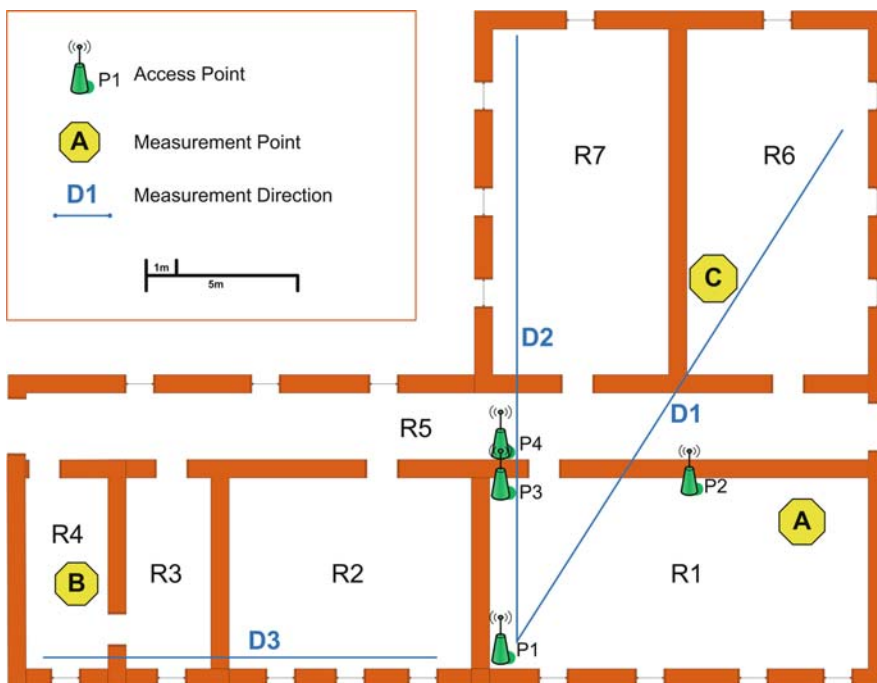
Fig. 1 Plan of the analyzed indoor environment

data transfer capacity was measured in different indoor points (possible positions of workstations) and in different configurations of the network elements (SISO, single-input multiple-output – SIMO, multiple-input single-output – MISO and MIMO) in order to achieve the optimum mean data transfer capacity.

2 Measurements, Results, and Discussions

2.1 The Distribution of the Electromagnetic Field

For evaluating the EMF level emitted by WLAN devices from the perspective of covering a certain area, the situation which has to be considered for the AP is that in which it transmits only the beacon signal necessary for synchronizing and broadcasting the information needed to establish the connections with the workstations. The measurement system settings have to respect the relevant characteristics of the EMF emitted by the AP: frequency range, operating channel, modulation technique, and certain parameters which are specific to the modulation type. We measured E component of the EMF emitted by a TRENDnet TEW–432BRP-type SISO AP in the analyzed indoor site, in a horizontal grid plane with step of 1 m. The AP was configured to emit on channel 9 (2443–2463 MHz) at a limited transmission rate of 18 Mbps in order to maintain constant amplitude of each emitted symbol. At the same time, the interval beacon has been modified from the default value of 100 ms to the value of 1 ms; this interval produces a duration and an intensity of the EMF which can be measured accurately by the spectral analyzer. Other relevant characteristics of the emitting source are modulation scheme – OFDM with QPSK, number of subcarriers – 52, subcarrier spacing – 315 kHz, OFDM symbol duration – 4 μs; maximum emitting power – 13 dBm. The FIELD NOSE measuring system (BASIC version) was used, being composed of the following elements: antenna with automatic positioning system, tripod, NOSE Basic measurement software, and the Anritsu MS2711D spectral analyzer. The dipole antenna is precision conical dipole antenna PCD8250 type, ARC Seibersdorf. In order to measure pulsed signals with a smaller duration, the measuring system was used in the Max Hold mode, with multiple sweeps. For attenuating the adjacent channel produced by consecutive subcarriers, resolution bandwidth (RBW) is established below or equal to 100 kHz [7]. The systematic overestimation of the fields was avoided by using the root mean square (RMS) detector. This type of detector imposes a measuring duration sufficiently large to allow the correct calculation of the real value from the measured samples. Figure 2 illustrates the spectrum measured when limiting the transmission rate at 18 Mbps for two cases: case 1: without traffic, beacon interval of 1 ms; case 2: with traffic, beacon interval of 100 ms, the workstation being situated at a sufficiently long distance from both (the AP and the measuring system) so that the measured EMF to be generated only by the AP.

The FIELD NOSE measuring system settings were the following: RBW = 30 kHz, VBW = 300 kHz, N (number of sweeps) = 40, sweep rate = 1 MHzps. The 315 kHz spacing between the subcarrier and the lack of the informational signal, which narrows the spectrum for each subcarrier, allows raising the RBW value at 100 kHz in measuring the field distribution. In all four situations considered, the positions of the AP were chosen near a wall at the same height (220 cm), three of them in the main room (R1) and one in the hallway (R5) connecting all seven rooms of the analyzed indoor environment (see Fig. 1). The walls of the measuring site are made of bricks and are 60 cm thick. The height of the rooms is 350 cm. The measuring points form a 1 × 1 m grid. The height of the measuring antenna was established at 110 cm (corresponding to the possible position of individual workstations). The field measurements were performed in order to identify the position of the radio

Measurement Data
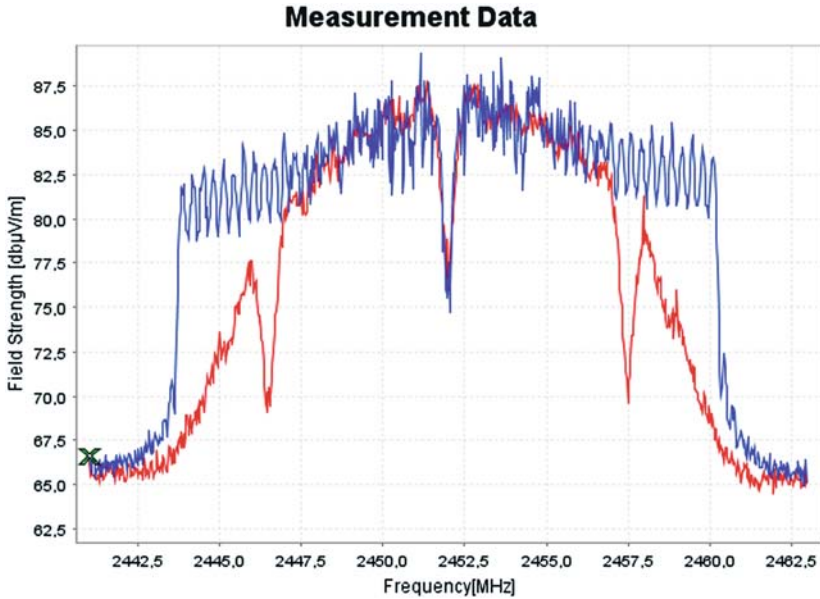
Fig. 2 Signal spectrum in channel 9 IEEE 802.11 g: (a) *red* – AP in idle mode; (b) *blue* – unidirectional (download) traffic

AP determining the best distribution of EMF in the seven rooms, knowing that the highest intensity of the EMF has to be obtained in the main room (R1). The results of the EMF distribution in the indoor site for four AP positions are illustrated in Fig. 3. It can be noticed that positions P1 and P3 ensure the best coverage of the analyzed indoor environment. Compared to P3, P1 ensures a better signal level in the rooms R3, R6, and R7. Position P3 offers a better coverage of R5, but this aspect is less important, R5 being a hallway.

2.2 Data Transfer Capacity for SISO and MIMO Systems

The measuring scheme comprises the MIMO or SISO AP, the workstation with MIMO or SISO WA, and a PC connected to the AP by UTP cable. The system configurations, for which the data transfer rate was analyzed, are (a) MIMO AP, MIMO WA; (b) MIMO AP, SISO WA; (c) SISO AP, MIMO WA; (d) SISO AP, SISO WA. The following 802.11 (*g* and *n*) wireless components, produced by TRENDnet, were used: MIMO APTEW–633GR, SISO AP TEW–432BPP, MIMO WA TEW–642UB, and SISO WA TEW-444 UB. In each situation, unidirectional traffic was applied, from the PC to the workstation, and the data transfer capacity was monitored for 5 min with the Wireshark 1.0.0 software installed on the workstation. To compare the proposed system configurations, MIMO AP was set to operate according to 802.11 g, the maximum transfer rate being 54 Mbps. For the AP position ensuring the best coverage of the entire indoor site, the data transfer capacity was analyzed according to the angular orientation of the AP and the WA. The angles considered for AP are 0°, 45°, 90°, and 135° and for WA 0°, 45°, 90°, 135°, 180°, 225°, 270°, and 315°. Three representative points were considered in the indoor environment (A, B, and C). Point A is situated in R1 room and allows studying the behavior of the system components when the LOS component is significant. Points B and C are situated beyond three, respectively two, walls distance from the AP, permitting
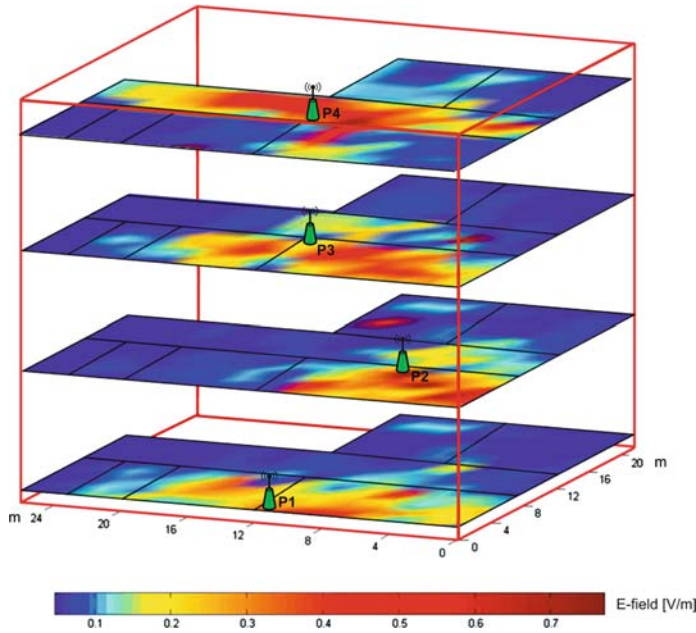
Fig. 3 The electromagnetic field distribution in the horizontal plane in the indoor environment when SISO AP is placed in four different positions

Table 1 Mean values and standard deviations of data transfer capacity (Mbps) according to the AP angular orientation

AP angle	0°	45°	90°	135°
Mean value, A position, MIMO AP	21.96	21.72	21.24	21.96
Standard deviation, A position, MIMO AP	0.66	0.96	0.68	0.60
Mean value, B position, MIMO AP	20.25	22.05	21.59	22.17
Standard deviation, B position, MIMO AP	1.96	0.99	1.13	0.61
Mean value, C position, MIMO AP	11.10	8.74	13.73	20.35
Standard deviation, C position, MIMO AP	2.55	2.99	2.84	1.87
Mean value, C position, SISO AP	9.44	9.44	9.44	9.44
Standard deviation, C position, SISO AP	1.49	1.49	1.49	1.49

analyzing the behavior of the system components in cases when the NLOS component is significant. Table 1 indicates the mean values and the standard deviations of the data transfer capacity belonging to points A, B, and C. As expected, the smallest standard deviation (1.49 Mbps) from the mean value (9.44 Mbps) was obtained in the case of SISO. For MIMO, the best behavior is obtained when orienting the AP at 135° (mean value: 20.35 Mbps; standard deviation: 1.87 Mbps).

For this orientation of the MIMO AP (135°), the variation of the data transfer capacity versus distance on the three directions (D1, D2, and D3 in Fig. 1) was measured. These three directions characterize the indoor environment not only from the perspective of the influence of propagation (walls, objects) but also from the perspective of positioning the wireless elements of the network. The analysis was performed comparatively for the SISO and MIMO system configurations. Figure 4 illustrates the variation of the data transfer capacity with distance for the three measurement directions. The gray bars represent the walls crossed in each direction. Figure 4 shows that, regardless of the analyzed direction, the data transfer capacity of the MIMO system is much higher and relatively
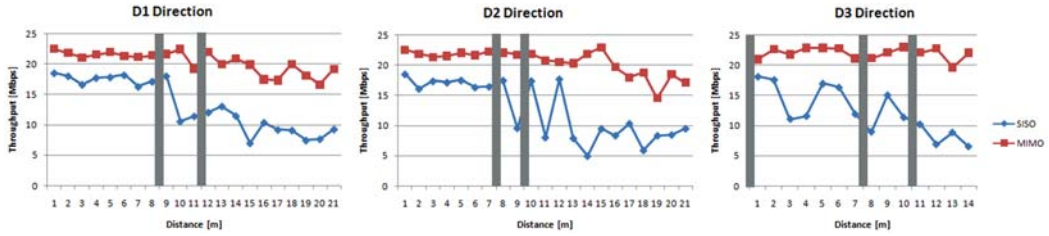
Fig. 4 Data transfer capacity of SISO and MIMO systems on D1, D2, and D3

constant at different distances. In case of the SISO system, the data transfer capacity decreases significantly as the distance to the AP increases and the number of walls crossed increases (e.g., for D3, after crossing three walls, the attenuation exceeds 50%). The influence of walls in the case of SISO is also emphasized by the fact that, when there are LOS conditions, the variation of the data transfer capacity is small and the mean value is close to that obtained with MIMO; in NLOS conditions, high variations occur when distance increases.

For the first two best covering AP positions (P1 and P3), the data transfer capacity was measured in some points representing possible positions of workstations, in all rooms, and for all four configurations (SISO, SIMO, MISO, and MIMO) of the wireless elements of the network. Figure 5 indicates the mean values of the data transfer capacity in each room and for all four configurations according to the position of the AP.

It may be noticed that, regardless of the position of the AP, the MIMO system displays the highest transfer capacity, its mean value being approximately the same for all rooms (around 21 Mbps). The lowest data transfer capacity is obtained by the SISO systems. The SIMO and MISO systems gained medium transfer values by comparison to the MIMO and the SISO systems, similar for all rooms. The mean values of the data transfer capacity in the entire indoor environment are indicated in Table 2.
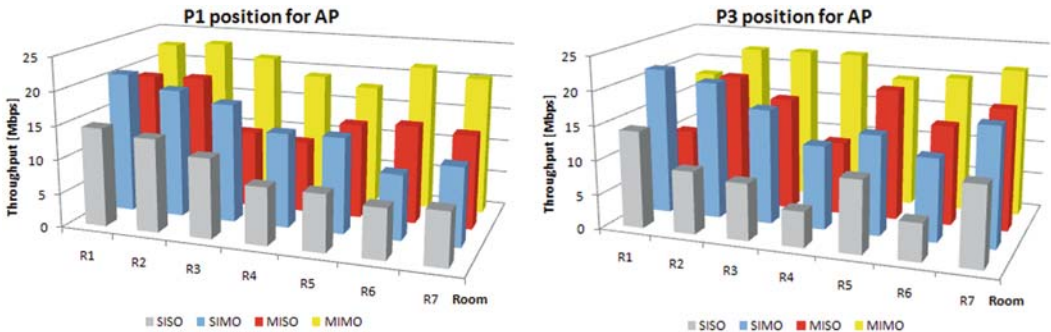
Fig. 5 Mean values of the data transfer capacity for P1 and P2 of the AP

Table 2 Mean values of the data transfer capacity of the entire indoor site

System	SISO	SIMO	MISO	MIMO
P1 AP position	10.29	15.17	14.59	21.45
P3 AP position	9.2	16.34	15.45	20.82

The mean values of the data transfer capacity measured for the four configurations in P1 and P3 of the AP are fairly close. This confirms the similar distribution of the EMF for P1 and P3 (Fig. 5). When considering only the basic configurations of the system (SISO and MIMO), the optimum position of the AP would be P1 (mean value of the data transfer capacity: 10.29 Mbps for SISO and 21.45 Mbps for MIMO).

3 Conclusions

This work analyzed the data transfer capacity of MIMO and SISO systems in an indoor environment composed of several rooms. The system configurations were set such as to allow a comparison of MIMO and SISO technologies against the specifications of the 802.11 g standard. The restrictions imposed in setting MIMO AP do not affect the validity of the results obtained when using the maximum transmission rate (300 Mbps) allowed by the 802.11n standard. Significant differences occurred depending on the type of the system (SISO, SIMO, MISO, and MIMO) and the position and orientation of the AP. The optimum position of the MIMO AP is in the corner of the room, having the vertical antennas horizontally aligned with the bisecting line of the two walls. This position guarantees a high mean value and a relatively constant data transfer capacity, regardless of the orientation of the WA of the workstation in the analyzed indoor environment. The measurements performed confirmed the better performances of MIMO technology as compared to SISO technology and emphasize the importance of the geometric positioning of MIMO AP as compared to SISO AP.

References

1. D. Franco, J. Lluis, R. Jordi, G. Alfred Multi-Antenna for MIMO Communications. Morgan & Claypool Publishers 2008.
2. K. Volker, Wireless Communications over MIMO Channels. Applications to CDMA and Multiple Antenna Systems. John Wiley & Sons Ltd, England, 2006.
3. A.A. Abouda, Characterization of MIMO Channel Capacity in Urban Microcellular Environment, PhD Dissertation, Helsinki, 2007.
4. J. Jeng-Shiann, A. I. Mary, Spherical-Wave Model for Short Range MIMO. IEEE Transactions on Communications 0090–6778, 2005.
5. A. Zelst Physical Interpretation of MIMO Transmissions. Proceedings Symposium IEEE, Eindhoven, 2003.
6. U. Trautwein, M. Landmann, G. Sommerkorn et al., System-Oriented Measurement and Analysis of MIMO Channels. Cost 273 TD(05) 063, Italy, 2005.
7. G. Schmid, P. Preiner, D. Lager et al., Exposure of General Public due to Wireless LAN Applications in Public Places. Radiat. Prot Dosimetry, vol. 124, 2007, doi:10.1093/rpd/ncm320.

Analysis of Ultra-wideband Impulse Radio Over Multimode Fiber Ranging System

J. George, D. Thelen, A. Chamarti, A. Ng'oma, and M. Sauer

Abstract Ultra-wideband impulse radio (UWB-IR)-based systems are well known for their inherent capability to provide accurate ranging [1–3]. Remote positioning of such systems using Radio over MultiMode Fiber (RoMMF) technology is advantageous, for it provides a cost-effective way of system deployment by the consolidation of head-end equipment. In this chapter, we describe the details of a system model for evaluating the performance of a ranging system employing UWB-IR over multimode fiber. As the system uses low data rate digital communication to obtain range information, its quality can be studied using Bit Error Ratio (BER). This model combines wireless and radio over fiber sections of the system to predict system performance in terms of BER.

1 Introduction

Ultra-wideband impulse radio location tracking and ranging systems have the advantage of providing accurate ranging information that results from the inherent capability of broadband pulses [1–3]. As per Federal Communications Commission (FCC) regulations, the Effective Isotropic Radiated Power (EIRP) of these devices is restricted to less than -41.3 dBm/MHz [4]. This restriction imposes significant limitations on the reach of these signals compared to the traditional 802.11 WLAN technology. One of the ways to overcome this UWB reach limitation is to use a fiber distribution network [5–9] with a centralized architecture.

In the first part of this chapter, we describe the details of a system model for evaluating the performance, in terms of BER, of a ranging system employing UWB-IR over multimode fiber. Such a system has two distinct parts: (i) a wireless section, including antennas and wireless propagation through air and (ii) a Radio over Multimode Fiber section, including electrical to optical (E/O) conversion, propagation through fiber, and optical to electrical (O/E) conversion. This system model combines both the wireless and radio over fiber sections of the system to predict performance in terms of BER. In time of arrival-based range measurement systems, a high BER would lead

J. George (✉)
Corning Incorporated, Corning, NY 14831, USA
e-mail: georgej@corning.com

to deviation of the time stamp, representing the time of flight between the systems that carry the distance information from actuality. The system model sheds light into the dominant impact of wireless distance, in comparison to fiber length, and the laser relative intensity noise (RIN) on system performance.

Toward the end of this chapter, in Section 4.1, correlation is made between the predictions of the model and experimental observations. The experiments in this regard were performed using commercially available UWB radios [10] and different lengths of multimode fibers.

2 System Model

In this section we describe the details of the system model used for analyzing the UWB-IR over multimode fiber ranging system. Figure 1 shows the schematic of an UWB-IR over multimode fiber ranging system.

The downlink and the uplink paths are identical, except that the signal coming from the remote tag (uplink) uses amplification before the optical domain conversion to account for the losses in the wireless section of the system. Being the more sensitive path, the following analysis is focused on the uplink path.
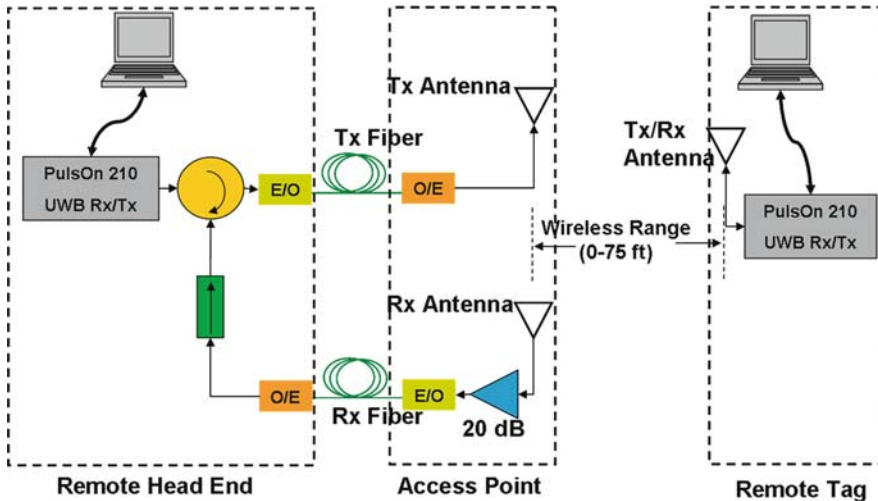
Fig. 1 Schematic of the experimental setup used for evaluating the ranging accuracy of UWB-over-fiber technology for different fiber lengths. The boxes named E/O stand for the 850 nm VCSELs and the boxes named O/E stand for photo detector trans-impedance amplifier (TIA) assemblies

2.1 Bit Error Ratio (BER) Calculation

Figure 2 shows the schematic of the uplink from the remote tag to the access point. The signal transmitted from the transmit antenna of the UWB module is ~ -6.25 dBm, as regulated by FCC.

After the signal is received by the receiver antenna, some small loss L_1 is used to compensate for connector losses. Then an amplification stage is used followed by additional small loss L_2 for filters, bias-tee, etc. In our calculations we assumed $L_{1,2} = -1$ dB. The output from the amplifier is
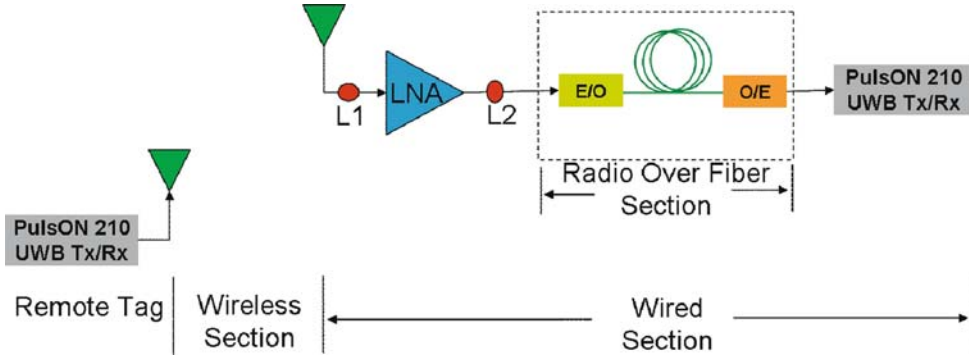
Fig. 2 Schematic of the uplink showing different sections as designated in the model

converted into the optical domain (E/O conversion) using an 850 nm VCSEL and further transmitted over fiber to the location where the centralized access points are placed. At this location the signals are converted from the optical domain to the electrical domain, using a photo detector, and further fed into a UWB receiver module.

The analysis described here computes the BER of the system starting from the remote tag. For binary antipodal modulation, the BER P_E is given by [11]

$$P_{\mathrm{E}} = \frac{1}{2}\,\mathrm{erfc}\left(\sqrt{\frac{E_{\mathrm{b}}}{N_{\mathrm{eff}}}}\right), \tag{1}$$

where E_b is the energy per bit at the receiver and N_{eff} is the effective noise. The ratio of E_b/N_{eff} is obtained in a similar fashion as described in [12]:

$$\frac{E_{\mathrm{b}}}{N_{\mathrm{eff}}} = \frac{(PRF/BPS)\,p_{\mathrm{TX}}\,g_{\mathrm{sys}}}{kT\,nf_{\mathrm{wired}}\,g_{\mathrm{wired}}\,n_{\mathrm{bw}}}, \tag{2}$$

where *PRF* and *BPS* are the pulse repetition frequency and the bits per second of the UWB-IR system, p_{TX} is the transmitted power from the remote tag, g_{sys} is the overall system gain, k is the Boltzmann constant, T is the operating temperature, nf_{wired} and g_{wired} are the noise figure and gain of the system, respectively, from the receiving antenna that is connected to the low noise amplifier, and n_{bw} is the noise bandwidth of the system.

The following two sections describe the details of the gain and noise figure calculations required in (2).

2.2 System Gain

The system gain is considered to have two major contributions: (i) the wireless channel loss (g_{WL}) and (ii) the amplifiers and the electrical to optical and optical to electrical conversions, including the transmission through the fiber (g_{wired}). The overall system gain, g_{sys}, is

$$g_{\mathrm{sys}} = g_{\mathrm{WL}}\,g_{\mathrm{wired}}. \tag{3}$$

The wireless channel loss, g_{WL}, is obtained as

$$g_{WL} = p_l \, g_{Tx} \, g_{Rx} \, r_{tx}(\theta) \, r_{rx}(\theta), \qquad (4)$$

where g_{TX} and g_{RX} are the transmit and receive antenna gains and θ is the angle between transmit and receive antennas. In this study, transmit and receive antennas are assumed to be vertical dipoles, and the angle would be the angle between the vertical and the line joining the centers of the two antennas. Since we are using vertical dipoles, and we know that $\sin(180-\theta) = \sin(\theta)$, θ would be the same for both transmit and receive antennas for various heights. r_{tx} and r_{rx} are the normalized radiation patterns of the transmit and receive antennas, which are obtained by normalizing the following equation for the vertical radiation pattern for a dipole [13]:

$$\mathrm{rad}_{vertical}(\theta) \cong \frac{120 \, \pi \, |I_0|^2 \sin^3 \theta}{8 \, \pi^2}, \qquad (5)$$

where I_0 is the antenna current. From (5), we get

$$r_{rx}(\theta) = \mathrm{rad}_{vertical}(\theta)/\mathrm{rad}_{vertical}(90°).$$

The wireless propagation path loss, p_l, is obtained by

$$p_l = \left(\frac{\lambda}{4 \, \pi} \right)^2 \frac{1}{r^n}, \qquad (6)$$

where r is the distance between the two antennas and n is the path loss exponent. $n = 1.6$ to 2 for line of sight in-building applications and $n = 4$–6 for in-building non-line of sight scenarios [14–15].

With reference to Fig. 2, the gain of the wired part of the system can be obtained using the gain concatenation formula [14–15]:

$$g_{wired} = g_{L1} \, g_A \, g_{L2} \, g_{FIB} \, g_{UWB} \qquad (7)$$

where g_{L1} and g_{L2} take into account connector losses, g_A is the gain of the LNA, g_{UWB} is the gain of the UWB receiver, and g_{FIB} is the loss of the fiber link given by

$$g_{FIB} = s_l^2 \, \eta_{LF}^2 \, T_{FIB}^2 \, r_d^2 \, \eta_{FD}^2 \, g_{TIA}, \qquad (8)$$

where s_l is the slope efficiency of the laser, η_{LF} is the laser to fiber coupling coefficient, T_{FIB} is the fiber loss, r_d is the responsivity of the photo detector, η_{FD} is fiber to detector coupling coefficient, and g_{TIA} is the gain of the TIA associated with the detector.

2.3 Link Noise Figure

To estimate the noise figure information required in the calculation of BER, we use the noise concatenation formalism [14–15] given by

$$nf_{wired} = nf_{L1} + \frac{(nf_A - 1)}{g_{L1} \, g_{Rx}} + \frac{(nf_{L2} - 1)}{g_{L1} \, g_{Rx} \, g_A} + \frac{(nf_{FIB} - 1)}{g_{L1} \, g_{Rx} \, g_A \, g_{L2}} + \frac{(nf_{UWB} - 1)}{g_{L1} \, g_{Rx} \, g_A \, g_{L2} \, g_{FIB}}. \qquad (9)$$

In (9), nf_{wired} is effective noise figure of the wired part of the system shown in Fig. 2. nf_{L1}, nf_{L2}, nf_{A}, nf_{FIB}, and nf_{UWB} are the noise figure of loss component L1, loss component L2, LNA, radio over fiber section, and UWB receiver, respectively. The noise figure of the loss components L1 and L2 is obtained by taking the reciprocal of their respective gain/loss and that of the amplifier and the UWB receiver come from specifications. nf_{FIB} of the radio over fiber section be obtained by [14–15]

$$nf_{\text{FIB}} = \frac{2\, g_{\text{FIB}}\, kT \; + \; I_{\text{d}}^2 \text{RIN}\, R_{\text{load}} \; + \; 2\, q\, I_{\text{d}}\, R_{\text{load}} \; + \; kT}{g_{\text{FIB}}\, kT}, \tag{10}$$

where RIN is the laser relative intensity noise; R_{load} and q are the load resistance and the elementary charge, respectively; $g_{\text{FIB}} < 1$ is the fiber attenuation, $I_{\text{d}} = I_{\text{bias}}\, s_{\text{l}}\, r_{\text{d}}\, g_{\text{FIB}}$ is the photodetector current with photodetector responsivity r_{d}, and I_{bias} is the laser bias current.

3 System Parameters

Relevant parameters of the UWB radios [10], laser, fiber, photodetector, and amplifier, based on typical product specifications, are summarized in Table 1. A noise bandwidth of 3.2 GHz, which is equal to the operating bandwidth of the UWB modules, was used. For the fiber link, standard high-bandwidth 50 μ_{m} MMF specifications were used. As laser, commercially available 10 Gb/s 850 nm VCSELs were considered in this study.

Table 1 Various parameters used in the study

Parameter	Value	Units
Laser slope efficiency, s_{l}	0.13	W/A
Receiver responsivity, r_{d}	0.65	A/W
Laser bias current, I_{bias}	5	mA
Laser RIN	−130	dB/Hz
Load resistance, R_{load}	50	ohm
LNA gain, G_{a}	20	dB
LNA noise figure, NF_{a}	3.5	dB
Fiber loss at 4.7 GHz	0.01	dB/m
UWB PRF	9.6	MHz
UWB BPS	150	Kbps
UWB gain, G_{UWB}	−1	dB
UWB noise figure, NF_{UWB}	4.7	dB

Note that the gain and noise figures are listed in dB. They are obtained by using relationships $G_{\text{a}} = 10 \log g_{\text{a}}$ *or* $\text{NF}_{\text{a}} = 10 \log nf_{\text{a}}$.

4 Simulation and Experimental Results

The most important objective of this study is to obtain an analysis of a UWB-based location tracking/ranging system deployed using radio over fiber technology. A ranging system usually provides the distance of a remote tag from an access point. The commercially available UWB [10] ranging system considered in this study has a bandwidth of 3.2 GHz centered around 4.7 GHz. In the following analysis, we assume line of sight communication between transmit and receive antennas.

4.1 Impact of Fiber Length

The BER computed using (1) is shown for different fiber lengths in Fig. 3a for a UWB ranging system using radio over fiber technology. The figure shows that the system performance is mainly impacted by the wireless distance, rather than the fiber length. This observation indicates that UWB-based location tracking/ranging signals can be distributed inside a building, using radio over fiber technology, without significant deterioration in system performance.

In order to verify this observation experimentally, we investigated the ranging accuracy of UWB over multimode fiber technology using the setup shown in Fig. 1. To perform the study, equal lengths of multimode fiber were used in transmit and receive directions. This is to comply with the ranging algorithm that uses half of the overall time of flight for estimating the range.

After inserting equal lengths of multimode fiber in both transmit and receive paths, the distance between the access point and the remote tag was increased from a distance of 0 to 22.86 m on a calibrated path. At each point the actual distance and the UWB measured distance were recorded. The maximum possible wireless distance was limited due to the size limitation of the measurement site.

Figure 3b shows the ranging error observed in the experiment for different fiber lengths. On correlating the experimental observations in Fig. 3b to the BER predictions in Fig. 3a, we can conclude
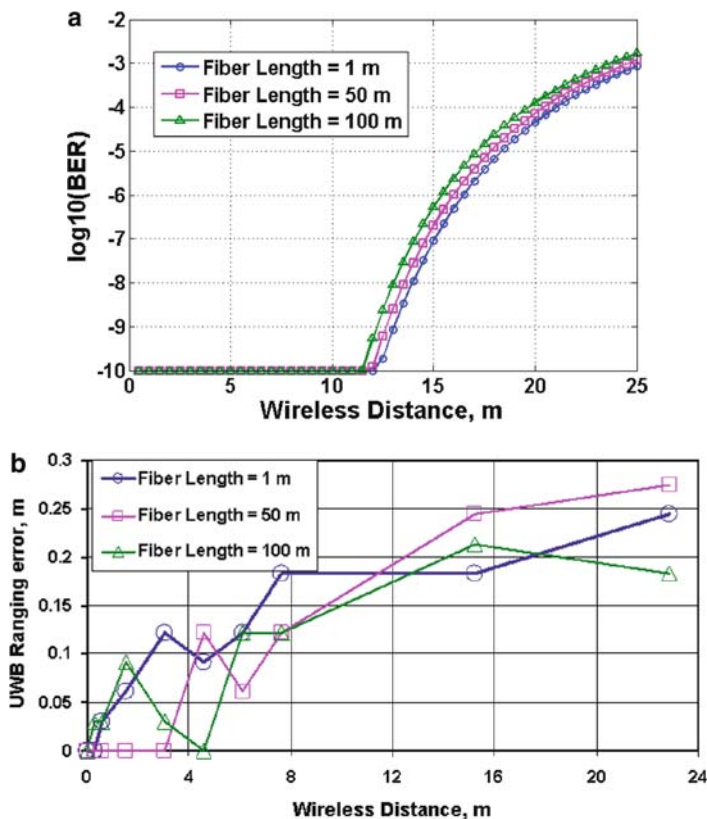
Fig. 3 (a) Simulated BER performance of the UWB over fiber system for different fiber lengths. (b) Measured ranging error for the UWB over fiber system for different fiber lengths

that the UWB ranging system shows increase in ranging error with wireless distance. BER is not a direct measure of the ranging error. However, the model was capable of pointing out significant impact of wireless distance on system performance, as observed in the experiments. From the above comparison it is also clear that for a fiber length of 150 m and for a wireless distance of 22.4 m, we have a BER that is better than 10^{-3}.

Figure 4 shows the computed system performance for a range of fiber lengths and for a range of wireless distances. From this graph we can observe that the BER for 300 m fiber distribution network is only better than 10^{-2} for a wireless distance of 25.4 m. However, it can be significantly improved to $\sim 10^{-4}$ if we can reduce the wireless distance to 20 m.
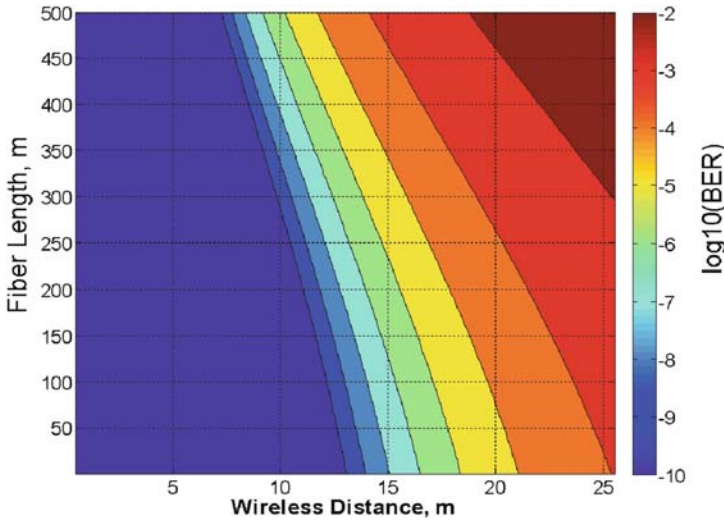
Fig. 4 System performance (BER) as a function of wireless distance and fiber length. The path loss exponent used was $n = 2$

4.2 Impact of LNA Gain

Figure 5 shows the simulated BER as a function of LNA gain for various fiber lengths. In all of these scenarios, we kept a constant wireless distance of 25 m. In general, a higher value of LNA gain provides improved system performance. However, a much larger gain could drive the laser into compression. From the figure it is clear that an optimum value of LNA gain can be obtained for a specific system.

4.3 Impact of LASER RIN

Finally, we investigated the effect of laser RIN on system performance. It is clear from Fig. 6 that RIN plays an important role on the UWB over fiber system performance. For instance, a RIN of -130 dB/Hz causes the BER to become as high as $\sim 10^{-1.5}$ for a wireless distance of 15 m and a nominal fiber length of 1 m. At the same time, a RIN of -140 dB/Hz improves the performance

Fig. 5 System performance (BER) as a function of LNA gain. In all of the above cases the wireless distance was kept constant at 25 m
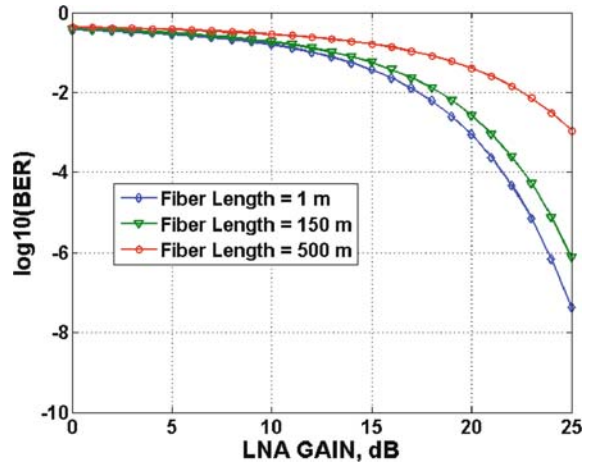
Fig. 6 System performance (BER) as a function of LASER RIN. In all of the cases the fiber length was kept constant at 1 m
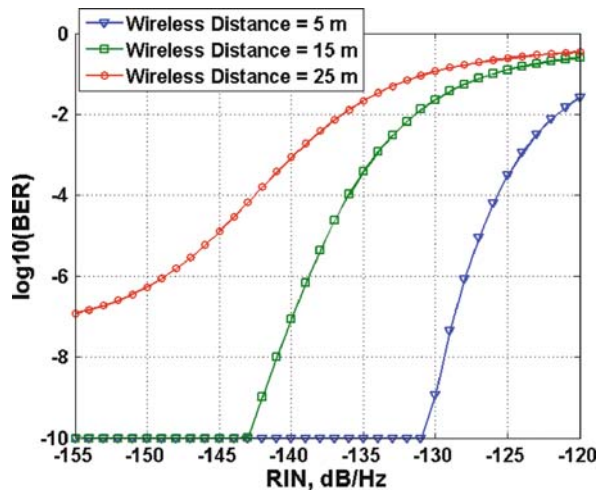
to $\sim 10^{-7}$ for the same scenario. In other words, this means that laser selection to obtain optimum system design is possible.

We also investigated system performance as a function of laser slope efficiency and observed that it was not significant.

5 Conclusions

A simulation framework was created for evaluating the performance of a radio over fiber, UWB ranging system in terms of BER. The estimated system performance, in terms of BER, was well correlated with experimental results in terms of ranging accuracy. The simulation studies show that the UWB-IR over fiber-based system performance mainly depends on (i) wireless distance and (ii) laser RIN.

References

1. S. Gezici, Z. Tian, G. B. Giannakis, H. Kobayashi, A. F. Molisch, H. V. Poor, and Z. Sainoglu, Localization via ultra-wideband radios: a look at positioning aspects for future sensor networks, IEEE Signal Processing Magazine, vol. 22, no. 4, pp. 70–84, 2005.
2. S. J. Ingram, D. Harmer, and M. Quinlan, Ultra-wideband indoor positioning systems and their use in emergencies, Position Location and Navigation Symposium, pp. 706–15, April 2004.
3. V. Schwarz, A. Huber, and M. Tuchler, Accuracy of a commercial UWB 3D location/tracking system and its impact on LT application scenarios, IEEE Conference on Ultra-wideband, pp. 599–603, 2005.
4. Federal Communications Commission (FCC), Revision of Part 15 of the Communications Rules Regarding Ultra-wideband (UWB) Transmission Systems, First report and order, ET Docket 98-153, FCC 02-48, Released April 2002.
5. M. Y. Wah, C. Yee, and M. L. Yee, Wireless ultra wideband communications using radio over fiber, IEEE Conference on Ultra wideband Systems Technologies, pp. 265–269, 2003.
6. B. Luo, L. C. Ong, M. L. Yee, Y. X. Guo, M. Y. W. Chia, Centralized UWB/WLAN distribution network using low cost radio over multimode fiber technology, IEEE Vehicular Technology Conference, pp. 799–801, 2005.
7. M. Sauer, A. Kobyakov, L. Fields, F. Annunziata, J. Hurley, and J. George, Experimental investigation of multimode fiber bandwidth requirements for 5.2 GHz WLAN signal transmission, IEEE Optical Fiber Communications Conference, p. 3, 2006.
8. M. Sauer, A. Kobyakov, J. Hurley, and J. George, Experimental study of radio frequency transmission over standard and high bandwidth multimode optical fibers, IEEE Microwave Photonics Conference, pp. 99–102, 2005.
9. M. Sauer, A. Kobyakov, and J. George, Radio Over Fiber for Picocellular Network Architecture Lightwave Technologies, pp. 3301–20, November 2007.
10. http://timedomain.com/
11. J. G. Proakis, Digital Communications, Fourth Edition, McGraw-Hill Publishing, New York, 2000.
12. C. G. Bilich, Bio-Medical Sensing using Ultra wideband Communications and Radar Technology: A Feasibility Study, IEEE Pervasive Health Conference and Workshops, pp. 1–9, 2006.
13. C. A. Balanis, Antenna Theory – Analysis and Design, second edition, John Wiley and Sons Inc., New Jersey, 1997.
14. H. Al-Raweshidy and S. Komaki, (eds.) Radio over Fiber Technologies for Mobile Communications Networks, Artech House, Boston, 2002.
15. C. H. Cox III, Analog Optical Links. Theory and Practice, Cambridge University Press, Cambridge, 2004.

Time Domain Transition Zone Diffraction on Convex Obstacles

P. Górniak and W. Bandurski

Abstract The chapter presents the derivation of a 2D time domain model of two bare conducting convex obstacles. The model includes amplitude diffraction and first-order transition zone diffraction, called the slope diffraction. The considered model is represented by its impulse response. Thanks to the introduction of some vital approximations of the expressions occurring in amplitude term and slope term of the impulse response; it can be given in a closed form. The presented approach can be extended for the case of more than two cascaded convex obstacles in the channel. The uniform theory of diffraction (UTD) formulated in the frequency domain is used in the derivation of the model. The correctness and accuracy of the derived model is verified by simulation of an ultra-wideband (UWB) pulse distortion.

Keywords Time domain model · Impulse response · Uniform theory of diffraction (UTD) · Ultra-wideband (UWB)

1 Introduction

The chapter presents the time domain (TD) modeling of diffraction caused by convex objects. We consider the soft polarization case. We propose to use deterministic UWB channel modeling for the channel with convex objects. Examples of such objects are round buildings, round pillars in buildings and rounded corridors in buildings. In our considerations, the transition zone diffraction is included. Therefore the slope diffraction is the key factor and cannot be omitted. When the UWB signal propagation is taken into account, the time domain modeling is the right choice.

In this chapter we derive the impulse response of two cascaded, perfectly conducting convex obstacles shadowing the transmitter and receiver. This impulse response can be obtained in a closed form. The proposed method can be extended for the cases of more than two cascaded convex obstacles.

W. Bandurski (✉)
Poznań University of Technology, Poznań, Poland
e-mail: bandurski@et.put.poznan.pl

2 Description of the Channel Model and Formulation of Its Transfer Function

An example of a convex object is a 2D bare hill. It can be modeled as a part of a circle, as shown in Fig. 1. This model was proposed by Bertoni [1]. We assume that the transmitted pulse approaches the receiver along one dominant ray, which is a creeping ray. The ray becomes attached to the hill at attachment point Q'. Then it travels along the arc of the hill. The ray leaves the arc of the hill tangentially at the shedding point Q. Thus, the transmitted pulse experiences
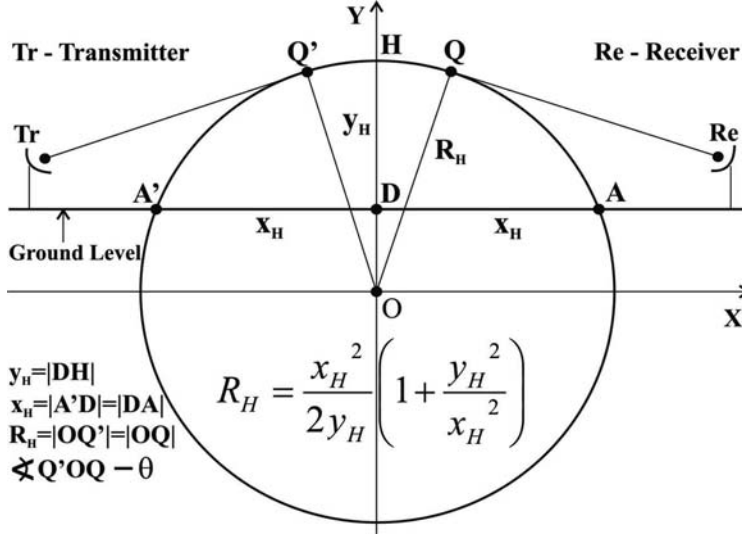
Fig. 1 Model of a bare hill

diffraction on the convex obstacle. The exact UTD expression for the amplitude term of the frequency domain diffraction coefficient of one convex conducting obstacle for soft polarization is given by (1) [2–4] and the parameters of the model are indicated in Fig. 1:

$$H_A(\omega) = H_{A1}(\omega) + H_{A2}(\omega) = -m\sqrt{\frac{2}{\beta}} \frac{e^{-j\pi/4} \cdot (1 - F(X_d))}{2\xi_d\sqrt{\pi}} + -m\sqrt{\frac{2}{\beta}} P_s(\xi_d). \qquad (1)$$

The diffraction coefficient (transfer function $H_A(\omega)$) given by (1) does not include the delay terms or the spreading factor. The parameters used in (1) are as follows:

$$m(\omega,R) = \left(\frac{\omega R}{2c}\right)^{1/3}, \quad \xi_d(\omega,\theta,R) = m(\omega,R)\theta, \quad X_d = \frac{\omega L \xi_d^2}{2cm^2} = \frac{\omega L \theta^2}{2c},$$

where $\beta = \omega/c$, c is the speed of electromagnetic wave propagation in free space, L is the distance parameter, and $F(X)$ is the transition function:

$$L = \frac{|TQ'| \cdot |QR|}{|TQ'| + |QR|}, \quad F(x) = 2j\sqrt{x}e^{jx} \int_{\sqrt{x}}^{\infty} e^{-ju^2} \, du.$$

The function $P(\xi_d)$ is the Pekeris caret function and $p^*(x)$ is the Fock scattering function [2,3]:

$$P_s(x) = p^*(x) \cdot e^{-j\pi/4} - \frac{e^{-j\pi/4}}{2x\sqrt{\pi}}, \quad p^*(x) = \frac{1}{\sqrt{\pi}} \int\limits_{-\infty}^{\infty} \frac{V(\tau)e^{-jx\tau}}{W_2(\tau)} d\tau, \quad W_2(\tau) = \frac{1}{\sqrt{\pi}} \int\limits_{\infty e^{j2\pi/3}}^{\infty} e^{-\frac{z^3}{3}} e^{\tau z} dz,$$

$$V(\tau) = \sqrt{\pi} Ai(\tau), \quad Ai(\tau) = \int\limits_{0}^{\infty} \cos\left(\tau z + \frac{z^3}{3}\right) dz.$$

The model of two cascaded convex obstacles is shown in Fig. 2.
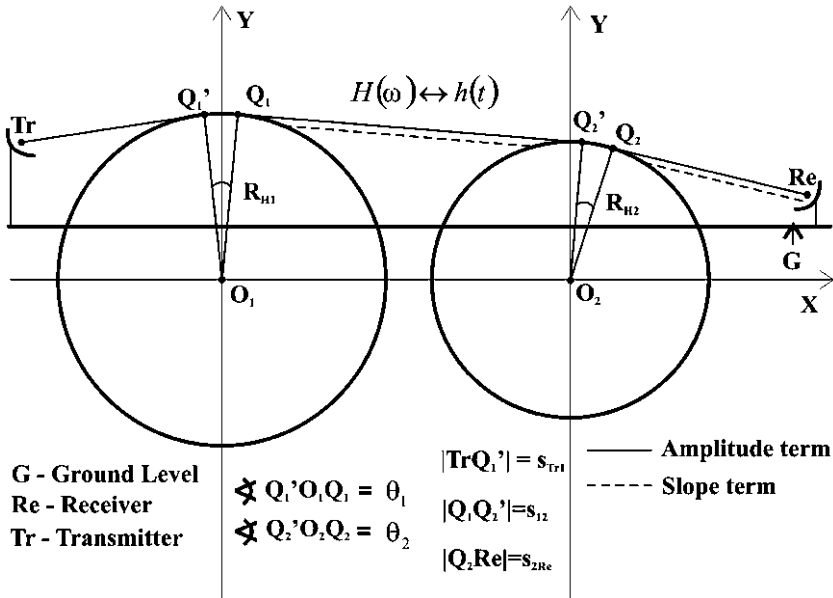
Fig. 2 Two cascaded convex obstacles shadowing the transmitter and receiver

When two convex objects are taken into account and the second object is in the transition zone of the first convex object, the frequency response of the "partial" channel has the following form:

$$[H_s(\omega,s) + H_A(\omega)]A(s)e^{-jk(\theta_1 R_{H1}+s)}, \tag{2}$$

where s is equal to distance $|Q_1Q_2'|$, $A(s)$ is the spreading factor, the input of the channel is at point Q_1', and the output of the channel is at point Q_2 (Fig. 2). The spreading factor and delay factor in (2) will not be considered in the derivation of the impulse response of the channel.

The slope term and amplitude term of (2) are related through the following equation:

$$H_s(\omega,s) = \frac{\partial H_A(\theta)}{s \partial \theta} . \tag{3}$$

After differentiation of the components of (1) we have

$$
\begin{aligned}
H_{S1}(\omega,s) &= \frac{\partial H_{A1}(\theta)}{s\partial\theta} = H_{S11}(\omega,s) + H_{S12}(\omega,s) + H_{S13}(\omega,s) \\
&= -\sqrt{\frac{2c}{\omega}}e^{-j\pi/4}\frac{j\omega L}{2c\sqrt{\pi}s} + \sqrt{\frac{2c}{\omega}}e^{-j\pi/4}\frac{L\cdot F(X_d)}{2c\sqrt{\pi}s} + \sqrt{\frac{2c}{\omega}}e^{-j\pi/4}\frac{1}{2s\sqrt{\pi}\theta^2},
\end{aligned}
\tag{4}
$$

$$
H_{S2}(\omega,s) = \frac{\partial H_2(\theta)}{s\partial\theta} = \frac{1}{s}\frac{\partial}{\partial\theta}\left(-m\sqrt{\frac{2}{\beta}}P_s\left(\xi_d\right)\right).
\tag{5}
$$

Function $P_s(\xi_d)$ occurring in (5) cannot be easily differentiated with respect to its argument. Therefore, we approximate $H_{A2}(\omega)$ with two different series. The first one is appropriate for bigger values of the argument ξ_d and the second one is applicable for smaller values of ξ_d. The first of the approximating series is given by Keller [2–4]:

$$
H_{A2>}(\omega) = \sum_{n=0}^{N}A_n\cdot\omega^{-1/6}\cdot e^{-\gamma_n\omega^{1/3}\theta}, \; A_n = \left(\frac{R}{2c}\right)^{1/3}\cdot j^{-1/6}\cdot\sqrt{\frac{c}{2\pi}}\cdot\frac{1}{\left[Ai'(q_n)\right]^2}, \; \gamma_n = -q_n\left(j\frac{R}{2c}\right)^{1/3},
\tag{6}
$$

where q_n are zeros of the Airy function and $Ai'(q_n)$ is the value of the derivative of the Airy function calculated for q_n. The values of q_n and $Ai'(q_n)$ can be found in [2]. The second approximating series is related to smaller values of ξ_d (down to 0). In this situation we propose to approximate the Fock scattering function by the following series [5]:

$$
p^*(\xi_d) \approx e^{j\pi/6}\sum_{n=1}^{N}\frac{\rho_n}{n!}\cdot j^{n/3}\cdot\xi_d^n, \; H_{A2<}(\omega) = m\sqrt{\frac{2c}{\omega}}e^{-j\pi/4}\cdot\left(\frac{1}{2\xi\sqrt{\pi}} - e^{j\pi/6}\sum_{n=0}^{N}\frac{\rho_n}{n!}j^{n/3}\xi_d^n\right).
\tag{7}
$$

The values of coefficients ρ_n can be found in [5,6].

The approximation of $H_{A2}(\omega)$ can now be written in the following form:

$$
H_{A2}(\omega) \approx \begin{cases} H_{A2>}(\omega) \; \xi_d > \xi_{dT} \\ H_{A2<}(\omega) \; \xi_d \leq \xi_{dT} \end{cases}.
\tag{8}
$$

Now, it is necessary to establish the value of ξ_d for which (8) can be approximated with sufficient accuracy (by this we mean the relative error less than 0.1%; at the same time, the number of series terms should be as small as possible). The calculations which we conducted have shown that the threshold value is $\xi_{dT} = 1.2$. The maximum required number of terms in (6) and (7) equals 6 and 10, respectively.

Having the approximation of $H_{A2}(\omega)$, we can write (5) in the following form:

$$
H_{S2}(\omega,s) \approx \begin{cases} H_{S2<}(\omega,s) \; \xi_d \leq 1.2 \\ H_{S2>}(\omega,s) \; \xi_d > 1.2 \end{cases} = \begin{cases} -\sqrt{\frac{2c}{\omega}}e^{-j\pi/4}\frac{1}{2s\sqrt{\pi}\theta^2} - \sum_{n=0}^{N}\frac{n}{s}B_n\theta^{n-1}\omega^{\frac{n}{3}-\frac{1}{6}} \; \xi_d \leq 1.2 \\ -\sum_{n=0}^{N}\frac{A_n}{s}\gamma_n\omega^{\frac{1}{6}}e^{-\gamma_n\omega^{1/3}\theta} \qquad\qquad \xi_d > 1.2 \end{cases},
\tag{9}
$$

where

$$B_n = (2c)^{\frac{1}{6}} \, R^{\frac{1}{3}} \frac{\rho_n}{n!} \left(\frac{R}{2c} \right)^{\frac{n}{3}} j^{\frac{n}{3} - \frac{1}{6}} \, .$$

3 Time Domain Version of the Diffraction Coefficient

In this section we show the transformation of (1) and (3) into the time domain. The time domain equivalents of components containing the transition function are obtained using the inverse Laplace transform. In this case transformation is performed by applying inverse Laplace transform of the $\mathrm{erfc}(p^{1/2})$ function in (10):

$$H_1(p) = \frac{1}{\sqrt{\pi}} \frac{R_H}{\sqrt{2D}} \sqrt{\pi X} e^{p \frac{X}{c}} \, \mathrm{erfc}\left(\sqrt{\frac{pX}{c}} \right) \, . \tag{10}$$

In the case of expressions which do not contain the transition function we use the one-sided inverse Fourier transform [6,7]:

$$f(t) = \mathrm{Re}\left[\overset{+}{f}(t_c) \right] = \mathrm{Re}\left[\frac{1}{\pi} \int\limits_0^\infty F(\omega) e^{j\omega t_c} d\omega \right], \tag{11}$$

where time t_c may be a complex number. In order to apply retransform (11) to (1) and (3), we must find the following integrals:

$$I_1(t) = \int\limits_0^\infty \omega^a e^{-\gamma \omega^{1/3} \theta} e^{j\omega t} d\omega, \quad I_2(t) = \int\limits_0^\infty \omega^a e^{j\omega t} d\omega. \tag{12}$$

Integral $I_1(t)$ is calculated using Taylor's series expansion of the factor $e^{j\omega t}$ around $\omega = 0$. Then $I_1(t)$ can be approximated by the following series:

$$I_1(t) \approx \frac{3}{(\gamma \theta)^{3(1+a)}} \sum_{n=0}^N \frac{j^n}{n!} \Gamma\left[3\left(n+1+a\right) \right] \left(\frac{t}{(\gamma \theta)^3} \right)^n. \tag{13}$$

For very small values of $t/(\gamma \theta)^3$, $I_1(t)$ converges for small N. After integration, $I_2(t)$ has the form

$$I_2(t) = \left(\frac{-1}{jt} \right)^{a+1} \Gamma\left(a+1\right) \, . \tag{14}$$

Basing on the above considerations, we can give the time domain equivalents of expressions which constitute (1) and (3):

$$\overset{+}{h}_{A11}(t) = -\frac{1}{\pi}\sqrt{\frac{c}{2\pi}}\frac{e^{-j\pi/4}}{\theta}\left(\frac{-1}{jt}\right)^{1/2}\Gamma\left(\frac{1}{2}\right), \quad \overset{+}{h}_{A2>}(t) = \frac{1}{\pi}\sum_{n=0}^{N}A_n\frac{3}{(\gamma_n\theta)^{\frac{5}{2}}}\sum_{m=0}^{M}\frac{j^m}{m!}\Gamma\left(3m+\frac{5}{2}\right)\cdot\left[\frac{t}{(\gamma_n\theta)^3}\right],$$

$$\overset{+}{h}_{A2<}(t) \approx \frac{1}{\pi}\sum_{n=0}^{N}B_n\theta^n\left(\frac{-1}{jt}\right)^{\frac{n}{3}+\frac{5}{6}}\Gamma\left(\frac{n}{3}+\frac{5}{6}\right)+\frac{1}{\pi}\sqrt{\frac{c}{2\pi}}\frac{e^{-j\pi/4}}{\theta}\left(\frac{-1}{jt}\right)^{1/2}\Gamma\left(\frac{1}{2}\right),$$

$$\overset{+}{h}_{S11}(t,s) = \frac{-1}{\pi}\sqrt{\frac{1}{2c\pi}}\frac{Le^{j\pi/4}}{s}\left(\frac{-1}{jt}\right)^{3/2}\Gamma\left(\frac{3}{2}\right), \quad \overset{+}{h}_{S13}(t,s) = \frac{1}{\pi}\sqrt{\frac{c}{2\pi}}\frac{e^{-j\pi/4}}{s\theta^2}\left(\frac{-1}{jt}\right)^{1/2}\Gamma\left(\frac{1}{2}\right),$$

$$h_{A12}(t) = \frac{L\theta}{2\pi\sqrt{2ct}(t+\frac{X}{c})}, \quad h_{S12}(t,s) = \frac{\partial}{\partial t}\left(\frac{L^2\theta^2}{s2c\pi\sqrt{2ct}(t+\frac{X}{c})}\right),$$

$$\overset{+}{h}_{S2<}(t,s) \approx \frac{1}{\pi}\sum_{n=0}^{N}\frac{nB_n}{s}\theta^{n-1}\left(\frac{-1}{jt}\right)^{\frac{n}{3}+\frac{5}{6}}\Gamma\left(\frac{n}{3}+\frac{5}{6}\right)-\frac{1}{\pi}\sqrt{\frac{c}{2\pi}}\frac{e^{-j\pi/4}}{s\theta^2}\left(\frac{-1}{jt}\right)^{1/2}\Gamma\left(\frac{1}{2}\right),$$

$$\overset{+}{h}_{S2>}(t) = \frac{-1}{\pi}\sum_{n=0}^{N}\frac{A_n}{s}\frac{3}{(\gamma_n\theta)^{\frac{5}{2}}}\sum_{m=0}^{M}\frac{j^m}{m!}\Gamma\left(3m+\frac{7}{2}\right)\left[\frac{t}{(\gamma\theta)^3}\right]^m.$$

The whole impulse response of the path $Q_{1'}-Q_2$ is equal to the expression $h_A(t)+h_S(t,s)$. Components $h_A(t)$ and $h_S(t,s)$ are described by the following formulas:

$$h_A(t) \approx \begin{cases} h_{A12}(t) + \text{Re}\left\{\overset{+}{h}_{A11}(t)+\overset{+}{h}_{A2<}(t)\right\} & \underset{f\in B}{\wedge}\xi_d(f)\le 1.2 \\ h_{A12}(t) + \text{Re}\left\{\overset{+}{h}_{A11}(t)+\overset{+}{h}_{A2>}(t)\right\} & \underset{f\in B}{\wedge}\xi_d(f)>1.2 \end{cases}, \tag{15}$$

$$h_S(t,s) \approx \begin{cases} h_{S12}(t,s)+ \\ \text{Re}\left\{\sum_{n=1,3}\overset{+}{h}_{S1n}(t,s)+\overset{+}{h}_{s2<}(t,s)\right\} & \underset{f\in B}{\wedge}\xi_d(f)\le 1.2 \\ h_{S12}(t,s)+ \\ \text{Re}\left\{\sum_{n=1,3}\overset{+}{h}_{S1n}(t,s)+\overset{+}{h}_{S2>}(t,s)\right\} & \underset{f\in B}{\wedge}\xi_d(f)>1.2 \end{cases}, \tag{16}$$

where B is the frequency band of the incident signal.

4 Model of the Channel with Two Convex Objects Shadowing the Transmitter and Receiver

The considered channel model is shown in Fig. 2. We assume that the slope of the field is zero when the field originates from the transmitter. We further assume that the receiver is in the far zone, so the slope of the field originating from the second obstacle equals zero [8]. Then the TD field at the receiver is defined by (17) (the time delay of the signal over the distance $\theta_{1/2}R_{1/2}$ is not included):

$$E_{\text{Re}}(t) = \left(E_2(t)\times h_A(t,L_{A12\text{Re}},R_2,\theta_2)+\frac{\partial E_2(t)}{\partial n}d(t,L_{s12\text{Re}},R_2,\theta_2)\right)A_2(s)\times\delta\left(t-\frac{s_{2\text{Re}}}{c}\right), \tag{17}$$

where

$$E_2(t) = E_1(t) \times h_A(t, L_{ATr12}, R_1, \theta_1) \times \delta\left(t - \frac{s_{12}}{c}\right) A_1(s),$$

$$\frac{\partial E_2(t)}{\partial n} = E_1(t) \times h_s(t, L_{sTe12}, R_1, \theta_1, s_{12}) \times \delta\left(t - \frac{s_{12}}{c}\right) A_1(s).$$

E_1 is the function of the field at point Q_1', where the creeping ray hits the first convex object. L_{A12Re} and L_{S12Re} are the distance parameters ensuring the continuity of the amplitude term and slope term of the field around the shadow boundary after the second convex object [8] and L_{ATr12} and L_{STr12} are the distance parameters ensuring the continuity of the amplitude term and slope term of the field around the shadow boundary after the first convex object [8]. The form of $d(t, L_{S12Re}, R_2, \theta_2)$ can be found through the operation of integration of $h_s(t,s)$ over argument t.

5 Simplifications of the Obtained Formulations

Now we calculate convolutions occurring in expression (17). A problem arises during calculation of the convolutions of functions containing singularities. If we need to calculate convolutions $x_1(t)*x_2(t)$ and both functions contain singularity at $t = 0$, we proceed as follows. To remove singularities, we integrate $x_1(t)$ n times and $x_2(t)$ m times. As a result we obtain

$$\underbrace{\int \dots \int}_{n} x_1(t)\, dt \times \underbrace{\int \dots \int}_{m} x_2(t)\, dt = y_1^n(t) \times y_2^m(t) = p(t)\,. \tag{18}$$

Next we differentiate $p(t)$ $m + n$ times to obtain

$$x_1(t) \times x_2(t) = \frac{\partial^{n+m}}{t^{n+m}} p(t)\,. \tag{19}$$

The procedure is applied to each convolution appearing in expression (17). Unfortunately, functions $y_1^n(t)$ and/or $y_2^m(t)$ in some cases are proportional to function $\text{arctg}(t^{1/2})$. Then convolution (18) cannot be obtained in the analytical way. In that case function $\text{arctg}(t^{1/2})$ is approximated by the following expression:

$$C_{a<}(t) = \begin{cases} a_1^k t + a_0^k \sqrt{t} & \text{for} \quad t < t_T \\ a_3^k + \frac{a_2^k}{\sqrt{t}} & \text{for} \quad t \geq t_T \end{cases}, \tag{20}$$

where $k = 1$ or 2.

Parameters a_n^k ($n = 0, 1, 2, 3$) and the threshold time t_T are determined by a minimization algorithm (e.g., genetic algorithm).

6 Verification of the Derived Impulse Response

In this section we examine the accuracy of the obtained results. In order to do this, we calculate the distortion of a UWB pulse caused by two cascaded convex obstacles. We set $E_1(t)$ to a particular UWB pulse $p(t)$:

Fig. 3 The shape of the distorted UWB pulse with the parameters $a = 3$ ns and $t_c = 1$ ns. Comparison of the results of the pulse distortion obtained with IFFT (a) with the results of the pulse distortion obtained through direct time domain calculations (b) and with the incident UWB pulse normalized to the amplitude of the distorted pulse (c). The values of parameters of the convex objects are $\theta_1 = 0.15$, $\theta_2 = 0.20$, $R_1 = 200$ m, and $R_2 = 150$ m

UWB pulse distortion (Amplitude + Slope diffraction)
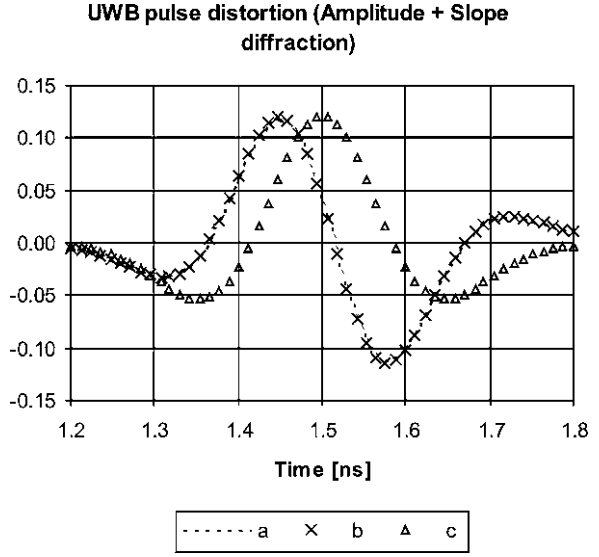
$$p(t) = \left[1 - 4\pi \left(\frac{t - t_c}{a}\right)^2\right] \exp\left(-2\pi \left(\frac{t - t_c}{a}\right)^2\right). \tag{21}$$

The achieved results are compared with the calculations obtained by means of IFFT of (2) (Fig. 3).

7 Conclusions

In this chapter we present the way for obtaining the time domain formulas for the field at the receiver when two convex obstacles are shadowing the transmitter and receiver. Numerical experiments show that the results obtained using the approximations presented in Section 6 are accurate compared to the results obtained by (17). However the former were obtained at a lot smaller complexity cost (Fig. 3). Although (17) relates to the soft polarization case, respective formulas can be derived for hard polarization, using a similar method to that applied for the soft polarization case. Further research should concern the non-perfect conducting convex obstacles, as well as a higher number of cascaded obstacles.

References

1. H. L. Bertoni, Radio Propagation for Modern Wireless Systems, Prentice-Hall Inc., Upper Saddle River, NJ, 2000.
2. D. A. McNamara, Introduction to the Uniform Geometrical Theory of Diffraction, Artech House, Boston, London, 1990.
3. P. H. Pathak, An asymptotic analysis of the scattering of plane waves by a smooth convex surface, Radio Science, vol. 14, no. 3, pp. 419–435, 1979.
4. P. Górniak and W. Bandurski, UWB pulse distortion in the channel containing cylindrical hill, European Conference on Antennas and Propagation, Nice, 6–10 November 2006.
5. N. A. Logan, General research in diffraction theory, Lockheed Missiles and Space Division, Tech. Rep. LMSD-288087, 1959.

6. P. H. Pathak, A time domain formulation of the uniform geometrical theory of diffraction for scattering from a smooth convex surface, IEEE Transactions on Antennas and Propagation, vol. 55, no. 6, pp. 1522–1534, 2007.
7. P. H. Pathak, Time-domain uniform geometrical theory of diffraction for a curved wedge, IEEE Transactions on Antennas and Propagation, vol. 43, no. 12, pp. 1375–1382, 1995.
8. G. Koutitas, A UTD solution for multiple rounded surfaces, IEEE Transactions on Antennas and Propagation, vol. 54, no. 4, pp. 1277–1283, 2006.

Benchmark Problems for Coupling and Scattering with Cavities of General Form

P.D. Smith, E.D. Vinogradova, S.B. Panin, Y.A. Tuchkin, and S.V. Vinogradov

Abstract The need for reliable and accurate prediction of electromagnetic wave coupling to, or scattering from, structures arises in many contexts. General-purpose computational codes have been extensively developed in the last few decades as computing power and resources have become widely available; they have had a significant impact in providing numerical solutions and insight into important coupling and scattering mechanisms. However, their accuracy, particularly for objects of some complexity, incorporating edges and re-entrant structures, can be difficult to assess. The strongly resonant features of cavity-backed apertures can present difficulties in accuracy and computational cost for such general-purpose numerical codes. This chapter presents a method of analytically regularizing the underlying integral equation governing diffraction from the structure, so that a well-conditioned system of equations is obtained. It generalizes the process of analytical regularization applied to cavities of spherical and other canonical shape [2, 3] in which the basic equations are transformed to a second-kind Fredholm matrix equation. It applies to axisymmetric bodies, and examples confirm that the condition number of the resultant system is well controlled even near-resonant frequencies and that solutions of guaranteed accuracy can be efficiently obtained.

Keywords Scattering and diffraction · Electromagnetic waves · Bodies of revolution · Apertures · Analytical regularization

1 Introduction

Cavity-backed apertures and related structures are widely used to simulate various types of antennas, open resonators, and waveguides. While diffraction from closed bodies with smooth surfaces has been intensively studied from both the analytical (e.g., see [1]) and numerical–analytical point of view, cavity-backed apertures are much less tractable to analytical methods, and the accuracy of present-day purely numerical methods (finite element, boundary element) can be difficult to ascertain, mainly because they rely on the computational solution of an underlying first-kind equation that is neither stable nor convergent [2]. Indirect criteria such as energy balance, solution "stabilization" with increasing size of the truncated system, or solution residual size are inconclusive. The only

P.D. Smith (✉)
Department of Mathematics, Macquarie University, Sydney 2109, Australia
e-mail: pdsmith@maths.mq.edu.au

practical tool is the condition number, identifying the number of exact digits in the solution of the truncated system, but it is not usually assessed, because of computational cost.

Thus, it is highly desirable to transform the initial equation of the first kind into one of the second kind, which, as is well known, possesses a stable and fast converging computational algorithm; any prescribed accuracy of numerical computation is obtained by the standard truncation technique; practically, the condition number of the truncated system will stabilize (i.e., converge to a limit) as the system size increases. This transformation can be effected by the functional analytic method of analytical regularization. Its practical construction in explicit analytical form for any given problem is challenging and has only been achieved for some limited diffraction classes. For canonically shaped open screens (spheres, spheroids, etc.) a transformation technique based on a semi-inversion procedure has been successfully applied [3]; the two-dimensional cavity diffraction problem has been solved for arbitrarily shaped structures, in both E- and H-polarizations [4].

In this chapter we describe the generalization of this method to three-dimensional axisymmetric problems. We consider the scalar wave diffraction problem with a Dirichlet boundary condition imposed on an arbitrarily shaped open smooth surface of revolution topologically equivalent to a sphere punctured with one circular hole. Two cases are satisfactorily treated: an axisymmetrically located vertical electric dipole exciting a perfectly electrically conducting screen and an acoustic plane wave illuminating an acoustically soft screen.

2 Formulation

An open smooth surface of revolution S_0 is formed by the rotation of a generating curve l_0 around the OZ-axis (see Fig. 1). The curve l_0 is a connected part of a smooth and non-self-intersecting curve l, whose ends are placed on the OZ-axis and which lies in the right half-plane of the ZOY-plane. One endpoint of l_0 lies on OZ. Let l_1 denote the portion of l complementary to l_0, so that $l = l_0 \cup l_1$. We call the surface S_1, obtained by rotation of the curve l_1, the "aperture"; it is the complement of S_0 in the closed *surface* $S = S_0 \cup S_1$; S is assumed to be *smoothly* isomorphic to a sphere. The curve l is described by a smooth parameterization $z = z(\tau)$, $\rho = \rho(\tau)$, $\tau \in [0, \pi]$, of the cylindrical coordinates of a point $p(z,\rho,\varphi) \in l$. It should satisfy the condition that the differential
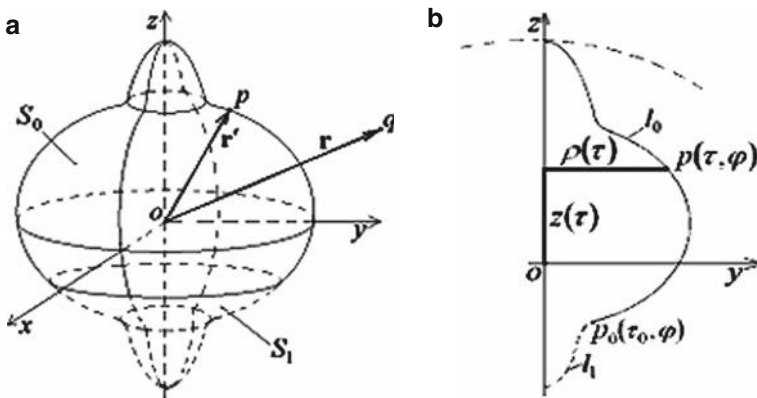
Fig. 1 (**a**) The screen of revolution and aperture surface and (**b**) the generating curve

of arc length $\ell(\tau) = \sqrt{\{z'(\tau)\}^2 + \{\rho'(\tau)\}^2}$ be positive, and the surface be smooth at poles, so that $z'(0) = z'(\pi) = 0$, $\rho(0) = \rho(\pi) = 0$. Choose τ_0 so that the contour l_0 corresponds to the interval $\tau \in [0, \tau_0]$.

Suppose the scalar wave $u_i(q)$, $q \in R^3$, is incident on the screen. The diffracted field $u_s(q)$ for the Dirichlet problem is to be found. It satisfies the Helmholtz equation, and a unique solution is guaranteed [1] by enforcing the boundary conditions $u_i(q) + u_s(q) = 0$, at each $q \in S_0$, the Sommerfeld radiation conditions, and a condition on the finiteness of field energy within any confined volume of space. This problem can be reduced to a Fredholm integral equation of first kind

$$\iint\limits_{S_0} j_D(p) \, G(q,p) \, ds_p = u_i(q), \quad q \in S_0, \tag{1}$$

where $j_D(p)$ is the unknown surface current density and Green's function is $G(q,p) = (4\pi)^{-1} e^{ikR(q,p)}/R(q,p)$, where k is the wave number, and $R(q,p)$ is the distance between q and p. Let $\xi(\tau) = \sqrt{\rho(\tau)/\sin\tau}$ and introduce the following unknown function X, which is defined over the whole surface S, proportional to $j_D(p)$ on the open surface S_0, vanishing on the aperture S_1:

$$X(\tau,\varphi) = \begin{cases} \xi(\tau)\,\ell(\tau)\,j_D(\tau,\varphi), & \tau \in [0, \tau_0], \varphi \in [0, 2\pi], \\ 0, & \tau \in (\tau_0, \pi], \varphi \in [0, 2\pi]. \end{cases} \tag{2}$$

We apply Fourier transforms to (1). Denote the mth azimuthal Fourier coefficients of the function $f(\tau,\varphi)$ by $f^m(\tau)$ so that

$$f(\tau,\varphi) = \sum_{m=-\infty}^{\infty} f^m(\tau) \, e^{im\varphi},$$
$$f^m(\tau) = \frac{1}{2\pi} \int_{-\pi}^{\pi} d\varphi \, e^{-im\varphi} f(\tau,\varphi).$$

The axial symmetry of the screen implies that (1) can be separated into the set:

$$\int_0^\pi d\tau_p \sqrt{\rho(\tau_p)\,\sin\tau_p} \; X^m(\tau_p) \, G^m(\tau_q, \tau_p) = \frac{1}{2\pi} u^m(\tau_q). \tag{3}$$

A careful analysis of the singularities of the azimuthal coefficient $G^m(\tau_q,\tau_p)$ of Green's function leads us to define the *remainder* function, for each index m,

$$D^m(\tau_q,\tau_p) = \xi(\tau_q)\xi(\tau_p) \, G^m(\tau_q,\tau_p) - g^m(\tau_q,\tau_p), \tag{4}$$

where $g^m(\tau_q, \tau_p)$ denotes the mth azimuthal Fourier coefficient of Green's function of the unit sphere. The choice of the scaling factor $\xi(\tau_q)\,\xi(\tau_p)$ is important in making the remainder as smooth as possible: It can be shown that

$$D^m(\tau, \tau+\delta) = \frac{1}{64\pi^2} \frac{\delta^2 \ln|\delta|}{\sqrt{\sin\tau\,\sin(\tau+\delta)}} \left([4m^2 - 1] \left\{ \frac{\ell^2(\tau)}{\rho^2(\tau)} - \frac{1}{\sin^2\tau} \right\} - 4k^2 \left(\ell^2(\tau) - 1 \right) \right)$$
$$+ O\left(\delta^3 \log|\delta| \right) \quad \text{as } \delta \to 0. \tag{5}$$

So (1) can be written in the form, for each index m,

$$\int\limits_0^\pi d\tau_p \ \sin \ \tau_p \ \left\{ g^m \left(\tau_q, \tau_p\right) + D^m \left(\tau_q, \tau_p\right) \right\} X^m \left(\tau_p\right) = \frac{1}{2\pi} \xi \left(\tau_q\right) \ u^m \left(\tau_q\right).$$

Fix m; expand all quantities in Fourier–Legendre series with normalized associated Legendre functions $\hat{P}_n^{|m|}$:

$$g^m \left(\tau_q, \tau_p\right) = \frac{1}{4\pi} \sum_{n=|m|}^{\infty} \frac{2}{2n+1} \hat{P}_n^{|m|} \left(\cos \ \tau_q\right) \hat{P}_n^{|m|} \left(\cos \ \tau_p\right), \tag{6a}$$

$$X^m \left(\tau\right) = \sum_{n=|m|}^{\infty} x_n^m \hat{P}_n^{|m|} \left(\cos \ \tau\right), \quad \frac{1}{2\pi} \xi \left(\tau\right) u^m \left(\tau\right) = \sum_{n=|m|}^{\infty} u_n^m \hat{P}_n^{|m|} \left(\cos \ \tau\right), \tag{6b}$$

$$D^m \left(\tau_q, \tau_p\right) = \frac{1}{4\pi} \sum_{k=|m|}^{\infty} \sum_{l=|m|}^{\infty} D_{kl}^m \hat{P}_k^{|m|} \left(\cos \ \tau_q\right) \hat{P}_l^{|m|} \left(\cos \ \tau_p\right). \tag{6c}$$

Insertion of these series transforms (5) to the following set of dual series equations for the Fourier–Legendre coefficients x_n^m $(n = |m|, \ |m+1|, \ldots)$, of $X^m (\tau)$:

$$\begin{cases} \sum\limits_{n=|m|}^{\infty} \frac{2}{2n+1} x_n^m \hat{P}_n^{|m|} \left(\cos \ \tau\right) = \ = \sum\limits_{n=|m|}^{\infty} \left(u_n^m - \sum\limits_{l=|m|}^{\infty} D_{nl}^m x_l^m \right) \hat{P}_n^{|m|} \left(\cos \ \tau\right), \ \tau \in [0, \tau_0] \\ \sum\limits_{n=|m|}^{\infty} x_n^m \hat{P}_n^{|m|} \left(\cos \ \tau\right) = 0, \qquad \tau \in (\tau_0, \pi]. \end{cases} \tag{7}$$

The system is equivalent to an operator equation of first kind in the Hilbert space given by the Meixner condition. The key steps in the process of analytical regularization, that removes its inherent ill-conditioning, are as follows. Represent the orthonormalized Legendre functions in terms of Jacobi polynomials via

$$\hat{P}_n^{|m|} \left(\cos \ \tau\right) = \sin^{|m|} \tau \ \hat{P}_{n-|m|}^{(|m|,|m|)} \left(\cos \ \tau\right).$$

Next, set $z = \cos \ \tau$. Multiply the first equation of system (7) by $(1+z)^m$, integrate over $[-1, t]$, and use the well-known Abel integral transform [2]:

$$\int\limits_{-1}^{t} (1+z)^m \ \hat{P}_s^{(m,m)} (z) \ dz = \frac{1}{\sqrt{\pi}} \left(s+m+\frac{1}{2} \right)^{-\frac{1}{2}} \int\limits_{-1}^{t} \frac{(1+x)^{m+\frac{1}{2}} \ \hat{P}_s^{\left(m-\frac{1}{2}, m+\frac{1}{2}\right)} (x)}{(t-x)^{\frac{1}{2}}} dx$$

to obtain a homogenous Abel integral equation, which has the general form

$$\int\limits_{-1}^{t} \frac{u (x)}{(t-x)^{1/2}} \ dx = 0, \tag{8}$$

for a certain function $u(x)$. This integral equation has the unique solution $u(x) = 0$. A similar substitution of an integral representation for the Jacobi polynomials in the second equation of system (7) likewise leads to a homogenous Abel integral equation. The solution of both integral equations leads to a system of dual series equations involving the orthonormal family of functions

$$\hat{P}_{n-|m|}^{(|m|-1/2,\ |m|+1/2)}(z),\quad n=|m|,|m|+1,|m|+2,\dots.$$

From this is easily obtained an algebraic system of the form

$$\left[\mathbf{I}+\mathbf{Q}^m\mathbf{D}^m\right]\mathbf{x}^m=\mathbf{Q}^m\mathbf{u}^m,\tag{9}$$

where the matrix $\mathbf{D}^m$ and vectors $\mathbf{x}^m,\mathbf{u}^m$ are, respectively, the array of normalized Fourier–Legendre coefficients $\hat{D}_{nl}^m$ and normalized components $\hat{x}_n^m,\hat{u}_n^m$ of $D^m(\tau_q,\tau_p)$ and $X^m(\tau)$, $u^m(\tau)$, defined by

$$\hat{x}_s^m=(s+1/2)^{-1/2}\,x_s^m,\quad \hat{D}_{nl}^m=\sqrt{n+1/2}\,\sqrt{l+1/2}D_{nl}^m,\quad \hat{u}_n^m=\sqrt{n+1/2}\,u_n^m,\tag{10}$$

and the matrix $\mathbf{Q}^m=\left(Q_{s,n}^m\right)_{s,n=|m|}^{\infty}$ has elements

$$\int_{\cos\tau_0}^{1} dx\,(1-x)^{|m|-\frac{1}{2}}\,(1+x)^{|m|+\frac{1}{2}}\,\hat{P}_{s-|m|}^{\left(|m|-\frac{1}{2},\ |m|+\frac{1}{2}\right)}(x)\,\hat{P}_{n-|m|}^{\left(|m|-\frac{1}{2},\ |m|+\frac{1}{2}\right)}(x)\tag{11}$$

utilizing the "incomplete scalar product" [3]. The compactness of the matrix operator $\mathbf{D}^m$ follows from the boundedness of the ortho-projection matrix $\mathbf{Q}^m$ and the rapid decay of the coefficients, according to

$$\sum_{s=|m|}^{\infty}\sum_{l=|m|}^{\infty}(1+s)\,(1+l)\,\left|D_{sl}^m\right|^2<\infty.\tag{12}$$

Thus, (9) is equivalent to a Fredholm operator equation of the second kind; its solution can be calculated to prescribed accuracy by truncation techniques.

3 Numerical Results

The accuracy of this approach is exemplified by the open prolate spheroidal shell and the non-canonical open shell generated by the *"Cassini Oval"* shown in Figs. 2 and 3; here $r(\tau)=\sqrt{z(\tau)^2+\rho(\tau)^2}$ is the polar radius of the generating curve. The prolate spheroid with major and minor semi-axes a and b is illuminated by a plane wave normal to the aperture; its aspect ratio is $b/a=0.15$. Figure 2 displays the monostatic cross section σ_0, computed from backscattered field, over the range $0<k<20$. As the truncation number $N=N_{\text{tr}}$ of the regularized system is increased, the condition number ν_N of the system approaches a limit, dependent upon k. This limiting value ν_N is displayed over the same range. A strongly resonant feature is visible near $k=16.6$; however, the condition number remains well controlled so that the accuracy of the solution is guaranteed. Away from resonance the condition number and solution accuracy are also well controlled. Results were validated against those obtained by a different method [3].
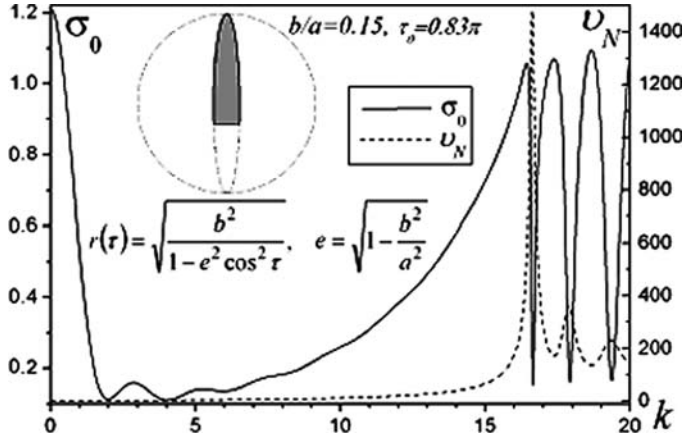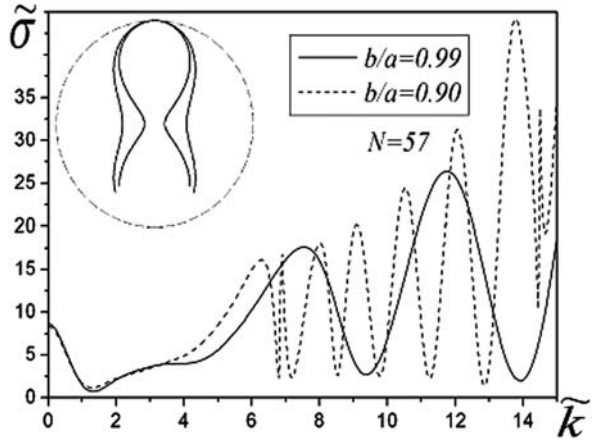
Fig. 2 Monostatic cross section σ_0 and condition number v_N as a function of k

Fig. 3 Monostatic cross
section of the Cassini oval

The Cassini oval is defined by

$$r(\tau)^2 = b^2 \left(\cos 2\tau + \left((a/b)^4 - \sin^2 2\tau \right)_{1/2} \right).$$

Revolution about its axis produces a highly resonant structure of two symmetrical cavities connected via narrow neck, with an aperture opened in one cavity. Robust well-conditioned solutions were obtained across the frequency band examined. The monostatic cross section σ_0 is shown in Fig. 3 for two different aspect ratios; the limiting value of the condition number v_N stabilized with a truncation number less than 57, over the range $0 < \tilde{k} = ka < 15$, remaining bounded by modest values over the range, even near resonant values.

4 Conclusions

A rigorous and effective approach for solving the scalar Dirichlet diffraction problem for an arbitrarily shaped open screen of revolution is described. The analytical regularization procedure transforms the underlying integral equation to an algebraic system of second kind, for which there are reliable numerical methods, permitting the problem to be efficiently solved with any prescribed accuracy. The condition number as a function of truncation number swiftly stabilizes for the various screens considered. On the whole the stabilization level of condition number is rather small even for screens of complex geometry. This behaviour of the condition number is perhaps the most significant advantage of the second-kind system (9). It allows us to obtain robust solutions with pre-specified accuracy for any frequencies including the resonant domain. Although analytical and analytical–numerical methods are rather more difficult to apply than the conventional numerical techniques of electromagnetics, they possess the unique advantage of providing robust, reliable solutions to scattering problems of guaranteed accuracy.

References

1. J. J. Bowman, T. B. A. Senior, and P. L. E. Uslenghi, Electromagnetic and Acoustic Scattering by Simple Shapes, Hemisphere Pub. Corp., New York, 1987.
2. A. Y. Poyedinchuk, Y. A. Tuchkin, and V. P. Shestopalov, New numerical–analytical methods in diffraction theory, Mathematical and Computer Modeling, vol. 32, pp. 1026–1046, 2000.
3. S. S. Vinogradov, P. D. Smith, and E. D. Vinogradova, Canonical Problems in Scattering and Potential Theory. Part II: Acoustic and Electromagnetic Diffraction by Canonical Structures, Chapman & Hall/CRC, Boca Raton, FL, 2002.
4. E. D. Vinogradova, Y. A. Tuchkin, and S. S. Vinogradov, Diffraction of H-polarized plane wave by cylindrical cavities of arbitrary shape, Proceedings of the 10th International Conference on Electromagnetics in Advanced Applications, Torino, Italy, 2007.

Accurate Modelling of Ultra-short Electromagnetic Pulse Scattering Using a Locally Conformal Finite-Difference Time-Domain Scheme

D. Caratelli, R. Cicchetti, M. Simeoni, and A. Yarovoy

Abstract A locally conformal finite-difference time-domain (LC-FDTD) scheme is proposed to accomplish the challenging task of accurately modelling electromagnetic scattering phenomena generated by the wave interaction with metallic and/or dielectric objects having complex geometries. The proposed technique is first validated by evaluating the resonant frequency of a dielectric resonator enclosed in a metallic cavity and then applied to the characterization of a realistic ground-penetrating radar scenario involving complex shaped metallic and dielectric objects with curved boundaries.

1 Introduction

The computation of the transient responses of complex metal-dielectric structures (radar targets, antennas, etc.) to ultra-short electromagnetic pulses requires accurate and fast numerical schemes. One of such techniques is the finite-difference time-domain (FDTD) algorithm [1]. However, in the conventional formulation proposed by Yee [1], each cell in the computational grid is implicitly supposed to be filled by a homogeneous material. For this reason, the adoption of well-posed orthogonal Cartesian meshes could be responsible for a reduced numerical accuracy when complex electromagnetic structures having curved boundaries have to be modelled. In such cases, locally conformal FDTD schemes (LC-FDTD) (see, for instance, [2]) provide clear advantages over the use of the *staircasing* approach or unstructured and stretched space lattices [1], potentially suffering from significant numerical dispersion and/or instability.

Here, a novel LC-FDTD scheme, based on the effective electrical parameters concept, is proposed. In particular, a static finite-difference approach is adopted to rigorously evaluate the intrinsic capacitance and conductance of each non-uniformly filled cell in the computational grid. Then, by using simple algebra, the effective permittivity and electrical conductivity of the generic cell are easily derived. In this way, the information regarding the physical and geometrical characteristics of the

───────────────────

D. Caratelli (✉)
Delft University of Technology, IRCTR, Delft, The Netherlands
e-mail: d.caratelli@tudelft.nl

electromagnetic structure under consideration is transferred to suitable position-dependent tensorial effective parameters. The computation of such quantities is carried out before the FDTD method time marching starts; hence, unlike in conformal techniques based on stretched space lattices, no additional corrections are required in the core of the numerical algorithm. Obviously, the proposed scheme has the same stability properties as the conventional FDTD formulation [1].

In Section 2, the description of the proposed formulation is presented by putting particular emphasis on the derivation of the effective electrical parameters. In order to assess the numerical accuracy and effectiveness of the proposed technique, several test cases have been considered. For the sake of brevity, only the computation of the fundamental resonant frequency of a rectangular metallic cavity loaded with a cylindrical dielectric resonator is presented in Section 3. The application of the proposed formulation to the modelling of ultra-short electromagnetic pulse scattering occurring in a realistic ground-penetrating radar (GPR) system intended to detect and characterize buried dielectric pipes is presented in Section 4. Finally, the conclusions are drawn in Section 5.

2 Theoretical Formulation

In the last years, several methods based on effective medium theory have been developed to evaluate the electromagnetic field distribution excited in structures having complex geometry [1–5]. These methods evaluate the effective dielectric constants for partially filled cells before the FDTD method time marching starts.

There are basically two approaches to obtain the effective dielectric constants for partially filled FDTD cells. One is the simplified finite-volume time-domain (FVTD) technique, which uses an approximated integral formulation [3]. The other is the averaging method [4]; such scheme calculates the effective dielectric constant by computing an area (or volume)-weighted average of the dielectric constant of the materials contained in the cell. This approach is easy to be implemented, but sensitive to the electric field polarization. In fact, when the considered electric field component is parallel to the material interface, the weighted area (or volume) average yields accurate results. On the contrary, this approach tends to become inaccurate when the electric field component results tilted with respect to the dielectric boundary surface.

In this contribution, a novel LC-FDTD method is introduced. This method employs an effective medium theory based on a rigorous electrostatic formulation to account for the electromagnetic field behaviour across dielectric boundaries and, consequently, to model complex objects more accurately. Arbitrarily shaped dielectric surfaces may generate partially filled cells in the FDTD computational grid, as shown in Fig. 1.

Where the given electric field component is parallel to the dielectric boundary and, consequently, continuous in each material contained in the cell, the corresponding effective permittivity and conductivity may be evaluated by using the conventional weighted volume average approach [4], as follows:

$$\left\{ \begin{matrix} \varepsilon \\ \sigma \end{matrix} \right\}_{\text{eff}} = \left\{ \begin{matrix} \varepsilon \\ \sigma \end{matrix} \right\}_1 v_1 + \left\{ \begin{matrix} \varepsilon \\ \sigma \end{matrix} \right\}_2 v_2, \tag{1}$$

v_1 and v_2 being the fractional volumes of the cell containing the materials with parameters $(\varepsilon_1, \sigma_1)$ and $(\varepsilon_2, \sigma_2)$, respectively. However, this scheme cannot distinguish between cells having the same fill factor and different geometrical properties. Moreover, if the considered electric field component is tilted with respect to the dielectric boundary (see Fig. 1), the discontinuity effect across the material interface cannot be accurately modelled using an averaging method. To overcome this limitation, a rigorous electrostatic approach is adopted here to evaluate the intrinsic capacitance C_{eff_p} and
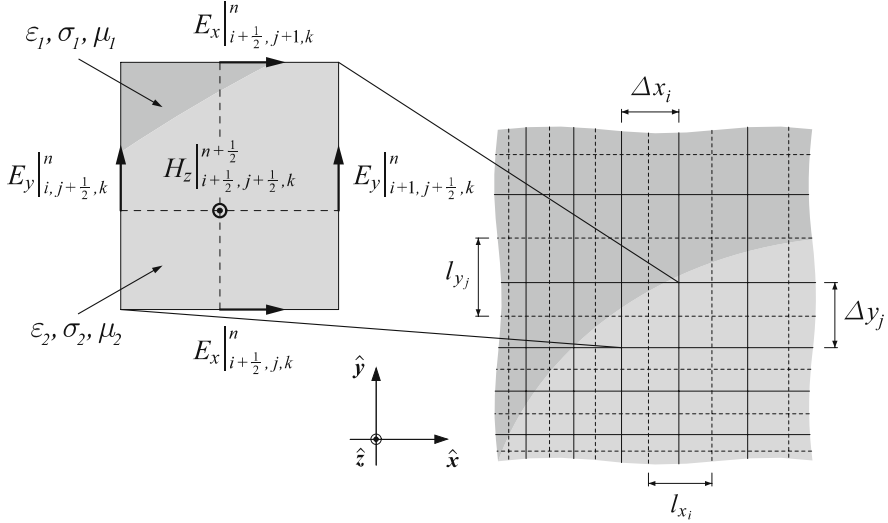
Fig. 1 Cross-sectional view of the FDTD computational grid in the presence of a curved boundary between different dielectric materials

conductance G_{eff_p} of each non-uniformly filled cell in the computational grid, relevant to generic electric field component E_p ($p = x, y, z$). By doing so, the tensorial effective material parameters, accounting for local inhomogeneities, may be easily derived as follows:

$$\left\{ \begin{array}{c} \varepsilon \\ \sigma \end{array} \right\}_{\text{eff}_p} = \frac{l_p}{A_p} \left\{ \begin{array}{c} C \\ G \end{array} \right\}_{\text{eff}_p} \quad (p = x, y, z), \tag{2}$$

where l_p and A_p denote the length and the cross-sectional area of the individual cell, respectively. The proposed algorithm entails solving the Poisson's equation

$$\nabla \cdot \left[\varepsilon(\mathbf{r}) \nabla \phi_p(\mathbf{r}) \right] = 0, \quad \mathbf{r} \in \tau_{C_p}, \tag{3}$$

subject to the boundary conditions

$$\begin{aligned} \phi_p(\mathbf{r}) &= \pm V/2, \quad \mathbf{r} \in S_{B\pm_p}, \\ \frac{\partial \phi_p(\mathbf{r})}{\partial n} &= 0, \quad \mathbf{r} \in S_{L_p}, \end{aligned} \tag{4}$$

$S_{B\pm_p}$ and S_{L_p} being the top, bottom, and side surfaces, respectively, of the cell volume τ_{C_p} ($p = x, y, z$) with outward normal $\mathbf{n}$. In (3)–(4), $\phi_p(\mathbf{r})$ is the electrostatic potential within the considered cell, regarded as an inhomogeneously filled, parallel plate, ideal capacitor, experiencing a voltage drop V. As outlined in [5], such an assumption holds since the finite-difference update equation of the generic electric field component E_p ($p = x, y, z$) at any FDTD grid location can be conveniently recast in the voltage-balance equation for an RC electric bipole, if the following interchanges are made:

$$E_p \leftrightarrow V = -l_p E_p,$$
$$\varepsilon_{\text{eff}_p} \leftrightarrow C_{\text{eff}_p} = \varepsilon_{\text{eff}_p} A_p / l_p, \tag{5}$$
$$\sigma_{\text{eff}_p} \leftrightarrow G_{\text{eff}_p} = \sigma_{\text{eff}_p} A_p / l_p.$$

In view of this, once the boundary-value problem (3)–(4) is solved using a suitable finite-difference or finite-element method, the individual intrinsic capacitance C_{eff_p} and conductance G_{eff_p} ($p = x, y, z$) may be rigorously determined as follows:

$$C_{\text{eff}_p} = W_{e_p} / \left(\tfrac{1}{2} V^2 \right),$$
$$G_{\text{eff}_p} = P_{d_p} / V^2, \tag{6}$$

where

$$P_{d_p} = \int\limits_{\tau_{C_p}} \sigma\left(\mathbf{r}\right) \left| \nabla \phi_p\left(\mathbf{r}\right) \right|^2 d\tau,$$
$$W_{e_p} = \tfrac{1}{2} \int\limits_{\tau_{C_p}} \varepsilon\left(\mathbf{r}\right) \left| \nabla \phi_p\left(\mathbf{r}\right) \right|^2 d\tau \tag{7}$$

denote the dissipated power and the electric energy stored in the cell volume τ_{C_p} ($p = x, y, z$), respectively. In this way, the electromagnetic field behaviour across arbitrarily shaped dielectric boundaries and wedges is properly taken into account in the evaluation of the effective tensorial parameters ($\varepsilon_{\text{eff}_p}$, σ_{eff_p}) for partially filled FDTD cells, improving the numerical accuracy of the algorithm over conformal FDTD schemes based on conventional weighted averaging approaches [4].

3 Numerical Validation

In order to validate the accuracy of the proposed LC-FDTD scheme a number of test cases has been considered. Here the results obtained for the computation of the fundamental resonant frequency of a dielectric resonator enclosed in a metallic cavity are presented. The structure under consideration, shown in Fig. 2a was already analysed in [6].

(a)   (b)
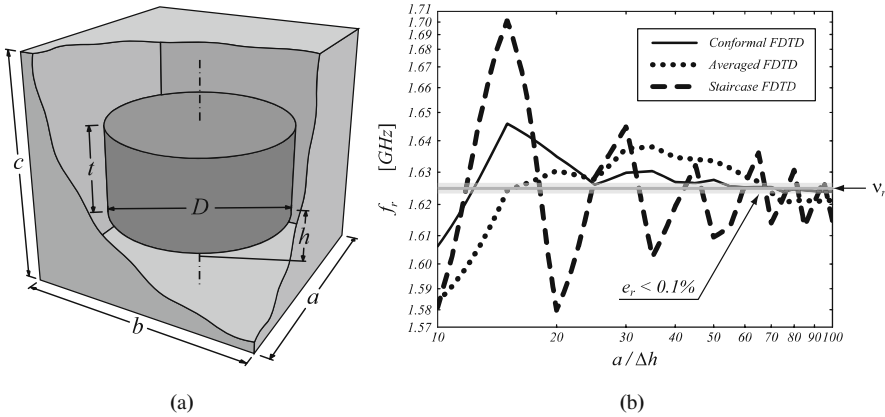
Fig. 2 Geometry of a dielectric loaded rectangular cavity (**a**) and behaviour of the fundamental resonant frequency f_r for different FDTD mesh sizes (**b**)

It consists of a perfectly conducting metallic cavity of dimensions $a = b = 50$ mm and $c = 30$ mm, loaded with a cylindrical dielectric (ceramic) puck having diameter $D = 36$ mm, height $t = 16$ mm, and relative permittivity $\varepsilon_r = 37$. The puck is suspended at a distance of $h = 7$ mm from the bottom of the cavity. Since the dielectric permittivity of the resonator is rather high, the effect of the orthogonal Cartesian mesh being not conformal to the resonator shape is expected to be noticeable. Here the structure is analysed by means of a standard FDTD scheme featuring the traditional staircase approximation of the resonator's contour and by means of the weighted averaging approach proposed in [4], and the LC-FDTD scheme detailed in Section 2. The numerical results obtained from these FDTD schemes are compared against the ones reported in [6] resulting from the use of a commercial transmission line matrix (TLM) method-based solver. To this end, a cubic FDTD mesh having fixed spatial increment Δh has been adopted to analyse the structure. As it appears in Fig. 2, this example clearly demonstrates the suitability of the proposed approach to efficiently handle complex structures with curved boundaries. The proposed LC-FDTD scheme introduces a significant improvement in accuracy over the *staircasing* approximation, converging very quickly to the reference value. The use of a relatively coarse mesh enabled by the LC-FDTD leads to reduced computational time and memory storage.

4 Ultra-short Pulse Ground-Penetrating Radar Application

In the subsurface exploration of fine objects such as pipes, cables, and voids, impulse and stepped-frequency continuous-wave (SFCW) radars are commonly employed. The detection of the mentioned targets requires a short radio pulse or, equivalently, a large bandwidth operation, in order to achieve an adequate range resolution. Thus the adoption of broadband radiating elements, such as spiral and bow–tie antennas, is essential [7]. The emphasis is here put on the electromagnetic modelling of an ultra-wideband cavity-backed bow–tie antenna pair for ground-penetrating radar (GPR) applications. A sketch of the structure geometry is shown in Fig. 3. As it appears, each radiating element, featuring two circularly ended flairs with angle $\Theta_f = 130°$ and length $l_f = D_c / 2 - s_c = 19$ cm, is assumed to be elevated to a height $h_a = 3$ cm over the ground, modelled as a lossy homogeneous half-space, where an infinitely long dielectric pipe is buried at a depth $h_p = 50$ cm. A suitable absorber-filled cavity is employed to reduce the antenna back-radiation level maintaining, at the same time, good impedance matching over the whole operating bandwidth [7].

To properly enlarge the antenna bandwidth, thus reducing late-time ringing phenomena, a resistive loading with the following Wu–King-like profile

$$\sigma_f(\rho) = \Omega_0 \frac{1 + \frac{\sigma_{\min}}{\Omega_0} - \frac{\rho}{l_f}}{\rho/l_f}, \qquad \sigma_{\min} = 10^{-4}\ \text{S/m} \tag{8}$$

is applied to the flairs of the considered radiators. In (8), ρ denotes the radial distance from the central delta gap. A voltage source of amplitude $V_g = 1$ V and internal reference resistance $R_0 = 50\ \Omega$ is employed to excite the transmit antenna (element no. 1), whereas the receive antenna (element no. 2) is terminated on a matched load. In particular, the excitation signal is a Gaussian pulse given by

$$\Pi_g(t) = V_g \exp\left[-\left(\frac{t - t_0}{\tau}\right)^2\right], \quad \tau = \frac{\sqrt{\ln 10}}{\pi f_{\max}}, \quad t_0 = 10\,\tau, \tag{9}$$
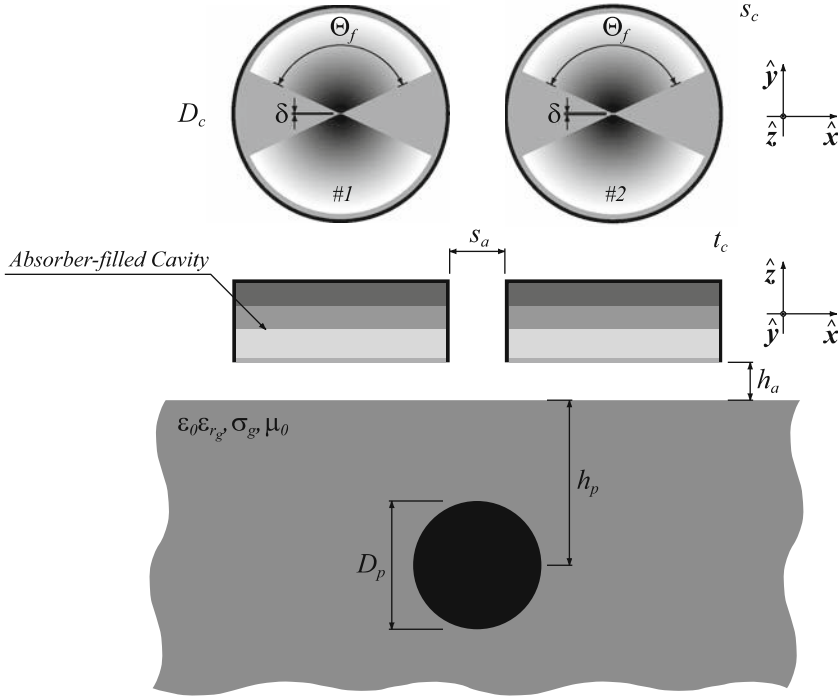
Fig. 3 Geometry of a cavity-backed resistively loaded bow–tie antenna pair for GPR applications. Structure characteristics: $s_c = 1$ cm, $t_c = 5$ mm, $\delta = 2.5$ mm, $s_a = 5$ cm, $D_p = 20$ cm

where the time constant τ is selected in order to have the source pulse significant energy in the frequency band up to $f_{max} = 1.5$ GHz. The conductivity parameter Ω_0 has been determined in order to guarantee good impedance matching over the frequency band 100 MHz to 1 GHz. To this end, a specific parametric analysis has been carried out. By doing so, the optimal value $\Omega_{opt} \cong 30$ S/m, useful to meet the mentioned bandwidth specifications, has been found [7].

Since the considered structure is reciprocal and symmetrical, the corresponding scattering matrix is completely described in terms of the S_{11} and S_{21} parameters, whose frequency behaviour for different electrical properties of the buried pipe is shown in Fig. 4a. As it appears from this figure, the antenna return loss is rather insensitive to the target that, on the other hand, has a remarkable effect on the coupling level between the radiating elements. This behavior is due to the subsurface diffraction processes and to the excitation of surface and creeping waves, which strongly depends on the electrical and geometrical characteristics of the buried scatterer.

It is worth noting that the peak level of the radio signal contribution diffracted by the pipe, and detected at the input terminals of the receive antenna essentially depends on of the difference, $\Delta\varepsilon_r = \varepsilon_{r_g} - \varepsilon_{r_p}$, between the relative permittivities of the ground and the pipe (see Fig. 4b). However, where such difference is negative, resonant phenomena, responsible for local minima in the aforementioned signal component, occur. Such physical process can be easily understood by looking at the spatial distribution of the electric field excited along the vertical cut-plane of the structure (see Fig. 5). As it can be noticed in Fig. 5, if the relative permittivity of the pipe is greater than that of the ground, the pipe acts as an electromagnetic lens responsible for a significant downward field focalization and, consequently, for the reduction of the radio signal at the receiver end. Such information can be usefully employed to optimize the detection of buried pipes in SFCW radar applications.
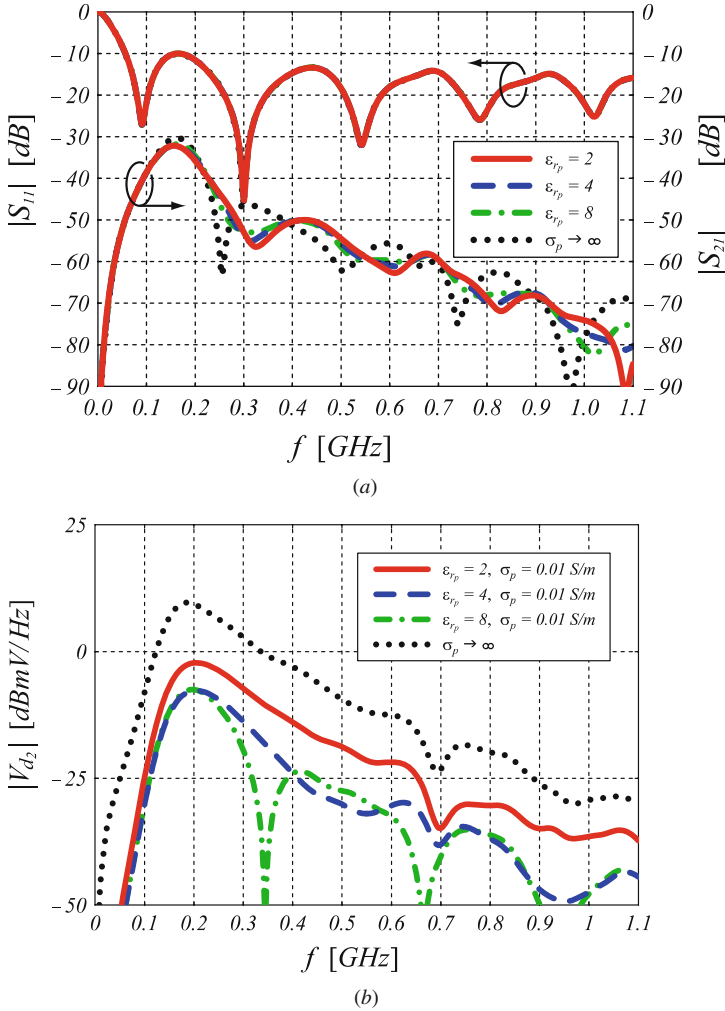
Fig. 4 Frequency behaviour of the bow–tie antenna pair for different electrical properties of the buried pipe: (**a**) scattering parameters and (**b**) radio signal diffracted by the pipe and detected at the input terminals of the receive antenna

5 Conclusion

A novel locally conformal FDTD scheme, useful to accurately analyse arbitrarily shaped dielectric structures, has been presented. The proposed approach is based on a electrostatic formulation, which rigorously evaluate the individual cell effective material parameters accounting for local inhomogeneities and the field polarization. The presented technique has been validated by computing the resonant frequency of a dielectric resonator enclosed in a metallic cavity, and then applied to the analysis of subsurface ultra-short pulse scattering phenomena arising from the electromagnetic field interaction with complex structures in realistic GPR scenarios. The obtained numerical results have provided a useful physical insight into subsurface scattering from buried targets. This information is useful to establish the required GPR dynamic range where the maximal received signal is due to the
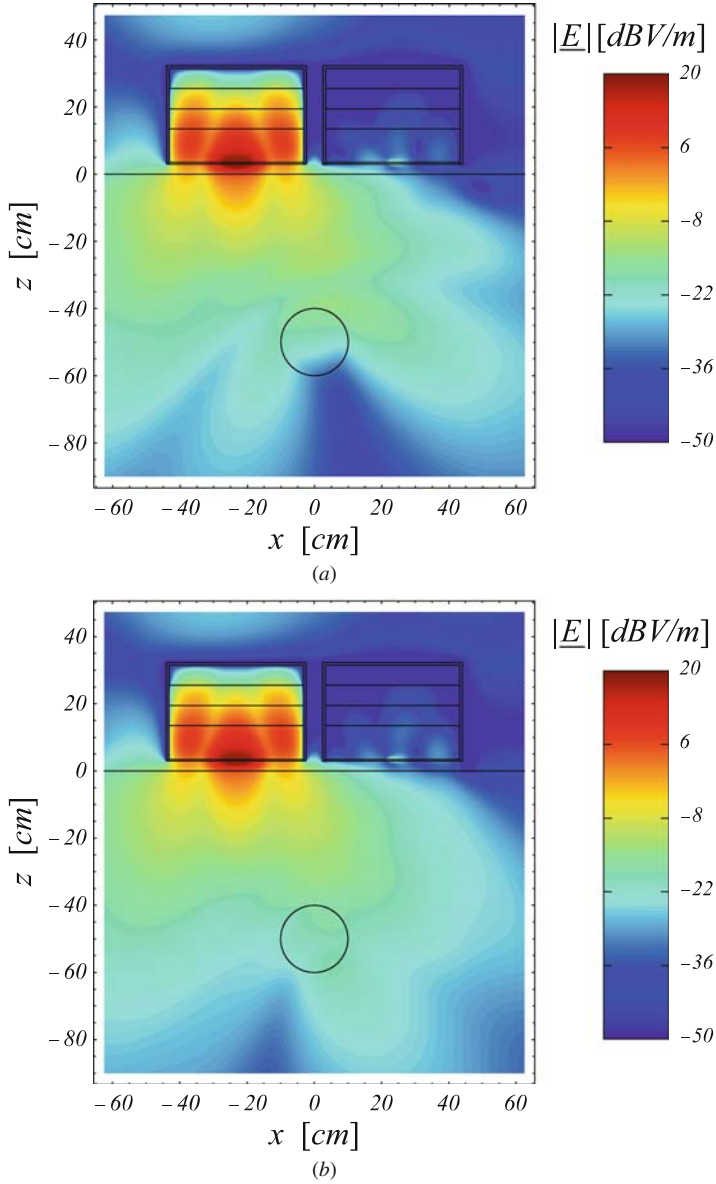
Fig. 5 Spatial distribution of the electric field excited along the vertical cut-plane of the antenna pair elevated over a lossy homogeneous half-space where an infinitely long dielectric pipe, having relative permittivity $\varepsilon_{r_p} = 2$ (**a**) and $\varepsilon_{r_p} = 8$ (**b**), is buried. A significant field focalization effect can be noticed if the buried pipe exhibits a larger relative permittivity. Working frequency $f = 500$ MHz

antenna coupling and the minimal detectable signal should be smaller than the weakest reflection from a thin dielectric pipe on the maximal expected depth.

References

1. A. Taflove and S. C. Hagness, Computational Electrodynamics: The Finite-Difference Time-Domain Method, Artech House, Norwood, 2000.
2. D. Caratelli and R. Cicchetti, A full-wave analysis of interdigital capacitors for planar integrated circuits, IEEE Transactions on Magnetics, vol. 39, pp. 1598–1601, 2003.
3. N. Kaneda, B. Houshmand, and T. Itoh, FDTD analysis of dielectric resonators with curved surfaces, IEEE Transactions on Microwave Theory and Techniques, vol. 45, pp. 1645–1649, 1997.
4. S. Dey and R. Mittra, A conformal finite-difference time-domain technique for modeling cylindrical dielectric resonators, IEEE Transactions on Microwave Theory and Techniques, vol. 47, pp. 1737–1739, 1999.
5. G. Marrocco, M. Sabbadini, and F. Bardati, FDTD improvement by dielectric subgrid resolution. IEEE Transactions on Microwave Theory and Techniques, vol. 46, pp. 2166–2169, 1998.
6. J. Chuma, C. W. Sim, and D. Mirshekar-Syahkal, Computation of resonant frequencies of dielectric loaded rectangular cavity using TLM method. Electronics Letters, vol. 35, pp. 1712–1713, 1999.
7. D. Caratelli, A. G. Yarovoy, and L. P. Ligthart, Full-wave analysis of cavity-backed resistively-loaded bow–tie antennas for GPR applications. Proceedings of the European Radar Conference, pp. 204–207, 2008.

Rigorous Modeling of Electromagnetic Wave Interactions with Large Dense Systems of Discrete Scatterers

E.H. Bleszynski, M.K. Bleszynski, and T. Jaroszewicz

Abstract A fast integral equation approach to numerical modeling of electromagnetic wave penetration through a medium composed of discrete scatterers is described. The method utilizes a periodic extension of the fast Fourier transform-based compression of the impedance matrix. The medium is modeled as a doubly periodic slab, infinite in two lateral directions, and composed of periodicity cells. The individual periodicity cell can be filled with periodically, nearly periodically, or randomly arranged scatterers. Important advantages of the approach are as follows: (i) large-scale calculations with several million unknowns per periodic cell are possible due to the use of the compression scheme; (ii) the approach is equally applicable in a wide range of frequencies, scatterer sizes, and scatterer separations; (iii) the approach facilitates extraction of the effective material parameters and eliminates detrimental effects of boundaries associated with using a finite-size cell as a medium sample; and (iv) the approach is applicable to investigating possible traveling waves in periodic and partly disordered systems.

Keywords Scattering · Integral equation · Periodic extension

1 Introduction

There is a significant interest in developing efficient algorithms for numerical simulation of interaction of electromagnetic waves with media consisting of large collections of discrete scatterers with either random, periodic, or partly disordered spatial distributions. Typical problems requiring such methods are propagation of wideband electromagnetic pulses through random media such as clouds or aerosols, as well as propagation through structured, periodic, or partly periodic materials composed of elements with dielectric and magnetic properties which allow one to attain the desired transmission and reflection properties.

In this paper we describe an efficient integral equation solution method, involving the fast Fourier transform (FFT)-based matrix compression [1], generalized to a laterally infinite periodic system (with the Green function periodic in the two orthogonal lateral directions). The system is modeled as a doubly periodic slab, infinite in two lateral directions, composed of periodicity cells. The

E.H. Bleszynski (✉)
Monopole Research, Thousand Oaks, CA 91360, USA
e-mail: elizabeth@monopoleresearch.com

generalized FFT-based compression scheme is characterized by the O($N \log N$) complexity with a minimal prefactor, where N is the number of unknowns *per periodicity cell*. This allows us to carry out numerical simulations with periodicity cells of several million unknowns. The individual periodicity cell can be filled with periodically, nearly periodically, or randomly arranged scatterers. A large number of unknowns per periodicity cell allow us to achieve a more realistic representation of the medium. We describe the formulation in Section 2. We note that a similar approach has been also applied to large finite periodic systems [2].

Approaches of extending a system of discrete scatterers to a laterally infinite periodic slab have been reported previously in the context of finite-difference methods [3,4] and recently in the context of the fast multipole method (FMM) [5,6]. We note that while the FFT-based compression presented here is ideally suited for dense media, the numerical complexity of the periodic FMM approach [5,6] may be more favorable for sparse materials. However, the FFT-based approach is uniformly valid for a wide range of element sizes and their separations, as well as it is applicable in a wideband frequency range, since it utilizes a frequency-independent multipole expansion. The FMM compression [7,8], on the other hand, requires different matrix compression algorithms in different frequency bands.

We finalize this chapter with two representative applications of the presented method (Section 3):

- Computation of transmission and reflection coefficients for a periodic slab composed of 100 layers of uniformly spaced dielectric spheres. We show that the system supports traveling volumetric waves and exhibits a band gap structure, as well as a very rapidly oscillating resonant behavior in the transmission bands, due to multiple reflection of the traveling waves from the slab faces.
- Extraction of the effective permittivity of a medium composed of randomly and densely distributed discrete dielectric scatterers. The medium is modeled by creating a periodicity cell filled with randomly distributed scatterers and by extending it to a laterally infinite periodic system. We verify that the periodicity does not introduce noticeable artifacts. We also note that the approach eliminates spurious effects due to boundaries of medium samples of finite size used in more conventional methods (see [9,10]).

Our approach can be used in numerous other applications, such as analysis of meta-materials and other composites, photonic crystals, or wave localization in random media.

2 Description of the Method

2.1 Integral Equations and Their Discretization for Periodic Systems

In this section we briefly summarize a problem of electromagnetic wave scattering from a system periodic in two lateral directions (x and y). We consider two types of problems: discrete scatterers in free space and discrete scatterers embedded in a dielectric/magnetic medium.

2.1.1 Discrete Scatterers in Free Space

As described above, we represent the medium as a slab, infinite in two lateral directions and composed of periodicity cells.

We model a periodicity cell (see Fig. 1) as a collection of M disconnected material regions (scatterers), $\mathbf{\Omega}_m$, in free space and confined to the periodicity cell of size $D{\times}D{\times}H$; in fact, the scatterers may also intersect the cell boundaries, provided the periodicity of the configuration is preserved.

Fig. 1 A single periodicity cell comprised of discrete scatterers embedded in free space; D_x denotes the period in the x-direction. The scatterers marked $\boldsymbol{\Omega_2}$ and $\boldsymbol{\Omega'_2}$ form a single object in the periodic system
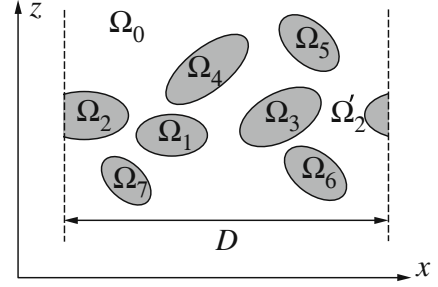
For a *single periodicity cell*, the system satisfies the PMCHWT [11] equations with the transmission boundary conditions on the surfaces of the scatterers[1]:

$$\mathrm{i} \int \mathrm{d}^2 r'\, G(\mathbf{r} - \mathbf{r}')\, W(\mathbf{r}') = -F^{\mathrm{in}}(\mathbf{r}), \tag{1}$$

where W is a vector comprised of electric and magnetic currents supported on interfaces between the consecutive regions Ω_m and the free space $\boldsymbol{\Omega_0}$, F^{in} represents the incident field, and G is a matrix describing couplings of the currents through the appropriate Green functions. We order the elements of the vectors and the matrix to correspond to the consecutive interfaces, $\partial\Omega_1, \ldots, \partial\Omega_M$. Hence, the current (column) vector $W = W(\mathbf{r}')$ has the form

$$W = \begin{bmatrix} W_{\partial\Omega_1} & W_{\partial\Omega_2} & \cdots & W_{\partial\Omega_M} \end{bmatrix}^{\mathrm{T}}, \tag{2}$$

where each of the components $W_{\partial\Omega_m}$ is a vector consisting of the electric and magnetic currents, $W_{\partial\Omega_m} = [\mathbf{J}_{\partial\Omega_m}\mathbf{M}_{\partial\Omega_m}]$. The incident field excites the exterior boundaries of the regions Ω_m, hence

$$F^{\mathrm{in}} = \begin{bmatrix} F^{\mathrm{in}}_{\partial\Omega_1} & F^{\mathrm{in}}_{\partial\Omega_2} & \cdots & F^{\mathrm{in}}_{\partial\Omega_M} \end{bmatrix}^{\mathrm{T}}, \tag{3}$$

with the components representing the incident electric and magnetic fields,

$$F^{\mathrm{in}}_{\partial\Omega_m} = [\mathbf{E}^{\mathrm{in}}_{\partial\Omega_m}\mathbf{H}^{\mathrm{in}}_{\partial\Omega_m}].$$

Finally, each entry in the matrix $G \equiv G(\mathbf{r} - \mathbf{r}')$ represents a coupling of a pair of interfaces (including the coupling of an interface with itself) through the Green function(s) of the region(s) adjacent to both of these interfaces,

$$G = \begin{bmatrix} \widehat{g_0} + \widehat{g_1} & \widehat{g_0} & \cdots & \widehat{g_0} \\ \widehat{g_0} & \widehat{g_0} + \widehat{g_2} & \cdots & \widehat{g_0} \\ \vdots & \vdots & \ddots & \vdots \\ \widehat{g_0} & \widehat{g_0} & \cdots & \widehat{g_0} + \widehat{g_M} \end{bmatrix}. \tag{4}$$

---

[1] Our approach applies also to the case of scatterers covered with thin material sheets. In such problems Eq. (1) contains additional surface current components as well as terms responsible for local current–current couplings.

In (4) hats over the Green functions denote 2×2 matrices

$$
\hat{g}_m(\mathbf{r}) = \begin{bmatrix} Z_0 \left[k \, \mu_m \, g_m(\mathbf{r}) + (k \, \varepsilon_m)^{-1} \, \nabla \, \nabla g_m(\mathbf{r}) \cdot \right] & i \, \nabla \times g_m(\mathbf{r}) \times \\ -i \, \nabla \times g_m(\mathbf{r}) \times & Z_0^{-1} \left[k \, \varepsilon_m \, g_m(\mathbf{r}) + (k \, \mu_m)^{-1} \, \nabla \, \nabla g_m(\mathbf{r}) \cdot \right] \end{bmatrix} \tag{5}
$$

with $Z_0 = \sqrt{\mu_0/\varepsilon_0}$, and the Green function

$$
g_m(\mathbf{r}) = e^{i k \sqrt{\varepsilon_m \mu_m} \, |\mathbf{r}|} / (4\pi \, |\mathbf{r}|), \tag{6}
$$

where ε_m and μ_m are the relative electric permittivity and magnetic permeability of the region Ω_m and k is the free space wave number (our convention is the $exp(-i\omega t)$ time dependence of the fields).

The free space Green function $\hat{g}_0(\mathbf{r})$ of (4) is given by an expression analogous to (5), but with $\varepsilon_m = \mu_m = 1$, and

$$
g_0(\mathbf{r}) = e^{i k |\mathbf{r}|} / (4\pi \, |\mathbf{r}|), \tag{7}
$$

In the case of a *periodic problem* we assume that the incident wave satisfies the pseudo-periodicity condition

$$
\mathbf{E}^{\text{in}}(x + mD, y + nD, z) = e^{i \alpha_0 \, mD + i \beta_0 \, nD} \, \mathbf{E}^{\text{in}}(x,y,z) \tag{8}
$$

(and similarly for the magnetic field), with pseudo-periodicity coefficients $(\alpha_0, \beta_0) \equiv \mathbf{q}_0$. For an incident plane wave, $\mathbf{E}^{\text{in}}(\mathbf{r}) = \mathbf{E}_0^{\text{in}} \, exp(i\mathbf{k} \cdot \mathbf{r})$, $\mathbf{q}_0 = (k_x, k_y)$ is simply given by the transverse component of the free space wave vector $\mathbf{k}$.[2]

In the case of a periodic problem, (1) retains its form, except that the *free space* Green function $\hat{g}_0$ in (4) is replaced by its pseudo-periodic counterpart

$$
\hat{G}_0(\mathbf{r}) = \begin{bmatrix} Z_0 \left[k \, G_0(\mathbf{r}) + k^{-1} \, \nabla \, \nabla G_0(\mathbf{r}) \cdot \right] & i \, \nabla \times G_0(\mathbf{r}) \times \\ -i \, \nabla \times G_0(\mathbf{r}) \times & Z_0^{-1} \left[k \, G_0(\mathbf{r}) + k^{-1} \, \nabla \, \nabla G_0(\mathbf{r}) \cdot \right] \end{bmatrix}, \tag{9}
$$

with G_0 satisfying the relation

$$
G_0(x + mD, y + nD, z) = e^{i \alpha_0 \, mD + i \beta_0 \, nD} \, G_0(x,y,z), \tag{10}
$$

and given, formally, by an infinite series of the functions $g_0(\mathbf{r})$ with arguments shifted by the multiples of the periods and multiplied by phase factors:

$$
G_0(x,y,z) = \sum_{m,n=-\infty}^{\infty} e^{i \alpha_0 \, mD + i \beta_0 \, nD} \, g_0(x - mD, y - nD, z). \tag{11}
$$

We stress that, for the periodic problem, the material Green function $\hat{g}_m$ in (4) remains *non-periodic*, since it only couples currents through the interior of a single scatterer.

---

[2]The formulation applies also to the case when $|\mathbf{q}_0| > k$, which corresponds to propagation of a traveling (non-radiating) wave.

2.1.2 Discrete Inclusions in a Dielectric/Magnetic Medium

The formulation discussed above can be generalized in a variety of ways to describe other physical systems. A typical example involves discrete elements embedded in a laterally infinite slab-type dielectric/magnetic region bounded by periodic (but not necessarily flat) surfaces. Such a system can be modeled by partitioning the slab into periodic cells and introducing explicit equivalent currents on the "upper" and "lower" boundaries of the slab, as well as on the surfaces of the scatterers.

For definiteness, we assume a "slab" region Ω embedded in the free space region Ω_0 and denote its upper and lower boundaries by $\partial\Omega_+$ and $\partial\Omega_-$, respectively. We consider a single periodicity cell of the system and assume it contains a set of M discrete embedded inclusions described as disconnected material regions Ω_m, $1 \leq m \leq M$. An example of such a configuration, for $M = 3$, is shown in Fig. 2, where one of the embedded inclusions intersects the boundary of the periodicity cell.

Fig. 2 A single periodicity cell in a slab-type infinite periodic structure with embedded inclusions; D denotes the period in the x-direction. The scatterers marked $\boldsymbol{\Omega_2}$ and $\boldsymbol{\Omega_2'}$ form a single object in the periodic system
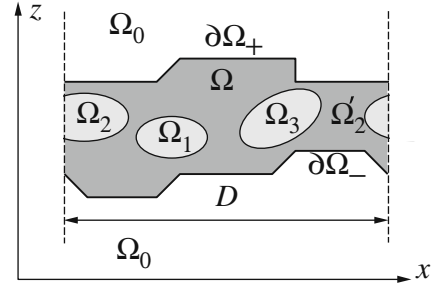
We also assume transmission boundary conditions on the surfaces of the materials (more general electric/magnetic thin-sheet boundary conditions can be treated in a similar way as for scatterers in free space).

As before, integral equations for such a system can be formally written in the form of (1) as follows:

$$\mathrm{i} \int \mathrm{d}^2 r' \, G(\mathbf{r} - \mathbf{r}') \, W(\mathbf{r}') = -F^{\mathrm{in}}(\mathbf{r}). \tag{12}$$

To specify the current vector W and incident field vector F^{in}, we order their elements to correspond to the consecutive interfaces, $\partial\Omega_+, \partial\Omega_-, \partial\Omega_1, \ldots, \partial\Omega_M$. Now W takes the form

$$W = \begin{bmatrix} W_{\partial\Omega_+} & W_{\partial\Omega_-} & W_{\partial\Omega_1} & \cdots & W_{\partial\Omega_M} \end{bmatrix}^{\mathrm{T}}. \tag{13}$$

The incident field excites only the exterior slab boundaries $\partial\Omega_\pm$, hence

$$F^{\mathrm{in}} = \begin{bmatrix} F^{\mathrm{in}}_{\partial\Omega_+} & F^{\mathrm{in}}_{\partial\Omega_-} & 0 \cdots 0 \end{bmatrix}^{\mathrm{T}}. \tag{14}$$

Finally, the impedance matrix takes the form

$$
G = \begin{bmatrix}
\widehat{G}_0 + \widehat{G}_\Omega & \widehat{G}_\Omega & \widehat{G}_\Omega & \cdots & \widehat{G}_\Omega \\
\widehat{G}_\Omega & \widehat{G}_0 + \widehat{G}_\Omega & \widehat{G}_\Omega & \cdots & \widehat{G}_\Omega \\
\widehat{G}_\Omega & \widehat{G}_\Omega & \widehat{g}_1 + \widehat{G}_\Omega & \cdots & \widehat{G}_\Omega \\
\vdots & \vdots & \vdots & \ddots & \vdots \\
\widehat{G}_\Omega & \widehat{G}_\Omega & \widehat{G}_\Omega & \cdots & \widehat{g}_M + \widehat{G}_\Omega
\end{bmatrix} . \tag{15}
$$

Here, the lowercase symbols $\widehat{g}_m$ refer to *non-periodic* Green functions defined in (5) (and describing couplings only through the interior material regions of the scatterers), while the uppercase $\widehat{G}_0$ and $\widehat{G}_\Omega$ are *pseudo-periodic* Green functions of the unbounded free space and the slab material region. $\widehat{G}_\Omega$ is given by expressions analogous to (9), (10), and (11) with G_0 replaced by the Green function of the infinite medium filled with the slab material.

2.2 Computation of the Method-of-Moments Matrix Elements

We compute matrix elements of the integral operator of (4) or (15) by using the Galerkin method with the RWG [12] basis functions defined on triangulated scatterer surfaces. As we discussed, the integral operator involves non-periodic Green functions for the material regions and pseudo-periodic Green functions in the background material and in the free space.

The difficulties in efficient computation of the pseudo-periodic Green functions (such as poor convergence of its series representation) are well known [13]. In our implementation we used a modification of the method described in [14], based on an adaptive application of the Kummer transform, either in spatial or spectral representation, supplemented by the Shanks transform.

However, despite adopting the above-mentioned acceleration algorithms, the direct evaluation of the matrix elements with the pseudo-periodic Green function (10) would still remain computationally quite expensive; a single evaluation of G would have taken several milliseconds. It is, therefore, preferable to tabulate the pseudo-periodic Green functions and to interpolate them when evaluating the integrals. For this purpose, we extract from $G(\mathbf{r})$ its part singular at $\mathbf{r} = 0$

$$
G(\mathbf{r}) = g(\mathbf{r}) + [G(\mathbf{r}) - g(\mathbf{r})] \equiv g(\mathbf{r}) + \Gamma(\mathbf{r}) \tag{16}
$$

and interpolate the regular function $\Gamma(\mathbf{r})$. At the same time, in carrying out singularity subtractions, we use only the singular term $g(\mathbf{r})$.

As a result, we can evaluate the matrix elements as the sum of the usual method-of-moments (MoM) matrix elements A^g with the Green function g and corrections A^Γ with g replaced by Γ. Schematically,

$$
A_{\alpha\beta} \equiv (\psi_\alpha, G\,\psi_\beta) = (\psi_\alpha, g\,\psi_\beta) + (\psi_\alpha, \Gamma\,\psi_\beta) \equiv A^g_{\alpha\beta} + A^\Gamma_{\alpha\beta}, \tag{17}
$$

where ψ_α and ψ_β are basis functions and $(\,\cdot\,,\,\cdot\,)$ denotes the inner product:

$$
(\psi_\alpha, g\,\psi_\beta) = \int \mathrm{d}^2 r_1\, \mathrm{d}^2 r_2\, \psi_\alpha(\mathbf{r}_1)\, g(\mathbf{r}_1 - \mathbf{r}_2)\, \psi_\beta(\mathbf{r}_2). \tag{18}
$$

The matrix elements of A^Γ involve also the gradient of $\Gamma(\mathbf{r})$, which we evaluate as the gradient of the interpolant of Γ. We use, respectively, tri-quadratic and tri-linear interpolations of Γ and $\nabla\Gamma$.

Since Γ and $\nabla\Gamma$ are smooth, the term $A_{\alpha\beta}^{\Gamma}$ can be evaluated by means of the conventional Gaussian quadratures.

We note here that the function Γ, as defined by (16), remains singular at periodic images of the point $\mathbf{r} = 0$, i.e., points $(D,0,0)$, $(0,D,0)$, etc. Therefore, interpolation of the term $\Gamma(\mathbf{r})$ might become inaccurate when the argument $\mathbf{r}$ approaches one of these points. We avoid, however, this difficulty by taking advantage of periodicity, which implies that $(\psi_\alpha, G\psi_\beta) = (\psi_\alpha, G\psi_{\beta'})$ for all periodic replicas $\psi_{\beta'}$ of the basis function ψ_β (we omitted here the pseudo-periodicity phases). We then evaluate the matrix element $(\psi_\alpha, G\psi_{\beta'})$ for that replica $\psi_{\beta'}$ whose support is located closest to the support of ψ_α. In this way the maximum coordinate values of the Green function argument in integral (18) do not exceed $\frac{1}{2}D$ plus the sum of the basis functions' support sizes (which are practically always much smaller than D).

We note that, since we use FFT-based matrix compression (to be discussed in Section 2.4), we do not need to evaluate the MoM (near-field) matrix elements in the vicinity of the singularities of Γ, *provided the near-field range is smaller than the periodicity D*. Should the latter condition be violated, it would be necessary to redefine Γ by subtracting more terms and, accordingly, carry out singularity subtractions not only at $\mathbf{r} = 0$ but also at its images, which would significantly add to the algorithm complexity.

2.3 Preconditioning and Relation to Multiple-Scattering Expansion

In order to accelerate convergence of iterative solutions to the discretized equation (1), we utilize a right-preconditioner Q specified as the inverse of the block-diagonal matrix composed of diagonal blocks coupling each scatterer with itself, i.e., $Q = \mathrm{diag}\left[A_{11}^{-1} A_{22}^{-1} \cdots A_{MM}^{-1}\right]$. The preconditioned matrix has then the form $AQ = I - C$, where the blocks of the matrix C are given by $C_{mm} = 0$ and $C_{mn} = -A_{mn}A_{nn}^{-1}$ for $m \neq n$. By expanding $(AQ)^{-1} = (I - C)^{-1}$ in powers of C, we could generate, precisely, the multiple-scattering expansion of the solution. However, as expected[3] we found in many strong-coupling problems that the multiple-scattering expansion diverges. Instead, we solve the original matrix equation $Ax = b$ as the preconditioned system $AQ\tilde{x} = b$ by means of a minimum-residual iterative method (such as GMRES [15]) and evaluate the final solution as $x = Q\tilde{x}$. This procedure always leads to a convergent result and, in typical problems, the described preconditioning method provides a significant (at least a factor of 5) convergence acceleration. For example, in a typical case of more than 1000 droplets of radii $\lambda/2$, at average relative distances of $\sim 4\lambda$, where λ is the wavelength of the incident wave, we found that the preconditioner reduces the number of iterations (for the residual norm of 1%) from 50 to 5.

2.4 Compression of the Impedance Matrix

In order to be able to handle problems with large numbers of scatterers or scatterers of large sizes, we use a generalization of the FFT-based (AIM [1]) impedance matrix compression. Since the method is standard, we describe it only briefly and emphasize modifications introduced in the periodic case.

As in the non-periodic case, we introduce, for each original basis function $\psi_\alpha(\mathbf{r})$, a "far-field-equivalent" basis function $\widehat{\psi}_\alpha(\mathbf{r})$ constructed as a superposition of point sources located at nearby nodes of a regular Cartesian grid. The strengths of these equivalent sources are chosen such as

---

[3]Divergence of the multiple scattering series has also been observed in other computational techniques, such as the T-matrix methods, and alternative solutions are also used there.

to reproduce, to the desired accuracy, the far field generated by the original basis function; the procedure is here the same as in non-periodic problems.

The matrix elements (17) are then represented as sums of near- and far-field contributions,

$$A_{\alpha\beta} = A_{\alpha\beta}^{\text{Near}} + A_{\alpha\beta}^{\text{Far}}. \tag{19}$$

The term $A_{\alpha\beta}^{\text{Far}}$ is evaluated by replacing the basis functions ψ_α with the far-field-equivalent sources on the Cartesian grid. Hence, the far-field matrix takes the form of a product of two sparse matrices representing mapping between the MoM basis functions and the Cartesian-grid equivalent sources, and a *Toeplitz* matrix representing coupling, through the periodic Green function G, of the nodes of the Cartesian grid. With this form of the matrix, the corresponding term in the matrix-vector multiplication can be evaluated by means of the FFTs.

At small distances between the supports of the basis functions ψ_α and ψ_β the resulting far-field matrix A^{Far} element is, obviously, not a good approximation to the exact MoM matrix element. Therefore, we compute the matrix A^{Near} by means of the (periodic) MoM and subtract from it the far-field matrix elements evaluated in terms of the equivalent sources. By construction, A^{Near} is sparse.

In the case of periodic problems, the above matrix compression procedure involves two new elements:

1. The criterion of the "nearness" of the basis functions is now based on the minimum distance between the supports of the actual basis functions and their periodic replicas. For instance, basis functions whose supports are located near the opposite boundaries of the periodicity cell may be in the near-field range since their periodic replicas are.
2. Another modification of the original algorithm is due to the fact that the Green function appearing in the far-field matrix is periodic in the directions x and y. Therefore, no zero padding is required in these directions, although padding in the z-direction remains. The absence of (x,y) padding results in about fourfold reduction of storage and matrix-vector multiplication time.

In a particular class of cases, where the minimum distance between the scatterers is larger than the near-field range, an even more efficient version of the FFT compression becomes applicable. In these circumstances, all couplings between different scatterers can be described by far-field interactions only. As a result, far-field subtractions in the matrix compression are not necessary, and the matrix fill time is practically negligible (e.g., 1 min for 200,000 unknowns on a single processor).

3 Applications

We discuss two representative applications of the presented approach: (a) computation of a band gap structure of a periodic medium and (b) extraction of effective material parameters from a medium of randomly and densely distributed scatterers.

3.1 Computation of a Band Gap Structure of a Periodic Systems

As one of the applications of our fast solver for periodic systems of scatterers we solved the transmission and reflection problem for an infinite two-dimensional array consisting of diamond spheres arranged in 100 equidistant layers. The ratio of the distance D between the sphere centers to the

sphere radius is $D/a = 0.45$, hence the spheres are densely packed. The relative electric permittivity of the spheres is $\varepsilon = 5.84$. The interest in this system is based on the fact that it is expected to support propagation of volumetric traveling waves [16,17].

In Fig. 3 we show the absolute value of the computed reflection coefficient R for the system as the function of the quantity kD in the range from $kD = 1.5$ to 3.5. The plot shows a well-defined band gap ($R \simeq 1$) in the range $1.96 \leq kD \leq 2.24$ and another gap starting at $kD = 3.2$. Outside the gaps, the transmission coefficients exhibit rapid resonant oscillations due to propagation of the traveling waves across the slab and their reflection from the slab boundaries. The rapid oscillations of R required computation for about 950 frequencies. The results are in agreement with those of [16,17], in which scattering on a single sphere was described analytically by the P-wave amplitudes.
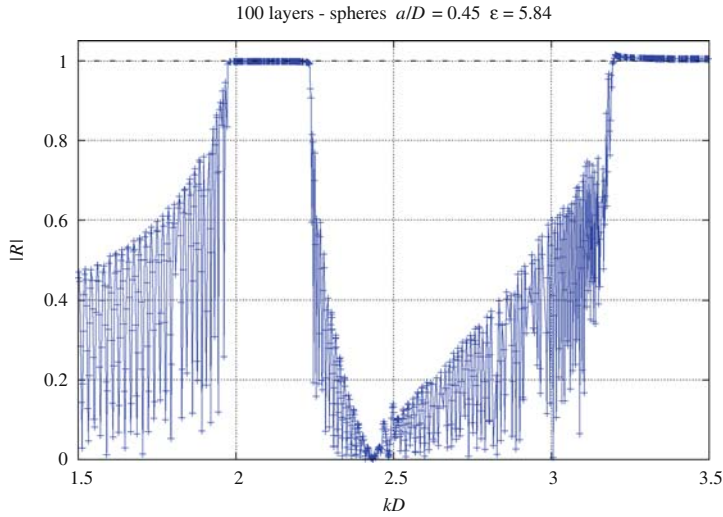
Fig. 3 The absolute values of the reflection coefficients R for a periodic slab containing 100 layers of spherical dielectric scatterers, plotted as the function of kD, where D is the distance between the scatterer centers

3.2 Extraction of Effective Material Parameters from Discrete Random Systems

3.2.1 Extraction of Effective Material Parameters from a Finite Sample of a Discrete Medium

Another of our goals in modeling periodic systems is to extract information on a behavior of large sets of randomly distributed scatterers. A typical problem is evaluation of reflection (R) and transmission (T) coefficients for a plane wave incident on a large slab of thickness H, filled with discrete scatterers. From the H dependence of R and T one can then extract information on the effective material properties. In particular, we may relate the transmission coefficient to the computed total scattering cross section $\sigma_{\mathrm{t}}(A)$ on a slab cell of lateral area A and parameterize it in terms of the mean free path ℓ. We find then

$$T_A\left(H\right) = 1 - \frac{\sigma_{\mathrm{t}}(A)}{2A} \simeq \mathrm{e}^{-\frac{1}{2}H/\ell}, \tag{20}$$

where the mean free path ℓ is understood as a complex (predominantly real) number. On the other, we can model the (infinite) slab as a dielectric of a certain effective permittivity ε_{eff} and obtain a relation $\ell^{-1} = -2\,\mathrm{i}\,k\left(\sqrt{\varepsilon_{\text{eff}}} - 1\right)$.

However, it is difficult to achieve an adequate accuracy in effective material parameter extraction by considering finite slabs, or slab cells, playing the role of "containers" holding discrete scatterers: Since we are filling a slab cell with discrete scatterers of some radii a, there is always an ambiguity in treating scatterers near the container surface; e.g., requiring that entire scatterers or only their "centers" (if they can be uniquely defined) are located inside the cell. Thus, necessarily, the cell sizes D and H are defined only to the accuracy $\sim a$. To reduce the geometrical error, we have to require D and H large compared to a, and since, for dense media, the mean free path is comparable to the scatterer size, we also have to require a large optical slab thickness.

As a result, when we increase H and the slab becomes more and more intransparent, the relative size of the boundary to the area contributions to the amplitude increases exponentially with H and, eventually, we are not probing the intrinsic properties of the medium, but rather the geometrical shape of the sample.

A possible way of reducing the error due to diffraction is to compare "containers" of the same shape and size, filled either with discrete scatterers or a continuous effective medium (see, e.g., [9,10] for spherical containers). Nevertheless, the error due to the uncertainty in the geometrical size of the random medium sample may remain significant.

As an example, consider a finite slab cell of lateral area $A = D^2$ and thickness H and suppose the diffractive effects of the slab boundaries can be neglected. If then we extract the mean free path by using (20) and require a relative error $\delta\ell/\ell$ in the extracted value, the errors in the cross section and area must satisfy[4]

$$\left|\frac{\delta\sigma_{\text{t}}}{\sigma_{\text{t}}} - \frac{\delta A}{A}\right| < T\,|lnT|\,\left|\frac{\delta\ell}{\ell}\right| \equiv C\left|\frac{\delta\ell}{\ell}\right|. \tag{21}$$

For instance, if $T = 0.01$, the coefficient in the expression above is $C \simeq 0.046$, and a 10% error in ℓ implies $\delta A/A = 2\,\delta D/D < 0.005$ and the uncertainty in the forward-scattering differential cross section $\delta\widehat{\sigma} < 0.04$ dB (the latter relation follows from $|\sigma_{\text{t}}| \sim \sqrt{10^{\widehat{\sigma}/10}}$). Since the uncertainty in the sample size is $\delta D \sim a$, the first of the conditions requires large D/a and the second necessitates a very high accuracy in the cross-sectional computation.

3.2.2 Extraction of Effective Material Parameters in the "Periodic Slab" Model

The difficulties in extracting effective material parameters from the behavior of finite-size medium samples largely disappear in our approach, i.e., in modeling a medium slab as a periodic structure. Periodic boundary conditions eliminate effects of lateral cell boundaries, and the low computational cost of the fast solution algorithm allows us to work with a sizable optical thickness of the slab and its sizable thickness in terms of the scatterer size (in the example discussed below we reach $H/\mathrm{Re}\,\ell \sim <$ 15.5 and $H/a \sim < 14$). However, the periodic slab model itself may, potentially, introduce artifacts through periodicity; we discuss this question below.

A critical problem in modeling a particulate medium as a periodic slab is to ensure that the results (e.g., the transmission and reflection coefficients) are not distorted by artifacts of periodicity. For instance, we should check that, e.g., $T(D,H;\gamma_D) \simeq T(2D,H;\gamma_{2D})$, i.e., that the reflection

---

[4]We also notice that, since the cross section $\sigma_{\text{t}}(A)$ is close to its geometrical limit $2A$, even small errors may cause the computed transmission coefficient to become negative.

coefficient for a cell of size D and a scatterer configuration γ_D is approximately the same as for a cell of size $2D$ and a scatterer configuration γ_{2D}. The difficulty in carrying out such tests quantitatively is, obviously, due to the fact that there must be some dependence of the results on the scatterer configurations γ. The criterion we use in assessing the applicability of the model is then that the difference between a given observable computed for different cell sizes should be comparable to the difference due to various scatterer configurations for the same cell, i.e., $|T(D,H;\gamma_D) - T(2D,H;\gamma_{2D})| \simeq |T(D,H;\gamma_D) - T(D,H;\gamma'_D)|$. Figure 4 shows that in our example this criterion holds: The difference between the results for the two cell sizes, $D = 3.6$ and $7.2\ \mu m$, is less than the statistical spread of computed points for the smaller cell size ($D = 3.6\ \mu m$).

Below we present some results of computations of the transmission coefficient T for single cells filled with discrete dielectric scatterers (spheres) in the non-periodic model and for the same cells in the periodic slab model. We have chosen parameters corresponding to very strong scattering, resulting in the mean free path ℓ comparable to the average distances between the scatterers. We considered the wavelength $\lambda = 1.5\ \mu m$ and took, as the scatterers, spheres of radii $a = 0.26\ \mu m$ and $\lambda = 0.102 + i\ 0.092$ (we do not consider this permittivity value realistic – it was merely chosen to ensure strong interactions). In generating random distributions of scatterers we chose the desired average scatterer–scatterer distance (always measured between the centers of scatterers) as $R_a = 0.65\ \mu m$ (the actually obtained average distances were slightly larger), and the minimum distance was set to $R_m = 0.55\ \mu m$ and achieved almost exactly. The number density of the scatterers was practically the same in all the configurations. With these parameters, the spheres are very closely packed and the mean free path is comparable to the inter-scatterer separation ($\mathrm{Re}\ell \simeq 0.649\ \mu m \simeq 1.18\,R_m$). The cell sizes were $D \times D \times H$ with $D = 3.6, 7.2$, and $0.6\ \mu m \leq H \leq 4.2\ \mu m$. For each of the cell sizes we generated at least 5 (usually 10 or more) different random configurations of scatterers.

A representative sample of the results is shown in Fig. 4, where we plot values of the transmission coefficient $|T|$, as a function of H, for the first five scatterer configurations, in order to indicate
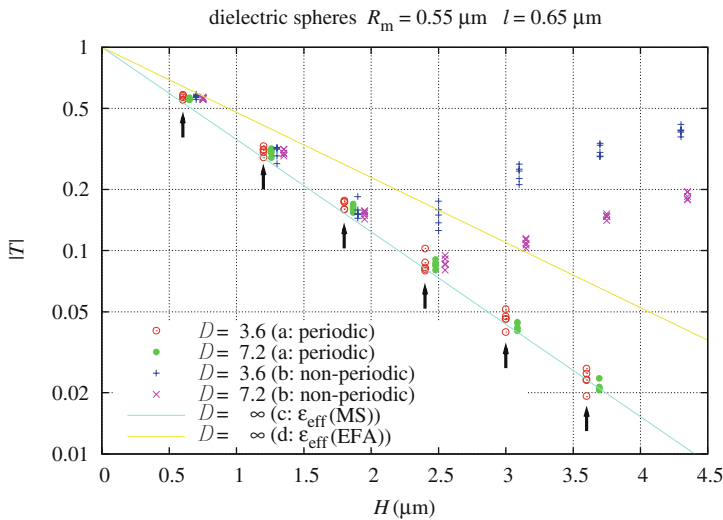
Fig. 4 The absolute values of the transmission coefficients T for periodic and non-periodic finite slabs filled with discrete scatterers. The data points are spread horizontally for better visibility; the actual values of the thickness H are indicated by *arrows*. Further details are described in the text

their typical statistical spread (similar results are obtained for the phase of *T*). The results can be summarized as follows:

- Numerical results obtained for the *periodic* slab with cells of sizes $D = 3.6$ and 7.2 µm are practically indistinguishable (cases marked (a) in Fig. 4). This indicates that the extension of the sample to the infinite periodic slab does not introduce noticeable artifacts.
- Numerical results obtained for finite, *non-periodic* cells of sizes $D = 3.6$ and 7.2 µm (cases marked (b) in Fig. 4) indicate that for thickness H exceeding about three mean free path lengths, the transmission coefficient starts displaying growing contributions from diffraction on the sample boundary, and hence the results become unreliable.
- The straight line (case marked (c) in Fig. 4) represents the fit of the periodic model transmission coefficient (data points (a)) with an exponential. It yields the multiple-scattering effective permittivity $\varepsilon^{(MS)}_{eff} = (0.9101 \pm 0.0024) + i(0.4810 \pm 0.0021)$.
- The straight line (case marked (d) in Fig. 4) represents predictions for the transmission coefficient obtained with the effective field approximation (EFA [18]) permittivity value $\varepsilon^{(EFA)}_{eff} = 0.896 + i\,0.339$, based on the forward-scattering amplitude for a single scatterer. The difference between the EFA- and multiple-scattering-based values of the permittivity is evidently significant.

Our example also shows that for simulations in which $|T|$ is small, the periodic slab model is much more economical than non-periodic cell models. A more detailed analysis indicates that, in order to reach the level $|T| \leq 0.02$ by using finite-size samples from the considered set, the minimum transverse size would have to be at least $D \geq 57.6$ µm. With the corresponding thickness $D = 3.6$ µm the number of scatterers would be at least about 33,000. The same accuracy can be obtained in the periodic model for the cell size $D = 7.2$ µm (or even $D = 3.6$ µm) with no more than 600 scatterers. Therefore, taking into account the additional fourfold cost saving in the periodic problem (no need of zero padding in the FFTs), the computational advantage of the periodic model over the non-periodic one is given by the factor of at least $4 \times (57.6/7.2)^2 = 256$.

4 Summary

We described an efficient numerical approach to computing scattering of electromagnetic waves on a periodic system of discrete dielectric/magnetic scatterers.

The method can be applied in a straightforward way to simulate scattering on a system strictly periodic in two dimensions. We described such an example in Section 3.1, where we considered scattering of a wave on a slab of periodically distributed diamond spheres of a finite but large thickness (100 layers of scatterers, hence each periodicity cell contains a set of 100 scatterers). We found effects of propagation of traveling waves in the slab and determined positions of band gaps, in which the slab becomes intransparent.

We also applied our approach to simulation of scattering on random distributions of scatterers and to extraction of the effective parameters of the medium. In this case the periodicity cell contains a large number of randomly distributed scatterers. We found that periodicity does not introduce spurious effects in determination of the effective medium parameters (differences between results for various cell sizes are smaller than the statistical spread of results for a fixed cell size). At the same time, periodicity eliminates detrimental effects of lateral boundaries appearing in computations for finite-size samples and allows us to achieve a high accuracy at a much lower cost than in comparable computations for finite samples of the medium.

In both types of applications the FFT-based compression utilized in our solver results in the algorithm complexity $O(N \log N)$, where N is the number of unknowns per periodicity cell.

References

1. E. Bleszynski, M. Bleszynski, and T. Jaroszewicz, AIM: adaptive integral method for solving large-scale electromagnetic scattering and radiation problems, Radio Science, vol. 31, pp. 1225–1251, 1996.
2. E. Bleszynski, M. Bleszynski, and T. Jaroszewicz, BLock-Toeplitz fast integral equation solver for large finite periodic and partially periodic array systems, IEICE Transactions on Electronics, vol. E87-C, pp. 1586–1594, 2004.
3. K. Kärkkäinen, A. Sihvola, and K. Nikoskinen, Analysis of a three-dimensional mixture with finite difference method, IEEE Transactions on Geoscience and Remote Sensing, vol. 39, pp. 1013–1018, 2001.
4. L. Jylhä and A. Sihvola, Microstructure-based numerical modeling method for effective permittivity of ceramic/polymer composites, Journal of Applied Physics, vol. 97, pp. 1041041–1041047, 2005.
5. Y. Otani and N. Nishimura, An FMM for periodic boundary value problems for cracks for Helmholtz' equation in 2D, International Journal for Numerical Methods in Engineering, vol. 73, pp. 381–406, 2008.
6. Y. Otani and N. Nishimura, A periodic FMM for Maxwell's equation in 3D and its applications to problems related to photonic crystals, Journal of Computational Physics, vol. 227, pp. 4630–4652, 2008.
7. R. Coifman, V. Rokhlin, and S. Wandzura, The fast multipole method for the wave equation: a pedestrian prescription, IEEE Antennas and Propagation Magazine, vol. 35, pp. 7–12, 1993.
8. H. Cheng, W. Y. Crutchfield, Z. Gimbutas, L. F. Greengard, J. F. Ethrigde, J. Huang, V. Rokhlin, N. Yarvin, and J. Zhao, A wideband fast multipole method for the Helmholtz equation in three dimensions, Journal of Computational Physics, vol. 216, pp. 300–325, 2006.
9. B. E. Barrowes, C. O. Ao, F. L. Teixeira, J. A. Kong, and L. Tsang, Monte Carlo simulation of electromagnetic wave propagation in dense random media with dielectric spheroids, IEICE Transactions on Electronics, vol. E83-C, pp. 1797–1802, 2000.
10. I. Bogaert and F. Olyslager, Exact full-wave simulation of finite pieces of metamaterials and extraction of effective material parameters, Proceedings of Metamaterials 2007, University "Rome Tre", 2007, pp. 609–612.
11. A. J. Poggio and E. K. Miller, Integral equation solution of 3-dimensional scattering problems, p. 218, in R. Mittra (ed.), Computer Techniques for Electromagnetics, Pergamon Press, Oxford, New York, 1973.
12. S. M. Rao, D. R. Wilton, and A. W. Glisson, Electromagnetic scattering by surfaces of arbitrary shape, IEEE Transactions on Antennas and Propagation, vol. AP-30, pp. 409–418, 1982.
13. G. Valerio, P. Baccarelli, P. Burghignoli, and A. Galli, Comparative analysis of acceleration techniques for 2-D and 3-D Green's functions in periodic structures along one and two directions, IEEE Transactions on Antennas and Propagation, vol. 55, pp. 1630–1643, 2007.
14. N. Guérin, S. Enoch, and G. Tayeb, Combined method for the computation of the doubly periodic Green's function, Journal of Electromagnetic Waves and Applications, vol. 15, pp. 205–221, 2001.
15. Y. Saad and M. H. Schultz, GMRES: a generalized minimal residual algorithm for solving nonsymmetric linear systems, SIAM Journal on Scientific and Statatistical Computing, vol. 7, pp. 856–869, 1986.
16. R. A. Shore and A. D. Yaghjian, Traveling waves on two- and three-dimensional periodic arrays of lossless scatterers, Radio Science, vol. 42, RS6S21, pp. 1–40, 2007.
17. R. A. Shore and A. D. Yaghjian, Correction to "Traveling waves on two- and three-dimensional periodic arrays of lossless scatterers", Radio Science, vol. 43, RS2S99, pp. 1–1, 2007.
18. L. L. Foldy, The multiple scattering of waves: I. General theory of isotropic scattering by randomly distributed scatterers, Physical Review, vol. 67, no. 3,4, pp. 107–119, 1945.

A Hybrid Method for Solving 2-D Inverse Scattering Problems

A. Semnani and M. Kamyab

Abstract In this chapter, hybrid method for solving two-dimensional inverse scattering problems is illustrated. In this method, a two-step optimization-based routine is used in which direct and expansion methods are utilized simultaneously to obtain more precise and fast reconstruction. In the first step, a coarse solution is achieved with the help of truncated cosine Fourier series expansion method. Then, with this solution as an initial guess for the second step, direct optimization is used to obtain a much more accurate solution of the problem. In both steps, finite difference time domain and differential evolution are used as an electromagnetic solver and global optimizer, respectively. The most important advantage of this method is that because of a suitable initial answer in direct optimization routine, sensitivity of the algorithm to the regularization parameter is decreased and convergence of the results is completely guaranteed. Performance of the proposed method is demonstrated for several two-dimensional relative permittivity profile reconstruction cases.

1 Introduction

Inverse problems are inherently nonlinear and ill-posed [1,2]. Therefore, these problems are usually considered in global optimization-based procedures and regularization terms are used to conquer the ill-posedness [3–5]. The general form of the cost function for optimization routine can be considered as

$$F = \sum_{i=1}^{I} \sum_{j=1}^{J} \sum_{t=0}^{T} \left\| \vec{E}_{ij}^{\text{sim}}(t) - \vec{E}_{ij}^{\text{meas}}(t) \right\|^2 + \lambda \times R(\varepsilon_r, \sigma, \mu), \tag{1}$$

in which, $\vec{E}_{ij}^{\text{sim}}$ and $\vec{E}_{ij}^{\text{meas}}$ are simulated and measured fields, respectively, $R(\varepsilon_r, \sigma, \mu)$ is the regularization term, and λ is the regularization factor. I and J are the number of transmitters and receivers, respectively, and T is the total time of measurement.

———————————

A. Semnani (✉)
Department of Electrical Engineering, K. N. Toosi University of Technology, Tehran, Iran
e-mail: a_semnani@eetd.kntu.ac.ir

Unfortunately, the conventional methods have two main drawbacks. The first is huge number of the unknowns especially in two-dimensional (2-D) and three-dimensional (3-D) cases which increases not only the amount of computations but also the degree of ill-posedness. The other disadvantage is the determination of regularization factor which is not straightforward at all.

It has been shown that instead of direct optimization of the unknowns, it is possible to expand them in terms of a complete set of orthogonal basis functions and optimize the coefficients of this expansion [6,7]. However, disadvantage of the expansion method is the imperfect accuracy due to limited number of expansion terms that are used.

In this chapter, hybrid method [8] for fast and accurate solving of 2-D inverse scattering problems is investigated. In the proposed method, a coarse solution is obtained by choosing relatively small number of terms in an expansion routine in the first step. Then, based on this answer as the initial guess of the direct optimization problem, a much more accurate solution is obtained in the second step.

A general form of the problem and a brief overview of truncated cosine Fourier series expansion method are presented in Section 2. In Section 3, the hybrid method is introduced and its advantages over direct and expansion methods are discussed. Finally in Section 4, several 2-D inhomogeneous case studies are considered and efficiency of the algorithm is studied for them.

2 Truncated Cosine Fourier Series Expansion Method

As a general case of the problem, we consider the relative permittivity profile reconstruction of an inhomogeneous 2-D medium surrounded by known media (free space here) as shown in Fig. 1.

The flowchart of the expansion method is presented in Fig. 2. If cosine basis functions are used for 2-D cases, the expansion of the relative permittivity profile in $x - y$ plane which is assumed to be homogeneous along z is expressed as
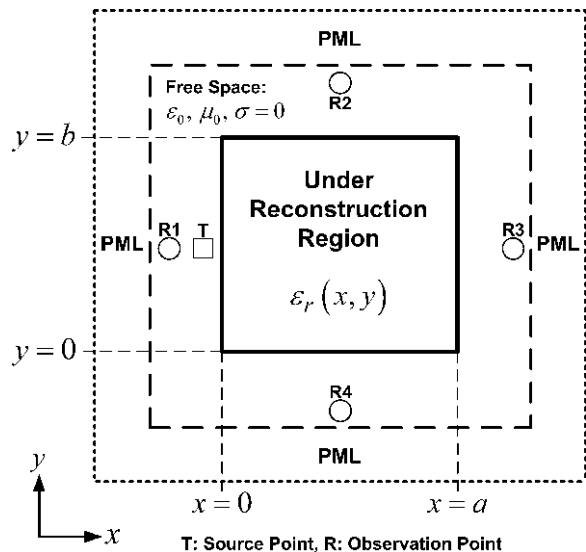
Fig. 1 Geometrical configuration of the problem [7]
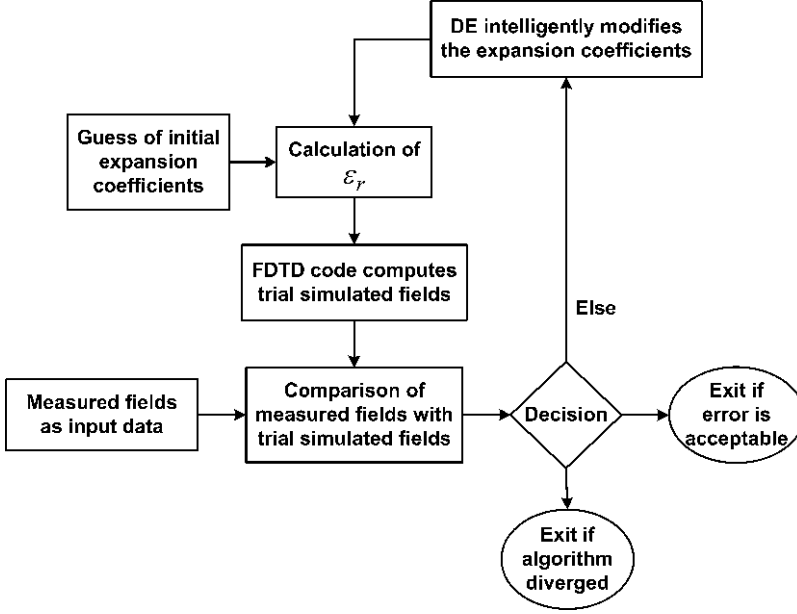
Fig. 2 Flowchart of expansion method [7]

$$\varepsilon_r\,(x, y) = \sum_{n=0}^{N} \sum_{m=0}^{M} d_{nm} \cos\left(\frac{n\pi}{a}x\right) \ \cos\left(\frac{m\pi}{b}y\right), \tag{2}$$

where a and b are the dimensions of the problem in the x- and y-directions, respectively, and the coefficients, d_{nm}, are to be optimized. In this case, the number of optimization parameters is $(N + 1) \times (M + 1)$ in comparison with conventional direct optimization methods in which this number is equal to the number of grid points of the problem. This results in a considerable reduction in the amount of computations.

There are some additional useful relations that can be applied during the optimization routine to have easier convergence [7]. If it is assumed that the relative permittivity has limited range of variation, i.e.,

$$1 \le \varepsilon_r\,(x, y) \le \varepsilon_{r,\,\text{max}}, \tag{3}$$

Then, we have

$$1 \le d_{00} \le \varepsilon_{r,\,\text{max}}, \tag{4}$$

$$1 \le \sum_{n=0}^{N} \sum_{m=0}^{M} d_{nm} \le \varepsilon_{r,\,\text{max}}, \tag{5}$$

$$1 \le \sum_{n=0}^{N} \sum_{m=0}^{M} (-1)^{n+m} d_{nm} \le \varepsilon_{r,\,\text{max}}, \tag{6}$$

and

$$1 \leq \sum_{n=0}^{N} \sum_{m=0}^{M} |d_{nm}|^2 \leq \varepsilon_{r,\max}^2.$$ (7)

As discussed in sensitivity analysis of expansion method in [7], small values of expansion terms reduce the accuracy of reconstruction, while large values cause oscillatory response or even divergence of the solution. Therefore, although the expansion algorithm leads to a fast reconstruction with a substantial reduction in the amount of computations, an important weakness is the imperfect accuracy due to limited number of expansion terms that can be used.

3 Hybrid Method

In order to obtain more precise reconstruction and improved well-posedness of the problem simultaneously, it is possible to use a two-step hybrid algorithm. This hybrid method benefits from advantages of both expansion and direct methods in solving inverse scattering problems. The flowchart of the hybrid algorithm is shown in Fig. 3. According to this flowchart, in the first step (expansion method), a coarse solution is obtained by choosing relatively small number of terms in a small number of iteration in an expansion routine. Then, taking this rough answer as the initial guess for direct optimization problem, a much more accurate solution is obtained in the second step (direct method). In both steps, finite difference time domain (FDTD) [9] and differential evolution (DE) [10] are used as electromagnetic solver and global optimizer routine, respectively. Because of a reliable initial estimation in direct optimization procedure, the probability of divergence of the optimization in second step is completely eliminated and the algorithm converges quickly.

4 Numerical Results

Performance of the hybrid method is studied for two different inhomogeneous and lossless case studies. For each case, direct and hybrid methods are compared in terms of the number of optimization iteration and reconstruction precision.

To make a better comparison between the methods, a supplementary evaluation function is defined as

$$E = \left[\frac{\sum_{p=1}^{P} \sum_{q=1}^{Q} \left(X_{\mathrm{org}}(p,q) - X_{\mathrm{rec}}(p,q) \right)^2}{\sum_{p=1}^{P} \sum_{q=1}^{Q} X_{\mathrm{org}}^2(p,q)} \right]^{1/2},$$ (8)

where P and Q are the numbers of FDTD grid points in the x- and y-directions, respectively. Also, X_{org} and X_{rec} are the original and reconstructed values, respectively.
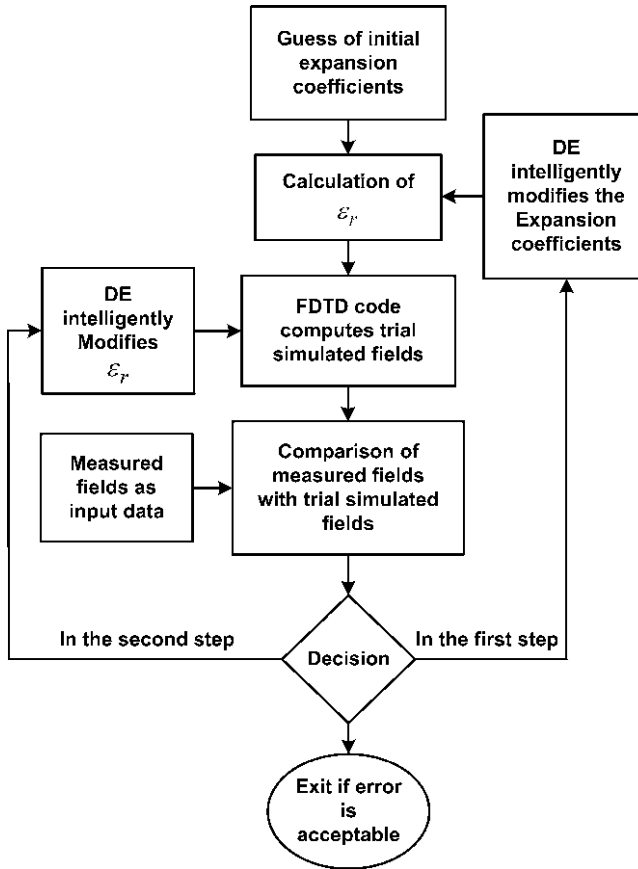
Fig. 3 Flowchart of hybrid method [8]

In the simulations of all test cases, one transmitter and four receivers are considered around the under-reconstruction region as shown in Fig. 1. Concerning the DE implementation, the population is chosen equal to 100 and the maximum iteration is considered to be 600 (equal to 300 for each steps of hybrid method). The mutation parameter and crossover probability are set to 0.5 and 0.8, respectively. The number of time steps is limited to 300 and a Gaussian waveform is used as the source of excitation.

4.1 Case Study No. 1

In the first sample case, we consider an inhomogeneous medium consisting of 10×10 cells. For the expansion method, the numbers of expansion terms in both directions are set to 5.

The original profile and reconstructed profiles by expansion, hybrid, and direct methods with the aid of total variation (TV) regularization [7,11] are shown in Fig. 4(a)–(d). It is seen that a suitable
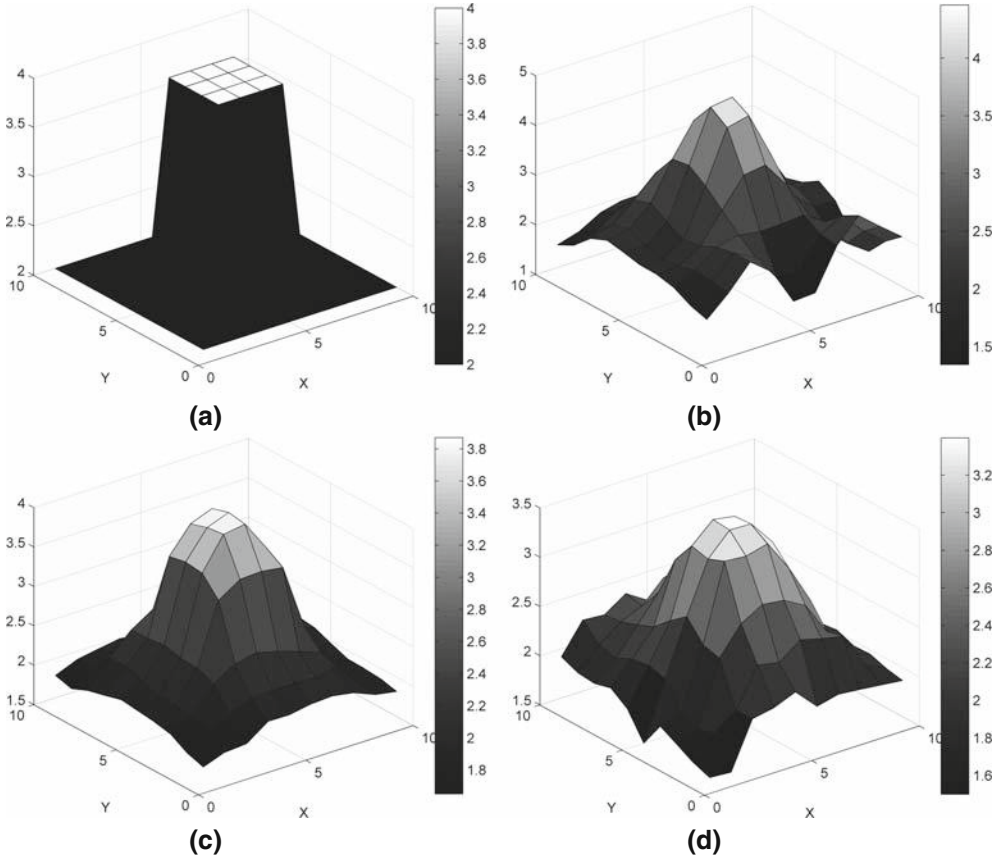
Fig. 4 Permittivity profile reconstruction of case study no. 1. (**a**) Original profile and reconstructed by (**b**) expansion method, (**c**) hybrid method, and (**d**) direct method

initial answer in hybrid method leads to a better reconstruction in comparison with direct method in a relatively small number of iterations.

4.2 Case Study No. 2

In the second example, another lossless and inhomogeneous medium again with 10×10 cells is considered. Again, the numbers of expansion terms in both directions are chosen equal to 5. The original profile and reconstructed profiles by expansion, hybrid, and direct methods with the aid of TV regularization are shown in Fig. 5(a)–(d), respectively. Again, it is observed that with the same condition of optimization parameters, hybrid method has better result in comparison with the direct optimization of the unknowns.

The values of evaluation function of all methods for both test cases are presented in Table 1. It is clearly seen that using hybrid method leads to less reconstruction error in comparison with direct method.
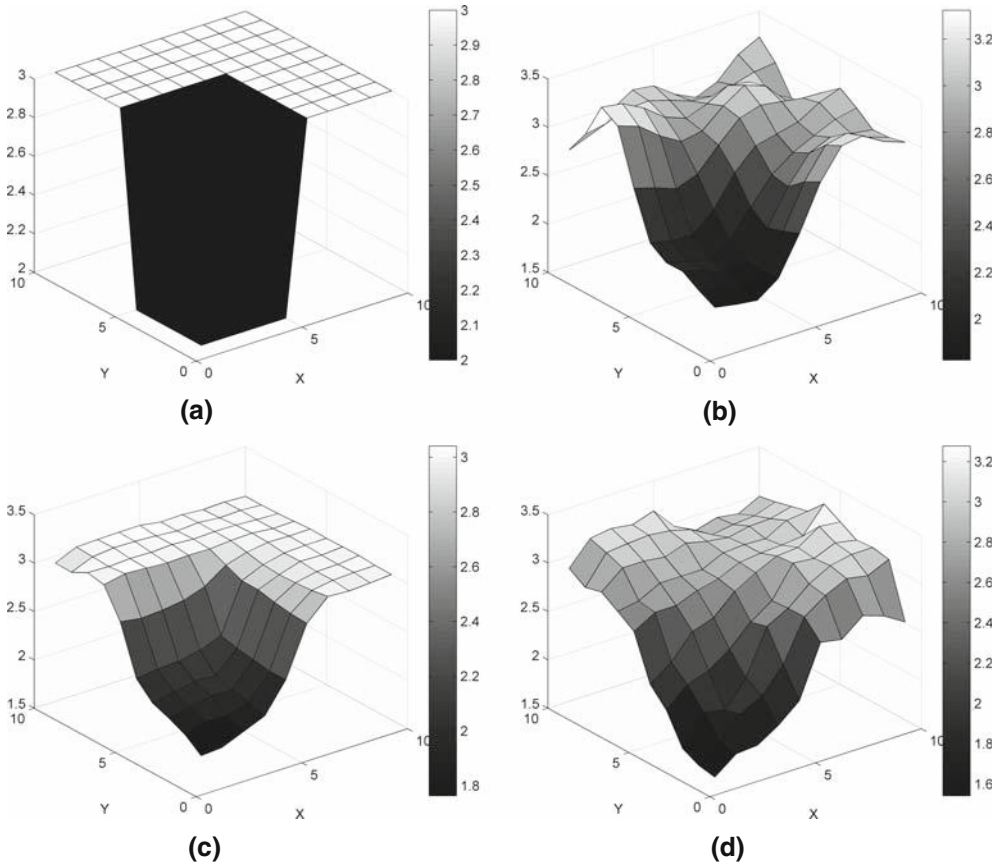
Fig. 5 Permittivity profile reconstruction of case study no. 2. (**a**) Original profile, reconstructed by (**b**) expansion method, (**c**) hybrid method, and (**d**) direct method

Table 1 Values of evaluation function of all methods for both test cases

	Expansion method (300 iterations)	Hybrid method (300 iterations)	Direct method (600 iterations)
Case study no. 1	0.1717	0.1290	0.1897
Case study no. 2	0.0650	0.0483	0.0749

5 Conclusion

An efficient technique which is based on combination of the truncated cosine Fourier series expansion and direct optimization methods has been studied for 2-D reconstruction problem. Both expansion and direct methods have limitations on precision and well-posedness, respectively. It has been shown that with the aid of hybrid method, it is possible to use the advantages of both methods in a single hybrid procedure to conquer the above limitations and solve the inverse scattering problems more quickly and accurately. The method has been examined for reconstruction of two inhomogeneous case studies. The results show that the hybrid method is able to reconstruct the unknown media

successfully with more precision and less probability of ill-posedness in comparison with expansion and conventional direct methods, respectively.

References

1. T. J. Cui, W. C. Chew, X. X. Yin, and W. Hong, Study of resolution and super resolution in electromagnetic imaging for half-space problems, IEEE Transactions on Antennas and Propagation, vol. 52, no. 6, pp. 1398–1411, 2004.
2. M. Donelli, G. Franceschini, A. Martini, and A. Massa, An integrated multiscaling strategy based on a particle swarm algorithm for inverse scattering problems, IEEE Transactions on Geoscience and Remote Sensing, vol. 44, no. 2, pp. 298–312, 2006.
3. M. Popovic and A. Taflove, Two-dimensional FDTD inverse-scattering scheme for determination of near-surface material properties at microwave frequencies, IEEE Transactions on Antennas and Propagation, vol. 52, no. 9, pp. 2366–2373, 2004.
4. I. T. Rekanos and A. Raisanen, Microwave imaging in the time domain of buried multiple scatterers by using an FDTD-based optimization technique, IEEE Transactions on Magnetics, vol. 39, no. 3, pp. 1381–1384, 2003.
5. M. Donelli and A. Massa, Computational approach based on a particle swarm optimizer for microwave imaging of two-dimensional dielectric scatterers, IEEE Transactions on Microwave Theory and Techniques, vol. 53, no. 5, 1761–1776, 2005.
6. A. Semnani and M. Kamyab, An enhanced method for inverse scattering problems using Fourier series expansion in conjunction with FDTD and PSO, Progress in Electromagnetics Research, vol. 76, pp. 45–64, 2007.
7. A. Semnani and M. Kamyab, Truncated cosine Fourier series expansion method for solving 2-D inverse scattering problems, Progress in Electromagnetics Research, vol. 81, pp. 73–97, 2008.
8. A. Semnani and M. Kamyab, An enhanced hybrid method for solving inverse scattering problems, Thirteenth Biennial IEEE Conference on Electromagnetic Field Computations (IEEE CEFC 2008), Athens, Greece, May 2008.
9. A. Taflove and S. C. Hagness, Computational Electrodynamics: The Finite-Difference Time-Domain Method, 3rd ed., Artech House, Norwood, MA, 2005.
10. R. Storn and K. Price, Differential evolution – a simple and efficient heuristic for global optimization over continuous space, Journal of Global Optimization, vol. 11, no. 4, pp. 341–359, 1997.
11. A. Abubakar and P. M. Van Den Berg, Total variation as a multiplicative constraint for solving inverse problems, IEEE Transactions on Image Processing, vol. 10, no. 9, pp. 1384–1392, 2001.

Time-Reversal-Based Signal Processing Techniques for Ultra-wideband Electromagnetic Imaging

M.E. Yavuz and F.L. Teixeira

Abstract Remote sensing of obscured objects has withdrawn attention from numerous fields. Depending on the nature of the specific applications, various approaches employing acoustical or electromagnetic (EM) waves have been developed. One such approach is the time-reversal (TR) technique which has originally been introduced in acoustics and involves the retransmission of signals acquired by a set of transceivers in a time-reversed fashion to exploit the invariance of the wave equation under TR. In this work, we review the TR-based signal processing techniques to achieve ultra-wideband (UWB) EM detection and imaging for distinct objects (targets) embedded in inhomogeneous media.

Keywords Time-reversal · Ultra-wideband electromagnetic waves · Time-domain DORT method · Space-frequency (SF) imaging · Statistical stability

1 Introduction

Remote sensing of obscured objects has withdrawn attention from numerous fields. Depending on the nature of the specific applications, various approaches employing acoustical or electromagnetic (EM) waves have been developed. One such approach is the time-reversal (TR) technique which has originally been introduced in acoustics [1] and involves the retransmission of signals acquired by a set of transceivers in a time-reversed fashion to exploit the invariance of the wave equation under TR (in lossless and stationary media). Among the unique capabilities TR offers are the super-resolution and statistical stability in inhomogeneous media which are not possible via the classical imaging methods utilizing the narrowband regime. As a result, the use of TR techniques has found steadily increasing interest in many applications including remote sensing and subsurface imaging [2, 3]. In this work, we review the TR-based signal processing techniques to achieve ultra-wideband (UWB) EM detection and imaging for distinct objects (targets) embedded in inhomogeneous media. We start by analyzing the eigenspace of the TR operator (TRO) which is obtained from the multistatic data matrix (MDM) whose elements correspond to the received signals from the distinct scatterers (e.g., depending on the application, malignant tumors, pipes, mines, unexploded ordnances, and trapped humans can be considered as the distinct scatterers) and (possibly inhomogeneous) background

M.E. Yavuz (✉)
Sensor Physics Group, Halliburton Energy Services, 3000 N Sam Houston Pkwy E, Houston, TX 77032, USA
e-mail: yavuz.5@osu.edu

combined. Each significant TRO eigenvalue can be associated with a specific scatterer in the domain and the corresponding eigenvector can later be utilized via synthetic backpropagation to achieve (selective) imaging of the scatterers in the probed domain. This constitutes the time-domain (TD)-DORT (decomposition of the TR operator after its French acronym [4]) method [3] which provides statistically stable images of the scatterers even in the presence of background clutter [5]. An alternative to TD-DORT method is the space-frequency (SF) imaging [6] which simultaneously utilizes both the spatial and the frequency information obtained from the TR array antennas. This is achieved via the singular value decomposition (SVD) of the newly created SF MDMs. While the left singular vectors provide spatial information, the right singular vectors yield the UWB frequency information for the imaging algorithm. In this work, the comparison of the two methods will be discussed along with their applicability ranges. For our simulations, we consider typical subsurface sensing scenarios where a limited aspect linear TR array is used to probe the (random) media with UWB signals. The random medium models are based on inhomogeneous soil models having spatially fluctuating random dielectric permittivities aiming to represent the random nature of the subsurface due to geophysical, meteorological, and other effects. However, it should be noted that the same algorithms can be adapted to different applications as in the case of microwave breast cancer detection, nondestructive testing, or through-wall human detection.

2 Time-Domain DORT and Space-Frequency TR Imaging

DORT method starts by obtaining an $N \times N$ MDM $K(\omega)$ (where ω is the frequency of operation) by probing the medium by an active TR array of N transceivers. In this case, each MDM element $[K(\omega)]_{ij}$ corresponds to the signal received at the ith antenna when the jth antenna is the transmitter. Since each element is associated with a different spatial location, this kind of MDM is labeled as the space–space MDM. In the frequency domain, TR of $K(\omega)$ is represented by its Hermitian conjugate $K^H(\omega)$, and hence, the TRO is defined by $T(\omega) = K^H(\omega)K(\omega)$. The SVD of the MDM is given by $K(\omega) = U(\omega)\Lambda(\omega)V^H(\omega)$, where $U(\omega)$ and $V(\omega)$ are unitary matrices and $\Lambda(\omega)$ is real diagonal matrix of singular values. The EVD of the TRO can be written as $T(\omega) = V(\omega)S(\omega)V^H(\omega)$, where $S(\omega) = \Lambda^H(\omega)\Lambda(\omega)$ is the diagonal matrix of eigenvalues. The columns of the unitary matrix $V(\omega)$ are normalized eigenvectors of the TRO ($v_p(\omega)$, $p = 1,\ldots,N$). For isotropic scattering from well-resolved point-like scatterers, each significant eigenvalue of the TRO is associated with a particular scatterer. Subsequent backpropagation of the corresponding eigenvector yields a wave front focusing on that scatterer [3]. Therefore, selective focusing on the mth scatterer is achieved by exciting the TRA with $N \times 1$ column vector $r_p(\omega)$ generated from $\lambda_m(\omega)$ and eigenvector $v_p(\omega)$ via $r_p(\omega) = K^H(\omega)u_p(\omega) = \lambda_p(\omega)v_p(\omega)$. This represents the single-frequency DORT method [3–5]. For ultra-wideband signals, eigenvalue decomposition can be applied at all the available frequencies and a time-domain signal can be generated via $r_p(t) = \text{IFT}(K^H(\omega)u_p(\omega)) = \text{IFT}(\lambda_p(\omega)v_p(\omega))$, where IFT denotes the inverse Fourier transformation. Backpropagation of these time-domain signals into the probed medium characterizes the TD-DORT method [3]. In cases where the background Green's function is not known (which is the case for most of the subsurface sensing scenarios), approximate Green's functions (G_0) can be used to obtain synthetic images of the probed medium by using the following TD-DORT imaging functional:

$$
\begin{aligned}
\mathbf{D}_p^\Omega(\bar{x}_s) &= \langle g_0(\bar{x}_s,t), \mathbf{r}_p(t) \rangle \Big|_{t=0} = \sum_{i=1}^{N} r_p^i(-t)_t^* G_0(\bar{x}_s,\bar{a}_i,t)\Big|_{t=0}, \\
&= \int_\Omega \lambda_p(\omega) v_p^T(\omega) g_0(\bar{x}_s,\omega) d\omega
\end{aligned}
\tag{1}
$$

where $g_0(\bar{x}_s,t) = [G_0(\bar{x}_s,\bar{a}_1,t),...,G_0(\bar{x}_s,\bar{a}_N,t)]^T$ is the approximate time-domain steering vector connecting any search point $\bar{x}_s$ in the probed domain to the antenna locations $\bar{a}_i$ for $i = 1,...,N$, r_p^i is the ith element of r_p, Ω is the operation bandwidth, and $*_t$ denotes convolution operation in time. Note that for well-resolved scatterers, the cross-range resolution of the DORT method is related to the classical diffraction limit which is directly proportional to the wavelength and propagation distance and inversely proportional to the effective aperture length of the TR array. When the well-resolvedness criterion is broken, eigenvectors of the signal subspace of space–space MDMs may become linear combinations of the Green's function vectors connecting the targets to the TR array, resulting in degradation of the final image. Another problem with the time-domain DORT stems from the eigenvalue decomposition step which creates eigenvectors with arbitrary frequency-dependent phase $\phi_{svd}(\omega)$. Direct combination of these eigenvectors creates incoherent time-domain signals which in turn severely affect the TD-DORT excitation signals. This is particularly important in inhomogeneous background media with strong multiple scattering where multipath components need to be coherently combined over the entire bandwidth at the target locations. Therefore, a pre-processing step should be applied to the space–space eigenvectors to obtain coherent time domain signals by canceling the arbitrary phase term $\phi_{svd}(\omega)$. Such pre-processing steps can be performed by projecting the incoherent eigenvectors onto the columns of the MDM [7] or by a phase smoothing algorithm which tracks the phase difference between the adjacent frequency eigenvectors [3]. The time-domain signals obtained for a random medium case with and without phase smoothing algorithm are shown in Fig. 1. The positive effect of phase smoothing algorithm is evident from the comparison of these plots.
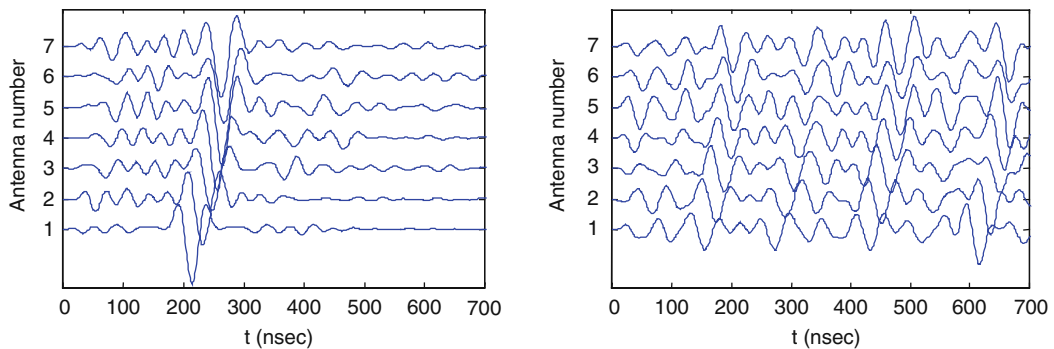
Fig. 1 Time-domain excitation signals obtained using the TD-DORT method for a random medium with (*right*) and without (*left*) phase smoothing algorithm

An alternative approach for pre-processing is based on the application of the SVD to an unconventional type of MDM which incorporates sensor location and UWB frequency data simultaneously. Such MDMs are denoted as the *space-frequency* (SF) MDMs. They were first introduced for their application with the MUSIC-type algorithms [8]. Here, we utilize them in the context of TR-based UWB imaging algorithms as discussed in what follows.

SF-MDMs can be obtained by transmitting an UWB pulse from the nth TRA antenna and recording the received signals by all the TRA receiver antennas to yield an $N \times M$ matrix given by

$$K_{SF}^n = \begin{pmatrix} k_{1n}(\omega_1) & \dots & k_{1n}(\omega_M) \\ \vdots & \ddots & \vdots \\ k_{Nn}(\omega_1) & \dots & k_{Nn}(\omega_M) \end{pmatrix}, \tag{2}$$

where each row consists of the uniform samples of the Fourier transform of the time-domain signal corresponding to the associated MDM element and M is the number of utilized frequency samples for the accurate frequency-domain representation. Once N of these individual SF-MDMs is obtained, SVD is applied to each of them to yield $K_{SF}^n = U_{SF}^n \Lambda_{SF}^n (V_{SF}^n)^H$ where U_{SF}^n is the $N{\times}N$ matrix of left singular vectors, V_{SF}^n is the $M{\times}M$ matrix of right singular vectors, and Λ_{SF}^n is the $N{\times}M$ matrix of singular values. Note that K_{SF}^n maps the frequency space onto the receiver space via $K_{SF}^n V_{SF}^n = \lambda_{SF}^n U_{SF}^n$ where λ_{SFi}^n is the ith singular value, V_{SFi}^n is the ith $M{\times}1$ right singular vector that represents the frequency content, and U_{SFi}^n is the ith $N{\times}1$ left singular vector containing spatial (sensor location) data. Note that the left singular vectors U_{SFi}^n for $i = 1,\ldots,N$ form an orthonormal set spanning the sensor location space and similarly right singular vectors V_{SFi}^n for $i = 1,\ldots,N$ form an orthonormal set spanning the frequency space. Inverse Fourier transformation can be applied to the right singular vectors to obtain time-domain signals which are *coherent* as SVD applied to the SF-MDM does not create arbitrary phase-dependent term as in the TD-DORT implementation. Therefore, the time-domain excitation signals to be backpropagated can be approximated as $s^n(t) = \sum_{k=1}^P \lambda_{SFk}^n V_{SFk}^n(t)$ where $V_{SFk}^n(t) = IFT(V_{SFk}^n(\omega))$ and P is the total number of time-domain signals included in the approximation which is determined by examining the singular values and the associated singular vectors. Time-domain signals corresponding to relatively small singular values and those with further incoherency are not included. The resulting time-domain signals provide the UWB frequency data but they do not possess any sensor location information. Therefore, we use the left singular vectors to provide the necessary amplitude and phase shifts to be applied to each TR antenna during backpropagation. For this end, we define a vector functional $f(a,z(t)) = \text{IFT}\{[A_0 e^{j\phi_o} z(\omega),...,A_N e^{j\phi_N} z(\omega)]^T\}$ where $z(t)$ is the time-domain signal to be used and $a = [A_0 e^{j\phi_o},...,A_N e^{j\phi_N}]^T$ is the $N{\times}1$ vector to determine the relative time delays and amplitudes. Utilization of this functional yields the time-domain vector $r_{SFi}^n(t) = f(U_{SFi}^n, s^n(t))$ which is to be backpropagated from the receivers. If the background medium is not known, approximate Green's functions can be utilized and the following imaging functional is obtained:

$$
\begin{aligned}
\mathbf{I}_{SFi}^n(\bar{x}_s) &= \langle g_0(\bar{x}_s,t), r_{SFi}^n(t) \rangle \Big|_{t=0} = \sum_{k=1}^N r_{SFik}^i(-t)_t^* G_0(\bar{x}_s,\bar{a}_k,t) \Big|_{t=0} \\
&= \int_\Omega (\mathbf{r}_{SFi}^n(\omega))^H g_0(\bar{x}_s,\omega) d\omega = \int_\Omega (s^n(\omega))^* (U_{SFi}^n(\omega))^H g_0(\bar{x}_s,\omega) d\omega
\end{aligned}
\tag{3}
$$

where $*$ represents complex conjugate operation. Note that this procedure is repeated for all $n = 1,\ldots,N$ and the resulting images are averaged via $I_{SFi}(\bar{x}_s) = 1/N \sum_{n=1}^N I_{SFi}^n(\bar{x}_s)$ and denoted as the SF image. Note that instead of the left singular vectors, one can also utilize the eigenvectors obtained from the DORT method at the central frequency for the spatial information [6]. A second kind of SF-MDM can be obtained by combining all the $\mathbf{K}_{SF}^n$ for $n = 1,\ldots,N$ into a single $N^2{\times}M$ matrix given as $\mathbf{K}_{SF}^{full} = [\mathbf{K}_{SF}^1; \mathbf{K}_{SF}^2; ...; \mathbf{K}_{SF}^N]^T$. This is denoted as the full SF-MDM. Similarly, SVD applied to this matrix yields $N^2{\times}N^2$ left and $M{\times}M$ right singular vectors. The right singular vectors of the full SF-MDM are very similar to the individual SF-MDM and can be utilized to obtain time-domain excitation signals for backpropagation. The sub-vectors of the left singular vectors can provide the sensor location data for the SF-imaging. For the sake of brevity, readers are referred to [6] for further details on the utilization of the full SF-MDM. Next, we apply both the TD-DORT and the SF-imaging to a subsurface detection scenario and demonstrate the similarities and differences between the two methods.

3 Simulation Setup, Results, and Discussions

We employ the finite difference time-domain (FDTD) method to simulate the forward and backward propagations (TM$_z$ case only). A grid of $N_x \times N_y = 200 \times 200$ cells with a spatial cell size of $\Delta s = 1.37$ cm is used with perfectly matched layers. The medium has a spatially fluctuating dielectric permittivity of $\varepsilon(r) = \varepsilon_m + \varepsilon_f(r)$ with a mean value of $\varepsilon_m = 2.908$ (dry sand). The fluctuating term $\varepsilon_f(r)$ is a zero mean Gaussian random variable with Gaussian correlation function. We employ $N = 7$ dipole transceivers which are fed by the first derivative of the UWB Blackmann Harris pulse at a central frequency of 400 MHz (corresponds to a wavelength of 32 Δs for ε_m). The central antenna is located at the origin of the simulation domain (i.e., $r_4 = (0, 0)\Delta s$). Only a single scatterer embedded at $(30, 80)\Delta s$ is considered in both homogeneous and a random medium defined by the variance $\delta = 0.03$ and correlation length $ls = 6\Delta s$. Figure 2 shows the corresponding eigenvalues for the TD-DORT method and singular values for the SF-imaging methods. It is observed that with increasing multiple scattering (randomness), the strengths of both the eigenvalues and the singular values increase. Additionally, the first dominant singular values obtained in homogeneous (HM) and random medium (RM) are close to each other and they exhibit similar time-domain signals (except fluctuations due to clutter in random medium) as can be seen in Fig. 3. Among the remaining non-dominant singular values, those obtained in RM are larger than the HM ones.
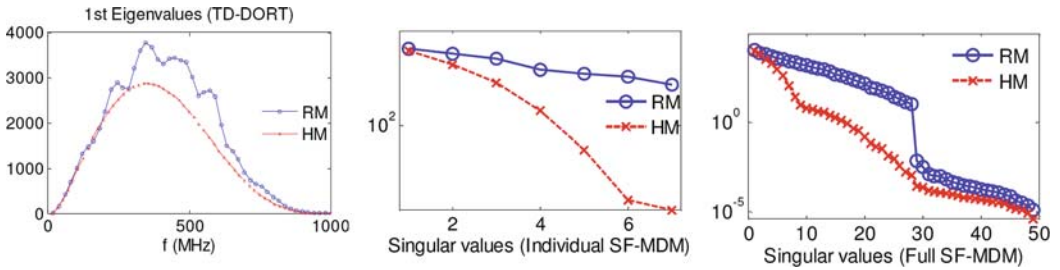
Fig. 2 The first eigenvalue distribution of the space–space MDM with respect to the frequency (*left*) and singular values of the individual (*center*) and full (*right*) space-frequency MDMs

The corresponding time-domain right singular vectors also behave quite differently. For RM case, the non-dominant right singular vectors are mainly due to clutter and not included in the approximation used for the excitation signal. Therefore, the first right singular vector can be used as the excitation signal with appropriate amplitudes and phase shifts dictated by the left singular vectors or TD-DORT eigenvectors at the desired frequency as shown in Fig. 4.

It is worth reminding that the excitation signals obtained by the SF-MDM processing do not require the phase smoothing algorithm as it is necessary for the TD-DORT method. In certain cases where multiple scattering is very large, this might pose a problem as the phase smoothing algorithm might fail to yield coherent time-domain excitation signals whereas SF-MDM processing will always yield coherent time-domain signals.

Figure 5 shows the final images obtained by both the TD-DORT and the SF-imaging methods in homogeneous and random media. Note that in terms of cross-range resolutions, both methods provide similar performances. However, in HM, TD-DORT slightly performs better [6]. As for the RM case, TD-DORT might suffer from phase-smoothing limitations for higher multiple scattering, whereas SF-imaging is not affected by the incoherent signals. Another important property is that both methods provide statistical stability (i.e., the results do not depend on the particular random
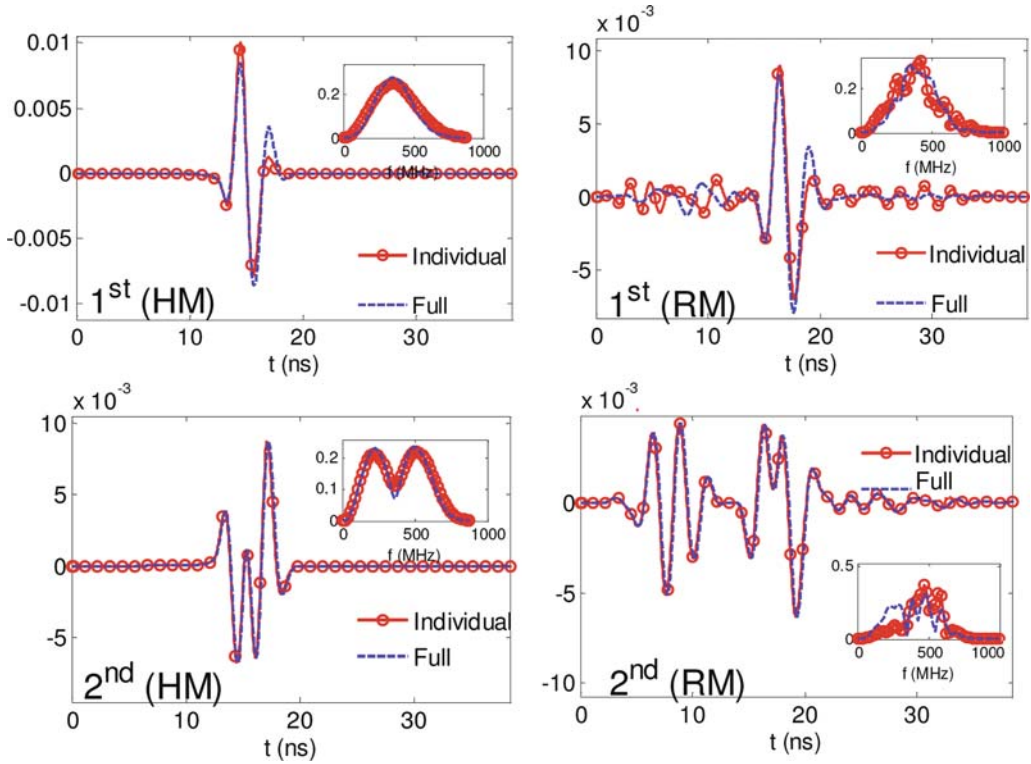
Fig. 3 The first two significant time-domain right singular vectors obtained in homogeneous and random media using both the individual and the full SF-MDM
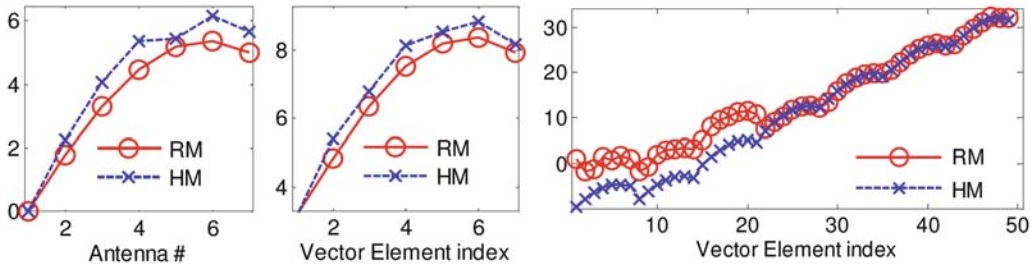
Fig. 4 Phase distribution of the most significant TD-DORT eigenvector obtained at the central frequency (*left*) and those of the left singular vectors of the individual (*middle*) and full (*right*) SF-MDMs

medium realization but to its statistical distribution) thanks to the frequency and spatial decorrelation achieved by the UWB and limited aspect nature of the simulation scenario.

4 Conclusions

In this chapter, we have reviewed two imaging methods based on the TR concept. Specifically, TD-DORT and SF-imaging methods which, respectively, utilize space–space and space-frequency
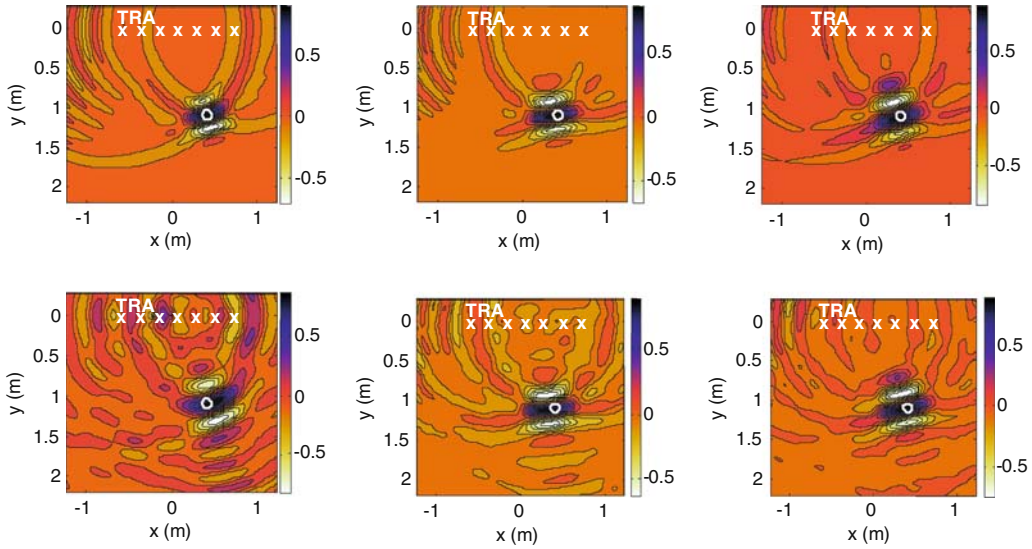
Fig. 5 Images obtained both in homogeneous (*top row*) and in random (*bottom row*) media by TD-DORT (first column), SF-imaging using individual (second column) and full SF-MDMs (thrid column)

MDMs are explained. For the TD-DORT method, eigenvector decomposition at each single frequency of the available bandwidth is utilized to obtain the necessary time-domain excitation signals after carrying out a phase smoothing algorithm. While this method performs well in homogeneous and relatively low clutter environments, due to the limitation of the phase smoothing algorithm, it fails at higher multiple scattering environments. On the other hand, SF-imaging utilizes unconventional MDMs to provide consistently coherent time-domain excitation signals regardless of the background clutter. Although TD-DORT cross-range performance is slightly better, SF-imaging might be favored in highly scattering environments. For a future study, we plan to combine both methods to exploit their advantages within a single algorithm. For further details on both methods and their possible utilizations in lossy and dispersive media, readers are referred to [3, 5, 6, 9].

References

1. M. Fink, D. Cassereau, A. Derode, C. Prada, P. Roux, M. Tanter, J. Thomas, and F. Wu, Time-reversed acoustics, Rep. Prog. Phys., vol. 63, pp. 1933–95, 2000.
2. M. E. Yavuz and F. L. Teixeira, A numerical study of time reversed UWB EM waves in continuous random media, IEEE Antennas Wireless Prop. Lett., vol. 4, pp. 43–46, 2005.
3. M. E. Yavuz and F. L. Teixeira, Full time-domain DORT for ultrawideband fields in dispersive, random inhomogeneous media, IEEE Trans. Antennas Propagat., vol. 54, no. 8, pp. 2305–15, August 2006.
4. C. Prada, S. Mannevile, D. Spoliansky, and M. Fink, Decomposition of the time reversal operator: detection and selective focusing on two scatterers, J. Acoust. Soc. Am., vol. 99, no. 4, 2067–76, 1996.
5. M. E. Yavuz and F. L. Teixeira, On the sensitivity of time-reversal imaging techniques to model perturbations, IEEE Trans. Antennas Propagat., vol. 56, no. 3, pp. 834–43, March 2008.

6. M. E. Yavuz and F. L. Teixeira, Space-frequency ultrawideband time-reversal imaging, IEEE Trans. Geosci. and Remote Sensing, vol. 46, no. 4, pp. 1115–24, April 2008.

7. J. G. Berryman, L. Borcea, G. Papanicolaou, and C. Tsogka, Statistically stable ultrasound imaging in random media, J. Acoust. Soc. Amer., vol. 112, no. 4, pp. 1509–22, October 2002.

8. B. Scholz, Towards virtual electrical breast biopsy: space-frequency music for trans-admittance data, IEEE Trans. Med. Imag., vol. 21, no. 6, pp. 588–95, June 2002.

9. M. E. Yavuz and F. L. Teixeira, Frequency dispersion compensation in time reversal techniques for UWB electromagnetic waves, IEEE Geosci. Remote Sensing Lett., vol. 2, pp. 233–37, April 2005.

Imaging of Distributed Objects in UWB Sensor Networks

R. Zetik and R.S. Thomä

Abstract The chapter proposes a new imaging algorithm. This algorithm is suitable for the imaging of extended objects in UWB sensor networks. Its comparison to the conventional range migration algorithm known from GPR or similar applications is given by a simulated example. The example shows disadvantages of the range migration algorithm for imaging in UWB sensor networks. Images obtained by the new proposed algorithm are easier to interpret and their quality is much higher.

Keywords Sensor networks · Imaging · UWB sensor

1 Introduction

Despite the excellent range resolution capabilities offered by UWB radar sensors, detection and localization performance can be significantly improved by cooperation between spatially distributed nodes of a sensor network. Moreover, distributed sensor nodes can acquire comprehensive knowledge on the structure of the unknown environment and construct an electromagnetic image which is related to the relative sensor-to-sensor coordinate system.

In [1] we presented an idea of the localization and imaging applications in a UWB sensor network. We presented measurement examples showing the potential of the sensor networks for imaging of its environment. These examples were based on migration algorithm [2,3] known from remote sensing, e.g., ground penetrating radar (GPR), or through-wall applications. In what follows we will refer to this migration algorithm as the range migration.

In this chapter we show that this algorithm is not suitable for the application in UWB sensor networks. We describe drawbacks of this migration algorithm that arise especially due to the different application scenario. In this chapter we propose a new imaging algorithm developed for the imaging of distributed objects in UWB sensor networks. We compare performance of the proposed imaging algorithm with the range migration by a simulated example.

R. Zetik (✉)
Electronic Measurement Research Lab, Ilmenau University of Technology, Ilmenau, Germany
e-mail: rudolf.zetik@tu-ilmenau.de

2 Imaging in GPR Applications vs. UWB Sensor Networks

The range migration algorithm fuses together signals measured by a sensor situated at different positions to produce a 2D image of the medium under test. Signals reflected from objects form traces in measured 2D data (range × cross-range). The shape of these traces depends on the measurement positions and geometrical as well as material properties of objects. Range migration algorithm cumulates reflected signals along these traces. This produces a focused image of the inspected environment. Range migration is described for the monostatic sensor, which uses the same antenna for the transmission and the reception of signals, by the following equation:

$$o(x,y) = \frac{1}{N} \sum_{n=1}^{N} R_n \left(\frac{2r_n\,(x,y)}{v} \right), \tag{1}$$

where $r_n(x,y)$ is the distance between the nth sensor and the $[x,y]$ position in the focused image, v stands for the propagation velocity. The quantity $(2r_{n(x,y)})/v$ is the round trip time which the electromagnetic (EM) wave needs to propagate from the transmitter to the position $[x,y]$ and back to the receiver. $R_n(\tau)$ is the impulse response measured at the nth sensor's position. First, range migration maps received impulse response $R_n(\tau)$ to the 2D "snapshot" according to

$$s_n(x,y) = R_n \left(\frac{2r_n\,(x,y)}{v} \right) = R_n \left(\frac{2\sqrt{(x - x_n)^2 + (y - y_n)^2}}{v} \right), \tag{2}$$

where $[x_n, y_n]$ are the sensor coordinates situated at the nth position. According to (2), a signal in the impulse response $R_n(\tau)$ reflected from some objects is mapped in the snapshot $s_n(x,y)$ as a circular trace around the sensor's coordinates $[x_n, y_n]$. This circular trace represents all probable positions of the object within this snapshot. Thus, the snapshot can be interpreted as a probability map. The idea behind the range migration is that by combining (summing) multiple snapshots according to (1) the probability map focuses at the objects' positions. This is true if objects are point-like scatterers. As illustrated in [4], the circular traces contained in different snapshots that are related to the same point-like object cross together at the position of this object.

However, what happens if objects are extended (distributed) and EM waves are rather reflected and not scattered back to the sensor as it is in the case of point-like objects. Figure 1 illustrates measured data and formation of the focused image using the range migration concept in case of an extended object. Signals reflected from this object form a linear trace in the measurement domain. Each reflected signal is mapped by the range migration as a circular trace around the sensor position in the focused image. However, each signal is reflected from different reflection points of this object. Therefore, circular traces do not intersect at one position. They even do not intersect at the object. As a result the image contains a set of circular traces and is impossible to interpret.

Thus, it seems that the range migration focuses only images of point-like objects. However, it is widely used in, e.g., seismology for the imaging of planar objects too. What makes the range migration applicable also for the imaging of extended objects? These are the following assumptions:

- Scanning of the medium under test must be dense enough
- Received signals must be bipolar

Fig. 1 Formation of the "focused" image in case of a distributed object
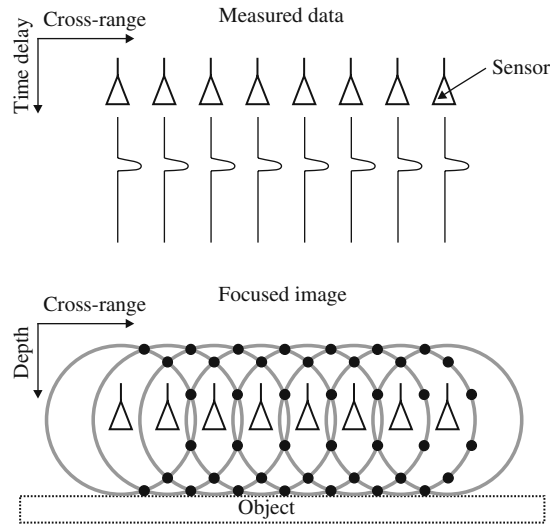
By increasing the density of measurement points, circular traces contained in snapshots intersect closer to the actual position of the focused object. This makes the object more focused and visible in the image. However, if measurement positions are distributed along a linear track, there arise "phantom" images of objects. Phantom images are symmetrical to the linear track of the sensor movement. They cause no problems in GPR or similar applications, where only a half of an inspected area (space) is of interest. Phantom images of objects situated in front of antennas appear in the focused image beyond antennas and do not disturb. Phantom images of objects situated behind antennas do not appear in the area of interest due to the use of directive antennas that do not see objects placed behind them.

If receive antennas provide bipolar signals for the range migration, then circular traces contained in snapshots intersect coherently at the position of the focused object (and its phantom image) and incoherently at other positions within the focused image. This significantly removes artifacts contained in the focused image and allows application of the range migration algorithm in GPR or similar applications.

However, imaging in a UWB sensor network must take into account some specifics resulting from the different application scenario. These can be summarized as follows:

- There is no half-space constriction; objects can be situated in the whole inspected area (space)
- The use of directional antennas is constrained; simple sensor nodes cannot usually provide information about the antenna orientation, which would be necessary for the proper data fusion
- Static sensor nodes are distributed in the network irregularly with low density
- Moving nodes do not have to be moved along linear track; they can follow arbitrary tracks selected even on purpose
- Sensor nodes must be usually self-localized by the network; the precision offered by the UWB technology is in an order of some centimeters

These specifics result in the following challenges for the migration algorithm:

- Symmetrical distribution or movement of sensor nodes gives rise to the disturbing phantom images

- Irregular and sparse density of the nodes prohibits correct data fusion; resulting image contains a number of artifacts and cannot be correctly interpreted
- The network topology influences focused image; it is actually mapped onto the objects in the image, thus some parts of extended objects are over-illuminated if seen by multiple sensor nodes, some parts are under-illuminated if there are no nodes in the network that can illuminate ("see") them
- Knowledge of node's positions is prerequisite for the correct range migration; the localization precision of some centimeters is not high enough to allow coherent signal processing, thus only an envelope of measured signals can be used; unfortunately this is unipolar signal and the advantage of bipolar signal processing as described above is lost.

Figure 2 demonstrates these most significant drawbacks of the range migration algorithm if applied for the imaging in a sensor network.

Fig. 2 Range migration in a UWB sensor network
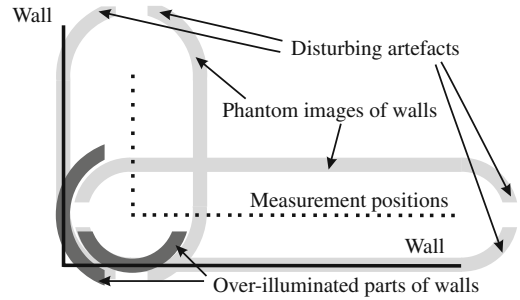
3 Generalized Imaging Algorithm

In [4] we have presented an imaging algorithm suitable for the imaging of small, point-like objects by a UWB sensor network. This algorithm is based on the cross-correlated imaging algorithm [5, 6]. In contrast to the range migration algorithm it does compute one snapshot $s_n(x,y)$ from not only one observation $R_n(t)$ (see (2)), but also from multiple spatially distributed observations. In [4], we have described how to advantageously select and combine observations from multiple sensor nodes for the imaging of point-like objects. The performance of this imaging algorithm was demonstrated by a measurement example. It demonstrated reduction of disturbing artifacts and improvement of the image interpretability.

In what follows we will describe this algorithm in more detail and adopt it for the imaging of distributed objects in a UWB sensor network. Let us assume a simple scenario, in which three sensor nodes (transceivers) are used for the imaging of an extended object – of a wall. Range migration algorithm proposes to compute three snapshots and add them to the focused image. This would result in the "focused" image containing three circular traces that would generally intersect beside the object.

Imaging algorithm presented [4] proposes to build a modified snapshot according to

$$
\begin{aligned}
s_{n\,\mathrm{mod}}(x,y) = R_n \left(\tfrac{2r_n}{v} \right) \left| R_n \left(\tfrac{2r_n}{v} \right) \right|^{-1} \cdot \\
\cdot A \left[\left| R_n \left(\tfrac{2r_n}{v} \right) \right|, \ \left| R_{r1n} \left(\tfrac{2r_{r1n}}{v} \right) \right|, ..., \left| R_{rN-1n} \left(\tfrac{2r_{rN-1n}}{v} \right) \right| \right]
\end{aligned}
\tag{3}
$$

where $A[\cdot]$ is an operator averaging N spatially distributed observations. This modification assumes that all N nodes can "see" the object. In case of point-like objects that scatter incident EM waves in all directions, sensor nodes can be situated arbitrarily in the object's vicinity and they will still "see" the object. However, an extended object reflects EM waves like a mirror. A sensor node can "see" only a small part of this object, which is observed under the perpendicular viewing angle. Therefore, there will be only small number (mostly only one) of nodes observing the same part of an extended object. Thus, it seems that the proposed modification of the modified snapshot computation cannot find an application for imaging of extended objects. However, by the imaging of an extended object also another object's part can contribute to the computation of the modified snapshot. Figure 3 illustrates the formation of a modified snapshot. Observation from sensor and its reference node 1 can be directly fused together. They observe the same part of the wall. Although reference sensor 2 does not observe the same part of the objects, its observation can also be used for the creation of the modified snapshot. It must only be translated to the correct position as shown in Fig. 3. If the averaging operator $A[\cdot]$ is, e.g., a geometrical mean all three circular traces are multiplied together. This leaves nonzero contribution to the focused image, computed according to (1) from the modified snapshots, only at the correct position of the object. Disturbing artifacts – circular traces – are removed from the focused image.

Fig. 3 Formation of the modified snapshots for the imaging of distributed objects
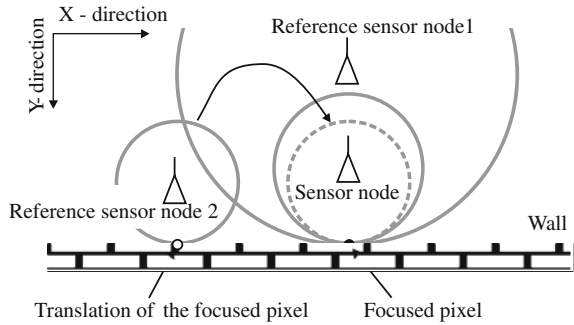
If an object or its part is observed by more sensor nodes, it is over-illuminated in the focused image. In contrary, if some part of an object is observed only by small number of nodes, it is under-illuminated. This significantly makes the interpretation of the focused image difficult or even impossible. Figure 4 illustrates it on a simple scenario. One sensor node is moved perpendicular and parallel to two extended objects (walls). Each wall is over-illuminated by an imaging algorithm at the position where the sensor is moved perpendicular to this wall. The over-illuminated positions are seen from multiple measurement positions. On the other hand, some parts of walls are even invisible due to the lack of measurement position, from which the sensor could see these parts.

In order to remove this drawback from the imaging algorithm, we propose to weight the snapshots before their summation as follows:

$$o(x,y) = \frac{1}{N} \sum_{n=1}^{N} W_n(x,y) A\left[R_n(x,y), R_{\text{ref}1n}(x,y),..., R_{\text{ref}Mn}(x,y)\right], \tag{4}$$

where $W_n(x,y)$ are weighing coefficients computed according to

Fig. 4 Projection of the
network topology on the
imaged objects

Projection of the network to pologyon the X -axis(Wall1)
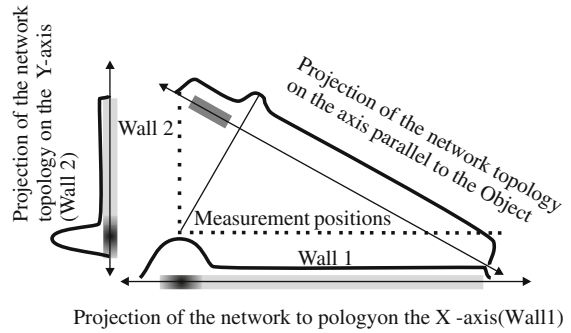
$$W_n\,(x,y) = \left(\sum_{i=1}^{N} p_i\,(x,y)\right)^{-1}.\tag{5}$$

where $p_i(x,y)$ is the probability that the ith node can contribute to the imaging of a part of the extended object at coordinates $[x,y]$ that is observed from the nth node position. Thus, weighing coefficients are inversely related to the number of measurement positions observing a specific part in the focused image. This way it is possible to equalize the illumination in the produced focused image.

4 Performance Comparison

Improved performance of the generalized weighed imaging algorithm in comparison to the range migration algorithm is illustrated by the following simulation example. Three walls and one point-like scatterer are inspected by a sensor node, a transceiver moving along an oval track. Its positions are assumed to be a priori known.

Figure 5 shows an image of this simulated environment obtained by the range migration algorithm. Especially walls are improperly mapped in this image. The over-illumination of some parts of the walls is due to neglecting spatial information of the network by this migration algorithm. Besides
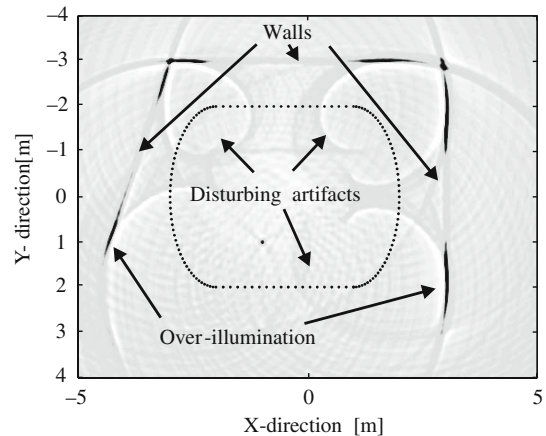
Fig. 5 Range migration

Fig. 6 Generalized imaging
algorithm
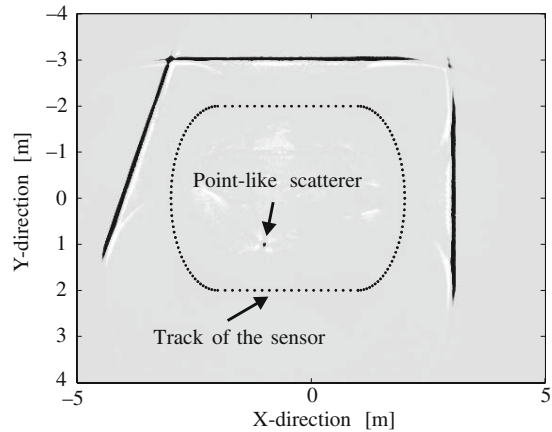
the over-illumination, the focused image is further corrupted by disturbing artifacts produced by the algorithm. Thus, the correct interpretation of this image is almost impossible.

Figure 6 illustrates the improvement of the focused image using the imaging algorithm proposed in this chapter. A geometrical mean computed from two observations was used as an averaging operator $A[\cdot]$ in (4). This averaging decreased the number of disturbing artifacts in the focused image. The over-illumination of the walls was removed by encountering the network topology in the data fusion using the weighing coefficients defined by (5). The increase of the objects quality is apparent.

5 Conclusions

The generalized algorithm proposed in this chapter and in [1] is a model-based imaging algorithm. It decreases disturbing artifacts in the image by making certain assumptions – a priori information about objects. It needs an adaptive selection of additional observations in order to compute modified snapshots. The selection must be done with respect to the object's interaction with the EM waves (scattering – point-like objects, reflection – extended objects). Although the selection cannot be always perfect due to the lack of the necessary observations, the resulting focused image contains significantly less disturbing artifacts. Moreover, by correct data fusion taking into account the topology of the network, the quality of the focused image clearly outperforms performance of the range migration algorithm.

References

1. R. S. Thomä, O. Hirsch, J. Sachs, and R. Zetik, UWB sensor networks for position location and imaging of objects and environments, EuCAP 2007, The Second European Conference on Antennas and Propagation, Edinburgh, UK, November 2007.
2. D. J. Daniels, Ground penetrating radar – 2nd edition, IEE, London, 2004.
3. J. M. Lopez-Sanchez and J. Fortuny-Guasch, 3-D Radar Imaging Using Range Migration Techniques, IEEE Transactions on Antennas and Propagation, vol. 48, no. 5, pp. 728–737, 2000.

4. R. Zetik and R. S. Thomä, Monostatic imaging of small objects in UWB sensor networks, accepted as an invited paper to the International Conference on Ultra-wideband (ICUWB 2008), Germany, 2008.
5. S. Foo and S. Kashyap, Cross-correlated back projection for UWB radar imaging, IEEE Antennas and Propagation Society Symposium, Piscataway, NJ, USA, vol. 2, 2004.
6. R. Zetik, J. Sachs, and R. S. Thomä, Modified cross-correlation back projection for UWB imaging: numerical examples, ICU 2005 IEEE International Conference on Ultra-wideband, Switzerland, September 2005.

Advanced Imaging by Space–Time Deconvolution in Array GPR

T.G. Savelyev, N.T. van Tol, A.G. Yarovoy, and L.P. Ligthart

Abstract Digital beamforming in array-based UWB radar delivers a high-resolution 3-D image of subsurface in GPR landmine detection while simultaneous data acquisition by elements of the array significantly increases the scanning speed. Such a GPR system with a single transmit antenna and a linear receive array has been developed in the Delft University of Technology. For online processing we propose an advanced imaging algorithm based on migration by regularized, parametric space–time deconvolution. The algorithm deconvolves a 3-D space–time array point spread function out of the data volume by means of FFT and inverse Wiener filter that is being controlled automatically with numerical criteria for stability and accuracy. The prior knowledge of GPR impulse response and ground impulse response is used to form a separate point spread function for each receiving antenna. The developed technique has been verified on experimental data for typical anti-personnel mines and compared with a classical migration by diffraction stacking.

Keywords Array radar · Ground penetration radar (GPR) · Deconvolution · Landmine detection · Migration · Near-field imaging

1 Introduction

Landmine detection by means of GPR remains a challenging direction for designing an UWB radar system and data processing algorithms. In recent years IRCTR developed an array-based GPR for vehicular use, which possesses such attractive specifications as compactness and reliability of the antenna system with a single transmit (Tx) antenna, high speed of data acquisition by multi-channel compact electronics, and capability to image a strip of 84 cm with a linear receive (Rx) array in one mechanical scan [1]. It is worth to mention that the GPR has been built on video impulse technology with a 30 ps rise time of transmitted pulse, system bandwidth from 0.3 to 3 GHz at –10 dB, time window of 20 ns, pulse repetition frequency of 525 kHz. A dielectric wedge antenna is used as transmit, and the Rx array is formed with 13 loop antennas with a separation of 7 cm (Fig. 1a). GPR impulse response for the central loop measured from a large metal plate is given in Fig. 1b. The

T.G. Savelyev (✉)

International Research Centre for Telecommunication and Radar, Delft University of Technology, Mekelweg 4, 2628CD Delft, The Netherlands
e-mail: t.g.savelyev@irctr.tudelft.nl
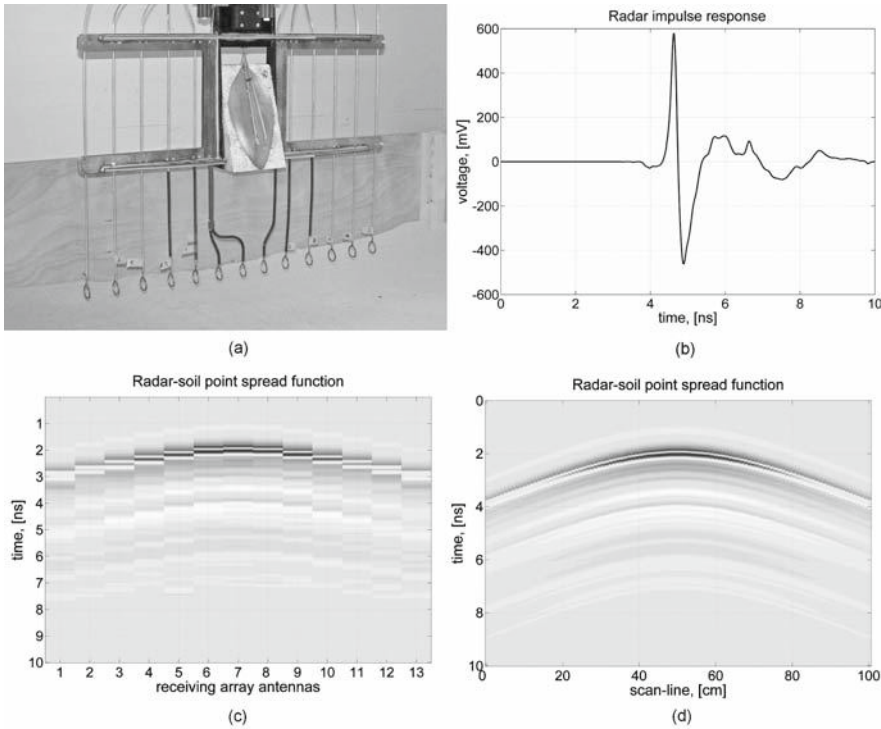
Fig. 1 Characteristics of array-based GPR: (**a**) antenna system; (**b**) radar impulse response for the central receive loop; (**c**) cross section of 3-D PSF over array for subsurface point scatterer; (**d**) cross section of 3-D PSF over mechanical scan

theoretical limit of data acquisition speed that provides appropriate image quality offline reaches 148 km/h.

A classical approach to GPR imaging employs migration by diffraction stacking that originates from seismic processing and to some extent it is equivalent to SAR. Diffraction stacking migrates the data in time domain by taking into account only true travel times of GPR signal and dielectric constant of the ground. Based on that, a novel 3-D imaging algorithm that combines focusing of the synthetic aperture with focusing of the real array aperture has been developed for our GPR and published in [2]. However, diffraction stacking is more suitable for offline processing due to high computational time.

Prior to imaging the GPR data need a certain pre-processing that includes suppression of uncorrelated thermal and quantization noise by low-pass filtering, compensation for random time drift of the electronics, background and clutter removal. Next to that, calibration is necessary to estimate "time zero" for every array channel and to correct for non-uniform footprint of Tx-antenna. One will find a detailed description of the pre-processing and calibration in [2].

A fast migration technique based on space–time deconvolution, that makes use of GPR impulse response and more properties of the ground, has been proposed in [3]. The idea behind is that a target signature can be treated as superposition of reflections from point-like scatterers that means convolution of a point spread function (PSF) with a true shape of the target. Radar-soil PSF is defined as a reflection from a point scatterer buried at a certain depth and received by GPR at different positions.

Figure 1c and 1d illustrate cross sections of 3-D PSF in the planes of the array and mechanical scan, respectively. Deconvolution of PSF out of the acquired data delivers a focused target image.

In this work we extend the approach of deconvolution to the case of array GPR with multiple PSFs. Deconvolution is performed with a Wiener inverse filter that automatically adjusts the regularization parameter to satisfy numerical criteria for stability and accuracy [4, 5]. This chapter consists of four sections. Sections 2 and 3 describe migration by deconvolution in 2-D and 3-D cases, respectively, and compare its performance with diffraction stacking for experimental data. Conclusions are summarized in Section 4.

2 Space–Time Deconvolution in 2-D Case

In 2-D case we consider a B-scan acquired with one Rx-antenna by mechanical scanning over a buried target. The deconvolution approach assumes that each acquired A-scan can be approximated in time domain as follows:

$$s\left(t\right) = \frac{d}{dt}\left[\frac{T_{a-g}T_{g-a}}{8\pi^2 R_t R_r c} g\left(t,d\right) \otimes h\left(t - \tau\right)\right] \otimes \Lambda\left(t\right) = w(t) \otimes \Lambda\left(t\right) \tag{1}$$

where T_{a-g}, T_{g-a} are the air–ground and ground–air transmission coefficients, respectively; R_t, R_r are the total path lengths from Tx-antenna to target and from target to Rx-antenna, respectively; c is the velocity of light; $g(t, d)$ is the ground impulse response depending on the two-way path length d in the ground; $h(t - \tau)$ is the GPR impulse response as a function of the signal travel time τ; $\Lambda(t)$ is the target impulse response. The formula takes into account that a point scatterer differentiates the incident electromagnetic wave. The terms preceding $\Lambda(t)$ constitute a radar-soil impulse response or 1-D PSF.

The GPR impulse response accounts for properties of Tx- and Rx-antennas and electronics. It can be estimated from a reflection from a large metal plate (Fig. 1b). The ground impulse response is given by the formula [3]

$$g\left(t,d\right) = \frac{d\sqrt{\mu\varepsilon'}\tan\delta}{2\pi\left[\left(t - d\sqrt{\mu\varepsilon'}\right)^2 + \left(0.5d\sqrt{\mu\varepsilon'}\tan\delta\right)^2\right]}, \tag{2}$$

where μ stands for the permeability of the ground, ε' is the real part of permittivity, and $\tan\delta$ is the loss tangent. These parameters are frequency dependent but here we use their values averaged over the GPR bandwidth.

Extending the 1-D case to 2-D gives the following formula:

$$b\left(x,t\right) = w\left(x,z_0,t\right) \otimes_{x,t} \Lambda_{z_0}(x,t), \tag{3}$$

where $b(x, t)$ is a B-scan acquired over line x, $w(x,z_0,t)$ is the 2-D PSF estimated beforehand for a certain depth of point scatterer z_0, operator $\otimes_{x,t}$ stands for 2-D convolution with the unknown scattering matrix of a target $\Lambda_{z_0}(x,t)$.

Formation of the 2-D PSF implies that a point scatterer is buried at a typical depth of landmine in the middle of B-scan. Every A-scan of the PSF needs computation of the first two terms under the differentiation operator in (1) and travel time of the signal propagating in the two media. This includes finding the refraction points on the ground surface, which can be done by solving a

fourth-order polynomial [2]. Note that for a given soil and measurement configuration one needs to compute the PSF only once so computational expenses is not an issue here. The estimated terms are to be convolved with the GPR impulse response delayed by the travel time. The result should be differentiated. The procedure repeats for all positions of the GPR with respect to the point scatterer. The last step is normalization of PSF by its 2-norm (square root from energy) which makes it non-dimensional and removes a possible gain. Figure 1d illustrates a PSF for a point scatterer buried at 6 cm depth in dry sand with $\varepsilon = 3.03$ and $\tan \delta = 0.08$.

Deconvolution is performed with a 2-D Wiener inverse filter that, from a mathematical point of view, does regularization in wavenumber-frequency domain. Physically the regularization parameter represents an inversed signal to noise ratio (SNR) which is unknown a priori. We developed a fast iterative algorithm that changes SNR by 1 dB unless the solution satisfies two numerical criteria for efficiency proposed in [5]. The first is energy ratio given by

$$\gamma = \frac{\left\|\hat{\Lambda}(x,t)\right\|}{\|b(x,t)\|} 100\%, \tag{4}$$

where operator $\|\circ\|$ stands for 2-norm of a matrix, $\hat{\Lambda}(x,t)$ is a deconvolution result for the current regularization parameter. The energy of signal after deconvolution should not exceed its original energy, i.e., γ should not be more than 100%. Otherwise the solution is unstable that means presence of artifacts in the focused image.

The second criterion represents error of deconvolution:

$$err = \frac{\left\|b(x,t) - w(x,z_0,t) \otimes_{x,t} \hat{\Lambda}_{z_0}(x,t)\right\|}{\|b(x,t)\| + \left\|w(x,z_0,t) \otimes_{x,t} \hat{\Lambda}_{z_0}(x,t)\right\|} 100\%. \tag{5}$$

From our experience the error should not exceed 25% as otherwise the focused image will be blurred.

Removal of the PSFs phase by deconvolution out of the wavenumber-frequency spectrum of the acquired B-scan results in a shift of the focused image. However, this shift is constant and easy to compensate for. Also one should remember that dimensions of the PSF, B-scan, and focused image are the same which provide a higher resolution than that of the diffraction stacking.

Figure 2 illustrates an example of 2-D migration. A raw B-scan acquired with the central array loop over an anti-personnel landmine PMN-2 buried at 6-cm depth in dry sand is shown in Fig. 2a. The pre-processed B-scan is shown in Fig. 2b. Images focused by diffraction stacking and deconvolution are given in logarithmic scale in Fig. 2c and d,, respectively.

The PSF shown in Fig. 1d was used for deconvolution. The efficiency criteria are 100% for the energy ratio and 11% for the error. Deconvolution provides a sharper image with dimensions of 1024×410 pixels in 5 s in MATLAB on average PC while diffraction stacking requires 71 s to produce an image of 44×101 pixels.

3 Array Space–Time Deconvolution in 3-D Case

In 3-D case, an array C-scan that consists of 13 acquired B-scans is used and formulas (3–5) become 3-D. Because the C-scan is sparse over the array (Fig. 1c) we use interpolation to obtain appropriate resolution such as 1 by 1 cm in the horizontal plane. A 3-D PSF is formed by combining 2-D PSFs, computed for each loop separately, and interpolating them in the same way as the acquired C-scan.
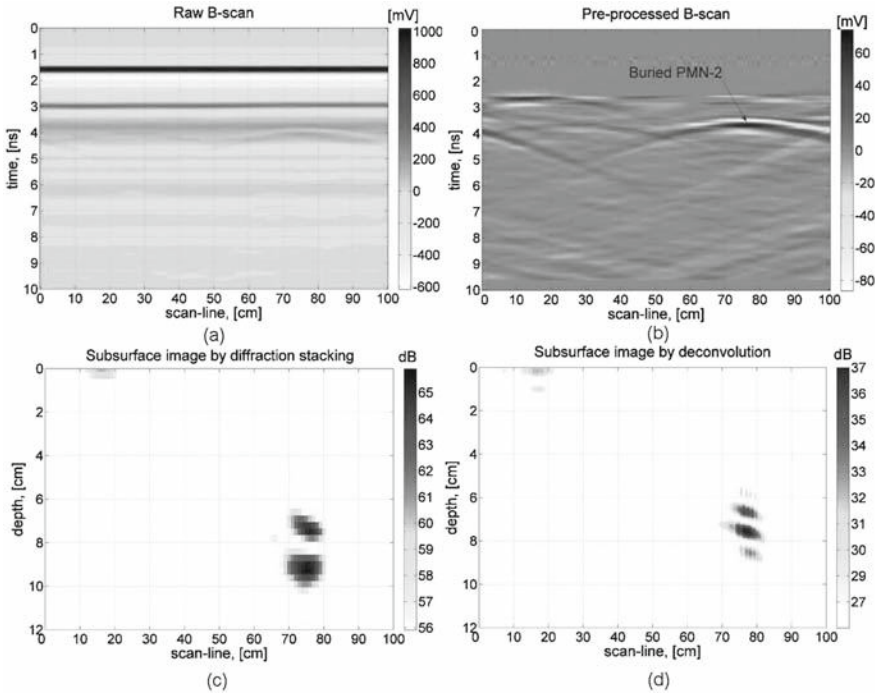
Fig. 2 2-D subsurface imaging: (**a**) raw B-scan by central receive channel; (**b**) pre-processed B-scan; (**c**) subsurface image focused by diffraction stacking; (**d**) subsurface image focused by deconvolution

To test the performance of deconvolution we selected a scenario when one landmine is buried in the middle of the aperture and the other is buried at the edge (Fig. 3a).

Diffraction stacking works without prior information about targets and images all of them in a selected 3-D grid. Figure 3b presents the focused image of the two landmines in the horizontal
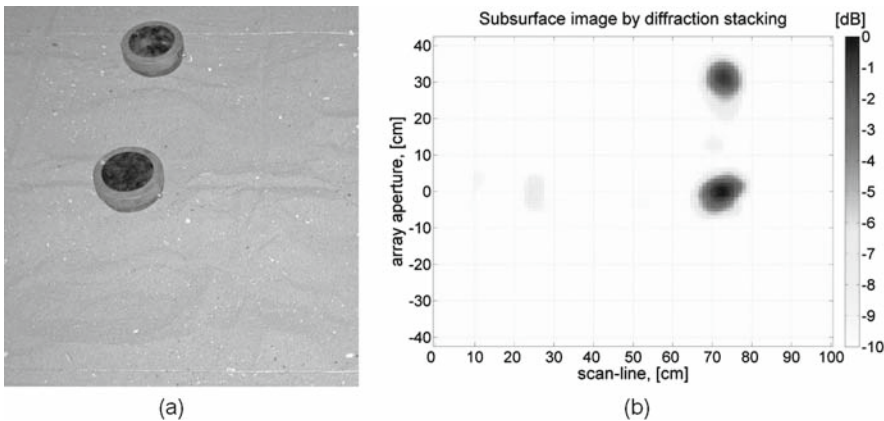
Fig. 3 3-D array imaging by diffraction stacking: (**a**) target scenario with one PMN-2 in the *middle* and one at the edge of the array aperture, buried at 5 cm depth; (**b**) focused image of the mines

plane. This 2-D image was obtained from the focused C-scan by means of alternating sign windowed energy projection (ASWEP) [6].

For deconvolution, a question arises where within the array aperture a point scatterer should be buried as its different positions give different PSF as shown in Fig. 4a and b. The use of only one PSF for a point scatterer in the middle images only the target in the middle (Fig. 4c). In practice, the number and positions of targets are unknown so we propose to use 13 PSFs obtained, respectively, for scenarios when a point scatterer is buried under each loop. Then 13 deconvolutions need be performed separately. Next to that, we should account for a fact that unnormalized PSF at the array edge is truncated and has lesser energy (Fig. 4b), which results in a weaker image of the target at the edge. This effect can be compensated for by weighting each deconvolution result with a factor of $1/\|PSF_k\|$. The next step deals with combination of the 13 deconvolution results. Our investigation showed that a solution giving the least number of artifacts is to form the final C-scan from pieces of the 13 migrated C-scans. Each piece represents a small area under the corresponding loop. The combined volume needs be smoothed by median filtering and projected by ASWEP. Figure 4c presents a result of the whole processing that clearly shows the two buried landmines. The multiple PSFs were deconvolved with 5% energy ratio and 25% error.

In terms of computational expenses, 3-D migration by deconvolution required 8 min for a $512 \times 101 \times 85$ migrated C-scan while diffraction stacking took 23 h to obtain a $27 \times 101 \times 85$ focused data volume. Note that both techniques work with the same acquired C-scan but the result of diffraction stacking has smaller dimensions due to a selected 3-D grid with $1 \times 1 \times 0.5$ cm cell.
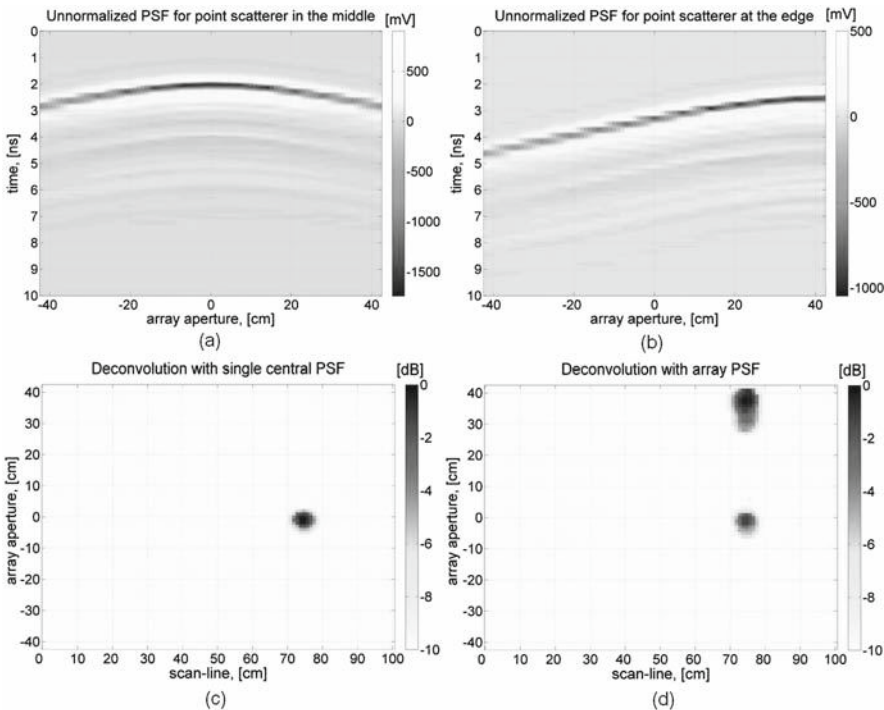
Fig. 4 3-D array imaging by deconvolution: (**a**) cross section of unnormalized PSF for point scatterer in the middle of the array aperture; (**b**) cross section of unnormalized PSF for point scatterer at the edge of the array aperture; (**c**) focused image by deconvolution with single, central PSF; (**d**) focused image by deconvolution with array PSF

4 Conclusions

A novel 3-D imaging algorithm has been developed for an array GPR which has a potential to be used in online processing. The algorithm takes into account GPR impulse response and such properties of the soil as dielectric constant, loss tangent, and transmission coefficients which are used to form an array point spread function (PSF). Deconvolution of array PSF out of the acquired data is done with a 3-D Wiener inverse filter that iteratively adjusts its regularization parameter until two efficiency criteria are satisfied. The criteria control numerically sharpness of the focused image and amount of artifacts. The developed algorithm has been tested on a realistic data set with two buried landmines. It can image the targets independently of their position within the array aperture. Comparison with a classical migration by diffraction stacking shows a huge difference in computational time, more specifically 23 h vs. 8 min by deconvolution. Deconvolution provides a sharper image for synthetic aperture formed in the mechanical scan direction but within the array aperture the image quality degrades when target is shifted from the middle. Further investigation will be conducted toward more accurate estimation of array PSF and combination of its deconvolution results. Influence of the burial depth needs a separate analysis as well.

References

1. A. G. Yarovoy, T. G. Savelyev, P. J. Aubry, P. E. Lys, and L. P. Ligthart, UWB array-based sensor for near-field imaging, IEEE Transactions on Microwave Theory and Techniques, vol. 55, pp. 1288–95, 2006.
2. T. G. Savelyev, A. G. Yarovoy, and L. P.Ligthart, Weighted near-field focusing in an array-based GPR, Radio Sci., vol. 43, RS4S11, doi:10.1029/2007RS003791, 2008.
3. B. Scheers and M. Acheroy, Migration technique based on deconvolution, in Daniels D. (ed.) Ground Penetrating Radar, second edition. IEE Radar, Sonar, Navigation and Avionics Series 15, Bodmin, Cornwall, UK, 2004.
4. T. G. Savelyev, L. van Kempen, and H. Sahli, Deconvolution techniques, in Daniels D. (ed.) Ground Penetrating Radar, second edition. IEE Radar, Sonar, Navigation and Avionics Series 15, Bodmin, Cornwall, UK, 2004.
5. T. G. Savelyev, T. Kobayashi, X. Feng., and M. Sato,. Robust target discrimination with UWB GPR, in Sabbath F., Mokole E. L., Schenk U., and Nitsch D. (eds.) Ultra-wideband, short-pulse electromagnetics 7, Springer, New York, 2007.
6. V. Kovalenko, Advanced GPR data processing algorithms for detection of anti-personnel landmines, Ph.D. dissertation, Delft University of Technology, The Netherlands, 2006.

Time-Domain Characterization of Asymptotic Conical Monopole

Dhiraj Kumar Singh and Devendra Chandra Pande

Abstract Impulse response of an ultra-wideband antenna needs to be determined to completely characterize it. Hence, knowledge of the input to the antenna and its response to the same along with a technique to relate them with the impulse response needs to be devised. Deconvolving the input and the output signals gives the impulse response of the system. A solution to the deconvolution problem is presented using an iterative method, wherein the iteration is applied over discrete data in time domain. Given the input and the measured output from an asymptotic conical monopole, which is an ultra-wideband system, a method is shown to determine the impulse response of the monopole. The uniqueness of the estimate of the impulse response is sensitive to the nature of the errors in input and output data acquired. Here, conjugate gradient method is employed to estimate the impulse response of the monopole antenna.

Keywords Asymptotic conical monopole · D-dot · TEM cell · Deconvolution · Conjugate gradient method

1 Introduction

The asymptotic conical monopole used here as an equipment under test (EUT) for estimation of impulse response, is a D-dot type of electromagnetic field sensor. The output voltage of the sensor is time derivative of the electric flux density. Pulsed electromagnetic field is generated using a pulse source and a transverse electromagnetic (TEM) cell. With the assumption that a uniform transverse electromagnetic wave exists within the cell, the asymptotic conical monopole sensor placed within and its output was recorded on an oscilloscope. Irrespective of the experimental setup, there might exist many solutions to deconvolution problem. The best solution should be aptly chosen. The minimum error solution will be a fair choice. The convergence to such a solution depends on the formulation of the problem and the approach adopted to arrive at the solution.

The method adopted is the conjugate gradient method. Given the output of the monopole and its input, an iterative procedure to estimate the impulse response is implemented. The instrumentation

D.K. Singh (✉)
Electronics & Radar Development Establishment, Bangalore, India
e-mail: dhiraj_lrde@rediffmail.com

used in the experiment is solar electronics CS115 source as input pulse generator, a TEM cell, and a 500 MHz agilent oscilloscope.

2 The Deconvolution Problem

A system can be completely characterized by its impulse response. The convolution for finite impulse response system is defined by *a[n]*

$$
\begin{aligned}
y[n] &= \sum_{k=0}^{K} a[k]x[n-k] = a[n] \otimes x[n] \\
&= x[n] \otimes a[n]
\end{aligned}
\tag{1}
$$

where, *y[n]* is the observed output and *x[n]* is the input to the system.

The above equation can be expanded for all values of *n* to represent a system of linear equations, which can be represented in the matrix form given as

$$
XA = Y,
\tag{2}
$$

where X represents the transform on the vector A to give the vector Y. The problem reduces to finding an inverse X transform. The possibility of X being a singular matrix prohibits us from directly solving the above equation. Hence the conjugate gradient approach, which is not affected by the singularity property of the matrix X, is employed. CG converges to a possible solution **A,** by minimizing the squared error

$$
\zeta^2 = <Xa - y; Xa - y> ,
\tag{3}
$$

where <:> denotes the inner product between two vectors. The minimization is performed in N steps, where N is the number of equations to be solved. Each iteration refines the estimate of a along a search direction, which is X orthogonal to all previous search directions.

The choice of a time-domain method over the conventional frequency-domain approach is adopted because the monopole considered is a wideband sensor. And hence to determine its characteristics, a huge range of frequencies has to be swept. This can be achieved simply by stimulating the monopole with a pulse of a few nano-seconds pulse width, thereby analyzing the monopole effectively.

In practical measurements, the exact knowledge of the time signals is not possible. As a result of bandwidth limitation of the time signal detector and the digitization and acquisition processes, the acquired waveform differs to a certain extent from the true signal. Denoting the acquired waveforms by

$$
x_w(t) = x(t) + x_e(t)
\tag{4}
$$

and

$$
y_w(t) = y(t) + y_e(t),
\tag{5}
$$

where $x_e(t)$ and $y_e(t)$ represent the error components, respectively.

And the corresponding frequency domain form is

$$[Y_w(j\omega) - Y_e(j\omega)] = H(j\omega).[X_w(j\omega) - X_e(j\omega)]. \tag{6}$$

Consequently, $H(j\omega)$ is given by

$$H(j\omega) = \frac{Y_w(j\omega)}{X_w(j\omega)}. \tag{7}$$

In practical solutions $x(t)$ is a band-limited signal, i.e., $X(j\omega)$ has a finite bandwidth and, consequently, there exists a region of frequencies approximation, $X(j\omega) \approx X_w(j\omega)$ is not a good one. The deconvolution $H_e(j\omega)$ will contain some fairly high values. These values can be viewed as a sequence of spikes. Upon the application of inverse Fourier transformation to $H_w(j\omega)$, the spikes that were concentrated in the frequency regions of small $X(j\omega)$ produce error contributions that are spread over the entire time-domain epoch. And if the error components are high, they may dominate the time-domain transformation, thereby hiding most of the details of $h_w(t)$. Hence a time-domain deconvolution method was adopted to thwart such errors.

3 Algorithm Description

The conjugate gradient algorithm is an iterative search procedure which calculates a set of approximate solutions $\{a_k\}$ obtained by searching along a set of direction vectors $\{p_k\}$. Efficiency of the search procedure results from reduction in the dimensionality of the error subspace. The error vector may be shown to be X-orthogonal to all previous search directions, on any given iteration. Thus, the minimum is achieved (to within available arithmetic precision) in at most N iterations. The algorithm followed is as given below. It is started off with an initial guess of A. By using any initial guess $[A]_0$ for the solution, the matrices $[R]$ and $[P]$ are generated, where

$$[R]_0 = [X][A] - [Y] \tag{8}$$

and

$$[P]_0 = -[X]^T[R], \tag{9}$$

where $[X]$ is the transformation matrix formed from the input vector; it is a toeplitz matrix. $[A]$ is the vector which needs to be determined. It represents the impulse response of the monopole. $[Y]$ is the vector which represents the discrete output signal.

$$[A]_{n+1} = [A]_n + t_n[R]_n, \tag{10}$$

where $t_n = \frac{|[X]^T[R]_n|^2}{|[X][P]_n|^2}$.

And $[R]$ and $[P]$ are obtained according to the relations

$$\begin{aligned} [R]_n &= [R]_{n-1} + t_{n-1}[X][P]_{n-1} \\ &\text{and} \\ [P]_n &= -[X]^T[R]_n + q_{n-1}[P]_{n-1} \end{aligned}, \tag{11}$$

$$q_{n-1} = \frac{\left|[X]^T [R]_n\right|^2}{\left|[X]^T [R]_{n-1}\right|^2}. \tag{12}$$

The advantage of the conjugate gradient method is that it is an iterative scheme that usually yields excellent results within J iterations where J is the number of independent eigenvalues of $[X]^{T*} [X]$. It has been shown that the conjugate gradient method converges to a solution even when $[X]^{T*}[X]$ is singular. For this case the iteration process is terminated once the solution stops converging (i.e., begins to oscillate).

4 Measurement Method

The monopole needs to be exposed to a uniform transverse electromagnetic pulse field to get its response to the pulsed field. In the absence of impulse radiating antenna, pulsed TEM field was simulated using a TEM cell of bandwidth 500 MHz and the pulsed source used for the experiment was a solar electronics made voltage source, commonly used for CS115 test of MIL-STD 461E, of rise time less than 2 ns. The pulser output at the other end of TEM cell and the monopole output have been recorded simultaneously in the two channels of the agilent 500 MHz oscilloscope. The measurement setup is shown in Fig. 1.

The monopole was driven with an input pulse of duration of 34 ns. The simultaneous display of the input to and the output from the sensor are as shown in Fig. 2. The discrete values of input and output were stored as vectors X and Y, respectively, in the text format from the scope which was utilized for further processing.

Fig. 1 Measurement setup
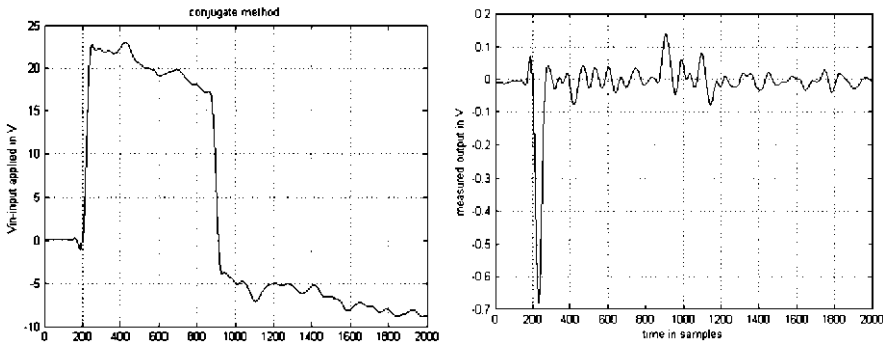
Fig. 2 Input and output signals from the oscilloscope

5 Results

The impulse response of the UWB monopole sensor is determined with a set of input output pairs. The responses obtained by applying conjugate gradient algorithm on one of the input–output pair are shown in Fig. 3.
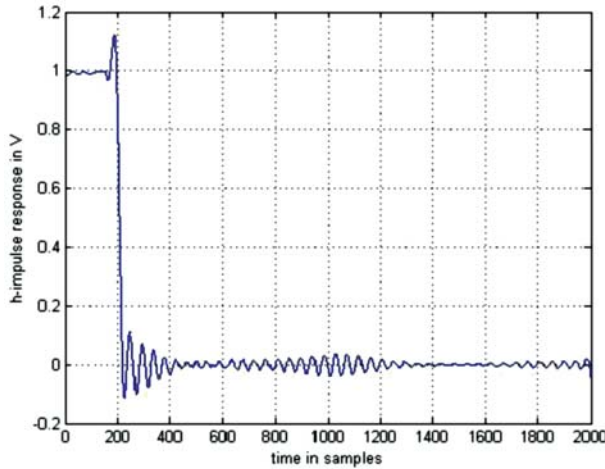
Fig. 3 Estimated impulse response

The signal obtained by convoluting the estimated impulse response and the actual input used to stimulate the monopole are shown below in Fig. 4.

The actual output as seen on the oscilloscope is shown in Fig. 5 and error in estimating A, i.e., the difference between the actual output signal and the signal obtained by convoluting input with the estimated response is shown in Fig. 6. The error in determining the system output to the given input using the estimated impulse response is given by (13).

$$error = XA - Y. \tag{13}$$
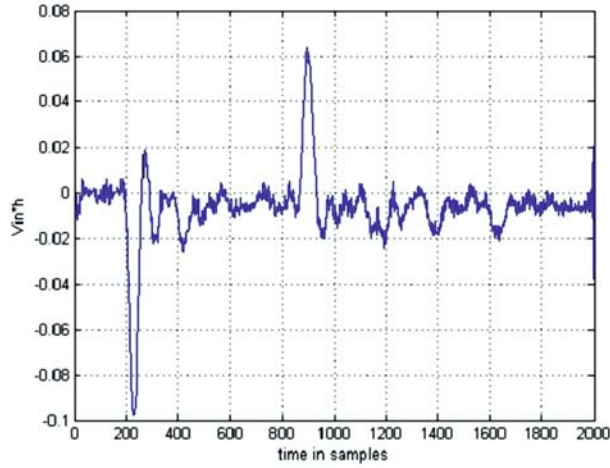
Fig. 4 Convolution of the given input and the estimated impulse response
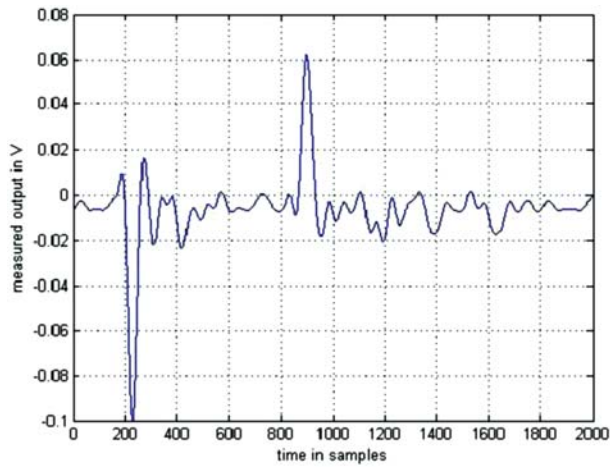
Fig. 5 Output as seen on the scope

The error parameters are also tabulated below:

Standard deviation in *error* = 0.0014
Variance of *error* = 1.8652*e*−006
Mean value of *error* = 2.5214*e*−008

The impulse response as estimated from another input–output pair for the same system is as shown in Fig. 7.

Fig. 6 Error in the estimation of output
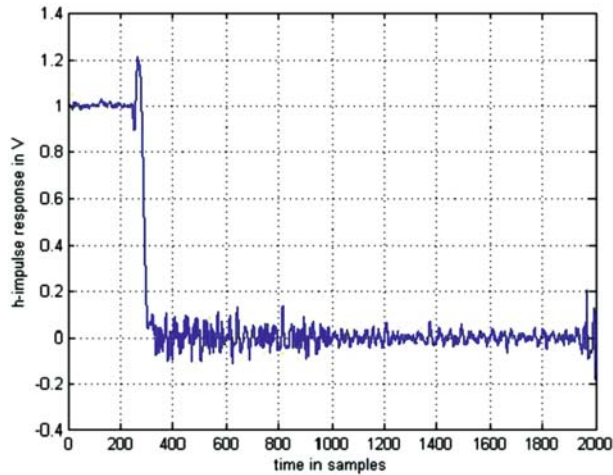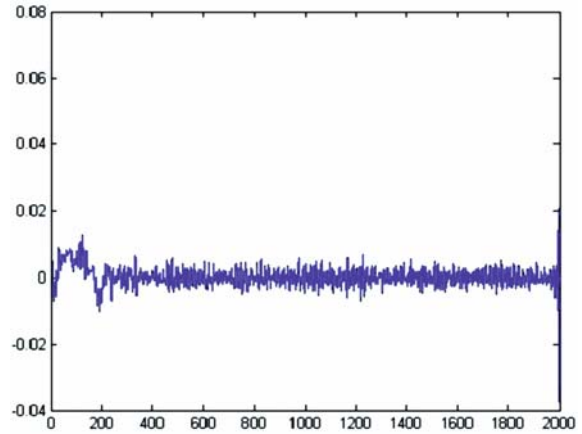
Fig. 7 Impulse response as determined for the same system from a different input–output pair

6 Conclusion

The impulse response of the system as determined from two different sets of input and output pairs are as shown in Figs. 4 and 7. The similarity is evident from the figures. Also, the statistical parameters of the *error* as shown above imply an acceptable error in determining the impulse response of a monopole. Time-domain simulation method of characterizing UWB monopole sensor using the conjugate gradient method was presented in this chapter. The measured antenna transfer function was found to be close to the simulated one indicating that we can use a software-based approach like MATLAB used here to determine the impulse response of the monopole sensor. Moreover, using the same technique, the impulse response of any other ultra-wideband LTI system can be determined.

References

1. T. K. Sarkar and D. D Weiner et. al., Impulse response determination in the time domain-theory, IEEE Transactions on Antenna & Propagation, vol. AP-30, no. 4, pp. 657–63, July 1982.
2. T. K. Sarkar and D. D Weiner et al., Some mathematical considerations in dealing with the inverse problem, IEEE Transactions on Antenna & Propagation, vol. AP-29, no. 2, pp. 373–79, March 1981.
3. T. Sarkar, F. I. Tseng, S. M. b o, S. A. Dianat, B. Z. Hollman, Deconvolution of impulse response from time-limited input and output: theory and experiment, IEEE Transactions on Instrumentation and Measurement, vol. IM-34, no. 4, pp. 541–46, December 1985.
4. Tapan K. Sarkar (ed.), Applications of conjugate gradient method to electromagnetics and signal analysis, Chapter 7, vol. 5, pp. 242–60, Elsevier-1991.
5. Edmund K. Millers (ed.), Time-domain measurements in electromagnetics, Chapter 3, pp. 87–93, 1986.

A TDFEM-Employed Temporal Second-Order Lagrange Interpolation for Three-Dimensional EM Radiation Problems

X. Wu and L. Zhou

Abstract This chapter investigates a new time-domain finite element method (TDFEM) based on Lagrange interpolation and high-order Whitney elements for temporal and spatial expansion, respectively. This approach is motivated by goals of achieving computational efficiency and further applying to ultra-wideband (UWB) antenna simulation. Traditional TDFEM scheme is based on Galerkin's method with a piecewise linear temporal expansion of the electric field. In this chapter, we use a second-order Lagrange interpolation polynomial instead of linear temporal expansion. Such a multistep interpolation scheme leads to a more robust interpolation and a more efficient approximation. Moreover, this method allows for a consistent time discretization of the electric field vector wave equation with the augmented perfectly matched layer (PML) regions. The novel scheme is first verified by applying on a canonical problem, i.e., the cavity resonance problem. The results achieved by this scheme were in close agreement with the analytical solution. We finally applied this scheme to a dipole antenna and compared the results from the TDFEM by using piecewise linear temporal basis function. We found that they were in good agreement with each other.

Keywords Time-domain finite element method · Second-order Lagrange interpolation polynomial · Temporal basis function · Electromagnetic radiation · Ultra-wideband antenna

1 Introduction

Recently, various new types of ultra-wideband (UWB) antennas with complex geometry structure and material distribution have become the most important devices in wireless communication as well as the radar systems. Researchers pay more attention toward modeling and simulating UWB-based antennas and radars.

Time-domain finite element method (TDFEM), among proposed computational electromagnetics methods in the past decade, has been demonstrated as a powerful technique for the accurate analysis of electromagnetic wave phenomena in relation to scattering and radiation [1]. TDFEM covers the drawbacks of finite difference time-domain (FDTD) method and time-domain integral equation (TDIE) method by tackling the unstructured mesh elements in the same manners as finite element

X. Wu (✉)
School of Electronic Engineering and Computer Science, Peking University, Beijing, P.R.China
e-mail: wuxiaeecs00@gmail.com

method (FEM) procedure does. Furthermore it generates sparse matrices in inhomogeneous media. Being a time-domain method, TDFEM is also attractive in its ability to compute the antenna response on many different frequencies in a single run.

Since the emergence of TDFEMs in 1980s, the point-match time-domain finite element method was first investigated by A. C. Cangellaris [2]. This method combined the simplicity of the explicit integration scheme of FDTD with the flexibility of conventional FEM. However, these methods have two obvious disadvantages. First, they employ node elements which cause difficulty in forcing boundary condition; second, they may encounter the leap-frog problems like FDTD. In order to suppress these problems, an unconditional stable inexplicit FETD algorithm was proposed in 1990s [3], which was based on electric (or magnetic) field second-order vector wave equation expanded by spatial vector FEM basis functions and the Newmark-β method for temporal discretization. Although this method is simple and stable, but it solves a huge sparse matrix equation in each time step. That is why TDFEMs did not receive serious attention until the early 2000s. They developed very rapidly after the implementation of perfectly matched layer (PML) in the area of electromagnetics [4]. PML is a landmark in the computational electromagnetics that clearly shows the potential of TDFEMs [5].

This chapter proposed a novel TDFEM by using second-order Lagrange interpolation polynomial temporal basis function. The motivation behind the research was to utilize the convergence and robustness of Lagrange interpolation polynomial [6]. In our algorithm, the electric field is expressed as a combination of piecewise second-order Lagrange interpolation polynomial function in time discretization and high-order Whitney element [7] on tetrahedrons in space discretization.

After the introduction, Section 2 covers a short review of frequent domain FEM as well as the outlines of the derivation of the time-domain FEM formulation. Section 3 introduces second-order Lagrange interpolation polynomial as temporal basis function resulting in a fully discretized system. In Section 4 the numerical results are exhibited with the typical cases that demonstrate the validity of the novel method. The last section concludes our current work.

2 Formulations

2.1 Frequent-Domain FEM Formulation

When an antenna in free space is considered, the infinite region can be truncated by Sacks PML [4], which can efficiently absorb the outward propagating electromagnetic waves. By letting $s = j\omega$, and $\vec{J}_0$ is the applied electric current source, then the Maxwell's equations can be expressed as

$$\nabla \times \vec{E} = -\left(s\left[\mu\right] + \left[\sigma_M\right]\right)\vec{H} = -s\mu_0 \overset{\leftrightarrow}{\Lambda}_M \vec{H}, \tag{1}$$

$$\nabla \times \vec{H} = \left(s\left[\varepsilon\right] + \left[\sigma_E\right]\right)\vec{E} + \vec{J}_0 = s\varepsilon_0 \overset{\leftrightarrow}{\Lambda}_E \vec{E} + \vec{J}_0, \tag{2}$$

where $\overset{\leftrightarrow}{\Lambda}_M = \left[\mu_r\right] + \left[\sigma_M\right]/s\mu_0, \overset{\leftrightarrow}{\Lambda}_E = \left[\varepsilon_r\right] + \left[\sigma_E\right]/s\varepsilon_0$ are the constants or tensors corresponding to the isotropic or anisotropic materials. From (1) and (2), one can get the following equation that the electric field satisfies:

$$\nabla \times \left(\overset{\leftrightarrow}{\Lambda}_M^{-1} \cdot \nabla \times \vec{E}\right) + \frac{s^2 \overset{\leftrightarrow}{\Lambda}_E}{c_0^2} \cdot \vec{E} = -s\mu_0 \vec{J}_0. \tag{3}$$

Equation (3) is valid for the whole calculated regions, but in the PML regions, $\overset{\leftrightarrow}{\Lambda}_M = \overset{\leftrightarrow}{\Lambda}_E = diag\left\{\gamma_y\gamma_z/\gamma_x, \gamma_z\gamma_x/\gamma_y, \gamma_x\gamma_y/\gamma_z\right\}$ $\gamma_i = 1 + \beta_i(i)/s$, $i = x, y, z$. c_0 represents the speed of light in the vacuum.

Afterward the entire volume will be divided into a series of tetrahedral. Taking inner product of (3) with a test function $\vec{N}_i$ (second-order Whitney edge elements [7]) and applying Green's first vector identity one can obtain the weak form of (3) [3]

$$\iiint_\Omega \left((\nabla \times \vec{N}_i) \cdot \overset{\leftrightarrow}{\Lambda}_M^{-1} (\nabla \times \vec{E}) + \vec{N}_i \cdot \frac{s^2 \overset{\leftrightarrow}{\Lambda}_E}{c_0^2} \vec{E} \right) dV = \iiint_\Omega \left(-s\mu_0 \vec{N}_i \cdot \vec{J}_0 \right) dV. \tag{4}$$

The electric field $\vec{E}$ can also be expanded as their linear combination. So (4) can be written algebraically so that the electric field can be solved for a given single frequency.

As for the case of UWB antennas is concerned, the frequent-domain FEM seems less efficient. In order to avoid the time cost for swept frequency in broadband simulation, we utilized the time-domain FEM, namely, the problems will be solved in time-domain directly.

2.2 Time-Domain FEM Formulation

Both sides of (4) are the function of s, by using the inverse Laplace transform and letting

$$\vec{E}(\vec{r}, t) = \sum_j e_j(t) \vec{N}_j(\vec{r}) \tag{5}$$

Equation (4) can be transformed into a time-domain formulation [8]

$$[L]\frac{d^2}{dt^2}\{e\} + [M]\frac{d}{dt}\{e\} + [S]\{e\} - \{p\} + \{q\} = \{f\}, \tag{6}$$

where

$$L_{ij} = \iiint_V \frac{1}{c_0^2}\vec{N}_i \cdot \vec{N}_j dV, \tag{7}$$

$$M_{ij} = \iiint_V \frac{1}{c_0^2}\vec{N}_i \cdot \bar{J} \cdot \vec{N}_j dV, \tag{8}$$

$$S_{ij} = \iiint_V (\nabla \times \vec{N}_i) \cdot (\nabla \times \vec{N}_j) \, dV + \iiint_V \frac{1}{c_0^2}\vec{N}_i \cdot \bar{C} \cdot \vec{N}_j dV, \tag{9}$$

$$p_i = \iiint_V \frac{1}{c_0^2}\vec{N}_i \cdot \sum_j (\bar{D} \cdot \vec{N}_j) dV, \tag{10}$$

$$q_i = \iiint_V (\nabla \times \vec{N}_i) \cdot \sum_j [\bar{F} \cdot (\nabla \times \vec{N}_j)] dV, \tag{11}$$

$$f_i = -\iiint_V \mu_0 \vec{N}_i \frac{\partial \vec{J}}{\partial t} dV, \tag{12}$$

$$\bar{J} = diag\left\{\beta_y + \beta_z - \beta_x, \beta_z + \beta_x - \beta_y, \beta_x + \beta_y - \beta_z\right\}. \tag{13}$$

$\bar{C}$ is a diagonal matrix with

$$\bar{C}_{xx} = (\beta_x - \beta_y)(\beta_x - \beta_z) \tag{14}$$

and $\bar{C}_{yy}$, $\bar{C}_{zz}$ are treated analogously by given cyclic permutation of (x, y, z); $\bar{D}$ and $\bar{F}$ are diagonal matrices as well, which involves temporal convolution terms

$$\bar{D}_{xx} = \beta_x (\beta_x - \beta_y)(\beta_x - \beta_z) \cdot e^{-\beta_x t *} e_j(t), \tag{15}$$

$$\bar{F}_{xx} = \left(\frac{\beta_y (\beta_x - \beta_y)}{(\beta_y - \beta_z)} \cdot e^{-\beta_y t} + \frac{\beta_z (\beta_x - \beta_z)}{(\beta_z - \beta_y)} \cdot e^{-\beta_z t} \right) * e_j(t), \tag{16}$$

Analogously, $\bar{D}_{yy}$, $\bar{D}_{zz}$, $\bar{F}_{yy}$, $\bar{F}_{zz}$ are yielded by cyclic permutation of (x, y, z). Equation (6) is a semi-discretized matrix system; in order to obtain the fully discretized system, $e_j(t)$ should be expressed by the certain time basis functions:

$$e_j(t) = \sum_m e_j^m T^m(t), \tag{17}$$

where e_j^m is unknown coefficient which corresponds to $e_j(t)$ at $t = t^m$ for integer m, for instance, $T(t) = 1 - |t/\Delta t|$ is linear temporal basis function ranging from $-\Delta t$ to Δt.

3 Second-Order Lagrange Interpolation Polynomial

3.1 Lagrange Interpolation Polynomial Function

In this section, we introduce the formulation of Lagrange interpolation. An interpolation can be defined as a function $I(x)$, which contains independent variable x and a number of parameters. For $n+1$ given points (x_i, y_i), $i = 0, 1,\ldots, n$, through suitable parameters, we can construct the interpolation function $I(x)$. For example, Lagrange interpolation polynomial function of degree n has analytical expression [6] as

$$I(x) = y_0 T_0^{(n)}(x) + y_1 T_1^{(n)}(x) + \ldots + y_n T_n^{(n)}(x), \tag{18}$$

where $T_0^{(n)}, \ldots, T_n^{(n)}$ denote the parameters in Lagrange interpolation formulation that can be calculated by the $n+1$ given points:

$$T_i^{(n)} = \frac{(x - x_0) \ldots (x - x_{i-1})(x - x_{i+1}) \ldots (x - x_n)}{(x_i - x_0) \ldots (x_i - x_{i-1})(x_i - x_{i+1}) \ldots (x_i - x_n)} \quad T_i^{(n)}(x_k) = \begin{cases} 1, if\ i = k \\ 0, if\ i \neq k \end{cases}. \tag{19}$$

Lagrange interpolation functions become popular since their computation cost is lower than other interpolation functions.

3.2 Temporal Discretization by Second-Order Lagrange Interpolation Polynomial Function

Unlike Reference [8] that used a linear temporal basis, here the electric field $e_j(t)$ is expressed in terms of a second-order Lagrange interpolation polynomial. In (18) and (19), let t represents the independent variable x, and $n = 3$, one can get the following expression defined in $[-\Delta t, 2\Delta t]$:

$$T(t) = \begin{cases} \frac{1}{2}(t/\Delta t)^2 + \frac{3}{2}(t/\Delta t) + 1 & -\Delta t \leq t \leq 0 \\ -(t/\Delta t)^2 + 1 & 0 \leq t \leq \Delta t \\ \frac{1}{2}(t/\Delta t)^2 - \frac{3}{2}(t/\Delta t) + 1 & \Delta t \leq t \leq 2\Delta t \\ 0 & \text{elsewhere} \end{cases}. \tag{20}$$

Equation (20) is our temporal basis function, which is shown in Fig. 1.

The stability of a scheme depends on the temporal discretization, that is, on the choice of the temporal basis and test functions. As usual, we apply the Newmark method in temporal discretization to obtain a stable scheme. In order to match the Newmark-β method [9] and our temporal basis function, we let the test function $W_n(t)$ be

$$W_n(t) = a_3 |t/\Delta t|^3 + a_2 |t/\Delta t|^2 + a_1 |t/\Delta t| + a_0 - \Delta t < t < \Delta t, \tag{21}$$

where the coefficients a_3, a_2, a_1, a_0 are determined by satisfying the Newmark-β method stability condition and our chosen temporal basis functions. In this way we get the test function $W_n(t)$ as

$$W_n(t) = 40 |t/\Delta t|^3 - 45 (t/\Delta t)^2 + 9 |t/\Delta t| + 1 - \Delta t < t < \Delta t. \tag{22}$$
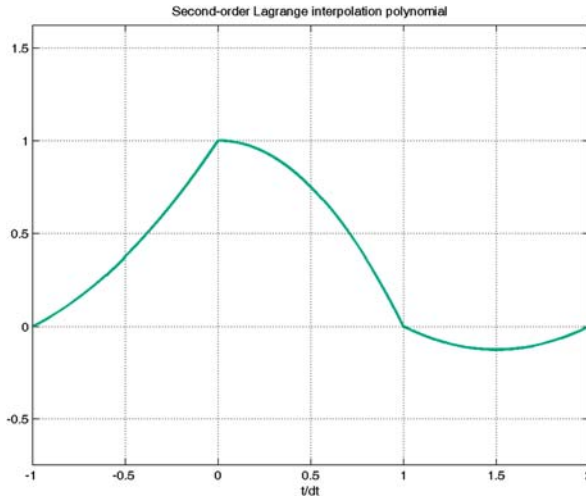
Fig. 1 The second-order Lagrange interpolation polynomial

Substituting (18) and (20) into (6), testing (6) with (22), we obtain the fully discretized system:

$$[L]\frac{1}{(\Delta t)^2}(e_{n+1} - 2e_n + e_{n-1}) + [M]\frac{1}{2\Delta t}(e_{n+1} - e_{n-1}) + [S](\beta_1 e_{n+1} + \beta_0 e_n + \beta_{-1} e_{n-1}) =$$
$$(\beta_1 f_{n+1} + \beta_0 f_n + \beta_{-1} f_{n-1}) + (\beta_1 p_{n+1} + \beta_0 p_n + \beta_{-1} p_{n-1}) - (\beta_1 q_{n+1} + \beta_0 q_n + \beta_{-1} q_{n-1})$$
(23)

where $\beta_1 = \beta_{-1} = 1/4$, $\beta_0 = 1/2$, which is found to exactly match the Newmark-β unconditional stable scheme in the non-PML region.

4 Numerical Experiments

A FORTRAN program based on the novel TDFEM is presented here in this section. The proposed new scheme is employed on canonical examples. In order to validate the accuracy and stability of the proposed scheme, a simple example of the excitation of a lossless cavity with perfectly conducting walls was studied. Then a dipole antenna was chosen for studying the radiation patterns.

For the source impulse as a function of time, we utilize Gaussian pulse in (24). The waveforms of source pulse and its spectra are given by Fig. 2, where $t_0 = 6T$, $f_0 = 1/T = 2946$ MHz:

$$V = \left(1 - \frac{(t - t_0)^2}{T^2}\right) exp\left[-0.5 \times \frac{(t - t_0)^2}{T^2}\right].$$
(24)
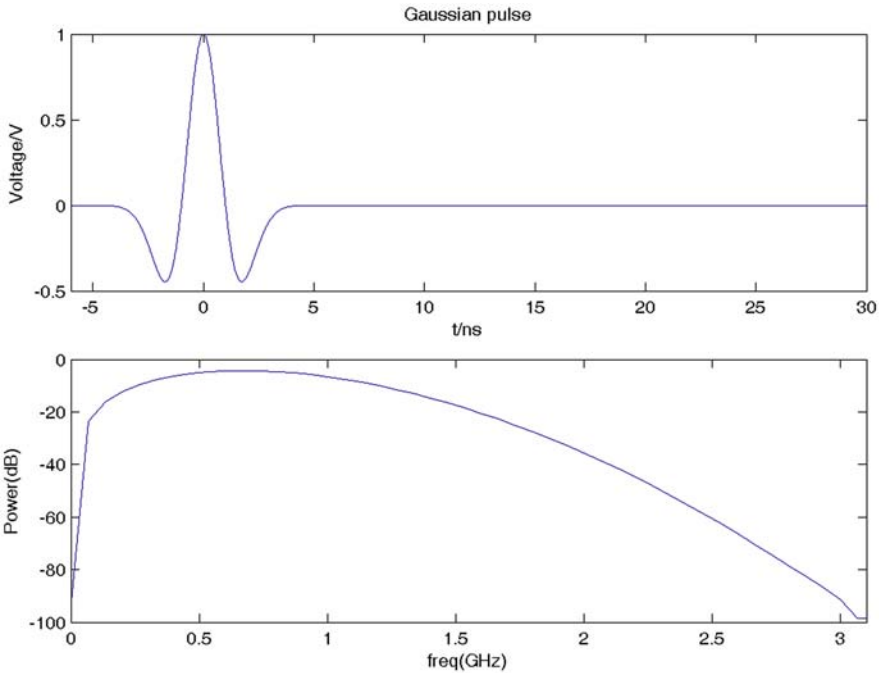
Fig. 2 The waveforms and spectra of Gaussian pulses

4.1 Cavity

The dimensions of the cavity are 0.072 m by 0.050 m by 0.072 m, and the exact resonant frequency for the TE_{101} mode is 2946 MHz. The simulations were performed over the time period $t = 0$–48 ns with the time-step of $\Delta t = 8$ ps and the resonant frequency was obtained by fast Fourier transformation of the time response. Table 1 illustrates the resonant frequency of the cavity for the TE_{101} mode by using several methods. It can be seen that the results from the TDFEM with second-order Lagrange interpolation temporal basis function are in good agreement with those from analysis method; thus the correctness and efficiency of our proposed approach was proven.

Table 1 The resonant frequency of the cavity for the TE_{101} mode

The employed method	Resonant frequency (MHz)	Relative error (‰)
Analysis method	2946	0
TDFEM + linear basis	2951	1.6970
TDFEM + second-order Lagrange interpolation	2947	0.3394
TDFEM + B-splines [10]	2947	0.3394

4.2 Dipole Antenna

The second case is a dipole antenna which is constructed from a perfectly electric conducting (PEC) wire as shown in Fig. 3, and with the feed source along y-axis. The lengths of the two poles are 0.025 m. For this antenna, we calculated the far field radiation patterns in time domain, which are shown in Figs. 4 and 5. They demonstrate the features of electric field value (the y-component and the z-component of the electric field, i.e., Ey and Ez, respectively) with respect to time and θ.

In order to verify the far field results obtained with the proposed method, we use Fourier transform to convert the results to radiation patterns at different frequencies and compare these patterns with those obtained by method in [8]. Figure 6 shows a comparison of the E-plane radiation pattern at 2.8 GHz. It can be seen that solutions from the novel TDFEM are in good agreement with those from method in [8].
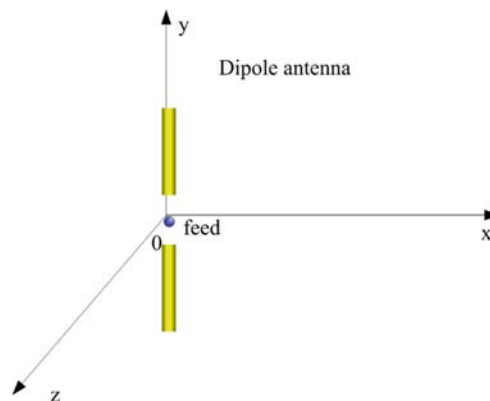
Fig. 3 Dipole antenna model
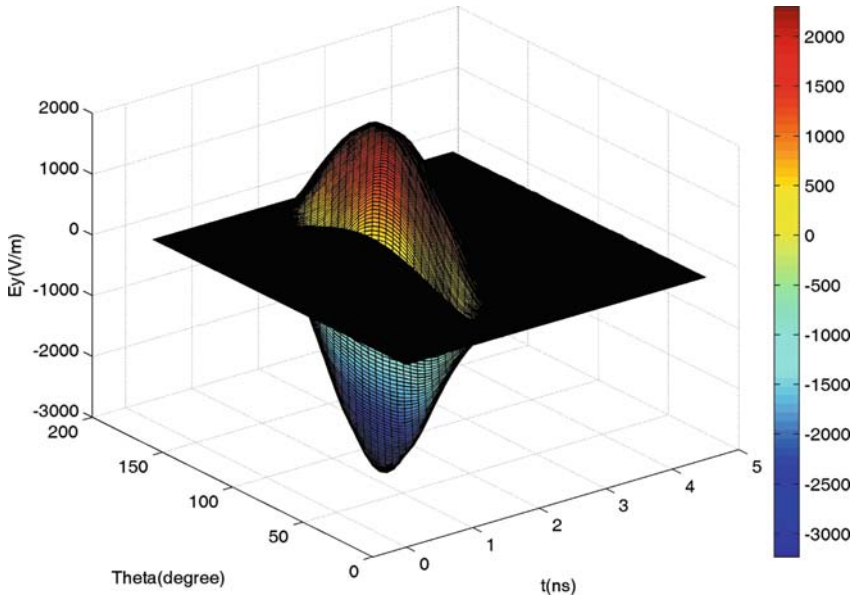
Fig. 4 The time-domain radiation pattern of a dipole antenna (*y*-component of the electric field)
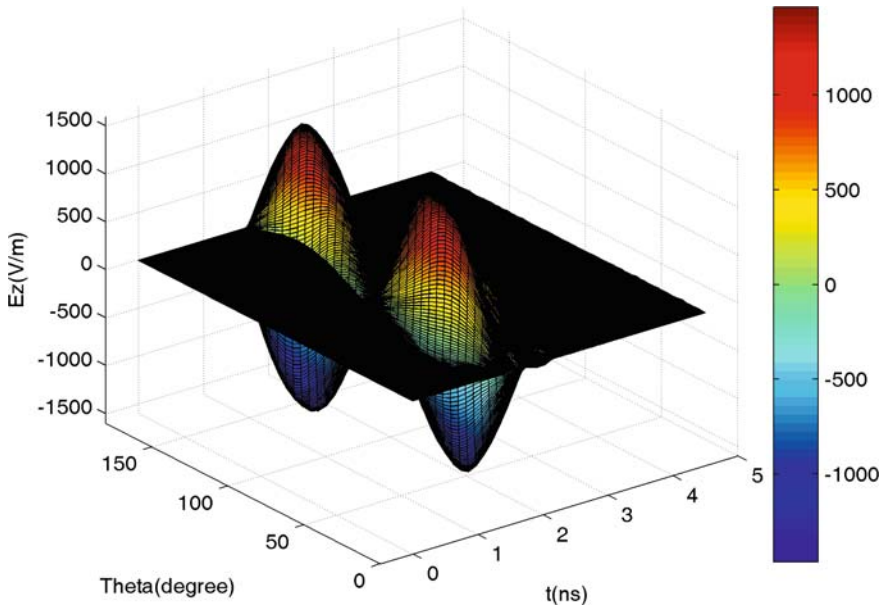
Fig. 5 The time-domain radiation pattern of a dipole antenna (*z*-component of the electric field)
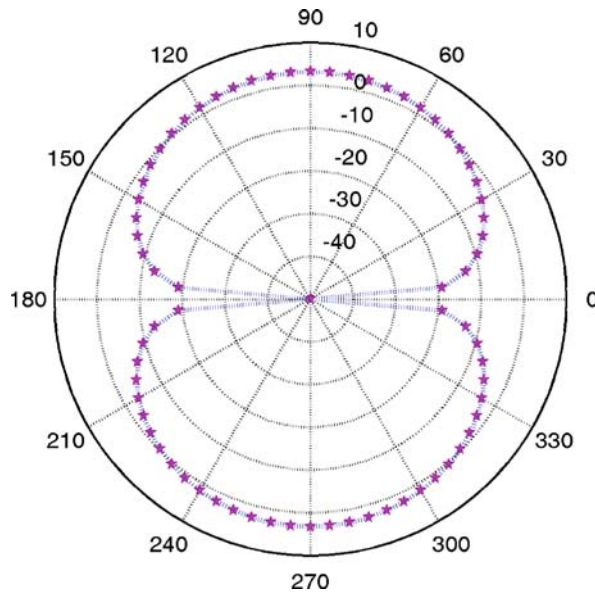
Fig. 6 The E-plane radiation pattern (dB) at 2.8 GHz, the line denotes the TDFEM with second-order Lagrange interpolation polynomial function; the stars denote the TDFEM with linear basis function

5 Conclusions

A novel time-domain finite element method for three-dimensional electromagnetic radiation problems is presented. The method uses second-order Lagrange interpolation polynomials as temporal basis functions, and it is shown to be unconditionally stable. Then the results were demonstrated that the stable and accurate scheme is achievable.

To sum up, with our proposed numerical technique, the computational efficiency and accuracy of TDFEM can be improved. This numerical technique can be used for general electromagnetic radiation problems.

References

1. J. M. Jin, The Finite Element Method in Electromagnetics, second edition. Wiley, New York, 2000.
2. A. C. Cangellaris et al., Point-matched time domain finite element methods for electromagnetic radiation and scattering. IEEE Transactions on Antennas and Propagation, vol. 35, no. 10, pp. 1160–73, 1987.
3. Stephen D. Gedney and U. Navsariwala, An unconditionally stable finite element time-domain solution of the vector wave equation, IEEE Microwave and Guided Wave Letters, vol. 5, no. 10, pp. 332–34, 1995.
4. Z. Sacks, D. Kingsland, R., and Lee et al., A perfectly matched anisotropic absorber for use as an absorbing boundary condition. IEEE Transactions on Antennas Propagation, vol. 43, no. 12, pp. 1460–63, 1995.
5. D. Jiao, J. M. Jin, E. Michielssen et al., Time-domain finite-element simulation of three-dimensional scattering and radiation problems using perfectly matched layers. IEEE Transactions on Antennas Propagation, vol. 51, no. 2, pp. 296–305, 2003.
6. Jinghong Zheng and Lap-Pui Chau, A motion vector recovery algorithm for digital video using Lagrange interpolation. IEEE Transactions on Broadcasting, vol. 49, no. 4, pp. 383–89, 2003.
7. J. Lee and Z. Sacks, Whitney elements time domain (WETD) methods. IEEE Transactions on Magnetics, vol. 31, no. 3, pp. 1325–29, 1995.

8. T. Rylander and J. M. Jin, Perfectly matched layers in three dimensions for the time-domain finite element method applied to radiation problems. IEEE Transactions on Antennas Propagation, vol. 53, no. 4, pp. 1489–99.
9. N. Newmark, A method of computation for structural dynamics. Journal of Engineering Mechanics Division, vol. 85 pp. 67–94, 1959.
10. Xia Wu and Lezhu Zhou, Application of B-spline temporal basis function in time-domain finite element method for three-dimensional EM radiation problem, 2008 A-P Symp. on EMC & 19th International Zurich Symposium. On Electromagnetic Compatibility, Singapore: 774–777.

TLM Simulation of Wave Envelopes Using Dynamic Phasors

D.W.P. Thomas, J.D. Paul, and C. Christopoulos

Abstract The TLM simulation of the slow-varying envelope of a carrier wave using the principle of dynamic phasors enables the TLM cell size to greatly exceed the normal $\lambda/10$ restriction. The TLM equivalent circuit necessary to simulate dynamic phasor propagation is described. Example results showing the performance of the technique for solving fundamental problems such as lossy propagation or the simulation of propagation in a medium with a constant dielectric are presented.

Keywords TLM · Dynamic phasor · Lossy propagation

1 Introduction

Many electromagnetic problems such as radio propagation, RADAR, or optical devices have time-dependent or non-linear behaviour which can best be simulated using time-domain differential techniques such as TLM or FDTD. However, the problem size often exceeds many wavelengths which make it computationally too expensive to solve using time-domain differential techniques. On the other hand, by using a dynamic phasor representation of the waveforms, simulation of the dynamic phasor amplitude and phase variation is only restricted by the carrier wave envelope bandwidth and the system time constants. The simulation in the time domain of electrically large problems then becomes more manageable.

The principle of dynamic phasors was first described in [1]. The carrier wave is represented by a phasor with a time-dependent amplitude and phase and it is this which is then applied to the simulation algorithm. In this chapter an approach for modelling dynamic phasor propagation with TLM is described. The theory of dynamic phasors is first described followed by a description of a dynamic phasor TLM node. Results for lossy propagation and propagation in a homogeneous dielectric medium are then presented to demonstrate the power of this approach, and conclusions and suggestions for future developments are given.

————————————————

D.W.P. Thomas (✉)

George Green Institute for Electromagnetics Research, The University of Nottingham, University Park, Nottingham NG7 2RD, UK

e-mail: dave.thomas@nottingham.ac.uk

2 Dynamic Phasors

Dynamic phasors are based on the time-averaged Fourier transform over the interval $\tau \in (t - T, t)$, the kth harmonic coefficient (or k-phasor) at time t is given by [1]

$$X_k(t) = \frac{1}{T} \int_{t-T}^{t} x(\tau) e^{-jk\omega_f \tau} = \langle x \rangle_k(t), \tag{1}$$

where $\omega_f = 2\pi / T$ is the fundamental angular frequency. Dynamic variations of these Fourier coefficients for moving time window are then simulated. In constructing the simulation formulation the following result is used [1]

$$\frac{dX_k}{dt} = \left\langle \frac{d}{dt} x \right\rangle_k - jk\omega_f X_k. \tag{2}$$

By applying (2) to the telegraphers equations for propagation in the z direction along a lossy line of per unit length parameters C, G, L and R which are the capacitance, conductance, inductance and resistance, respectively, we obtain

$$\frac{d^2 X_k}{dz^2} - CL \frac{d^2 X_k}{dt^2} - (GL + RC + 2jk\omega_f CL) \frac{dX_k}{dt} - (R + jk\omega_f L)(G + jk\omega_f C)X_k = 0. \tag{3}$$

Equation (3) suggests that dynamic phasor propagation can be represented by propagation along a transmission line with complex conductivity and resistivity:

$$\begin{aligned} \mathbf{G} &= G + j\omega C \\ \mathbf{R} &= R + j\omega L \end{aligned}. \tag{4}$$

The TLM [2] implementation of dynamic phasor simulation therefore is achieved with a node that has complex conductivity and resistivity as given by (4). Care must be taken to note that the terms are distributed and for large cell sizes the lumped equivalent circuits will not be valid. A formulation for the cell using distributed parameters has to be used as given by the Norton equivalent circuit in Fig. 1, where v_L^i and v_R^i are the incident voltage pulses from the left and right, respectively, $Z_0 = \sqrt{L/C}$, $Z_{tl} = \sqrt{\mathbf{R}/\mathbf{G}}$ and the other quantities are calculated at each time step. It then follows that by using

$$\begin{aligned} T_1 &= \frac{1}{Z_0 \sinh(\Delta z \sqrt{\mathbf{GR}})} \\ T_2 &= \frac{1 - \coth(\Delta z \sqrt{\mathbf{GR}})}{Z_0} \end{aligned}, \tag{5}$$
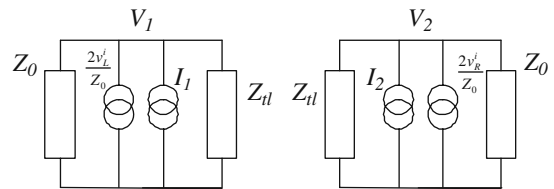
Fig. 1 TLM cell circuit for the simulation of dynamic phasors

then

$$\begin{bmatrix} V_1 \\ V_2 \end{bmatrix} = \frac{2}{Z_0} \begin{bmatrix} \frac{Z_0+Z_{tl}}{Z_0 Z_{tl}} - T_2 & -T_1 \\ -T_1 & \frac{Z_0+Z_{tl}}{Z_0 Z_{tl}} - T_2 \end{bmatrix}^{-1} \begin{bmatrix} v_L^i \\ v_R^i \end{bmatrix}. \tag{6}$$

The left and right reflected pulses v_L^i, v_R^i, respectively, are then calculated from

$$\begin{bmatrix} v_L^r \\ v_R^r \end{bmatrix} = \begin{bmatrix} V_1 \\ V_2 \end{bmatrix} - \begin{bmatrix} v_L^i \\ v_R^i \end{bmatrix}. \tag{7}$$

These reflected pulses then propagate to the adjacent nodes to form the incident pulses for the next time step which is normally termed the connection process [2]. In this formulation the connection process can be viewed as reproducing the first two terms in (3) and the other terms are given by the cell circuit solution (5–7). Note also that the TLM scattering and connection process is here carried out with complex voltage phasor pulses.

Often in TLM it is useful to a circuit to the nodes to represent more complex medium properties [2, 3]. At the simplest level extra capacitance or inductance is added using a TLM stub in the cells. This can also be done in the dynamic phasor representation but the extra component must also be added to the distributed complex conductance and reactance. For example, to added extra capacitance Cs to the dynamic phasor TLM cell the equivalent circuit becomes as given in Fig. 2, where

$$\mathbf{G}_c = G + j\omega(C + C_s), \tag{8}$$

$$T_{c1} = \frac{1}{Z_0 \sinh\left(\frac{\Delta z}{2}\sqrt{\mathbf{G}_c \mathbf{R}}\right)} \tag{9}$$

$$T_{c2} = \frac{1-\coth\left(\frac{\Delta z}{2}\sqrt{\mathbf{G}_c \mathbf{R}}\right)}{Z_0}$$
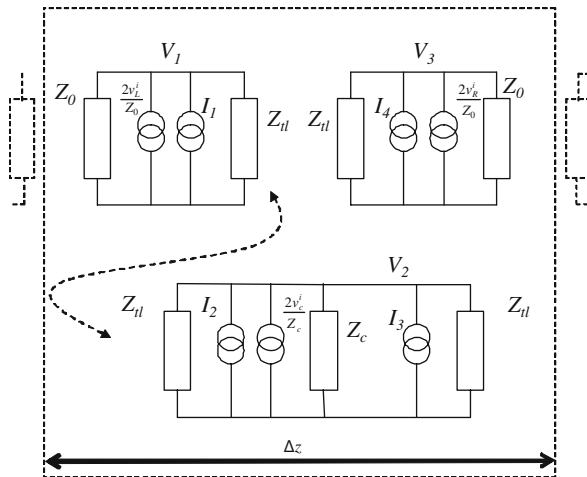
Fig. 2 Norton equivalent circuit of a dynamic phasor TLM cell with capacitive stub added

It then follows that

$$
\begin{bmatrix} V_1 \\ V_C \\ V_2 \end{bmatrix} = \begin{bmatrix} \frac{Z_0+Z_{tl}}{2Z_{tl}} - \frac{Z_0}{2}T_2 & -\frac{Z_0}{2}T_1 & 0 \\ -\frac{Z_C}{2}T_1 & \frac{2Z_C+Z_{tl}}{2Z_{tl}} - Z_C T_2 & -\frac{Z_C}{2}T_1 \\ 0 & -\frac{Z_0}{2}T_1 & \frac{Z_0+Z_{tl}}{2Z_{tl}} - \frac{Z_0}{2}T_2 \end{bmatrix}^{-1} \begin{bmatrix} v_L^i \\ v_C^i \\ v_R^i \end{bmatrix}, \tag{10}
$$

where Z_C is the capacitance stub impedance [2], v_C^i is the incident pulse on the capacitive stub and the reflected wave on the capacitive stub is found from $v_C^r = V_C - v_c^i$.

The other pulses can be found using (7) and the connection process as before. For 2D and 3D TLM the central section in Fig. 2 can represent the coupling to the orthogonal directions in the nodes. The scattering matrix can then be solved. For example for a symmetric 2D shunt node of a homogeneous linear frequency independent material this reduces to a scattering matrix given by

$$
S = 0.5 \begin{bmatrix} -e^{-\gamma l} & e^{-\gamma l} & e^{-\frac{\gamma l}{2}} & e^{-\frac{\gamma l}{2}} \\ e^{-\gamma l} & -e^{-\gamma l} & e^{-\frac{\gamma l}{2}} & e^{-\frac{\gamma l}{2}} \\ e^{-\frac{\gamma l}{2}} & e^{-\frac{\gamma l}{2}} & -e^{-\gamma l} & e^{-\gamma l} \\ e^{-\frac{\gamma l}{2}} & e^{-\frac{\gamma l}{2}} & -e^{-\gamma l} & -e^{-\gamma l} \end{bmatrix}. \tag{11}
$$

3 Results

To illustrate the TLM simulation of dynamic phasors, the propagation of a pulse with a 1 GHz carrier frequency and modulated by a Gaussian envelope along a lossy transmission line with characteristics is given in Table 1. The first example in Fig. 3 shows the TLM simulation of the complete waveform using standard TLM cells of length $\Delta z = 1.5$ cm ($\lambda/20$) compared with the dynamic phasor simulation of the waveform using cells of length $\Delta z = 30$ cm (λ). Two profiles are shown. One is after

— DF TLM at 0.2 ns
···· TLM at 0.2 ns
— TLM at 0.1 ns
–·– DF TLM at 0.1 ns
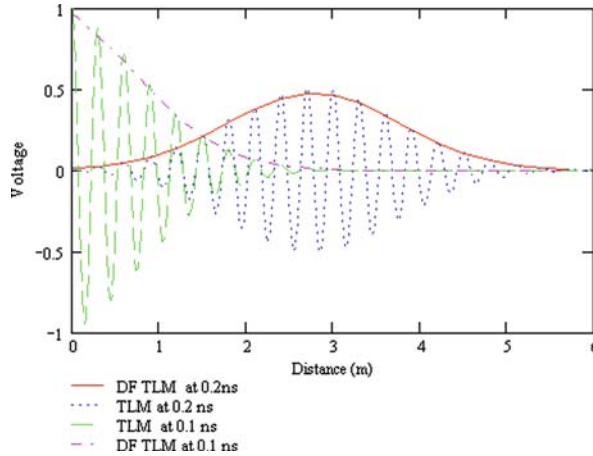
Fig. 3 Simulated propagation on a lossy transmission line using both normal TLM and TLM with dynamic phasors

Table 1 The optimized values of compact low-pass filter

R	L	G	C
0.1 Ω/m	166.7 nH/m	0.0001 s/m	66.67 pF

Fig. 4 Simulated propagation with capacitive stubs representing a relative permittivity = 4 using both normal TLM and TLM with dynamic phasors
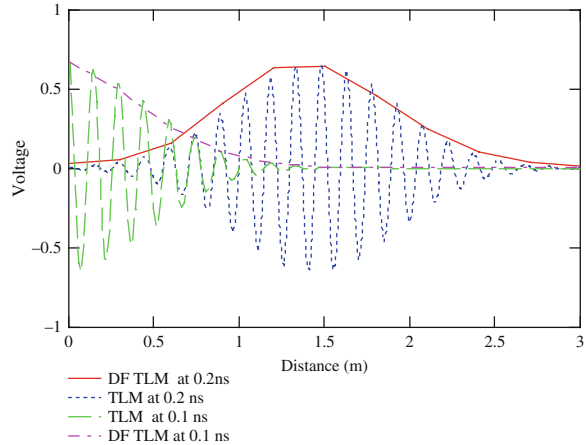
propagation for 10 ns and the other after 20 ns. The dynamic phasor simulation reproduces the same attenuation as for the normal TLM simulation.

In the second example the propagation is lossless but an extra capacitance of 20 pF is added as a stub in the cell centres to represent a halving of the propagation velocity and the characteristic line impedance as for a medium of relative permittivity $\varepsilon_r = 4$. Figure 4 shows the resulting waveforms simulated both with conventional TLM and TLM simulation of dynamic phasor. Two profiles are shown. One is after propagation for 10 ns and the other after 20 ns. The dynamic phasor simulation also reproduces the same propagation delay.

The final example is the predicted interference pattern for two 424×10^{12} Hz sources separated by 6 μm deduced using a 2D TLM shunt mesh with a cell size 1 μm. Figure 5 shows the TLM simulation compared with the theoretical pattern and observed at a distance of 0.4 mm. Notice the main differences between simulation and theoretical prediction are due to the discrete representation of phase differences in this formulation.
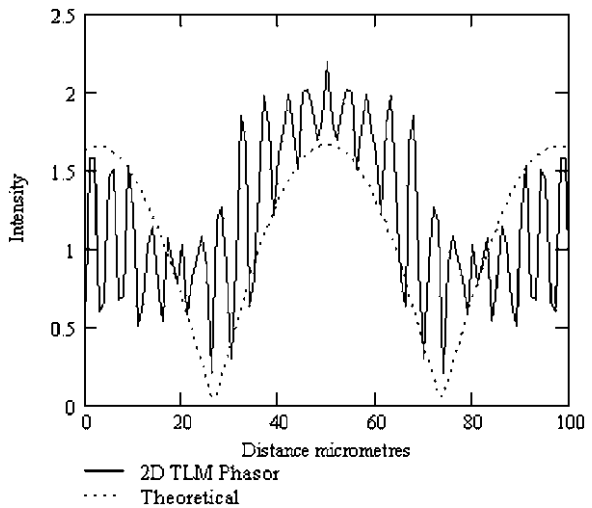
Fig. 5 Simulated interference pattern of two 424×10^{12} Hz sources separated by 6 μm deduced using a 2D TLM shunt phasor mesh with a cell size 1 μm (1λ) and compared with theoretical pattern from point sources

4 Conclusions

A method for simulating the dynamic phasor amplitude of a carrier wave using the TLM methodology has been described. Results show that good agreement with standard TLM can be achieved but with a much greater cell size and corresponding reduction in computation time. This is a powerful technique which will enable large problem spaces to be studied with the time-domain TLM technique.

References

1. A. M. Stanković, Analysis of asymmetrical faults in power systems using dynamic phasors, IEEE Transactions on Power Systems, vol. 15, no. 3, pp. 1062–68, August 2000.
2. C. Christopoulos, The Transmission-Line Modelling Method TLM, IEEE Press, 1995. ISBN 0-7803-1017-9.

Analysis of Anisotropic Microwave Circuits with Several Metallized Interfaces

C. Boularak, M.L. Tounsi, A. Khodja, R. Touhami, and M.C.E. Yagoub

Abstract This chapter presents a new theoretical analysis of multilayered anisotropic microwave circuits based on a modified spectral-domain approach (SDA). The number of conducting strips/slots located on several interfaces of dielectric layers can be arbitrary set. The numerical solutions obtained by this technique are discussed and compared with published data. Furthermore, original configurations based on three-level metallized couplers were computed and validated using neural network models. The efficiency of the proposed technique is demonstrated through the determination of dispersion characteristics such as effective dielectric constant, normalized phase velocity, and characteristic impedance.

Keywords Microwave circuits · Anisotropic · Multilayer · Numerical method · Green's functions

1 Introduction

Primarily due to their advantages over isotropic substrates, the use of anisotropic materials as microwave substrates has become popular in a variety of devices, including directional couplers, random antennas, and non-reciprocal integrated circuits [1, 2]. In addition, since isotropic MIC substrates may exhibit anisotropic properties at higher millimeter-wave frequencies, analyzing the anisotropic behavior of substrates is critical for accurate device design. In fact, passive elements in conventional RF/microwave anisotropic circuits use transmission line sections and waveguides in different configurations, thereby achieving the desired functionality and meeting performance specifications. This functionality is largely achieved by the use of coupled transmission lines [3]. In electromagnetic (EM) theory, the coupled power is function of the physical dimensions of the structure, the mode of propagation, the frequency of operation, and the direction of propagation of the primary power. The coupling mechanism must be accurately described. Since, most of the coupled structures are primarily realized using only two metallized interfaces, an accurate circuit design must be performed including anisotropic effects as well. To reach that target, the authors have used an efficient computation technique based on extension of spectral domain approach (SDA) for analysis of many anisotropic microwave circuits with several conducting strips/slots located on several

C. Boularak (✉)

Instrumentation Laboratory, Faculty of Electronics and Informatics, USTHB University, Bab Ezzouar 16111, Algiers, Algeria
e-mail: boularak_chafik@hotmail.com

interfaces of dielectric layers [4, 5]. These circuits are very useful in the design of many microwave components for wireless communications.

   This technique uses a transfer matrix expression between tangential components of EM fields on two consecutive interfaces H_i and H_{i+1}, which make the evaluation of Green's functions easier. The proposed method exhibits attractive features: (i) The use of Fourier transform allows the conversion of convolution integrals equations into algebraic products, avoiding the evaluation of complex integrals. (ii) The SDA method is numerically more efficient than others working in space domain since the anisotropic and multilayer problems can be resolved by a simple product of different transfer matrices. (iii) The coupling phenomena between different conducting interfaces can be resolved using superposition theorem. (iv) The solution obtained by this method is stationary by nature. Thus, the solution is insensitive to the first-order error associated with the basis functions.

2 Spectral Domain Method Formulation

Figure 1 shows a cross section of the circuit under analysis. The conductors are assumed to be perfectly conducting and infinitesimally thin, and the substrates are assumed to be biaxially anisotropic such that ε and μ are diagonal tensors.

   The first step consists of a transform coordinate system from (x, y, z) to (u, y, v) coordinate system (Fig. 1) to simplify the evaluation of EM field components and boundary conditions at all dielectric interfaces. Maxwell's equations are then Fourier transformed to the spectral domain. Hence, tangential components of the EM field are expressed in a dielectric layer i ($i = 1,\ldots, N$) as
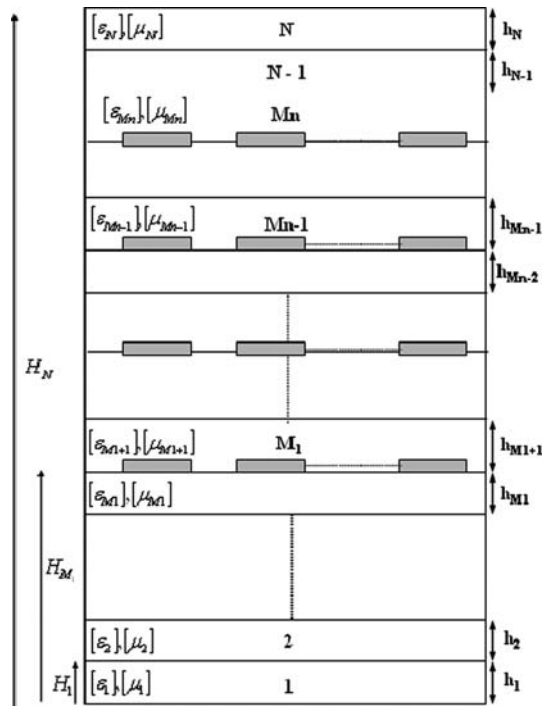
Fig. 1 Cross section of the analyzed multilayer circuit

$$\tilde{E}_{ui} = \frac{-\omega\mu_y}{\rho^*}\tilde{H}_{yi}, \tag{1}$$

$$\tilde{E}_{vi} = \frac{\omega\mu_y\alpha_n\beta\delta\varepsilon}{\rho^*\rho_\varepsilon}\tilde{H}_{yi} - j\frac{\varepsilon_y\rho^*}{\rho_\varepsilon}\frac{\partial\tilde{E}_{yi}}{\partial y}, \tag{2}$$

$$\tilde{H}_{ui} = \frac{\omega\varepsilon_y}{\rho^*}\tilde{E}_{yi}, \tag{3}$$

$$\tilde{H}_{vi} = \frac{-j\mu_y\rho^*}{\rho_\mu}\frac{\partial\tilde{H}_{yi}}{\partial y} + \frac{\omega\alpha_n\beta\varepsilon_y\delta\mu}{\rho^*\rho_\mu}\tilde{E}_{yi}, \tag{4}$$

with $\rho^* = \sqrt{(\alpha_n^2 + \beta^2)}$, $\rho_\mu = (\alpha_n^2\mu_x + \beta^2\mu_z)$, $\rho_\varepsilon = (\alpha_n^2\varepsilon_x + \beta^2\varepsilon_z)$, $\delta\mu = (\mu_x - \mu_z)$, $\delta\varepsilon = (\varepsilon_z - \varepsilon_x)$.

The normal EM field components must satisfy to the following wave equations:

$$\frac{\partial^4(\tilde{E}_{yi}, \tilde{H}_{yi})}{\partial y^4} + \left(f_{1i}^e, f_{1i}^h\right)\frac{\partial^2(\tilde{E}_{yi}, \tilde{H}_{yi})}{\partial y^2} + \left(f_{2i}^e, f_{2i}^h\right)(\tilde{E}_{yi}, \tilde{H}_{yi}) = 0, \tag{5}$$

where

$$f_1^e = k_0^2\left(\varepsilon_{rx}\mu_{rz} + \varepsilon_{rz}\mu_{rx}\right) - \alpha_n^2\left(\mu_x/\mu_z + \varepsilon_x/\varepsilon_y\right) - \beta^2\left(\varepsilon_z/\varepsilon_y + \mu_x/\mu_y\right)$$

and

$$f_2^e = -\left(k_0^2\varepsilon_{rx}\varepsilon_{rz}\mu_x/\mu_y - \mu_x(\alpha_n^2\varepsilon_x - \beta^2\varepsilon_z)/(\varepsilon_y\mu_y)\right), \left(\alpha_n^2 + \beta^2\mu_z/\mu_x - k_0^2\varepsilon_{ry}\mu_{rz}\right)$$

k_0 is the free wave number. The f_1^h and f_2^h coefficients can be easily obtained from f_1^e and f_2^e simply by permuting between ε and μ. The general solution of (5) may be written as

$$\tilde{E}_{yi} = A_i^e \sinh\left(\gamma_{ei}^a.(-1)^k.(y - H_i)\right) + B_i^e \cosh\left(\gamma_{ei}^b.(-1)^k.(y - H_i)\right), \tag{6}$$

$$\tilde{H}_{yi} = A_i^h \sinh\left(\gamma_{hi}^a.(-1)^k.(y - H_i)\right) + B_i^h \cosh\left(\gamma_{hi}^b.(-1)^k.(y - H_i)\right), \tag{7}$$

where $k = 1$ for $i \geq m_i$, $k = 2$ for $i \leq m_i$ (m_i = metallized interface) and

$$\gamma_{ei}^a = \sqrt{\frac{-f_1^e - (f_1^{e2} - 4f_2^e)^{1/2}}{2}}; \; \gamma_{ei}^b = \sqrt{\frac{-f_1^e + (f_1^{e2} - 4f_2^e)^{1/2}}{2}}, \; \gamma_{hi}^a = \sqrt{\frac{-f_1^h - (f_1^{h2} - 4f_2^h)^{1/2}}{2}};$$
$$\gamma_{hi}^b = \sqrt{\frac{-f_1^h + (f_1^{h2} - 4f_2^h)^{1/2}}{2}}$$

2.1 Evaluation of the Impedance Green's Functions

The boundary conditions that require the tangential fields between two consecutive anisotropic layers (i and $i+1$) at $y = H_i$ can be expressed as

$$\vec{\Re}_{i+1}\Big|_{y=H_i} - \vec{\Re}_i\Big|_{y=H_i} = \vec{\Im}_i, \tag{8}$$

where

$$\vec{\Re}_i\Big|_{H_i} = \big[\, \tilde{E}_{ui}\ \tilde{E}_{vi}\ \tilde{H}_{ui}\ \tilde{H}_{vi}\,\big]^T_{y=H_i}\,,\ \vec{\Im}_i = \big[\, 0\ 0\ \tilde{J}_{vi}\ -\tilde{J}_{ui}\,\big]^T_{y=Hi}$$

and $\tilde{J}_{ui}$, $\tilde{J}_{vi}$ represent the current sources at the conducting interface.

From (1) and (3), two transfer matrix relations that relate the EM fields at $y = H_i$ (or H_{i-1}) to the EM fields at $y = H_{i-1}$ (or H_i) are, respectively, obtained in the form of

$$\vec{\Re}_i\Big|_{Y=H_i} = [M]_i\ \vec{\Re}_i\Big|_{y=H_{i-1}}\,, \tag{9}$$

$$\vec{\Re}_i\Big|_{y=H_{i-1}} = [M]_i^*\ \vec{\Re}_i\Big|_{y=H_i}\,, \tag{10}$$

$[M]_i$ and $[M]_i^*$ represent the transfer matrix whose elements depend on frequency, propagation constant β, and anisotropic layer properties.

The application of the boundary conditions to the tangential components of EM fields on $y = H_i$ in absence of metallization leads to the following form:

$$\vec{\Re}_i\Big|_{y=H_i} = [M]_i\ \vec{\Re}_{i-1}\Big|_{y=H_{i-1}}\,, \tag{11}$$

$$\vec{\Re}_i\Big|_{y=H_{i-1}} = [M]_i^*\ \vec{\Re}_{i+1}\Big|_{y=H_i}\,. \tag{12}$$

In order to obtain the impedance function at the metallized interface m_1, we used the superposition theorem. This means that there is no conducting interface at $m_2, m_3, \ldots, m_n$.

Thus,

$$\vec{\Re}_{m1}\Big|_{y=H_{m1}} = [M]^{1,m1}\ \vec{\Re}_1\Big|_{y=0}\,, \tag{13}$$

$$\vec{\Re}_{m1+1}\Big|_{y=H_{m1}} = [M]^{*N,m1+1}\ \vec{\Re}_N\Big|_{y=H_N}\,, \tag{14}$$

where $[M]^{1,m1} = \prod\limits_{i=1}^{i=m1} [M]_i$, $[M]^{*N,m1+1} = \prod\limits_{i=N}^{i=m1+1} [M]_i^*$. The boundary conditions at $y = 0$, $y = H_{m1}$, and $y = H_N$ imposes the following requirements:

at $y = 0$:

$$\vec{\Re}_1\Big|_{y=0} = \big[\, 0\ 0\ \tilde{H}_{u1}\ \tilde{H}_{v1}\,\big]^T_{y=0}\,, \tag{15}$$

at $y = H_{m1}$:

$$\vec{\Re}_{m1+1}\Big|_{y=H_{mi}} - \vec{\Re}_{m1}\Big|_{y=H_{mi}} = \vec{\Im}_{m1}\,, \tag{16}$$

at $y = H_N$:

$$\vec{\Re}_N\Big|_{y=H_N} = \big[\, 0\ 0\ \tilde{H}_{uN}\ \tilde{H}_{vN}\,\big]^T_{y=H_N}\,, \tag{17}$$

with

$$\vec{\Im}_{m1} = \left[\, 0\ 0\ \tilde{J}_{vm1}\ -\tilde{J}_{um1}\,\right]^T_{y=Hm1}.$$

After replacing (15), (17), into (13), (14), and substituting the resulting expressions into (16), we obtain impedance relations between field and currents at the conducting interface m_1:

$$\vec{\psi}_{m1} = [Z]_{11,uv}\,.\vec{J}_{m1}, \tag{18}$$

where

$$\vec{\psi}_{m1} = \left|\, \tilde{E}_{um1}\ \tilde{E}_{vm1}\,\right|^T_{y=H_{m1}},\ \vec{J}_{m1} = \left|\, \vec{J}_{um1}\ \vec{J}_{vm1}\,\right|^T.$$

Following the same formulation, we can evaluate the impedance form at different conducting layers $(m_2, m_3, ..., m_n)$.

2.2 Evaluation of the Coupling Impedances

The influence of the interface plane m_1 on m_2 and m_2 on m_1, can be described, respectively, as follows:

$$\left.\vec{\Re}_{m2}\right|_{Y=H_{m2}} = [M]^{m1,m2}\,\vec{\Re}_1\Big|_{Y=H_{m1}}, \tag{19}$$

$$\left.\vec{\Re}_{m1}\right|_{Y=H_{m1}} = [M]^{*m2,m1}\,\vec{\Re}_1\Big|_{Y=H_{m2}}, \tag{20}$$

where

$$[M]^{m1,m2} = \prod_{i=m1}^{i=m2} [M]_i,\ [M]^{*m2,m1} = \prod_{i=m2}^{i=m1} [M]_i^*.$$

Therefore, the coupling impedances between the metallized interfaces m_1 and m_2 can be expressed via (18), (19), and (20) as

$$\vec{\psi}_{m1} = [Z]_{12,uv}\ \vec{J}_{m2},\ \vec{\psi}_{m2} = [Z]_{21,uv}\ \vec{J}_{m1}. \tag{21}$$

This procedure can then be generalized for the calculation of the coupling impedances between all arbitrary metallized interfaces M_i (with $i = 1, 2, 3, ..., n$).

Finally, we obtain the Green dyadic matrix:

$$\begin{pmatrix} \vec{\psi}_{m1} \\ \vec{\psi}_{m2} \\ . \\ \vec{\psi}_{Mn} \end{pmatrix} = \begin{bmatrix} [Z]_{11,uv} & [Z]_{12,uv} & .. & [Z]_{1Mn,uv} \\ [Z]_{21,uv} & [Z]_{22,uv} & .. & .. \\ .. & .. & .. & .. \\ [Z]_{Mn1,uv} & & & [Z]_{MnMn,uv} \end{bmatrix} \begin{pmatrix} \vec{J}_{m1} \\ \vec{J}_{m2} \\ . \\ \vec{J}_{Mn} \end{pmatrix}. \tag{22}$$

After switching back to (x, z) coordinates, the Galerkin's technique was used, leading to an algebraic homogeneous system in order to calculate the propagation constant.

3 Characteristic Impedance

Another critical quantity to evaluate is the characteristic impedance. Because of the hybrid mode, the definition of the characteristic impedance is not unique. We shall use hereafter the power–voltage definition for slot mode and power–current for strip mode:

For slot mode:

$$Z_c = \frac{V^2}{2P}. \tag{23}$$

For strip mode:

$$Z_c = \frac{2P}{I_z^2}, \tag{24}$$

where V is the voltage across the slot and I_z is the total conduction current in the strip:

$$V = \int\limits_{-w/2}^{w/2} E_x(x).dx, \; I_z = \int\limits_{-w/2}^{w/2} J_z(x).dx.$$

V (or I_z) can be evaluated since integrand E_x (or I_z) is defined by the field series expansion within the slot (or strip) and by the known amplitudes of the basis functions P is the time-averaged power flow:

$$P = real \sum_{i=1}^{N} \int\limits_{-a/2}^{a/2} \int\limits_{Hi-1}^{Hi} (E_{xi}H_{yi}^* - E_{yi}H_{xi}^*).dydx. \tag{25}$$

By applying Parseval's theorem, (25) becomes

$$P = real \sum_{n=-\infty}^{+\infty} \left(\sum_{i=1}^{Mn} \int\limits_{Hi-1}^{Hi} (\tilde{E}_{xi}\tilde{H}_{yi}^* - \tilde{E}_{yi}\tilde{H}_{xi}^*).dy \right). \tag{26}$$

4 Numerical Results

4.1 Unilateral Circuits

The three-line coupler mode impedances and phase velocities were computed for anisotropic material with various $\varepsilon_{xx}/\varepsilon_{yy}$ ratios ($h_1/H = 0.1$, $h_1/a = 0.1$, $f = 1$ GHz). As shown in Fig. 2, all characteristic impedance modes decreased by increasing the $\varepsilon_x/\varepsilon_y$ ratios. It is interesting to note that Z_{ee} is quite larger than Z_{eo} and Z_{oo} due to the lower capacitance value of this mode. Figure 3 shows that the equalization of phase velocities is achieved for $\varepsilon_x = 2.5 \, \varepsilon_y$. The computed results agree well with [6].

Fig. 2 Characteristic impedance modes versus $\varepsilon_{xx}/\varepsilon_{yy}$
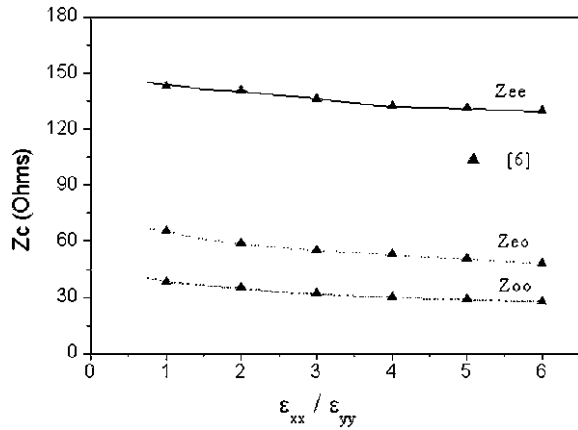
Fig. 3 Normalized phase velocity versus $\varepsilon_{xx}/\varepsilon_{yy}$
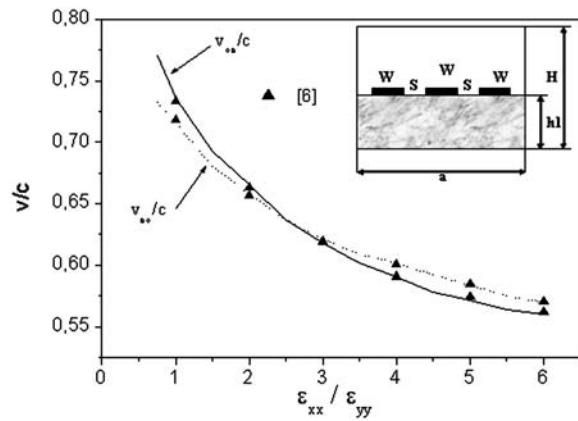
4.2 Bilateral Circuits

The analysis of two-layer three-coupled microstrip lines on uniaxially anisotropic sapphire substrates ($\varepsilon_{x1} = \varepsilon_{x2} = \varepsilon_{z1} = \varepsilon_{z2} = 9.4$, $\varepsilon_{y1} = \varepsilon_{y2} = 11.6$) is presented in the first example. Figures 4 and 5 show the dispersion characteristics, the frequency dependence of the odd and even modes of effective permittivity and characteristic impedance ($2a = 20$ mm, $b = 6$ mm, $h_1 = h_2 = 1$ mm, $h_3 = 2$ cm, $w/h_1 = 1$, $s/h_1 = 0.5$). The computed results show good agreement with [7].

The second example consists of a coupled structure which makes use of a backed conductor to couple two coplanar waveguides on the same side of an isotropic substrate ($\varepsilon_r = 2.5$, $w = 1$ mm, $s = 0.5$ mm, $d = 5$ mm, $2a = 100$ mm, $b = 10$ mm, $h_1 = h_3 = 60$ mm, $h_2 = 0.635$ mm). It is shown from Figs. 6 and 7 that ε_{eff} and Z_c of even and odd modes are almost identical for $L < 5$ mm. However, if $L > 5$ mm the backed conductor is wide enough to cover the two coplanar waveguides on the other side of substrate and a significant difference is observed between the even and odd modes. The computed results were compared to [8] and a good agreement is observed. The larger differences observed in Fig. 6 for larger values of L can be explained by the necessity to increase the number of the basis functions in the Galerkin's procedure to obtain a good convergence.

Fig. 4 Effective permittivity versus *f*
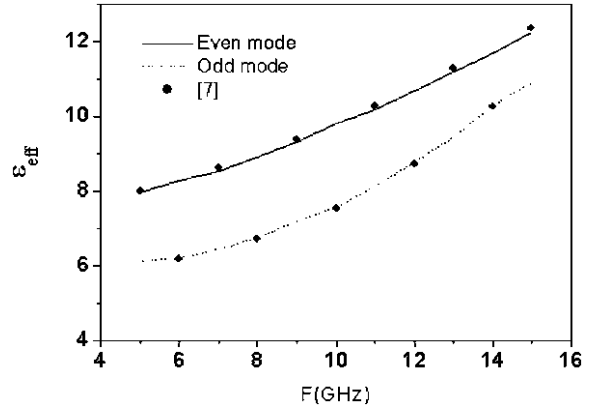
Fig. 5 Characteristic impedance versus *f*
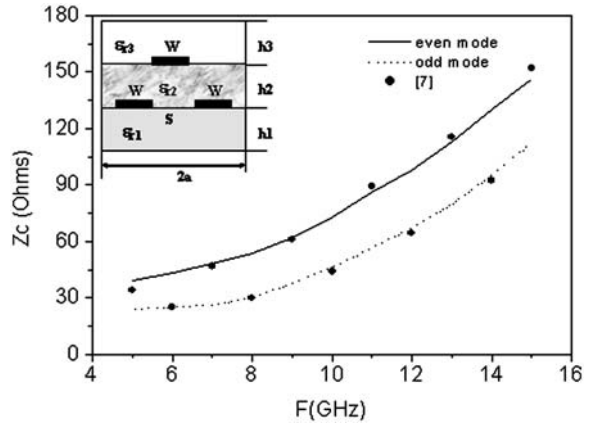
Fig. 6 Effective permittivity versus *L*
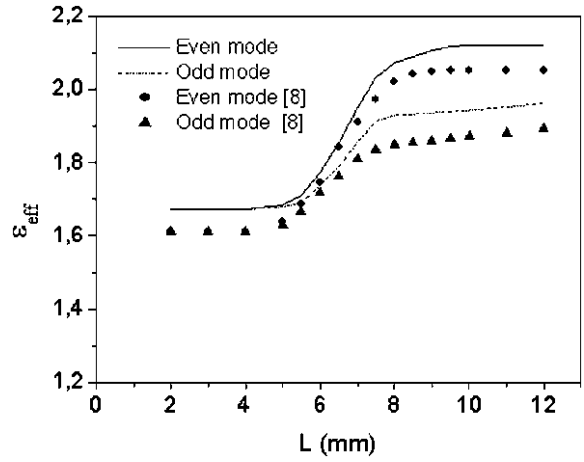
Fig. 7 Characteristic impedance versus L
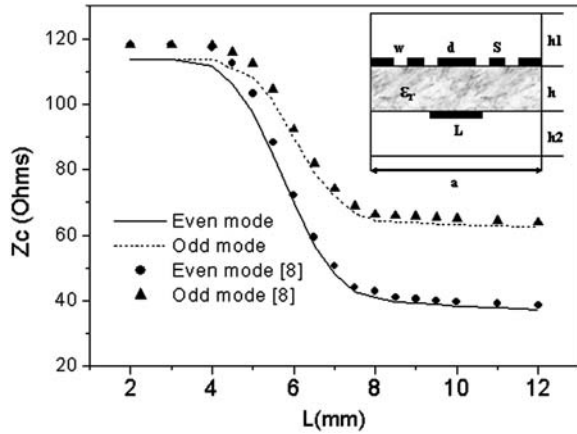
4.3 Three-Level Metallized Circuits

Figures 8 and 9 illustrate the modeling results of a multilayer parallel-coupled microstrip structure suitable for miniaturized MMICs. It consists of two dielectric layers (e.g., silicon oxynitride), isolated by a common ground plane, over a grounded dielectric substrate (e.g., GaAs). The strips are located on two different layers and coupled to each other through a rectangular aperture on the common ground plane ($\varepsilon_{r1} = \varepsilon_{r2} = 5$; $h_1 = h_2 = 5\mu$m; $\varepsilon_{r3} = 12.9$, and $h_3 = 25$ mils). It is shown that ε_{eff} and Z_c of the even and odd modes depend strongly on the strip, in particular for narrow strips ($2w/h<4$). This influence becomes weak for high values of the strip width. A good agreement was observed with regard to [9].

The last circuit consist of a three levels microstrip coupler, including four dielectric layers in which 2 and 3 are anisotropic with ($\varepsilon_{rx2} = 6.64$, $\varepsilon_{ry2} = 6.24$, $\varepsilon_{rz2} = 5.56$; $\varepsilon_{rx3} = 2.35$, $\varepsilon_{ry3} = 2$, $\varepsilon_{rz3} = 3.5$, $\mu_{rx3} = 2.75$, $\mu_{ry3} = 2$, $\mu_{rz3} = 3.5$). We can observe through Fig. 10 that the thickness h_2 influences considerably the even mode permittivity, in particular, for the low values of h_2 where the dispersion is high. On the other hand, for high values of h_2, the dispersion becomes weak. We
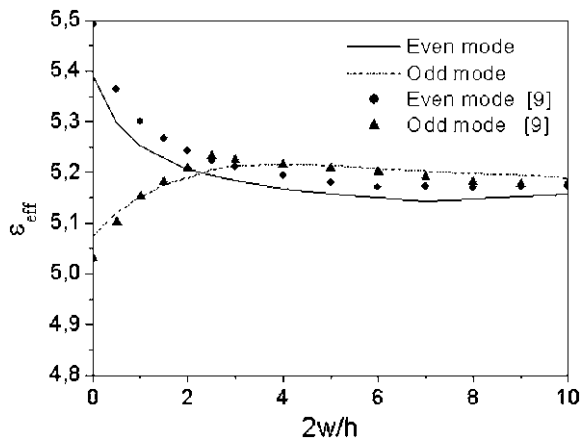
Fig. 8 Effective permittivity versus $2w/h$

Fig. 9 Characteristic
impedance versus 2*w/h*
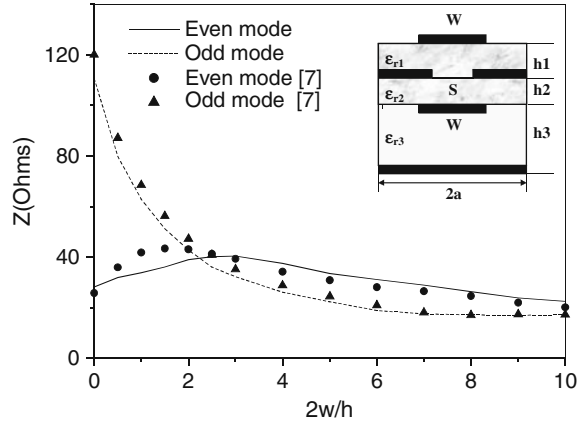
Fig. 10 Even-mode ε_{eff}
versus *F* for several values
of h_2
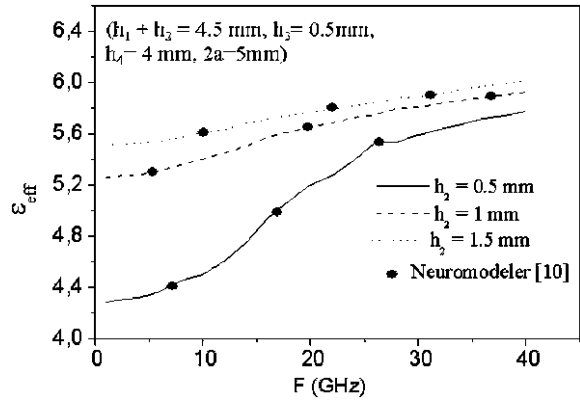
also note that the ε_{eff} increases with h_2. The same observation can be made versus h_3 (Fig. 11)
($h_1 = 4$ mm, $h_2 = 0.5$ mm, $h_3 + h_4 = 4.5$ mm) where ε_{eff} increases with h_3. So, the dispersion is
higher for $h_3 = 1$ mm. In addition, it is interesting to observe that the influence of h_2 is higher than
that due to h_3. The computed results were compared with those simulated by the *Neuromodeler*

Fig. 11 Even-mode ε_{eff}
versus *F* for several values
of h_2
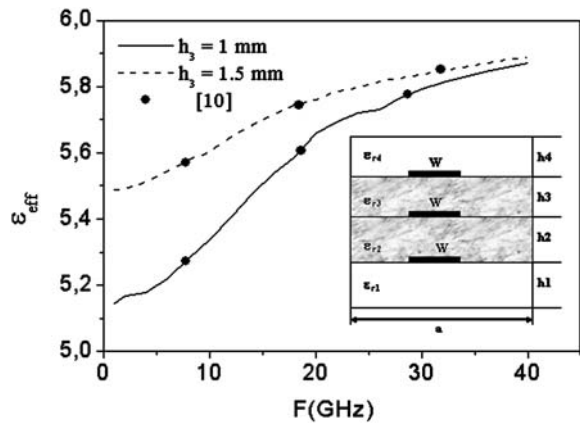
software [10] which exploits the neural network technique. The neural models of the effective permittivity were generated with an average training error of 0.01% and maximum test error lower than 0.9%, confirming the reliability of these models.

5 Conclusion

In this chapter, a contribution to the analysis of planar microwave circuits was proposed with an arbitrary number of anisotropic dielectric layers and metallized levels. The permittivity and permeability tensors were assumed to be diagonal. This analysis was applied to circuits with one, two, and three metallized interfaces but can be easily generalized to multi-level of metallization.

References

1. K. Radhakrishnan et al., Fullwave analysis of multiconductor transmission lines on anisotropic inhomogeneous substrates,' IEEE Transactions on Microwave Theory and Techniques, vol. 47, pp. 1764–70, September 1999.
2. T. Q. Ho et al., Analysis of bilateral fin-lines on anisotropic substrates, IEEE Transactions on Microwave Theory and Techniques, vol. 40, pp. 405–9, February 1992.
3. T. Itoh et al., A generalized spectral domain analysis for coupled suspended microstrip lines with tuning septums, IEEE Transactions Microwave Theory and Techniques, vol. 26, pp. 820–6, October 1978.
4. M. L. Tounsi, R. Touhami, and M. C. E. Yagoub, Generic spectral immittance approach for fast design of multilayered bilateral structures including anisotropic media, IEEE Microwave and Components letters, vol. 17, no. 6, pp. 409–11, June 2007.
5. M. L. Tounsi et al., Analysis of the mixed coupling in bilateral microwave circuits including anisotropy for MICs and MMICs applications, Progress In Electromagnetics Research, vol. 62, pp. 281–315, 2006.
6. L. Yu and B. Rawat, Quasi-Static Analysis of three-line microstrip symmetrical coupler on anisotropic substrates, IEEE Transactions on Microwave Theory and Techniques, vol. 39, no 8, pp. 1433–37, August 1991.
7. C. Seo and C. Woong Lee, Analysis of two-layer three-coupled microstrip lines on anisotropic substrates, IEEE Trans. Microwave Theory Tech., vol. 42, pp. 160–2, January 1994.
8. Chun-Lin Liao, C. Hsing Chen, A novel conductor-backed coplanar-waveguide coupled structure, Asia Pacific Microwave Conf, Singapore, vol. 2, pp. 299–302, November 1999.
9. S. Kunasani and C. Nguyen, Multilayer aperture-coupled broadside microstrip lines IEEE MTT-S Digest, pp. 1367–9, 1999.
10. Q. J. Zhang, NeuroModeler v. 1.2, Carleton University, Ottawa, Canada, 2000.

A Novel High-Miniaturized Semi-fractal Branch-Line Coupler Using Loaded Coupled Transmission Lines

M. Nosrati and M.S. Fealy

Abstract In this chapter, a compact branch-line coupler (BLC) is designed and developed using the previously proposed model of coupled transmission lines and taking up employment of fractal technique on this model. This proposed model is also analyzed using equivalent circuit model. The size reduction of this new BLC is reported about 79% with a comparable performance.

1 Introduction

Compact size and high-performance microwave branch-line couplers are demanded in many communication systems. The branch-line couplers have several applications in the design of microwave elements such as amplifiers, mixers, and phase shifters. At the lower frequency of the microwave band, the size of the conventional branch line is very large in printed circuit. Therefore, the size reduction of this element is highly important in modern communication systems. In order to reduce the size of this element, several types of BLC have been designed and proposed in previous works. For example, the combination of short high-impedance transmission lines and shunt-lumped capacitors were considered in [1–3]. In these works, the size reduction has been improved to some extent; however, they still have a very large size in printed circuit boards.

In [6], a compact model of the loaded coupled transmission lines has been introduced for the size reduction and a small size BLC has been designed using this proposed model. Figure 1 shows the proposed model in [6].

In this chapter, a highly compact model of the loaded coupled transmission lines is introduced using employment of the fractal technique on the previously proposed loaded coupled model in [6] for further size reduction in this type of BLC. A novel miniaturized BLC is designed and analyzed at 900 MHz on a 0.762-mm thick substrate with a relative dielectric constant $\varepsilon_r = 3.5$. Increasing in the electrical and the magnetic coupling and making the best use of the vacant space in the structure of the conventional BLC are two important features of the new BLC.

M. Nosrati (✉)
Azad University, Kermanshah Branch, Zip. C: 69311-33145, Kermanshah, IRAN
e-mail: nosrati_1359@yahoo.com

Fig. 1 The proposed model
in [6]
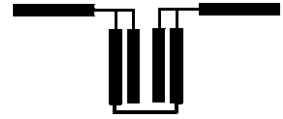
2 Analysis Procedure

In [6], the simple transmission line been has replaced by the proposed model and the foursome transmission lines are assumed as a load for the two bisected simple transmission lines. Referring to the structure in Fig. 1, in order to achieve a further size reduction, existing vacant space in this layout can be used for implementation of other loaded coupled transmission lines. For this purpose, in this chapter, the existent simple transmission line in foursome loaded model is again replaced by another foursome loaded one using fractal technique and then, a new model is proposed with furthermost coupling among their transmission lines as shown in Fig. 2.

In order to make a comprehensive analysis, at the first step, the network model of the folded four-coupled transmission lines is obtained as shown in Fig. 3(a).

As discussed in [7], the equivalent circuit of two cascade elements can be derived. If the two elements have the same characteristic impedance ($Z_1 = Z_2 = Z$), the relationships of the inductors and capacitors indicated in Fig. 3(b) in term of the characteristic impedance given in Fig. 3(a) are given as follows:
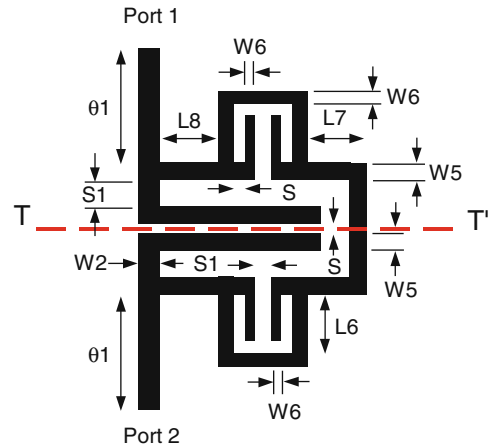
Fig. 2 The new semi-fractal
proposed model
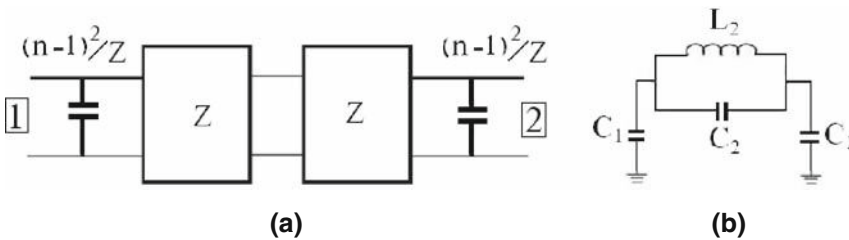
Fig. 3 (**a**) The network model of the folded four-coupled transmission lines (**b**) its equivalent circuit model

$$C_1 = \frac{1}{Z}, \tag{1}$$

$$C_2 = \frac{-1}{2Z}, \tag{2}$$

$$L_2 = 2Z. \tag{3}$$

The series capacitor in Fig. 3(b) must be increased to compensate for additional negative capacitor, so designed element using this technique – large capacitance, low inductance – is extremely compact due to the fact that no redundant elements have been used to ease the realization.

Similar to [6], the constituent parameters of the proposed model can be obtained using the even and odd modes analysis around of the symmetric plane T–T' in Fig. 2.

3 Design of the Proposed BLC

As stated in previous section, in [6] a series of mathematical equations was derived for the determination of foursome transmission line's constituent parameters using the even and odd modes analysis. It is necessary to state that the second foursome transmission lines as a load in the structure is symmetry and it can thereby obtain its transmission line's constituent parameters by the same way.

In order to determine the constituent parameters of the proposed semi-fractal model, the approximation values are initially obtained using [6], and then they are optimized using ADS full-wave simulator software.

At the next step, the quarter-wave length lines in the conventional BLC are replaced by the optimized model and a compact BLC is designed by this technique. It is observed that the return loss is obtained more than that of the conventional BLC after replacement of the new model with the simple quarter wavelength. In order to compensate this further loss, similar to the first model, a second model is developed using applying several changes as shown in Fig. 4.

Figure 5 shows the final structure of the proposed branch-line coupler using two new semi-fractal models. Finally, the frequency response of the compact BLC is simulated by ADS full-wave simulator. Figure 6 shows the frequency responses of the two branch-line couplers.
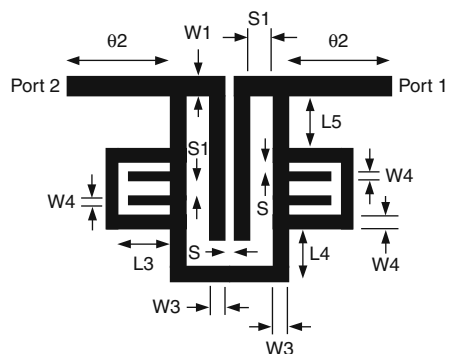
Fig. 4 The new modified model

Fig. 5 The layout of new
compact BLC
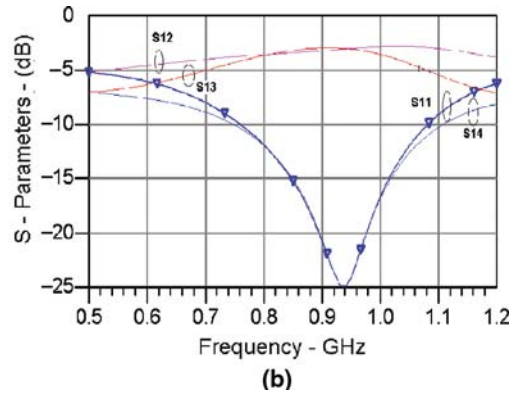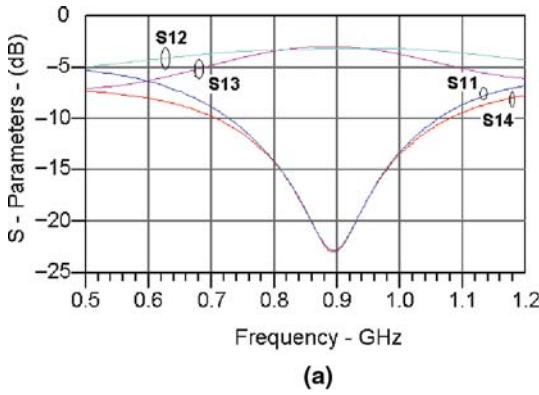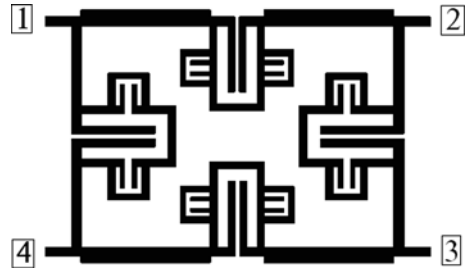
Fig. 6 The frequency responses of (**a**) the conventional BLC (**b**) the novel BLC

It is observed that the performances of the two BLCs are desirably comparable as shown in Fig. 6. The optimized physical dimensions of the proposed compact BLC are given in Table 1.

Table 1 The optimized physical values of the proposed BLC

L7 mm	L6 mm	L5 mm	L4 mm	L3 mm	L2 mm	L1 Mm
1.9	1.89	1.05	0.7	5.35	8	6.5
W6	W5	W4	W3	W2	W1	W8
0.7	1.6	0.8	0.9	1.715	2.91	1.4

$S = 0.2$ mm in all of the coupled transmission lines.

4 Conclusion

A novel highly compact semi-fractal branch-line coupler has been designed and developed using foursome loaded coupled transmission lines. Increase in the electrical and the magnetic coupling and making the best use of the vacant space in the structure of the conventional BLC are two important features of the new BLC. The size reduction of this new BLC has reported about 79% with a comparable performance as compared with the conventional BLC.

References

1. Kh. Hettak, G. A. Morin, M. G. Stubbs, Compact MMIC CPW and asymmetric CPS branch-line couplers and Wilkinson dividers using shunt and series stub loading, IEEE Transactions on Microwave Theory and Techniques, vol. 53, no. 5, pp. 1624–35, May 2005.
2. S-S. Liao and P-T. Sun, A novel compact-size branch line coupler, IEEE Transactions on Microwave Theory and Techniques, vol. 15, no. 9, pp. 588–90, September 2005.
3. R. W. Vogel, Analysis and design of lumped and lumped-distributed element directional coupler for MIC and MMIC applications, IEEE Transactions on Microwave Theory and Techniques, vol. 41, no. 9, pp. 2116–25, December 1993.
4. Hirota, T. A. Minakawa and M. Murauchi, Reduced-size branch-line and rate-race hybrids for uniplanar MMICs, IEEE Transactions Microwave Theory and Techniques, pp. 270–75, August 2002.
5. C. Y. Ng, M. Chongcheawchamnan, M. S. Aftanasar, Miniature X-band branch-line coupler using photo-imageable thick-film materials, Electronic letters, vol. 37, no. 19, pp. 1167–68, September 2001.
6. M. Nosrati and S. Karbasy, A novel compact branch-line coupler using four coupled transmission lines, published in Microwave and Optical Technology Letters, December 2007.
7. J. A. G. Malherbe, Ph.D. Microwave Transmission Line Filters. Artech House, pp. 24–26 and 71–79, 1979.

New Coplanar Low-Pass Defected Ground Structure (DGS) Filter

A. Batmanov, A. Boutejdar, A. Balalem, A. Omar, and E. Burte

Abstract This chapter presents the design of a new compact low-pass defected ground structure filter (DGS LPF). The proposed structure is based on coplanar waveguide (CPW) lines and $\lambda/4$ resonators. The filter provides three transmission zeros within the stop-band and offers bandwidth of 8.3 GHz, namely from 3.1 to 11.4 GHz. The stop-band rejection is more than -20 dB. Filter dimension is as low as $4 \times 23.4\,\text{mm}^2$. An equivalent circuit model is used to investigate the filter characteristics. The proposed low-pass filter has been fabricated and its characteristics measured. Good agreement between electromagnetic simulation, equivalent circuit simulation, and measurements has been obtained.

Keywords Low-pass filter (LPF) · Defected ground structure (DGS) · Coplanar waveguide (CPW) · *λ/4* resonators · HF filters

1 Introduction

Low-pass filters are essential components of most microwave and mobile communication systems [1]. Such systems usually require compact filter structures. Additionally, such filters must have a high rejection in their stop-band.

Defected ground structures add an extra degree of freedom in microwave circuit design [2]. The defect in the ground of a planar transmission line (e.g., microstrip, coplanar, and conductor backed coplanar waveguides) is equivalent to a parallel connected inductor (L), capacitor (C), and resistor (R) as was shown in [3]. This leads to a rejection of the signal at a certain frequency band determined by the shape of the defect. Consequently, this opens the door to a wide range of applications [2, 3].

Coplanar waveguides (CPW) have gained wide interest, since shunt connections can be easily done without a need for via holes. This makes the CPW ideal for use with surface-mounted components and simplifies the manufacturing process [4–6]. So far, different low-pass filters implementation with microstrip defected ground structures and CPW structures have been developed with moderate results [7–11].

In this work, a compact low-pass defected ground structure filter has been designed, implemented, and measured. The behavior of the structure has been simulated using an electromagnetic solver

----

A. Batmanov (✉)

Chair of Semiconductor Technology, University of Magdeburg, Magdeburg, Germany

e-mail: anatoliy.batmanov@ovgu.de

in addition to a lamped-element equivalent circuit model. Both simulations have shown that the proposed filter introduces three transmission zeros and a very high rejection in the stop-band. These results have been confirmed by the measurements. The proposed low-pass DGS filter has been developed for a stop-band ranging from 3.1 to 11.4 GHz, with a stop-band rejection of more than –20 dB.

2 Low-Pass DGS Filter Topology

Figure 1 shows the schematic diagram of the proposed low-pass DGS filter structure. It has been constructed by combining $\lambda/4$ open-ended stub resonators with DGS resonators. Two DGS slots are etched in the ground plane and located on both sides of the center conductor. The newly proposed DGS slot consists of two square heads and a connecting slot with a gap of 1 mm. The CPW lines used for this filter were designed to have a characteristic impedance of 50 Ω. This impedance corresponds to G/W/G of 0.2/2.8/0.2 mm, see Fig. 1. The filter has been built on a Ro4003c substrate that has a relative dielectric constant of 3.38 and a thickness of 0.813 mm. The substrate is covered by a copper layer with a thickness of 35 μm. Geometrical parameters of the filter structure are $a = 6.3$ mm and $l = 7.7$ mm. The total area of the low-pass filter is 24.0×23.4 mm^2. Figure 2 shows the insertion and return losses of the simulated structure with the dimensions stated above.
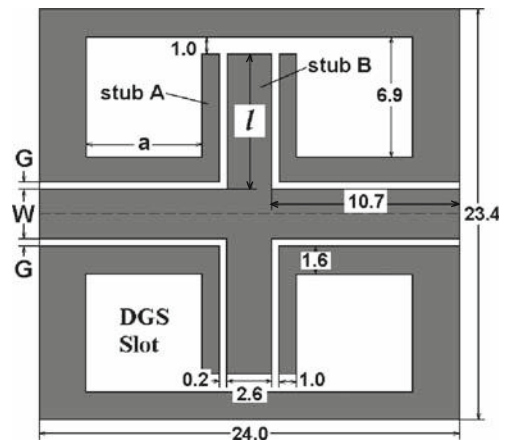
Fig. 1 Schematic diagram of the proposed coplanar low-pass DGS filter
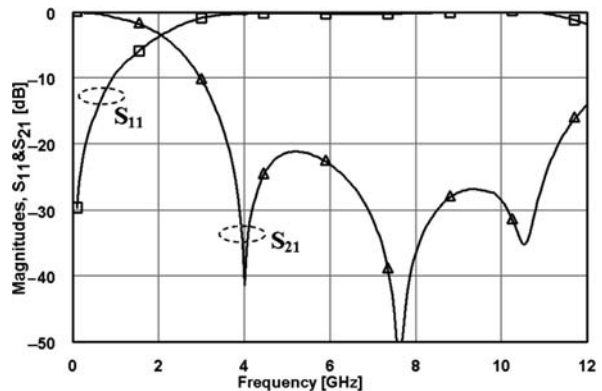
Fig. 2 EM simulation result for the proposed coplanar low-pass DGS filter

3 Electromagnetic and Equivalent Circuit Simulations

The electromagnetic simulations have been carried out using the full-wave 2.5-D MoM simulator SONNET [12]. The equivalent circuit simulation has been performed using the commercially available EM simulator AWR Microwave Office [13]. Figure 3 shows the lumped-element equivalent circuit model for the proposed low-pass DGS filter. Due to the stubs A (see Fig. 1), the DGS slots operate as a shunted series resonator at the corresponding $\lambda/4$. These stubs resonate when the length is equal to $\lambda/4$, which is responsible for the transmission zero occurring at 4 GHz. In order to verify that, the physical length of the stub A is compared to the effective wavelength at the first transmission zero frequency, which is given by [1]

$$\lambda_g = \frac{c}{\sqrt{\varepsilon_{\mathrm{r.eff}}} f_z},$$ (1)

where c is the speed of light in free space, $\varepsilon_{\mathrm{r.eff}}$ is the effective dielectric constant, and f_z is the transmission zero frequency.

Fig. 3 Equivalent circuit model of the proposed coplanar low-pass DGS filter
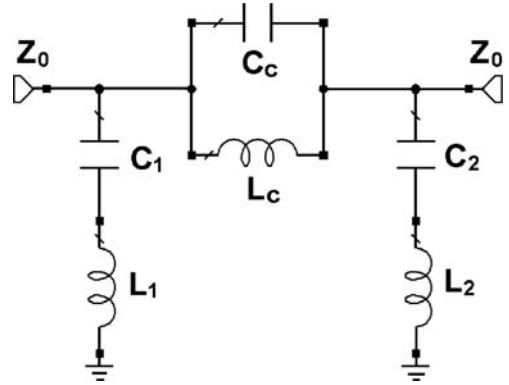
The effective dielectric constant $\varepsilon_{\mathrm{r.eff}}$ and the transmission zero frequency have been extracted from the electromagnetic simulation. The theoretically calculated effective wavelength λ_g at the first transmission zero frequency is 49.2 mm. The physical length of the stub A is approximately equal to $\lambda_g/4$.

Similarly the stubs B which are connected to the central transmission line operate as shunted series resonator at the corresponding $\lambda/4$, which is responsible for the transmission zero that occurs at 7.6 GHz.

In order to understand the reason behind the transmission zero occurring at 10.55 GHz, the current density distribution on the filter metallization has been calculated using EM MoM simulator SONNET [12]. Figure 4 shows this distribution at the third transmission zero frequency of 10.55 GHz.

From Fig. 4 it can be clearly seen that there is a coupling between both open-end stubs and the stubs within the DGS slots, since the current density has both maxima and minima at the stub metallization. Such a coupling is a mixed one, i.e., inductive and capacitive together. Therefore, a parallel resonator can represent this coupling [14].

The next step is to construct the equivalent circuit of the proposed low-pass structure, which has two shunted series resonators coupled to each other by a mixed coupling element (parallel resonator).

Fig. 4 Current density distribution at the third transmission zero frequency of 10.55 GHz
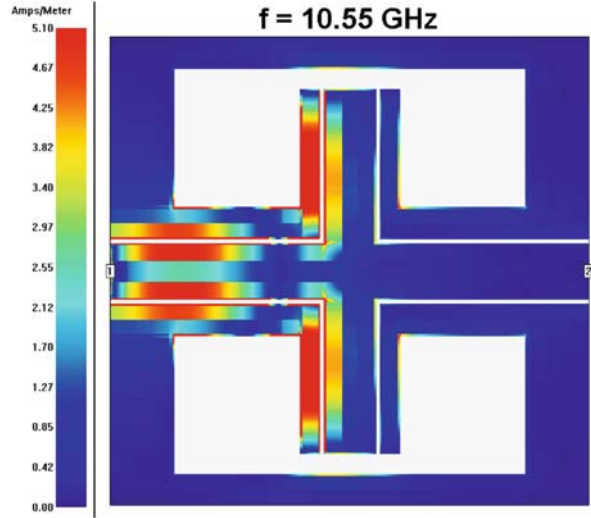
Referring to Fig. 3, the first resonator C_1L_1 represents the stubs inside the DGS slots, while C_2L_2 represents the open-end stubs connected to the center line and the parallel resonator C_cL_c represents the mixed coupling between these stubs.

The equivalent circuit extraction method has been used to extract the values of the circuit parameters. The resonance frequency ω_{0i} is given in term of the resonant circuit elements by

$$\omega_{0i} = \frac{1}{\sqrt{L_iC_i}}, \tag{2}$$

where L_i and C_i are inductance and capacitance of the resonator, respectively, which is responsible for the each transmission zero.

The shunted series resonator L_1C_1, corresponded to the first transmission zero at 4.0 GHz, has impedance given by

$$Z_1 = j\omega L_1 + \frac{1}{j\omega C_1}. \tag{3}$$

The transmission coefficient S_{21} is easily shown to be given by

$$S_{21} = \frac{2Z_0}{2Z_0 + Z_1} = \frac{2Z_0}{2Z_0 + j\omega L_1 + \frac{1}{j\omega C_1}}. \tag{4}$$

The 3 dB cutoff frequency point ω_c is defined through

$$|S_{21}| = \frac{2Z_0}{\sqrt{4Z_0^2 + \left(\frac{\omega_c^2 - \omega_0^2}{\omega_0^2 \omega_c C_1}\right)^2}} = \frac{1}{\sqrt{2}}. \tag{5}$$

Rearranging (5), the capacitance of the equivalent circuit model is given by

$$C_1 = \frac{(\omega_c^2 - \omega_0^2)}{2\sqrt{2}Z_0(\omega_0^2\omega_c)}. \tag{6}$$

Substituting back in (2), the inductance value L_1 can be determined as

$$L_1 = \frac{2\sqrt{2}Z_0\omega_c}{(\omega_c^2 - \omega_0^2)}. \tag{7}$$

Similar calculation can be used to extract the element parameters for the shunted series resonator L_2C_2 which is responsible for the transmission zero at 7.6 GHz.

At high frequency the equivalent circuit is represented by the parallel coupled resonator L_cC_c while the series resonators are in the rejection state. The equivalent impedance of the parallel resonator is given by

$$Z_c = \frac{1}{1/j\omega L_c + j\omega C_c}. \tag{8}$$

Substituting (8) in (5), the parallel capacitance C_c can be defined as

$$C_c = \frac{\omega_c}{2Z_0(\omega_0^2 - \omega_c^2)} \tag{9}$$

than the inductance L_c can be determined from (1).

The extracted circuit parameters are $L_1 = 3.95$ nH; $C_1 = 0.40$ pF; $L_2 = 0.87$ nH; $C_2 = 0.56$ pF; and $L_c = 1.45$ nH; $C_c = 0.15$ pF. Equivalent circuit simulations have been carried out and the lumped element parameters have been adjusted to meet the EM response. Both EM and equivalent circuit simulation results for the proposed low-pass filter are in good agreement with each other as shown in Fig. 5.
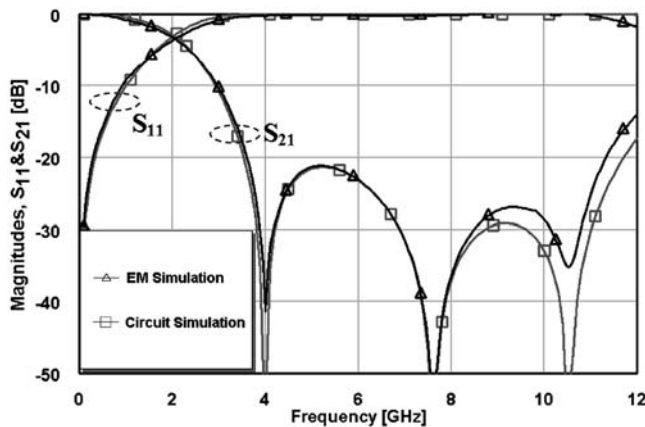
Fig. 5 EM and equivalent circuit model simulation results for the proposed coplanar low-pass DGS filter

4 Control of the Filter Characteristics

Some parameters are affecting the transmission zero frequency positions such as the geometrical parameters *a* and *l* (see Fig. 1). Figure 6 shows the influence of the length of the open-end sections *l* on the filter response. As can be seen, increasing the length of the stub shifts the second and third transmission zeros to lower frequencies and vise versa. Basically, changing the length of these stubs should only affect the second transmission zero. However, due to the narrow gap between the stubs, any change of the dimensions of each would affect the coupling between them. Therefore the third transmission zero is also shifted to a lower frequency band.

By changing the dimension *a* from the outer sides, mainly, the length of the stubs that are responsible for the first transmission zero is changing. Therefore, by increasing the distance *a* the first transmission zero is shifted to a lower frequency band while the other two transmission zeros remain at the same positions. Figure 7 shows the filter response with different values of the distance *a*.
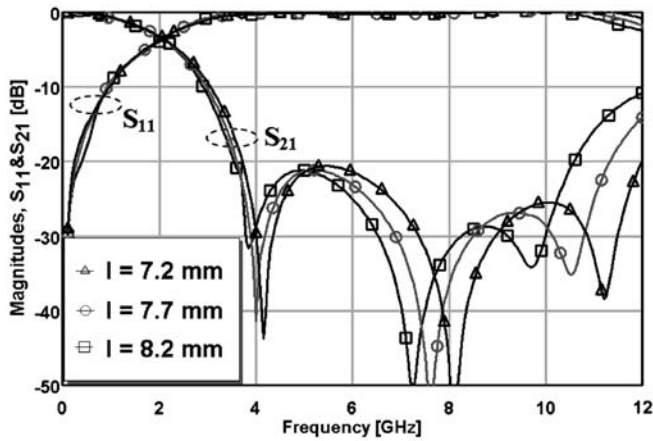
Fig. 6 EM simulations for the different values of the length of the open-stabs *l*
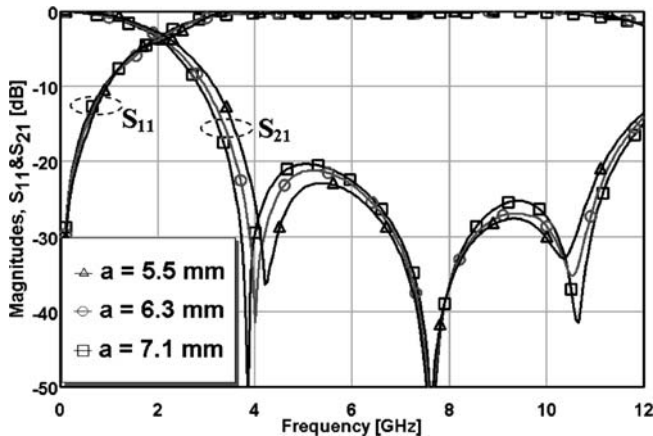
Fig. 7 EM simulations for the different values of the geometrical parameter α

5 Experimental Results

The proposed filter has been designed, simulated, and optimized, then fabricated and measured. The dimensions of the measured filter are $a = 7$ mm, $l = 7.7$ mm, see Fig. 8. The filter has 3 dB cutoff frequency of 1.5 GHz, and three transmission zeros located at 4, 7.6, and 10.55 GHz. The highest insertion loss at the passband is better than 0.8 dB, and the highest group delay is better than 0.21 ns. Figure 8 shows photo of the fabricated filter. The measurements are shown in Fig. 9. A very good agreement between the simulated and measured result is achieved at except the third transmission zero position which is shifted to a lower frequency. This most probably occurred due to impacting the metallization thickness which has not been taken into account in the simulation results.
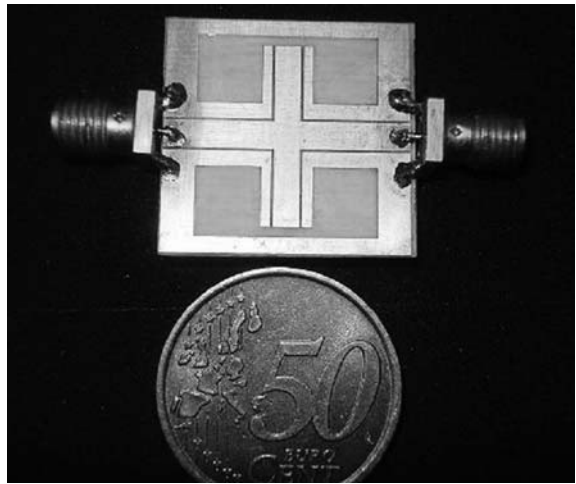
Fig. 8 Photo of the fabricated coplanar low-pass DGS filter
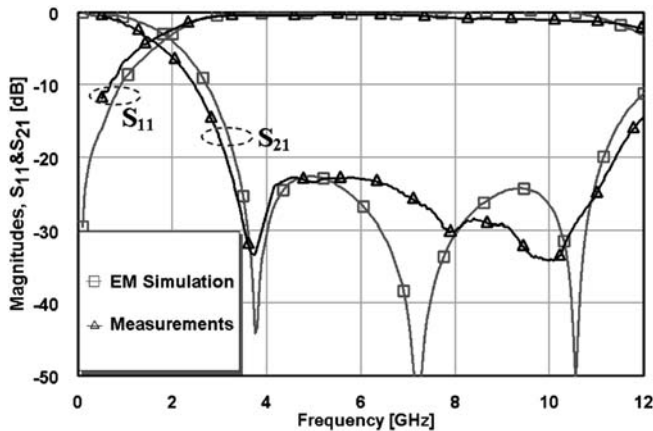
Fig. 9 EM simulated and measured results of the proposed coplanar low-pass DGS filter

6 Conclusion

This chapter presents a new compact high-performance coplanar low-pass DGS filter with improved stop-band. The proposed filter shows wide and deep stop-band characteristics. The structure has been simulated using a MoM EM simulator as well as a lumped-element equivalent circuit model. The proposed low-pass filter provides three transmission zeros within the stop-band and a bandwidth of 8.3 GHz, from 3.1 to 11.4 GHz. The stop-band rejection is more than -20 dB. The filter has been fabricated and measured. Good performance is observed in the pass-band of the filter. Significant improvement over ripples, an excellent harmonic suppression, and enlarged stop-band bandwidth are obtained. The proposed coplanar low-pass DGS filter is smaller than conventional CPW components.

References

1. G. L. Matthaei, L. Young, and E. M. T. Jones, Microwave filters, impedance-matching networks, and coupling structures, McGraw-Hill, New York, 1980.
2. J.-S. Lim, J.-S. Park, Y.-T. Lee, D. Ahn, and S. Nam, Application of defected ground structure in reducing the size of amplifiers, IEEE Microwave and Wireless Components Letters, vol. 12, no. 7, p. 261, July 2002.
3. Y. Chung, S.-S. Jeon, D. Ahn, J.-J. Choi, and T. Itoh, High isolation dual-polarised patch antenna using integrated defected ground structure. IEEE Microwave and Wireless Component Letters, vol. 14, no. 1, pp. 4–6, Janurary 2004.
4. Anatoliy Batmanov, Ehab K. I. Hamad, Edmund P. Burte, and Abbas S. Omar, Design of H-shaped low actuation-voltage RF-MEMS switches, Proceedings. Asia-Pacific Microwave Conference, Yokohama, Japan, December 2006.
5. Anatoliy Batmanov, Ahmed Boutejdar, Edmund P. Burte, and Abbas S. Omar, New compact MEMS-switch controlled tunable DGS coplanar bandpass filter, Proceedings ESSDERC- ESSCIRC conference, Munich, Germany, pp. 438–41, September 2007.
6. Anatoliy Batmanov, Abbas S. Omar, and Edmund P. Burte, Design of low actuation-voltage high isolation S-band MEMS capacitive switches, in Proceedings Micro- and Nano- Engineering International. Conference (MNE), Copenhagen, Denmark, September 2007.
7. A. Boutejdar, A. Elsherbini, L. Haiwen, and A. Omar Improvement of microstrip low pass filter's characteristics using a optimized number of new multi-ring defected ground structure (DGS). Microwave and Optical Technology Letters, vol. 17, no. 12, pp. 1405–8, June 2007.
8. Ahmed Boutejdar, Adel Elsherbini, and Abbas S. Omar, A novel technique to transform a fractal lowpass to bandpass filter using a simple combination of defected ground structure and gap capacitive, Proceedings Asia-Pacific Microwave Conference, Yokohama, Bangkok, Thailand, December 2007.
9. Ahmed Boutejdar, Adel Elsherbini, and Abbas Omar, A new cross-head defected ground structure (CDGS) for a compact lowpass filter with a wide stopband, Proceedings of the 37th European Microwave Conference (EuMC), Munich, Germany, October 2007.
10. Anatoliy Batmanov, Nikolaus Spiliotis, Ahmed Boutejdar, Abbas S. Omar, and Edmund P. Burte, Control of bandwidth and resonant frequency of a new coplanar bandpass filter, Proceedomgs Asia-Pacific Microwave Conference, Yokohama, Bangkok, Thailand, December 2007.
11. A. Balalem, A. R. Ali, J. Machac, and A. Omar, Quasi-elliptic microstrip low-pass filters using an interdigital DGS slot. IEEE Microwave and Wireless Components Letters, vol. 17, no. 8, August 2007.
12. Sonnet Suite, Ver.10.52, Sonnet Software, Liverpool, NY, 2005.
13. AWR Microwave Office, Ver. 5.51, http://web.awrcorp.com
14. J. S. Hong, and M. J. Lancaster Microwave Filters for RF/Microwave applications. John Wiley and Sons, Inc. 2001.

Bandwidth Enhancement and Further Size Reduction of a Class of Miniaturized Elliptic-Function Low-Pass Filter

M. Nosrati, S. Abbaspour, and A. Najafi

Abstract In this chapter, a new model for further reducing the size and increasing the bandwidth (BW) of a class miniaturized elliptic-function low-pass filter is presented. A compact elliptic-function low-pass filter using microstrip stepped-impedance semi-hairpin resonators is also developed and then, a multiple cascaded filter using semi-hairpin resonators is designed by this technique. The overall bandwidth (BW) of the proposed low-pass filter is reported to be increased by more than 40% with a size reduction about 80% compared with the conventional ones.

Keywords Filter · Semi-hairpin resonator

1 Introduction

Low return-loss, high harmonics suppression and the increasing of bandwidth are some important features of a demandable low-pass filter and this is a demanding work.

On the design of a low-pass filter, in several studies has been tried to achieve a maximum bandwidth (BW) accompanied with size reduction and high performance [1–4]. There are different methods for the size reduction of low-pass filters in these studies, but the return-loss has not been improved in some of them and the harmonics suppression has been achieved for narrow stop-band in the other studies. For example in [2], a wide-band low-pass filter has been designed but, its return loss is not very well and harmonics suppression in its narrow stop-band is not very good. Thereafter, in [5] a compact elliptic-function low-pass filter has been proposed using microstrip stepped-impedance hairpin resonator. This filter has a desirable behavior in harmonics suppression and a wide stop-band but in return, its bandwidth has been decreased in compared with the one designed in [2].

Recently, a low-pass filter has been developed and proposed in [6]. This one has a miniaturized size and high harmonics suppression with a wide stop-band. In order to increase bandwidth and reduce size, in this chapter a model of the stepped-impedance hairpin resonator is proposed. The layout of this low-pass filter is shown in Fig. 1.

M. Nosrati (✉)

Department of Electrical and computer Engineering, Ilam Azad University, Ilam, Iran

e-mail: nosrati_1359@yahoo.com

Fig. 1 The stepped
impedance hairpin resonator
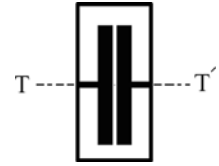
The prototype filter is synthesized from the equivalent circuit model and is shown in Fig. 2. This structure provides a wide band-pass with high harmonics suppression in a wide stop-band. To optimize the performance of this filter, electromagnetic simulation is used to tune the dimensions of the prototype filters. There is a 40% enhancement of the bandwidth in performance of this filter in comparison with the LPF designed in [5].

Fig. 2 The equivalent circuit
of the proposed model

(a)   (b)
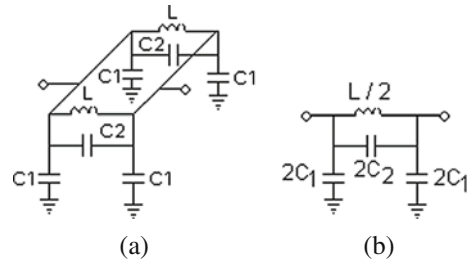
2 The Stepped-Impedance Semi-hairpin Resonator

In order to increase bandwidth and reduce size, the layout of proposed low-pass filter in [6] can be mirrored around the T–T$'$ plane and by this way the structure shown in Fig. 1 can be obtained.

This structure consists of two parallel simple transmission lines and a symmetric capacitance load parallel coupled lines in miniature.

Similar to [6], the equivalent π-network circuit of the two part of proposed model which are symmetrical around the T–T$'$ plane can be derived. Due to the fact that these two parts are parallel together, their equivalent circuit can be obtained in terms of lumped element as shown in Fig. 2.

Referring to the equivalent circuit of the proposed model, it is observed that two inductors are parallel together and all of the capacitances also are parallel together.

Considering the simple primary impedance equations for an inductor and a capacitor, it is obvious that the more the inductance reduces, its bandwidth increases, the more the capacitor increases, and in return, the harmonics suppression improves.

In [5], the relationships between lamped and distributed elements have been derived using ABCD matrix and their equivalent circuit models. Equations (1–4) show these relationships again:

$$C_{22} = \frac{Z_e - Z_o}{2\omega Z_e Z_o \cot(\beta_c l_c)}, \tag{1}$$

$$C_2 = \frac{1}{\omega Z_e \cot(\beta_c l_c)}, \tag{2}$$

$$L = \frac{Z_0 \sin(\beta_a l_a)}{\omega}, \tag{3}$$

$$C_1 = \frac{1 - \cos(\beta_a l_a)}{\omega Z_0 \sin(\beta_a l_a)}. \tag{4}$$

From (1–4), it is observed that C_{22}, C_2, L, and C_1 are depended on l_a, Z_0, W, and l_c and the resonance frequency of stepped-impedance semi-hairpin is a function of them, so these parameters can be tuned for a special resonance frequency. Figure 3 shows the different microstrip low-pass filters using different stepped-impedance semi-hairpin resonators designed at 3-dB cutoff frequencies f_1, f_2, and f_3 GHz.

Fig. 3 The different low-pass filter designed for different resonance frequencies
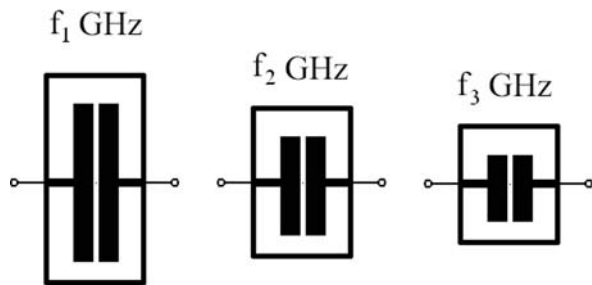
3 Multiple Cascaded Low-Pass Filter

By using the equality of the proposed and the conventional stepped-impedance hairpin resonators shown in previous section, a novel low-pass filter can be designed using multiple cascaded resonators. Figure 4 shows the layout and its equivalent circuit model of this proposed low-pass filter.

To optimize the performance of this filter, electromagnetic simulation is used to tune the dimensions of the prototype filters and a novel low-pass filter is designed for a 3-dB cutoff frequency of 3.26 GHz on a 25-mil-thick substrate with relative dielectric constant $\varepsilon_r = 10.2$. Figure 5 shows the simulated frequency response of the proposed low-pass filter obtained using the Agilent ADS simulator.
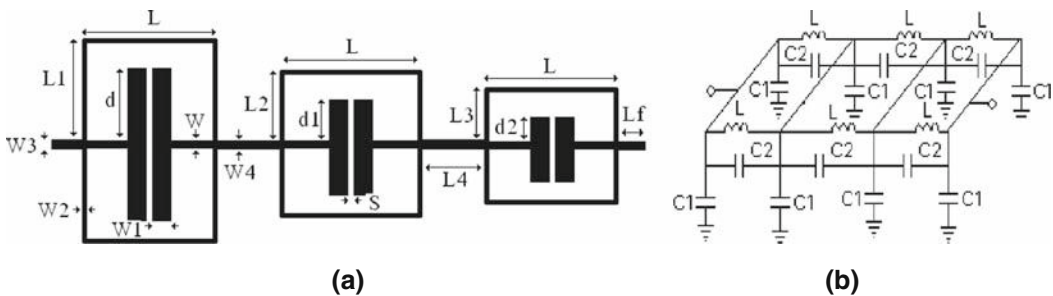
Fig. 4 (**a**) The proposed compact multiple cascaded low-pass filter (**b**) its equivalent circuit model
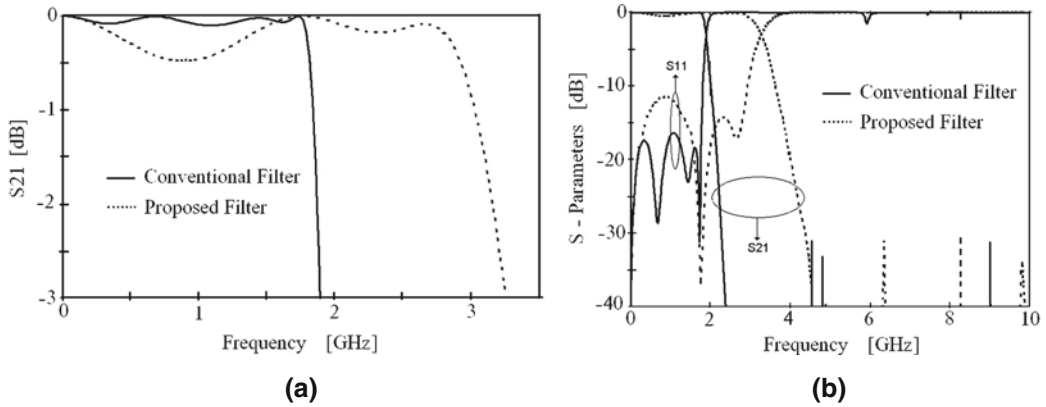
Fig. 5 (**a**) S21 within the 3-dB bandwidth; (**b**) the simulated frequency response of the proposed and conventional low-pass filters

The proposed low-pass filter has a 3-dB pass band from dc to 3.26 GHz and its return-loss is better than −12 dB and the rejection greater than 30 dB within stop-band.

In order to compare the performance of the proposed low-pass filter with the conventional one, their frequency responses are shown in Fig. 5.

As shown in Fig. 5 the return-loss of the proposed low-pass filter is not much better and the harmonics suppression is same and the sharpness is lower than those of the conventional low-pass filter and there is a bandwidth enhancement in the performance of the proposed low-pass filter (40%). The optimized dimensions of the proposed low-pass filter are listed in Table 1.

Table 1   The optimized values of compact low-pass filter

Parameter	Value (mm)	Parameter	Value (mm)
Lf	4	d1	2.2
L	2.44	d2	1.6
L1	3.84	W	0.46
L2	3.44	W1	0.5
L3	2.84	W2	0.12
L4	1.4	W3 = W4	0.56
D	2.6	S	0.2

4 Conclusion

In order to increase the bandwidth and reduce the size of the conventional stepped-impedance hairpin resonator, a novel model of this resonator has been proposed.

Using this proposed model a low-pass elliptic-function filter has been designed and introduced using multiple cascaded semi-hairpin resonators. This new low-pass filter provides a sharp cutoff frequency response and low insertion loss with a very compact size. The performance of this filter is comparable respect to the conventional low-pass filter with a size reduction about 80 and 40% bandwidth enhancement.

References

1. J. T. Ku, M. J. Maa, and P. H. Lu, A microstrip elliptic-function filter with compact miniaturized hairpin resonator, The Philosophical Transaction of the Royal Society London, vol. A247, pp. 529–551, IEEE Microwave Guided Wave letter, vol.10, pp. 94,95, March 2000.
2. F. Giannini, M. Salerno, and R.Sorrentino, Design of low-pass elliptic filters by mean of cascaded Microstrip rectangular elements, IEEE Transactions on Microwave Theory and Techniques, vol. 30, pp. 1348–53, September 1982.
3. S. Y. Lee and C. M. Tsai, New cross-coupled filter design using improved hairpin resonator, IEEE Transactions. Microwave Theory and Techniques, vol. 48, pp. 2482–90, December 2000.
4. D. Ahn, J. S. Park, C. S. Kim, J. Kim, Y. Qian, and T. Itoh, A design of the low-pass filter using the novel microstrip defected ground structure, IEEE Transaction Microwave Theory Techniques, vol. 49, pp. 86–92, January 2001.
5. L-H. Hsieh and K. Chang, Compact elliptic-function low-pass filters using microstrip stepped-impedance hairpin resonators, IEEE Transaction Microwave Theory, vol. 51, no. 1, pp. 193–9, January 2003.
6. M. Nosrati and A. Najafi, A novel high compact elliptic-function low-pass filter, IEEE Applied Electromagnetics Conference, December 2007.

A Miniature 3.1 GHz Microstrip Bandpass Filter with Suppression of Spurious Harmonics Using Multilayer Technique and Defected Ground Structure Open-Loop Ring

A. Boutejdar, A. Batmanov, A. Omar, and E. Burte

Abstract In this chapter a cascaded bandpass filter composed of three open-loop $\lambda/2$ resonators is proposed. The three elements are electromagnetically coupled. They are placed on the top of a multiplayer structure. Electromagnetic simulation of the cascaded bandpass filter shows good results in both passband and in stopbands. The filter provides two 3-dB attenuation pole frequencies f_1 at 2.95 GHz, f_2 at 3.25 GHz, and a center frequency f_0 at 3.1 GHz. In order to develop and to miniaturize this planar three-pole microstrip bandpass filter, two ideas are developed and implemented that are based on DGS technique and the coupling matrix method. Using DGS resonators on the ground structure, a compact filter with improved response has been realized. The proposed filter has been fabricated on a substrate with dimensions of ($0.57\lambda_g \times 0.28\lambda_g$). The simulated and measured results show good agreement and validate the proposed approach.

Keywords Cascaded method · Bandpass filter · Open-loop-resonator · DGS · Multilayer technique

1 Introduction

Recently, defected ground structures (DGSs) with various configurations for microwave and millimeter wave applications have been reported [1–2]. DGS is realized by etching off a defected pattern from the ground plane [5]. An etched defect disturbs the shield current distribution in the ground plane. This disturbance can change characteristics of a transmission line such as line capacitance and inductance. This gives rise to an increase in the effective capacitance and inductance of a transmission line, respectively. Thus, an *LC* equivalent circuit can be used to model the proposed DGS circuit. [3–4]. The use of DGS represents a very successful approach to achieve significant size reduction. Such a technique can be used in various kinds of components such as lowpass filters and bandpass filters, as well as RF phase shifters. Planar bandpass filters [5] have been extensively studied and exploited as key circuit blocks to implement in-band transmission and out-of-band rejection. To meet the requirements in modern wireless communication, much effort has been made in the past years to develop a variety of compact bandpass filters with sharp and deep rejection outside the passband by generating transmission zeros or attenuation poles. Recent advance in

A. Boutejdar (✉)
Chair of Microwave and Communication Engineering, University of Magdeburg, Magdeburg, Germany
e-mail: ahmed.boutejdar@ovgu.de

high-temperature superconducting (HTS) circuits and microwave monolithic integrated circuits (MMIC) has additionally stimulated the development of various planar filters, especially narrow-band bandpass filters that play an important role in modern communication and electronic systems [6]. In order to improve the selectivity and efficiency of spectrum utilization, filters with two or more transmission zeros have been demanded. In order to obtain compact three-pole microstrip bandpass filters with two transmission zeros, low rejection band performance, low insertion loss in passband and high selectivity, several structures were proposed such as end-coupled slow-wave resonators, slow-wave open loop resonators, and slow-wave open stub-tapped resonators. Other techniques involve employing cross-coupling and quasi-elliptic filters which are able to place the transmission zeros near the cutoff frequencies so that higher selectivity with less resonators can be obtained. Multiple transmission zeros were obtained by using suitable input, output, and interstage tapped couplings. Quarter-wavelength ($\lambda/4$) open stubs and capacitively coupled gaps were introduced in the conventional coupled-line filter structure to create the transmission zeros at stopband was proposed by Boutjdar et al. [7]. The trisection and quadruplet microstrip bandpass filters based on folded $\lambda/4$ resonators were proposed to achieve a symmetrical structure with one or two transmission zeros. However, the resultant circuit topology is also large in size. The compact hairpin filter with asymmetric tapping feed lines to produce transmission zeros was also discussed in Boutjdar et al. [8]. Other two transmission zeros, in [9], were realized using open stub lines and DGS circles. In [10], a slow-wave resonator filter using two coupled hairpin microstrip folded lines was presented. The bandpass filter, designed at the fundamental resonant frequency of the resonator, shows low insertion loss in the passband.

In this chapter, a new type of compact microstrip bandpass filters with slow-wave effect realized using open-loop DGS resonators on a multilayer structure has been developed. Transmission zeros can be implemented on both sides of the passband.

2 Characteristics of the DGS Element

The proposed open-loop ring DGS shown in Fig. 1 is etched in the ground plane and consists of two capacitive arms, which are connected to a rectangular slot, with the same dimensions. The etched slot (DGS) is equivalent to a capacitance. The metal area between the two arms on the top layer corresponds to an inductance. The conventional circuit parameters can be extracted using electro-magnetic simulations by matching to a one pole Butterworth bandstop filter response, as discussed in [11]. The open-loop slot in the ground plane acts as a parallel resonant circuit. It can be modeled by an LC circuit as shown in Fig. 2 (left). The values of L and C can be computed using

$$C_P = \frac{5f_c}{\pi \left(f_0^2 - f_c^2\right)} \quad \text{and} \quad L_p = \frac{250}{C_p(\pi f_0)^2}. \tag{1}$$

The values of the cutoff frequency f_c and resonance frequency f_0 can be found from the transmission characteristics of the open-loop slot as shown in Fig. 2 (right). The simulation results of the ring slot show one-pole lowpass filter characteristics. It is clear that employing the slot in the metallic ground plane increases the effective permittivity, leading to an increase of the effective inductance of the microstrip line. From Fig. 3 we can see the dependence of the resonance frequency (cutoff frequency) on the dimensions of the ring shape on the top and bottom layers. The etched arm has a significant effect on the resonance frequency. Actually, it is well known that an attenuation pole can

Fig. 1 Layout of the
open-loop cell
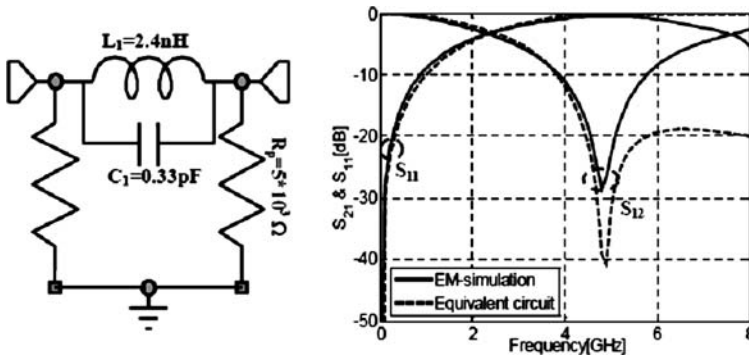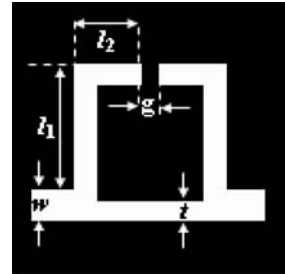
Fig. 2 Equivalent circuit of the DGS Element (*left*) and simulation results (*right*)
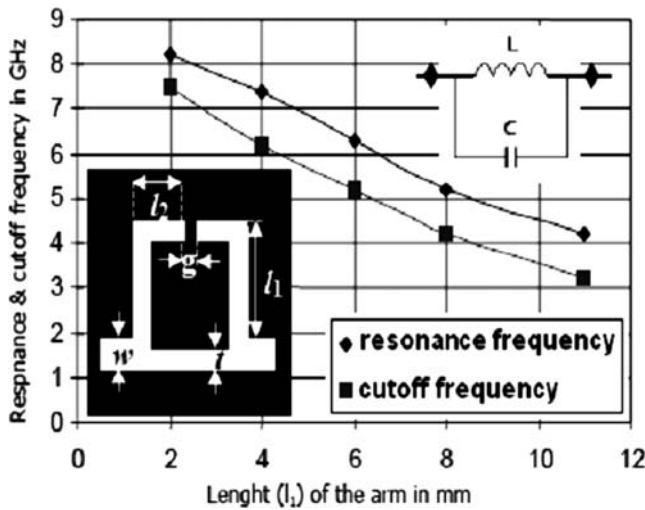
Fig. 3 Resonance and cutoff frequencies versus the length l1

be generated by combining inductive and capacitive elements. This explains the frequency character-
istic of the proposed ring-DGS element. Figure 3 shows that if g is kept constant while l_1 is varied, it
is easy to control the positions of the cutoff and attenuation poles. This means that the length of gap
(arm) controls the effective series inductance of a microstrip. The microstrip line on the top of the

substrate has a width of $w = 1.9$ mm to obtain a 50 Ω characteristic impedance. The substrate dielectric constant is 3.38 and its height is $h = 0.813$ mm. The DGS cell is simulated using Microwave Office. Simulation results are depicted in Fig. 2 (right), which resembles the characteristics of a one-pole LPF.

3 Design of the Proposed Compact BPF

In order to improve the performance of the classical bandpass filter shown in Fig. 4, a multilayer structure is used. The new structure is similar to the original filter but the central DGS resonator is moved to the bottom layer as shown in Fig. 5. This proposed geometrical idea is based on the use of several stacked layers. This was found to improve the performance and reduce the overall size of the filter. The new bandpass filter has the same bandwith (10%) and the same center frequency ($f_0 \approx 3.1$ GHz) but with improved passband characteristics. We designed and fabricated this filter using commercially available electromagnetic simulators. The cutoff and resonance frequencies have not changed from their previous positions, but the advantage is that, the new LPF is 30% more compact than the conventional one [5], as Figs. 5 and 6 show

In order to obtain the coupling matrix of the new topology, the specifications of the filter are defined and then the desired parameters are extracted by using an optimization-based scheme [6].
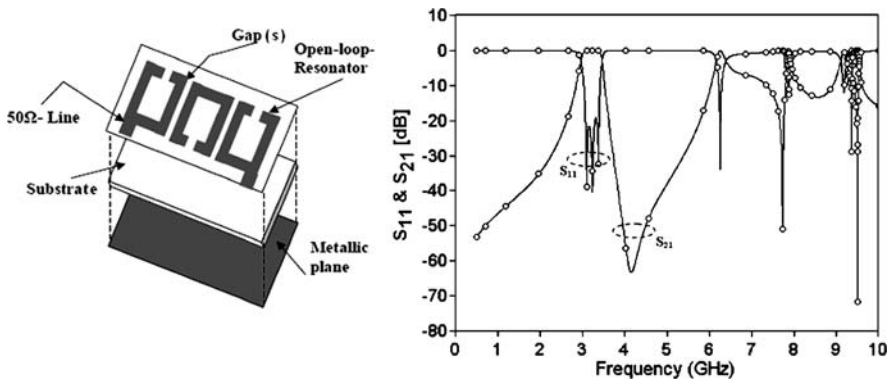
Fig. 4 Three-dimensional view of the cascaded BPF (*left*) and its EM simulation result (*right*)
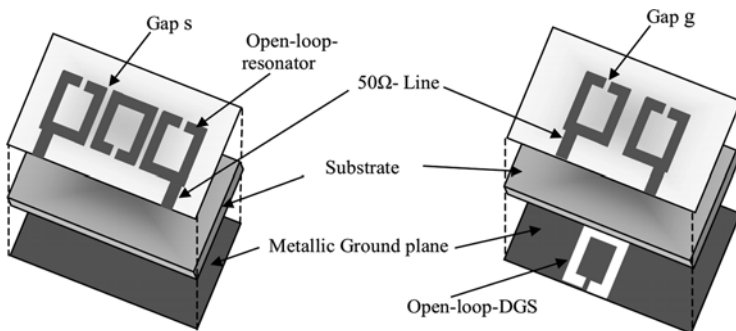
Fig. 5 Three-dimensional view of the transformation of cascaded BPF (*left*) to compact multilayer BPF (*right*)

The coupling coefficient and quality factor curves are then used to realize the obtained coupling coefficients. In our case a third order filter has been assumed, which has a bandwidth $BW = 300$ MHz, return loss $RL = 20$ dB, and center frequency $f_0 = 3.1$ GHz. The obtained coupling matrix from the optimization scheme is given by

$$m = \begin{bmatrix} 0 & 0.1255 & -0.151 \\ 0.1255 & 0 & 0.1255 \\ -0.151 & 0.1255 & 0 \end{bmatrix}. \tag{2}$$

The external quality factors are $q_{in} = q_{out} = 0.9479$. The full-wave EM software IE3D is used to extract the coupling coefficients and external quality factors. The value of the coupling spacing s in the proposed filter is 0.8 mm (see Fig. 6 (left)). The normalized coupling matrix and quality factors can be expressed in terms of fractional bandwidth FBW, M and q as

$$FBW = (BW)(f_0^{-1}), \tag{3}$$

$$M = (m)(FBW), \tag{4}$$

$$Q = (q)(FBW)^{-1}, \tag{5}$$

$$M = \begin{bmatrix} 0 & 0.0121 & -0.0146 \\ 0.0121 & 0 & 0.0121 \\ -0.0146 & 0.0121 & 0 \end{bmatrix}, \tag{6}$$

$$\Rightarrow Q_1 = Q_2 = 5. \tag{7}$$

The proposed DGS bandpass filter has been simulated on a Rogers RO4003 substrate with a relative dielectric constant ε_r of 3.38 and a thickness h of 0.813 mm. Simulation one was performed using Sonnet and Microwave Studio^{TM} simulators. The simulation results of the proposed bandpass filter are shown in Fig. 6 (right).
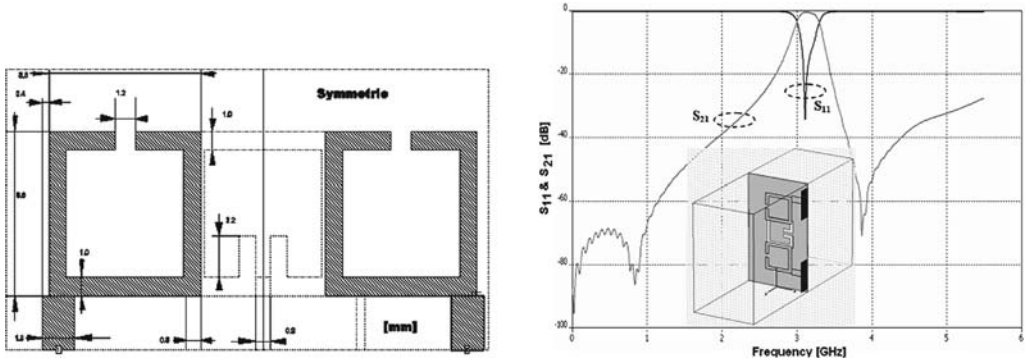
Fig. 6 Two-dimensional view of the proposed BPF (*left*) and its EM simulation result (*right*)

4 Distribution of the Magnetic Field at the Passband and the Stopband

The objective of this short investigation is to verify the dependence of the equivalent circuit elements (capacitance and inductance) on the surface as the distribution electromagnetic field. The simulation results are shown in Fig 7(a) and 7(b). The microstrip structure is divided into two regions. In region I
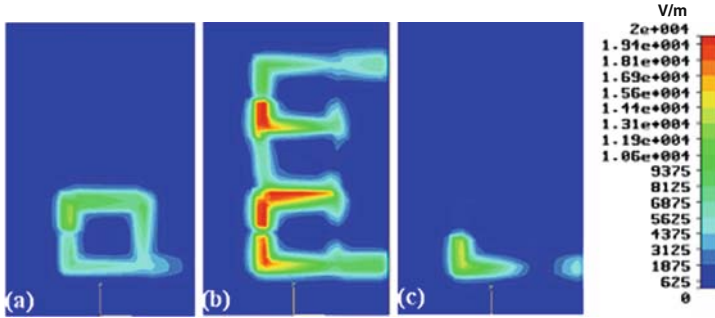
Fig. 7(a) Electric field distributions at (**a**) $f = 2$ GHz, (**b**) $f_0 = 3.1$ GHz, and (**c**) $f = 4$ GHz
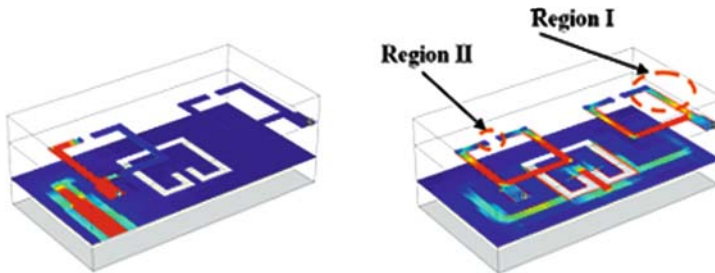
Fig. 7(b) Magnetic field distributions at $f = 4.0$ GHz (*left*) and at $f_0 = 3.1$ GHz (*right*)

the electric field is highly concentrated in the gap; hence any change in dimensions of the gap affects the effective capacitance of the structure. In region II the electric field nearly vanishes. It means that the length of the arms (l_1 and l_2) does not affect the effective capacitance of the filter structure. On the other hand, the current is distributed throughout the whole structure. Therefore any change in the length of the meander arm strongly affects the magnetic field distribution and hence the surface current, which in turn leads to a change in the effective inductance of the structure. Therefore, that region I corresponds to a capacitance and region II corresponds to an inductance. The full structure corresponds then to an *LC*-resonator.

5 Design and Fabrication of the Proposed BPF

Figure 8 shows photographs of the fabricated BPF filter. The simulations of the proposed BPF are performed using CST Microwave Studio and Microwave Office. The simulation results show that the designed filter has a good sharpness factor, symmetrical response, and small losses in the passband
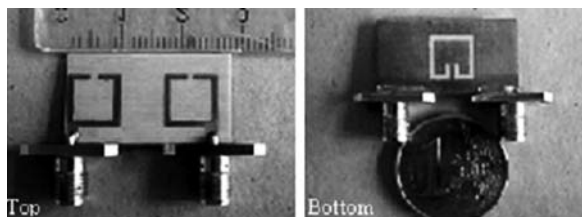
Fig. 8 Photographs of the fabricated open loop DGS bandpass filter
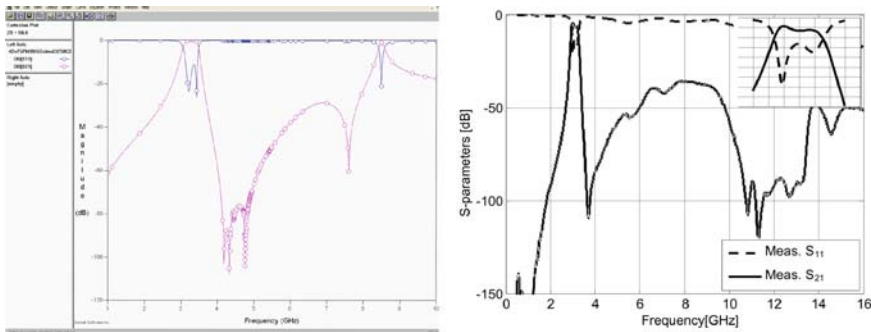
Fig. 9 EM simulation results (*left*) and measured result (*right*) of the proposed BPF

as shown in Fig. 9 (left). In order to verify the simulation results, the filter has been fabricated and measured using an HP8722D network analyzer. The BPF has been fabricated on a substrate with a relative dielectric constant ε_r of 3.38 and a thickness h of 0.813 mm. The measurements and the simulation results are shown in Fig. 9 (right). A very good agreement between simulations and measurements has been obtained. In the passband, the measured insertion and return losses are less than –5dB and −15dB, respectively. The results show significantly improved performance over the filters previously presented in [10, 11]. The proposed structure is more compact compared to the conventional microstrip filters. The losses have been caused due to mismatching effects and the manufacturing errors [12].

6 Conclusion

A coupling structure for open-loop ring DGS bandpass filter has been proposed to suppress harmonics and to make its implementation less challenging. The presented experimental results of the fabricated filter demonstrate its potential. Two transmission zeros are positioned above and below the passband, which gives good attenuation characteristics. A significant size reduction has been accomplished using a novel DGS technique and multiplayer method.

References

1. A. Abdel-Rahman, A. K. Verma, A. Boutejdar, and A. S. Omar, Compact stub type microstrip bandpass filter using defected ground plane, IEEE Microwave and Wireless Components Letters, vol. 14, pp. 136–38, 2004. (MTT-Journal).
2. A. Boutejdar Elsherbini, Adel, Omar Abbas Sayed, Improvement of bassband and sharpness factor of parallel coupled microstrip bandpass filters using discontinuities correction, Mediterranean Microwave Symposium 2007. Budapest, pp. 121–24.
3. J.-S. LIM, C.-S. KIM, Y.-T. LEE, D. AHN, and NAM, Design of LPFs using DGS and compensated microstrip line, Electronics Letters, vol. 38, no. 22, pp. 1357–58, October 2002.
4. A. Batmanov, A. Boutejdar, A. S. Omar, and E. P. Burte, 2D quasi-fractal periodic de-fected ground structure for coplanar waveguide Proceedings IEEE AP-S International Symposium. Manchester Grand Hyatt, San Diego, USA, 5–12 July, 2008.
5. C. Kim, J. S. Park, A. Dal, and J. Kim, A novel 1-D periodic defected ground structure for planar circuits, IEEE Microwave Guided Wave Letters, vol. 10, pp. 131–33, April 2000.
6. J. S. Hong and M. J. Lancaster, Microstrip Filters for RF/Microwave Applications. Wiley, New York, 2001.

 7. A. Boutejdar, G. Nadim, and A. S. Omar Compact bandpass filter structure using an open stub quarter-wavelength microstrip line corrections Proceedings of the 35th EuMC, Paris, 2005.
 8. A. Boutejdar, A. Elsherbini, A. Balalem, J. Machac, and A. S. Omar Design of new DGS hairpin microstrip bandpass filter using coupling matrix method, Proceedings of PIERS'2007, Prague, 2007, pp. 261–65.
 9. Ahmed Boutejdar, A. Elsherbini, and A. S. Omar, A compact microstrip multi-layer lowpass filter using triangle slots etched in the ground plane, Proceedings of the 36th European Microwave Conference 2006 (EuMC), Manchester, UK, September 2006.
10. A. Boutejdar, A. Elsherbini, A. Balalem, J. Machac and A. S. Omar, Design of new DGS hairpin microstrip bandpass filter using coupling matrix method, Progress in Electromagnetics Research Symposium (PIERS). PIERS 2007 in Prague, Czech Republic, August, 2007.
11. D. AHN, J. S. PARK, C. S. KIM, Y. QIAN, and T. ITOH, A design of the low-pass filter using the novel microstrip defected ground structure, IEEE Transactions on Microwave Theory and Techniques, vol. 49, no. 1, pp. 86–93, January, 2001.
12. A. Boutejdar, A. Elsherbiny, and A. S. Omar (Invited), A novel method to obtain a large reject-band with a compact bandstop filter using detected ground structure (DGS) coupled resonators Mediterranean Microwave Symposium Genova, Italy September, 2006.

Modeling Broadband Antennas for Hot Electron Bolometers at Terahertz Frequencies

I. Türer, X. Gaztelu, N. Ribière-Tharaud, A.F. Dégardin, and A.J. Kreisler

Abstract There is a strong need for wideband and sensitive receivers for radio astronomy and remote sensing applications in the terahertz (THz) region. Superconducting hot electron bolometer (HEB) mixers are a competitive alternative to conventional mixer technologies in the THz range. The aim of this chapter is to model antennas coupled to HEBs belonging to an array working in the 1–7 THz range, typically. Several broadband antenna types were investigated before selecting the log-periodic structure. In order to perform experiments in microwave-devoted anechoic chambers, the antenna working frequency band has been scaled down to the 2.25–17.5 GHz range. We have so measured a front-to-side gain ratio of 18 dB at center frequency, which is quite satisfactory for HEB THz imaging arrays. Experimental results performed with scaled models, as compared with simulations performed with a commercially available finite element software, exhibited on the whole good matching within a 2–3 octave bandwidth.

Keywords Terahertz · Wideband antennas · Log-periodic planar antenna · Antennas for imaging arrays · Superconducting bolometers

1 Introduction

After more than three decades of niche applications in the space sciences, molecular spectroscopy, and plasma diagnostics, the terahertz (THz, spanning from 0.5 to 10 THz, typically) field has seen a true renaissance. While major strides continue to be made in submillimeter wave astronomy and remote sensing, the past few years have witnessed an unprecedented expansion of THz applications, components, and instruments. However, this frequency band is still one of the less explored regions of the electromagnetic spectrum, due to a lack of sources and detectors, although there are so many potential applications [1, 2].

Superconducting hot electron bolometer (HEB) mixers are a competitive alternative to conventional mixer technologies in the THz range. A HEB typically consists of an ultra-thin (a few 10 nm thick) superconducting microbridge ($0.5 \times 0.5 \ \mu m^2$) coupled with a planar antenna. We develop HEBs for imaging systems in the 1–7 THz range, made from high-T_c superconducting

I. Türer (✉)
SUPELEC/Laboratoire de génie électrique de Paris (LGEP); CNRS UMR 8507; UPMC Univ Paris 06; Univ Paris Sud 11, Gif-sur-Yvette, France
e-mail: ahmed.boutejdar@ovgu.de

YBa$_2$Cu$_3$O$_{7-\delta}$(YBCO) thin films deposited on MgO substrates [1]. As the operating conditions are based on heterodyne detection, the electromagnetic input signal is down converted to an intermediate frequency (in the microwave range) by means of a THz local oscillator.

As superconducting YBCO is totally reflective to the THz electromagnetic radiation, the YBCO device is connected to a planar antenna for optimizing the coupling with the incident radiation, as shown in Fig. 1.
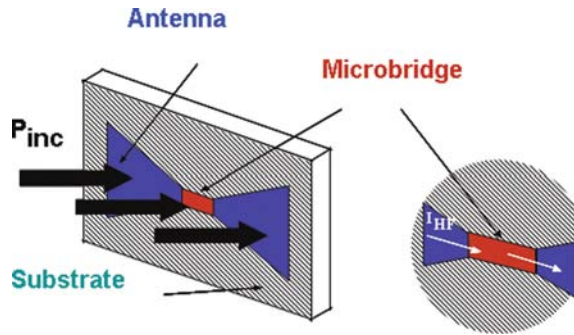
Fig. 1 Planar antenna structure connected to a HEB superconducting microbridge

The targeted 1–7 THz range, which is much larger than the center frequency, requires ultra-wideband (UWB) antenna technology, so to ensure a sufficient impedance match throughout the band, aiming at power loss less than 10% due to reflections at the antenna terminals. To reach adequate coupling between antenna and the HEB device, the impedance value of the antenna should be close to the resistance value of the YBCO microbridge, which is $\approx 100\ \Omega$, typically, as testified by the resistive transition measurement shown in Fig. 2.
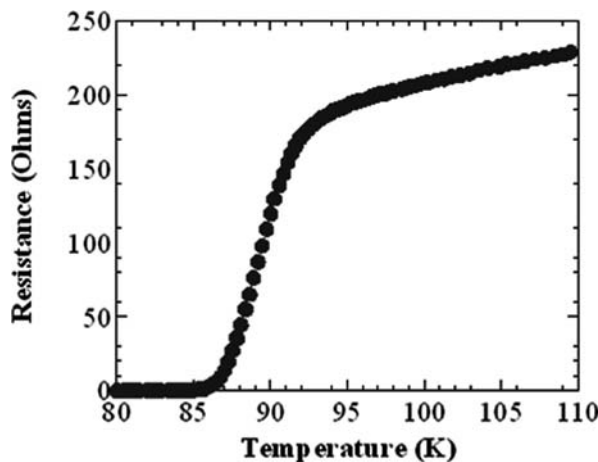
Fig. 2 Resistive superconducting transition of an YBCO HEB (after [1])

UWB requirement has had a substantial effect on antenna design. Given that antenna research for most narrowband systems is relatively mature, coupled with the fact that the antenna has been a fundamental challenge of the UWB system, UWB has attracted a great deal of interest in antenna design by providing new challenges and opportunities for antenna designers. The main challenge

in UWB antenna design is to achieve a wide impedance bandwidth while still maintaining high radiation efficiencies [3].

In the next sections, UWB antenna requirements will be listed at first, before explaining log-periodic antenna properties. After designing a THz log-periodic antenna with the help of empirical formulas, the THz antenna will be scaled down to the microwave region to perform experiments, the results of which will be finally compared to simulations.

2 Planar Antennas for the Terahertz Range

2.1 UWB Antenna Geometry

The purpose of the antenna is to couple power from a wave in free space into a device that is much smaller than one wavelength. We currently develop integrated planar antennas because of their advantages, as compared to waveguide coupling, such as cheaper fabrication, better accuracy, and robustness, particularly at higher frequencies. Planar antennas are good candidates for easy integration into THz pixel arrays, as well [4].

Antenna characteristics such as impedance, radiation pattern, or polarization behavior are invariant to a change of the physical size if a similar change is also made in the operating frequency or wavelength. In other words, the performance is invariant if the electrical dimensions remain unchanged [5]. To design a UWB antenna, two principles should be considered: self-complementarity and self-similarity. Self-complementarity is the property of invariance as the metal part is replaced by the dielectric part, as shown in Fig. 3. Babinet's equivalence principle states that the input impedances Z_1 and Z_2 of two planar complementary antennas are related to the characteristic impedance η of free space as [6]

$$Z_1 Z_2 = \eta^2 \big/ 4. \tag{1}$$

Self-similarity is the property of invariance that the electromagnetic behavior can be similar at the multiple scales where the shape reproduces itself.
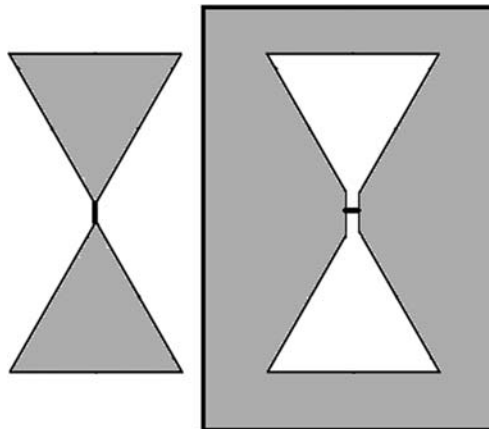
Fig. 3 Complementary antennas
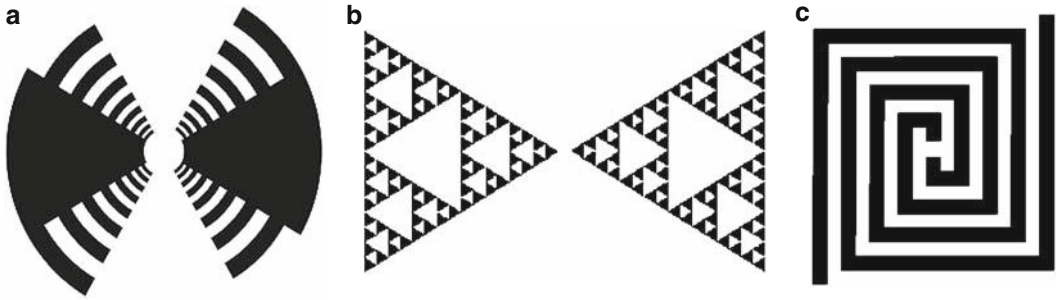
Fig. 4 **(a)** Log-periodic, **(b)** Sierpinski fractal, **(c)** square spiral

Log-periodic, Sierpinski fractal and square-spiral antennas, as shown in Fig. 4, have been investigated before finally selecting log-periodic antennas because of their larger bandwidth and quasi-constant impedance behavior.

2.2 Log-Periodic Antenna

A log-periodic antenna has been developed, to be used as a coupling element between free space and the superconducting microbolometer. The geometrical parameters of the antenna are detailed in Fig. 5. The expected bandwidth of this 8 pseudo-dipole (or 8-arm) log-periodic antenna – which belongs to the family of "frequency-independent antennas" – spans from 0.9 to 7 THz with a center frequency of 2.5 THz according to our specifications. The key design parameter of a log-periodic antenna is the scale factor τ, which is defined as the ratio of sequential radii R_n and R_{n+1}, so that for our 8 pseudo-dipole structure, one gets

$$\tau = \frac{R_{n+1}}{R_n} \cong 1.1365. \tag{2}$$

Working principles of log-periodic antennas were firstly investigated, and to understand how these antennas work, we have sought empirical considerations. For instance, one arm could be considered as active only when its length L is one-fourth of the effective wavelength λ_{eff}, so that

$$L = \lambda_{\mathrm{eff}}/4, \text{ with } \lambda_{\mathrm{eff}} = \lambda_o/\sqrt{\varepsilon_{\mathrm{eff}}}, \tag{3}$$
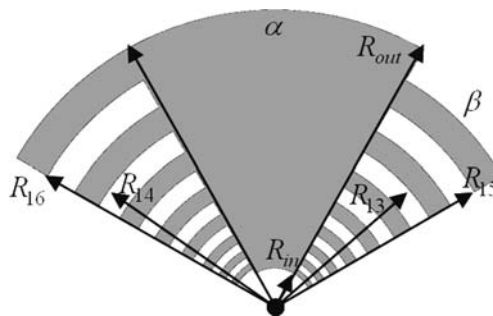
Fig. 5 8-arm log-periodic antenna

where ε_{eff} is the effective relative permittivity of the antenna medium.

The frequency limits $f_{\min}$ and $f_{\max}$ of the log-periodic antenna can be determined as follows. The lowest and highest frequencies are obtained when the longest and shortest arms are having values, respectively,

$$L_{\max} = 2\pi R_{out}\beta/360°, \quad L_{\min} = 2\pi R_{in}\beta/360°, \tag{4}$$

where β is the arm angle and R_{out} (resp. R_{in}) the outer (resp. inner) radii of the structure (see Fig. 5). These length values are related to the effective (or antenna) wavelengths including the substrate, so that

$$L_{\max} = \lambda_{\text{eff}-\max}/4 \quad \text{and} \quad L_{\min} = \lambda_{\text{eff}-\min}/4. \tag{5}$$

These effective values are then converted to their free space counterparts to obtain the minimum and maximum frequencies as

$$\lambda_{\max} = \lambda_{\text{eff}-\max} \times \sqrt{\varepsilon_{\text{eff}}} \quad \text{and} \quad \lambda_{\min} = \lambda_{\text{eff}-\min} \times \sqrt{\varepsilon_{\text{eff}}}, \tag{6.1}$$

$$f_{\min} = c/\lambda_{\max} \quad \text{and} \quad f_{\max} = c/\lambda_{\min}, \tag{6.2}$$

where c is the velocity of light in vacuum.

2.2.1 Impedance Behavior of Log-Periodic Antennas

To understand the impedance behavior of log-periodic antennas, some hypothetical cases have been investigated at first. In theory, frequency independence is only achieved if the outer radius is infinitely large and the inner radius is infinitesimally small. In applications, we have to restrict antenna dimensions with regard to desired bandwidth. As the inner radius of the log-periodic antenna increases, impedance inconsistency occurs at high frequencies. Similarly, the outer radius is responsible for the lowest frequency. To prove this property, two different log-periodic antennas exhibiting the same scale factor τ were investigated, both on substrates of dielectric constant $\varepsilon_r = 10$. The first antenna, having both smaller inner (2.8 µm) and outer (22 µm) radii is called as Antenna 1, while the second one (Antenna 2) has larger radii (5.2 and 40 µm, respectively). Both antenna impedances are plotted in Fig. 6, as obtained from simulation software CST Microwave Studio® [7].

If the antennas were immersed in free space the antenna impedance would oscillate around 189 Ω, according to Babinet's equivalence principle (1). In the case of a dielectric–air interface, it has been suggested [4] to replace (1) by

$$Z_{ant} = \frac{\eta}{2}\frac{1}{\sqrt{\varepsilon_{\text{eff}}}}, \quad \text{where} \quad \varepsilon_{\text{eff}} = (\varepsilon_r + 1)/2. \tag{7}$$

From this rough approximation, the antenna impedance would be equal to 80 ε for an MgO substrate ($\varepsilon_r = 10$). For better design, however, the above-mentioned software was used to specify an empirical expression converging to $\varepsilon_{\text{eff}} \cong (\varepsilon_r + 5)/2$ for an electrically thick MgO substrate.

Another issue to be considered is the effect of the ground plane under the substrate. In Fig. 7, the effect of the ground plane can be seen. There is a ground plane 50 µm apart from Antenna 3. The other antenna (Antenna 4) is operating without any ground plane. Both structures are operating in free space. At integer multiples of $\lambda/2$, Antenna 3 exhibits interference effects revealed by impedance peaks. Also, at higher frequencies, less effect of ground plane is observed because of electrically
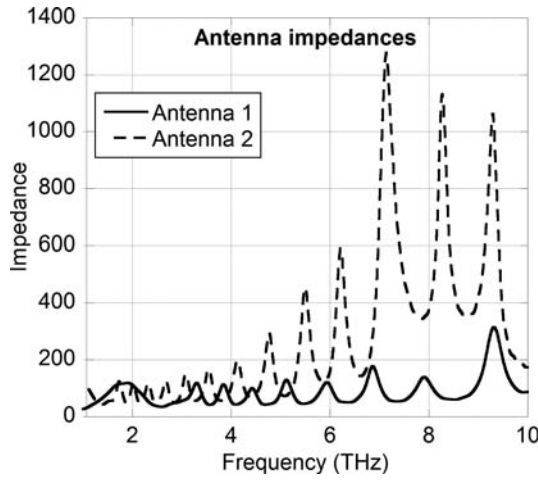
Fig. 6 Impedance effect of inner radius
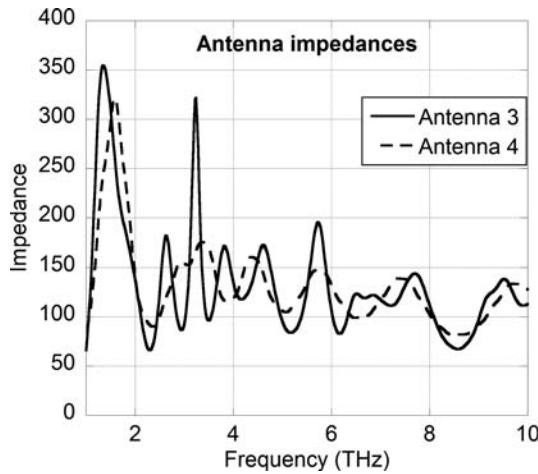
Fig. 7 Ground plane effect

Table 1 Radii of Antennas 1 to 4

Parameter		Antenna 1	Antenna 2	Antenna 3	Antenna 4
Inner radius (μm)	R_{in}	2.8 μm	5.2 μm	1 μm	1 μm
Outer radius (μm)	R_{out}	22 μm	40 μm	58 μm	58 μm
Radius factor	τ	1.1365	1.1365	1.289	1.289

larger distance between the antenna and ground plane. Antennas 3 and 4 both have inner and outer radii of 1 and 58 μm, respectively. The radii of Antennas 1 to 4 are gathered in Table 1.

2.2.2 Scaling from THz to Microwave Region

After having considered some elementary working principles of log-periodic antennas, we have designed a THz log-periodic antenna with the help of our empirical approach. In order to perform

experiments, the antenna working frequency band has been scaled down to the microwave region (2.25–17.5 GHz, typically), with a scaling factor such that 6.07 GHz is equivalent to 2.5 THz so that scaling the microwave model to terahertz by a factor of ~ 411 (the ratio of substrate thicknesses). THz and large-scale antenna parameters are given in Table 2. CST Microwave Studio$^{\circledR}$ was used to simulate the electromagnetic characteristics of this antenna. In Fig. 8, surface currents J_s are plotted for 2, 6, and 10 GHz, after approximately scaling down from 1, 2.5, and 4 THz, respectively.

Table 2   8-arm antenna parameters (THz and scaled model)

Parameter		THz values	GHz values
Inner radius	R_{in}	7.5 μm	3 mm
Outer radius	R_{out}	58.1 μm	23.2 mm
Radius factor		1.1365	1.1364
Frequency range	f_{min}-f_{max}	0.9–7 THz	2.25–17.5 GHz
Flare angle (Fig. 5)		60º	60º
Arm angle (Fig. 5)		90–αº	90–αº
Substrate thickness	T_s	250 μm	102 mm
Substrate relative permittivity	ε_r	10	10

It is observed that the designed antenna works well in the desired frequency band. At low frequencies, the log-periodic antenna behaves like a bow-tie antenna, as expected. At the center frequency (6 GHz), the active arm is the fourth one nearest to the antenna center. It is also worth mentioning that at 10 GHz, there is more than one arm resonating.
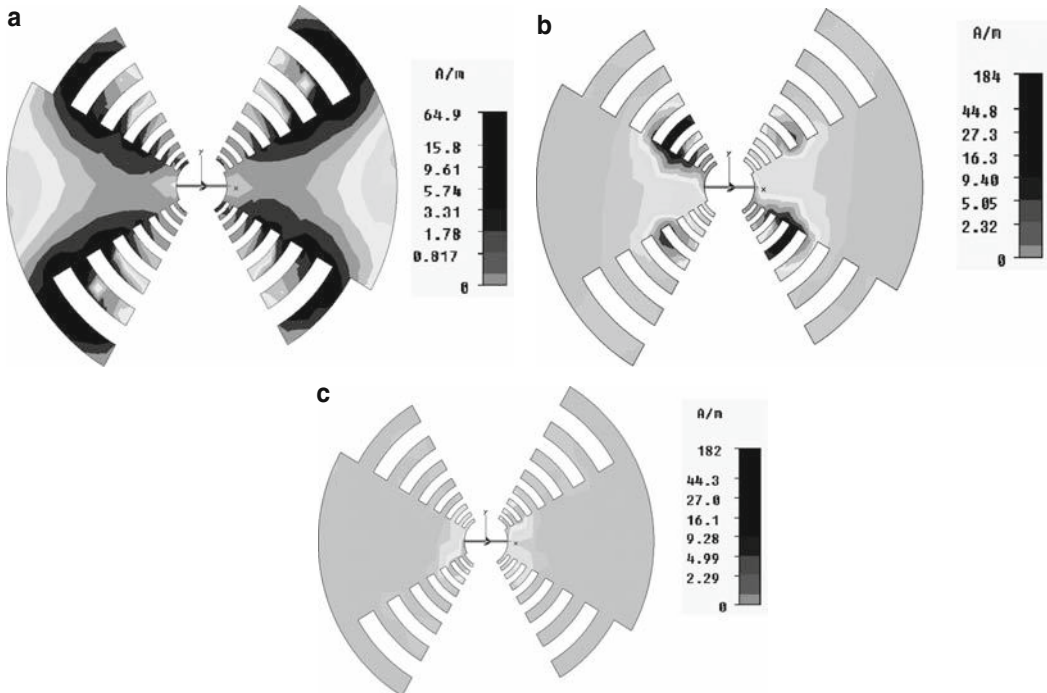
Fig. 8   (**a**) J_s at 2 GHz, (**b**) J_s at 6 GHz, (**c**) J_s at 10 GHz

3 Experiment and Simulation Compared

To realize the large-scale antenna, we have scaled the THz antenna according to Table 2. Issues arose from having electrically thick ($\sim$10 cm) and MgO-equivalent substrates ($\varepsilon_r = 10$) which were needed and supplied to realize the large-scale model. We have dealt with different sizes of substrates for mechanical implementation requirements [8, 9]. In order to get a symmetric antenna feed, a *balun*(*bal*ance/*un*balance) device should be used. However, to design a wideband *balun* and integrate it onto a very thick substrate is not an easy task. We have considered a simple solution consisting in feeding the antenna symmetrically through the substrate with two coaxial cables, the inner conductors being connected to the two halves of the antenna. The transition between these cables and the source coaxial cable could then be performed by using a commercially available wideband 0–180° hybrid phase shifter. Finally, for cross-checking purposes, a large-scale experimental log-periodic antenna on an MgO-equivalent substrate ($\varepsilon_r = 10$) was tested by simulation software and measurements which were performed in anechoic chambers (Fig. 9).
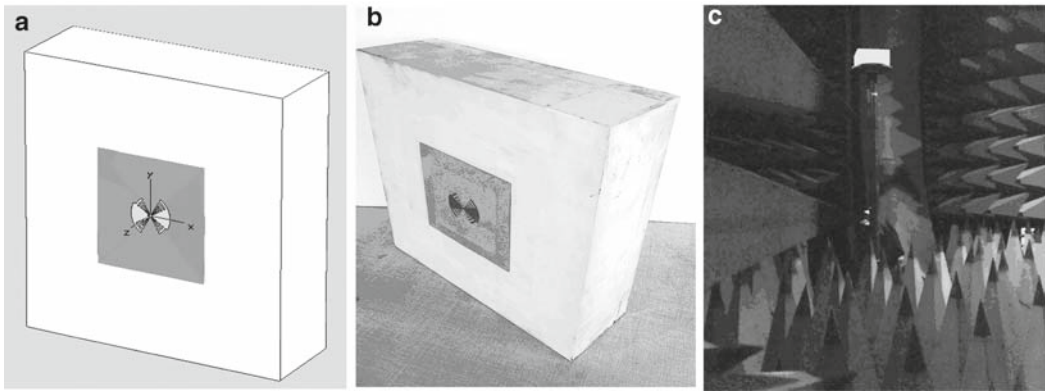
Fig. 9 **(a)** Simulation model, **(b)** experimental large-scale antenna, **(c)** anechoic chamber (SUPELEC/DRE)

For 2, 6, and 10 GHz, gain patterns are compared with those obtained from CST Microwave Studio® simulations. CST simulation was carried out with the efficiency of $\sim 40\times10^6$ cells. Gain patterns for E-plane (-*xz*) and H-plane (-*yz*) for 2, 6, and 10 GHz are plotted in Fig. 10.

At low frequency, such as 2 GHz, there is a main lobe around 0°. Main lobe widths are quite comparable and in the bore-side direction the gain difference is quite small. However, there are some imperfections near 70° at 2 GHz which might be due to the actual setup of the anechoic chamber such as spurious reflections cables. Near 70° the peak point is shifted and may be ascribed to small experimental orientation errors. Nevertheless, at 2 GHz, the result is satisfactory for both E- and H-planes. Near center frequency (6 GHz), we see gain decay near 0°. After 20°, there is an increase about 10 dB. The same remark can be made about the frequency shifting effect (orientation error). It is worth to say that at 90° the side lobe level is quite small ($\sim$ –10 dB) which is desirable to reduce electromagnetic cross talk between the elements of linear arrays of HEB detectors. Overall, however, there is a good match between experiment and simulation.

At 10 GHz, until 45° results can be considered alike. But after this value, there is mismatch between measurement and simulation. At 10 GHz, indeed, even the smallest experimental details such as soldering imperfections or anechoic chamber spurious reflections can affect the results meaningfully. Because of electrically large structure, there are losses due to substrate high order modes also affecting the results badly.
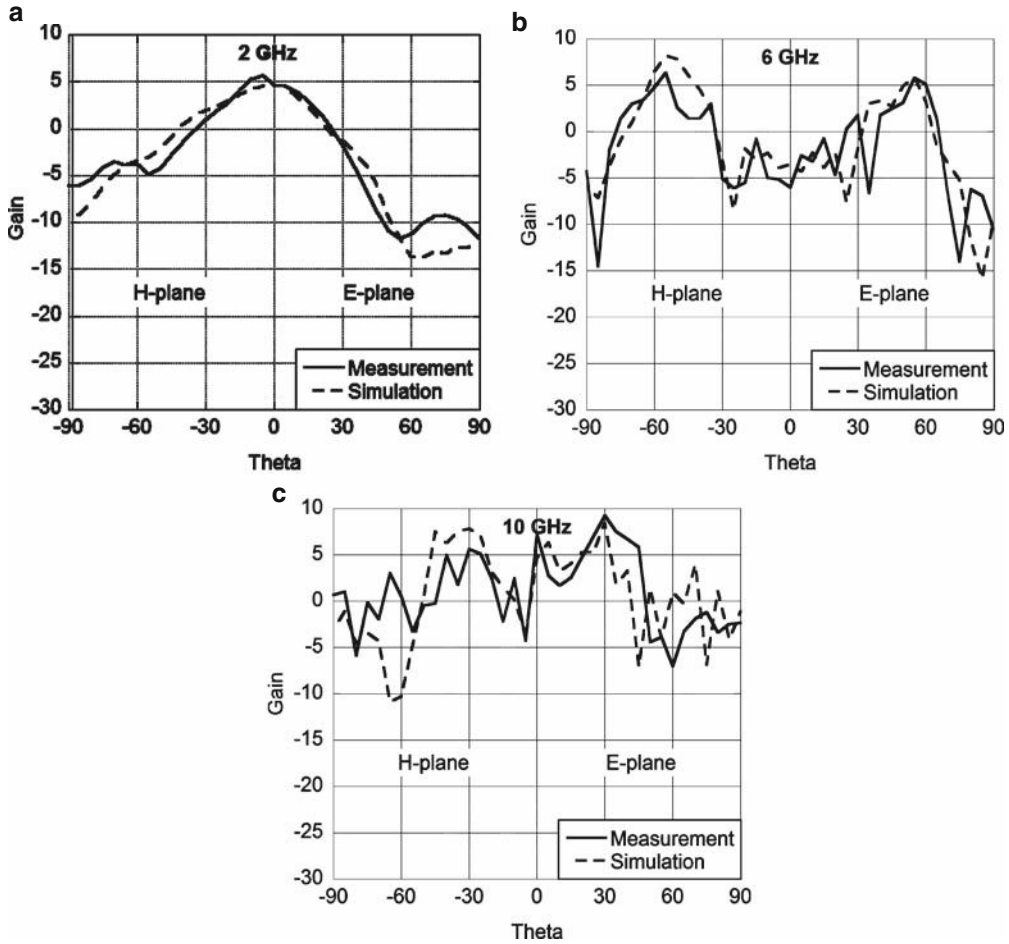
Fig. 10 (**a**) Gain at 2 GHz, (**b**) gain at 6 GHz, (**c**) gain at 10 GHz

4 Conclusion and Future Works

Several different types of UWB antennas were investigated before the selection of log-periodic antenna. To realize the large-scale model, needed substrates were obtained from the market. Afterward, we have fabricated and characterized a GHz large-scale model. The substrate, having a high dielectric permittivity, keeps the energy and prevents complete radiating to free space. In order to avoid back radiation at least, a back metal has been placed under the substrate. A better solution might be to place a high permittivity material over the substrate, such as a lens. Both improvements are compatible with HEB THz mixer block technology. Finally, we have proven that the simulation results were confirmed by measurements.

This work is going to lead to the final design of linear arrays of HEB detectors.

References

1. A. J. Kreisler, A. F. Dégardin, and M. Aurino et al., New trend in terahertz detection: high Tc superconducting hot electron bolometer technology may exhibit advantages vs. low Tc devices, IEEE International Microwave Symposium (IMS 2007), Honolulu, Hawaii, USA, June 2007, Proceedings, pp. 345–48.
2. P. H. Siegel, P. de Maagt, and A. I. Zaghloul, Antennas for terahertz applications, IEEE Antennas and Propagation Society International Symposium 2006.
3. Johnna Powell, Antenna Design for Ultra Wideband Radio, Master thesis, Massachusetts Institute of Technology, 2004.
4. E. N. Grossman, Lithographic antennas for submillimeter and infrared frequencies, Electromagnetic Compatibility, 1995. Symposium Record. 1995 IEEE International Symposium on Volume 14–18, pp. 102–107, 1995.
5. C. A. Balanis, Antenna Theory: Analysis and Design, Third edition, John Wiley and Sons, New York, 2005.
6. J. A. Kong, Electromagnetic Wave Theory, EMW Publishing, Cambridge, 2000.
7. CST Microwave Studio®, www.cst.com.
8. Emerson&Cuming, Microwave Products, www.eccosorb.com (Eccostock material).
9. Rogers Corporation, www.rogerscorporation.com (Duroid material).

Investigation on the Phase Center of Ultra-wideband Monopole Antennas with Band-Stop Functions

A. Mohamed and L. Shafai

Abstract A method for determining the phase center location of ultra-wideband monopole antennas is presented and used to investigate its movement within the frequency band of the antenna. It is then used to study the effects of different band-stop designs on the degree of the phase center movements. It is shown that some designs can adversely affect the phase of the radiated field, by displaying larger phase center movements. For improved performance of the UWB antennas, such designs must be avoided.

Keywords Phase center · Band-stop functions · Ultra-wideband antennas · Monopole antennas · Circular monopoles

1 Introduction

The proposed use of ultra-wideband (UWB) communication services, over the bandwidth of 3–10 GHz, has increased the research interest on design and performance studies of UWB antennas, especially monopole types with omnidirectional radiation patterns. However, other services already operate within this band. Thus, to eliminate the interference between the existing and upcoming ultra-wideband communication services, UWB Antennas with band-stop functions are being investigated [1–3]. A common approach is to implement certain features in the antenna structure, like half wavelength slots at the center frequency of stop-band, to cause resonances and current concentration around the features to eliminate radiation at the required frequencies. These additional design features naturally affect the antenna performance, especially the phase of the far field patterns over its wide frequency band. This is due to the fact that the new antenna becomes effectively two separate antennas, the original UWB antenna and the added feature, whose radiation cancels that of the original antenna within the desired band. For this reason, the phase performance of the new antenna can become more complex, as the two antennas have their own separate phase centers, with subsequent interactions. Here, the phase center is defined as a point where from the radiation of the antenna

---

A. Mohamed (✉)

Department of Electrical and Computer Engineering, The University of Manitoba, Winnipeg, Manitoba, Canada, R3T 5V6

e-mail: halim@ee.umanitoba.ca

originates. Since, the location and intensity of the current distribution on the original UWB antenna changes within its wide frequency band, the resulting phase center location of the composite antenna will change within the band. This means, different frequency components of a wideband pulse will radiate from different regions of the antenna, with subsequent deteriorating effect on the radiated pulse at the far fields. Thus, it is important that in designing a band-stop feature a configuration be selected such that it does not have a detrimental effect on the phase center location of the resulting composite antenna. To demonstrate this phenomenon the problem of phase center location and its movement within the required band are investigated for a few common designs. It is shown that indeed some designs are inferior and must be avoided.

Spheroidal, conical, and teardrop monopole antennas are some of the traditional UWB antennas with excellent electrical characteristics. However, they are three-dimensional structures and also difficult to fabricate. Monopole disc antennas, with circular, elliptical, and trapezoidal shapes, can also provide UWB impedance bandwidths, but have simpler two-dimensional geometries and are easier to fabricate. In 1992, Honda and others proposed a circular monopole TV antenna operating at 90–770 MHz [4]. These antennas can be designed to cover both existing and upcoming UWB communication applications and have omnidirectional radiation patterns over the entire frequency of operation [5]. For these reasons, in this study circular monopole type designs are selected. Since their radiation is mostly near the horizontal plane, between $\theta = 60°$ and $90°$, the phase center locations are determined for this angular range. However, the antenna configurations are angular dependent and create angular-dependent phases in the frequency domain, which in turn causes distortion in the time-domain signal that is not symmetric along the azimuth angle ϕ. To understand this phenomenon, the computations are made in the principal and diagonal planes $\phi = 0°$, $45°$, and $90°$. For a circular UWB monopole antenna, over the frequency band of 3–11 GHz, this study was reported by authors in [6]. This chapter investigates the effect of including different band-stop features in the circular UWB monopole on its overall phase center behavior. The feature studies are spiral, circular arc slot, and two different fork-type structures.

2 Antenna Design

An antenna using a circular monopole of radius 10 mm at 1 mm distance from a 120×120 mm^2 square ground plane is studied. The width of the feeding strip is 1.5 mm, Fig. 1a. It is designed to work over the frequency band of 3.1–10.6 GHz, and the lower frequency edge is determined using the formula described in [7]. Then, different slot features are included inside the circular antenna to create a stop-band centered at 5.5 GHz, to eliminate interference with the IEEE802.11a, working in the frequency band of 5.15–5.825 GHz. Four different slot shapes are used for this study including spiral, circular arc, fork, and ring shape slots. The total length of each slot is half wavelength at the center frequency of the stop-band, at 5.5 GHz. The slot widths are 2 mm and create a stop-band from 5 to 6 GHz. The spiral slot is an Archimedean one with 0.5 mm separation between arms [1].

The circular arc slot has an outer radius of 8 mm and its center is at $Z = 10$ mm. The fork is a circular metal arc of width 2 mm, an outer radius of 4.5 mm, center at $Z = 10$ mm and attached to the feed region through a strip 1.5 mm high and 2 mm wide. The ring slot is a circular arc of outer radius 4.5 mm and center at $Z = 10$ mm, attached to the feed region through two strips 1.5 mm high and 2 mm wide. They are shown in Fig. 1b, 1c, 1d, and 1e, respectively.
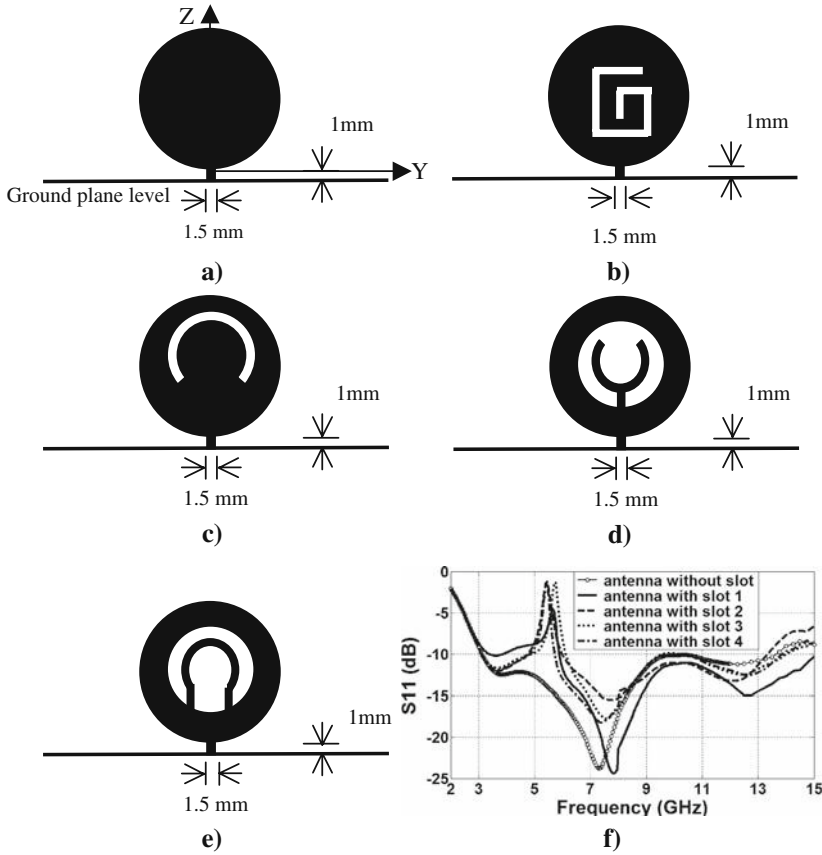
Fig. 1 Circular monopole antenna with different types of slots, (**a**) antenna without slot, (**b**) antenna with slot 1, (**c**) antenna with slot 2, (**d**) antenna with slot 3, (**e**) antenna with slot 4, (**f**) return loss curves of the antennas

3 Phase Center Determination

In this chapter, the antenna phase center is defined as the origin of a sphere, over which the phase of the radiated E_θ field is nearly ($\leq 7°$ phase variation) constant over the frequency band of operation from 3 to 11 GHz, for θ from 60° to 70°, at the three principal $\phi = 0°$, 45°, and 90° planes. HFSS (high-frequency structure simulator based on the finite element method) is used for simulation of the configurations, and computation of the radiated E_θ field, and its phase for different θ ranges at $\phi = 0°$, 45°, and 90° planes. Figure 2 shows the geometry for calculating the phase center, where O (0, 0, 0) is the origin of the coordinates, and O$'$ (0, 0, Z_0) is the phase center location. Because of the symmetry, it is assumed that the phase center will move on the Z-axis. R is the distance from the origin to the far field point and r is the distance from the phase center location to the same observation point. Both R and r are much larger than Z_0 and R and r can be considered parallel. The radiated far field can be expressed as [8, 9]

$$\bar{E}(R,\theta,\phi) = f(\theta,\phi)\frac{e^{-jK_0R}}{R}e^{j\psi(\theta,\phi)}, \tag{1}$$

Fig. 2 Geometry for phase center calculation of UWB circular monopole antennas of Fig. 1
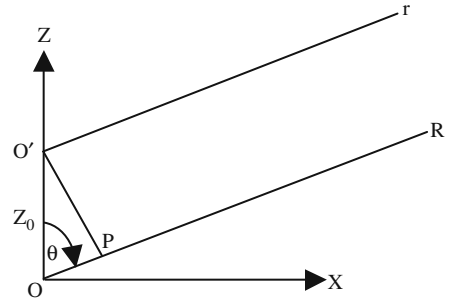
where $f(\theta, \phi)$ is the amplitude pattern, K_0 is the free space propagation constant, and $\psi(\theta, \phi)$ is the phase distribution of the radiated field. From Fig. 2, R and r are related as

$$R = r + Z_0 \cos\theta. \tag{2}$$

Then the phase of the radiated field can be expressed as

$$\psi(\theta, \phi) - K_0 Z_0 \cos\theta - K_0 r. \tag{3}$$

At the phase center point $O'(0, 0, Z_0)$ the phase term in (3) becomes independent (or nearly independent) of θ and ϕ. Using the HFSS results, for the phase distribution of the E_θ far field, in (3) the antenna phase centers, with and without the stop-band are determined for the three principal $\phi = 0°$, 45°, and 90° planes.

4 Results and Observations

The simulation results using HFSS software are used to obtain the phase of the E_θ radiated field with respect to origin O (0, 0, 0). Then this information is used to calculate the phase center of each antenna using the procedures described in Section 3. Figures 3a and 4a show the phase center locations of the circular monopole antenna without slot, for two different θ ranges of 80–90° and 70–80°, where the radiated field is strong. From these figures it can be seen that the phase center movement increases at higher frequencies, where there is also a big difference in the three $\phi = 0°$, 45°, and 90° planes. Figures 3b and Fig. 4b show the same results for the antenna with slot 1(spiral slot), in which the phase center movements in all three ϕ planes are similar up to 9 GHz, with no detrimental effect on the overall performance of the phase center curves. Figures 3c and Fig. 4c show the results for the antenna with slot 2 (circular arc), where the phase center movements are similar in all three ϕ planes, with better performance at high frequencies. Thus, this band-stop slot design improves the overall performance of the phase center carves in all three principal $\phi = 0°$, 45°, and 90° planes. This is due to the fact that this circular arc slot was placed away from the feed region and is symmetric around the Z-axis. Figures 3d and Fig. 4d show the results for the antenna with slot 3 (fork). It can be seen that the double effect of metal removal and the inclusion of a circular arc in the bottom of the radiator, attached to the center of the feed region, did not disturb the performance of the phase center curves. However, this configuration did not improve the phase center performance. Figures 3e and Fig. 4e show the phase center movement curves for the antenna with slot 4 (ring slot), where it can be seen that the effect of metal removal along with the inclusion of a ring attached to
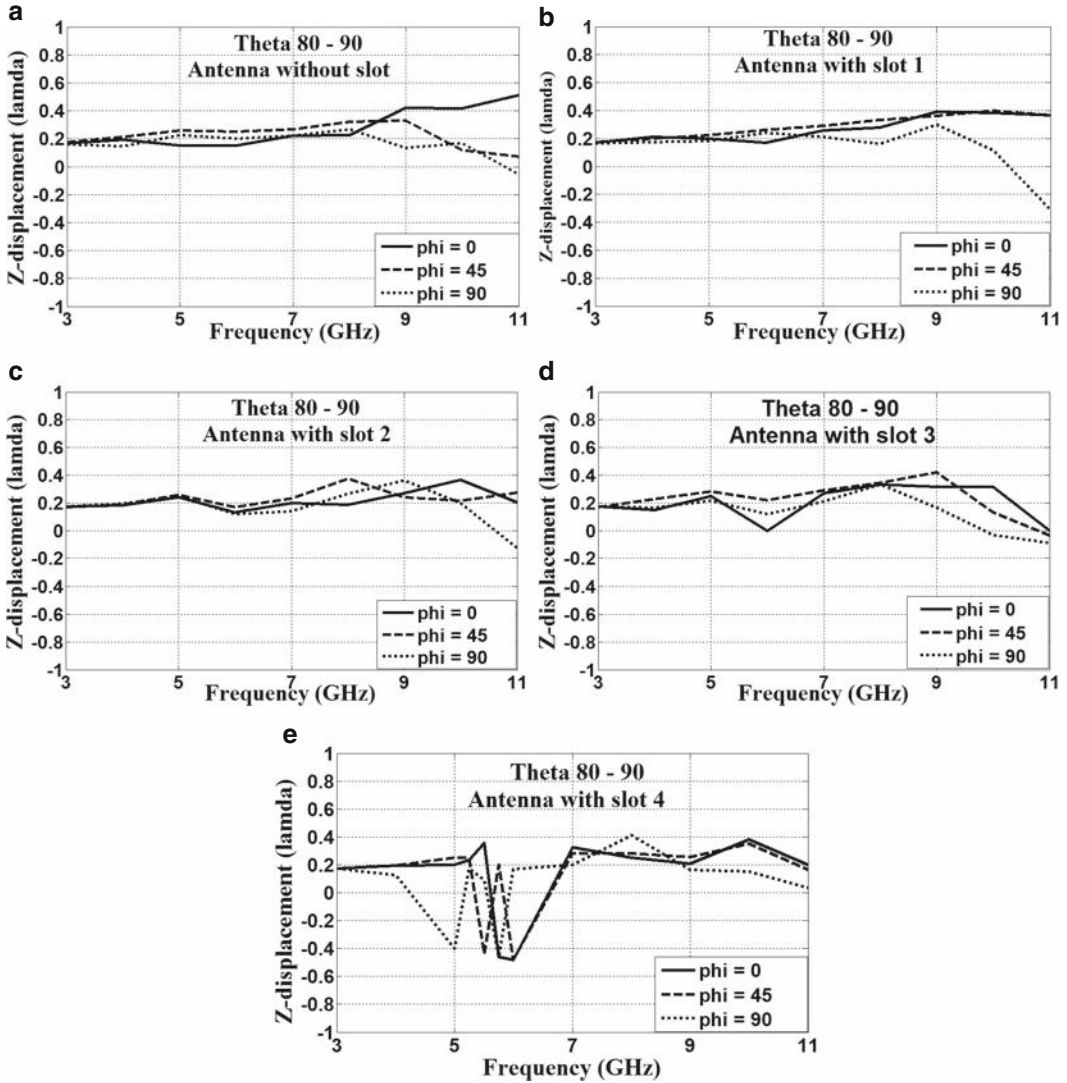
Fig. 3 Displacements on Z-axis (in λ units) correspond to the minimum change in the phase of the radiated E_θ for the θ range from 80° to 90°, at $\phi = 0°$, 45°, and 90° planes. (**a**) Antenna without slot; (**b**) antenna with slot 1; (**c**) antenna with slot 2; (**d**) antenna with slot 3; (**e**) antenna with slot 4

the feed region of the antenna has a noticeable deteriorating effect on the overall performance of the phase center curves.

Table 1 summarizes the maximum range of the phase center movement on the Z-axis for each antenna, over the entire frequency band and at the three principal $\phi = 0°$, 45°, and 90° planes. It should be noted that this range can be smaller if one is interested in the phase center movement in one or two planes only. Based on the phase center movement curves with frequency, the phase center for each antenna could be determined over the entire frequency band at the three principal planes of $\phi = 0°$, 45°, and 90°, for θ range from 60° to 90°. However, some variation in the far field phase
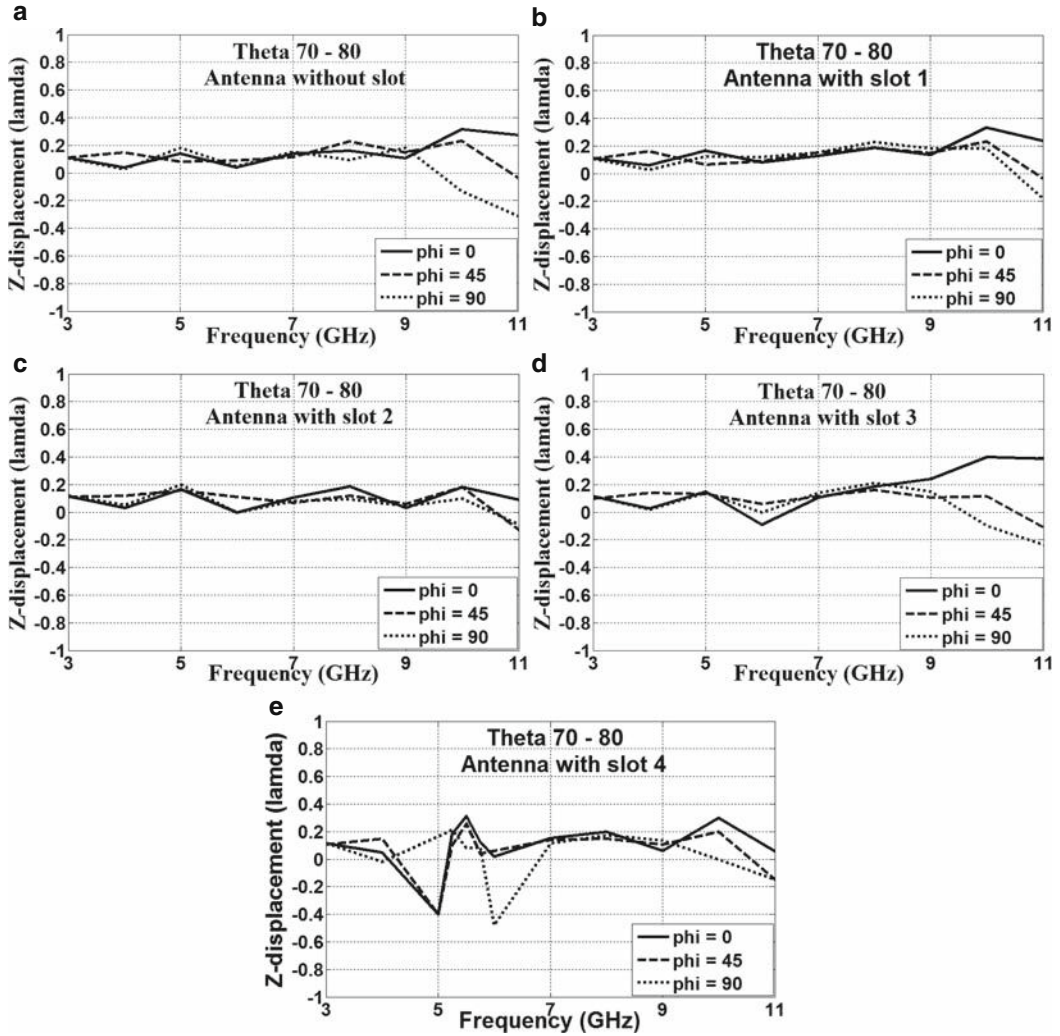
Fig. 4 Displacements on Z-axis (in λ units) for minimum change in the radiated E_θ phase for θ range from 70° to 80°, at $\phi = 0°$, 45°, and 90°. (**a**) Antenna without slot. (**b**) Antenna with slot 1 (spiral). (**c**) Antenna with slot 2 (circular arc). (**d**) Antenna with slot 3 (fork). (**e**) Antenna with slot 4 (ring)

Table 1 Maximum phase center movement ranges at $\phi = 0°$, 45°, and 90° planes for the studied antennas, over 3–11 GHz

θ range, deg.	Antenna without slot	Antenna with slot 1	Antenna with slot 2	Antenna with slot 3	Antenna with slot 4
70–90	0.6 λ	0.7 λ	0.5 λ	0.6 λ	0.9 λ
50–90	0.6 λ	0.7 λ	0.6 λ	0.7 λ	0.9 λ

will be present and must be tolerated, in order to easily find the phase center location over the entire band, and all principal planes.

5 Conclusions

The current distribution and the active regions of UWB monopole antennas at different frequencies can be affected by inclusion of resonant features in the antenna structure, near or connected to the feed point. However, by carefully selecting the feature shape and position, the phase center curves of such antennas can be stabilized in all three principal $\phi = 0°$, $45°$, and $90°$ planes at θ from $60°$ to $90°$. In this study, the E-plane phase center of a UWB circular monopole antenna with different features for band stop function was calculated at each frequency and determined for the entire band. It was found that certain feature shapes have small, or even beneficial, effects on the antenna phase center behavior, while others deteriorate the performance. Examples of Phase center location behaviors for different θ ranges were illustrated.

References

1. A. Mohamed and L. Shafai, Ultra wideband circular monopole antenna with spiral-slots for band-notch function, URSI Meeting, Ottawa, Canada, 22–26 July 2007.
2. A. J. Kerkhoff and H. Ling, Design of a band-notched planar monopole antenna using genetic algorithm optimization, IEEE Transactions on Antennas and Propagation, vol. 55, no. 3, pp. 604–10, March 2007.
3. J. K. Kim and S. Park, Analysis of the small band-rejected antenna with the parasitic strip for UWB IEEE Transactions on Antennas and Propagation, vol. 54, no. 6, pp. 1688–92, June 2006.
4. S. Honda, M. Ito, H. Seki, and Y. Jinbo, A disc monopole antenna with 1:8 impedance bandwidth and omni-directional radiation pattern, Proceedings on ISAP, pp. 1145–48, September 1992.
5. P. P. Hammoud and F. Colomel, Matching the input impedance of a broadband disc monopole, Electronics Letters, vol. 29, pp. 406–7, February. 1993.
6. A. Mohamed and L. Shafai, Investigation on the phase centre of ultra wideband circular monopole antennas, IEEE AP-S International Symposium, San Diego, USA, 5-12 July 2008.
7. N. P. Agrawall, G. Kumar, and K. P. Ray, wide-band planar monopole antennas, IEEE Transactions on Antennas and Propagation, vol. 46, no. 2, pp. 294–95, February 1998.
8. A. Helaly, A. Sebak, and L. Shafai, Phase centre movement in linear phased array antennas, IEEE AP-S International Symposium, vol. 3, pp. 1166–69, 7–11 May, 1990.
9. H. Moheb, A. Sebak, and L. Shafai, Phase centre analysis of array antennas and its significance for microwave landing system, 7th ICAP International Conference, pp. 213–16, 15–18 April, 1991.

Improvements to the Time-Domain Response
of the Double-Ridged Horn

J.S. McLean and R. Sutton

Abstract The double-ridged horn is widely used in frequency-domain measurements and can exhibit a nearly 20:1 impedance bandwidth, albeit with substantial and undesirable pattern variations as well as anomalies related to input impedance match and power transfer. The horn is frequently employed in EMC measurements and it is also being adapted as a UWB and time-domain, short-pulse test antenna. In this chapter we examine it with regard to its time-domain performance

1 Introduction

The double-ridged (DR) horn [1–6] is widely used in frequency-domain measurements and can exhibit a nearly 20:1 impedance bandwidth, albeit with substantial and undesirable pattern variations as well as anomalies related to input impedance match and power transfer. The horn is frequently employed in EMC measurements and it is also being adapted as a UWB and time-domain, short-pulse test antenna [3–6]. Therefore, we examine it here with regard to its time-domain performance.

As noted in [1] and [2], there are many commercially available versions of this design. Close inspection of these commercial units shows that they are for the most part derivatives of a single design presented some time ago in a detailed research report [7] and subsequent journal paper [8]. This work, in turn, apparently drew on the general approach presented in what is perhaps the seminal publication on DR horns [9].

The non-ideal frequency-domain behavior of this horn can be broadly delineated into two categories:

1. Pattern control or frequency-domain power pattern degradation over certain limited frequency ranges as noted in [1] and [10]: These degradations cause variations in the on- and off-axis time-domain responses as noted in [6].

J.S. McLean (✉)
TDK R&D Corp., Cedar Park, TX, USA
e-mail: jmclean@tdkrf.com

2. Narrowband frequency-domain spikes in the input VSWR with attendant dips in the magnitude of the frequency-domain transfer function or gain in all directions: These anomalies manifest themselves in the time domain as ringing. They were first observed in [7, 8] and are typically located above the upper end of the operating frequency range. For the particular design examined here, which is representative of a broad class of commercially available antennas, one exists near 18.5 GHz. Thus, the associated time-domain ringing exhibits a period on the order of 50 picoseconds.

In addition to the non-ideal behavior manifested in the frequency domain, an additional short-coming of the DR horn is most apparent in time-domain measurements. Significant and unavoidable reflections occur at the mouth of the horn at the lower end of the operating frequency range. In addition to this, the cutoff phenomenon in the double-ridged waveguide feed necessarily causes reflections at the feed for sufficiently low frequencies. These two distinct and spatially separated regions of reflection can cause ringing in the time-domain response horn. This ringing has a relatively long period, on the order of 1 ns or longer. Thus, compared to a TEM horn with a perfectly matched feed, the double-ridged horn might be considered as inferior since such a TEM horn exhibits reflection localized to the mouth region and therefore does not exhibit such pronounced ringing.

A cutaway view of a typical DR horn is shown in Fig. 1. The design is very similar to that given in [7] with the exception of some differences in the feed region, the backing cavity, and the curvature of the ridges. The distance between the ridges at the feed point is 1.25 mm. The center conductor of the coaxial feed line is 1.25 mm in diameter. The distance from the coaxial feed to the mouth of the horn is 178 mm. This rendition is actually taken from a solid model used as part of a numerical simulation. The horn is often produced without the walls that are perpendicular to the H-plane of the horn, that is, the vertical side wall in the figure. Here we examine the design in Fig. 1 with and without the side walls.
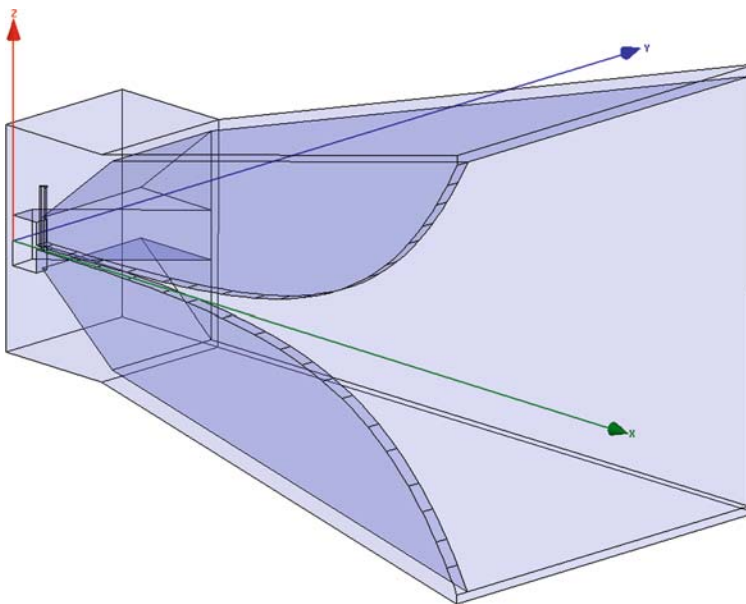
Fig. 1 Cutaway view of double-ridged horn. The mouth dimensions are 254 mm (*w*) by 143 mm (*h*). At the feed point, the gap between the ridges is 1.25 mm. The ridge width is 9 mm

2 The Time-Domain Response of the Double-Ridged Horn

The time-domain response of the double-ridged horn was determined via frequency-domain measurements of the port-to-port scattering parameters of pairs of horns situated in an anechoic chamber. The measurements were taken using a vector network analyzer over a frequency range of 10 MHz to 20 GHz with 16001 frequency points. From these measurements the complex frequency-domain transfer functions were determined using a complex three-antenna approach as described in [6] and then inverse Fourier transformed to obtain the time-domain impulse responses.

In Fig. 2, the time-domain impulse response as defined in [6] of the DR horn shown in Fig. 1 is plotted for five directions in the E-plane. As can be seen, the horn exhibits a fast rise time and a reasonably sharp initial pulse followed by quasi-periodic ringing with a period of approximately 1 ns. The high-frequency ringing is due both to a notch in the transfer function near 18.5 GHz as well as truncation of the frequency-domain data at 20 GHz. Comparison of the data here with data given in [6] shows that the high-frequency ringing of this design is much less pronounced. This is due to a modification of the horn involving a reduction in the distance between the ridges at the feed point. As will be discussed later, reducing this distance has a very marked and beneficial effect on the performance of the horn. From the data in Fig. 2, it can be seen that the shape of the impulse response is fairly similar to that of the on-axis response even for directions 60 degrees off of bore sight in the E-plane.
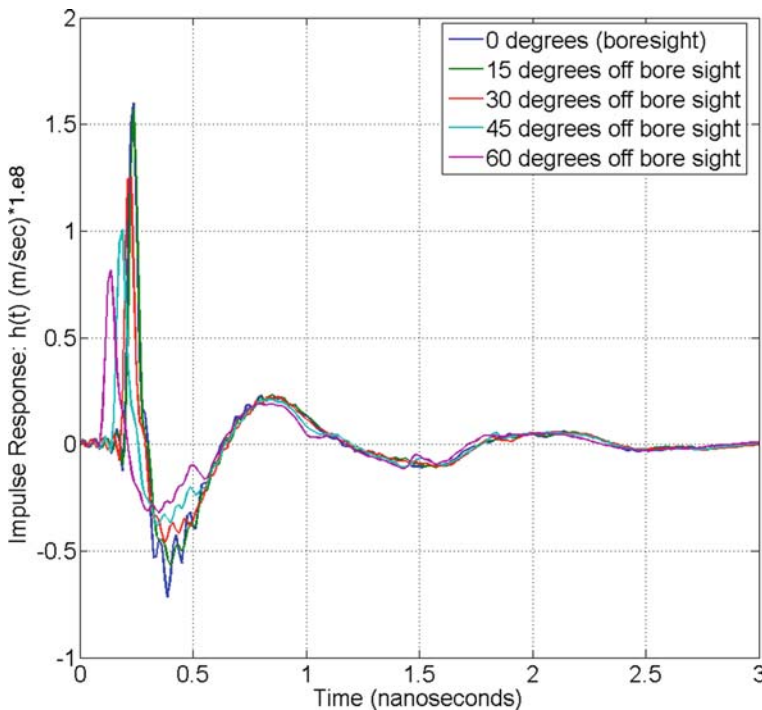
Fig. 2 Time-domain impulse response of horn on- and off-axis in E-plane

In Fig. 3, the time-domain impulse response is plotted for five directions in the H-plane. As can be seen, the response in the H-plane is not as consistent with direction as it is in the E-plane. In previous publications, it has been noted that the frequency-domain, H-plane power pattern of the
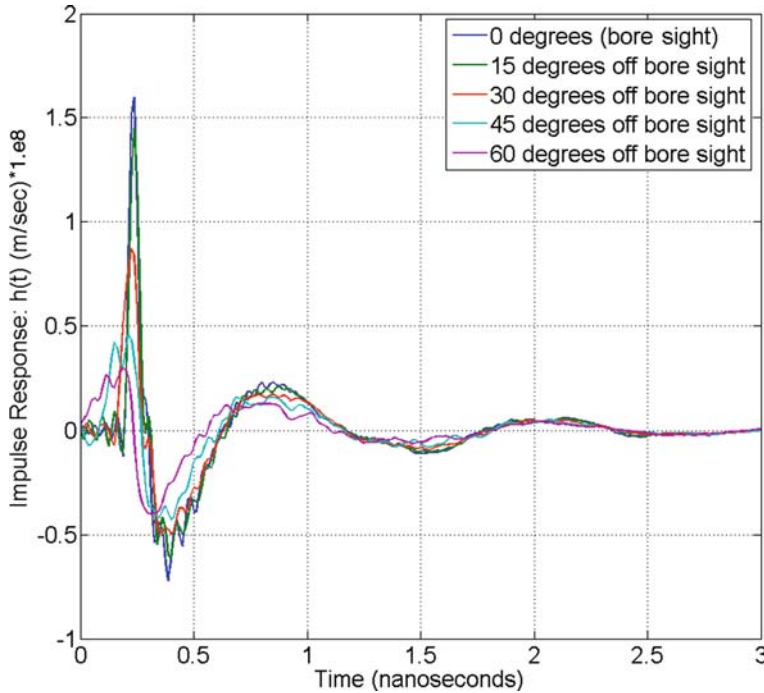
Fig. 3 Time-domain impulse response of horn on- and off-axis in H-plane

DR horn varies much more with frequency than does the E-plane pattern. Specifically, it can be seen that the early-time response is what degrades most significantly as the direction is moved off the bore sight in the H-plane.

In Figs. 4 and 5, the time-domain impulse response of the DR horn without the side walls, the walls perpendicular to the H-plane, is plotted for directions in the E- and H-planes, respectively. Interestingly, the on-axis impulse response is greatly improved over that obtained with the side walls in place. However, the consistency of the response with direction is degraded, especially in the H-plane. Again, the early-time response varies most strongly with direction. It is documented that removal of the side walls results in a broader H-plane power pattern at the low end of the operating frequency range. However, here it is clear that the operation at the high end of the operating frequency range is also strongly affected by the presence or absence of side walls. That is, the fine detail of the early-time response is noticeably changed by the absence of side walls.

In Fig. 6, the on-axis impulse responses of the DR horn with and without side walls are compared to that of a precision TEM horn employing a ground plane. The TEM horn is a Farr Research model TEM-1. The impulse response of the TEM horn was determined using the same equipment and approach as was used to determine the response of the DR horn. The measured impulse response data appears to agree well with published data for the TEM-1. As can be seen the initial spike in the response of the DR horn is almost identical to the impulse response of the TEM horn. However, the initial peak of the response of the DR horn is followed by ringing. In the case of no side walls the response is only slightly inferior to that of the TEM horn.

The on-axis frequency-domain response of the DR horn without side walls is reduced in magnitude over its lowest octave compared to the response with the side walls. It is believed that this reduction in response in the vicinity of the relatively sharp cutoff imposed by the double-ridged
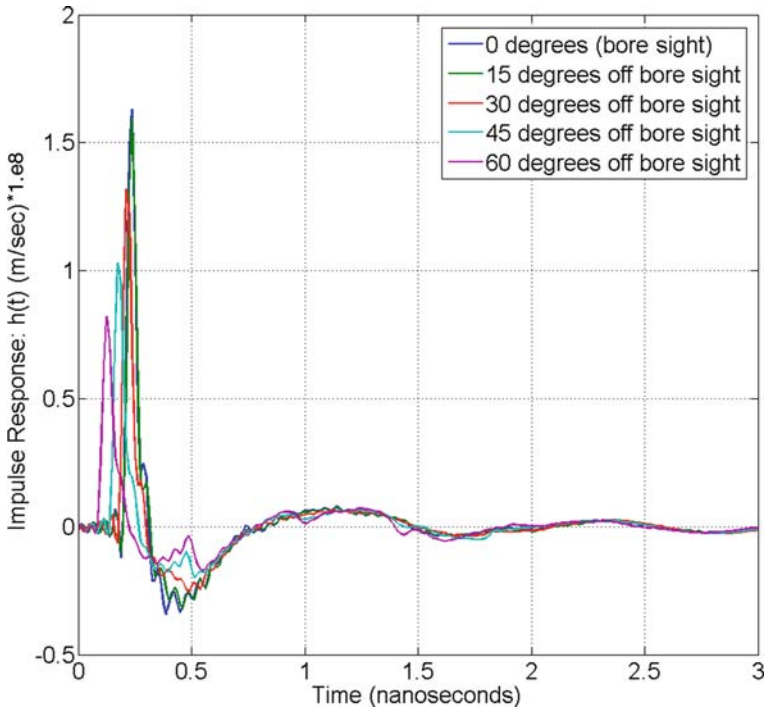
Fig. 4 E-plane off-axis response of the DR horn with no side walls
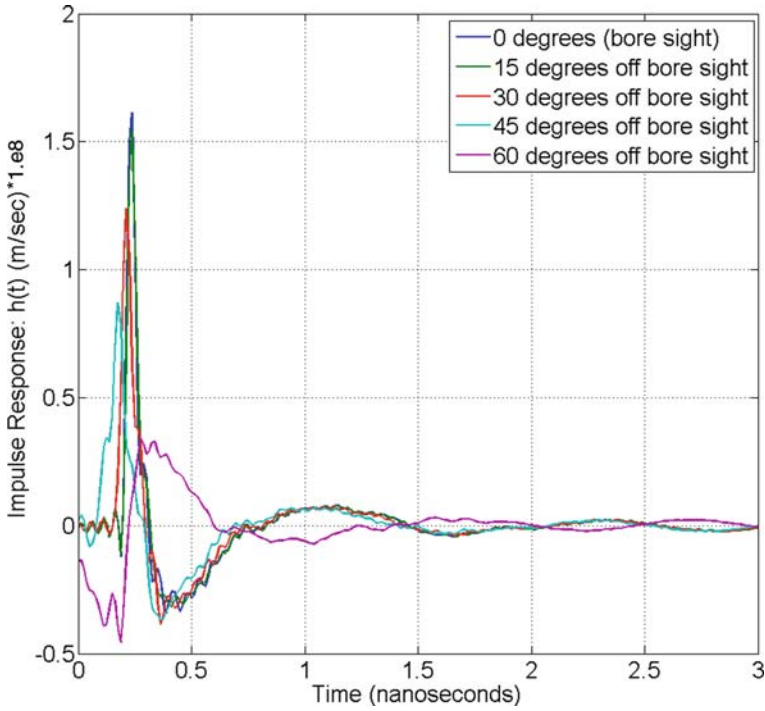
Fig. 5 H-plane off-axis response of the DR horn with no side walls
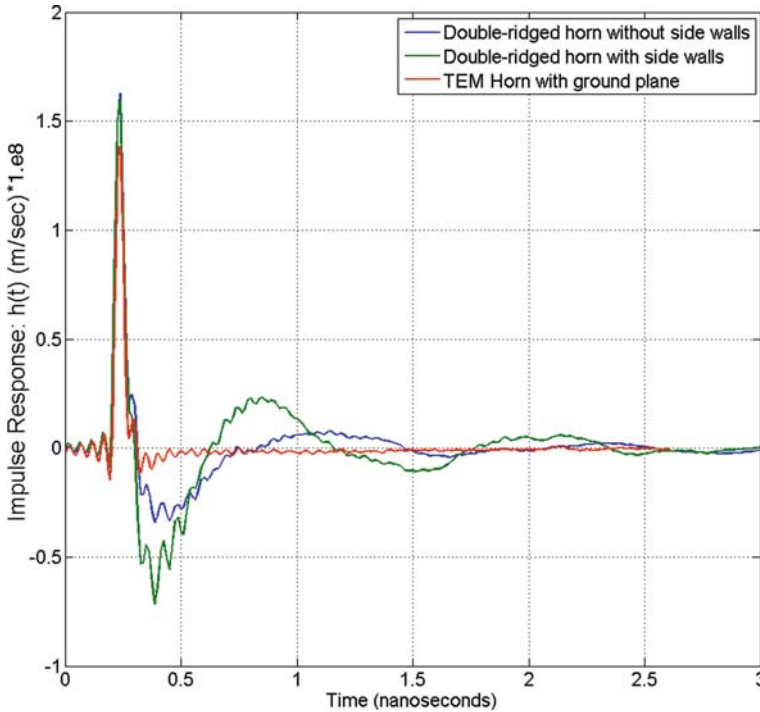
Fig. 6 On-axis time-domain impulse response of DR horn with and without side walls compared to that of a TEM horn employing a ground plane. As can be seen the response of the DR horn with no side walls is reasonably similar to that of the TEM horn

waveguide is responsible for the very much improved time-domain response. However, as noted earlier, the improved on-axis response is accompanied by strongly degraded off-axis response.

The presence or absence of side walls plays a role in making the horn conducive to supporting trough modes [11, 12]. These modes strongly affect the frequency-domain radiation pattern of the horn and hence the time-domain impulse response. In particular the excitation of the so-called TE_{30} hybrid mode [11], a mode that is predominantly guided by the trough region, severely degrades the frequency domain radiation pattern and can be shown to be indirectly responsible for the multi-lobed pattern discussed in [1] and [10]. That is, this mode is excited at the feed point and then converts to an even higher order mode as it propagates down the horn resulting in the multi-lobed pattern.

3 Conclusions

The double-ridged horn is a reasonably capable short-pulse antenna. Two detractors from its short-pulse response are primarily responsible for its less than ideal behavior. The first, frequency-dependent pattern degradation, which leads to inconsistent on- and off-axis pulse response, has been shown to be primarily due to coupling to the TE_{30} hybrid mode in the feed region. If the TE_{10} hybrid mode can be excited exclusively, the horn exhibits a well-behaved pattern. Since these modes are orthogonal in uniform guide, it should, in principle, be possible to excite only the TE_{10} hybrid mode. However, it does not appear to be possible to discriminate against the TE_{30} mode by forcing it to be cutoff throughout the entire operating frequency range of the horn. The second problem, narrowband spikes in input VSWR, which lead to notches in the frequency-domain transfer function

and ringing in the impulse response, is more difficult to comprehensively treat but has been shown to also be related to high-order modes of the three-dimensional volume behind the feed. This aspect is affected by the asymmetry of the feed, but cannot be eliminated by enforcing symmetry. Nor can placing a load behind the feed eliminate it. The feature is, however, very strongly influenced by the dimension of the feed gap, the distance between the ridges at the feed, and the dimension of cavity behind the feed parallel to the E-plane of the horn.

In several publications, it has been noted that the general reduction of the size of the feed region ameliorates both of these problems. However, this also results in degradation of the low-frequency response. We have found that the single most effective change to be made to the horn is the reduction of the gap dimension. This (1) lowers the cutoff frequency of the TE_{10} hybrid mode, (2) greatly reduces coupling to the TE_{30} mode, and (3) greatly reduces coupling to modes in the cavity behind the feed. Thus, it simultaneously addresses nearly all of the shortcomings of the double-ridged horn design. Unfortunately, as noted in [9], such an approach results in a horn matched to a lower impedance than 50 Ω. However, the introduction of a coaxial tapered transmission line transformer should mitigate this problem without introducing deleterious features in the time response.

Finally, it is possible to fabricate such a horn without walls perpendicular to the H-plane. As has been shown, the on-axis time-domain impulse response of such a horn is very much superior to that obtained when the side walls are present. The response is only slightly inferior to that of a TEM horn employing a ground plane. It would be most useful if the response of this horn could be further improved to be more similar to that of the TEM horn. Employing a transmission line transformer to allow the use of a tighter gap appears to be one sound approach for improving the performance of this device.

References

1. C. Bruns, P. Leuchtmann, and R. Vahldieck, Analysis and simulation of a 1–18 GHz broadband, double-ridged horn antenna, IEEE Transactions on Electromagnetic Compatibility, vol. 45, no. 1, pp. 55–60, February 2003.
2. C. H. G. Santos Henrique, M. M. Afonso, R. S. Alípio, Ú. C. Resende, M. A. O. Schroeder, L. A. L. Santos, Approximated raising of the curvature of a double-ridged waveguide horn antenna in a computational model, Proceedings of the 2007 SBMO/IEEE MTT-S International Microwave & Optoelectronics Conference, pp. 435–38, 2007.
3. Z. Zhang and R. E. Diaz, Simulation of broadband double-ridged horn in high-fidelity material characterization using finite-difference time-domain method, in Proceedings in the IEEE 2005 International Symposium Antennas and Propagation, pp. 561–64, 2005.
4. J. S. McLean, A. Medina, R. Sutton, H. Foltz, and J. Li, Investigation into the underlying physical mechanisms for high frequency pattern degradation in broadband, double-ridged horns, AMTA Symposium 2006, Austin, TX.
5. W. Sörgel, F. Pivit, and W. Wiesbeck, Comparison of frequency domain and time domain measurement procedures for ultra wideband antennas, Proceedings of the 25th Annual Meeting and Symposium of the Antenna Measurement Techniques Association, pp. 72–76, Irvine, CA, October 2003.
6. J. S. McLean, Armando Medina, Robert Sutton, H. D. Foltz, Junfei Li, Measurements of UWB Antenna Pattern Descriptors, in Proceedings of the 2006 AMTA Europe Symposium, Munich, 4 May, 2006.
7. J. L. Kerr, Broadband Horns, Tech. Report ECOM-3319, AD714994, August 1970.
8. J. L. Kerr, Short axial length broad-band horns, IEEE Transactions on Antennas and Propagation, vol. AP-21, pp. 710–14, September 1973.
9. K. L. Walton and V. C. Sundberg, Broadband Ridged Horn Design, Microwave Journal, March 1964.
10. V. Rodriguez, New broadband EMC double-ridge guide horn antenna, RF Design, pp. 44–50, May 2004.
11. F. F. Dubrovka, G. A. Yena, P. Y. Stepanenko, and V. M. Tereschenko, Ultra wideband double ridged horns with rectangular aperture, in Proceedings of the International Conference on Antenna Theory and Techniques, pp. 590–93, September 2003.
12. J. R. Montgomery, On the complete eigenvalue solution of ridged waveguide, IEEE Transactions Microwave Theory and Techniques, vol. MTT-19, pp. 547–55, June 1971.

The Folded Horn Antenna

E.G. Farr, L.H. Bowen, C.E. Baum, and W.D. Prather

Abstract Antennas for radiating high-power mesoband (medium-bandwidth) electromagnetic signals are critical to the mission of upsetting electronics at a distance. When operated at frequencies of a few hundred megahertz, RF weapons require highly efficient antennas that can fit into a small volume. Most of the existing antennas, such as pyramidal horns, are too large to fit onto certain platforms of interest. To address this challenge, we investigate the folded horn, which has aperture dimensions of 0.5 × 2 wavelengths, and a depth of 1.5–2 wavelengths. This antenna has a nearly focused aperture field, due to a parabolic fold in the H-plane. We report here on the fabrication and testing of the first folded horn, operating at 3 GHz. After a number of iterations, we obtained a realized gain of at least 10 dBi over 3–5 GHz, an aperture efficiency of 80%, and a return loss below –10 dB over 2.8–3.35 GHz. This design could be adapted to high-voltages, and it could work well in a two-antenna array, with two antennas positioned back to back, driven by a differential source.

1 Introduction

We introduce here a new antenna, the folded horn. This antenna was first proposed by C. E. Baum for radiating high-power mesoband (medium-bandwidth) signals from a very compact package with high efficiency and moderate gain [1]. It was intended to operate at a frequency of a few hundred megahertz, for the application of upsetting electronics at a distance. In this chapter we provide the first experimental results for the folded horn.

The advantage of a folded horn over a pyramidal horn is that it has no dimension larger than 2 wavelengths. The requirement to keep the antenna size small becomes apparent at lower frequencies. For example, at 200 MHz, where the wavelength is 1.5 m, a folded horn with aperture dimensions of 0.5 × 2 λ and depth of 1.7 λ has a size of 0.75 × 3 × 2.6 m. An antenna of this size can fit onto the bed of a truck while looking sideways. However, for example, a pyramidal horn would not fit into such a limited space at this frequency.

E.G. Farr (✉)
Farr Research, Inc., Albuquerque, NM, 87123, USA
e-mail: efarr@farr-research.com

In this chapter, we build and test the first prototype low-power folded horn, operating at a nominal operating frequency of 3 GHz. We tried several iterations, resulting in a design that satisfies our requirements over 3–5 GHz. We also describe alternative configurations, and we suggest further improvements that could result in either improved performance or a more compact size. We begin now with a description of the folded horn.

2 Folded Horn Design and Analysis

We describe here the basic design and operation of the folded horn, and we provide an analysis of its performance. A sketch of the folded horn and photos of the devices are shown in Fig. 1. This device consists of three parts: the feed section, the parabolic bend, and the aperture section. At its design frequency of 3 GHz, this antenna has an aperture of $0.5 \times 2\ \lambda$, and a depth of $1.75\ \lambda$.
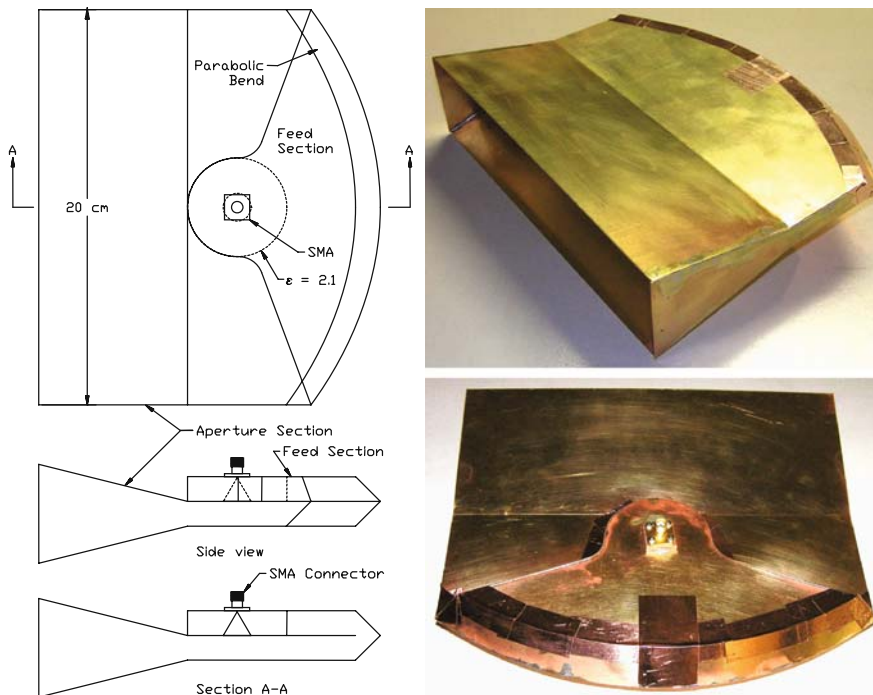
Fig. 1 The folded horn, model FH-1E (*left*), and photos of the *top* and *bottom* views (*right*)

The folded horn works as follows. The antenna is driven by an SMA connector that is positioned at the focus of the parabolic bend. Waves in the feed section expand in the H-plane until they reach the parabolic bend. After reflecting off the parabolic bend, the waves are focused in both E- and H-planes. The waves then proceed into aperture section, in which the fields are expanded in the E-plane. The fields remain focused in the H-plane, because of the parabolic bend. The fields in the E-plane are only slightly out of focus, because there is little difference in ray path length between the central and extreme rays.

A sketch of the aperture electric fields appears in Fig. 2. On the left, we see that the electric fields protrude only slightly from the aperture, due to a slight defocus in the E-plane. On the right,
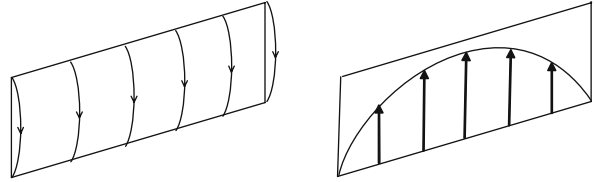
we observe that the electric field magnitude varies approximately as a cosine function across the aperture, because of the metal walls on either side.

We begin the analysis by calculating the level of defocus in the aperture fields. We do so by calculating the path length difference between a central ray and an extreme ray in an E-plane cut through the aperture section, which has a length of $\frac{3}{4}$ λ. We find the extreme ray has a length of 0.79 λ, compared to a direct path length down the center of 0.75 λ, resulting in a path length difference of 0.04 λ. So the aperture is essential in focus.

Next, we calculate the boresight gain of such an aperture field distribution, assuming a focused aperture of size 0.5×2 λ. We use the standard formula, $G = (e4\pi \ \lambda^2) \ A$, where A is the aperture area, λ is the wavelength, and e is the aperture efficiency. Because of the cosinusoidal field distribution, $e = 8/\pi^2 = 0.81$, according to [1]. For this aperture, $A = \lambda^2$, so we have $G = 32/\pi = 10.2 = 10.1$ dBi at the design frequency.

If one assumes a focused aperture, then the fields are similar to those of an open-ended waveguide (OEWG) [2, pp. 290–291]. In this case, the pattern functions are described by

$$F_H(\theta) \ = \ \frac{1 + \cos(\theta)}{2} \ \frac{\cos\left[\frac{\beta a}{2} \ \sin(\theta)\right]}{1 - \left[\frac{2}{\pi} \ \frac{\beta a}{2} \ \sin(\theta)\right]^2} \ , F_E(\theta) \ = \ \frac{1 + \cos(\theta)}{2} \ \frac{\sin\left[\frac{\beta b}{2} \ \sin(\theta)\right]}{\frac{\beta b}{2} \ \sin(\theta)}, \tag{1}$$

where the long and short aperture dimensions are a and b, respectively; $\beta = 2\pi/\lambda$, and θ is the angle from boresight. We plot these pattern functions later in this chapter, next to our experimental data. A more accurate formulation would take into account the defocusing in the E-plane, using the expressions for the E-plane sectoral horn [2, pp. 306–310]. This has the same H-plane expression, but a different E-plane expression, which may be useful for larger E-plane opening angles.

3 Folded Horn Description

We now provide the details of our folded horn, model FH-1E. A sketch of the configuration was shown earlier in Fig. 1, and photos are shown in Figs. 1 and 3. This antenna is designed to operate at 3 GHz, or a wavelength of λ = 0.1 m. Thus, the aperture is 0.05×0.2 m (0.5×2 λ), which makes the antenna small enough to allow easy construction and testing. The FH-1E was designed so it could be constructed entirely from flat pieces of sheet metal, with bends only in a single plane of curvature.

A number of features near the feed point require clarification. The feed point is located at the center of a cylinder, which is also the apex of the feed section and the focus of the parabolic bend. The radius of the cylinder surrounding the feed point was chosen to be λ/4 at the design frequency, 3 GHz, in air. This was chosen so the short circuit at the edge of the cylinder would look like an open circuit at the feed.
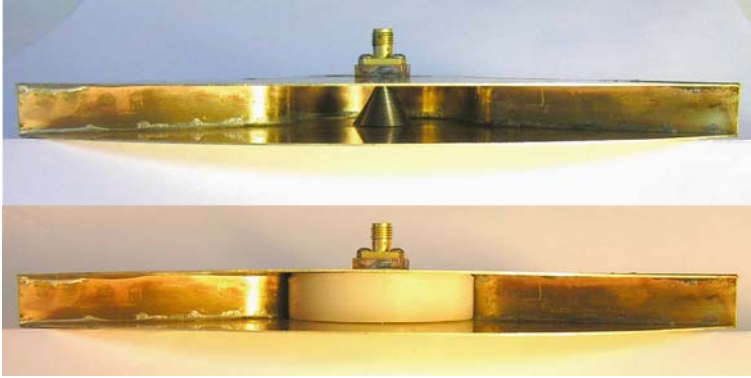
Fig. 3 Feed point detail of the FH-1E, before (*top*) and after (*bottom*) adding the dielectric disk

We tried a number of different feed point designs before arriving at the final design, shown in Figs. 1 and 3. The feed point initially consisted of simply extending the center pin of the SMA connector all the way through the cavity, with a solder connection to the other side. In this configuration, we found that the antenna worked best near 5 GHz, which was well above our target frequency of 3 GHz. To reduce the operating frequency, we increased the electrical size of the disc by filling it with a dielectric material (Teflon, $\varepsilon_r = 2.1$). However, this still left us with an impedance spike at the feed point, as was apparent from TDR measurements. Thus, we replaced the straight pin with a cone embedded within the dielectric disc. The impedance of the cone was $\sim$50 Ω in the presence of the dielectric, using the standard expression for a cone above a ground plane. Details of the evolution of the feed point, including data obtained at intermediate steps, are provided in [3].

The shape of the parabolic bend also requires some clarification. The height of the feed section was $\lambda/8$, and it was desirable to keep the entire feed section within the $\lambda/2$ height of the aperture. To conserve space, the bend was implemented as an abrupt 180° bend, using two 45° reflectors, as shown in Fig. 4. The dotted arrows show the path of a typical ray. With this configuration, all rays have the same path length around the bend, which keeps the wavefront in focus.

Fig. 4 Detail of the 180° bend, showing a typical ray path
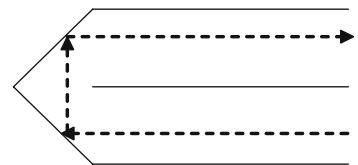
4 Data

We characterized the antenna on our *PATAR*® time-domain antenna range. The source for this system is a Picosecond Pulse Labs model 4015C step generator, which drives a Farr Research model TEM-1-50 sensor. The 4015C is a high-speed pulser with a negative 4 V voltage step, with a fall time of 20 ps. The antenna under test was placed 4 m from the aperture of the TEM sensor. The output of the AUT was recorded using a Tektronix model TDS8000 sampling oscilloscope, with a model 80E04 sampling head.
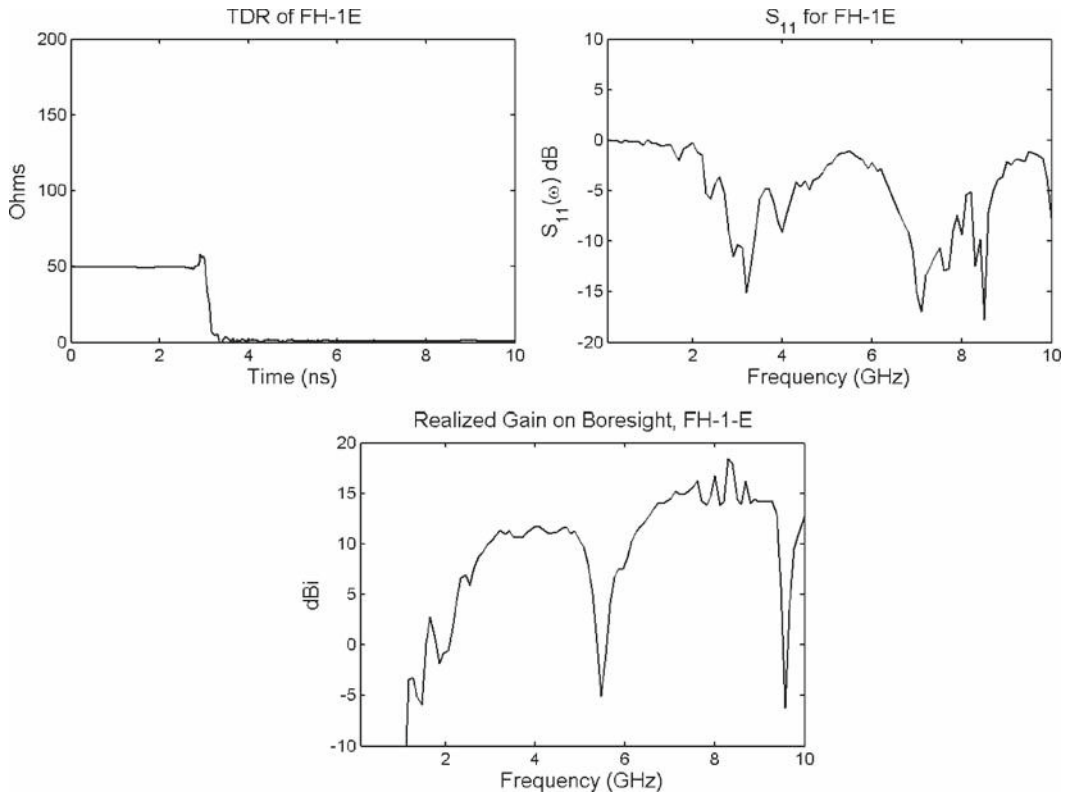
Fig. 5 TDR, S_{11}, and realized gain on boresight for the FH-1E

In Fig. 5 we provide the TDR, S_{11}, and boresight realized gain of the FH-1E. Recall that realized gain is the gain reduced by return loss. The TDR at the feed point tapers smoothly from 50 to 0 Ω, as it should. The S_{11} dips near 3 GHz the intended operating frequency. The realized gain is ≥ 10 dBi over a frequency range of 3–5 GHz, which is consistent with our earlier predictions at 3 GHz. The frequency range over which the return loss is –10 dB or better is 2.8–3.35 GHz.

The antenna patterns in the H- and E-planes are shown in Fig. 6 at 3, 4, and 5 GHz. Alongside these, we plot the theoretical patterns of an OEWG with similar aperture dimensions. We see that the H-plane pattern is much narrower than the E-plane pattern, which we expect because of the aperture shape. The measured patterns are quite similar to the theoretical predictions; however, we observe higher H-plane sidelobe levels in our experimental data than in the OEWG theory.

5 Improvements to the Folded Horn

We summarize here the improvements to the folded horn that will be worth investigating in the future. First, it should be possible to further adjust the feed point to reduce the return loss over a broader frequency range. One might try varying the radius of the cylinder, the angle of the feed cone, and the dielectric constant of the disk.

Second, one might investigate the effect of the opening angle of the antenna in the E-plane, θ_E, as shown in Fig. 7. We have configured the aperture height to be $\lambda/2$, but a larger aperture height
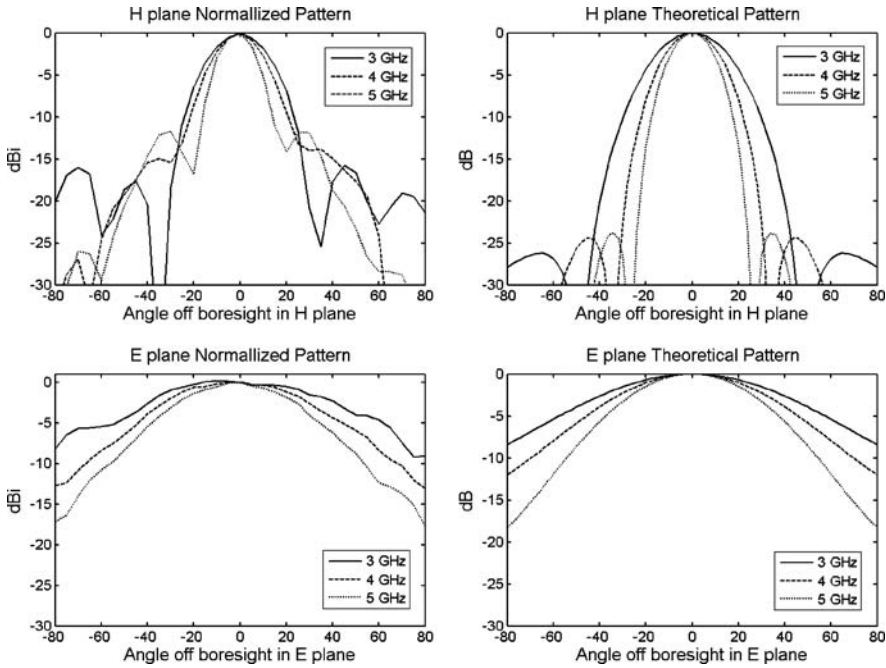
Fig. 6 Antenna patterns for the FH-1E in the H-plane (*top*) and E-plane (*bottom*) at 3, 4, and 5 GHz. Both experimental data (*left*) and theoretical predictions (*right*) are shown

Fig. 7 Adjustment of the opening angle in the E-plane to optimize gain
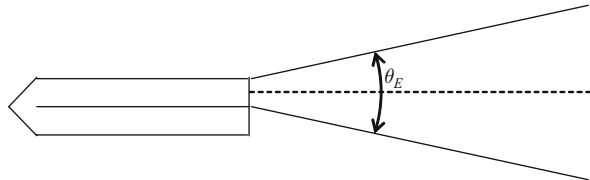
and larger θ_E might provide even more gain, with little disturbance to the focus in the E-plane. The current version has a difference in path length of just 0.04 λ, but it could probably tolerate the larger value that would come with a larger θ_E.

Third, one could imagine a two-element array of folded horns stacked in the E-plane, in order to increase the aperture size. Such a device could be driven with a differential source, with equal-but-opposite output voltages. One might consider stacking two antennas similar to the FH-1E, but there might not be sufficient space between the two antennas for the high-power mesoband source. A better idea might be to use two bi-folded horns, as shown in Fig. 8. In this case, each of the bi-folded horns has, beginning at the feed point, an expansion section in the H-plane, a parabolic bend, a straight section, a straight bend, and an expansion section in the E-plane.

Finally, when adapting the design to higher voltages, two modifications may be useful. First, the Teflon cylindrical disk will be replaced with oil. Second, one might place a sharpening switch at the apex of the cone in the feed section. (In its simplest form, this is nothing more than a gap in the center conductor.) A sharpening switch would be challenging to implement in a dual configuration, because both switches would have to fire simultaneously, with low jitter.

Fig. 8 Two bi-folded horns, positioned around a high-voltage source with differential output
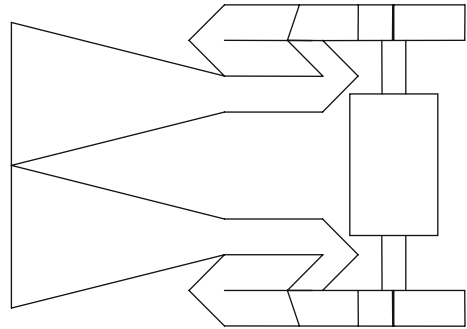
6 Conclusions

We have built and tested a folded horn, which is a compact antenna with moderate gain. After a number of iterations, we achieved a realized gain of 10 dBi or greater over a frequency range of 3–5 GHz. This was quite close to our predictions at 3 GHz, and it might be considered to be quite good performance for such a small antenna. The return loss was below –10 dB over a frequency range of 2.8–3.35 GHz. The measured antenna pattern was quite close to that of an OEWG, except that the experimental data had higher H-plane sidelobe levels than predicted by the theory.

A number of areas are worth investigating to improve the folded horn, as described in Section 5. These include investigations on refining the feed point, and increasing the E-plane opening angle. Two antennas may be arrayed in the E-plane, each with either a single- or bi-folded design. The bi-folded design may be necessary to allow space for the source.

References

1. C. E. Baum, More antennas for the switched oscillator, Sensor and Simulation Note 493, August 2004.
2. W. L. Stutzman and G. A. Thiele, *Antenna Theory and Design*, Second edition, New York, Wiley, 1998.
3. E. G. Farr, L. H. Bowen, C. E. Baum, and W. D. Prather, The folded horn antenna, Sensor and Simulation Note 520, December 2006, available at www.Farr-Research.com. Sensor and Simulation Notes are available from the authors, or from the editor of the series, Dr. Carl E. Baum, Carl.E.Baum@IEEE.org; Dept. of Elect. & Comp. Eng. MSC01 1100, 1 University of New Mexico, Albuquerque, NM 87131-0001.

Numerical Analysis of Small Slotted Ultra-wideband Antenna Based on Current Distribution for Bandwidth Enhancement

Y.R. Naumar, T.A. Rahman, R. Ngah, and P.S. Hall

Abstract A few years after the early investigation on ultra-wideband (UWB) wireless system, considerable research efforts have been put into the design of UWB antennas and systems for communications. These UWB antennas are essential for providing wireless wideband communications over very short distances at very low power densities. This chapter presents numerical analysis of a small slotted UWB antenna by studying its current behavior. The active and neutral zones of antenna are determined before applying slots on its patch radiator. This is due to any modification applied on this active zone means disturbing its current distribution and affect to its impedance characteristics. It is shown from simulated and measured results that L and U slotted on the patch antenna result an UWB bandwidth. This simulation was performed by using the Zeland simulation software.

Keywords Small antenna · Current distribution · Ultra-wideband antenna · Bandwidth enhancement · Slotted antenna

1 Introduction

A number of techniques have been developed in past to design antennas with wide band impedance matched characteristics. The use of beveling technique, cutting notches at bottom, dual feed, slotted on patch radiator are some examples of techniques used to improve the impedance bandwidth [1–4]. As far as slots cut on the patch radiator of antennas are concerned, it is necessary to identify active and neutral zones in antennas where any modification in these areas will affect the impedance bandwidth. They can be identified with the study of their currents behavior. The geometry of the antenna implies the current courses and makes it possible to identify active and neutral zones in the antenna, thus it will be possible to fix which elements will act on each characteristic.

The active zone is the matching and radiator zone. Acting on matching and radiating areas allows controlling the bandwidth [1]. Zone closed to feeding point is the active zone. The neutral zones where geometry modifications are useless because neither the radiation pattern nor the matching bandwidth is much influenced.

──────────────────

Y.R. Naumar (✉)

Wireless Communication Centre, Faculty of Electrical Engineering, Universiti Teknologi Malaysia, Johor Bahru, Malaysia

e-mail: vannebula2001@yahoo.com

2 Current Distribution Behaviors

Three different geometries of antennas with their current behavior are investigated such as conventional rectangular, rectangular with two notches, and pentagonal as shown in Fig. 1. The study of the current flow on a planar monopole antenna reveals that it is mostly concentrated in the vertical and horizontal edges. The notches and bevels at edges of antenna have disturbed their current flow. When properly designed, the bevels and notches improve significantly the impedance bandwidth at upper frequency.
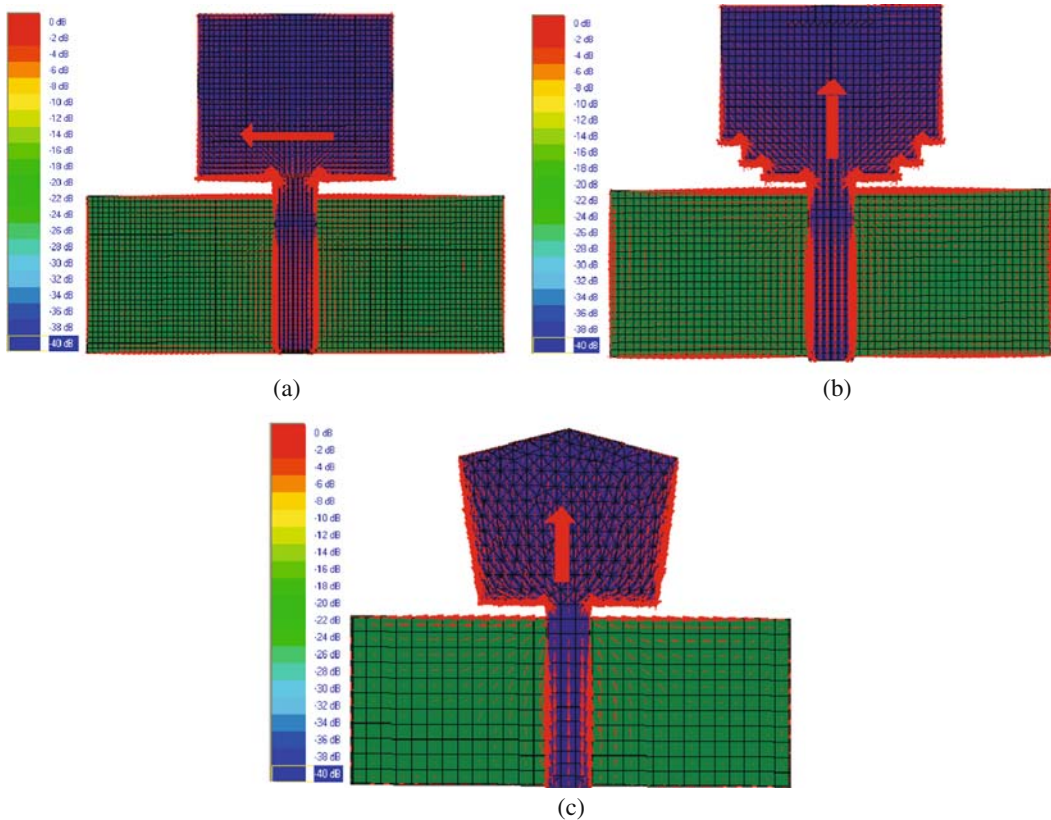
Fig. 1 Simulated current distribution for three model antennas with affect to the impedancebandwidth: (**a**) conventional rectangular, (**b**) rectangular with two notches, and (**c**) pentagonal

It is observed that the horizontal currents distributions are focused on the bottom edge of conventional rectangular patch as shown in Fig. 1(a). Besides, the horizontal component is also greater than the vertical on this part of the antenna. The discontinuity occurred from cutting notch or beveling at the bottom side of a rectangular antenna has enforced the excitation of the vertical current mode in the structure, which presents a very wide bandwidth. Much current density occurs closed to the feeding edge, while at the top of antenna; the current levels are not too strong as shown by simulated result in Fig. 1b and 1c. The field supported by these currents would be mainly confined between the bottom part of the rectangular antenna and the ground plane; this is due to the small distance, a small fraction of wavelength, of this edge to the ground plane [5]. Thereby, this part acts as a matching element. Matching bandwidth is due to the shape of the antenna closed to the feeding point, where

currents are the strongest. It is possible to enlarge or reduce it in accordance with the application to implement by modifying its geometry close to this one.

2.1 Return Loss

Figure 2 shows the return loss performance of those antennas. The conventional rectangular antenna has the smallest impedance bandwidth. The return loss starts degrading its performance at 7.5 GHz with respect to –10 dB, this is due to more horizontal current mode occurs in the whole structure which degrade the polarization properties and the impedance bandwidth performance of the antenna [5].
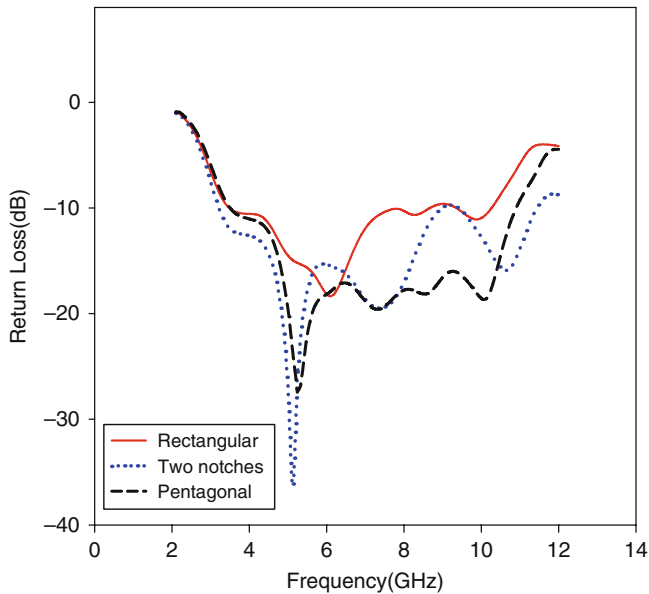
Fig. 2 Simulated return loss for three model antennas with affect to the impedance bandwidth

In order to modify the equivalent characteristic impedance on the antenna, the distance of the bottom edge to the ground plane and the bottom profile of the monopole should be varied. By varying the edges closed to the feeding point means modifying the current path on the antenna. It is clearly shown from the simulated result the double notches at the base of the antenna and bevels have demonstrated to shift upward the upper edge frequency of the bandwidth.

2.2 The Neutral Zones

Through literature reviews [1, 6] and simulation observation, there are four types of current distribution modes in the antenna surface: vertical current mode, horizontal current mode, diagonal current mode, and asymmetry current mode. In this section the current behavior of pentagonal antenna is studied. By observing the current distribution flow, the pentagonal has a diamond neutral zone. In this zone, the current levels are not too strong but they are not at zero level. Normally, this zone occurs at the middle of the antenna structure. The neutral zone for each frequency appears at

different position. This is due to the different current mode behavior at every frequency. Study on current distribution of planar monopole antenna by transmission line modeling (TLM) was performed in [6].

The neutral zone can be used to simplify the antenna structure and integrate other function of the systems such as antenna circuits. This investigation has been proposed in [1], but not much explanation given. How to determine the neutral zone is not explained in detail. From simulation observation, as long as the size and the position of the neutral zone are precisely determined, this zone can be removed with no much influence on the radiation pattern and the matching bandwidth.

Figure 3 presents the neutral zones for 5, 8, and 10.5 GHz of pentagonal antenna. From observation, each frequency has a different neutral zone size and position. The neutral zones of 5 and 8 GHz have the same size. This neutral zone size is determined by observing the current distribution mode in the antenna surface. The slot size is precisely measured in order not to degrade the antenna performance. This size is analyzed and optimized by Zeland simulation software. The optimum size
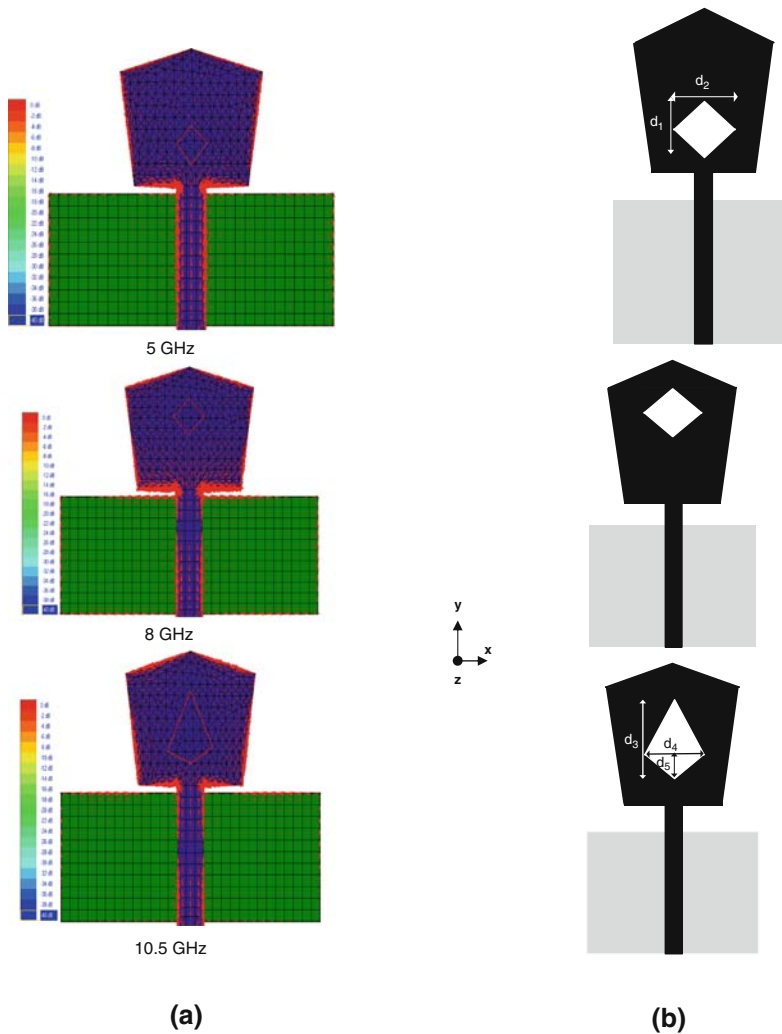
Fig. 3 Neutral zones for 5, 8, and 10.5 GHz of pentagonal antenna: (**a**) neutral zones of current distribution, (**b**) geometry of neutral zones
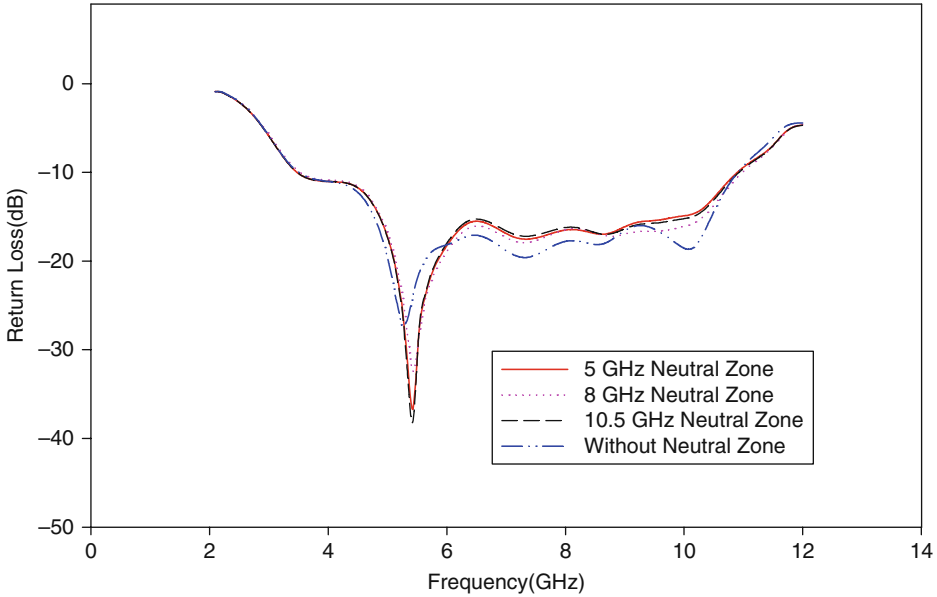
Fig. 4 The simulated return loss for various diamond slots of pentagonal antenna at 5 GHz

of diamond slot at 5 and 8 GHz is $d_1 \times d_2$ of 4×4 mm, while $d_3 \times d_4 \times d_5$ of $6 \times 4 \times 2$ mm at 10.5 GHz. The effect of this diamond slot to the return loss performance of pentagonal antenna is described in Fig. 4.

Figure 4 shows the simulated return loss for pentagonal antenna with and without diamond neutral slot. The antenna with their diamond neutral zone slots are simulated at 5 GHz. It is shown that the simulated return loss for all types of diamond slots does not influence the impedance bandwidth with respect to –10 dB. Thus, by identifying the neutral zone and active zones on an antenna, the size of antenna can be reduced and its characteristic can be controlled.

3 A Small Slotted UWB Antenna

As shown from the previous simulated result the neutral zones of pentagonal are most located at the middle of the patch. Thus, this small proposed slotted UWB antenna is designed by adding L and U couple slots at the edges of patch. The slots shape is designed very carefully by studying the current flow distribution which will give input impedance improvement. Analysis has proved the theory of slots in [2].

3.1 Antenna Geometry

To validate the simulated result, an antenna prototype has been developed. Figure 5 shows the UWB antenna printed on the FR$_4$ substrate of $\varepsilon_r = 4.6$. The pentagonal antenna is vertically installed above a ground plane (l_{grd}) of 11 mm. The optimum feed gap (h) to the ground plane is found to be 1.5 mm. The dimension of substrate is chosen to be 30×30 mm^2 ($W_{sub} \times L_{sub}$) in this study. Antenna has a pentagonal patch with a width (w) of 15 mm and a length (l) of 12 mm. The slot lengths of l_{s1}, l_{s2}, l_{s3}, and l_{s4} are 6, 9, 3, and 6.5 mm. The slot width is 0.5 mm in order to improve the bandwidth above 10 GHz.
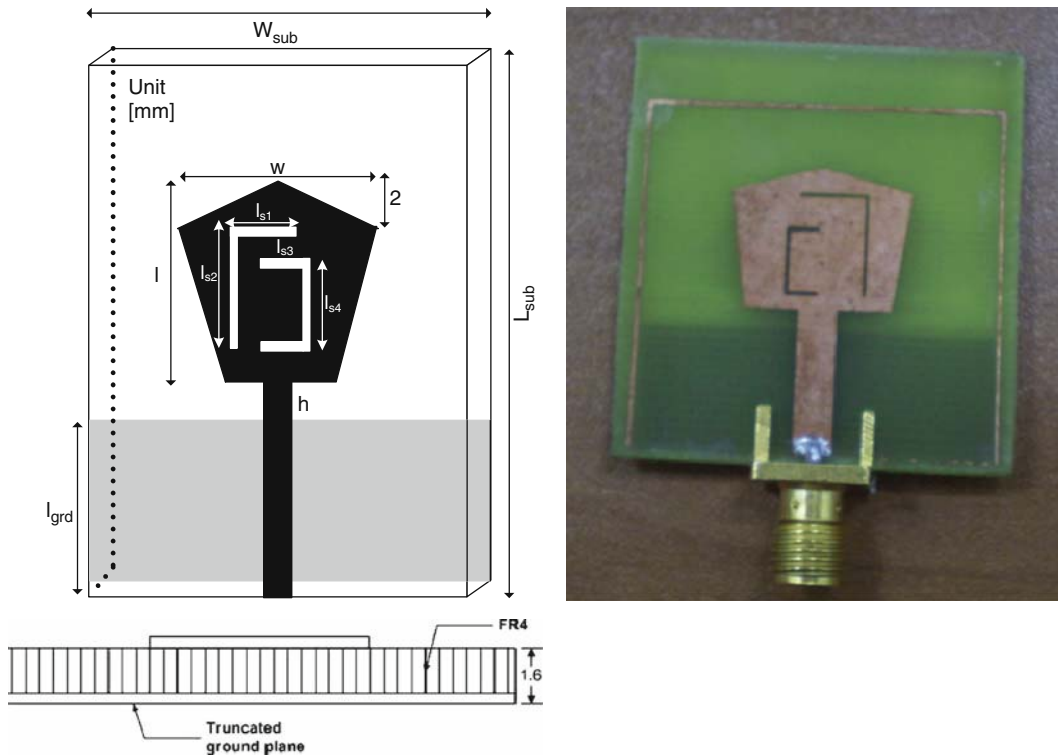
Fig. 5 The geometry and photograph of L and U slotted UWB antenna

The L and U slotted antenna with current distribution at 3, 6, and 9 GHz is presented in Fig. 6. It is shown that the vertical current is most concentrated near to the slots edges for all frequency range. It is also noticed that, the current distribution is less on the area between both slots without degrading its performance. This area is known as neutral zone.

3.2 Impedance and Pattern Bandwidth

The simulated and measured return loss is shown in Fig. 7. The measured return loss is slightly shifted to the simulated one, but they still cover 2.5–10.1 GHz as what the UWB required. From the simulation, the U slot improves the upper dip resonance of 10.3 GHz and the L slot improves the lower dip resonance of 5.3 GHz. The coupling of both slots has shown a very good return loss below –10 dB. The length of L slot is 14.5 mm approximately equal to 0.25λ at 5.3 GHz, and the length of U slot is 11.5 mm approximately equal to 0.4λ at 10.3 GHz. In addition, since the antenna is fed by a micro-strip line, misalignment can result because etching is required on both sides of the dielectric substrate. The alignment error results degradation to the antenna performance.

Figures 8 and 9 show the simulated and measured E and H planes for 4 and 5.8 GHz, respectively. The results show that the radiation patterns are changing as the frequency increases. The H planes show a good omni directional for both frequency ranges. The E-planes are relatively broad and slightly distorted at 5.8 GHz.

3 GHz   6 GHz

9 GHz
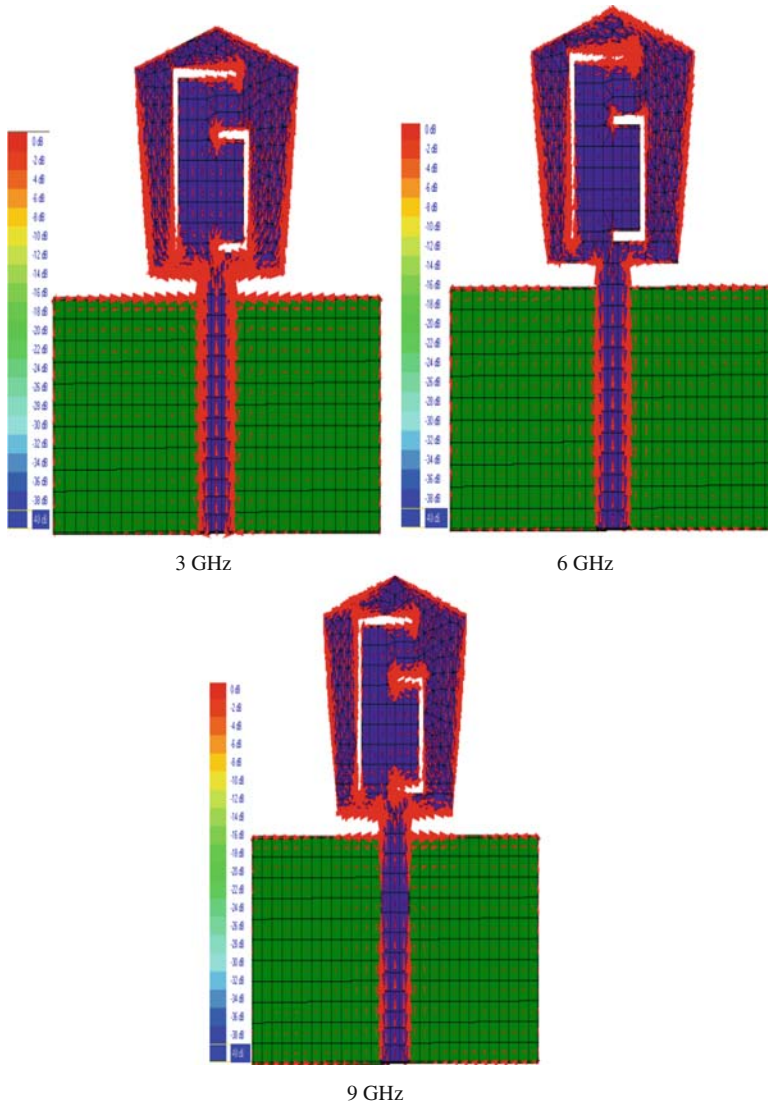
Fig. 6 Current distribution for L and U slotted UWB antenna
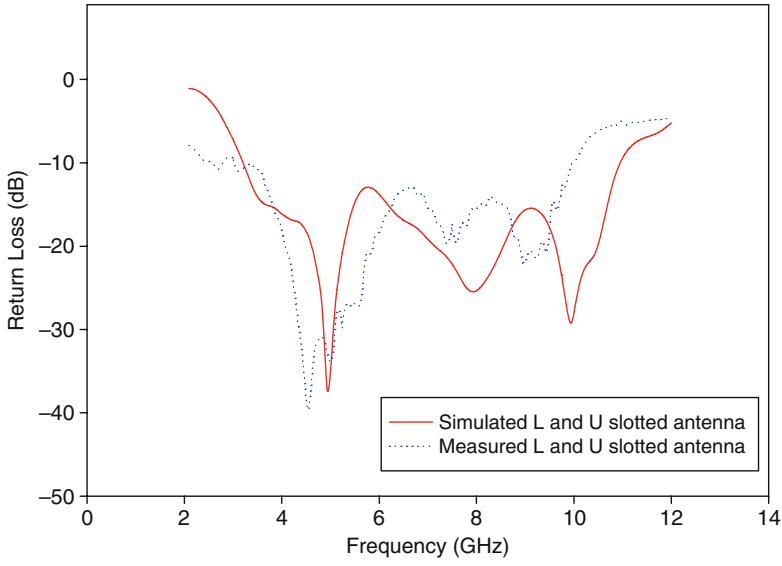
Fig. 7 The measured and simulated return loss for L and U slotted UWB antenna

E-plane at 4 GHz   H-plane at 4GHz
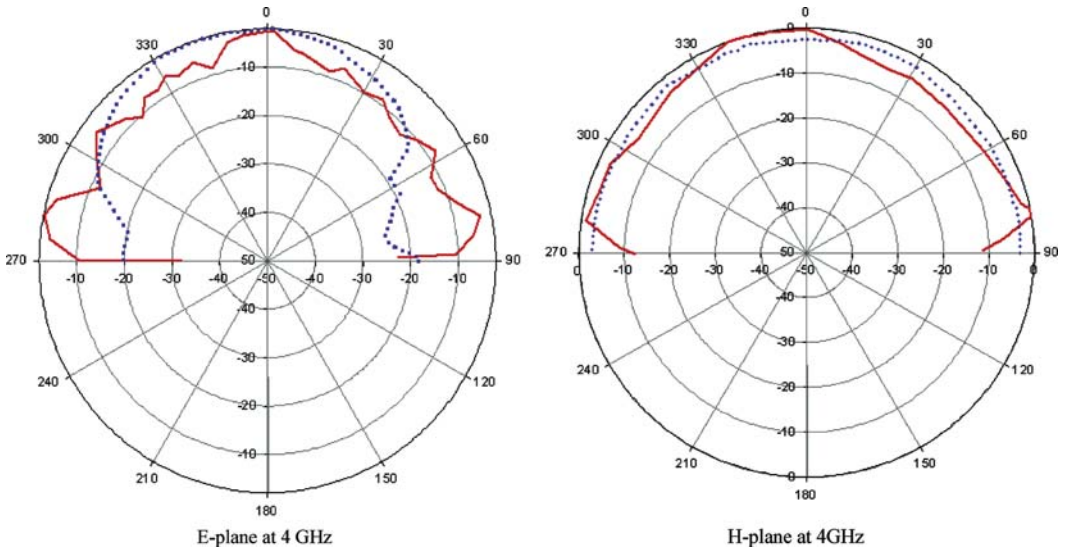
Fig. 8 The measured (solid) and simulated (dotted) radiation pattern for L and U slotted UWB antenna at 4 GHz
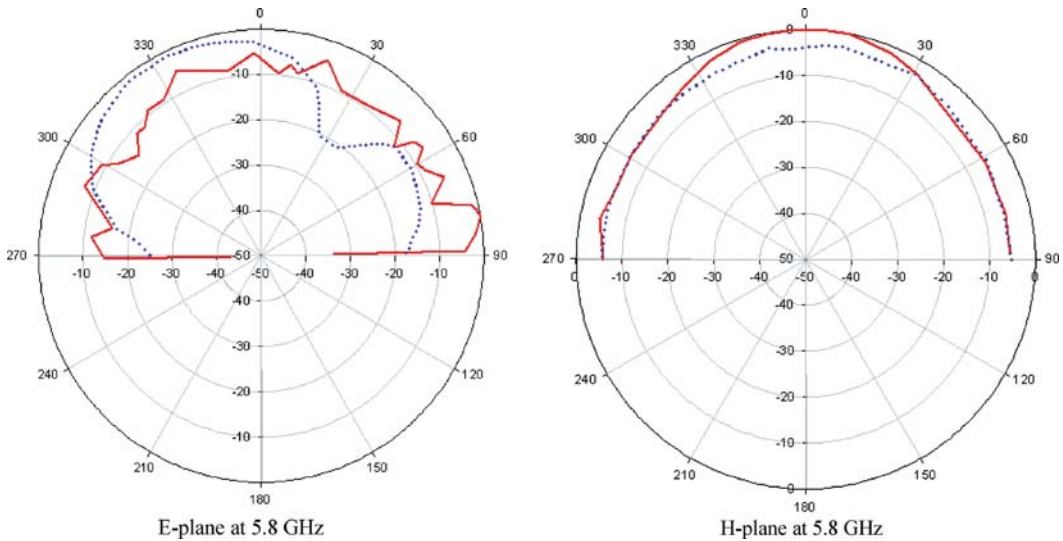
Fig. 9 The measured (solid) and simulated (dotted) radiation pattern for L and U slotted UWB antenna at 5.8 GHz

4 Conclusion

Numerical analysis of L and U slotted UWB antenna based on current distribution for bandwidth enhancement was presented in this chapter. It has been shown in this chapter, the proposed slots has improved the antenna impedance bandwidth. Before applying the L and U slots on this UWB antenna, the active and neutral zones have been determined to analyze the behavior of current distribution. This is due to any modification applied on this active zone affect its impedance bandwidth. Finally, this proposed antenna was successfully designed, developed, and tested.

References

1. Y. Pele, A. Mahe, S. Chousseaud, P. Y. Toutain, Garel, Ireena, Antenna design with control of radiation pattern and frequency bandwidth, IEEE Antenna and Propagation Society International Symposium, vol. 1, pp. 783–86, 20–25 June 2004.
2. Zhi Ning Chen, et al., Planar antennas, IEEE Microwave Magazine, vol. 7, no. 6, pp. 63–73, December 2006.
3. H. Seok, and Choi, et al., A new ultra-wideband antenna for UWB applications, Microwave and Optical Technology Letters, vol. 40, no.5, pp. 399–401, 5 March 2004.
4. Nader Behdad and Kamal Sarabandi, A compact antenna for ultra wideband applications, IEEE Transactions on Antennas and Propagations, vol. 53, no. 7, July 2005.
5. E. Antonino-Daviu, et al., Wideband double–fed planar monopole antennas, Electronics Letters, vol. 39, no. 23, 13 September 2003.
6. Daniel Valderas, et al., Design of UWB folded-plate monopole antenna based on TLM. IEEE Transaction on Antenna and Propagation, vol. 54, no. 6, June, 2006.

Design and Experiment of an Ultra-wideband Dual-Pulse Radiating Antenna

Z. Sitao, L. Guozhi, Y. Chaolong, S. Xiaoxin, F. Yajun, S. Lei, X. Wenfeng, and Z. Yufeng

Abstract A method to widen the microwave spectrum by radiating two pulses of different FWHM is presented. Based on this method, a high-power ultra-wideband dual-pulse radiating antenna is developed. The antenna is made up of a half-impulse radiating antenna (IRA) over a ground plane. The diameter of the reflector is 3 m with focal length 1.2 m and the ground plane is a rectangle of metal with length of 4 m and width of 3 m. Three TEM horns are adopted to feed two pulses into the reflector. The antenna can radiate two different bipolar pulses with peak-to-peak width of 1.7 ns and 3 ns effectively. The 3 ns bipolar pulse is after 1.7 ns bipolar pulse with a delay of 12.5 ns. Simulation analysis and experiments on the antenna are performed. Good agreements between calculated and measured results are obtained. The radiated spectrum of the 1.7 ns pulse covers from 240 MHz to 400 MHz, while the radiated spectrum of the 3 ns pulse covers from 110 MHz to 210 MHz. The radiated spectrum of the combined 1.7 ns and 3 ns dual-pulse with a 12.5 ns delay covers from 100 MHz to 430 MHz. Results show that radiating the combined pulses is a more effective method to widen the microwave spectrum than radiating a single pulse.

Keywords Ultra-wideband · Dual-pulse · Radiation · Antenna · Spectrum

1 Introduction

Ultra-wide spectrum electromagnetic pulse is in demand for a number of applications including impulse radar, target identification, and communication [1, 2, 4]. As a result, extending the spectrum of the radiated pulse is one of the main research interests. We presented an approach to extend the spectrum by radiating two pulses with different pulse widths and developed a pulse driver producing two types of bipolar pulses with peak-to-peak width of 1.7 ns and 3 ns. The purpose of this chapter is to develop an antenna to radiate the two output pulses of the driver synchronously or within some interval. The antenna is comprised of a half impulse radiation antenna (half-IRA) over a ground plane. Three TEM horns are introduced to feed two types of bipolar pulses to the reflector. The schematic of the antenna is shown in Fig. 1. Simulation analysis and experiments on the characteristics of the antenna system were performed. Both results are consistent with each other. Results show that radiating the combined pulses is an effective method to extend the radiated pulse spectrum.

Z. Sitao (✉)
Northwest Institute of Nuclear Technology, Xi'an 710024, China
e-mail: zhu_sitao@sina.com

Fig. 1 Schematic of the reflector
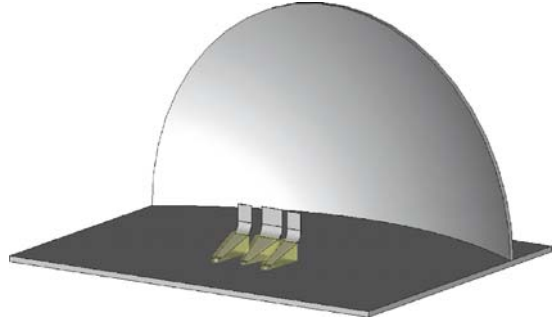
2 Design of the Antenna

2.1 Design of the Reflector

Reflector IRA is the most popular ultra-wideband (UWB) antenna for its good directivity [3–5]. A common paraboloidal reflector is shown in Fig. 2. The relation between the *F/D* ratio and the subtended angle θ is as follows:

$$F/D = \frac{1}{4} \cot\left(\frac{\theta}{2}\right),$$ (1)

where *F* is the focal length and *D* is the diameter of the reflector. The electric characteristic of the antenna will be better with a lager *F/D*, but more energy will lose with a larger portrait size, so *F/D* of 0.4 is chosen.

Fig. 2 The half-IRA
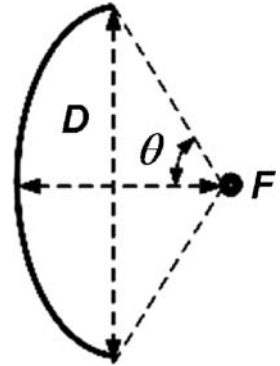
The parabolic reflector is an aperture antenna. When the impulse power in the coaxial feed line is fed into the aperture plane outright, single-polarized, symmetrically and synchronously, the rE_{p-p} merit of the radiated far field on the boresight is [6]:

$$rE_{p-p} = \frac{1}{2\pi c}\sqrt{\frac{\eta S}{Z_0}} \left[\left|\max \frac{\partial V(t)}{\partial t}\right| + \left|\min \frac{\partial V(t)}{\partial t}\right|\right]$$ (2)

where $V(t)$ is the feed voltage in the coaxial feed line, Z_0 is the impedance of the coaxial feed line, S is the area of the aperture, and η is the wave impedance in the free space. Equation (2) indicates that rE_{p-p} of the antenna is proportional to D. Considering the practical applications of this type of antenna, a half-IRA over a ground plane is developed as shown in Fig. 2. The diameter of the reflector is 3 m and the ground plane is a rectangle of metal with length of 4 m and width of 3 m.

2.2 Design of the Feeds

The feed design determines the radiation performance of the antenna with certain structure and parameters of the paraboloidal reflector. Generally, some design points of the feeds must be taken into account: (1) high feed efficiency, (2) launching a spherical TEM wave into the reflector, (3) low aperture blockage, (4) rotationally symmetric feed beam, (5) the field on the rim of the paraboloidal reflector aperture is about –10 dB of that on the center. We chose the F/D of the reflector 0.4 and θ 64°, so the –10 dB beam width of the H plane is 128° and 64° for the E plane.

To locate the radiation centers of the two pulses with peak-to-peak width of 1.7 ns and 3 ns, the 1.7 ns pulse from the 50 Ω feed line is fed into one TEM horn, radiation center of which is on the focus of the reflector. The 3 ns pulse is divided into two signals with a power splitter, then the two signals transmit from a 100 to 50 Ω gradual change line are fed into two TEM horns synchronously, which are centrosymmetric about the focus of the reflector. The two feeds form a horizontal duality array and its equivalent radiation center is on the focus. The schematic structure of the feeds is shown in Fig. 3.
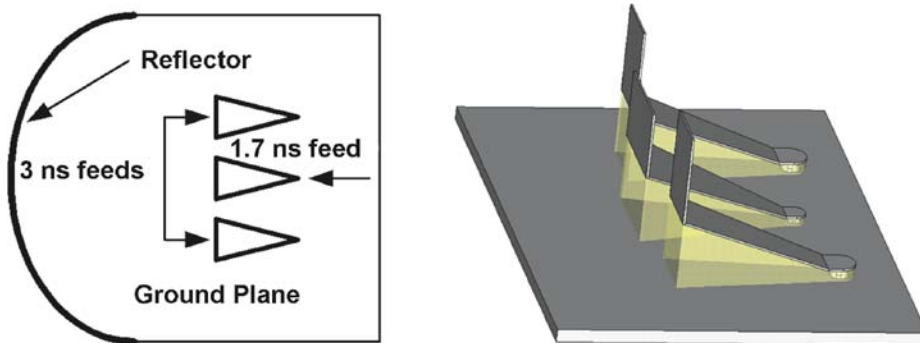
Fig. 3 Structure schematic of the feeds

The geometry dimensions of the feeds are optimized by the numerical calculation. The performances of the triangle plate TEM horn feeds with different lengths, flare angles, and loading conductors of different lengths at the end are calculated. The optimization objects include the feed efficiency of the horn, VSWR, rE_{far}, the ratio of the forward rE_{far} to the backward one, and the –10 dB beam width of the H plane and E plane. The relative position of the three feeds is optimized by taking account of the interaction. The two 3 ns feeds aperture plane is 60 mm behind the 1.7 ns feed and the distance between the two 3 ns feeds is 400 mm.

3 Numerical and Experimental Results

The numerical method is applied to calculate the radiation performance of antenna system. The calculated model is identical to the real structure. The typical waveforms of the two types of bipolar pulses with peak-to-peak width of 1.7 ns and 3 ns used in numerical simulation and experiments are illustrated in Figs. 4 and 5. The risetime of the 1.7 ns feed pulse is 800 ps and 1 ns for the 3 ns feed pulse. The 3 ns bipolar pulse is after 1.7 ns bipolar pulse with a delay of 12.5 ns.

Fig. 4 1.7 ns feed pulse
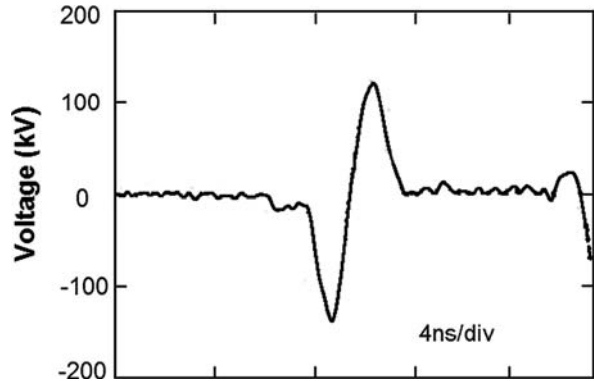
Fig. 5 3 ns feed pulse
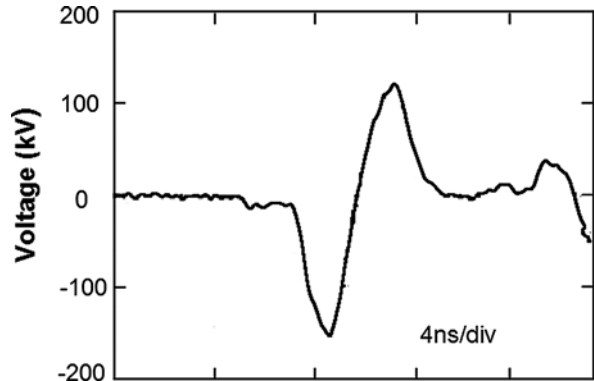
The field patterns of 1.7 ns and 3 ns pulses achieved from simulation and experimental results are shown in Figs. 6 and 7. The numerical (solid line) and experimental (dashed line) patterns are in good agreement. The –3 dB beam widths of the 1.7 ns and 3 ns radiation field from calculation and measured results are listed in Table 1.

Figure 8 shows the numerical and experimental results of the radiation field of the combined pulses on the boresight at a distance of $r = 75$ m. They are in good agreement with each other when ignoring the influence of the ground.

Radiated spectra of 1.7 ns pulse, 3 ns pulse, and combined pulses are shown in Figs. 9, 10, 11. Detailed data of their spectrum are listed in Table 2. The band ratio reaches over 4 by radiating the combined pulses, much larger than that by radiating a single pulse. The simulation result does not include the ground scattering effects in Fig. 11.a while the experimental result includes the effects
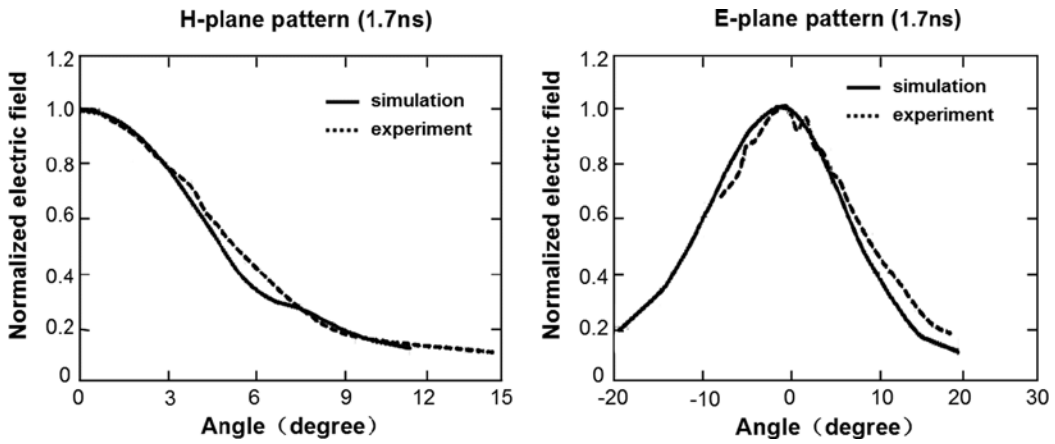
Fig. 6 The field patterns of 1.7 ns pulse on the H plane (*left*) and the E plane (*right*)
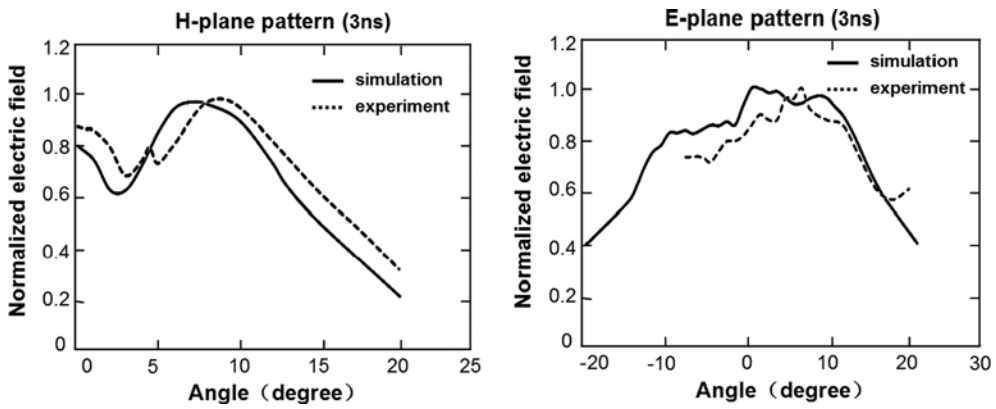
Fig. 7 The field patterns of 3 ns pulse on the H plane (*left*) and the E plane (*right*)

Table 1 The –3 dB peak power beam width of radiation field at $r = 75$m

Pulse		H plane	E plane
1.7 ns	Simulation	7°	14°
	Experiment	6°	14°
3 ns	Simulation	25°	27°
	Experiment	24°	25°

in Fig. 11.b, which makes the difference. Notches and peaks in Fig. 11.b are the consequence of spectrum interference between the two radiation pulse and the ground scattering.

4 Summary and Conclusions

An antenna system consisting of a half-reflector over a rectangular ground plane and three TEM feeds is developed. It can radiate two types of bipolar pulses with peak-to-peak width of 1.7 ns and

(a) Simulation   (b) Experiment
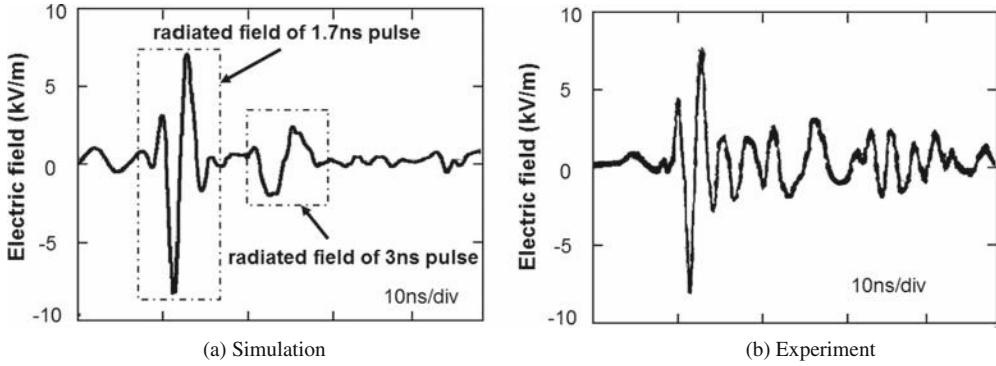
Fig. 8 Boresight radiation field of the combined pulse at a distance of $r = 75$m. (**a**) Simulation, (**b**) experiment

(a) Simulation   (b) Experiment
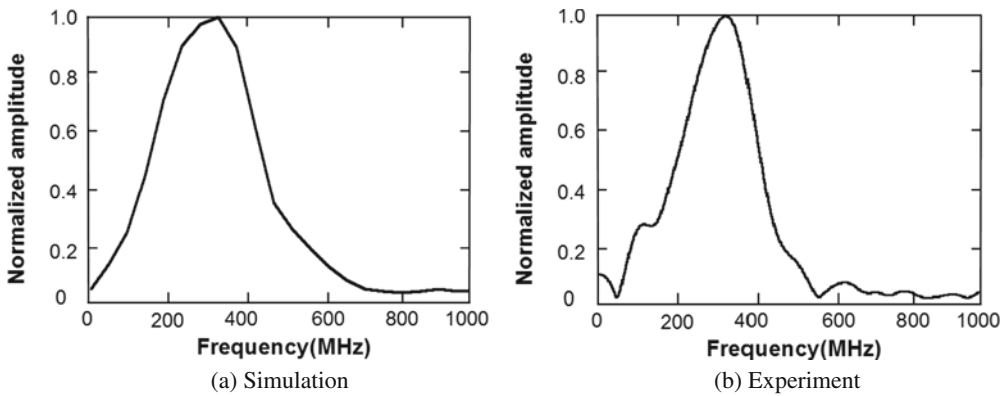
Fig. 9 Radiated spectrum of the 1.7 ns pulse: (**a**) simulation, (**b**) experiment

(a) Simulation   (b) Experiment
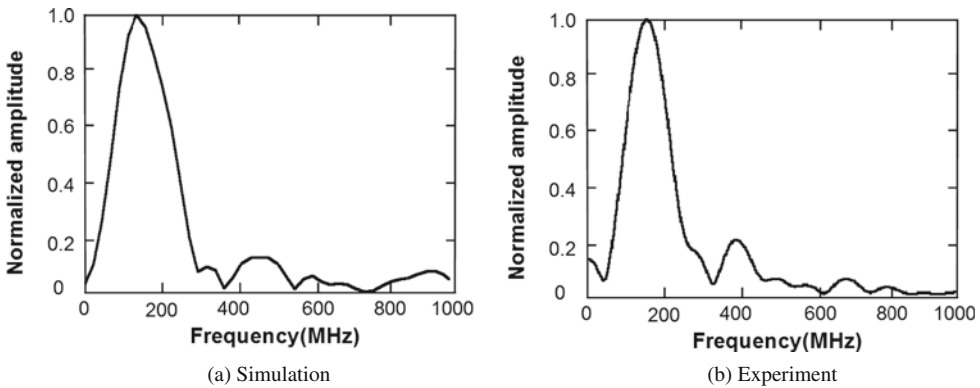
Fig. 10 Radiated spectrum of the 3 ns pulse: (**a**) simulation, (**b**) experiment

3 ns effectively. The radiated spectrum of the 1.7 ns pulse covers the frequency band from 240 MHz to 400 MHz, and 3 ns pulse corresponds to the band of 110–210 MHz. While the radiated spectrum combined with 1.7 ns and 3 ns pulses with a 12.5 ns delay spreads over a wider frequency band from

(a) Simulation
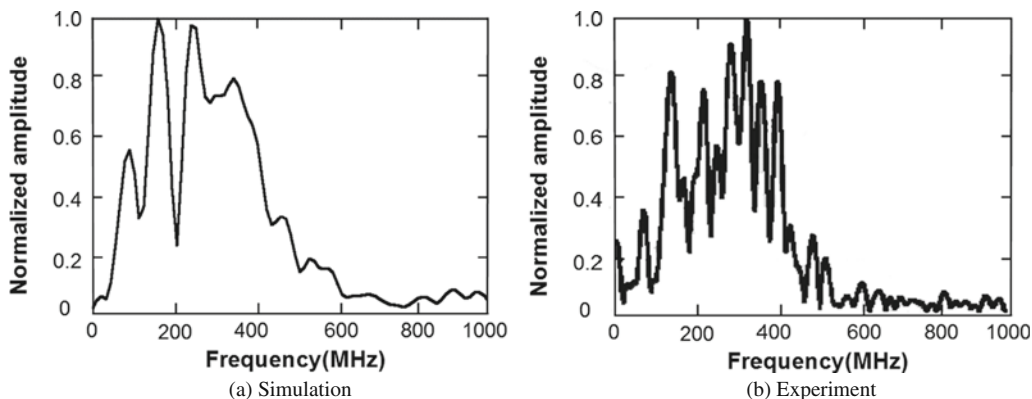
(b) Experiment

Fig. 11 Radiated spectrum of the combined 1.7 ns and 3 ns pulses: (**a**) simulation, (**b**) experiment

Table 2 Spectrum range of the boresight electric field

	1.7 ns pulse	3 ns pulse	1.7 ns and 3 ns combined pulses
Simulation	160–450 MHz	75–250 MHz	85–430 MHz
Experiment	240–400 MHz	110–210 MHz	100–430 MHz

100 MHz to 430 MHz. Results show that radiating the combined pulses is an effective method to expand the radiated pulse spectrum.

References

1. S. Jaruwatandilok, A. Ishimaru, and Y. Kuga, Optimum wireless communication through unknown obscuring environments using the time-reversal principle: theory and experiments, Ultra-wideband, Short-pulse Electromagnetics 8, Carl E. Baum, Alexander P. Stone, and J. Scott Tyo (eds.), Plenum Press, New York, p. 105, 2007.
2. A. O. Boryssenko, D. L. Sostanovsky, and Elen S. Boryssenko, Portable imaging UWB radar system with two-element receiving array, Ultra-wideband, Short-pulse Electromagnetics 8, Carl E. Baum, Alexander P. Stone, and J. Scott Tyo (eds.), Plenum Press, New York, p. 153, 2007.
3. Carl E. Baum and Everett G. Farr, Impulse radiating antennas, Ultra-wideband Short-pulse Electromagnetics1, H Bertoni et al. (eds.), Plenum Press, New York, 1993.
4. Carl E. Baum, et al., JOLT: a highly directive, very intensive, impulse-like radiator, Proceeding of the IEEE, vol. 92, no. 7, July 2004.
5. L. H. Bowen, E. G. Farr, and W. D. Prather, A high-voltage cable-fed impulse radiating antenna, Ultra-wideband, Short-pulse Electromagnetics 8, Carl E. Baum, Alexander P. Stone, and J. Scott Tyo (eds.), Plenum Press, New York, p. 9, 2007.
6. X. L. Liu, Ultra wide-band high power antenna research, Doctor Thesis of Xi'an Jiao Tong University, 2003.

A Novel UWB Planar Antenna with Notch Cut for Wireless Communications

A. Alshehri and A.R. Sebak

Abstract A novel printed antenna with a trimmed notch cut, fed by a simple microstrip line, is proposed and described. It is designed and fabricated for ultra-wideband (UWB) wireless communications under the band (3.1–10.6 GHz). This antenna is composed of a planar rectangular patch with notch cut and a transition step fed by a microstrip line with a partial ground plane. A parametric study is carried out to optimize the proposed patch antenna. The measured 10 dB return loss bandwidth for the designed antenna is 7.5 GHz. The proposed antenna provides a good radiation pattern and a relatively flat gain over the entire frequency band. The design details and related results are presented and discussed.

Keywords Antenna · Printed antenna · UWB communications · Patch antenna

1 Introduction

The frequency band of 3.1–10.6 GHz was allocated for ultra-wideband (UWB) technology in 2002 by the Federal Communications Commission (FCC) [1]. Since then, it has received high attention because it is a promising solution for short range high speed indoor mobile communications as well as the emerging reconfigurable and software-defined wireless networks. Therefore, several shapes and designs of UWB antennas such as square, circular, pentagonal, hexagonal, elliptical, and trapezoidal shapes have been proposed to satisfy UWB specifications [2, 3]. However, some shapes like the square and circular planar monopole antennas have a drawback of a relatively small impedance bandwidth [4]. To enhance the impedance bandwidth, several bandwidth enhancement techniques have been proposed. These techniques include the use of an asymmetrical feed arrangement [4], a partial ground plane [5], adjusting the gap between radiating element and ground plane [6], beveling radiating element [7], beveling ground plane [8], cutting slot in the ground plane beneath the microstrip line [2], and cutting two notches in the radiating element or using steps to control the impedance stability [3].

In this chapter, a new UWB planar patch antenna is proposed. We use various bandwidth enhancement techniques including adjusting the gap between radiating element and ground plane, partial

A. Alshehri (✉)
EXPEC Advanced Research Center, Saudi Aramco, Dhahran, Saudi Arabia
e-mail: abdullah.shehri.8@aramco.com

ground plane, using steps to control the impedance stability, and notch cut technique. The notch cut from the radiator is also used to miniaturize the size of the planar antenna [6]. The proposed antenna is composed of a planar rectangular patch with notch cut and a transition step fed by a microstrip line with a partial ground plane. The commercially available simulation software HFSS is used to design and optimize the antenna [9]. In this design, an impedance bandwidth of 7.5 GHz (3.1–10.6 GHz) for −10 dB return loss is obtained. The proposed antenna provides an acceptable radiation pattern and a relatively flat gain over the UWB frequency band. In addition, a parametric study is carried out to optimize the antenna and provide more information about the effects of its geometrical parameters.

2 Antenna Structure

Figure 1 illustrates the geometry of the proposed planar patch antenna. It consists of a planar rectangular patch with notch cut and a transition step fed by a microstrip line with a partial ground plane. A Cartesian coordinate system (x, y, z) is oriented such that the bottom surface of the substrate lies in the x–y plane. The antenna and the partial ground plane are oppositely etched on the sides of Rogers RT/Duroid 5880 substrate with a thickness of 1.575 mm and a relative permittivity $\varepsilon_r = 2.2$. The substrate size of the proposed antenna is 40×32 mm^2. The dimensions of the rectangular patch are $w = 22$ mm and $h = 16.33$ mm. The transition step of $w_1 \times h_1 = 17$ mm $\times$ 2.5 mm is attached to the rectangular patch. To reduce the overall size of the printed antenna and to get better impedance matching, a rectangular-shaped notch with dimensions of $l_s \times w_s = 5.6$ mm $\times$ 13 mm is symmetrically cut in the top middle of the radiator and both top edges of the patch are trimmed. The rectangular-shaped partial ground plane has dimensions 9.5×40 mm^2. The radiator is fed through a microstrip line having a length 10.5 mm and width $w_f = 3.6$ mm to ensure 50-Ω input impedance with a feed gap $g = 1.0$ mm. The 50-Ω microstrip line is printed on the same side of the substrate as the radiator. The feed gap "g" can be used to adjust the impedance matching.
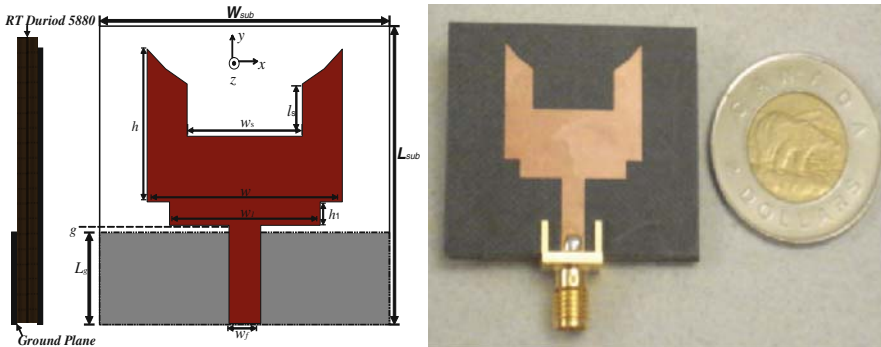
Fig. 1 Geometry and prototype of the proposed antenna

3 Parametric Studies

The parametric study is carried out to optimize the antenna and provide more information about the effects of the essential design parameters. The antenna performance is mainly affected by geometrical parameters, such as the dimensions related to the notch cut, the transition step, and the feed gap.

3.1 Notch Cut

The effect of the rectangular-shaped notch dimensions (l_s, w_s) on the return loss is studied. As shown in Fig. 2, the width of the notch affects the impedance matching, especially at the middle frequencies. It experiences mismatch when the width increases. Also, the lower edge frequency of the bandwidth is slightly shifted to higher frequencies and the higher frequencies are slightly shifted to lower frequencies once the width increases. On the other hand, the length of the notch slightly influences the impedance matching. Therefore, the effects of the notch cut parameters are very limited. It is also noted that the notch can be used to reduce the size of the radiator provided that the current distribution has low density in the notch part [6].

Fig. 2 Effects of notch width
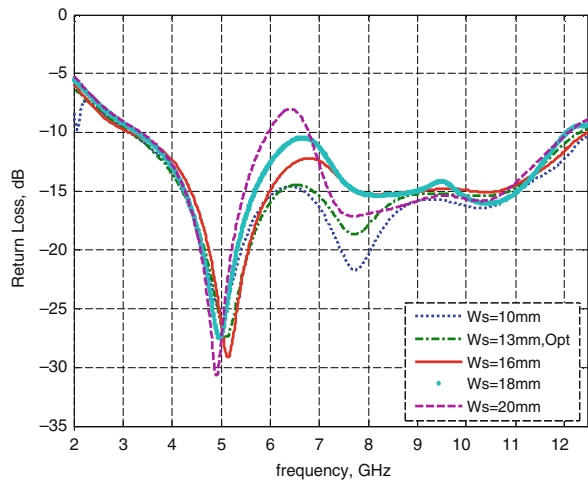
3.2 Transition Step

The effect of transition step width is plotted in Fig. 3. It greatly impacts the matching impedance for the entire band. The step width highly affects the whole band. When the width decreases, the middle and higher frequencies are greatly affected and exhibit mismatch. In contrast, when the width increases to be the same as the radiator width, the lower and higher frequencies are greatly affected and exhibit mismatch. In addition, the transition step height affects the entire band drastically (but figure is not shown for brevity). It is observed that when the height is getting smaller, the whole band is affected. Consequently, the transition step is very important technique since it influences the coupling between the radiator and the ground plane and provides a well-matched traveling mode and smooth impedance transition between the feed line and the radiator.

3.3 Feed Gap

Figure 4 shows the effect of the feed gap (g) between the radiator and the upper edge of the ground plane. The feed gap drastically affects the entire frequency band. When the feed gap is getting smaller, it affects the first half of the operational bandwidth (low and middle frequencies). On the

Fig. 3 Effects of step width
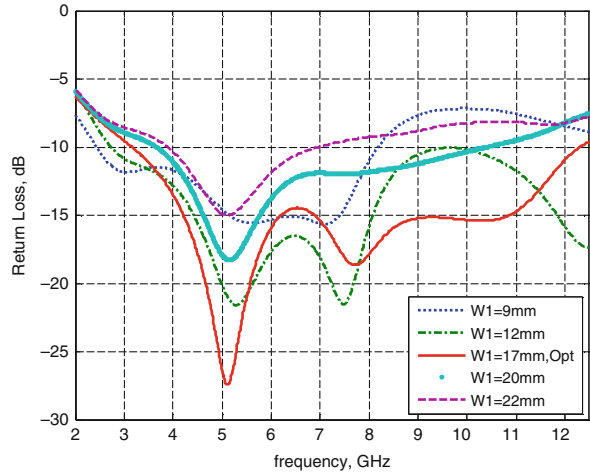
Fig. 4 Effects of feed gap
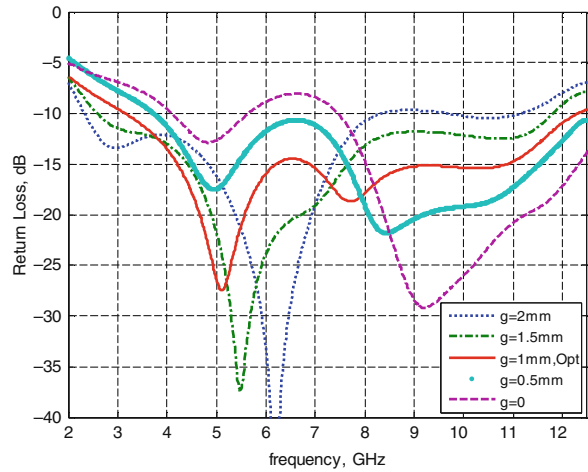
other hand, when it is getting larger, it affects the second half of the operational bandwidth (middle and high frequencies). The feed gap thus has to be precisely tuned to achieve the desirable impedance matching [6].

4 Experimental Results

Based on the parametric study and current distributions, the optimized antenna is designed and constructed as shown in Fig. 1. The return loss (S_{11}) of the proposed antenna is measured. As depicted in Fig. 5, the measured and simulated results are shown for comparison and indicate a reasonable agreement. The measured 10 dB return loss bandwidth of the antenna is approximately 7.5 GHz (3.1–10.6 GHz) and the antenna shows stable behaviors over the band. Thus, the measurement confirms the UWB characteristic of the proposed patch antenna, as predicted in the simulation.

Fig. 5 Simulated and measured return loss
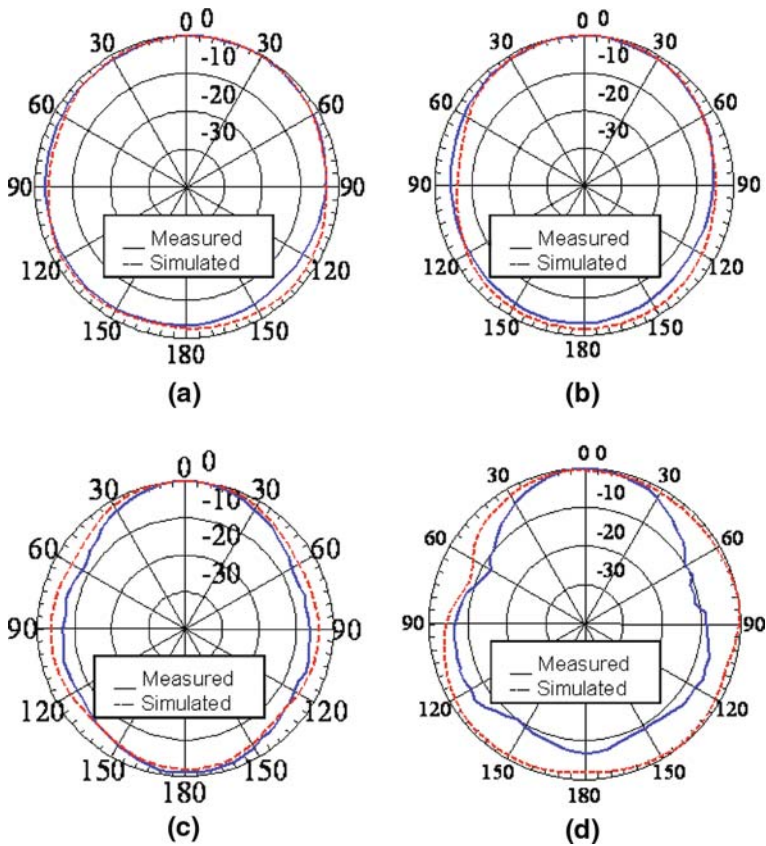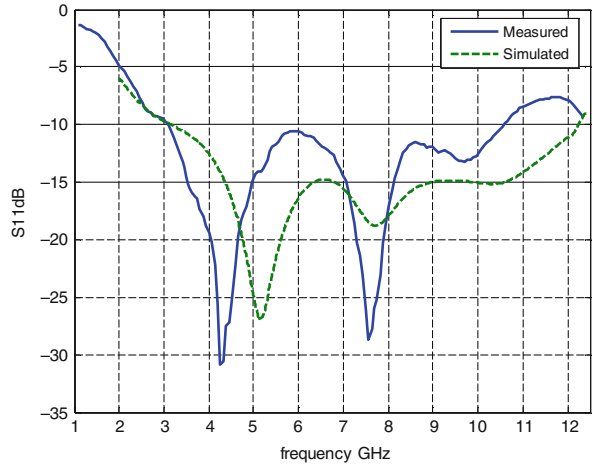
Fig. 6 H-plane radiation pattern at (**a**) 3.5 GHz, (**b**) 5.5 GHz, (**c**) 7.5 GHz, (**d**) 9.5 GHz
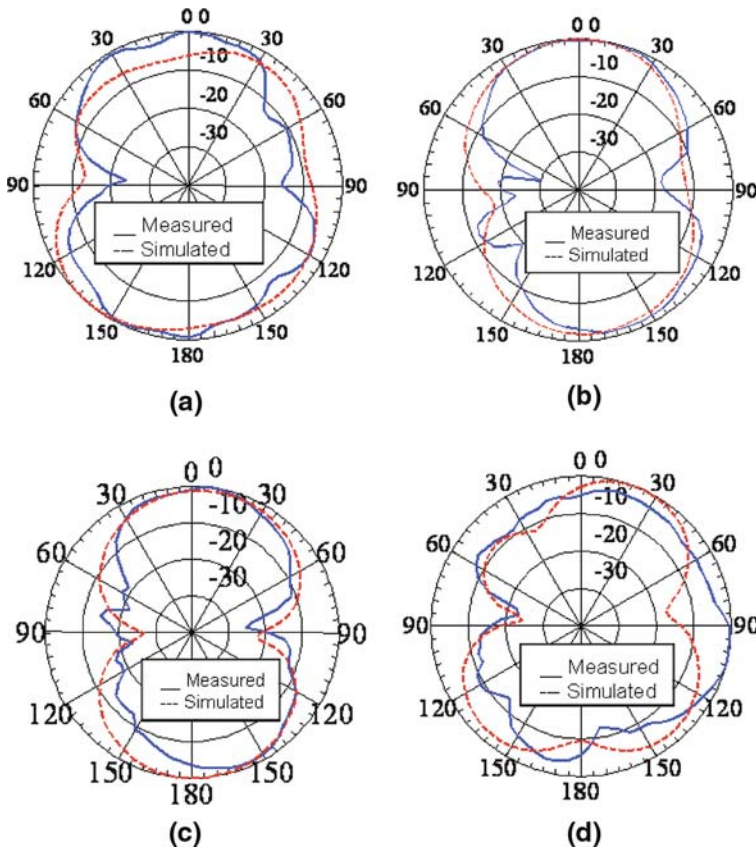
Fig. 7 E-plane radiation pattern at (**a**) 3.5 GHz, (**b**) 5.5 GHz, (**c**) 7.5 GHz, (**d**) 9.5 GHz

The radiation characteristics of the proposed antenna are also investigated. Figures 6 (a, b, c, and d) and 7 (a, b, c, and d) illustrate the simulated and measured H-plane and E-plane radiation patterns, respectively, at 3.5, 5.5, 7.5, and 9.5 GHz. The proposed antenna is characterized by an omnidirectional pattern in the H-plane (x–z plane) while it is a quasi-omnidirectional pattern in the E-plane (y–z plane). These results imply that radiation patterns are acceptable over the UWB bandwidth. The simulated antenna gain versus frequency is shown in Fig. 8. It varies from 3.5 dBi to 4.7 dBi over the operating frequency range, resulting in the maximum gain variation of 1.2 dB.

5 Conclusion

A novel planar patch printed antenna with a trimmed notch cut, fed by a simple microstrip line, is proposed and described. It is designed and constructed for UWB wireless communications. Several techniques have been applied to the designed antenna including the use of a transition step, feed gap, partial ground plane, and notch cut. The measured bandwidth for the designed antenna is 7.5 GHz. The parametric study is carried out to address the effects of the step, notch cut and feed gap on the proposed antenna characteristics and hence optimize it. The antenna provides a good radiation pattern and a relatively flat gain over the entire frequency band.

Fig. 8 Simulated gain
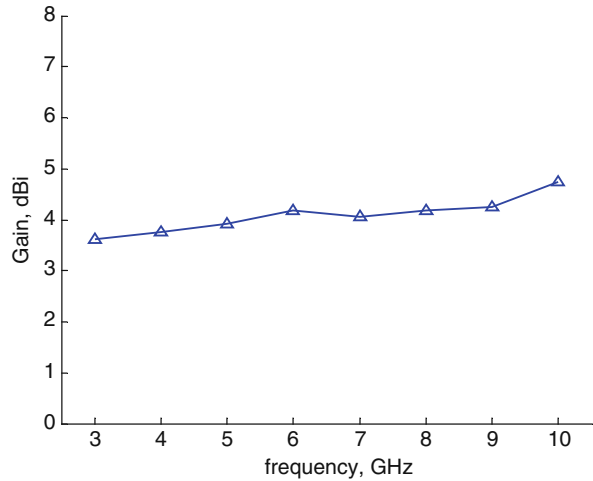
References

1. Federal Communication Commission, First report and order, revision of part 15 of the commission's rules regarding ultra-wideband transmission system. FCC, 2002.
2. C. Huang and W. Hsia, Planar elliptical antenna for ultrawideband communications, Electronics Letters, vol. 41, pp. 296–7, 2005.
3. S. Su, K. Wong, and C. Tang, Ultra-wideband square planar monopole antenna for IEEE 802.16a operation in the 2–11 GHz band, Microwave and Optical Technology Letters, vol. 42, pp. 463–6, 2004.
4. M. Ammann and Z. Chen, An asymmetrical feed arrangement for improved impedance bandwidth of planar monopole antennas, Microwave and Optical Technology Letters, vol. 40, pp. 156–8, 2004.
5. Z. Low, J. Cheong, and C. Law, Low-cost PCB antenna for UWB applications, IEEE Antennas and Wireless Propagation Letters, vol. 4, pp. 237–9, 2005.
6. Z. Chen, T. See, and X. Qing, Small printed ultrawideband antenna with reduced ground plane effect. IEEE Transactions on Antennas and Propagation, vol. 55, pp. 383–8, 2007.
7. M. Ammann and Z. Chen, Wideband monopole antennas for multi-band wireless systems IEEE. IEEE Antennas and Propagation Magazine, vol. 45, pp. 146–50, 2003.
8. W. Wang, S. Zhong, and S. Chen A novel wideband coplanar-fed monopole antenna. Microwave and Optical Technology Letters, vol. 43, pp. 50–52, 2004.
9. HFSSTM, v10, Ansoft Corporation Software, Pittsburgh, PA, USA.

Ultra-wideband 4 × 4 Phased Array Containing Exponentially Tapered Slot Antennas and a True-Time Delay Phase Shifter at UHF

J. Schmitz, M. Jung, J. Bonney, R. Caspary, J. Schüür, and J. Schöbel

Abstract For angular scanning a true-time array is developed for UHF ultra-wideband (UWB) applications in time and/or frequency domain. It is based on a 4 × 4 array with antipodal exponentially tapered slot antennas (ETSA, Vivaldi) and a 3-bit phase shifter. Distances of antenna elements are designed to be compromise between gain, scanning angle, side/grating lobe levels. The uniform spaced and fed array maximizes the overall gain. After defining the antenna shape, corrugations are introduced to improve antenna matching and gain pattern. Nine equally spaced beam positions for a 90° scanning angle are induced by an optimized 3-bit phase shifter on high permittivity substrate, while 4 bits are usually needed. Parasitic resonances are avoided by using PIN diodes in single pole double throw configuration. All components and the complete array system are simulated and verified in frequency domain with good agreement. Adaptation to UWB pulses is possible.

Keywords Antenna · Antipodal exponentially tapered slot antennas · Vivaldi antenna · True-time phase shifter

1 Introduction

Standard radar and tracking systems use phased antenna arrays for narrow band transmission [1, 2]. Therefore, designing procedures for the antenna array in order to optimize parameters like gain, low side lobe and grating lobe levels, antenna element distance a are straight forward. Techniques like non-uniform power distribution (Dolph–Tchebysheff distribution) are often used [1, 2]. Following constraints can be used to fix the antenna element distance in order to reduce grating lobes for phased arrays:

1. boresight transmission with grating lobes at $\pm 90°$:

$$a/\lambda \leq 1 \tag{1}$$

2. no grating lobe within a scanning angle of $\pm \Theta_0$:

$$a/\lambda \leq \frac{1}{1 + |\sin \Theta_0|} \tag{2}$$

J. Schmitz (✉)
Rheinmetall Waffe Munition GmbH, Heinrich-Erhardt-Straße 2 D-29345 Unterlüß, Germany
e-mail: juergen.schmitz@rheinmetall.com

For the chosen frequency band of 500 to 1000 MHz the critical frequency for avoiding grating lobes is the upper limit. Thus, for both equations and a specified scanning angle of $\pm45°$, maximum element distances of 0.3 and 0.17 m can be calculated. In contrast, low frequency transmission is limited by antenna aperture size. Ultra-wideband antennas like logarithmic periodical types usually have sizes which are half wavelength of the lower frequency limit and thus at least 0.3 m aperture size. The array design for a frequency band of one octave is an ill-conditioned optimization problem. For a prototype system the element distance of 0.3 m is chosen. Calculating the array factor at 1 GHz for a 4×4 array, nine equidistant scanning positions of above mentioned scanning angle are defined. The single antenna element needs an HPBW of 90° which results in a gain of about 5 dBi.

The next section describes the design of an exponential tapered slot (Vivaldi) antenna which is often used for ultra-wideband array applications. Simulation and measurement results are presented. Specification, design, and measurement results of an optimized 3-bit true-time delay phase shifter follow. All beam positions are fixed and should be independent from frequency variations. The third section shows the complete transmission system and its measurement results containing the phase shifter and the 4×4 antenna array Table 1.
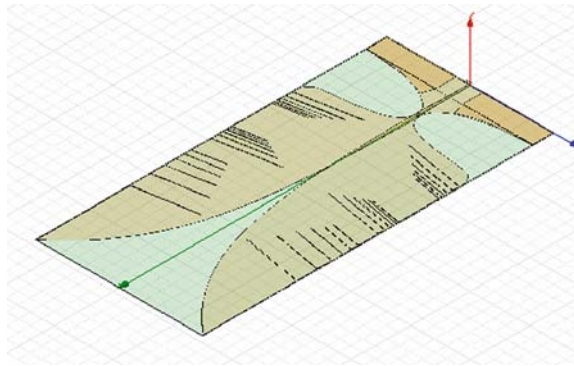
Fig. 1 Vivaldi antenna

2 Exponential Tapered Slot Antenna

The used Vivaldi antenna is separated into three distinguished parts: antenna foot reflector, symmetrical double-strip feeding, and antenna blades. The dimensions are 280 by 590 mm^2 on a 1.52 mm RO4003 substrate. The shape of the foot is approximately exponential. It is symmetrically distributed on both sides with a tapered feed for 50 Ω symmetrical double-strip line as seen in Fig. 1. The reflector is crucial for end-fire characteristics and matching.

Table 1 Blade function and parameters of the Vivaldi antenna shown in Fig. 1

$f_n(x) = M_n \cdot x + A_n + B_n \cdot e^{(Cn \cdot x)}$		
	$n =$ aperture	$n =$ back
M	−0.0175	0
A	−5.9259145	1.0759145
B	2.85	2
C	0.0078764423	0.1

The main difficulty in the design is the relatively small aperture of roughly $\lambda/2$ at the lowest frequency. The blade geometry follows exponential parameterized curves (Table 1) that are slightly tilted to gain an overlap at the line-to-blade transition. For improving the matching in the specified frequency band corrugations are inserted at the outer blade edges. They are arranged in a 10° tilted comb with a displacement of a quarter wavelength. The corrugation dimensions are corresponding to the blocked frequencies with relatively high impedance, due to the small slot width of 1 mm. There is a good agreement between the simulation and measurements for matching and antenna patterns in both planes (Fig. 2).
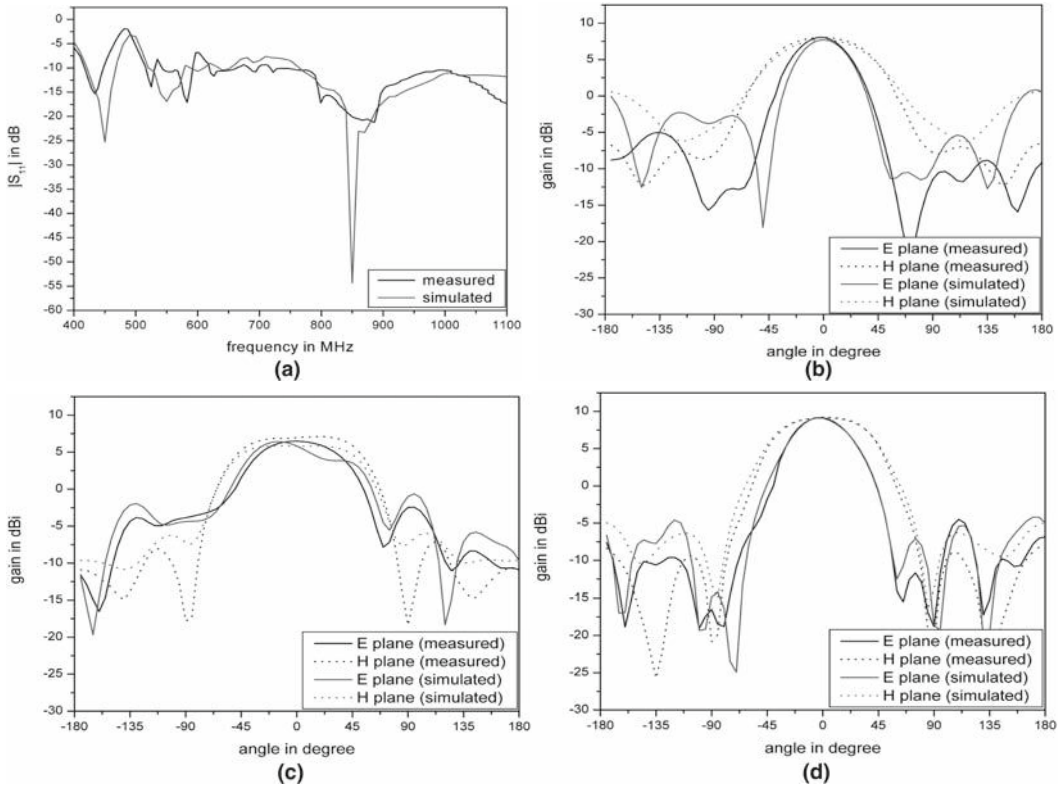
Fig. 2 Antenna simulation vs. measurement. (**a**) Matching, (**b**) 500 MHz, (**c**) 750 MHz, (**d**) 1000 MHz

3 3-Bit True-Time Phase Shifter

A total number of nine beams are required, which are distributed equally over a comparatively large angular scan range of ±45°. The beam angle Θ is independent of frequency if the signal is delayed between neighboring antenna elements by a constant time delay $\Delta T = (a/c) \cdot \sin \Theta$ for an element spacing of a. The corresponding phase shift increases linearly with frequency. Due to the large angular range, the nonlinearity in the sinus term cannot be neglected and time delays do not correspond well to conventional binary partitioning of the phase shifter stages (i.e., T, $2T$, $4T$, etc.). Therefore, the phase shifters are optimized with respect to optimum phase tolerances at minimum hardware

effort. Using two phase shifter stages leads to unacceptable phase errors. With three stages, eight different delays can be realized, but these are mutually interdependent. Therefore, an additional degree of freedom is introduced by different fixed delays (electrical length in "zero state") of the individual phase shifters, which results in significantly lower inherent phase errors.

The block diagram of the phase shifter system is depicted in Fig. 3. The signal is distributed via broadband three-stage Wilkinson dividers to the individual phase shifters [3, 4]. The latter are switched-line designs, which are made highly symmetrical to achieve good phase/delay tolerances. The insertion delays are defined exclusively by different lengths of straight transmission lines. The optimization of the phase shifter configuration consists of two tasks:

- finding the optimum combinations of switching states for all beams to achieve overall low phase errors and
- finding the optimum time delays for a given combination of switching states including the optimum "zero state" time delays.

Fig. 3 Block diagram of the phase shifter system. The phase shifters for the inner and outer antenna elements have different configurations
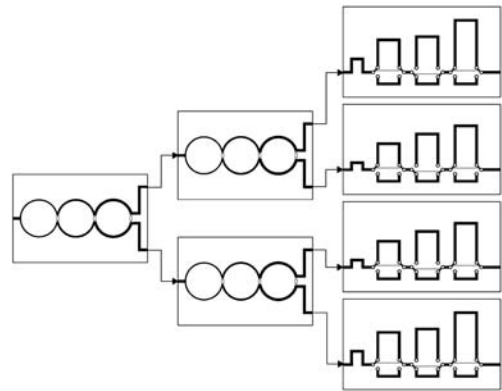
A Monte-Carlo technique was used to find the optimum combination of switching states, which minimizes the overall error in time delay for all states. For each set of switching states the optimum time delays are determined employing an error minimization technique. The results of the optimization are compiled in Table 2 showing the non-binary switching scheme. An average (maximum) inherent deviation of the time delay ΔT of 14 ps (22 ps) is inherent in the design.

Table 2 Delays and switching configurations of the optimized phase shifters. All time delay numbers are in picoseconds. Beams 6–9 (not shown) are inverse configurations of beams 1–4

	Beam angle	Nominal ΔT	Phase shifter 1 Delay stages			Phase shifter 2 Delay stages			Phase shifter 3 Delay stages			Phase shifter 4 Delay stages		
			512	542	1108	364	543	724	364	543	724	512	542	1108
Beam 1	45°	708				X	X		X	X	X	X	X	X
Beam 2	33.75°	556						X		X	X		X	X
Beam 3	22.5°	383					X		X	X				X
Beam 4	11.25°	195		X		X	X		X		X			X
Beam 5	0°	0		X				X			X		X	

The switched-line configuration includes a ring-like structure, half of which is decoupled by the off-state switches. In an ultra-wideband application it is likely or even unavoidable that the frequency range of use includes one or more resonances of the ring. This is illustrated in Fig. 4a. The switches employ series-shunt combinations of PIN diodes to attain a high isolation (25–30 dB and above), which is necessary to avoid the parasitic resonances in the off-state paths, see Fig. 4b. The input and output lines are kept on ground potential when switching off all diodes is done simultaneously. Therefore, the inductors will not impede fast switching.
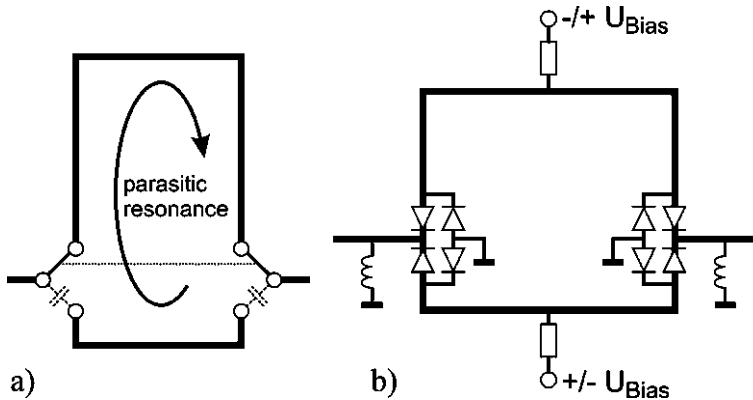
Fig. 4 (**a**) Parasitic resonance in a switched-line phase shifter, (**b**) Conceptual design of a single phase shifter stage

The system was realized using high-dielectric-constant boards (RO3210 or AD1000). Figure 5 shows the individual phase shifter boards and the complete system. The characterization of the phase shifters shows a good accuracy of the insertion phase/delay. If the average of the delay deviates from the design value, a certain beam pointing error will occur. If there is a spread in the time delays, the side lobe level will be degraded. The average delay deviations are between –21 and +18 ps, while the average time delay spread amounts to 1…20 ps depending on the beam. A large part of the average delay deviations are caused by the tolerances of the RF board dielectric constant. In Fig. 6 the transmission behavior in phase and absolute value for exemplary beams are compiled. The $|S_{21}|$ exhibits a frequency-dependent behavior, which is mainly caused be the rather long transmission lines. Return loss (not shown) is better than 10 dB at all ports for all states.
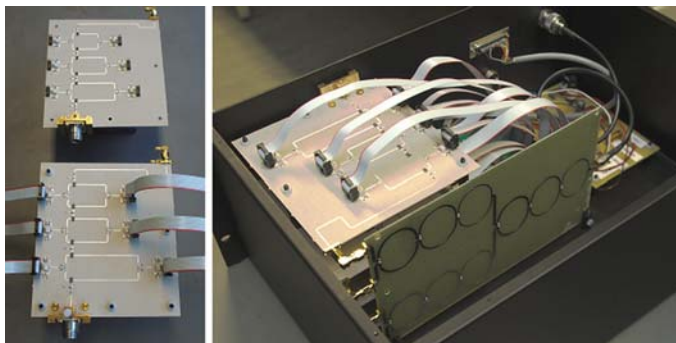
Fig. 5 Photographs of individual boards and complete phase shifter system
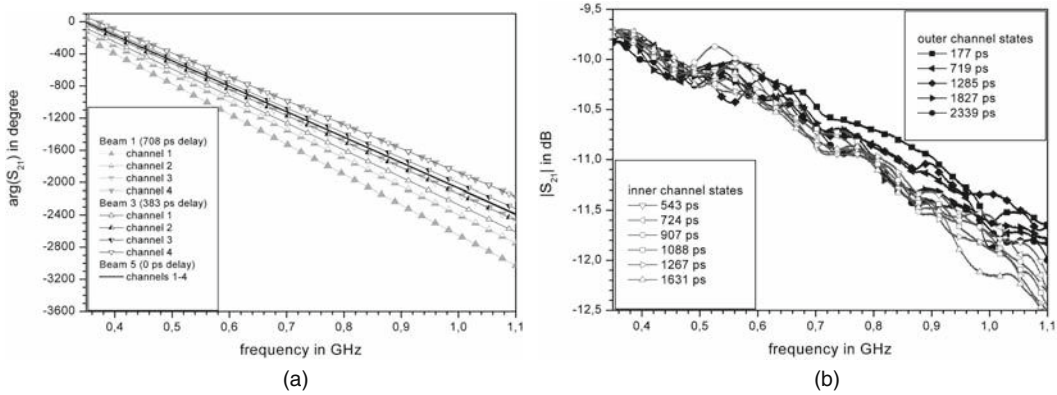
Fig. 6 Transmission behavior for exemplary beams in phase and absolute value of the phase shifter system. 6 dB dividing ratio of the Wikinson divider are included. (**a**) Phase, (**b**) Absolute value

4 True-Time Delay 4 × 4 Antenna Array

Figure 7 depicts the complete 4 × 4 antenna array containing the above designed exponential tapered slot antenna. The element distance is 0.3 m. The housing is built from Rohacell$^{®}$ and foamed PVC. In order to get the gain patterns for each switched beam position in E and H plane the antenna array is fed by the phase shifter followed by four parallel Wilkinson dividers.

Fig. 7 4 × 4 antenna array with exponential tapered slot antennas

Figure 8 shows the beam rosettes exemplary in H plane. The envelopes of each beam rosette follow qualitatively the specific pattern of the single antenna (compare Figs. 2 and 8). At 1000 MHz grating lobes occur as expected. Table 3 shows the measured gains of the array in H plane in comparison to a calculated gain of a single antenna element and the array factor. At low frequencies the array gains are about 3 and 4 dB lower than expected. The strictly linear model of pattern multiplication does not include effects like cross talk and coupling between antenna elements, etc. For 500 and 750 MHz the antenna element distances are to low to reduce cross talk.
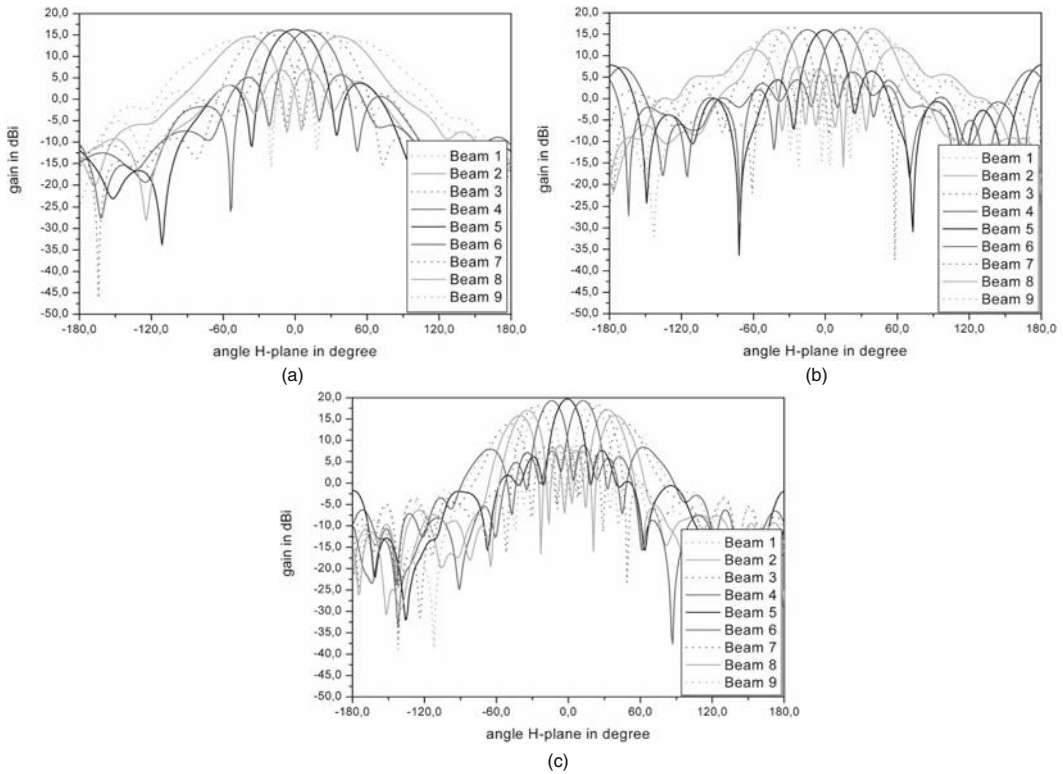
Fig. 8 Beam rosettes of the 4 × 4 phased array in H plane. (**a**) 500 MHz, (**b**) 750 MHz, (**c**) 1000 MHz

Table 3 Antenna gains at 500, 750, 1000 MHz

f in MHz	Gain in H plane in dBi	Single antenna with array factor in dBi
500	15.20	19.16
750	15.82	18.90
1000	19.38	21.03

5 Conclusions and Further Research

A UHF ultra-wideband 4 × 4 phased array antenna system is presented. After specifying the main functional parameters like number of beams, scanning angle, beam positions, and antenna element distance the main components are developed. In order to maximize gain and minimize grating lobes, an ill-conditioned optimization problem occurs because antenna aperture size and element distance are contradictory. As compromise the antenna size and element distance of 0.3 m are chosen to be equal. An exponential tapered slot antenna is developed. Simulation and measurement results show excellent agreement. A true-time delay phase shifter is designed and optimized for nine equidistant beam positions at a scanning angle of ±45°. Deviations of the implemented delays from the theoretical results are within ±20ps. The insertion phase of each beam state is a linear function of frequency which describes the true-time behavior of the phase shifter. This is verified be measuring the beam

patterns at each position within the frequency band of 500 to 1000 MHz. Grating lobes occur at high frequencies. At lower frequencies gain degradation is measured because of coupling and/or cross talk effects of neighboring antenna elements.

Adaptation of the array system to transient UWB pulses is a topic for further research especially for high power electromagnetic systems.

References

1. C. A. Balanis, Antenna Theory, Second edition, Wiley & Sons, New York, 1997.
2. R. C. Hansen, Phased Array Antennas, Wiley & Sons, New York, 1998.
3. D. M. Pozar Microwave Engineering, Third edition, Wiley & Sons, New York, 2001.
4. J. Schöbel, J. Schüür, R. Caspary, J. Schmitz, M. Jung, A True-time-delay Phase Shifter System for Ultra-wideband applications. ITG-Fachbericht of German Microwave Conference 2008, ISBN 978-3-8007-3086-5, pp. 182–5, Hamburg (GER), 2008.

Planar Elliptical Differential Antenna for UWB Applications

G. Quintero, J.F. Zürcher, and A.K. Skrivervik

Abstract Differential antennas are becoming of great interest for UWB systems because of the simplicity to connect them to an input amplifier. In this chapter a planar elliptical differential (PED) UWB antenna fed by coplanar striplines is investigated. This allows the antenna to be in the same plane as the circuit board, reducing the size of the system, and facilitating the connection to the input amplifier or LNA.

Keywords UWB antennas · Elliptical dipole · Differential antennas · Transfer function · Planar antennas

1 Introduction

Differential antennas are becoming of great interest for UWB systems because of the simplicity to connect them to an input amplifier. This type of antenna can be connected directly to the system without using an external balun, or balanced to unbalanced transition, thus reducing size and complexity of the UWB system. Most of differential antennas reported in literature are fed with coaxial cables perpendicular to the antenna plane [1, 2]. This could be of use for some applications, but it may be a problem for systems with strong space limitations.

In this chapter we investigate a planar elliptical differential (PED) UWB antenna fed by coplanar striplines. This allows the antenna to be in the same plane as the circuit board, reducing the size of the system and facilitating the connection to the input amplifier or LNA.

2 Antenna Descriptions

The proposed antenna is shown in Fig. 1. It is an elliptical dipole fed by a coplanar stripline (CPS) with a total size of 5.0×3.4 cm. The ellipses have a semi-major axis of 9.5 mm and a semi-minor axis of 7.6 mm. They are rotated at their center by 40°. The purpose of this rotation is to increase the

G. Quintero (✉)
Laboratoire d'Electromagnétisme et d'Acoustique (LEMA), Ecole Polytechnique Fédérale de Lausanne (EPFL), Lausanne Switzerland
e-mail: gabriela.quintero@epfl.ch

Fig. 1 PED antenna
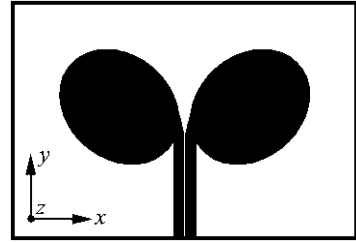
directivity in the *Y–Z* plane with respect to the classical elliptical dipole. The peak radiation is in the +*y* direction, avoiding with this unnecessary radiation toward the feeding system.

A coplanar stripline structure is shown in Fig. 2. The substrate used is Rogers RO4003 with 0.508 mm thickness and $\varepsilon_r = 3.38$. The impedance of the lines was calculated using the formulas in [3]. With $d = 0.25$ mm and $w = 1.5$ mm, an impedance of 107 Ω was obtained.

Fig. 2 Coplanar stripline, transversal cut
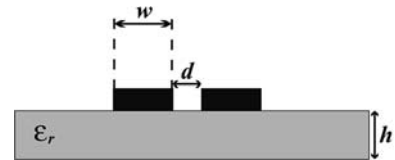
3 Transfer Function

Considering a system with two identical antennas oriented face to face at a distance *R* from each other, the transmission coefficient S_{21} can be easily measured. The system transfer function $H(\omega)$ is equal to the S_{21} and is defined as

$$H(\omega) = H_t(\omega)H_{ch}(\omega)H_r(\omega), \tag{1}$$

where $H_t(\omega)$, $H_r(\omega)$, and $H_{ch}(\omega)$ refer to the transfer functions of the transmitting antenna, the receiving antenna, and the free space channel, respectively.

The voltage transfer function relates the received voltage at the antenna load to the generator voltage at the transmit antenna [4]. Therefore, it can as well be written as follows:

$$H(\omega) = \frac{V_r(\omega)}{V_t(\omega)}e^{jkR}. \tag{2}$$

The amplitude $|H(\omega)|$ can be calculated from Friis' transmission equation [5]. In our case, both transmitting and receiving antennas are assumed to be identical and with the same polarization. Therefore, the characteristic impedances and the antenna gains are considered to be identical. $|H(\omega)|$ simplifies to

$$\frac{V_r(\omega)}{V_t(\omega)} = \left(1 - |S_{11}|^2\right)\left(\frac{\lambda}{4\pi R}\right)G(\theta, \phi). \tag{3}$$

The phase component of the transfer function is given by the channel propagation constant and by the phase constant of both antennas.

$$\angle H(\omega) = \angle S_{21} = \angle H_t + kR + \angle H_r. \tag{4}$$

If we consider the signal in time domain, the channel component of the phase corresponds to the displacement of the transmitted pulse, from one antenna to the other. However, this does not take into account the phase distortion inside the antennas. Therefore, this last component has to be added in the analytical calculation of the transfer function.

4 Simulations

Simulations of the antenna were done using Ansoft HFSS. The antenna was first simulated with a wave port to verify the impedance of the differential lines. The impedance given by the software corresponds to the impedance calculated analytically. Having a good estimation of the impedance, the antenna was finally simulated using a lumped port with 107 Ω as reference impedance. The return loss and the radiation properties were practically the same using any of the ports. Once the return loss was obtained, the transfer function was calculated as follows.

Using a discrete sweep in HFSS, the S_{11}, gain, and radiated E-fields were obtained. The return loss and the gain are used to compute the amplitude of the transfer function, as mentioned in the previous section. The phase of the radiated E-field depicts the phase constant of the antennas. The total system transfer function was calculated using the following equation:

$$H(\omega) = S_{21} = \left(1 - |S_{11}|^2\right) G(\theta, \phi) \left(\frac{\lambda}{4\pi R}\right) e^{jkR} e^{j2\angle E(\theta, \phi)}. \tag{5}$$

The above equation was resolved using Matlab and the impulse response at the receiving antenna was extracted. A Gaussian pulse with central frequency $f_C = 6.85$ GHz and fractional bandwidth $BW = 0.8$ was generated in time domain and used as input signal. The input pulse was transformed into its frequency representation using a standard fast Fourier transform (FFT). The received signal in the Fourier domain can then be recovered by multiplying the spectrum of the input pulse by the transfer function of the antenna system. The time domain representation of the received pulse is obtained by applying an inverse FFT.

5 Measurements

Three different antenna measurements were done to characterize the antenna: differential return loss, transfer function of the antenna system (from where the antenna gain was calculated), and radiation pattern. The measurement techniques are described in this section, and the results are compared to simulations.

5.1 Return Loss

Measurements of a differential antenna cannot be made directly with a conventional vector network analyzer (VNA). A VNA has typically two coaxial cables connected at each port. The coaxial cables are unbalanced whereas the antenna to be measured has a balanced input.

To obtain the differential return loss of the PED antenna, each line of the CPS line is connected to a port of the VNA. Treating each line as an unbalanced port, a post calculation of the differential return loss is done using the following equation:

$$S_{diff} = 20 \log_{10} \left| \frac{1}{2}(S_{11}^2 + S_{22}^2) - \frac{1}{2}(S_{12}^2 + S_{21}^2) \right|. \tag{6}$$

The CPS lines cannot be connected directly to the VNA ports. A two-port measurement jig was implemented, as described in [6]. The antenna connected to the jig is shown in Fig. 3. The measurements obtained at the VNA ports contain as well the information of the jig. In order to eliminate the effect of the jig, a de-embedding has to be done to obtain the return loss at the antenna reference plane.

Fig. 3 PED antenna with jig
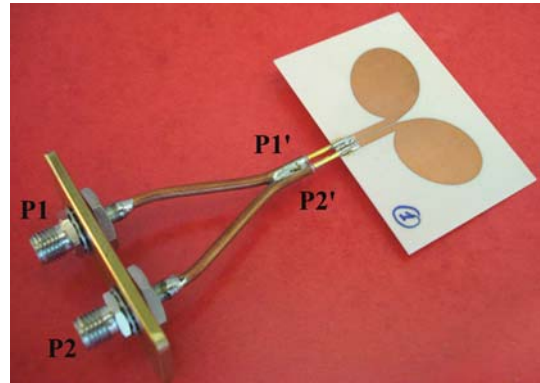
The scattering matrix of the antenna (S') at ports P1′ and P2′ can be calculated using the following matrix [7]:

$$S' = \begin{bmatrix} S_{11}e^{2\gamma_1 d_1} & S_{12}e^{(\gamma_2 d_2 + \gamma_1 d_1)} \\ S_{21}e^{(\gamma_1 d_1 + \gamma_2 d_2)} & S_{22}e^{2\gamma_2 d_2} \end{bmatrix}, \tag{7}$$

where γ is the propagation constant and d the length of the jig lines. Short-circuiting the two terminals of the jig to the cables' ground, the transmission characteristics of the lines (attenuation α and phase β) can be obtained. Assuming a perfect short circuit and symmetry of the jig terminals, $S_{11}' = S_{22}' = -1$ (total reflection). The propagation constant γ of the lines can be obtained from

$$S_{11} = -e^{-2(\alpha+j\beta)d} = -e^{-2\gamma d}, \tag{8}$$

$$\gamma d = -\frac{\ln(-S_{11})}{2} \tag{9}$$
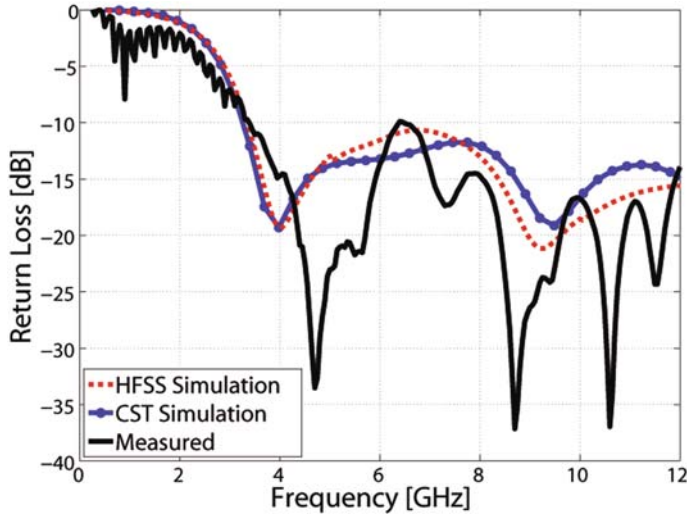
Fig. 4 Measured and simulated S_{11}

The S-parameters of the antenna are calculated substituting the values of the S' matrix in (5.1). In Fig. 4 the measured return loss, obtained after de-embedding, is plotted together with simulation results from HFSS and CST Microwave Studio. Measurements and simulations are in good agreement. They are below -10 dB in the UWB band. The measured return loss has ripples in the entire band, which is commonly found in S_{11} measurements of UWB antennas. This is due to the small size of the antenna and the standing waves produced by the antenna currents in the cable.

5.2 Transfer Function Measurements

An external balun was used to measure the two-port transmission coefficient. The S-matrix of the balun (back to back) was measured (Fig. 5) and later subtracted from the whole S-parameters measurement of the two antenna system. The S-parameters measurement was done inside an anechoic chamber with the two antennas located one meter apart in a foam support. The antennas were positioned face to face, transmitting and receiving in the $+z$ direction. The measured S-parameters are compared with simulations in Figs. 6 and 7 shows the antenna with balun together with the balun back to back.

To have low distortion of the transmitted pulse, the phase of the transmission coefficient has to be linear. Figure 8 shows the transfer function (S_{21}) of the antenna system in amplitude and phase along with the measured values. The phase shows to be linear in the UWB band. It can be seen a good agreement between measurements and simulations. To illustrate this, the signal in time domain is plotted in Fig. 9, where the input signal is compared to the simulated and measured received signals (right of the figure). We notice that there is indeed only a small dispersion and distortion of the signal.

The S-parameters of the PED antenna system were obtained after de-embedding of the half-balun at each antenna. The S-parameters of the PED antenna are compared with the simulated values from HFSS in Fig. 10. The measured value is above -10 dB after 6 GHz, which is clearly an effect of the mismatch of the balun. As seen in Fig. 5, the insertion loss of the balun increases after 6 GHz.
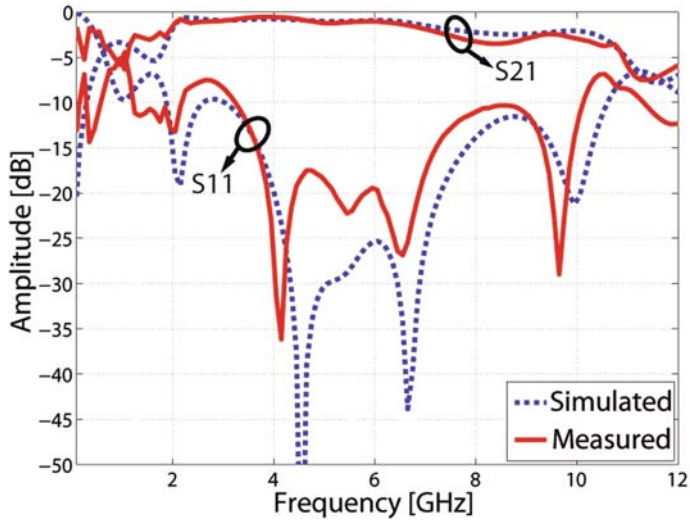
Fig. 5 Balun *S*-parameters

Fig. 6 *S*-Parameters of PED antenna system with balun
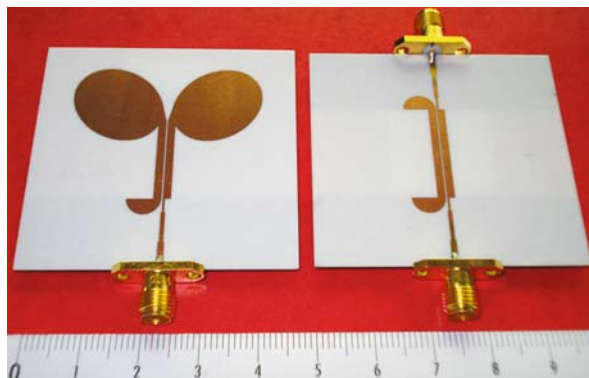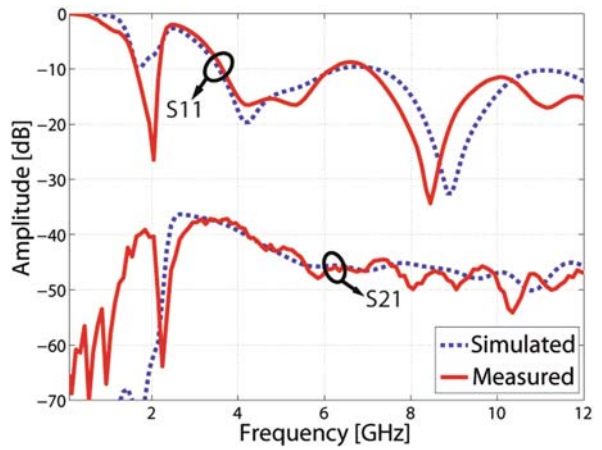
Fig. 7 PED antenna with balun and Balun back to back
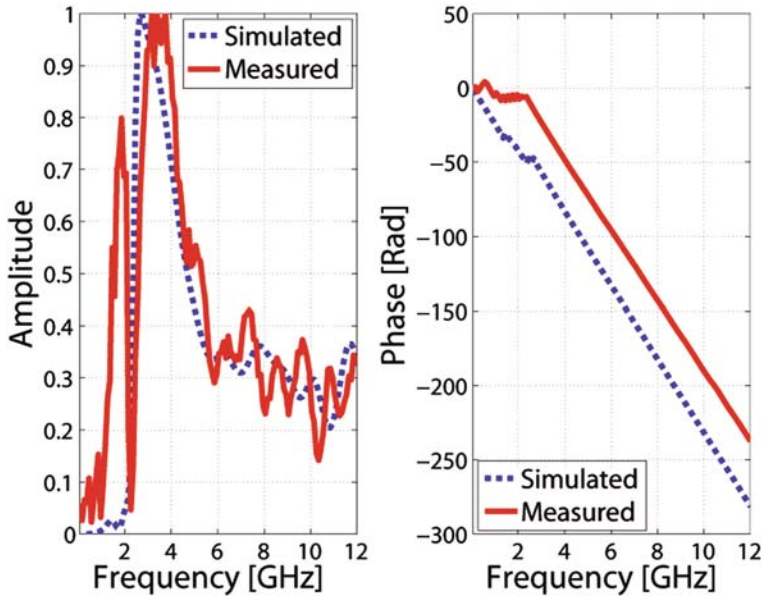
Fig. 8 PED antenna with balun transfer function, amplitude, and phase

Fig. 9 Time domain signal simulated and measured
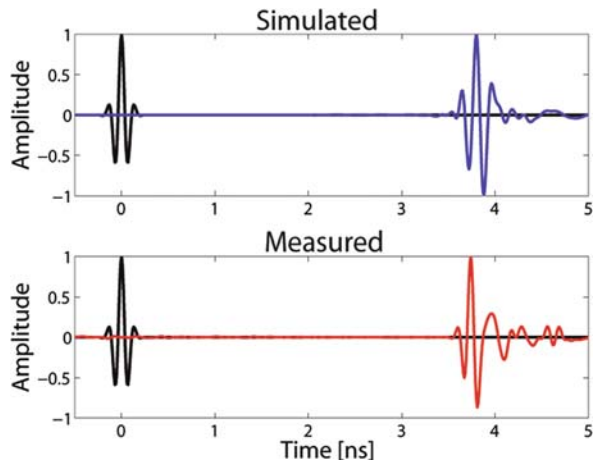
The phase of the transmission coefficient and its normalized amplitude are shown in Fig. 11. The phase shows again a good agreement between simulations and measurements, being linear in the UWB band. The measured transmitted pulse in Fig. 12 is clearly more dispersed than the simulated one. This is due to the de-embedding, showing that it is not possible to eliminate all the effects of the balun in the antenna.

Fig. 10 PED antenna system
S-parameters
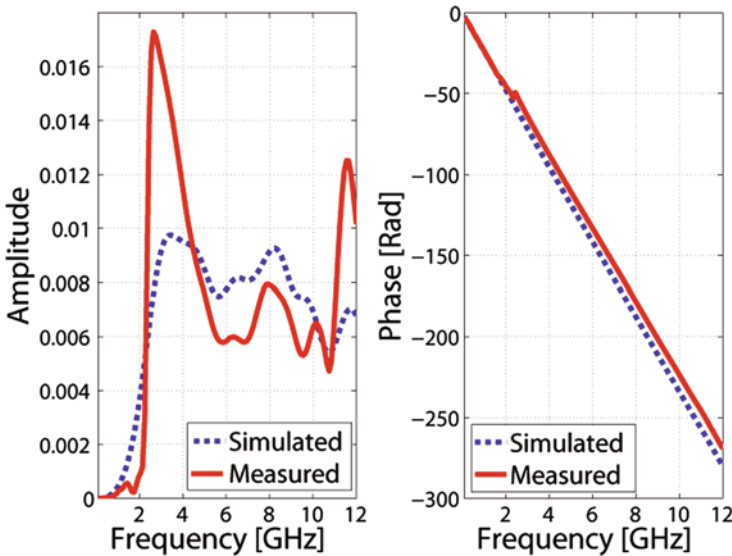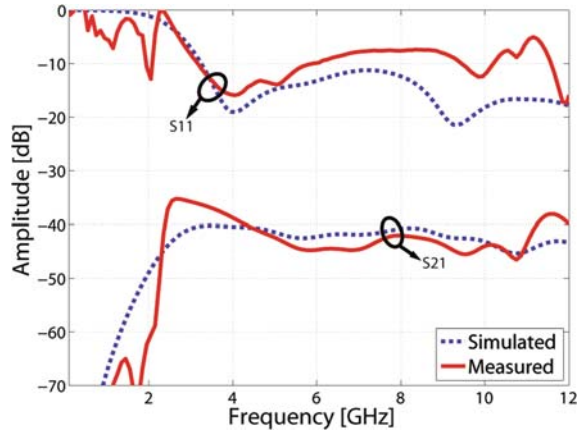
Fig. 11 PED antenna transfer function, amplitude, and phase

5.3 Gain and Radiation Pattern

Gain measurements of the PED antenna with and without balun were calculated from the measured transfer function shown in the last section, using (3.3). In Fig. 13, the gains are plotted, showing good concordance between simulation and measurements. The gain of the PED antenna with balun is lower than the PED antenna (without balun) after 5.5 GHz, which is due to the mismatch of the balun.

Radiation pattern measurements were done with the PED antenna with balun inside an anechoic chamber. The measurements show that radiation of the antenna is stronger in the $+y$ direction. The radiation in the $-y$ direction is 5 dB lower than in the $+y$ direction; showing with this the increased directivity of the PED antenna with respect to a classical elliptical dipole. The pattern is symmetric in the *Y–Z* plane as expected. In the *X–Y* plane, the asymmetry of the pattern is due to the mismatch of the balun, not feeding in a perfect symmetrical way the antenna (Fig. 14).

Fig. 12 Time domain signal simulated and measured
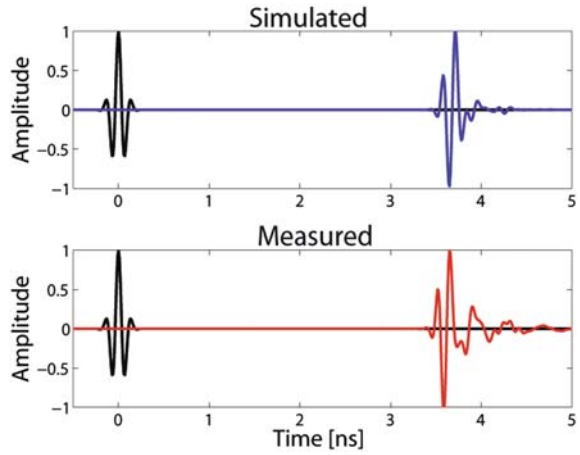
Fig. 13 PED antenna gain in the UWB band (3.1–10.6 GHz)
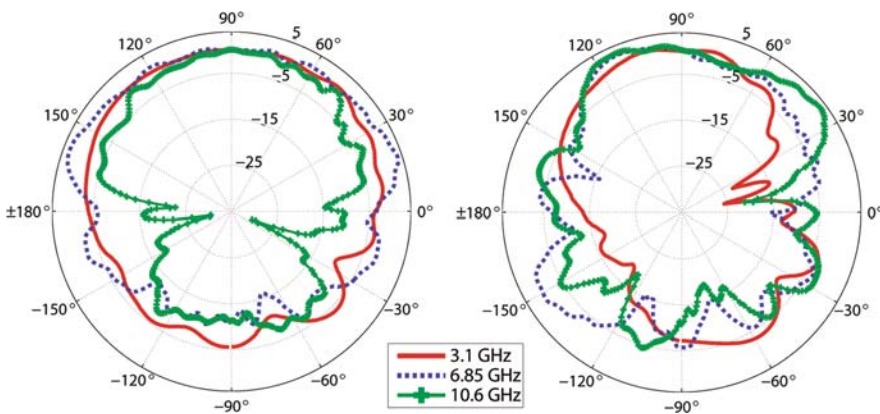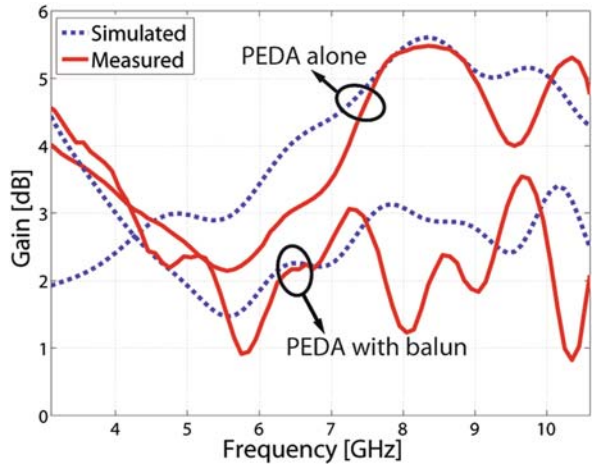
Fig. 14 Radiation pattern in the *Y–Z* plane and *X–Y* plane.

6 Conclusions

In this chapter, we presented a planar elliptical antenna that could be used in UWB differential systems. The transmission coefficient of an antenna system was analytically described. The equation agrees well with measurements. The gain of the measured antenna can be directly extracted using the same procedure. A measurement technique to obtain the differential return loss was discussed. The impulse response of the Tx/Rx system was computed, showing the limited dispersion of the system. Radiation pattern measurements prove the increased directivity of the PED antenna compared to a conventional dipole. Its maximum radiation is in the $+y$ direction, radiating 5 dB less toward the feeding structure.

References

1. C. Zhang, J. H. Wang, and Y. Han, Coupled planar dipole UWB antenna design For wearable computer, in IEEE International Conference in Microwave and Millimeter Wave Technology, 2007.
2. J. Powell and A. Chandrakasan, Differential and single ended elliptical antennas for 3.1–10.6 GHz ultra wideband communication, in IEEE Antennas Propagation Society International Symposium, 2004, pp. 2935–38.
3. B. C. Wadell, Transmission Line Design Handbook, 1991.
4. D. M. Pozar, Waveform optimizations for ultrawideband radio systems, IEEE Transactions on Antennas and Propagation, vol. 51, pp. 2335–45, September 2003.
5. C. A. Balanis, Antenna Theory. Analysis and Design, Second edition, John Wiley & Sons, Inc., New Jersey, 2005.
6. K. Duncan Palmer and M. W. van Rooyen, Simple broadband measurements of balanced loads using a network analyzer, IEEE Transactions on Instrumentation and Measurement, vol. 55, pp. 266–272, February 2006.
7. R. E. Collin, Foundations for Microwave Engineering, Second edition, McGraw-Hill, New York, 1992.

Array Antenna for Directed Radiation of High-Power Ultra-wideband Pulses

V.I. Koshelev, V.V. Plisko, and K.N. Sukhushin

Abstract This chapter presents the results of investigations of a 64-element array developed for radiation of directed ultra-wideband wave beams with multimegavolt effective potential. The array is excited from a 1-ns length bipolar pulse generator with the output impedance of 12.5 Ω. The total output impedance of a feeder system used for pulse distribution by the array elements is 0.78 Ω. The array aperture is 1.41 × 1.41 m. The peak power pattern FWHM in two orthogonal planes is 10º.

Keywords Pulse excited antennas · Directive antennas · Planar arrays · Antenna arrays feeds · Electromagnetic beams · Ultra-wideband radiation

1 Introduction

In order to realize remote sounding of radar objects with high space resolution, it is necessary to have sources for directed radiation of short ultra-wideband (UWB) radiation pulses with multimegavolt effective potential $E_pR \sim 10$ MV, where E_p is the electric field peak strength in the far-field zone at a distance R. The highest radiation stability is realized when using UWB sources based on the radiator excitation from one generator of high-voltage pulses. This is important at recognition of the sounding objects. Among the given type of UWB sources one can choose the sources based on impulse radiating antenna (IRA) [1] and arrays of combined antennas [2] where radiation pulses with megavolt effective potential have been obtained. Theoretical estimations, without taking into account power losses in a feeder system, have shown [3] that at the same apertures of IRA and the array with the number of elements equal to $\sim$100, the utmost value of E_pR for the combined antenna array is $\sim$1.5 times higher than for the IRA. An additional stimulus for our investigations is the promising application of controlled time delay lines installed in front of each combined antenna in an array. This can allow realizing the wave beam steering mode in the limits of ±45º [4].

In the previously developed [2, 5] UWB sources based on the excitation of 16-element arrays by bipolar voltage pulses the series-connected coaxial wave impedance transformer and power divider with cable feeders were used. This type of construction had two restrictions: small number of channels in the power divider and elements in the array, respectively, as well as a low level of voltage pulse amplitudes or a short lifetime of a source. The latter was stipulated by the cable breakdown. In

V.I. Koshelev (✉)
Institute of High Current Electronics, SB RAS, 2/3 Akademichesky Ave., Tomsk 634055, Russia
e-mail: koshelev@lhfe.hcei.tsc.ru

order to eliminate these drawbacks, a feeder system presenting a combination of the wave impedance transformer and power divider was suggested. To realize the suggested approach, a 8×8-array of combined antennas excited by a 1-ns length bipolar voltage pulse was developed. The order of the work was the following. Initially, an array antenna project was developed. The most difficulties were in the region of connection of the array elements with the divider. Owing to this, a 2×2-module of the array was fabricated and studied and only then the array was made completely. The results of investigations are presented in the same succession.

2 Design of a High-Directivity Array Antenna

An array (Fig. 1) consists of 64 (8×8) elements fixed at a metal plate. A combined antenna [5] optimized to a 1-ns length bipolar exciting pulse was used as an array element. The combined antenna dimensions are $0.15 \times 0.15 \times 0.16$ m. The distance between the centers of the elements is 0.18 m. The array aperture is 1.41×1.41 m.

Fig. 1 64-Element array

A design of a 64-channel power divider with simultaneous impedance transformation has been developed to transmit a bipolar voltage pulse from the generator to the array antenna elements. Structurally, the 64-channel power divider consists of three series-connected stages of four-channel dividers (1, 2 and 3 in Fig. 2). The wave impedance at the first stage input (1) equals to the wave impedance at the bipolar pulse generator output being equal to $12.5\,\Omega$. The starting wave impedance of the first stage arm of the divider is $12.5 \times 4 = 50\,\Omega$. The summary impedance of the feeders of

Fig. 2 64-Channel power divider
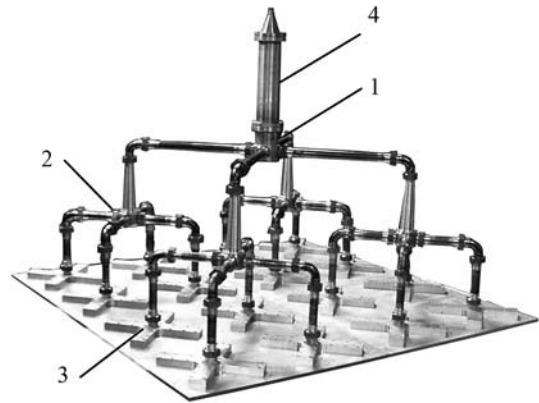
16 array elements to which each arm of the first stage is loaded equals to $50/16 = 3.125\,\Omega$ and the summary impedance of feeders of 64 elements equals to $50/64 \approx 0.78\,\Omega$. In order to minimize reflections at the impedance transformation, a compensated exponential transition was used. The impedance of the latter was calculated by the formula:

$$\rho(x) = \rho(0)\exp\left\{\ln\left(\frac{\rho(l)}{\rho(0)}\left[\frac{x}{l} - 0.133\sin\left(2\pi\frac{x}{l}\right)\right]\right)\right\},$$

where $\rho(0)$ and $\rho(l)$ are the values of the initial and final impedances of the transition.

The transmission lines are filled with transformer oil for insulation. The total length of one arm of the divider is 1.2 m. To match the divider input impedance and the wave impedance of measuring devices a wave transformer of the length 0.315 m ranging from 50 to $12.5\,\Omega$ was used (4 in Fig. 2). Figure 3 presents the normalized waveforms of the voltage pulses at the input U_g and output U_d of one of the divider channels. It is obvious from the diagram that the pulse waveform has got insignificant distortions. However, the pulse amplitude at the divider output is 6.5 times less than the amplitude at the input whereas in the ideal case it should be four times diminished. This is mainly related to the losses in a dielectric.
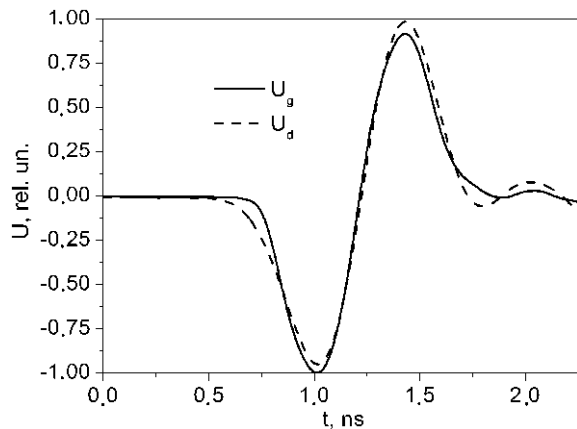
Fig. 3 Voltage pulse waveforms at the input U_g and output U_d of a 64-channel divider

Estimations show that power losses in a feeder system including a wave transformer (4) are reaching 60% of the input power. Decrease of power losses is related to the gas insulation application. The non-uniformity of the amplitudes at the divider outputs is not higher than 5%.

3 2×2-Module of Array Antenna

In order to check the engineering solutions, an array module has been fabricated presenting the last stage of a 64-channel power divider with a four-element (2×2) array antenna (Fig. 4). To match the input divider impedance with the wave impedance of a test bipolar pulse generator and measuring devices, a 0.3-m length wave transformer was used ranging from 50 Ω to 13.4 Ω (input impedance of the last divider stage).

Fig. 4 A four-element array antenna. **1** – array elements, **2** – power divider, **3** – wave transformer
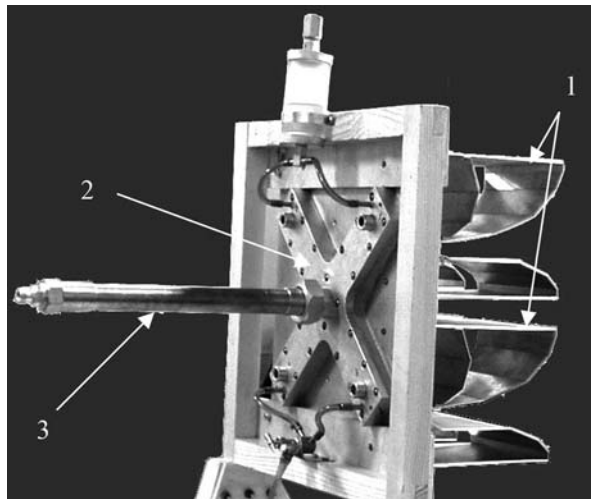
Figure 5 presents the transmission coefficient of the divider with the wave transformer versus frequency. Measurements of identity of the divider channels that were made revealed that in the frequency band of 0.1–2.5 GHz the difference of the transmission coefficient of the divider channels is not higher than 0.5 dB. Figure 6 presents the normalized bipolar generator pulses and the ones at the divider output. The division factor was equal to 2.13. For an ideal divider it should be equal to 2. The pulse at the output has got a small distortion owing to the frequency dispersion in the wave transformer and divider.

Figure 7 presents the peak power patterns for the array and single antenna. It is seen that though the single antenna pattern is asymmetric in a vertical plane, the array pattern is symmetric both in horizontal and vertical planes. The pattern FWHM is 40° for H- and E-planes.

Figure 8 presents the voltage standing wave ratio (VSWR) of the four-element array and divider with a wave transformer loaded to the matched resistors. VSWR rise at high frequencies for the array is related to the VSWR element influence. Resonances at low frequencies are related to the interaction of the antennas both between each other and with the elements of the array construction. Figure 9 presents the peak field strength versus the number of elements in the array. The line corresponds to the field strength of a one-element field E_{p1} multiplied by the number of elements. The measured values of the field strength are lower because of the interaction between the elements. At

Fig. 5 A transmission coefficient of a four-channel divider with a wave transformer
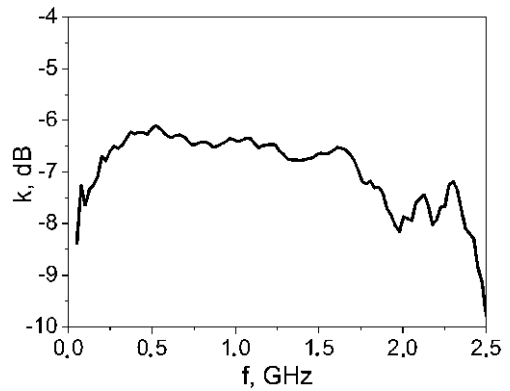
Fig. 6 Waveforms of generator bipolar pulse (**1**) and the one at the divider output (**2**)
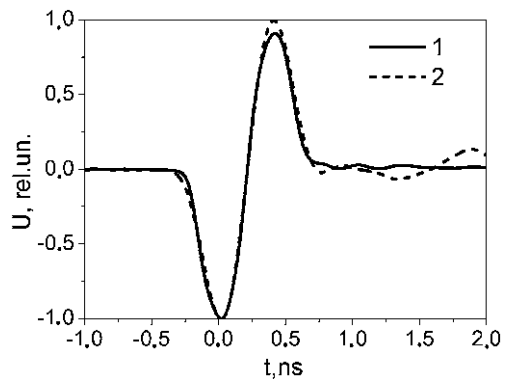
Fig. 7 Patterns of a single antenna (**1**) and four-element array (**2**)
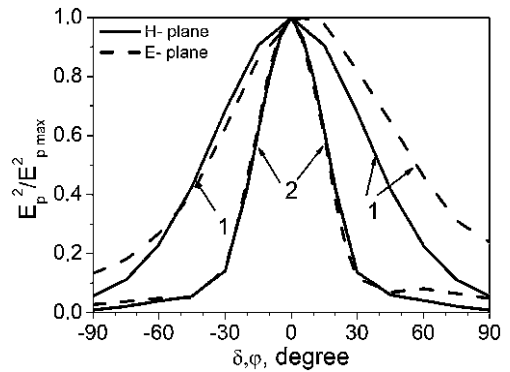
the galvanic connection of the output apertures of vertical elements the field strength is increased approximately by 3%. Figure 10 presents the waveform of radiated pulse. At the bipolar voltage pulse amplitude of the generator $U_g = 135$ V the effective potential $E_p R = 355$ V, where R is the distance to the measuring point in the far-field zone, and here $k_E = E_p R / U_g = 2.63$. Using the methods stated in [6], the directivity factor $D_0 = 17$ and the efficiency by energy $k_w = W_{rad}/W_g = 0.8$ were found, where W_{rad} is the radiated energy, W_g is the energy of the generator pulse. The efficiency by

Fig. 8 VSWR of the divider
with a wave transformer
(**1**) and four-element array
(**2**)
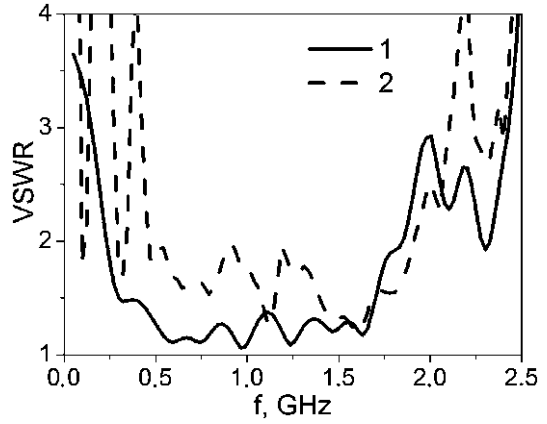
Fig. 9 Electric field strength
versus the number of
elements in the array with
(**1**) and without (**2**) galvanic
connection of output
apertures
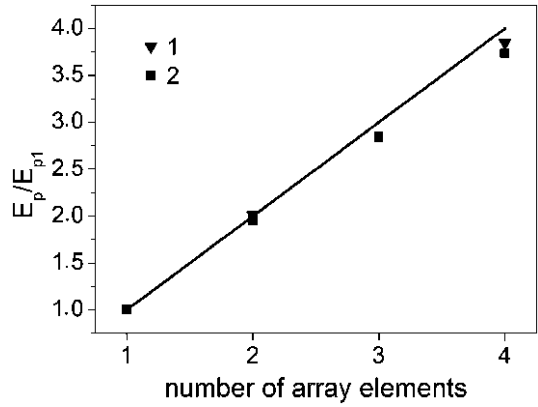
Fig. 10 A waveform of the
pulse radiated by a 2 ×
2-array module
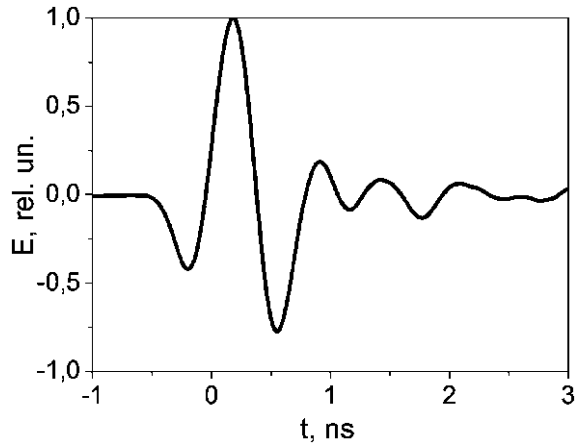
the peak power $k_p = P_{rad}/P_g = 0.5$, where P_{rad} is the peak power of the radiation pulse, P_g is the peak power of the voltage pulse. The measured value of E_p exceeded by 15% the value calculated by the formula

$$E_\mathrm{p} = \frac{1}{R}\sqrt{30 P_\mathrm{g} k_\mathrm{p} D_0}.$$

4 Investigation of a 8×8-Array Antenna

Figure 11 presents the effective potential of the array versus the distance to the receiving antenna. It is seen that the far-field zone begins at a distance exceeding 13 m. Figure 12 presents the peak power patterns of a 64-element array measured in the far-field zone. The pattern FWHM is 10° in both planes. The level of the cross-polarized radiation is less than 0.5%.

Figure 13 presents the waveform of the pulse radiated by a 64-element array in the direction of the pattern main maximum. Figure 14 shows the root-mean-square deviation of the pulse waveform in the limits of ±5° relative to the pulse waveform in the main direction that achieves 20% at the edges of the angular range. This indicates that the radar objects will be sounded by the wave beam with practically similar waveform of the pulse.
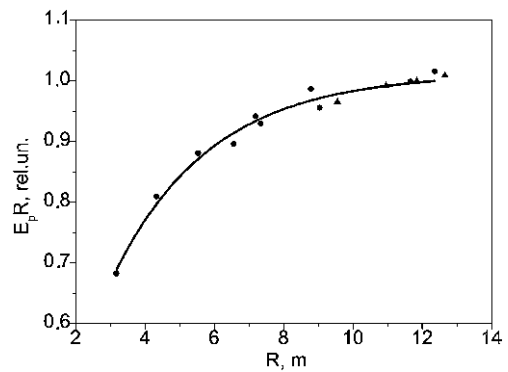
Fig. 11 Effective potential versus the distance between the receiving antenna and the array
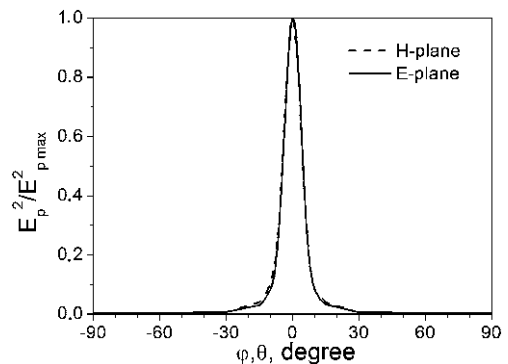
Fig. 12 Patterns of a 64-element array in E- and H-planes

Fig. 13 Waveform of the
pulse radiated by the 8 ×
8-array antenna
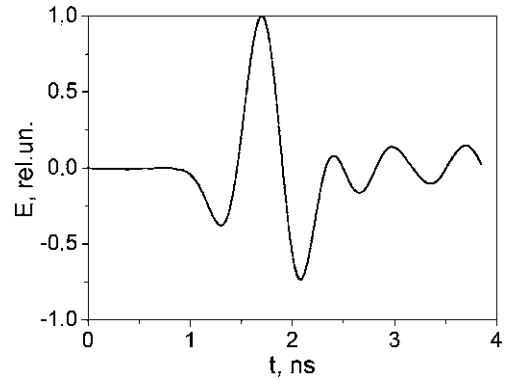
Fig. 14 Root-mean-square
deviation of the pulse
waveform
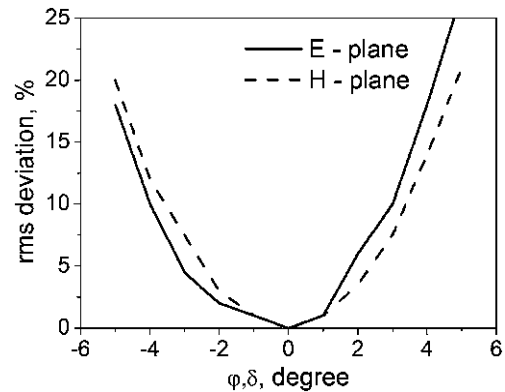
5 Conclusion

A 64-element array with the power divider for excitation from one generator by a 1-ns length bipolar
pulse has been created. The radiation is linearly polarized. The pattern width of the array at a half-
level of the peak power is 10° in E- and H-planes at a small change of the waveform of the radiated
electromagnetic pulse.

The array antenna was used in the UWB radiation source [7]. Radiation pulses with the effective
potential of 2.8 MV at the pulse repetition rate of 100 Hz were obtained. In order to increase the
effective potential of radiation up to 10 MV, it is necessary to quadruplicate (16 × 16) the number
of elements in the array, to decrease power losses in a feeder system by substituting the oil isolation
for the gas one and to increase the amplitude of a bipolar voltage pulse at the array input by 1.5–
2 times up to 300–400 kV. The latest task is the most difficult owing to high strength of the field
(∼1 MV/cm) in a bipolar pulse former [7] resulting in parasitic electric discharges limiting the
voltage pulse amplitude at the generator output.

References

1. C. E. Baum, W. L. Baker, W. D. Prather, J. M. Lehr, J. P. O'Loughlin, D. V. Giri, I. D. Smith, R. Altes, J. Fockler,
    D. McMillan, M. D. Abdalla, and M. C. Skipper, JOLT: A highly directive, very intensive, impulse-like radiator.
    Proceedings of the IEEE, vol. 92, pp. 1096–109, 2004.

2. V. P. Gubanov, A. M. Efremov, V. I. Koshelev, B. M. Kovalchuk, S. D. Korovin, V. V. Plisko, A. S. Stepchenko, and K. N. Sukhushin, Sources of high-power ultrawideband radiation pulses with a single antenna and a multielement array. Instruments and Experimental Techniques, vol. 48, pp. 312–320, 2005.
3. V. P. Belichenko, V. I. Koshelev, V. V. Plisko, Yu. I. Buyanov, S. N. Litvinov, Estimation of an utmost efficient potential of ultrawideband radiating systems, Proceedings of the 14th Symposium on High Current Electronics, Tomsk. Russia, 391–4, 2006.
4. V. I. Koshelev and V. V. Plisko, Interaction of ultrawideband radiators in linear array with wave beam steering, Proceedings of the 14th Symposium on High Current Electronics. Tomsk, Russia, 413–16, 2006.
5. A. M. Efremov, V. I. Koshelev, B. M. Kovalchuk, V. V. Plisko, and K. N. Sukhushin, Generation and radiation of high-power ultrawideband nanosecond pulses. Journal of Communications Technology and Electronics, vol. 52, pp. 756–764, 2007.
6. Yu .A. Andreev, Yu. I. Buyanov, and V. I. Koshelev, A combined antenna with extended bandwidth. Journal of Communications Technology and Electronics, vol. 50, pp. 535–543, 2005.
7. V. I. Koshelev, A. M. Efremov, B. M. Kovalchuk, V. V. Plisko, K. N. Sukhushin, High-power source of ultrawideband radiation wave beams with high directivity, Proceedings of the 15th Symposium on High Current Electronics. Tomsk, Russia, pp. 383–386, 2008.

Ultra-wideband Active Receiving Array Antenna with Dual Polarization

V.I. Koshelev, E.V. Balzovsky, and Yu. I. Buyanov

Abstract This chapter presents results of the investigations directed to creation of large ultra-wideband active receiving array antennas with dual polarization. The array element is made on the basis of two crossed electric dipoles. Each arm of the dipoles is loaded to the single-stage FET amplifier. Four such elements form a 2×2 module being a component of a multielement array antenna.

Keywords Dipole antennas · Planar arrays · Active arrays · Antenna measurements · Radar polarimetry · Ultra-wideband radiation

1 Introduction

Transmitting and receiving array antennas in high-power ultra-wideband (UWB) radar should be separated in space. This is stipulated by different operation conditions of transmitting and receiving array antennas and first of all conditions by peak power. The demands made to the arrays and, respectively, to their design are essentially different. The transmitting array antennas are developed on the basis of combined antennas and provide radiation of high-power UWB pulses with linear and dual polarization at the expense of dividing into orthogonal sub-arrays and pulse delay in time [1]. The elements of the receiving arrays should have a broad passband for small distortion of UWB signals reflected from sounded objects, small sizes that are important when changing a direction to an object within wide limits, and they should provide simultaneous recording of orthogonal components of the electric field in each pulse. Creation of fully polarimetric UWB radars will allow increasing their possibilities on object detection and recognition.

Antennas based on active crossed electric dipoles completely satisfy the demand made to receiving array antennas for UWB radar. At the first stage of investigations a single electric dipole with an active element based on a single-stage FET amplifier has been developed and experimentally studied [2]. The investigations have shown that minimum pulse distortions are realized when using a sectional dipole with resistive loads. This chapter presents a successive realization of the suggested approach on creation of active multielement receiving array antennas with dual polarization.

V.I. Koshelev (✉)

Institute of High Current Electronics, SB RAS, 2/3 Akademichesky Ave., Tomsk 634055, Russia

e-mail: koshelev@lhfe.hcei.tsc.ru

2 Array Antenna Element

Two crossed 48 × 48-mm dimension dipoles are made by the printed-circuit method on a 1-mm thick foil-clad glass-fiber plastic. The arms of the dipoles are loaded directly to the active element presenting a single-stage FET amplifier [2]. The supply voltage equals to 3 V. The consumption current of the array antenna element is 100 mA. Four active elements have got the coaxial feeders connected to a balancing unit in order to carry out investigations. The developed balancing unit consists of a phase inverter (providing phase shifting by 180º) and a two-stage ring summation unit. Figure 1 presents a physical configuration of an element of the active receiving array antenna with dual polarization together with a balancing unit.

Fig. 1 The element of active receiving dual-polarized array antenna (1) with a balancing unit (2)
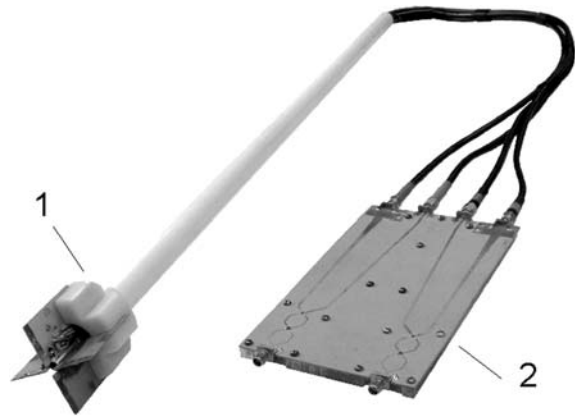
The same balancing unit is used at the output of the 2 × 2-module and multielement array, therefore it deserves careful study. Figure 2 presents the design of one channel of the balancing unit. The input ports 1, 2 and the output port 3, the phase inverter 4 of the length $L = 100$ mm, the strip line 5, and a two-stage ring summation unit 6 are placed on the 162 × 98-mm dimension printed-circuit board made of a 1-mm thick foil-clad dielectric FLAN-5. The elements disposed at the rear side of the plate are indicated by dashed lines. The second channel is placed at the same dielectric plate as a mirror image relative to the horizontal axis.

The phase inverter 4 consists of two exponential transitions from a microstrip line to the double-wire one joined toward each other. As a result of this connection of the lines, the "strip" and the "ground" at point A change their places at point B providing the 180° phase inversion. The electrical length of the uniform microstrip line 5 is equal to the electrical length of the line 4. The elements of
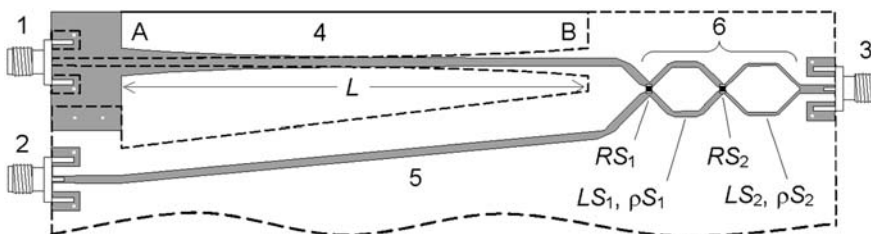
Fig. 2 Design of one channel of the balancing unit

the ring summation unit have got the following parameters: $RS_1 = 240\ \Omega$, $RS_2 = 100\ \Omega$, $\rho S_1 = 61\ \Omega$, $\rho S_2 = 82\ \Omega$. The length of the lines $LS_1 = LS_2$ corresponds to a quarter of the wavelength at the frequency of 2 GHz. The measured passband of a separately manufactured phase inverter is 0.15–10 GHz at VSWR ≤ 2.

The developed balancing unit has got the following characteristics. The amplitude response from the input 1 to the input 3 (Fig. 2) is no less than –3.5 dB in the range of 0.4–3.3 GHz except a narrow resonance at the frequency of 1.25 GHz where the amplitude response descends to –6 dB. The isolation between the ports 1 and 2 is no less than 10 dB in the range of 0.5–3.5 GHz. The measured VSWR at the ports 1 and 2 is not higher than 2 in the frequency range of 0.2–4.8 GHz.

Investigations of the array antenna element and the arrays were made in the time domain. A combined antenna [3] excited by a 0.5-ns length bipolar voltage pulse generator was used as a source of UWB radiation pulses with linear polarization. A TEM antenna of the dimension 1200 × 500 × 80 mm and effective length of 4 cm was used as a reference one to compare the waveforms of the recorded pulses. Pulse waveforms recorded by the dipole with orientation coinciding with the plane of polarization and orthogonal dipole are presented in Fig. 3 (curves 1 and 2, respectively). Polarization isolation between the channels is not less than 25 dB. For comparison, Fig. 3 presents the waveform (four times decreased) of the pulse recorded by the TEM antenna (curve 3).

Fig. 3 Pulses recorded by the dipole coinciding with the plane of polarization (1) and orthogonal dipole (2). *Curve 3* corresponds to pulse recorded by TEM antenna (four times decreased)
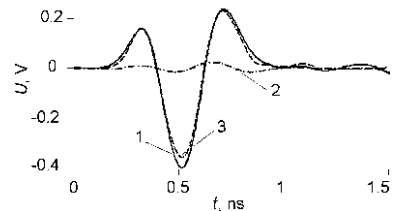
The root-mean-square deviation (σ) of the waveforms of the pulses received by the antennas is not higher than 0.15. The effective length of the active dipole antenna is 1 cm. The operating range of the measured fields is restricted from below by self-noises and from above by saturation of active elements. Special investigations were carried out taking into account possibility of influencing the active receiving antenna by high-power UWB pulses from the transmitting array antenna. It was shown that the active array antenna element survives after being influenced by a pulsed field with the strength up to 6 kV/m. However, long-time oscillations were observed here after the main pulse.

3 2 × 2-Module of Array Antenna

The array antenna module (Fig. 4) consists of four (2 × 2) crossed active dipoles 1, a dielectric base 2 of dimension 160 × 160 mm, a group of summation units 3, and feeder lines covered with an absorbing material 4. The distance between the centers of the dipoles d varied in the limits of 48–100 mm, the distance from the dipole arms to the dielectric base was 140 mm.

Figure 5 presents the block diagram of the array antenna module. Initially, the signals of the similar arms of active dipoles are summated in-phase and then an antiphase component is extracted. The dipoles are conditionally divided into vertical and horizontal. The vertical channel dipoles have got in all for upper and four lower arms. The signals of four upper dipole arms are summed in-phase in the summation unit 1 and the signals of the lower arms are summed in the summation unit 2. To extract the antiphase component corresponding to the vertical polarization, a balancing unit 3

Fig. 4 Array antenna module
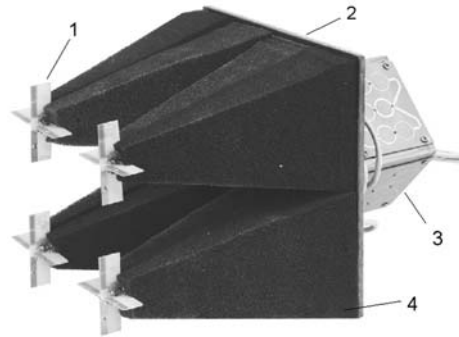
Fig. 5 Block diagram of array antenna module
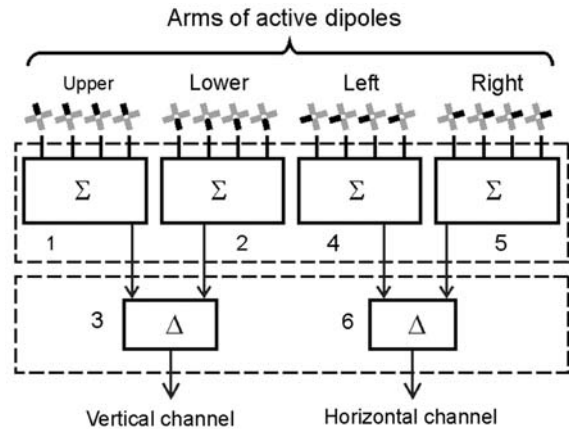
is used. The summation units 4 and 5 and a balancing unit 6 are used, similarly, for the horizontal channel.

The group of summation units consists of four similar printed-circuit boards. Three summation units are placed at 60×67-mm dimensional plates made of a 1-mm thick foil-clad dielectric FLAN-5. The passband of the summation unit ranges from 0.3 to 3.5 GHz at VSWR of ≤ 1.5 at each of four input ports. An amplitude response from each input port to the output port is not less than –7 dB in the indicated frequency band.

The waveforms of the pulses recorded by the array antenna module at $d = 48$, $d = 64$, and $d = 80$ mm are presented in Fig. 6 (curves 2–4, respectively). At $60 \leq d \leq 100$ mm the waveform of the recorded pulses was changed insignificantly. The effective length of the array antenna module was equal to 2.2 cm. At $48 \leq d < 60$ mm there were observed the change of the pulse waveform and increase of the effective length up to 2.35 cm that could be explained by mutual influence of the neighboring dipoles. The root-mean-square deviations of the waveforms of the pulses recorded by the TEM antenna (Fig. 6, curve 1) and the array antenna module were $\sigma = 0.24$, $\sigma = 0.34$ and $\sigma = 0.36$ at $d = 48$, $d = 64$, and $d = 80$ mm, respectively. Polarization isolation between the channels was no less than 25 dB.

Figure 7 presents the measured patterns of the array antenna module in two planes. Here, a pattern is an angular dependence of the square of the maximum voltage value at the array antenna output during a pulse. Increase of the distance between the elements results in the increase of the array

Fig. 6 Pulses recorded by the antenna module
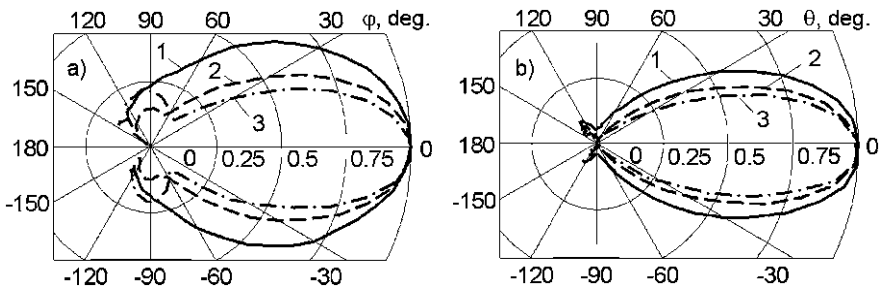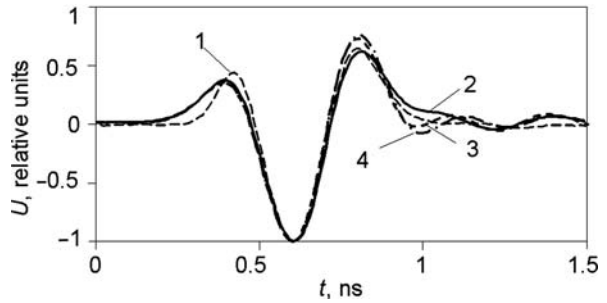
Fig. 7 The pattern by peak power of the array antenna module at H-plane (**a**) and E-plane (**b**). *Curves* 1–3 correspond to *d* equal to 48, 64, and 80 mm

antenna directivity and decrease of the angle range where the waveform of the recorded pulses is preserved. Figure 8 presents the root-mean-square deviation of the recorded pulse waveforms in different directions versus the pulse waveform in the main direction. These distortions are additional besides the waveform distortions in Fig. 6.

Direct connection of the array antenna module to the Tektronix TDS6604 digital oscilloscope in a shielded room has shown that the oscilloscope noises essentially exceed the array antenna module ones. The voltage corresponding to the oscilloscope noise level was equal to 450 μV. Connection of an UWB linear amplifier between the output of the array antenna module and the oscilloscope input increased the noise level up to 3 mV. Taking into account that the gain of linear amplifier is 36 dB, the noise level at the array antenna output can be evaluated as 50 μV. Saturation of the active elements

Fig. 8 Root-mean-square deviation of recorded pulse waveforms in different directions versus pulse waveform in the main direction. Measured (*solid*) and calculated (*dashed*) curves 1–3 correspond to *d* equal to 48, 64, and 80 mm
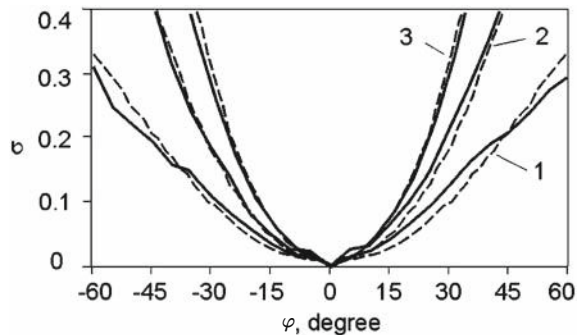
of the array antenna module occurs at the high field strength. At the field strength of 50 V/m (the array antenna module output voltage of 1.1 V), the root-mean-square deviation of the waveform of recorded pulses from the waveform at small fields is $\sigma = 0.1$. Assuming that a pulse can be recorded at the signal/noise ratio of 10 dB, a dynamic range of the array antenna module can be estimated at the level of 70 dB.

4 Multielement Array Antenna

A modular approach was used to construct a 16-element dual-polarized array antenna. The array antenna (Fig. 9) consists of four similar modules that have together 16 crossed dipoles 1 and 4 summation units 2. The output signals of the antenna modules are united in the summation unit 3. Antiphase signals corresponding to two polarizations are extracted into a balancing unit 4.
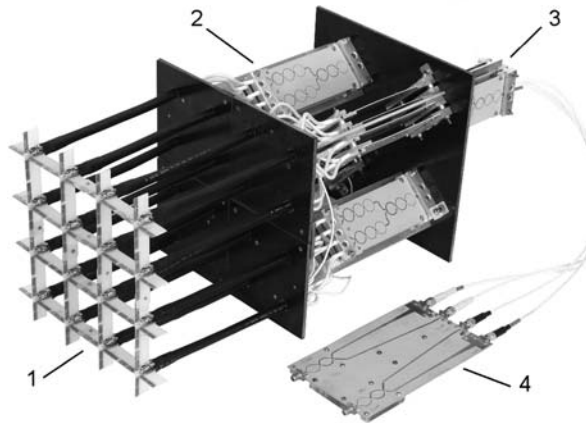
Fig. 9 16-Element dual-polarized array antenna

The distance between the dipole centers is 52 mm, and the dipole length is 48 mm. The distance between the dipoles and the dielectric support is equal to 150 mm and can be filled with an absorbing material. The consumption current is 1.6 A at a 3-V supply voltage. The array antenna dimensions are $21 \times 21 \times 56$ cm, the weight is 2.6 kg.

Measured (solid curves) and calculated (dashed curves) patterns by peak power in H- and E-planes are presented in Fig. 10a and 10b, respectively. The root-mean-square deviation of the recorded pulse waveforms in different directions versus the pulse waveform in the main direction is presented at Fig. 11. At a half peak power level the width of the pattern is equal to 40 degrees and the root-mean-square deviation $\sigma \leq 0.2$.

The waveform of the pulse recorded with the array antenna is presented in Fig. 12 (curve 1). The root-mean-square deviation from the waveform of the pulse recorded with the TEM antenna (curve 2) is $\sigma = 0.2$. The array antenna effective length is 4.5 cm. The polarization isolation between the array antenna channels is not less than 25 dB.
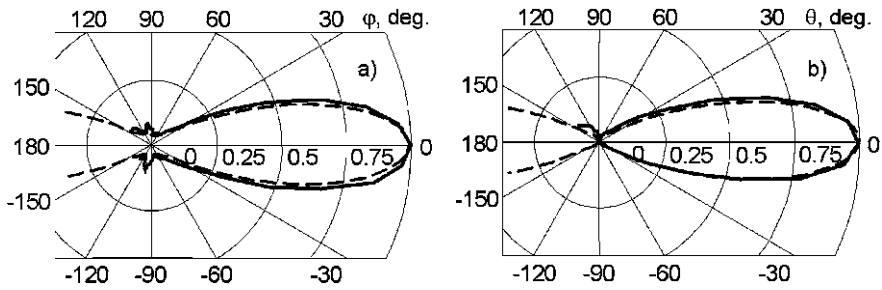
Fig. 10 Measured (*solid curves*) and calculated (*dashed curves*) patterns by peak power of 16-element array antenna at H-plane (**a**) and E-plane (**b**)

Fig. 11 The root-mean-square deviation of recorded waveforms in different directions versus the main direction
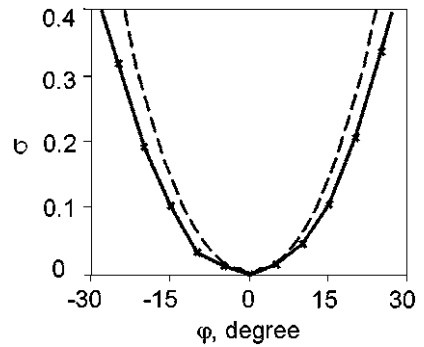
Fig. 12 Pulses recorded by 16-element array antenna (1) and TEM antenna (2)
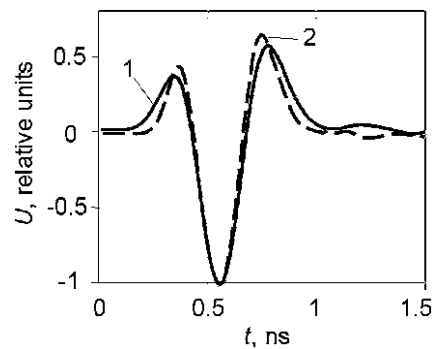
5 Conclusion

An approach to the creation of multielement active receiving array antennas with dual polarization for investigation of UWB signals reflected from radar objects was suggested and substantiated. The next stage of investigations in this direction is development of active steering receiving array antennas. To provide a protection of a receiving array antenna from direct radiation of an UWB source is an important problem as well. The latter is possible to be realized both due to application of absorbing materials and control of active elements of an array antenna.

References

1. A. M. Efremov, V. I. Koshelev, B. M. Kovalchuk, V. V. Plisko, and K. N. Sukhushin, Generation and radiation of high-power ultrawideband nanosecond pulses, Journal of Communications Technology and Electronics, vol. 52, pp. 756–64, 2007.
2. E. V. Balzovsky, Yu. I. Buyanov, and V. I. Koshelev, An active antenna for measuring pulsed electric fields, Russian Physics Journal, v**ol.** 50, 503– 8, 2007.
3. A. M. Efremov, V. I. Koshelev, B. M. Kovalchuk, V. V. Plisko, and K. N. Sukhushin, High-power sources of ultrawideband radiation with subnanosecond pulse length, Proceedings of the 14th Symposium on High Current Electronics. Tomsk, Russia. pp. 446–9, 2006.

Modeling of Broadband Antennas for Room Temperature Terahertz Detectors

Alexander Scheuring, Ibrahim Türer, Nicolas Ribière-Tharaud, Annick F. Dégardin, and Alain J. Kreisler

Abstract The purpose of this chapter is to present modeling investigations dedicated to planar broadband antennas with nearly frequency-independent characteristics. These antennas are used to couple efficiently terahertz radiation to semi-conducting YBCO bolometers of high impedance (kΩ range). Both detector and antenna structures are attached on thin substrates to avoid losses due to substrate high-order modes. The antenna properties (radiation diagram, reflection coefficient, input impedance) have been investigated by software modeling with regard to the need of high impedance and high bandwidth. By modifications of conventional concepts (spiral antenna, log-periodic dipole array), an impedance increase of about 50% could be achieved while maintaining wideband properties at the same time. For extreme high antenna impedance we propose a novel design of a grounded multi-tail dipole antenna. The reached antenna impedance maximum for this structure is 2 kΩ for a bandwidth of 10% at the center frequency $f = 2$ THz. All concepts were proven by measurements of large-scale models in anechoic chambers (in the 1–4 GHz range, typically).

Keywords Terahertz antennas · Wideband antennas · High-impedance antennas · Bolometric detectors · Large-scale models

1 Introduction

Several technologies have been proposed to develop terahertz detectors with broadband spectral response. We focus on uncooled thermal detectors of the bolometer type based on semi-conducting $YBa_2Cu_3O_{6+x}$ thin films (hereafter referred as YBCO): room temperature detectors promise a low-priced usage in multi-pixel terahertz cameras, for instance.

The working principle of a bolometer is shown in Fig. 1. Dependent on its intensity, an incident radiation changes the electrical resistivity of the bolometer. By applying an external current or voltage biasing DC source, this thermal effect can be detected as a variation of the voltage or current, respectively, which can be read out by a CMOS electronic circuit.

In our case a typical $50 \times 50\ \mu m^2$ detection area limited by lateral gold contact pads is patterned in a 0.3 μm thick YBCO film [1]. To improve the terahertz radiation coupling efficiency, a planar

A.J. Kreisler (✉)

SUPELEC/Laboratoire de génie électrique de Paris (LGEP); CNRS UMR 8507; UPMC Univ Paris 06; Univ Paris Sud 11, Gif-sur-Yvette, France

e-mail: alain.kreisler@supelec.fr

Fig. 1 General principle of a
bolometer: Absorbed
radiation is detected as a
change of the thermometer
impedance
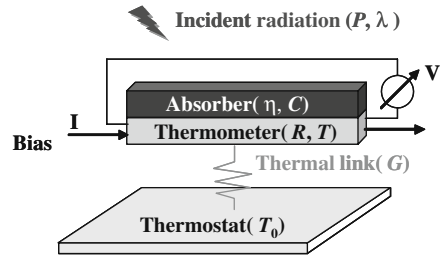
antenna is required. In this context, the challenges concerning the antenna structure are on the one hand the requirement of a large bandwidth (1–4 THz, typically) and on the other hand the difficult matching of the antenna to the device due to the extremely high resistivity of the sensing material ($\rho = 300$–$600\ \Omega$cm), leading to a resistance of the bolometric device as high as 10 MΩ, in the case of a meander-shaped sensing planar geometry, for instance.

A possibility to overcome this high impedance is to change the metal contacts from a lateral setup to a metal-YBCO-metal tri-layer structure as shown in Fig. 2. By using a thin YBCO layer and increasing the area of the contact pads, the detector impedance can be reduced significantly down to the range $Z_{\text{det}} = 1$–10 kΩ. For the antenna impedance a value of $Z_{\text{A}} = 1$ kΩ was defined as our design goal.

Fig. 2 Cross section of a thin
film metal-YBCO-metal
tri-layer structure for a
reduced detector impedance
($t_{\text{metal}} = 200$ nm; $t_{\text{YBCO}} =$
300 nm)
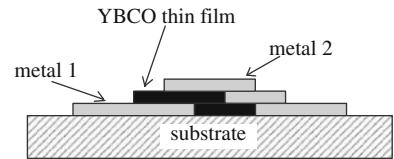
In Section 2 theoretical basics of planar wideband antennas are discussed in context to the required antenna properties (radiation pattern, impedance). In Section 3 results of software modeling and large-scale measurements in the gigahertz range of convenient antenna concepts are presented.

2 Basics of Wideband and High-Impedance Planar Antenna Structures

With regard to the operation in planar multi-pixel arrays, the utilized antenna structures have to fulfill different requirements concerning size, radiation pattern, and, as previously mentioned, bandwidth and impedance.

The size of an antenna is important for different issues like image resolution, gain or thermal capacitance, which limits the speed of the detector. For the shape of the radiation pattern, it is necessary to have a strong main lobe in the desired detection direction, in our case perpendicular to the substrate plane, to improve the radiation coupling. Moreover, side lobes should be minimized to avoid errors caused by cross talk effects between adjacent pixels. Concerning the large bandwidth issue, there exist different approaches in literature like angular, self-complementary, or log-periodic antennas, which promise nearly frequency-independent antenna characteristics [2].

To understand how to adjust the antenna impedance to the high desired value, one has to consider the working principle of antennas. For doing this, a general schematic of an antenna is shown in Fig. 3. We remind that an antenna can be considered as a degenerate transmission line consisting

Fig. 3 General schematic of
an antenna coupled to a
transmission line
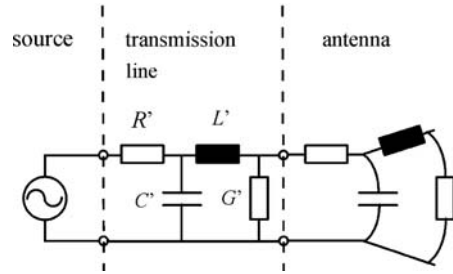
of capacitive (C') parts, inductive (L') parts, and losses caused by non-ideal properties of substrates (G') and the finite conductivity of metals (R').

For low loss materials the impedance of a transmission line can be calculated according to

$$Z_{line} = \sqrt{\left.\frac{R' + j\omega L'}{G' + j\omega C'}\right|_{R',G' \to 0}} = \sqrt{\frac{L'}{C'}}. \tag{1}$$

From (1) it can be seen that the impedance of a line, and consequently of an antenna, can be increased by increasing the inductive parts and by decreasing the capacitive parts. This can be done by selecting narrow line structures for higher inductance and by a wide spacing between the metal parts of the antenna to reduce the field coupling for a lower capacitance. In the following section this approach is used for different antenna types.

3 Simulation and Experimental Results

The cross section of an investigated terahertz sensor pixel is shown in Fig. 4. The antenna and the YBCO detector are attached on a free-standing silicon dioxide (SiO$_2$, of relative permittivity $\varepsilon_{SiO2} = 3.73$) membrane with a thickness $t_{mem} = 300$ nm. The membrane is fabricated on a polyimide substrate ($t_{poly} = 2$ μm; $\varepsilon_{poly} = 3.5$). This setup is the same for all considered terahertz antennas. With the low thickness of the membrane and a low permittivity of the used materials, the distortion of the radiation pattern and a decrease of the impedance can be suppressed. All simulations, both in the terahertz and gigahertz range, were performed with CST Microwave Studio® finite elements software [3].

For testing conveniently the antenna properties with currently available anechoic chamber, large-scale models were designed for the frequency range $f = 1$–4 GHz and fabricated on a Rogers®
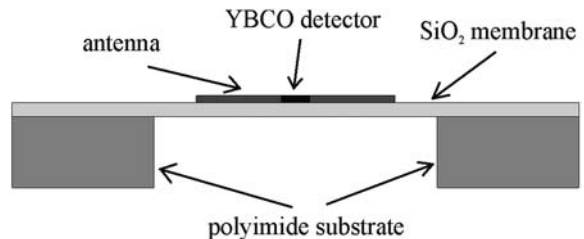
Fig. 4 Schematic of a
detector pixel setup. Antenna
and detector are attached on a
free-standing membrane
($t_{mem} = 300$ nm) to suppress
high-order substrate modes

RT/Duroid 6010LM substrate ($t_{sub} = 1.27$ mm, $\varepsilon_{sub} = 10.2$, tan $\delta_{sub} = 0.0023$) with a copper metallization ($t_{met} = 35$ μm).

3.1 Angular Concept: Spiral Antenna

Two different models of spiral antennas are shown in Fig. 5. The antenna in Fig. 5a is self-complementary and hence exhibits, following Babinet's principle, a constant impedance of $Z_A = 60\pi$ Ω ≈ 189 Ω. The structure in Fig. 5b has the same aperture size, but in order to increase Z_A, the line width is smaller and the slot distance is higher. Simulation results for the impedance are compared in Fig. 6.

Fig. 5(a) Layout of a terahertz self-complementary spiral antenna ($W_{line} = W_{slot} = 5$ μm; $L = 120$ μm) **(b)** Modified spiral antenna for a high antenna impedance ($W_{line} = 2$ μm; $W_{slot} = 8$ μm; $L = 114$ μm)
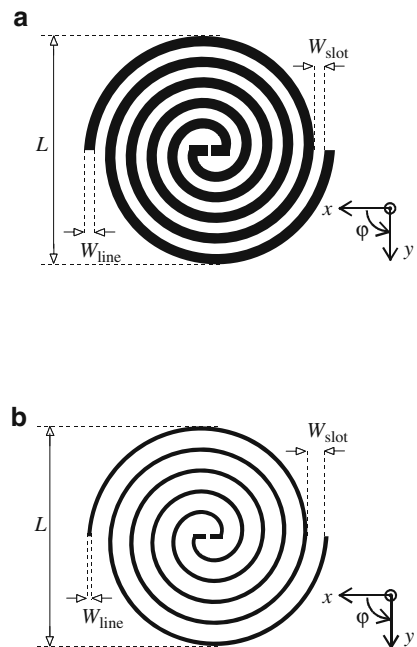
The curves exhibit similar features for both structures. While the imaginary part is slightly decreasing with frequency, the real part is nearly constant over the complete frequency range. For the second structure, the impedance could be increased to about 50%. The corresponding reflection parameter (S_{11}) of this latter antenna is shown in Fig. 7 for two reference impedances. The highest possible bolometer impedance to provide a reflection below –10 dB is therefore ~ 500 Ω.

The radiation pattern exhibits one main lobe perpendicular to the substrate plane without side lobes over the entire frequency range. The radiation patterns for frequencies $f = 2$ THz and $f = 4$ THz are depicted in Figs. 8 and 9, respectively.

In order to check the consistency between simulation and experiment, the simulated antenna characteristics of a large-scale antenna were compared to the results measured in the anechoic chamber. Typical radiation patterns for the higher spiral impedance for $f = 1$ GHz and $f = 3.5$ GHz are depicted in Figs. 10 and 11, respectively, showing a good agreement between measurement and simulation.

Fig. 6 Comparison of the impedance characteristic of both regular (a) and high impedance (b) spiral antennas (see Fig. 5)
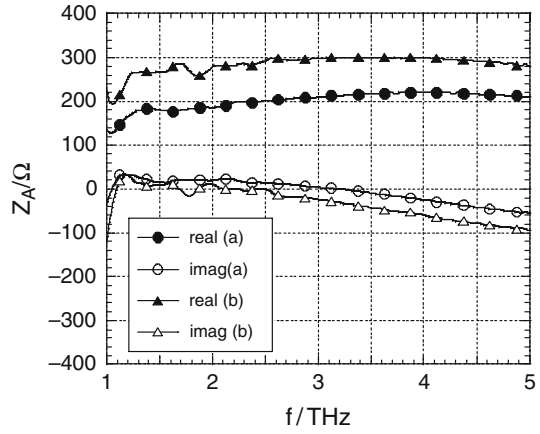
Fig. 7 Reflection parameter of the high-impedance spiral antenna for different reference impedances Z_{ref}
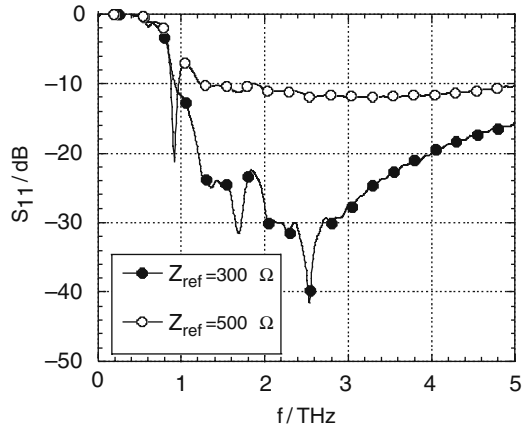
Fig. 8 Simulated radiation pattern of the spiral antenna at $f = 2$ THz for $\phi = 0°$ (●) and $\phi = 90°$ (○)
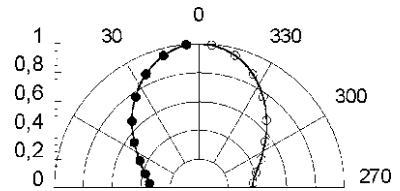
Fig. 9 Simulated radiation pattern of the spiral antenna at $f = 4$ THz for $\phi = 0°$ (●) and $\phi = 90°$ (○)
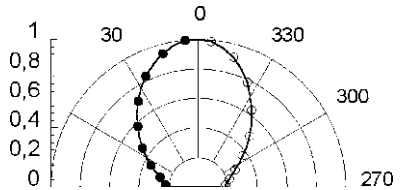
Fig. 10 Simulated (*solid*)
and measured (*hollow*)
radiation pattern at $f = 1$ GHz
for $\phi = 0°$ (●, ○) and $\phi =$
$90°$ (■, □)
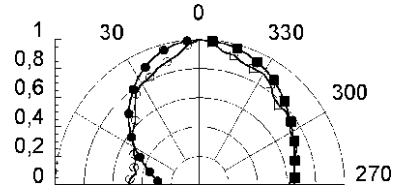
Fig. 11 Simulated (*solid*)
and measured (*hollow*)
radiation pattern at $f =$
3.5 GHz for $\phi = 0°$ (●,○)
and $\phi = 90°$ (■, □)
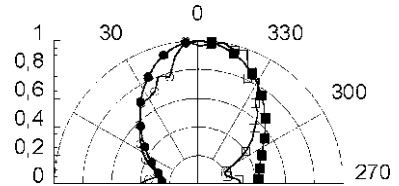
3.2 Log-Periodic Concept: Dipole Array

As an alternative approach, we propose a dipole array antenna. Typically a dipole antenna is used as a half wavelength resonator. It exhibits a low impedance because of the maximum of the current density at the central feed point. By changing the working mode to a full wave resonance, the current at the center decreases to zero from which results, at least in theory, an infinite impedance value. Because of the narrow bandwidth of a single dipole, this concept was extended to a log-periodic array structure to cover the desired frequency range. The antenna layout is shown in Fig. 12. The limitations of real antennas are given by the geometrical parameters. As a consequence of the finite line width, the average impedance of our antenna array is $Z \approx 300$ Ω.

The impedance vs. frequency plot is illustrated in Fig. 13.

From the S_{11} parameter curve (Fig. 14) it can be seen that the reflection remains below the –10 dB line for a reference impedance $Z_{ref} = 400$ Ω.

The results of the radiation pattern are similar to that of the spiral antenna. An example is shown in Fig. 15.
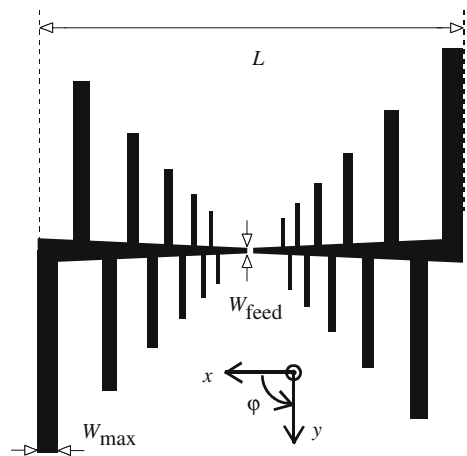
Fig. 12 Layout of the
log-periodic dipole array
($W_{feed} = 2$ μm; $W_{max} =$
7.2 μm; $L = 151$ μm)

Fig. 13 Impedance characteristic of the log-periodic dipole array (see Fig. 12)
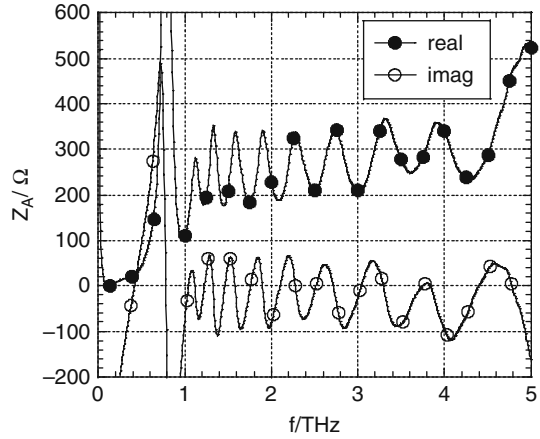
Fig. 14 Reflection parameter of the log-periodic dipole array for different reference impedances Z_{ref}
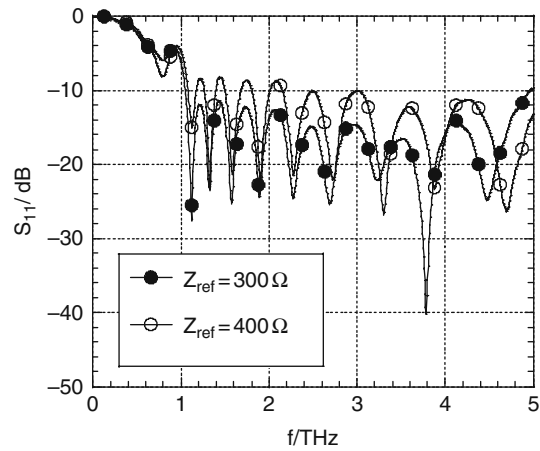
Fig. 15 Simulated radiation pattern of the dipole array at $f = 2$ THz for $\phi = 0°$ (●) and $\phi = 90°$ (○)
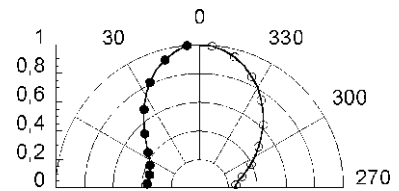
The large-scale measurement results show a good correlation with simulations, as shown in Fig. 16, for instance.

3.3 Novel Concept: Grounded Multi-tail Dipole Antenna

As shown in Sections 3.1 and 3.2, our approach of designing high-impedance antennas was successfully applied for two different antenna concepts. Compared to typically used designs, the impedance

Fig. 16 Simulated (*solid*)
and measured (*hollow*)
radiation pattern of the dipole
array at 3.5 GHz for $\phi = 0°$
($\bullet$, $\circ$) and $\phi = 90°$ ($\blacksquare$, $\square$)
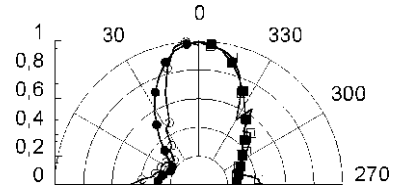
could be increased by some 50% by keeping broadband characteristic at the same time. The extreme high impedance of 1 kΩ could not be reached, however. Therefore we used the effect of the mutual coupling technique [4] to achieve a further enhancement of the impedance value.

In our approach, a dipole antenna was placed parallel to a back metal. The distance between dipole and ground plane was $d = 10$ μm for the terahertz structure. The coupling effect leads to very high, but narrow impedance peaks. To increase the frequency range the dipole was extended by several tails of slightly different lengths (multi-tail dipole antenna structure), as shown in Fig. 17.

The simulated impedance curve is shown in Fig. 18. For a reference impedance of 2 kΩ a bandwidth of about 10% around the center frequency f_0 (here $f_0 \approx 2$ THz) was achieved. This can be seen in the S_{11} curve (Fig. 19). In the frequency range corresponding to the antenna impedance match, the
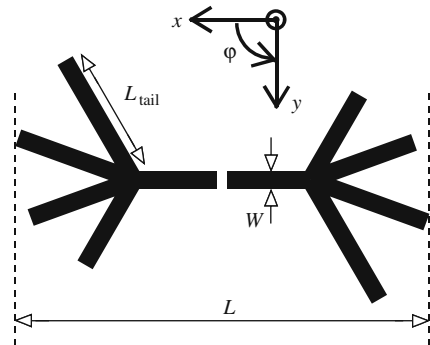
Fig. 17 Layout of the
multi-tail dipole antenna
($W = 5$ μm; $L_{\text{tail}} = 37$ μm;
$L = 118$ μm)
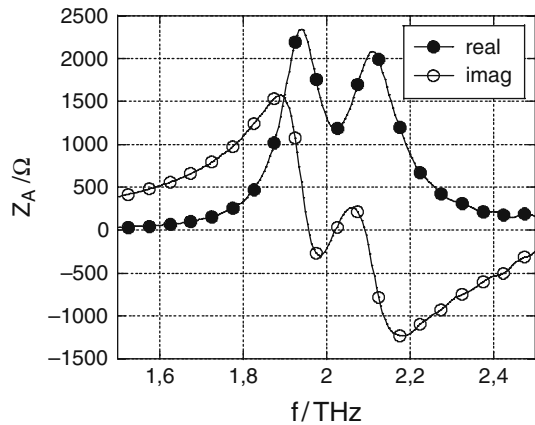
Fig. 18 Impedance
characteristic of the multi-tail
dipole antenna (see Fig. 17)

Fig. 19 Reflection parameter
of the multi-tail dipole
antenna
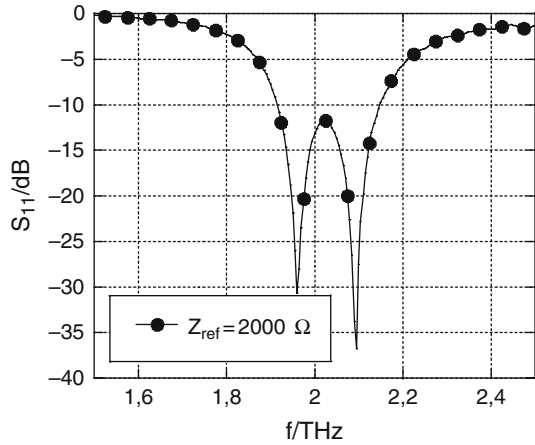
radiation pattern exhibits a main lobe similar to the two former antennas. For example, the radiation pattern at $f = 2.1$ THz is shown in Fig. 20.

For testing the large-scale model in the anechoic chamber, the structure was attached on a ECCOSTOCK® HiK500F substrate ($w_{sub} = l_{sub} = 305$ mm, $t_{sub} = 6.35$ mm, $\varepsilon_{sub} = 10$, $\tan\delta_{sub} < 0.002$). In contrast to the terahertz antenna membrane, in this massive and thick substrate many modes propagate. This results in side lobes in the antenna pattern, as shown in Fig. 21, which confirms the necessity of thin substrates. Simulation and measurement results are in good agreement for the main lobe. Simulation exhibits higher side lobe levels, however.

Fig. 20 Simulated radiation
pattern of the multi-tail dipole
antenna at $f = 2.1$ THz for
$\phi = 0°$ (●) and $\phi = 90°$ (○)
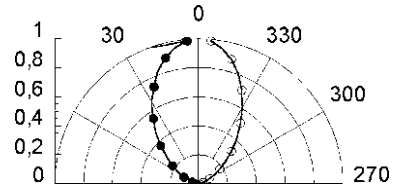
Fig. 21 Simulated (*solid*)
and measured (*hollow*)
radiation pattern of the
multi-tail dipole antenna at
$f = 2.1$ GHz for $\phi = 0°$ (●, ○)
and $\phi = 90°$ (■, □)
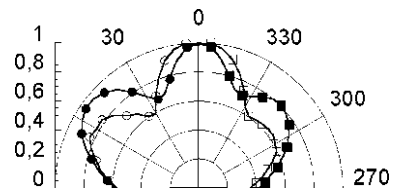
4 Summary

We have proposed different approaches for the design of wideband antennas which are necessary for an efficient radiation coupling to semi-conducting YBCO room temperature detectors that exhibit high impedance, in the kΩ range.

Starting from ultra-wideband self-complementary spiral antennas, an impedance increase of 50% could be achieved by tuning the geometrical parameters. Afterward a full wave dipole array was

introduced. With the very small current density at the feed point, very high impedance (theoretically infinite) is possible. Both approaches are limited by the geometrical constraints of the fabrication technologies. Therefore the maximum reached impedance values are in the range of 300–500 Ω over a frequency range of three octaves. In the third part the mutual coupling effect of a novel multi-tail dipole in front of a metal back plane was proposed to design a highly resistive antenna structure ($Z = 2$ kΩ). One the one hand the ground plane makes such high impedance possible; on the other hand it limits the bandwidth significantly, in our case to about 10%. For the verification of the simulation results, large-scale models were fabricated to operate in the gigahertz range and measured in an anechoic chamber; scaling was performed by wavelength in vacuum with a geometrical factor in the 350–800 range. Simulation and measurement show a good agreement for all scaled models. Only qualitative agreement between terahertz and gigahertz simulations could be achieved; however, insofar as the radiation patterns are concerned. This is due to approximate scaling of the dielectric substrate characteristics, which will be addressed in further investigations.

References

1. M. Longhin, A. J. Kreisler, and A. F. Dégardin, Semiconducting YBCO thin films for uncooled terahertz imagers, Materials Science Forum, vol. 587–588, pp. 273–77, 2008.
2. C. A. Balanis, Antenna theory: analysis and design, Third edition, John Wiley & Sons, New York, 2005.
3. http://www.cst.com.
4. C. Sydlo, Planar terahertz antenna optimisation, IEEE/ACES International Conference on Wireless Communications and Applied Computational Electromagnetics, pp. 878–82, 2005.

100 THz Broadband High-Power Antennas – Results of Modeling and Antennas Future Applications

A. Podgorski, W. Prather, S. Yakura, and J. MacGillivray

Abstract The purpose of this publication is to demonstrate the results of supercomputer modeling of broadband antennas operating up to 100 THz. The aim of modeling was to achieve the highest possible antenna gain and peak power, the highest gain uniformity and lowest sidelobes, while maintaining the smallest antenna aperture and lowest multi-antenna coupling.

Keywords Teraherz (THz) · Broadband · Antennas · Modeling · Applications

1 Introduction

Bridging the gap between microwave frequency region (100 GHz) and optical frequency region (100 THz) occupies minds of many scientists, as the THz region of the EM spectrum could provide advantages in the area of imaging, communication, and possibly high-power atomic interactions that could benefit security, defense, medical field, and non-destructive testing.

Majority of current research at terahertz frequencies is based on narrowband approach and falls into category of passive and active. At normal temperatures, all objects are constantly emitting relatively low level of terahertz rays that are easy to detect with passive narrowband terahertz systems. However, active terahertz systems that fire terahertz rays at an object and analyze the radiation reflected back or going through do not need to be restricted to narrowband. In our opinion, the presented broadband terahertz antenna technology should advance non-linear interaction for pulse sharpening, focusing, or shortening and it should benefit development of space radar systems.

The modeling results addressed in this publication are based on research in the area of 100 GHz broadband antennas, sensors, high-power generators, and single pulse 5 ps receivers [1, 2]. In the modeling process, entire terahertz frequency region extending from 100 GHz to 100 THz was covered using three TEM-Horn antennas – one operating from 100 GHz to 1 THz [3], the second from 1 to 10 THz, and the third from 10 to 100 THz. The low frequency of operation of each modeled antenna was determined by size of the antenna aperture (mouth of the antenna), while the upper frequency was limited by angular opening of the horn. High power capability of antennas was assured by use of teflon septum coating.

A. Podgorski (✉)
Air Force Research Laboratory, Kirtland AFB, NM 87117, USA
e-mail: a.podgorski@ieee.org

2 Broadband Antennas

2.1 General Information

Very low beam dispersion of laser systems that are dependent on signal amplitude, allows achieving angular resolution of approximately 1 milli-radian. For the broadband electrical systems to compete with the optical systems, the aspect of angular resolution is of primary importance. The very low angular resolution of 1 milli-radian, similar to resolution of lasers, was obtained for the first time in broadband, time-domain millimeter wave systems operating in the 5–70 GHz frequency range [1]. The millimeter wave antenna of [1], that had radiating diameter of only 10λ at the highest frequency of operation, allowed achieving 1 milli-radian angular resolution using the pulse rise time sensing rather than pulse amplitude sensing. Narrowband laser, that uses pulse amplitude sensing, would require 1000λ radiating diameter to achieve the same, 1 milli-radian angular resolution.

Proposed design of modeled broadband terahertz antennas is based on [1] and the 3D view of the antenna required for modeling is presented in Fig. 1. In all cases the 3D models were created using robust, trillion cell CAD-based Cartesian mesh generator for finite difference time domain (FDTD) method. Depending on the frequency of operation of the modeled antenna, appropriate Cartesian mesh with number of cubic cells required for the FDTD code was generated.

During the modeling process of three different antennas the only parameters that were changed were size of the cubic cell (6 µm, 0.6 µm, 60 nm), and length of the antennas (50 mm, 16.5 mm, 5 mm). Considering that all antenna dimensions, except the length, were scaled proportionally to the wavelength at the highest frequency, minimal change in the value of calculated parameters occurred, and consequently only few diagrams representing specific model parameters are shown. As such, for all antennas the achieved gain is presented, while only for one antenna the size of the antenna beam (E-field) plot and rise time of the generated E-field are included.
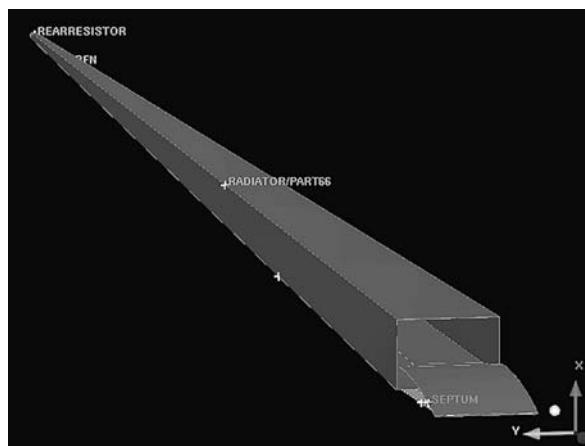
Fig. 1 3D view of the antenna used for modeling of all terahertz antennas

2.2 Broadband Antenna Operating in the Frequency Range of 100 GHz to 1 THz

Modeling of antenna operating in the frequency range of 100 GHz to 1 THz, required $10,000 \times 500 \times 400$ cells mesh that was generated by the Cartesian mesh generator. The size of each cubic mesh was confined to 6 μm that corresponds to 0.02λ at 1 THz, the highest frequency of operation. Our calculation was done on a 100 processor supercomputer (SC) and required 15 hours of computation time. Calculated E-field of Fig. 2 shows uniform beam that corresponds to 1.8 mm size of the antenna mouth. Beam dispersion is limited to ± 18 milli-radians or $\pm 1°$.

Calculated rise time of the generated E-field in y directions of Fig. 3 shows 500 fs rise time at the center of the beam, and it indicates 1 THz as the maximum frequency of operation. The calculation shows that, by using the pulse rise time sensing method, the ± 5 milli-radians or $\pm 0.3°$ angular resolution is achievable with the diameter of the mouth of the horn limited to only 7λ.

Comparison between Figs. 2 and 3 reveals the advantage of using the pulse rise time sensing method over the amplitude method. The steep slops of the rise time graph are indicative of very high sensitivity of the method.

The most important parameters of any antenna are visualization of the E-field in front of the antenna and the gain. Figure 4 shows the calculated E-field at the center of the beam and the power gain of the antenna in reference to the aperture based power gain. According to Fig. 4, the antenna can operate up to 1.5 THz.

Considering the importance of antenna ability to operate under high-power conditions during modeling teflon septum coating, limited to only one layer of cells, was used. It was expected that
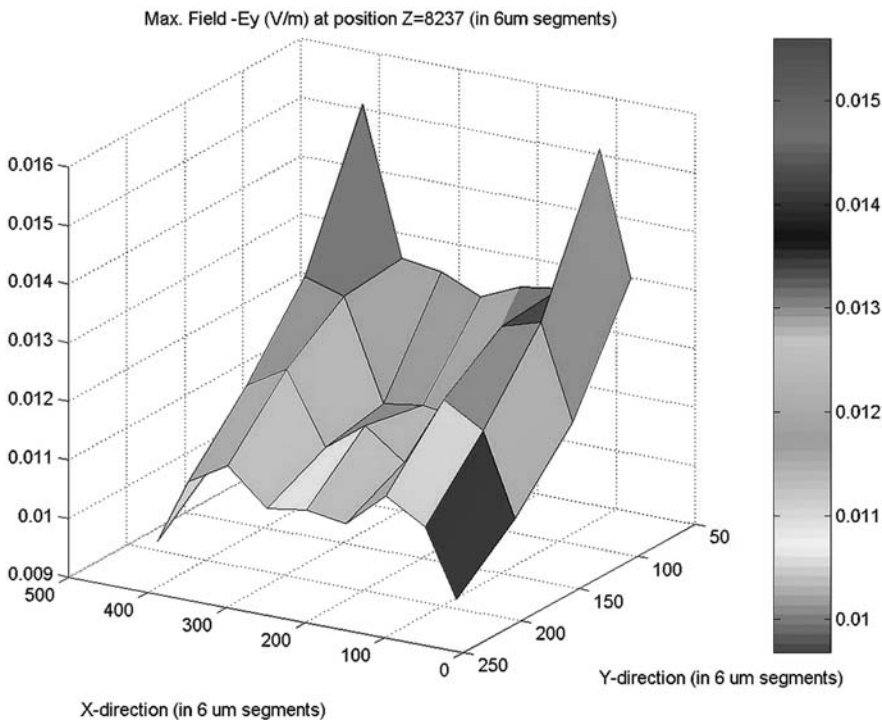
Fig. 2 Calculated antenna beam – Ey-field plot
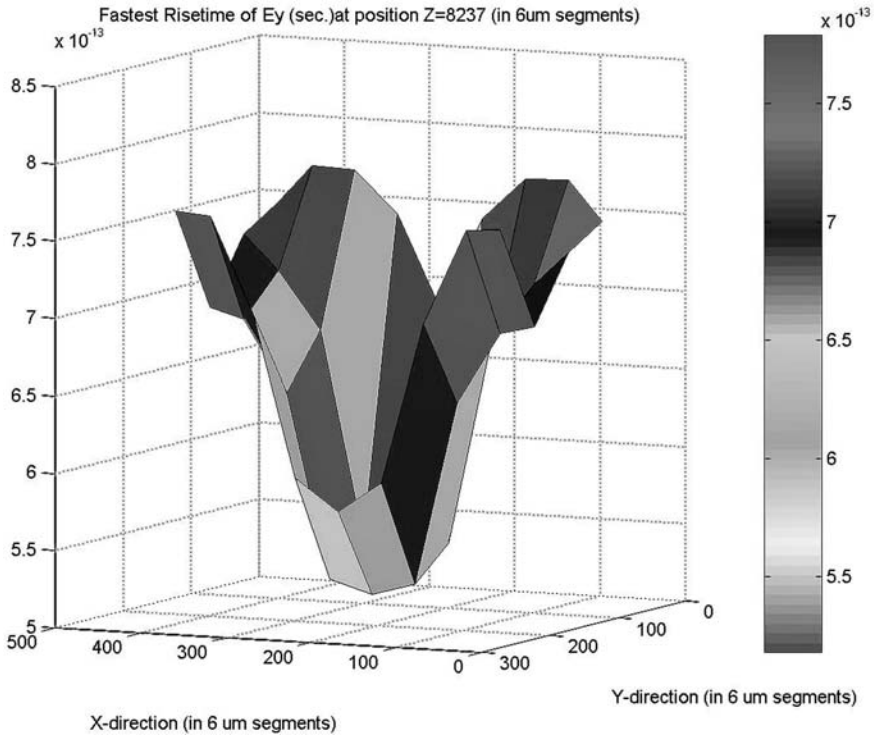
Fig. 3 Calculated rise time of the generated Ey-field
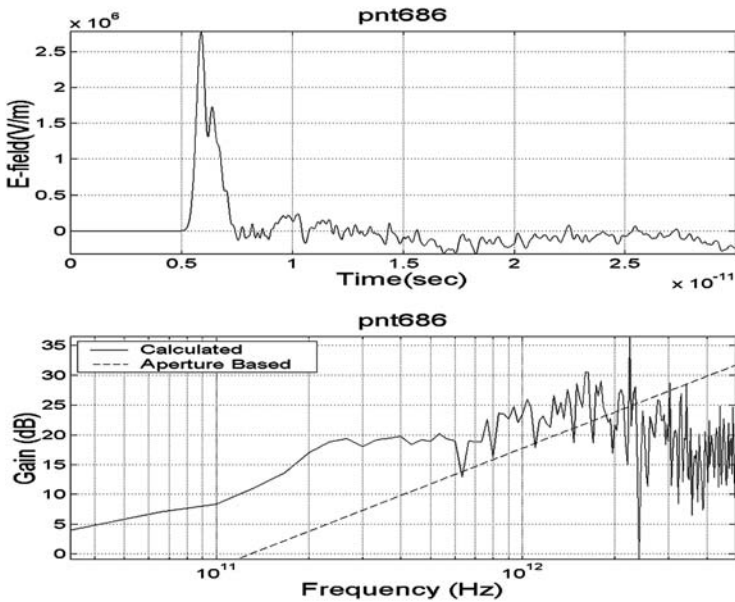
Fig. 4 Calculated E-field and power gain of the 100 GHz to 1 THz antenna – 6 μm grid size, no dielectric coating

as in our previous experiments, use of teflon coating would result in an increase of peak power of approx. 1000 times and reduction of maximum frequency of operation and gain. Figure 5, that shows the calculated E-field at the center of the beam and the power gain of the antenna in reference to the aperture based power gain, clearly indicates reduction of the maximum frequency of operation from 1.5 THz for the antenna without teflon (Fig. 4) to 1.2 THz and reduction of power gain by approximately 3.8 dB.
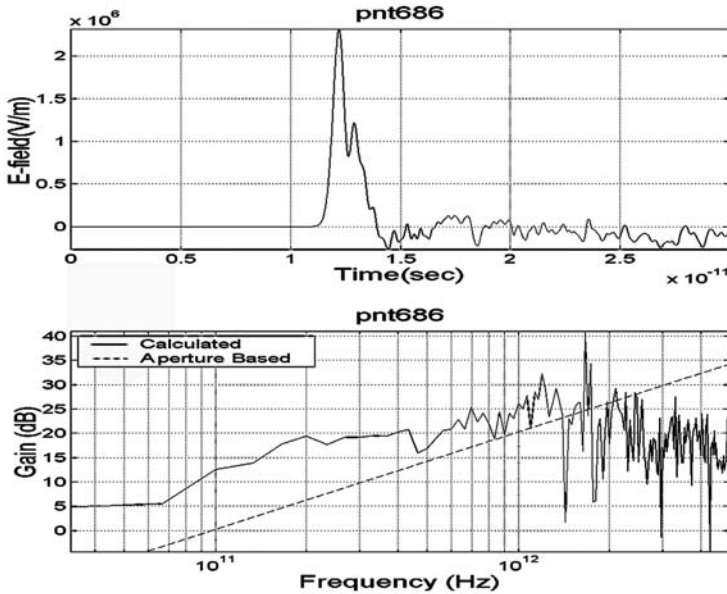
Fig. 5 Calculated E-field and power gain of the 100 GHz to 1 THz antenna – 6 μm grid size, teflon coating

Correctness of antenna design process was verified by calculating how power gain and operational bandwidth are affected by shortening the antenna. The power gain and frequency response of half-length antenna is shown in Fig. 6.

Comparing Fig. 6 (shortened antenna), with Fig. 4 (optimally designed antenna), indicates frequency bandwidth reduction from 1.5 THz to 850 GHz and 6 dB power gain reduction. Optimization of an antenna is of primary importance.

Furthermore, we also verified that accuracy of computation was only minimally affected when the grid size was changed from the nominal 6 to 0.6 μm.

2.3 Broadband Antenna Operating in the Frequency Range of 1–10 THz

Modeling of antenna operating in the frequency range of 1–10 THz required $32,000 \times 500 \times 400$ cells mesh that was generated by the Cartesian mesh generator. The size of each cubic mesh was confined to 0.6 μm that corresponds to 0.02λ at 10 THz, the highest frequency of operation. Our calculation was done on a 500 processor supercomputer (SC) and required 27 hours of computation time therefore only limited number of results is presented.

As in case of antennas operating in frequency range of 100 GHz to 1 THz, the antenna's high power capability (use of septum teflon coating) was verified. Figure 7 shows the calculated E-field
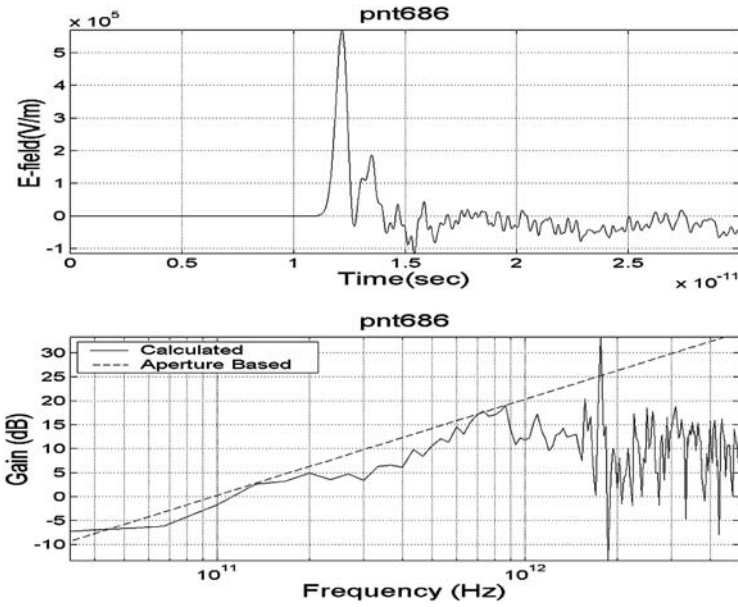
Fig. 6 Calculated E-field and power gain of the half length 100 GHz to 1 THz antenna – 6 μm grid size, no dielectric coating
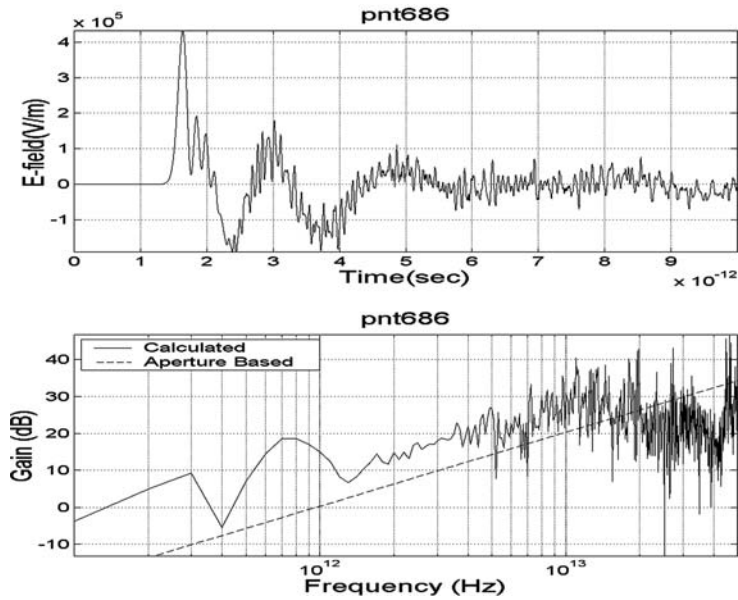
Fig. 7 Calculated E-field and power gain of the 1–10 THz antenna – 0.6 μm grid size, teflon coating

at the center of the beam and the power gain of the antenna in reference to the aperture-based power gain. The figure indicates 12 THz as maximum frequency versus computed 16 THz for antenna without teflon. Furthermore, for teflon-coated antenna 2 dB power gain reduction occurred.

2.4 Broadband Antenna Operating in the Frequency Range of 10–100 THz

Modeling of antenna operating in the frequency range of 10–100 THz required $100,000 \times 500 \times 400$ cells mesh that was generated by the Cartesian mesh generator. The size of each cubic mesh was confined to 60 nm that corresponds to 0.02λ at 100 THz, the highest frequency of operation. Our calculation was done on a 1000 processor supercomputer (SC) and required 77 hours of computation time. Realizing the cost associated with computation we only planned to make two runs. Unfortunately, during the automated mesh generation process an error occurred and it was discovered only during the analysis of the SC run.

Should the conditions permit, the 10–100 THz antenna mesh will be regenerated and the modeling process will be repeated. However, on the base of the results obtained for antennas operating in the 100 GHz to 1 THz and 1–10 THz, we anticipate that for the antenna without teflon coating, the pulse peak E-field should be in the vicinity of 100 kV/m and maximum frequency of operation should reach 150 THz. We foresee that the antenna power gain should be similar to power gain in the lower frequency antennas and be in the range of 10–30 dB. In our judgment, addition of teflon coating should reduce the frequency of operation from 150 THz to approx. 120 THz and reduce the peak power gain by approx. 1 dB. However, an accurate verification of our prediction will only be possible if the modeling of the 10–100 THz antenna will be repeated.

3 Applications of Broadband Antennas

Our modeling results let us to believe that the broadband terahertz antennas could benefit development of terahertz radar systems (stratospheric [4] and anti-collision radar) and THz imaging (IR, Raman and terahertz spectroscopy, terahertz microscopy).

3.1 Terahertz Radar Systems

As it was shown during AMEREM 2006 presentation [4], broadband stratospheric radar systems, using THz antenna, are capable of operating over the height of 5 km above the Earth, with an angular resolution of 1 milli-radian that is corresponding to angular resolution of 15 m at a distance of 15 km. Such systems can detect targets, even as small as few centimeters in size, and even if they are covered with variety of stealth absorbers.

Considering that, the bands above 100 GHz are currently free from other transmitters, an easily placement of anti-collision radar systems will be possible. The high time resolution of broadband radar systems will result in reduction of time errors that are normally associated with the movements of the radar transmitter/receiver and targets – particularly valid in a very dense traffic.

3.2 Terahertz Imaging

Broadband THz antennas will offer a new way for the development of imaging systems such as IR, Raman, terahertz spectroscopy, and terahertz microscopy. Current nano-technology research could benefit from a new tool that will allow visualization at the molecular level and therefore it will allow creating structures with new properties. The broadband technology offers advantages, not available with the use of narrowband technology, such as "sub-nanometer" level resolution, time-resolved imaging allowing visualization of non-linear system, thin coating interfaces, and spectroscopic material visualization.

4 Conclusions

Most important conclusion from our modeling is that for the first time, broadband high gain antennas operating up to 100 THz allow reaching femtosecond rise time and kilowatt peak power. We conclude that single high gain and high-power broadband antenna will allow achieving power density of TW/m^2. One can only foresee that use of an antenna array focused to a single point could result in reaching peak power density of PW/m^2. Results show that, using the pulse rise time sensing method, available only with broadband antennas, milli-radian angular resolution is achievable for antennas that, at highest frequency, have the size of the mouth limited to 7λ. Such angular resolution is not achievable in a narrowband system.

References

1. A. S. Podgorski, K-Band Shoot Through Obscuration (STO) and Training Scoring System Technology Demonstration, Final Report for Naval Air Warfare Center Training Systems Division, 12350 Research Parkway, Orlando, FL 32826-3275, March 15, 2002.
2. A. S. Podgorski, 100 GHz Broadband High Power Antennas, Chapter 33, Ultra-wideband Short-Pulse Electromagnetics 7, Springer, Germany 2007.
3. A. S. Podgorski, W. D. Prather, S. J. Yakura, and J. T. MacGillivray, Modeling of THz Broadband High Power Antennas, Proceedings of 2007 North America URSI Meeting, Ottawa, Canada, July 2007.
4. A. S. Podgorski, W. D. Prather, S. J. Yakura, and J. T. MacGillivray, THz Technology in Application to Space Radar Systems, Proceedings of AMEREM 06 Conference, Albuquerque NM, USA, July 2006.

Traveling-Wave Switches and Marx Generators

C.E. Baum

Abstract This chapter considers a possible technique for reducing the rise time of high-voltage switches by placing an array of smaller voltage switches in a traveling-wave geometry. This same technique can also be incorporated in a Marx generator.

1 Introduction

As technology pushes toward faster pulse-power systems, one searches for better design concepts. What are perceived to be limitations may perhaps be overcome by new design concepts. This chapter addresses switching and Marx generator speed by incorporating them in transmission-line geometries. This leads to the related concepts of traveling-wave switch and traveling-wave Marx generator.

2 Traveling-Wave Switch

In [1] fundamental limits for switching speed are based on the arc inductance for the shortest switch-electrode spacing for a given voltage across the switch. This in turn requires the highest dielectric strength switching medium, this also being influenced by any requirement for repetitive switching, requiring switch recovery before the next pulse. By rapidly charging the switch some improvements can be gained, but this has its limits.

By analogy to traveling-wave or distributed amplifiers [2], let us have a switch-closure propagate along a line array of switches as indicated in Fig. 1. With differential charging voltages $\pm V_{\mathrm{ch}}$ across the whole array of N switches, each switch initially has a voltage of $2\,V_{\mathrm{ch}}/N$ across it. This is accomplished by some high-impedance resistive grading network, say N resistors, each of resistance R across each switch.

One then triggers switch 1, which, in turn, overvolts switch 2, and on to switch N. The switches and associated electrical connections form the center conductor of a transmission line along which waves can propagate. As each switch closes it sends out two waves which can be designated as forward and backward. Each wave has amplitude V_{ch}/N, adding up to V_{ch} for the whole array. Ideally

C.E. Baum (✉)

Department of Electrical and Computer Engineering, The University of New Mexico, Albuquerque, New Mexico
e-mail: carl.e.baum@ieee.org

Fig. 1 Traveling-wave switch
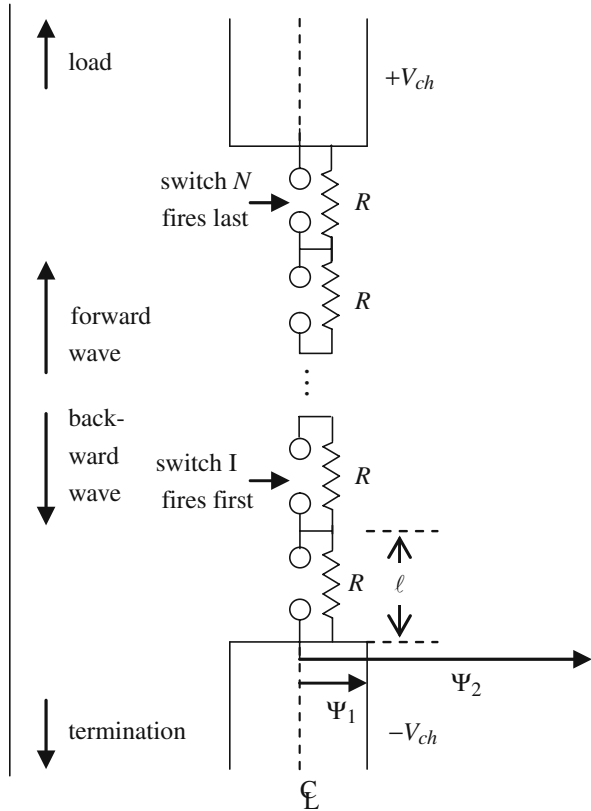
the wave speed approaches the speed of electromagnetic propagation in the surrounding dielectric medium (near c in the case of various gases). In this case the forward wave has a rise time limited approximately by that of a single switch, each switch contributing to the sharpening of the wave front. The backward wave is, of course, highly dispersed and appropriately terminated for negligible reflection.

The transmission-line characteristics of this array then need consideration. Letting Z_c be the characteristic impedance at both ends of the array, we then need to have the switch array have the same transmission-line characteristic impedance. Thinking of a lumped-element transmission line, let each switch and associated conductors have length l and consider their inductance L_0 and capacitance C_0. We need to match these to

$$L' = \mu f_g = \frac{L_0}{l}, f_g = \frac{1}{2\pi} \ln\left(\frac{\Psi_2}{\Psi_1}\right)$$

$$C' = \varepsilon f_g^{-1} = \frac{C_0}{l}, Z_c = \left[\frac{L'}{C'}\right]^{1/2},$$

(1)

$\mathrm{v} = [\mu\varepsilon]^{-1/2} =$ wave propagation speed in medium
$\mu =$ permeability of medium (typically μ_0)
$\varepsilon =$ permittivity of medium
$\Psi_1 =$ inner diameter of coaxes at both ends of switch array
$\Psi_2 =$ outer diameter of coaxes at both ends of switch array

This will make both the wave speed and characteristic impedance match that of the coaxes at both ends of the switch array.

For single-channel switches one can partially compensate for the switch inductance by increasing the radius of the conductors between the switches to greater than Ψ_1. This also increases the capacitance for a portion of the cell length, l. So some compromise may be inevitable.

Another approach utilizes multichannel switch concepts discussed in [3]. As illustrated in Fig. 2, one might have hollow circular cylinders (of radius Ψ_1) with switching occurring between the ends of these truncated cylinders. One might also have longitudinal slots to increase transit time isolation between arcs crossing the same switch gap (see [3] for further discussion). Another possible use for the hollow cylinders is the use of this central path for optical (or other) propagation from one switch gap to the next for the forward wave.

Fig. 2 Array of multichannel switches

possible slots to promote multi-channeling
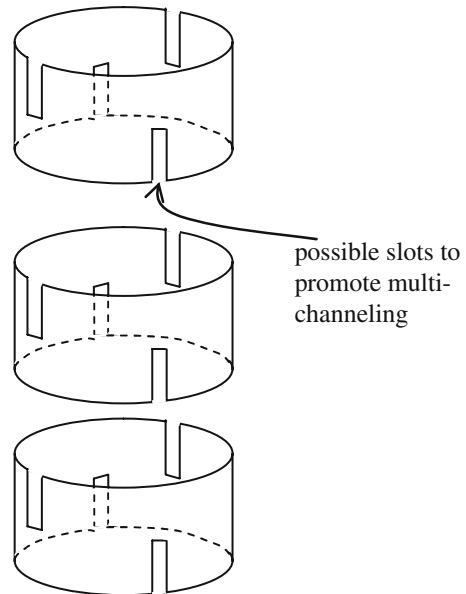
3 Traveling-Wave Marx Generator

Now by a simple substitution for each switch section of length l in Fig. 1, let us substitute a Marx-generator section as in Fig. 3. The connections between successive switches are replaced by two high-ε dielectric blocks. As such, these dielectric pieces act like conductors at high frequencies, thereby becoming part of the waveguide structure. Their radius takes the role of Ψ_2 (or a little larger, depending on the switch geometry).

Now the two transmission lines at each end of the switch array are initially uncharged. Each section, consisting of dielectric-switch-dielectric (with electrical connections) is now charged to $\pm V_0$ across the switch by a differential charging network (as in [4]), including a neutral (or reference zero voltage) connection with suitable isolating impedances so as not to load significantly the Marx generator after Marx erection. The neutral then also establishes the initial zero voltage on the two transmission lines at the ends of the switch array.
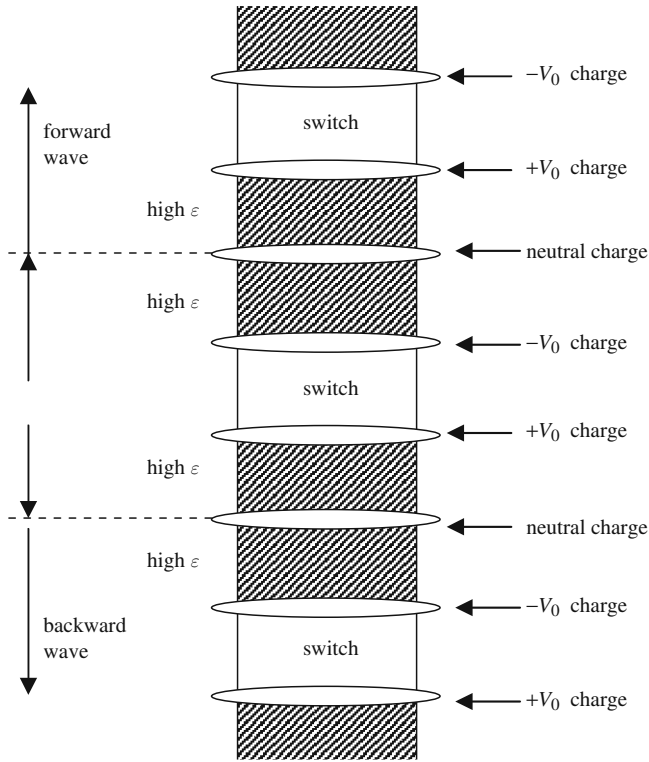
Fig. 3 Section of traveling-wave Marx generator

4 Concluding Remarks

The traveling-wave Marx generator is then quite similar to the traveling-wave switch. The difference lies in how the switches are charged. There is still much to be optimized. For example, what should be the ratio of switch rise time to the transit time l/v for each section. Also the switches need not all be identical; one may taper their characteristics as one goes from switch 1 to switch N.

References

1. J. M. Lehr, C. E. Baum, and W. D. Prather, Fundamental Physical Considerations for Ultrafast Spark Gap Switching, Switching Note 28, June 1997, pp. 11–20, in E. Heyman, B. Mandelbaum, and J. Shiloh (eds.), Ultra-wideband, Short-Pulse Electromagnetics 4, Kluwer Academic/Plenum Publishers, New York, 1999.
2. F. E. Terman, Electronic and Radio Engineering, McGraw Hill, New York, 1955.
3. C. E. Baum and J. M. Lehr, Some Considerations for Multichannel Switching, Switching Note 31, January 2002.
4. C. E. Baum and J. M. Lehr, Charging of Marx Generators, Circuit and Electromagnetic System Design Note 43, September 1999, Parallel Charging of Marx Generators for High Pulse Repetition Rate, pp. 415–22, in P. D. Smith and S. R. Cloude (eds.), Ultra-wideband, Short-Pulse Electromagnetics 6, Kluwer Academic/Plenum Publishers, 2002.

High-Voltage and High-PRF FID Pulse Generators

V.M. Efanov, M.V. Efanov, A.V. Komashko, A.V. Kriklenko, P.M. Yarin, and S.V. Zazoulin

Abstract Several types of pulse generators with amplitude from 200 to 10 kV, rise time from 200 to 50 ps, pulse duration from several nanoseconds to 100 ps have been developed. At amplitude of 100–200 kV maximum pulse repetition frequency (PRF) in continuous operation can reach 2–5 kHz. Testing of such pulse generators has been performed, and the tests have shown that total efficiency can reach more than 60% at pulse duration of 1–2 ns. Tests have also revealed that electric strength of connectors and transmitting cables rapidly decrease at pulse repetition frequency of 1 kHz and higher. At an amplitude of 10 kV, a rise time of about 100 ps, a pulse duration of 0.5 ns, and an operating frequency of 200 kHz in continuous mode have been reached. The jitter of the delay time between an external triggering pulse and the output high-voltage pulse from the generator is about 10–20 ps. A new type of pulser, which forms voltage pulses with amplitude of 5–10 kV, rise time of 0.5–1 ns, pulse duration of 1–2 ns, operating at pulse repetition rate of 3–6 MHz, has been developed.

Keywords Pulse source · Fast ionization devices (FID) · High voltage

1 Introduction

High-voltage nano- and picosecond pulses are used in laser, accelerator, radar applications as well as in many other fields of technology and research. Forming of voltage pulses with peak power from several megawatts to tens of gigawatts and pulse duration of 1–100 ns traditionally is done using spark gaps and thyratrons, but short lifetime, switching instability, and low pulse repetition rate are imposing significant limits for certain applications.

FID GmbH has developed a series of turn-on all-solid-state FID (fast ionization devices) and turn-off DRD (drift recovery diodes) switches with a peak power of more than 1 GW and is offering several types of nano- and picosecond pulse generators with unique set of specifications.

2 High-Voltage FID Picosecond Pulse Generators

Figure 1 shows the pulse generator FPG 200-1PN with maximum peak amplitude of 200 kV into 50 Ω. The rise time is 200 ps, pulse duration is about 1 ns, and maximum PRF is 1 kHz. The

V.M. Efanov (✉)
FID GmbH, Burbach, Germany
e-mail: vlad@fidtechnology.com

Fig. 1 FPG 200-1PN pulse generator

dimensions of the pulser are $480 \times 500 \times 160$ mm; the weight is about 30 kg. Figure 2 shows an output pulse of FPG 200-1PN.

A block diagram of the generator is shown in Fig. 3.

FPG 200-1PN can operate in internal and external triggering modes. For external triggering it is necessary to apply pulses with amplitude of 5 V and 100–1000 ns duration. Delay time between an external triggering pulse and high-voltage output pulse is 290 ns. If the PRF is up to 100 Hz then delay time drift during the first 20 min is 1.5 ns. If PRF is up to 1 kHz then the delay time is increased by 2.5 ns during the first 15–20 ns. The increase of the delay time is caused by heating up structures
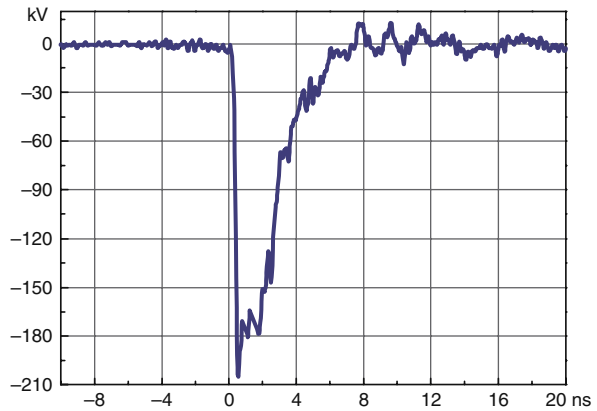
Fig. 2 FPG 200-1PN pulse shape
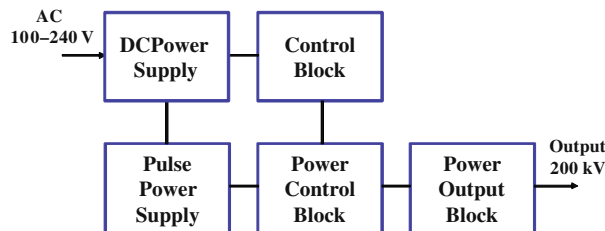
Fig. 3 FPG 200-1PN block diagram

and electronic components inside the generator to 40–50°C. In further operation delay time remains stable if ambient air temperature is constant within 2–3°C range. Delay time stabilization circuits have been developed which allow limiting temperature drift to 100–200 ps for temperatures from +20 to +50°C.

A very important specification of the pulser operation is jitter. Measurements of this parameter of FPG 200-1PN have shown that jitter of the output pulse relative to triggering pulse is not more than 30 ps. Jitter is not affected by heating of the generator and its repetition rate. At the same time it was found that jitter is increased to 50–70 ps if the rise time of a triggering pulse is increased from 1–3 to 20–30 ns.

Amplitude stability of output pulses is about 1–1.5% and, as research has shown, is dependent on stability of power supplies used.

FPG 200-1PN pulse generator has adjustable amplitude of the output pulses in the range of 100–200 kV.

Lifetime testing of FPG 200-1PN was performed at maximum amplitude of 200 kV and maximum PRF of 1 kHz during 10 days of continuous operation for 8 hours per day. After 42 hours of operation Teflon insulation of an output cable connector was broken. Most likely the cause of breakdown was in non-uniformity of Teflon layer. When lifetime testing was finished, all major operating specifications were measured. No changes from initial state were observed.

Pulse generator FPG 30-10PN is forming voltage pulses with amplitude of 30–40 kV into 50 Ω load at maximum PRF of 10 kHz. Rise time is about 100 ps, pulse duration is 0.5–1 ns. The pulser is air cooled and operates from 100 to 240 V AC mains.

Figure 4 shows an oscillogram of a pulse generated by FPG 10-100PN with maximum pulse repetition rate of up to 100 kHz in continuous mode. Voltage amplitude is up to 10 kV, rise time is 100 ps, and jitter is less than 20 ps. Testing of FPG 10-100PN has been performed at 100 kHz in continuous non-stop mode for 8 hours. During the first 10 min the delay time between triggering and output pulse has increased from 115.50 to 115.85 ns. During the next hour the delay time has risen to 115.89 ns and remained stable until the end of the test with an accuracy of 20–30 ps. Jitter during the whole test remained constant in the range of 15–20 ps. The pulser has a standard housing of 480 × 460 × 120 mm and a weight of about 20 kg. It uses a forced air cooling and requires input power of 100–240 V AC.
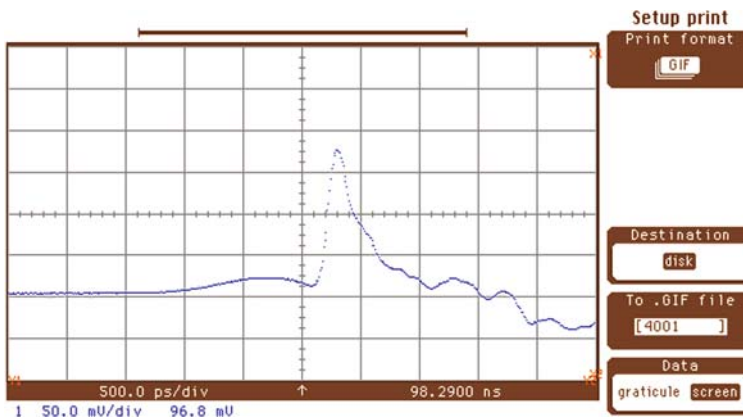
Fig. 4 FPG 10-100PN Pulse shape

Increasing the PRF to higher than 10 kHz in pulsers with rise time of about 100 ps requires significant improvement of cooling of output block with FID and DRD switches. At the same time it is necessary to lower the amplitude of output voltage pulses.

At 1 MHz in continuous nonstop mode maximum voltage is 1.5–2 kV with rise time of 100 ps and pulse duration of 0.5–1 ns.

In burst mode the amplitude of pulses can be up to 10 kV for a 1 MHz burst. Rise time in this case can be about 100 ps.

Figure 5 shows pulse generator FPG 10-6000 NP which has maximum PRF of up to 6 MHz in a burst with duration of up to 100 ms. Oscillograms of pulses are shown on Fig. 6. Rise time is 1 ns, pulse duration is about 2 ns. Amplitude stability of output pulses during the whole burst is 2%. At the amplitude of 1–2 kV maximum PRF in burst can be up to 20 MHz. Figure 7 shows an oscillogram of such pulses. Rise time at 20 MHz PRF and 1–2 kV can be in the range from 0.5 to 2 ns. Total efficiency of pulsers with PRF of 1–20 MHz reaches 80%, which permits operation with air or water cooling, keeping compact dimensions.

In most cases nano- and picosecond pulses are used with 50 Ω loads, but it is possible to make variants of pulse generators capable of operation into loads less or more than 50 Ω.

All pulsers feature overheating protection as well as the capability to withstand short and open circuit conditions for a short duration.

Fig. 5 FPG 10-6000 NP
Pulse generator
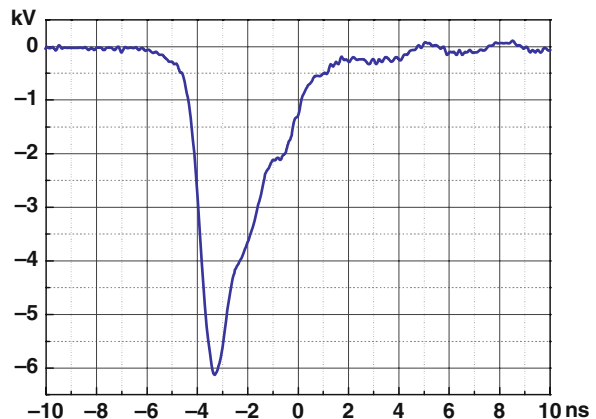
Fig. 6 FPG 10-6000 NP
Pulse shape
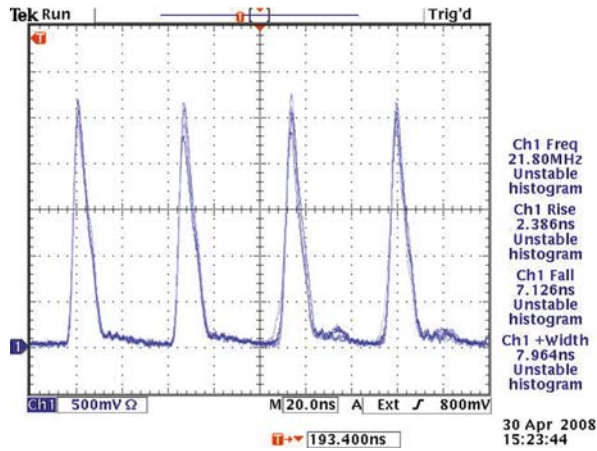
Fig. 7 2 kV pulses following each other

3 Conclusion

Further progress of nano- and picosecond pulse generator technology based on FID and DRD will improve efficiency and consequently development of more compact and higher repetition rate models. In the nearest future FID GmbH will be able to demonstrate pulsers with amplitude of 100 kV, rise time of 100 ps, pulse duration of about 1 ns, PRF of up to 1 kHz with dimensions of about 200 × 120 × 50 mm. Pulse repetition rate at 1–5 kV will reach 100 MHz.

Experimental and Theoretical Investigation of Directional Wideband Electromagnetic Pulse Photoemission Generator

P.V. Petrov, V.I. Afonin, D.O. Zamuraev, E.V. Zavolokov, N.V. Kupyrin, Yu. N. Lazarev, Yu. O. Romanov, Yu. G. Syrtsova, I.A. Sorokin, A.S. Tischenko, G.I. Brukhnevich, N.P. Voronkova, L.Z. Pekarskaya, and V.S. Belolipetskiy

Abstract The effect of electromagnetic wave generation by the electric current pulse propagating at the superluminal velocity along a conducting surface might be promising to create a high-power wideband microwave generator. The system comprising a plane vacuum photodiode with a transparent anode and using laser radiation to initialize electron emission is a variant to realize this scheme of electromagnetic pulse generation. This chapter presents results of experimental researches in characteristics of such radiating element with the cesium-antimonide cathode of Ø50 mm. The performed researches have shown that the generated wideband pulse ($f_0 \approx 3.3$ GHz, $\Delta f / f_0 \sim 1$) propagates in the direction corresponding to specular reflection of the incident laser radiation. Under the voltage of about 50 kV the electric field strength of 44 kV/m at the distance of 1.3 m has been recorded that corresponds to the generator power ~ 10 MW.

Keywords Electromagnetic pulse · Directional radiation · Photoemission · Vacuum photodiode · Superluminal velocity

1 Introduction

One of the promising techniques to generate high-power super-wideband directional electromagnetic (EM) radiation is based on using the photoemission current pulse propagating at the superluminal velocity along the irradiated surface capable of producing electron emission [1,2]. This scheme of generation is an interesting one for the following reasons:

1. High-power pulses in centimeter wavelength range are produced: EM radiation power is proportional to the area of the emitter surface and increases with decreasing pulse duration
2. The generated EM pulse is a directional one: It propagates in the direction corresponding to the specular reflection of the initiating radiation
3. The signal spectral composition is a super-wideband one: A super-wideband video pulse of short duration is radiated

P.V. Petrov (✉)
Russian Federal Nuclear Centre – Institute of Technical Physics, Snezhinsk, Russia
e-mail: pvpetrov@mail.ru

2 Microwave Generation Scheme

The simplest system that allows the realization of this scheme [3,4] comprises the plane vacuum photodiode with a transparent anode and an accelerating voltage between them (Fig. 1).

The emitted electron current pulse is formed on the photocathode under the plane front of initiating radiation. The electrons are accelerated in the interelectrode gap, pass through the grid anode, and generate above the anode the accelerated electron current pulse that propagates along the anode surface at the superluminal velocity:

$$\vec{j} = \vec{j}(\vec{r}, t - x/v_{ph}), \quad v_{ph} = c/\sin(\theta) > c, \tag{1}$$

where c is the velocity of light and θ the angle of initiating radiation incidence.

Since the thickness of the arising dipole layer is essentially less than the characteristic wavelength of the generated radiation, we can use the dipole approximation to estimate the generated field characteristics. In the far zone in the direction of EM pulse propagation at distance R the EM field amplitude is defined by the second time derivative of the electron dipole moment surface density above the anode $\ddot{P}_z(t)$ and the area of the radiator surface S [2]:
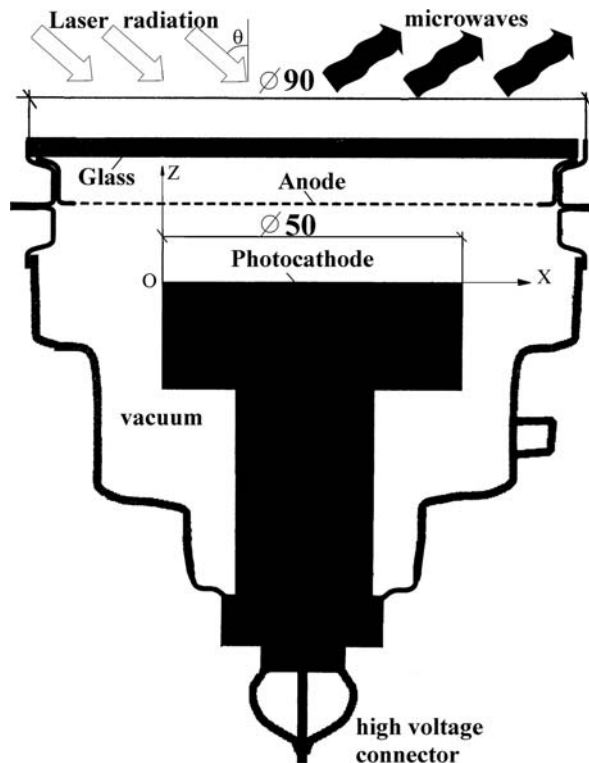
Fig. 1 Radiator scheme

$$E^w \sim H^w \approx \frac{2\,\sin(\theta)}{c^2 R} S\ddot{P}_z\,(t - R/c)\,. \qquad (2)$$

For estimations the second time derivative of the dipole moment surface density can be obtained from the one-dimensional model of dipole layer formation [3].

For the radiator with photodiode voltage U_0, photocathode lateral dimension D, and the separation between the cathode and anode L this approach gives the following expressions for the limiting electromagnetic radiation (EMR) parameters [1–4]:

duration: $T_0 \sim 2\pi\,(\gamma - 1)^{-1/2}\,L/c$;
divergence: $\theta_D \sim cT_0/D$;
the electric field amplitude in the far zone:

$$E^w \sim 10^5\,(\gamma - 1)^2\,(D/L)^2\,/R \quad (\text{V/m})\,.$$

In this context the power of the laser that irradiates the photocathode must be not less than $q \sim 1.4\,\times\,10^3\,(D/L)^2\,(\varepsilon/Y)\,(\gamma - 1)\,\sqrt{\gamma^2 - 1}$ (W), and pulse duration essentially less T_0.

Here ε is the quantum energy of the laser radiation, Y the photocathode quantum yield, $\gamma = 1 + eU_0/\left(mc^2\right)$, and e, m the electron charge and mass.

Despite these relations are derived without regard to the generated fields influence on the electron current formation they give qualitative idea of functional dependences of EM radiation on the diode parameters. It is clear that in order to generate high-power EMR it is needed to enlarge the radiator surface area, the dipole moment surface density, which is proportional to the accelerated electron energy and to decrease the time of the dipole layer formation. In this connection the system with small accelerating gaps, high accelerating voltage and high density of the emitted electron current is of the most interest.

Varying radiating element parameters and choosing different sources of photon radiation we can obtain a variety of devices that generate directional super-wideband microwave EM pulse [2–5].

3 Radiator Description

To investigate EMR in the photoemission radiator we used the vacuum system (Fig. 2) with cesium-antimonide (SbCs) photocathode of diameter Ø50 mm, quantum yield $Y \approx 0.05$ electron/photon (irregularity less than 30%). An orthogonal grid with a transparency of $\sim$70% was used as the anode. The emission was initiated by the plane wave front (divergence $\leq$0.3 mrad) of the second-harmonic radiation of the neodymium laser (duration $\sim$ 1 ps, wavelength $\lambda = 532$ nm). The angle of incidence of the laser radiation upon the photocathode surface was 45°. The separation between the cathode and anode varied from 1 to 4 mm.

The accelerating electric field between the cathode and anode was produced by a pulsed voltage generator developed on the basis of Vedenskiy scheme. This generator provides an output voltage pulse with amplitude up to 60 kV, pulse duration about 10 ns, and the leading edge 2 ns (Fig. 3). To synchronize the laser radiation pulse and the voltage pulse, the generator is started by the pulse produced by the reflection of the portion of the laserradiation fundamental harmonic at the early amplification stage.
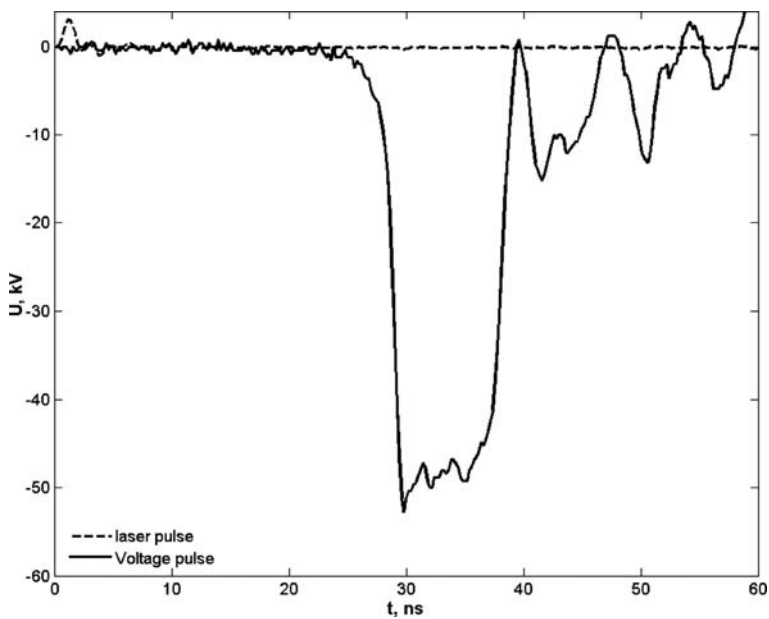
Fig. 3 The oscillogram of 50 kV amplitude voltage pulse applied to the radiator

4 Simulation

One- and two-dimensional codes based on self-consistent solution of the Maxwell–Vlasov set of equations [1–5] were applied to compute EMR characteristics.

   The property that defined this radiator is that two EM waves are produced: the first propagates in the free half-space above the anode in the direction corresponding to the specular reflection of the incidence and the second propagates in the waveguide formed by the cathode and anode. The field of the second wave being added to the emitted electron space charge results in effective decrease of
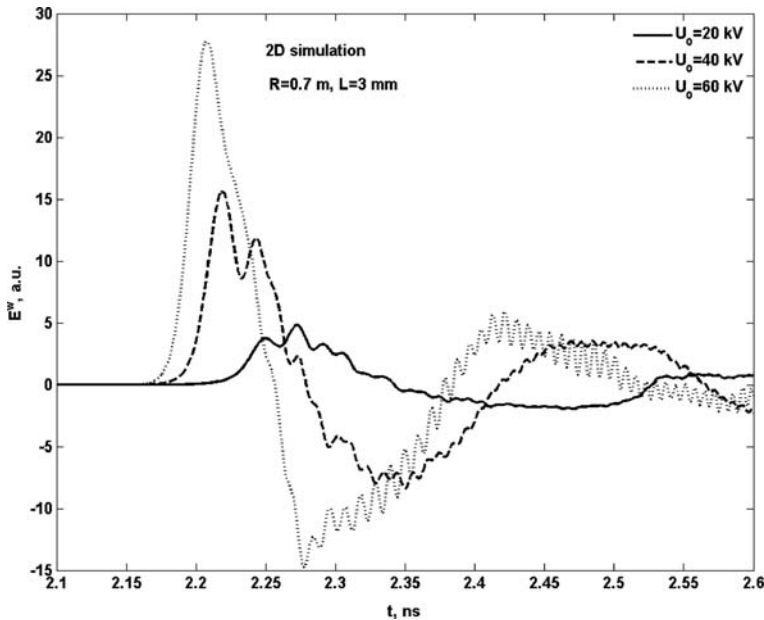
Fig. 4 The calculated time dependence of the magnetic field in the radiator far zone with accelerating voltage $U = 60 \, \mathrm{kV}$ and the gap between the anode and cathode $L = 3$ mm

the accelerating potential in the diode and accordingly the decrease of the ultimate attainable anode current density.

Figure 4 presents the typical form of EMR generated in the radiator far zone. The EM field amplitude increases and the pulse duration decreases with the increase of the accelerating voltage and the decrease of the accelerating gap sizes.

Computational results have shown that numerical simulation agrees with the analytical estimations of functional dependences of the EM field amplitude on the photodiode parameters.

5 Experiments

The dependence of the EMR amplitude in the radiator far zone on the laser radiation energy, the accelerating gap sizes, and the applied pulse voltage was measured in experimental researches.

IPPL detectors [6] (relative error about 5%) and oscillograph recorder DPO71604 (bandwidth 16 GHz) were used for electromagnetic field measurements. Figure 5 shows the oscillogram of the electric field at a point 1.3 m distant from the radiator in the anechoic camera.

Measurement results of the dependence between the EMR amplitude and the applied voltage are shown in Fig. 6.

The radiation pattern was taken in the plane of the laser radiation incidence to define the traveling direction of the generated radiation and estimate its divergence. Pursuant to the theory in the case of the infinitely long radiating element the arising EM radiation will propagate in the direction corresponding to specular reflection of the laser pulse incidence. For the finite-size radiator some deflection from this direction is observed for the generated EMR toward the radiator (Fig. 7).

By increasing the laser radiation energy EMR parameters reach asymptotic values.
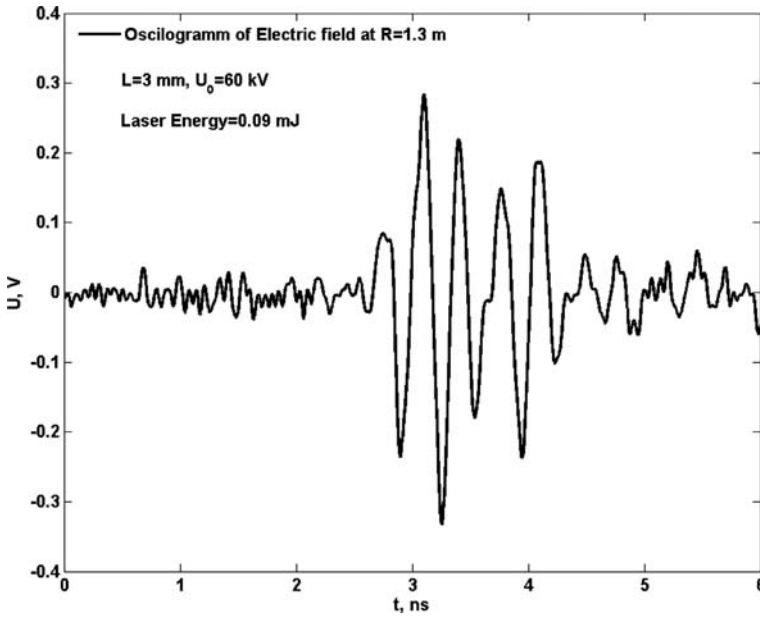
Fig. 5 The oscillogram of EMR pulse at 1.3 m distant from the radiator with the interelectrode gap 3 mm and applied voltage pulse 60 kV
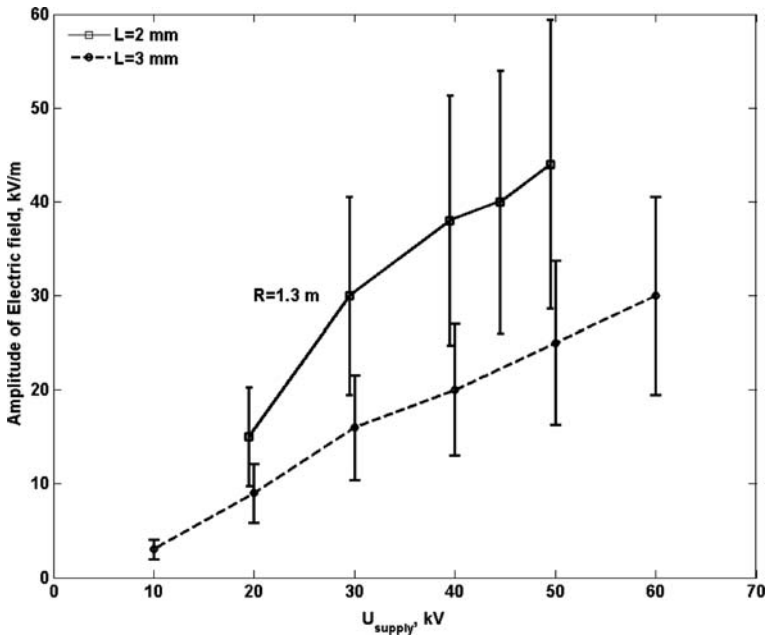
Fig. 6 The dependence of the electric field amplitude at 1.3 m distant from the radiator with the accelerating gap 2.3 mm on the applied voltage
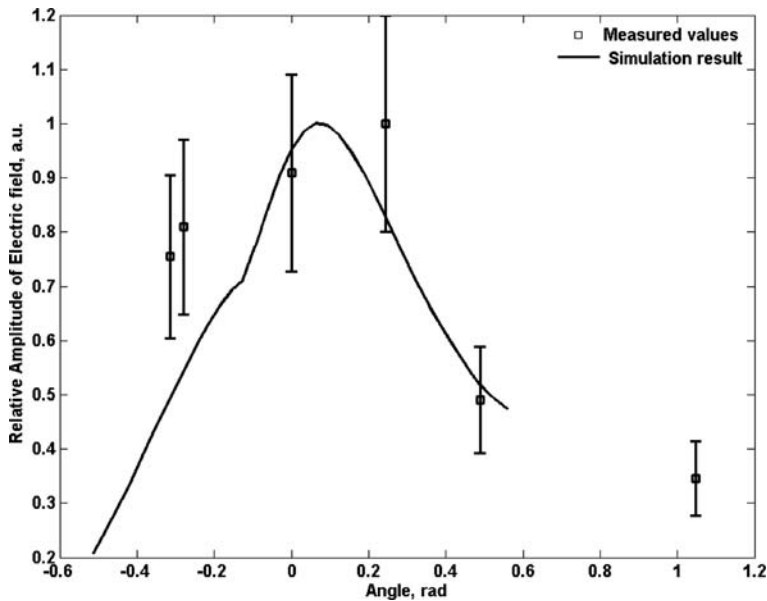
Fig. 7 The calculated and measured values in the experiment angular distribution of the electric field amplitude for the radiator with the accelerating voltage 20 kV and gap 3 mm

6 Conclusions

The obtained experimental results should be considered as the preliminary estimation of the generated electromagnetic radiation characteristics. This is connected with the fact that the applied apparatus is not capable to provide the required measurement quality of very short electromagnetic pulses (several tens of picoseconds).

Nevertheless the agreement of experimental and theoretical estimations confirms the efficacy and promise of the presented scheme of generation.

References

1. N. J. Carron and C. L. Longmire, Electromagnetic pulse produced by obliquely incident X-rays, IEEE Transactions on Nuclear Science, vol. NS-23, no. 6, pp. 1897–1902, 1976.
2. Y. N. Lazarev and P. V. Petrov, Microwave generation using a superluminal source, Journal of Experimental and Theoretical Physics, vo. 88, pp. 926–935, 1999.
3. P. V. Petrov, Y. N. Lazarev, and Y. G. Syrtsova, Microwaves generation by a superlight source at limiting current densities, Plasma Physics Report, vol. 29, pp. 449–457, 2003.
4. P. V. Petrov, Y. N. Lazarev, and Y. G. Syrtsova, Photoemission pulsed source of wide band directional electromagnetic radiation, Technical Physics, vol. 49, pp. 1477–1485, 2004.
5. Y. N. Lazarev and P. V. Petrov, High-gradient accelerator based on a superlight source, Technical Physics, vol. 45, pp. 955–961, 2000.
6. K. Y. Sakharov, Supershort electromagnetic pulse radiators and their parameters measuring methods, Moscow State Institute of Electronics and Mathematics, Moscow, 2006.

The GIMLI: A Compact High-Power UWB Radiation Source

P. Delmote and B. Martin

Abstract This chapter presents the design and performances of a compact, general-purpose, high-power ultra-wideband (UWB) source named GIMLI. The system was designed for dual use, homeland security and military applications. It is powered by a compact, coaxial 12-stage Marx generator with a rise time lower than 25 ns and an operating voltage up to 360 kV. A fast monocycle pulse is sharpened using a pulse former (MPF). The shaper stage comprises a switching module including a peaking and a grounding multi-channel spark gap under a N_2 pressure of 6 MPa. The module is followed by a monopulse-to-monocycle converter based on a coaxial Blumlein pulse forming line. The bipolar signal measured at the output of the MPF has a duration shorter than 2 ns with a rise time of 250 ps. The peak-to-peak output voltage is 250 kV on a 50 Ω resistive load. Repetitive operation of the MPF has been experienced with a 200 Hz Tesla transformer developed by the CEA (*Commissariat à l'Energie Atomique*). Electromagnetic energy is focused by a dedicated antenna. The designed antenna is a TEM half-horn with two ridges which improve the low-frequency focusing. High-power radiation tests show that the field measured at a distance of 9 m from the TEM Horn-antenna is higher than 120 kV/m.

Keywords UWB · High power · Source · GIMLI

1 Introduction

Formerly dedicated to radar applications, high-power UWB sources are now typical devices for dual use applications. Indeed, time and frequency characteristics of UWB pulses can offer new possibilities in bio-electric cell treatment, bio-fouling prevention but also for defence and homeland security applications. These include fast boat and car neutralization, improvised explosive devices disruption and wideband jamming.

To explore the offered possibilities of high-power UWB sources for security purposes, a project was launched in 2005 by the French-German Research Institute of Saint-Louis (ISL) which is supported by both French and German departments of defence. The aim of this study is to design a transportable prototype providing a pulsed electric field in the 1 MV figure of merit class (product of

P. Delmote (✉)
French-German Research Institute of Saint-Louis, High Power Microwave Group, Saint-Louis, France
e-mail: philippe.delmote@isl.eu

the distance by the electric field in the far field region). A covered spectrum between 100 MHz and 1 GHz was expected for the applications considered. The presented source called GIMLI (*Générateur d'Impulsions Modulées en Largeur et en Intensité*) is the result of this project. It is a test bench for the next generation embedded UWB source.

The first section of this chapter deals with the design of GIMLI. It includes a short presentation of the ISL Marx generator followed by the description of the monocycle pulse former and its performances. The design of the half-horn antenna is detailed at the end of this section.

Results of high-power radiation tests are discussed in the second section. Finally, the chapter concludes with the perspectives of the research work.

2 Design and Realization of GIMLI Prototype

GIMLI is made of three sub-systems depicted in Fig. 1. Following paragraphs detail the design of each block.
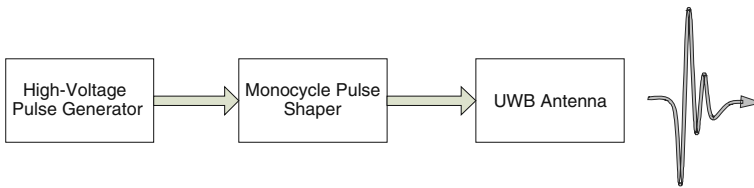
Fig. 1 Block diagram of the GIMLI prototype

2.1 High-Voltage Pulse Generator

The compact high-voltage generator used in the GIMLI is a standard ISL-Marx pulser. This former Flash X-ray radiography driver built at ISL comprises 12 stages. Each stage includes eight sector-shaped $SrTiO_3$ capacitors of 1.1 nF, two 30 kΩ charging resistors and two spherical half-spark gaps in their middle. All parts are packed in a resin compound to improve both electrical and mechanical strength (Fig. 2). The resulting elementary stages are surrounded by a stainless steel cylinder with a 25-mm thick polyethylene jacket.
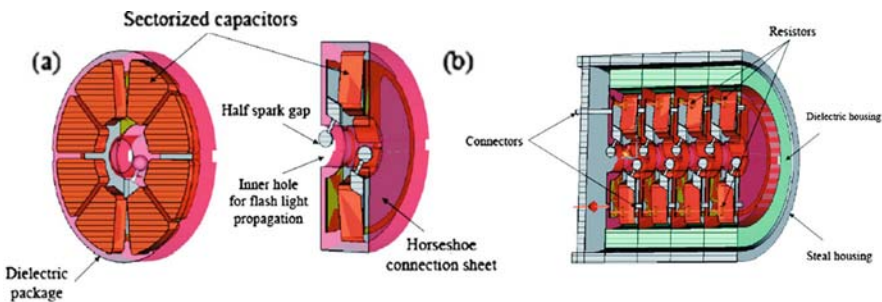
Fig. 2 3D cutaway view of an elementary stage with sectorized capacitors (**a**) and (**b**) and four stages mounted in the housing

The capacitor stages show a hole in their middle allowing the UV flashlight emitted by successive breakdowns to propagate throughout the generator. UV produces a pre-ionization which helps the erection mechanism.

The charging voltage can reach 50 kV. Nevertheless, a nominal voltage of 25–30 kV is sufficient to drive the shaper with a 350 kV pulse. In this case the rise time is about 15–25 ns.

Despite the poor pulse repetition rate (PRF) of 2 Hz, the Marx has been chosen for the GIMLI prototype. Further development will focus on this sub-system to improve the PRF in the range of 100 Hz.

2.2 Monocycle Pulse Shaper

The pulse shaper is of major importance in a high-power UWB source. Indeed, in GIMLI, the expected bandwidth from 100 MHz to 1 GHz requires a pulse length of 2 ns. Therefore, the sub-microsecond output pulse of the Marx must be sharpened in order to cover the specified wide spectrum.

We have found that monocycle presents several interesting features for high-power UWB [1]. As shown in Fig. 3, there is no DC component in the spectrum of the bipolar pulse. This kind of pulse avoids residual charges on the antenna after several bursts and the short circuiting of radiators is not required, increasing the human operator safety. It also reduces the risk of parasitic flashovers caused by the low-frequency and DC contents. Moreover, as there are only a few low-frequency contents in the input signal of the antenna, the radiated fields could be focused more efficiently. Finally, the fast mid-cycle falling edge of bipolar pulses enhances the figure of merit due to the high di/dt.

Two methods of monocycle pulse shaping have been published in the literature [2, 3]. Both are based on the active conversion of a monopulse to a monocycle. The principle is illustrated in Fig. 4. The slow Marx output is sharpened by a switching stage providing a fast monopulse. This pulse is then converted into a monocycle through a pulse forming block.

In practical terms, the MPF of GIMLI comprises two spark gaps as the pulse sharpener and a Blumlein pulse forming line as the converter. Both spark gaps are mounted in a 90 mm outer diameter brass vessel that can be pressurized up to 6 MPa with N_2 or air or a mixture of two gazes such as air/SF_6 (Fig. 5).

The first spark gap (U1) is a peaking switch that boosts the voltage rise rate up to 500 kV/ns. Its brass electrodes are conical in order to increase the active surface and then to reduce the erosion.
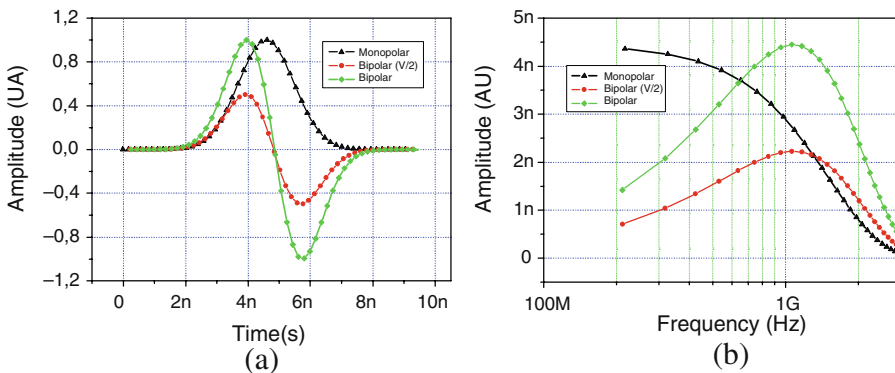
Fig. 3 Comparison between monopolar pulse and monocycles in time (*left*) and frequency (*right*) domains
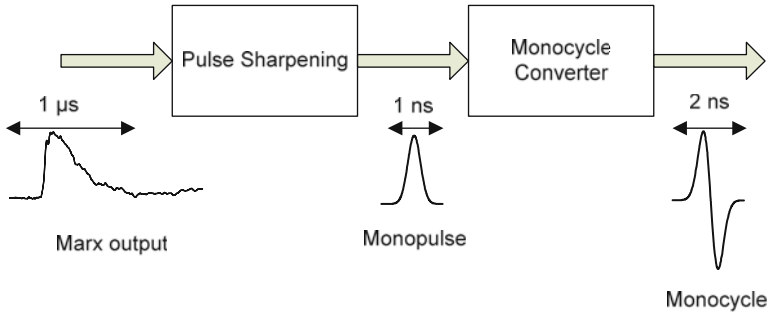
Fig. 4 Principle of monocycle pulse shaping with active converter
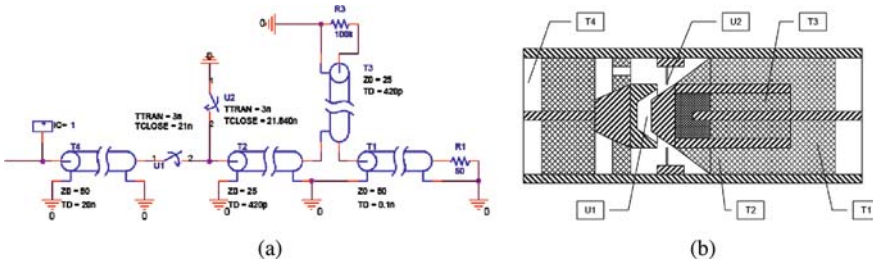
Fig. 5 Electrical equivalent circuit of the MPF (**a**) and simplified cutaway view of the monocycle pulse former (**b**)

The second gap (U2) is an annular grounding switch sharing a common electrode with the peaking. This setup allows the UV light of the first breakdown to pre-ionize the second gap so as to reduce its jitter. The 'jagged' geometry of the grounding switch was chosen to ensure simultaneous multi-channel discharge. The high rising rate of the peaking allows an extreme over voltage of the 12 field enhancement sites around the grounding switch. The voltage variation across the sub-millimetre gaps reaches 1 MV/ns.

The multi-channel operation of the grounding switch has been experimentally checked. To perform this verification, a clean new set of electrodes has been installed and then removed after one single discharge. After the test, the shared electrode exhibits 12 impacts, each located in front of the field enhancement sites of the annular jagged electrode.

The Blumlein-based monocycle converter is depicted in Fig. 5b. In this coaxial structure, an intermediate part is used as internal conductor of line T2 and external conductor of line T3. The insulation of lines T2 and T1 is made of polypropylene (PP) with a dielectric constant of 2.3. To adjust the time delay between line T3 and T1, the insulator surrounding the open end of T1 is made of a higher relative permittivity (dielectric: polyacetal (POM); $\varepsilon_r = 3.7$). A specific open circuit ensures a good termination of T1 up to 4 GHz. Finally, the profile of the internal conductor shows three diameter transitions to keep the impedance constant along the lines. The dimensions of the realized monocycle converter (Fig. 6) were optimized using the 3D EM simulation software CST MS.

The typical output signal of the MPF measured on a 50 Ω resistive load is shown in Fig. 7a. The maximum amplitude when the MPF is driven by the 12-stage Marx is 250 kV and the pulse length is 1.8 ns.
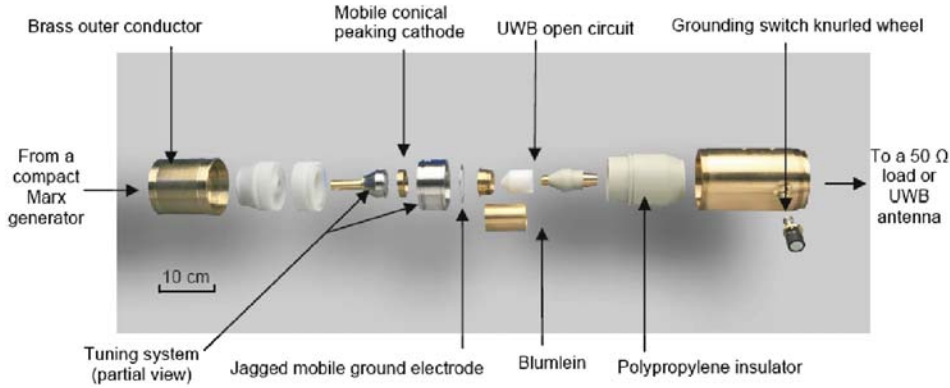
Fig. 6 Exploded view of the designed pulse former
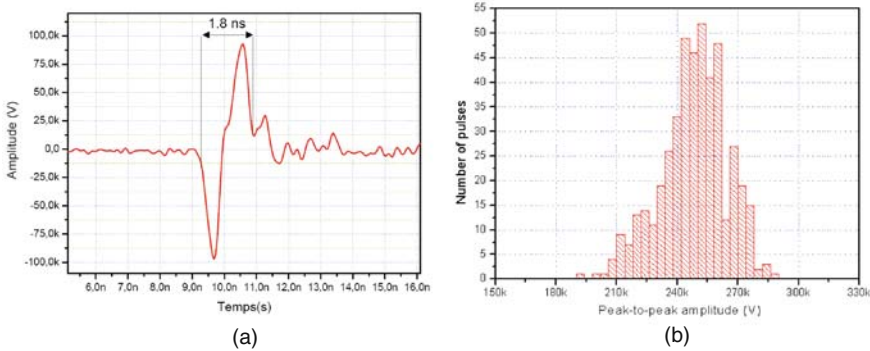
Fig. 7 Typical output of the MPF driven by a 210 kV Marx generator (**a**) and distribution of the peak-to-peak amplitude during a burst of 500 pulses at a repetition rate of 200 Hz (**b**)

Tests in repetitive mode of the MPF were carried out in collaboration with the CEA in the CESTA facility (*Centre d'Etude Scientifique et Technique d'Aquitaine*). The Marx was replaced by a Tesla transformer with the same output voltage but with a repetition rate of 200 Hz. The histogram in Fig. 7b presents the distribution of the peak-to-peak amplitude of the monocycles during a 500 pulses burst at a repetition rate of 200 Hz. The mean amplitude is about 250 kV with a standard deviation of 6.6%. During repetitive sequences, an additional peaking spark gap was inserted downstream of the MPF. With a sub-nanosecond rise time, it allows the MPF over voltage and then increasing the rise rate of the switching block. Voltage rise rates of 2 MV/ns were measured. In that case, the maximum amplitude was 440 kV. The output peak power is greater than 1 GW.

2.3 High-Power Antenna

In order to radiate a very high-power UWB pulse in the axial direction with maximal efficiency, the emitting antenna has to be

- broadband to cover the spectrum of the pulse delivered by the associated pulse generator and to avoid mismatch effects;
- highly directive with symmetrical pattern to ensure maximal axial gain and to minimize unintended effects due to parasitic side lobes;
- designed to provide a good compromise between high-frequency performances and risk of flashover due to high-voltage feeding;
- designed to ensure a good compromise between directivity even at low frequency and compactness.

The chosen antenna is based on a travelling wave antenna and a double ridged half-TEM horn. Using half-antenna lying on a metallic ground plane allows us to minimize the radiating element size and to avoid the problem of balanced excitation at very high voltage. On the other hand, this choice decreases the general efficiency as the local ground plane is never of infinite size. The input of the antenna is made by dedicated transition between a coaxial guide and a strip line; the dielectric used is PTFE. The measured S_{11} parameter is less than –15 dB in the range of 120 MHz to 6 GHz. Expected gain is between 10 dB at 200 MHz and 14 dB at 1.5 GHz (Fig. 8).

(a)   (b)
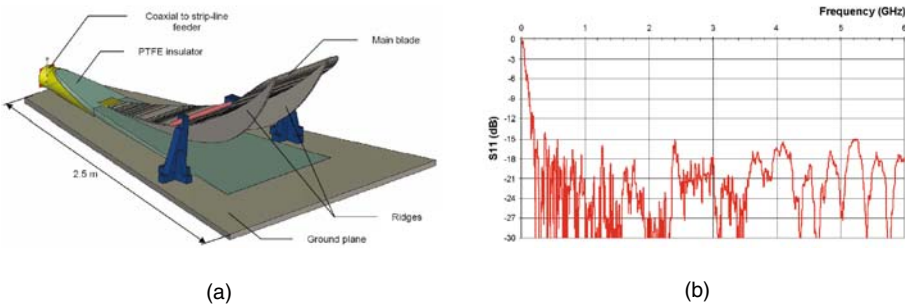
Fig. 8 CAD view of the antenna (**a**) and measured S11 parameter (**b**)
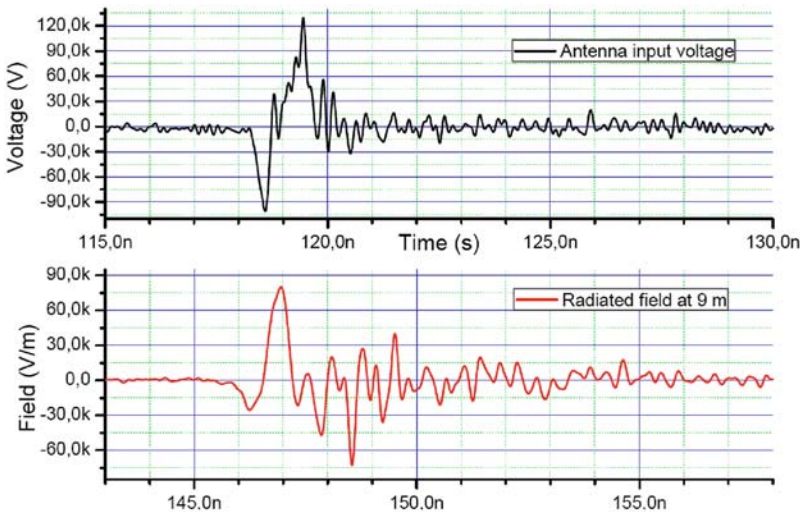
Fig. 9 Measured transient electrical field radiated by GIMLI in the axial direction

3 High-Power UWB Radiation

Radiation tests were performed in the ISL anechoic chamber. The MPF was set to deliver the fastest possible rise time. The peak-to-peak radiated field at a distance of 9 m was measured to be 152 kV/m for a 230 kV bipolar excitation (Fig. 9). Extra oscillations are visible on the monocycle leading to a resonant trail in the radiated field. In fact, there is a ringing in the Blumlein structure that induces a superimposed 2.5 GHz oscillation once the first half-period of the monocycle is generated.

4 Conclusion and Perspectives

The described monocycle pulse former shows a great potential for UWB-embedded applications. Voltage variation of 10^{15} V/s can be achieved using the multi-channel 'jagged' crowbar. The total radiated power is above 500 MW. The covered bandwidth is between 100 MHz and 1.1 GHz with a secondary band between 1.3 and 1.8 GHz. A resonant contribution around 2.5 GHz is also superimposed on the trail of the signal. The radiated field in the axial direction is in the range of 11–13 kV/m at a distance of 100 m. Further studies and experiments are conducted in order to increase amplitude and directivity of the radiated field and to insert MPF generator inside the antenna to reduce the size of the prototype.

References

1. B. Martin, P. Delmote, and B. Jecko, Design of an ultra compact UWB pulse former, presented at 16th International Pulsed Power Conference, Albuquerque, NM, USA, 2007.
2. Y. Yankelevich and A. Pokryvailo, A compact former of high-power bipolar subnanosecond pulses, IEEE Transactions on Plasma Science, vol. 33, pp. 1186–91, 2005.
3. Yu. A. Andreev, V. P. Gubanov, A. M. Efremov, V. I. Koshelev, S. D. Korovin, B. M. Kovalchuk, V. V. Kremnev, V. V. Plisko, A. S. Stepchenko, and K. N. Sukhushin, High-power ultrawideband electromagnetic pulse source, presented at 14th International Pulsed Power Conference, Dallas, Texas, 2003.

Classification of Electromagnetic Effects at System Level

F. Sabath

Abstract High-power electromagnetic (HPEM) environments are capable of causing effects like malfunctions, performance degradation, interferences, and destructions in electronic and electrical systems. Due to the large plurality of effects a scientific and systematic discussion requires a classification, which abstracts the essential information. This chapter presents a systematic classification of electromagnetic (EM) effects. The presented system enables an assessment and comparison at EM effects on system level.

Keywords Electromagnetic effects · Classification · Intentional electromagnetic interference (IEMI)

1 Introduction

The last two decades have witnessed an increased interest in high-power electromagnetics (HPEM), particularly the generation of high-power electromagnetic fields and their effects on electronics. As components for high-power microwave (HPM), wideband (WB), and ultra-wideband (UWB) technologies have achieved notable progress, high-power systems difficult or impossible to build 10 years ago are now being used for an increasingly wide variety of applications. With the advent of HPEM sources capable of producing output powers in the GW range, there has been interest in using HPEM devices in military defense applications to disrupt or destroy offensive electronic systems. In numerous publications it has been reported that terrorists have the possibility to interrupt and/or damage sensitive electronics by generating intentional electromagnetic interferences (IEMI) [1–3].

Electronic components and subsystems (e.g., microprocessor boards) are essential parts of modern civil and military systems like airplanes, communication, IT infrastructure, traffic management, or safety systems. Since these electronic components began to control safety critical functions, concern grew over the vulnerability of electronic systems. Therefore the susceptibility of critical systems is of vital interest since a setup or failure in these systems could cause major accidents or economic disasters. The increase of non-metallic materials like carbon-fiber composite as well as the decrease of signal levels results in a decreased susceptibility level of electronic systems. As a consequence, the investigation of the susceptibility of electronic systems as well as their protection and hardening against HPEM threats is of great interest.

F. Sabath (✉)
Federal Ministry of Defence; Armaments Directorate IV 6, Fontainengraben 150,
53123 Bonn, Germany
e-mail: frank.sabath@ieee.org

Due to the design and the functionality of electronics, the employed HPEM test environment, and the setup of susceptibility tests, the observed effects differ significantly from each other. In addition manufacturers of electronic systems are reluctant to have the susceptibility data of their systems be published and discussed in public. Therefore a scientific discussion needs a categorization of HPEM effects that (1) summarizes the essential information without giving away too much detail on the system and (2) enables a comparison of different manifestations of HPEM effects in different systems.

Effects caused by an HPEM environment can be characterized in a variety of ways. For example observed effects can be described by attributes of the physical mechanism as follows:

- bit flip,
- latch-up,
- flashover,
- wire melting, and
- bond wire destruction.

Alternatively one can classify EM effects by the duration of the effect and the need of human intervention, to recover normal operation. Such a scheme could range from "no effect" over "temporary effect" to "permanent effect" (e.g., destruction).

A third approach for classification of EM effects is by the implication on the main (or critical) function of the system [4,5]. The categories can range from "no effect" over "interference" and "degradation" to "loss of main function" or "mission kill."

This chapter will discuss advantages and disadvantages of each of these effect classification techniques in regard to system level assessment. A categorization scheme which is most useful to classify system level effects in regard to the comparison and analysis will be presented.

2 Classification of EM Effects

Susceptibility tests demonstrate that HPEM environments capable of causing cause interferences, malfunctions, upsets, and destructions in electronic equipments, even if they comply with standard EMC specifications or military hardening requirements. These induced effects in electronic systems are commonly referred to as intentional electromagnetic interference (IEMI).

Over the last few years a large variety of electronic and electrical components, equipment, and systems have been scrutinized to collect information on the physical mechanism of IEMI, critical parameter of the threat, as well as possible protection measures [6–8]. In order to develop a knowledge base which is of general value and independent of specific target systems, diverse systems and categories of systems (e.g., automotive, computer, IT systems, motherboards) were tested. The diversity of systems under test resulted in a large bunch of manifestations of HPEM-causing effects. Consequently, a comparison and analysis of the obtained raw data is difficult and a great challenge. The only way to analyze the effects data and identify tendencies or principles is to extract the essential information by a categorization.

2.1 Effect Classification by Mechanism

Initially, HPEM susceptibility investigations were performed to discover the physical mechanism of interference and destruction as well as the effective electromagnetic coupling. Consequently, the

characterization used to analyze susceptibility data focused on the physical mechanism, causing the observed effect.

Such a mechanism-based classification scheme is shown in Table 1. The first category "U" has an academic quality and is of minor interest for practical work. "No effect" data are useful in HPEM analysis, from a hardening and protection perspective, as it gives immunity level of the equipment or system to the HPEM environment. All other categories can be subdivided into interference and destructive effects. The shown two-stage classification follows the practical classification process. During a susceptibility test an observed effect can be easily mapped to interference (e.g., the system recovers) or destruction. The identification of which destruction mechanism applied needs additional detailed examinations of the system (e.g., opening of ICs and detailed on-chip investigation). As the destructive effects are of permanent nature usually the time consumption of such additional examination is no problem. In contrast, the temporary nature of interferences requires a real-time measurement of signals and additional measurements which enable observation, storage, and analysis of internal stages of the system under investigation.

The classification by mechanisms enables the analysis of the impact of threat parameter on a particular mechanism. For example, Camp and Garbe [9] used the quantities "breakdown failure rate" (BFR) and "breakdown threshold" (BT) to describe the impact of signal attributes of fast transient pulses (e.g., peak electric field) on the breakdown (category I.4) of personal computer systems.

Table 1 presents an example of a classification of EM effects by mechanism. As the categories are defined in regard to observed effects on systems under test, some explanation and discussion are necessary.

Usually, a bit flip results in a corruption of a data stream, which can be identified and/or corrected by an appropriate data coding. As the majority of observed bit flips impact transferred or stored user data, this effect is of temporary nature and results in a reduction of the data transfer rate or in a temporary malfunction of screens. But it should be mentioned that a bit flip has the potential to cause a latch-up (hang-up) of software.

Table 1 Classification of EM effects by mechanism

Category		Effect	Description
	U	Unknown	Unable to determine due to effects on another component or not observed
	N	No effect	No effect occurs
Interference	I.1	Noise	Raised noise level on signal and power lines, which results in flashing of displays or reduced data rates
	I.2	Bit flip	Injected signals alternate bits of a datastream
	I.3	Failure	Malfunction of the system/component due to EM interference
	I.4	Break down	Hang-up or crashing of software
Destruction	D.1	Latch-up	Injected signal causes latch-up in semiconductor components
	D.2	Flashover	On chip flashover/flashover in components
	D.3	On chip wire melting	Wires on chip are melted by injected energy
	D.4	Bond wire destruction/wire melting on PCB	Wires on PCB and/or bond wires in semiconductor devices are melted by injected HPEM energy

The categories failure and breakdown, as described in Table 1, are part of the transition from interference to destruction. The focus of the categorization, shown in Table 1, is on the physical mechanism. Therefore every effect on software is classified as interference and only hardware-related effects are classified as destruction. From the view point of a user a hang-up or crashing of software might be as bad as the physical destruction of a hardware component.

Generally a latch-up can be resolved by power cycling of the affected component or system. Latch-up is classified as a destructive effect due to its destructive nature as not every system or application (e.g., avionics) permits a power cycling.

The main drawback of the classification by mechanism is the fact that the classification categories contain sensitive (and therefore classified) information on the system under investigation. While talking about a real-life military used electronic equipment or avionics, no one would admit a destruction of hardware (HW) or a damage of software (SW). As the affected component is useless in any case, the specific realization of destruction is of no interest from the operational point of view. In addition the description of any kind of interference effect (I.1–I.4) does not contain sufficient information to assess the effect in regard to the operational efficiency. For example a bit flip that occurs only during the exposure to a UWB field pulse can be detected and corrected by a channel coding. Even if the coding is not able to correct the bit flip, the system will be back to full operation after the exposure has vanished.

2.2 Effect Classification by Duration

The NATO RTO SCI 132 task group tried to overcome the discussed disadvantages of the classification by mechanism and suggested a classification that assesses the observed effects from the viewpoint of a user or operator. Therefore, the classification introduced by NATO RTO SCI 132 task group used the duration and the need of human intervention as a deciding parameter. An improved version of this classification scheme was presented by Nitsch and Sabath at the AMEREM 2006 [10].

The duration of an HPEM effect provides the user with information on how long the desired function will be disturbed or broken down. The duration of an effect as a function of the threatening HPEM environment affords an estimation of status of an electronic system. The initial as well as the version improved by Nitsch and Sabath used a mixture of the effect duration, the need of human intervention, and destruction of components as differentiators. From a systematic point of view it is desired to use one single differentiator only. Consequently, a revision results into the classification listed in Table 2.

The main advantage of this classification is that (1) effects are characterized independent from the particular system and the main function and (2) by objective criteria. Only the decision between categories T and H does not support aspect (2) without restrictions. At this point the need for human intervention requires some explanation: In most cases a hang-up in a software or program (e.g., in the system software) can only be solved by a manually initiated reboot of the computer or a restart of the software. The situation becomes more complicated if the system software of an IT system (e.g., computer network, server) runs through an automatic reboot but the status of normal operation requires a manual start of an application software (or data stream). Some test engineers tend to classify this situation with category "T" as the system itself recovers without human intervention. As the main function needs the manual start of software the situation can be categorized as "H." In the practical case the decision depends if the test focuses on the main application (this will lead to H) or the basic system (T).

Table 2 Classification of EM effects by duration

Cat.	Duration	Description
U	Unknown	No effect occurs or the duration of an effect has not been observed (e.g., observer was unable to determine the duration due to effects on another component)
E	During exposure only	Observed effect is present only during exposure to HPEM environment; system functionality is completely available after HPEM environment has vanished
T	Some (follow-up) time after exposure	Effect is present some time after HPEM environment has vanished, but system recovers without human intervention Follow-up time is shorter or equal to typical reaction/operation cycle of the system
H	Persistent until human intervention	Effect is present until human intervention (e.g., reset, restart of function). Due to the effect the system is not able to recover to normal operation within an acceptable period (e.g., typical reaction/operation cycle of the system) No replacement of hardware or reload of software is necessary
P	Permanent or until replacement of HW/SW	Effect is permanent; usual interactions of an operator or user does not recover normal operation Effect has damaged hardware to the point that must be replaced or software to the point that it must be reloaded

The fact that the classification by duration does not provide information on the operational impact of the HPEM effect turns to a disadvantage if it comes to the assessment in regard to the main functionality or the mission of the system. For example, a faulty display, which is present for some follow-up time after the HPEM environment has vanished (category T), can be critical in one case and totally out of interest in another case. A broken maintenance data panel (category P) does not influence a running engine and has therefore no operational impact.

2.3 Effect Classification by Criticality

If HPEM effects are analyzed and assessed in regard to the operational impact and the functionality of the system, operational condition (e.g., critical periods of time, critical functions, minimum performance) must be taken into consideration. On the other hand such an analysis is working on a higher level of abstraction, as no details on the physical mechanism are needed.

Table 3 Classification of EM effects by criticality

Level	Effect	Description
U	Unknown	Unable to determine due to effects on another component or not observed
N	No effect	No effect occurs or the system can fulfill its mission without disturbances
I	Interference	The appearing disturbance does not influence the main mission
II	Degradation	The appearing disturbance reduces the efficiency and capability of the system
III	Loss of main function (mission kill)	The appearing disturbance prevents that the system is able to fulfill its main function or mission

Nitsch and Sabath introduced a classification of effects by its criticality for the main function or mission in [10] (Table 3). This classification provides the essential information on the functionality isolated from its duration.

Compared with previously discussed classifications the classification by criticality requires analysis of the observed effect and its impact on the function of the system in regard to a particular application. Therefore this classification depends on the application and its operational conditions. Due to this fact test engineers will hardly be able to map an observed effect on a criticality level without assistance of system specialists.

In addition the classification scheme contains aspects that are of interest for system specialists. In particular, the effect description provides a relation between observed effects and the hardening status of the system under consideration. For example if no effect (N) has been observed the system can be assessed as immune to the specific threat. If observed effects belong to the level interference (I) or degradation (II) the system is susceptible to the specific threat. Finally, a system that shows a level III effect (mission kill) definitely must be assessed as vulnerable.

From the aspect of the operational efficiency or operational restrictions, which are caused by the HPEM environment, sometimes criticality and the duration of the status (effect) are desired parts of information. As the classification by criticality (Table 3) and the classification by duration (Table 2) present the information as a function of one isolated criterion both classifications could be combined. Combinations with a practical relevance are listed in Table 4.

Table 4 Combination of duration and criticality

	Criticality level					
	U	N	I	II	III	
Duration	U	U	N			
category	E			E.I	E.II	E.III
	T			T.I	T.II	T.III
	H			H.I	H.II	H.III
	P			P.I	P.II	P.III

At this point it should be noticed that the combined classification carries two of four parts of information that are needed to determine the impact of the observed effect on complex systems. The missing parts of information are the operation value of the contributed functionality and requirements. For example an effect of category H.II of a subsystem results in E.I if it is acceptable that the subsystem is running on a lower performance level for some time. In another case any effect E.I I or higher results in a criticality level III if an undisturbed functionality is required.

3 Examples

In this section the theoretical presentation of classification schemes will be illustrated discussing examples typical for IT networks. In the experiment components of a generic IT network (e.g., WAN box, LAN box, server, PC) were exposed to a radiated HPEM environment. During the experiment the network operation was simulated by an FTP file transfer through the exposed component. Consequently, FTP traffic (data rate as well as retransmissions) can be used to assess the effect of the HPEM exposure on the network function.

Figure 1 depicts a category E behavior of the data transmission. Times of exposure to a narrowband signal, with a duration of less than 400 ns, are marked by dashed red lines. It can clearly be
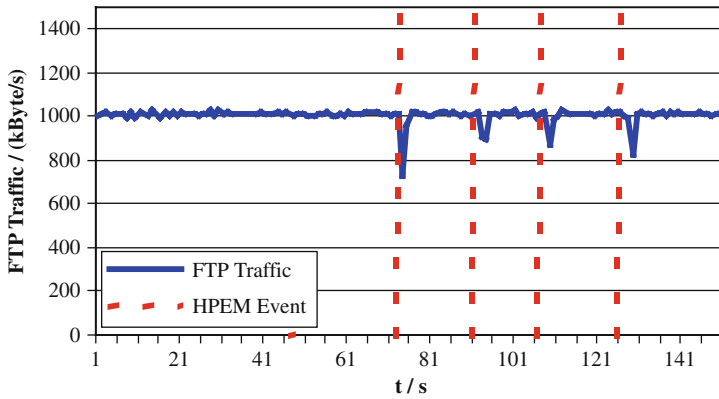
Fig. 1 E effects observed in a data transmission in an IT network

seen that every exposure causes a notch in the data traffic, which means that the data transmission decreases for at least one monitoring cycle. As the data traffic is back on the normal level within less than five monitoring cycles, it is most likely that the effect will not be observed by a user and does not affect network services. Therefore the effect can be categorized as E.I.

The effect shown in Fig. 2 is more severe as the HPEM exposure results into a total loss of data traffic for more than 50 s. The system is able to come back to normal operation without any intervention of the operator. This behavior is characteristic of a category T effect. The impact of the data transmission loss depends on the sensitivity of the running network service. A user who runs a simple data transmission would hardly notice a reduction of data transfer. In contrast, a network service with high requirements on unbroken connection would face a total breakdown (mission kill).

A data traffic curve that is typical for H and P effects is shown in Fig. 3. The exposure of the system under test to a narrowband HPEM field (dashed line) caused a collapse of the data transmission. A hang-up of the operation software or a damage of hardware components requires an operator-initiated reset (H effect) or replacement of components (P effect).
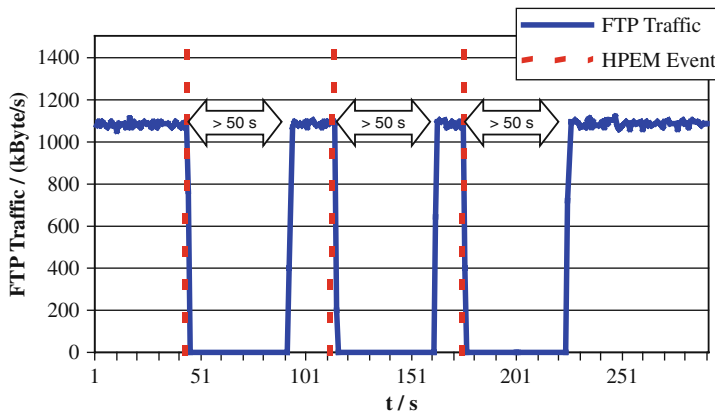
Fig. 2 T effect observed in a data transmission in an IT network
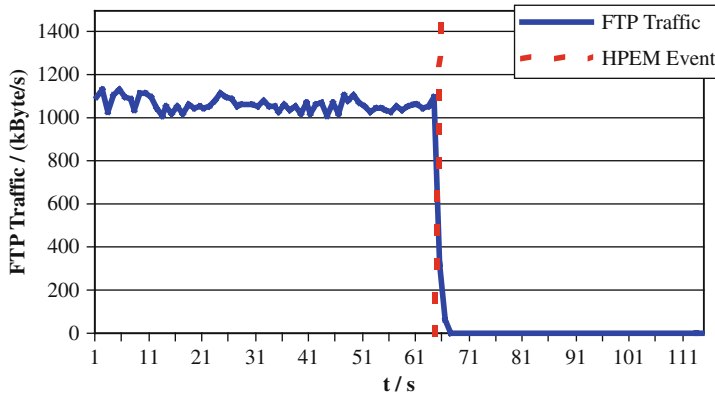
Fig. 3 H effect or P effect observed in a data transmission in an IT network
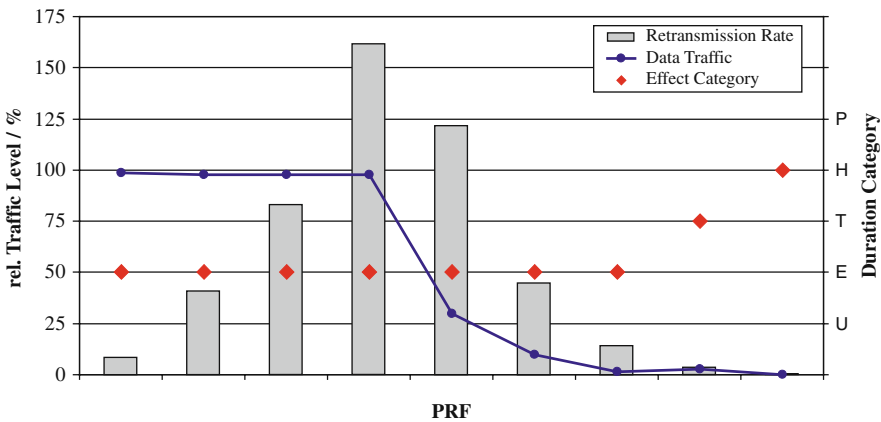
Fig. 4 Effects on data transmission in an IT network caused by UWB field signals

Figure 4 presents data that were collected during an exposure of selected components of an IT network to short pulse field signals with various pulse repetition frequencies (PRFs). The exposure of 10 s duration started after at least 10 s of stable data transfer. The observed effects were categorized regarding data transfer level and the rate of resubmitted data packets. For the lowest four pulse repetition frequencies the data traffic showed no effect and stayed on 100% level. During the exposure the system compensated corrupted data (caused by bit-flip) by an increase of the resubmission rate. The resubmission level returned to the normal (low) level after the field was switched off. Therefore the effect on the resubmission rate was categorized as E effect. From a point of view that focuses on the overall system performance these tests could also be categorized as N (no effect) as the system is able to handle the corrupted data internally, with no effect on the data traffic as well as on the network operation.

Figure 4 shows significant different situations for higher PRFs. The exposure to a burst with the intermediate three PRFs caused a temporary decrease of the data transmission. This is typical for a category E effect. The exposure to a burst with the next PRF was able to initiate a reboot of exposed network component. As a result the data transmission on the IT network stopped for a reboot cycle, which was longer than the 10 s exposure time.

Finally, the exposure to a burst with the highest PRF caused a hang-up in the exposed component. The effect was categorized as H effect as a manual switch off was required to return the network into normal operation.

4 Conclusions

This chapter addressed the need of a scientific discussion for a categorization of HPEM effects, which (1) provides the essential information and (2) enables a comparison of different manifestations of HPEM effects. In particular, the classification by (1) physical mechanism, (2) duration, and (3) criticality were presented in this chapter. The advantages and disadvantages of the presented classification techniques in regard to a system level assessment on HPEM effects were discussed.

Finally it was shown that a combination of the classification by duration and the classification by criticality is most useful to assess the impact of HPEM-causing effects. The combined classification allows a determination of the classification on system level using the categorization on equipment level in combination with the operational value of the contributed functionality.

References

1. M. W. Wik, R. L. Gardner, and W. A. Radasky, Electromagnetic terrorism and adverse effects of high power electromagnetic environments, Supplement to Proceedings of the 13th International Zürich Symposium on EMC, Zürich (CH), 13, 1999.
2. W. A. Radasky, Intentional electromagnetic interference (EMI) – test data and implications, Proceedings of the 14th International Zurich Symposium on EMC, Zürich (CH), 14, 2001.
3. M. Ianoz and H. Wipf, Modelling and simulation methods to assess EM terrorism effects, Proceedings of the 13th International Zurich Symposium on EMC, Zürich (CH), 13, 1999.
4. R. Hoad, N. Carter, D. Herke, and S. Watkins, Trends in EM susceptibility of IT equipment, IEEE Transactions on EMC, vol. 46, no. 3, pp. 390–395, 2004.
5. D. Giri and F. Tesche, Classification of intentional electromagnetic environments (IEME), IEEE Transactions on EMC, vol. 46, no. 3, pp. 322–328, 2004.
6. D. Nitsch, M. Camp, F. Sabath, J. L. ter Haseborg, and H. Garbe, Susceptibility of some electronic equipment to HPEM threats, IEEE Transactions on EMC, vol. 46, no. 3, pp. 380–389, 2004.
7. M. Backström and K. G. Lovstrand, Susceptibility of electronic systems to high-power microwaves: summary of test experience, IEEE Transactions on EMC, vol. 46, no. 3, pp. 396–403, 2004.
8. C. Mojert, D. Nitsch, H. Friedhoff, J. Maack, and M. Camp, UWB and EMP susceptibility of modern computer networks, Proceedings of EMC Zürich 2001, Zurich, Switzerland, February 2001.
9. M. Camp and H. Garbe, Susceptibility of personal computer systems to fast transient electromagnetic pulses, IEEE Transactions on EMC, vol. 48, no. 4, pp. 829–833, 2006.
10. D. Nitsch and F. Sabath, Electromagnetic Effects on Systems and Components, Book of abstracts AMEREM 2006, July 2006.

Measurement of EM Field Inside a Cruising Aircraft: Potential Problems for the Use of Mobile Phones on Board

A. Kohmura, J. Picard, N. Yonemoto, and K. Yamamoto

Abstract Electromagnetic (EM) emissions from portable electronic devices (PEDs) carried onboard aircraft can interfere with avionic systems. Several onboard systems using EM waves have been planned, such as mobile communications and UWB (ultra-wideband) entertainment services distribution. Manufacturers of this system develop schemes to avoid electromagnetic interference by the transmissions (emissions) of mobile phones with avionic systems; some local-specific problems still remain. The purpose of this chapter is to investigate to what extent non-GSM transmissions from the ground base stations reach inside a cruising aircraft. The EM field at the base station frequency bands is measured in a cruising small aircraft.

Keywords Mobile phone system onboard aircraft · EM field measurement in the air · Electromagnetic interference (EMI) · Direct connection · Control signal

1 Introduction

It is well known that electromagnetic (EM) emissions from portable electronic devices (PEDs) carried onboard aircraft can interfere with avionic systems [1]. In these 15 years, more than 200 anomalies, which are suspected to be triggered by the usage of PEDs, have been reported by airlines in Japan [2]. Generally, the use of PEDs, including mobile phones, is therefore limited in aircraft.

On the other hand, several onboard systems using EM waves have been planned, such as mobile communications and UWB (ultra-wideband) entertainment services distribution. Commercial services offering passengers the use of GSM (global system for mobile communications) mobile phones on aircraft are also set to start soon throughout the world [3, 4]. Though manufacturers of this system develop schemes to avoid electromagnetic interference by the transmissions (emissions) of mobile phones with avionic systems, some local-specific problems still remain. For example, it is not clear if all portable phones on board are truly disconnected from ground stations. These queries arise especially in the case of the uses of non-GSM mobile phones, which are not targeted by the system.

A. Kohmura (✉)
Electronic Navigation Research Institute, Tokyo, Japan
e-mail: kohmura@enri.go.jp

The purpose of this chapter is to investigate to what extent non-GSM transmissions from the ground base stations reach inside a cruising aircraft. The EM field at the base station frequency bands is measured in a cruising small aircraft.

2 Mobile Phone Systems

2.1 Japanese Mobile Phone Systems on the Ground

In Japanese mobile communications, PDC (personal digital cellular) of the second generation and CDMA (code division multiple access) of the third generation are adopted as transmission methods. The CDMA is known as a good jamming-resistant method. The above two methods are used in 800, 1500, and 2000 MHz bands, as shown in Fig. 1.
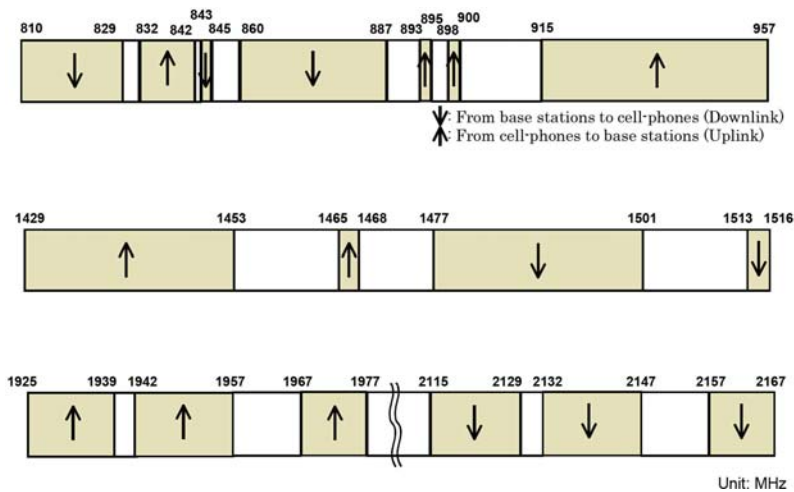
Fig. 1 Frequency allocation for mobile phones in Japan: (**a**) 800 MHz band allocation; (**b**) 1500 MHz band allocation; and (**c**) 2000 MHz band allocation

Some handsets sold in Japan are also compatible with GSM for international roaming purpose. There is also a move to introduce GSM to onboard systems in Japanese domestic flights with these compatible handsets [5].

2.2 Mobile Phone Systems on Airplanes

The trial of the use of mobile phones on airplanes has now started in response to passengers' demands. It will come into wide use soon. The mobile communication system enables passengers to use their mobile phones on board by placing small base stations in the cabin. The system will be available at the non-critical phase (i.e., excluding take off and landing) and at altitudes higher than 10,000 feet [6]. The system has been developed for the GSM transmission method using the 1800 MHz band, since this method has the largest market in the world.

The transmission power of target GSM phones in the cabin is kept low, controlled by the low power base stations (pico-cells) that link the phones to terrestrial communications via satellite. This scheme makes use of a behavior of mobile phones whereby phones control their radiating power in inverse relation to connection accessibility.

Another scheme is also investigated that makes mobile phones inactive by increasing the noise level around frequency bands used by terrestrial mobile communications, except the 1800 MHz band [7]. (Hereinafter, the eradiated radio wave (noise) is called the "control signal" in this chapter.) However, the scheme requires radiation of appropriate power in a wide frequency band in order to achieve a sufficient level of performance, while these jamming control signal emissions have to comply with the emission regulations for avionic equipments set by the radio technical commission for aeronautics (RTCA) [8]. Also, this method has the potential to jam terrestrial communications, especially in non-GSM countries. Therefore, the control scheme will not be readily accepted by the Japanese government commission of communications from the standpoint of fairness and efficiency of frequency resources use.

Consequently, only the former technique of suppression of radiation from mobile phones using pico-cells on board is realizable at the present moment. The problem with this technique is that it is efficient only for the transmission method employed, GSM, and does not work for mobile phones that use other methods. Thus, in a non-GSM country, when a passenger turns on his/her non-GSM mobile phone intentionally or unintentionally, it may radiate a very strong signal as the phone tries to maintain its link with the distant ground station. It could thus interfere with avionic systems.

This chapter treats two concerns. One is the possibility of a direct link connection between onboard mobile phones and ground stations. Another is damage to terrestrial communications in the case of the control signal being used on board above non-GSM countries.

3 EM Field Measurement in a Cruising Aircraft

3.1 Measurement Setup

The EM field at the three bands mentioned in Section 2.1 is measured using a wideband antenna connected to a spectrum analyzer on a cruising aircraft Beechcraft Model 99 aircraft. The measurement setup is shown in Fig. 2. It consists of a battery-powered portable spectrum analyzer (Anritsu MS2721B) and a discone antenna (band 500–3000 MHz, gain 2–4 dBi). The antenna is placed on the window-side seat behind the wing with vertical polarization. The EM field over Yamagata Airport, Japan, is recorded at altitudes from 1500 feet (469 m) to 7000 feet (2130 m) with a 500-foot interval. At each altitude, the aircraft flew in geographically identical positions on a straight line (32 km) along the runway of the Yamagata Airport.

3.2 E-Field Cross Section in the Sky

Figure 3 describes the maximum observed E fields cross section with altitudes over the Yamagata Airport runway (from 38º 30′N, 140º 34′E to 38º 47′N, 140º 38′E). The maximum values in each band are picked up and displayed.

In Fig. 3, 54–70 dB μV/m have been observed inside the aircraft. Generally, the E-field space cross sections are supposed to decrease with altitude. However, Fig. 3 shows spotty hot (high
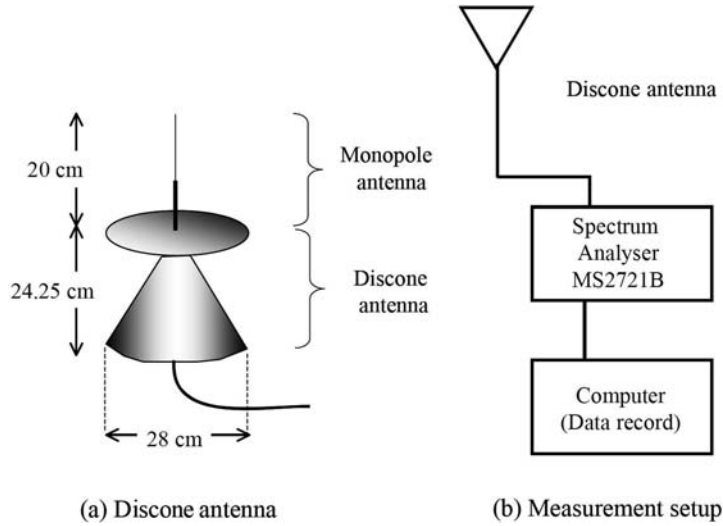
Fig. 2 Measurement setup: (**a**) discone antenna and (**b**) measurement setup

intensity) results, especially in Fig. 3(c), at 7000 feet. Figure 4 describes the geometric image of the measurement. Gradual attenuation with altitude is due to the transmission loss of the signal propagating away from the ground base station, supposed to be caused by shoulders of the base station beam. Also, these strong spots are attributed to reception of a beam top from a
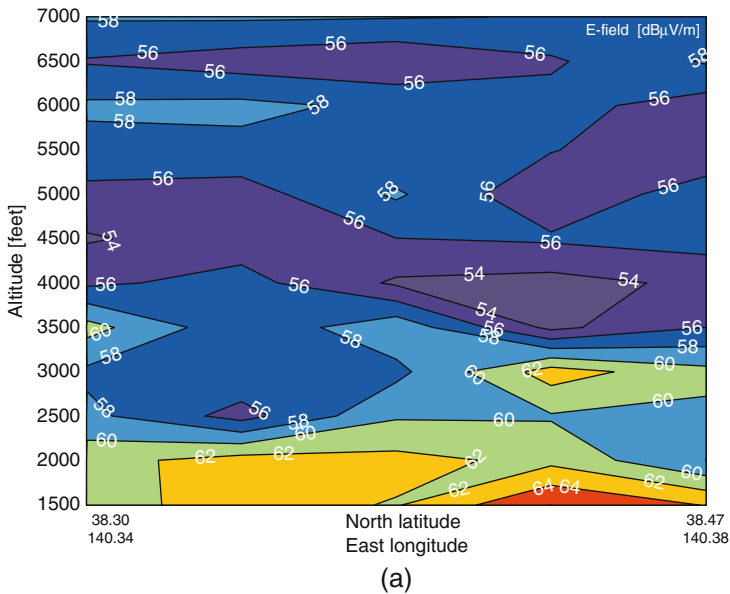
Fig. 3 Maximum observed E field from ground base stations in the 800 MHz band (**a**), 1500 MHz (**b**), and 2000 MHz (**c**) over Yamagata Airport

(b)

(c)
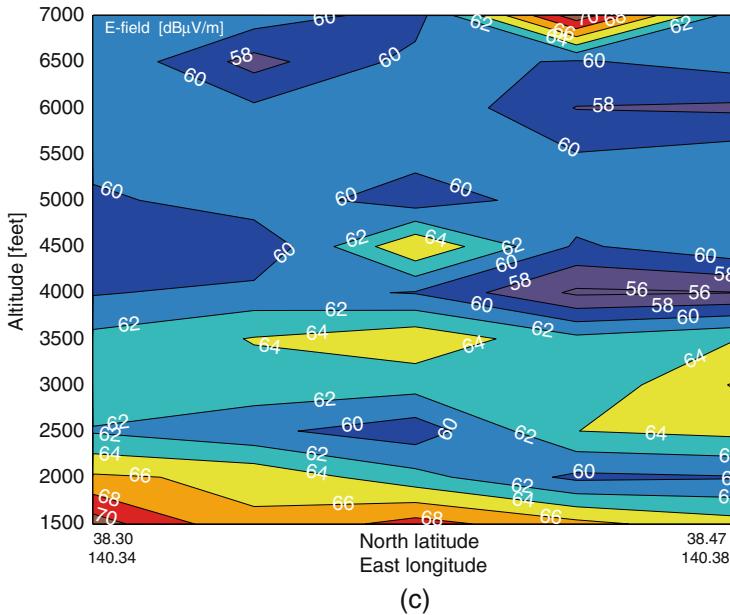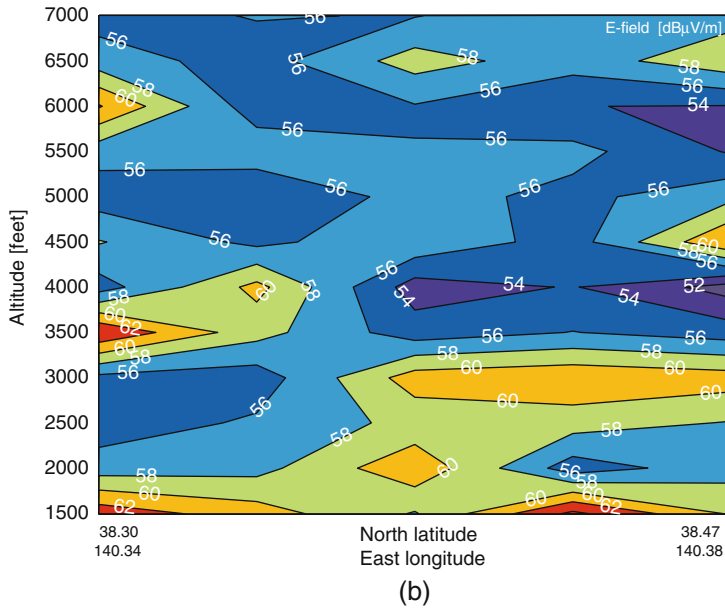
Fig. 3 (continued)

geographically far ground base station. This is possible on this flight, since the measured linear region, 32 km (105,000 feet), is much longer than the altitudes (1500–7000 feet) shown in Fig. 4. This result indicates the possibility of the existence of a spot where passengers can briefly connect their non-GSM phone in the air, even if ground base station antennas are tilted to the ground.
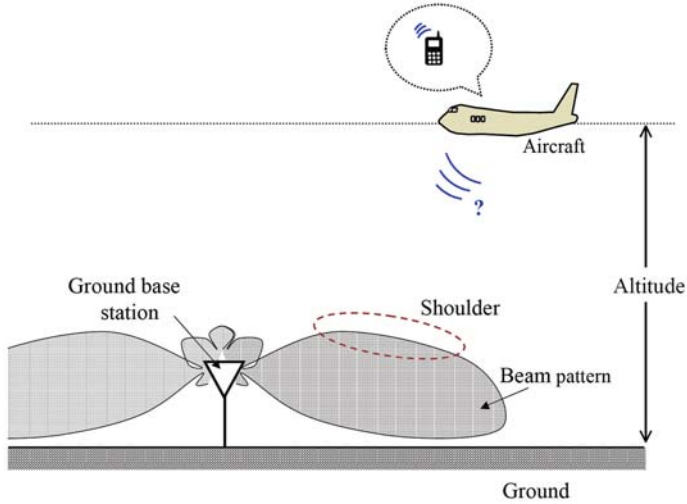
Fig. 4 Geographic measurement image

3.3 E-Field Estimation in the Sky

Characteristics (direction pattern, power), positions, and the number of ground base stations are not made public for security reasons. Therefore, the ground base station is supposed to be an isotropic source. In this investigation, the maximum E field at each altitude will thus be obtained when the aircraft is directly overhead the hypothetical base station.

The dashed line in Fig. 5 indicates the theoretical free space E field with distance (corresponding to the altitude axis) away from a transmitting antenna. Also, the plotted dots show the measured maximum E-field value depending on the altitude, from 1,500 to 7,000 feet, in each frequency band allocated for ground base stations in Japan. Frequency band details are indicated in Fig. 1 with downarrows.
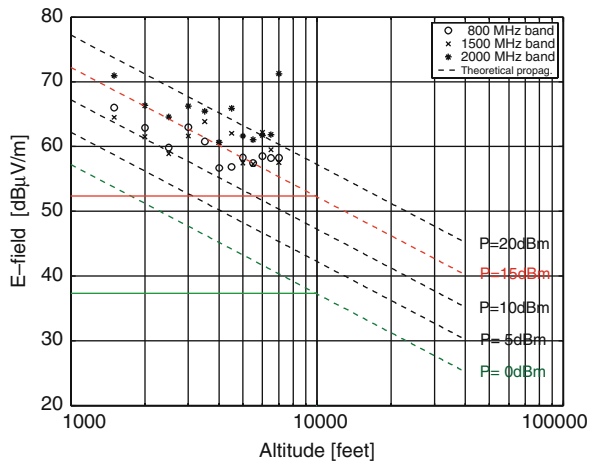
Fig. 5 Maximum measured E field and theoretical propagation to altitudes

The theoretical free space E field is obtained as follows:

$$E_{\text{theo}} = \frac{\sqrt{30P\,G_t}}{r},$$

(1)

where E_{theo} (V/m) is the free space E field (hereinafter called "theoretical propagation") at distance r (m) away from a transmitting antenna which has the gain Gt and transmitting power P (W). Formula (1) is derived by the power density at a reception antenna P_r (W):

$$P_r = \frac{P}{4\pi r}\,G_t$$

(2)

and E field at a reception point E_{theo} [9]:

$$E_{\text{theo}} = \sqrt{120\pi\,P_r}.$$

(3)

Since the theoretical propagation line in the case $P = 15$ dB m (red dashed line) in Fig. 5 fits observed maximum values (dots), it is supposed to be the transmitting power to skyward direction from the hypothetical ground base station. Note that the gradient of (1) does not change even if transmitting power P changes (see dashed lines in Fig. 5). Hence, the worst case of the cabin reaching E value is estimated around 52 dB μV/m at 10,000 feet, where the onboard mobile phone system will be turned on. It is approximated to be about 35–40 dB μV/m at higher altitudes where general commercial jet planes cruise 30,000–40,000 feet (9,150–12,200 m).

On the other hand, the reception sensitivity of a typical CDMA phone is approximately –110 dB m [10]. It is 26 dB μV/m at 870 MHz in E-field unit, smaller than the estimated cabin-reaching E field. It means that direct connection can be established between ground base stations and non-GSM phones on board, even at cruising altitudes. On such an occasion, mobile phones will burst their maximum allowed power 0.8 W for Japanese CDMA phones and 2 W for non-1800 MHz GSM phones.

3.4 Control Signal Influence

As feared, installing only a pico-cell is not enough to avoid establishment of a direct link between the cabin and ground base stations. Here, the use of a control signal is investigated by switching the relation between the ground and the cabin. Applying (1) to the case of leakage from an aircraft fuselage, control signal influence on terrestrial communications is investigated. Here, the onboard control signal is assumed to be an isotropic source. The fuselage attenuation is not considered in this calculation since conventional aircraft window material acrylic plate has few EM shielding effects. Therefore the fuselage attenuation can be ignored in a worst-case discussion.

For example, when a 0 dB m control signal is emitted from a cabin cruising at 10,000 feet, the E field that reaches the ground is estimated to be 37.2 dB μV/m (see green dotted line in Fig. 5). In the investigated Yamagata region, the control signal leakage is less than observed base station transmissions at 1500 feet, thus considered to be non-harmful for terrestrial communications. Appropriate control signal power that can control non-GSM phones on board well and does not disturb terrestrial communications should be chosen by (1). The way to set a guideline for the control signal power was shown.

4 Conclusion

The potential problems of installing mobile phone systems on board have been discussed through EM field measurement in the air. The possibility of direct connection between non-mobile GSM phones in the cabin and ground base stations is presented. In order to install this system in non-GSM countries, mechanisms must be considered to cut direct links from non-GSM phones to ground stations. For the typical solution that uses control signals, guidelines for choosing an adequate level are also presented. For the practical use, both electrical and mechanical solutions should be found. Shielding techniques for aircraft will be useful as well. Finally, flight safety when the system is installed in non-GSM countries can be ensured.

References

1. N. L. Armstrong et al., Investigation of the electromagnetic interference thereat posted by a wireless network inside a passenger aircraft, IEEE Transactions on EMC, vol. 50, no. 2, pp. 277–284, 2008.
2. K. Yamamoto, et al., PED interference reporting system in Japan, Seventh International Symposium on Electromagnetic Compatibility and Electromagnetic Ecology, June, 2007, pp. 220–223.
3. D. Hughes, 'Wired' airline cabins, Aviation Week & Space Technology, April 2008.
4. D. Hughes, Connectivity era arrives, Aviation Week & Space Technology, April 2008.
5. Go ahead! Plans for mobile phones on board Star Flyer plans in the spring of 2009, Asahi-Shinbun (Daily newspaper), December 19, 2007 (in Japanese).
6. T. Espiner, Ryanair announces in-flight mobile, cnet news, http://news.cnet.com/2100-1039_3-6110920.html?hhTest=1, August 30, 2006.
7. Questions about OnAir, http://www.onair.aero/admin/fil/Q&As%20about%20OnAir%20Apr%2008[1].pdf, April 2008, p. 7 Q&A28.
8. RTCA DO-160F, Environmental Conditions and Test Procedures for Airborne Equipment, Section 21, Category M.
9. J. D. Kraus and R. J. Marhefka, Antennas for All Applications, McGraw-Hill, New York, 2002
10. Y. Akamine et al., RF-IC system for W-DAMA: evaluation of prototype for W-CDMA mobile terminal, IEICE, Technical Report of IEICE. ICD, vol. 102, no. 340, September 2002, pp. 59–64 (in Japanese).

A New Method of Interference Evaluation Between UWB System and Wireless LAN Using a GTEM Cell

Shinobu Ishigami, Masashi Yamada, Kaoru Gotoh, Yasushi Matsumoto, and Masamitsu Tokuda

Abstract We propose a method of interference evaluation between the UWB and the wireless LAN using the GTEM cell that can test the receiver with a built-in type antenna. The interference evaluation was conducted between wireless LAN IEEE802.11a and DS-UWB. As a result, even when the UWB signal is smaller than the receiver noise of wireless LAN, the throughput characteristics deteriorate compared to the case of noninterference. Moreover, the signal of the DS-UWB was nearly equivalent to the AWGN in the case of throughput variation of 64QAM. We evaluated the separation distances in regulation limits of FCC and Japan. The measurement results for the amplitude probability distribution (APD) of the interfering UWB signal are also discussed.

1 Introduction

Ultra-wideband (UWB) technology is a wireless system that transmits the signal at high-speed transmission rate of 100 megabits per second (Mbps) – 480 Mbps with low-power spectrum density in the distance within 10 m. The federal communications commission (FCC) has allocated the frequencies from 3.1 to 10.6 GHz and from 22 to 29 GHz for the unlicensed use of the UWB. And so a dedicated frequency cannot be allocated for UWB system. We should consider carefully the interference problem between UWB and existing W-LAN or other wireless systems because the UWB system will be used over the frequencies that are allocated for the existing wireless systems.

The FCC [1] and the recommendation of ITU-R [2] defined the spectrum mask of UWB in terms of equivalent isotropic radiation power (EIRP). An EIRP is calculated by an electric field at the condition of a certain distance. An apparatus that can generate an intended electric field is required for interference evaluations. Moreover, the interference evaluations between wireless communications systems are usually performed in all measuring apparatuses connected. However, it is difficult to connect the communication system (receiver) of an antenna built-in type to the measuring apparatus.

S. Ishigami (✉)
National Institute of Information and Communications Technology, Tokyo, Japan
e-mail: shinobu@nict.go.jp

A transverse electromagnetic (TEM) waveguide can apply an intended field to the receiver of the built-in antenna type. A GTEM cell, which is applicable for several gigahertz, is useful as a test fixture that can be carried out an interference evaluation of the UWB.

In this chapter, we propose a new method of the interference evaluation between the UWB and the wireless LAN using the GTEM cell that can test the receiver with the antenna built-in type. The interference experiments are conducted between the direct-sequence spread spectrum UWB (DS-UWB) and the IEEE 802.11a wireless LAN. Moreover, the separation distances between the UWB and the wireless LAN are evaluated.

2 Evaluation of GTEM Cell

2.1 GTEM Cell

A TEM waveguide is an apparatus that can examine the immunity test by setting the equipment under test in the TEM electromagnetic field. A GTEM cell is an improved type of the TEM waveguide so that the cell can be used at frequencies above several gigahertz [3]. EMC measurements using a TEM waveguide are specified in IEC 61000-4-20 [4]. Figure 1 shows the schematic of the GTEM cell.
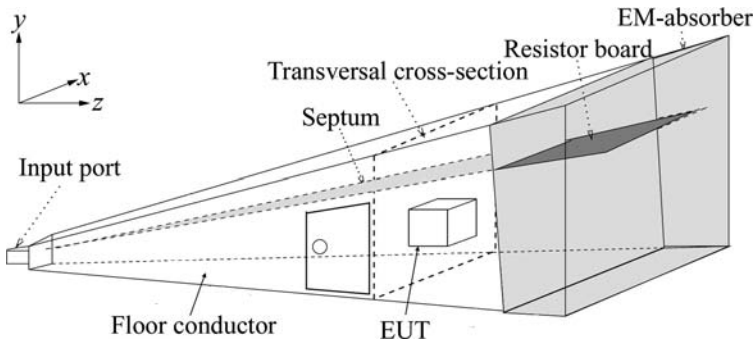
Fig. 1 A schematic of GTEM cell

The relation between the electric field at the point of the half of the septum height, E, and the net power consumed in the cell, P_{net}, is shown as

$$E = \frac{\sqrt{Z_0 P_{net}}}{h},\tag{1}$$

where Z_0 is characteristic impedance of the GTEM cell, and h is septum height. Z_0 and h are given by the structure of GTEM cell. If higher order modes are not generated, a propagation loss in the GTEM cell can be ignored. The approximated electromagnetic field can be provided by (1).

2.2 Measurement Method and Result

The frequency response of the electric field at the GTEM cell is measured. The septum height, h, and the septum width, w, are 1.0 m and 1.2 m, respectively. According to the IEC 61000-4-20, the

maximum EUT size is $h = 0.33$ m, $l = 0.72$ m, and $w = 0.72$ m in the case of our GTEM cell. Meanwhile, dimensions of a laptop computer used for the examination are 0.27 m height, 0.25 m depth, and 0.35 m width. The dimensions of the computer meet the requirements of EUT specified in IEC 61000-4-20.

The frequency response at the center point of the GTEM cell was measured with an isotropic electric field probe. The CW signal with a power of 30 dBm was fed into the GTEM cell. The measured values were compared with the approximated ones that were calculated by (1). When the difference between the measured and theoretical values in each frequency is within ± 3 dB, we determine the GTEM cell as an applicable device for the evaluation. Figure 2 shows the measurement result. The frequency response satisfied the requirement of the range of ± 3 dB from 3 to 6 GHz.
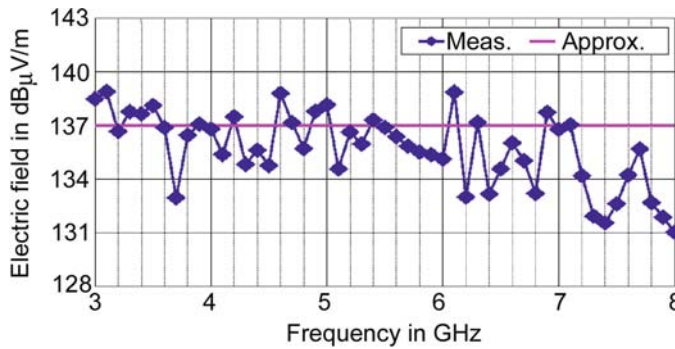
Fig. 2 Measured and theoretical values of electric fields at the center of the cell

3 Interference Evaluations

3.1 Specification of Measuring Instrument

Wireless LAN IEEE802.11a was used as a victim receiver in this interference evaluation. The specification of wireless LAN is shown in Table 1. For the interference source, DS-UWB transmitter is used. The DS-UWB specification is shown in Table 2. Figure 3 shows spectra of the DS-UWB and the wireless LAN.

Table 1 Specification of IEEE802.11A

	Specifications
Transmission scheme	OFDM
Frequency band	5.15–5.25 GHz
Frequency bandwidth	20 MHz
Modulation	BPSK, QPSK, 16QAM, 64QAM

3.2 Interference Evaluation of DS-UWB to W-LAN

Figure 4 shows a setup for the interference measurement. The laptop computer with a terminal of wireless LAN IEEE802.11a was placed at the center point of the GTEM cell. The wireless-LAN signal was added to the DS-UWB signal and those signals were applied to the GTEM cell with a

Table 2 Specification of DS-UWB

	Specifications
Transmission scheme	DS-SS
Center frequency	4.0 GHz
Nominal frequency band	3.0 GHz–5.0 GHz

Fig. 3 Spectra of DS-UWB and wireless LAN
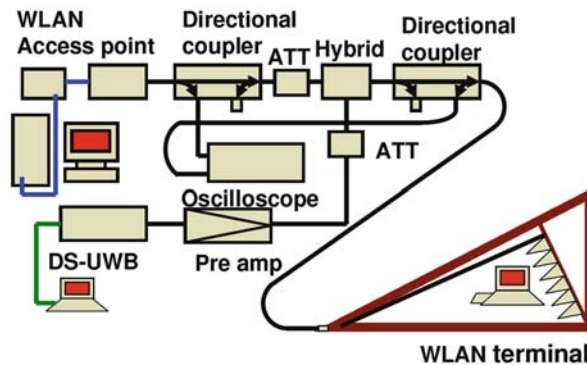
Fig. 4 Setup for interference measurement

coaxial cable. A receiver noise of the wireless LAN, *N*, and the wireless-LAN signal power, *C*, and the signal power of the DS-UWB, *I*, were defined at the input port of the GTEM cell, respectively. The term *N* was obtained by the comparison of the throughput variation in the receiver noise with the Gaussian noise added from the outside.

The interference test between the DS-UWB and the wireless LAN IEEE802.11a was conducted using the GTEM cell by measuring the throughputs for the various *I/N* ratio to the change of *C/N* ratio. A modulation scheme of the wireless LAN was fixed to BPSK or 64QAM in the measurements.

Figures 5 and 6 show the measurement results. The throughputs were degraded with the increase of *I/N* ratio. In cases of *I/N* ratio = –4.5 dB and –1.5 dB, the throughputs were degraded more than that of the noninterference case. In addition, the throughput of the DS-UWB in the case of *I/N* ratio = 0 agreed with that in a case where the Gaussian noise is added as the interference signal, *I*, instead of the UWB signal. Therefore, the signal of the DS-UWB is nearly equivalent to the additive white Gaussian noise (AWGN) in a case of throughput of 64QAM. The qualitative nature of throughputs in the case of BPSK is the same as the result of 64QAM. However, the signal of the DS-UWB is
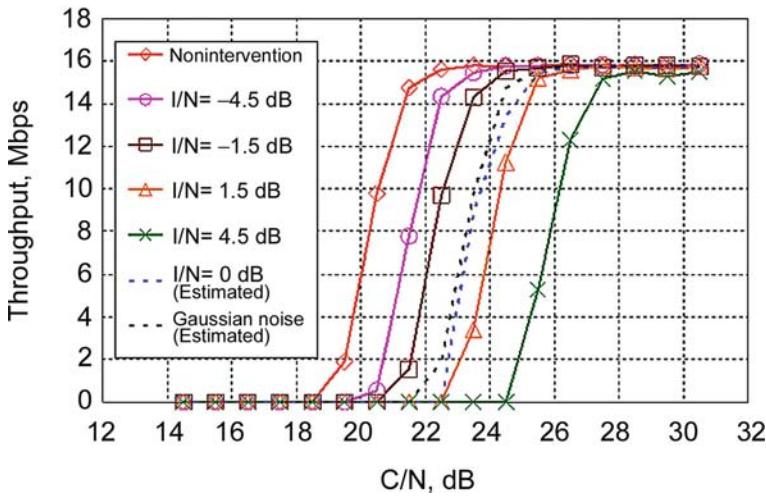
Fig. 5 Measurement results of throughputs in the case of 64QAM
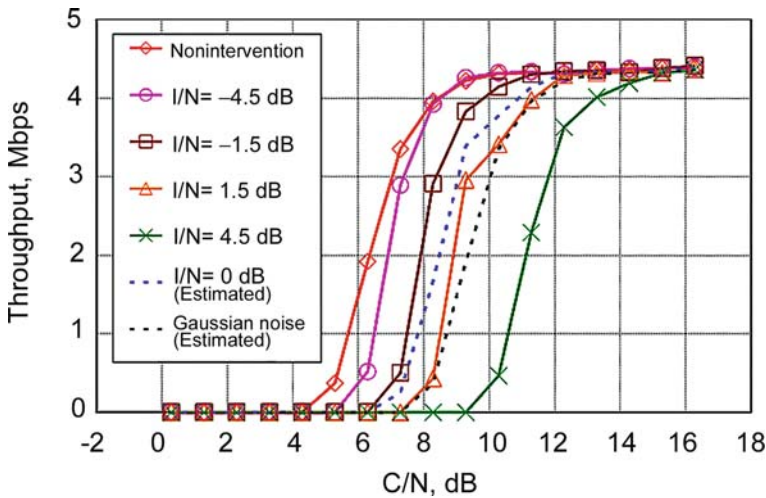
Fig. 6 Measurement results of throughputs in the case of BPSK

not equivalent to the AWGN in a case of the throughput of BPSK because the throughput of the DS-UWB is different from the Gaussian noise at the condition of I/N ratio $= 0$.

3.3 Evaluation of Separation Distance

A separation distance is defined as a distance between an antenna of the interference source and an antenna of the victim receiver. The separation distance is evaluated using the result of the throughput characteristics.

The minimum receiver sensitivity (MRS) of the wireless LAN in a case of 64QAM is -66 dBm/20 MHz. The receiver noise of the wireless LAN at the input port of the GTEM cell, N_0, was measured as -118 dBm/MHz. A transmission loss between the input port and the antenna output of the wireless-LAN receiver can be calculated as 44 dB using the Friis transmission equation. The gain of the receiving antenna was assumed to be 0 dB. A C/N ratio that corresponds to minimum receiver sensitivity, CNR_{min64QAM}, can calculate as the following equation:

$$CNR_{\mathrm{min64QAM}} = -66 - \{-118 - 44 + 10\log{(20\,\mathrm{MHz})}\} = 23\,\mathrm{dB}.$$

The blue dashed lines denote the MRS in the case of CNR_{min64QAM}. The separation distance, r, is given as

$$r = \frac{\sqrt{30 P_{EIRP}}}{E},\tag{2}$$

where E is electric field strength of the DS-UWB at the center point of GTEM cell. We apply the regulation limits of US (FCC) and the Japan/EU to the equivalent isotropic radiated power (EIRP), P_{EIRP}. The regulation limit in Japan is -70dBm/MHz in EIRP, and US regulation limit is -41.3dBm/MHz in EIRP at the frequency of 5.21 GHz.

Figure 7 shows the evaluation results. The separation distance of a severe condition, i.e., $I/N = -4.5$ dB, was 0.36 m in the case of Japan/EU limit. Throughput degradations of the wireless LAN receiver may be avoided at the distance of 0.36 m or more. The separation distance in C/N ratio that corresponds to the minimum receiver sensitivity of the wireless LAN is 0.21 m when we assume that the maximum permissible degradation in throughput caused by the interference is about 50% of the throughput under the interference-free condition. Therefore, probably UWB system on practical
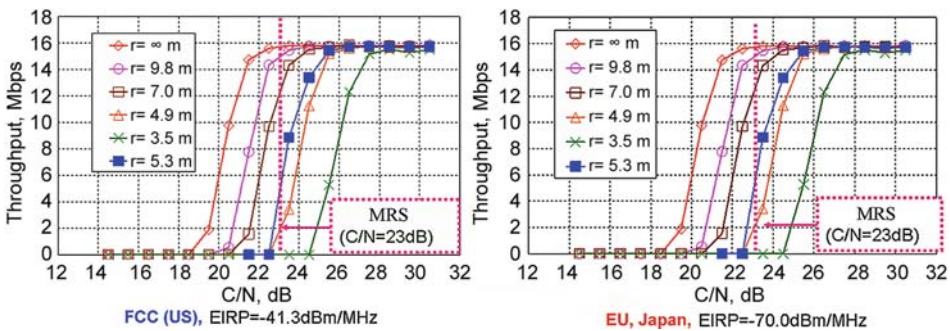
Fig. 7 Evaluated separation distances in regulation limits of US (*left*) and EU/Japan (*right*)

use hardly influences wireless LANs. In contrast, the separation distance of a severe condition was 9.8 m in the case of US limit. The wireless LAN receiver needs the separation distance of about 10 m or more to avoid the throughput degradations. In the case of the *C/N* in the minimum receiver sensitivity, the separation distance was 5.3 m.

4 APD Measurement of UWB Signal

The impact of interference depends not only on the power of the interfering signal but also on the statistical properties of the interfering waveform. Note that an amplitude probability distribution (APD) is defined by the part of time in which the signal amplitude exceeds a certain threshold. It is shown [6, 7] that the BEP (bit error probability) of a wireless system under interference can be directly calculated using a simple closed form of the APD of the interfering signals under some conditions. Considering the above background, additional measurements were conducted to obtain the APD of the DS-UWB signal. Following the necessary conditions of APD measurement to allow the results to be correlated with the degradation in the performance of the victim system [6, 7], the measurement conditions were as follows:

1. We set the APD measurement bandwidth to be 300 kHz, considering the subchannel bandwidth of IEEE 802.11a (312.5 kHz). The number of the subchannel of IEEE 802.11a is 52.
2. We adjusted the system noise level of the APD measurement apparatus to be equivalent to the internal noise level of the victim receiver.
3. The sampling frequency for the APD measurement was 10 MHz, which is sufficiently higher than the measurement bandwidth (300 kHz).

Figure 8 shows the measured APD of the DS-UWB signal at each measurement frequency. Note that the APD is plotted at 10 typical subcarrier frequencies. Note also that the power of the interfering UWB signal used for the APD measurement corresponds to $I/N = 0$ dB in Fig. 5, which means that the separation distance is 5.3 m in Fig. 7. It is found that the shape of the measured APD curve depends on the measurement frequency and that at some frequencies the APD clearly differs from a
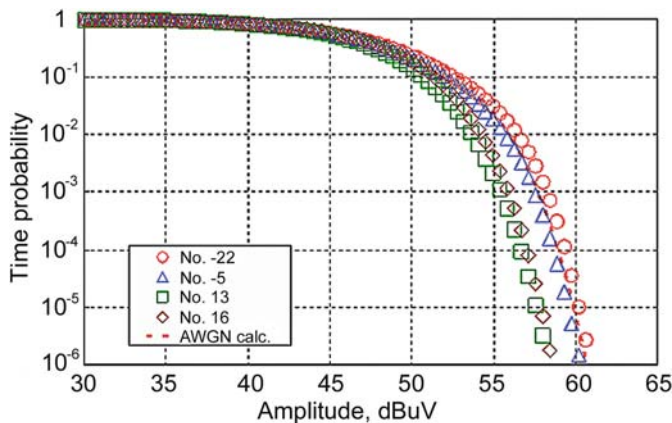
Fig. 8 APD of DS-UWB signal measured at each subcarrier frequency

calculated APD of AWGN. Thus, it can be concluded that the amplitude distribution of the in-band DS-UWB signal cannot be assumed to be AWGN. However, it should be noted that the total effect of the interference on the throughput degradation is nearly the same as that of the AWGN, as shown in Section 3.2.

5 Conclusions

In this report, we proposed a method of the interference evaluation between the UWB and the wireless LAN using the GTEM cell that can test the receiver with the antenna built-in type. It was confirmed that the GTEM cell could be used in the frequency range of DS-UWB by the evaluation of the frequency response.

The interference evaluation was conducted between wireless LAN IEEE802.11a and DS-UWB. As a result, even if the UWB signal is smaller than the receiver noise of wireless LAN, the throughput degrades. Moreover, the signal of the DS-UWB was almost equivalent to the AWGN in the case of the throughput variation of 64QAM.

We evaluated the separation distances in the regulation limits of US and Japan/EU. As a result, the wireless LAN receiver needed the separation distance of 0.36 m or more to avoid interference in the case of Japan/EU regulation limit. The separation distance in *C/N* ratio that corresponds to the minimum receiver sensitivity of the wireless LAN is 0.21 m. Therefore, probably UWB system on practical use hardly influences wireless LANs. In contrast, the separation distance of a severe condition was 9.8 m in the case of US limit. The wireless LAN receiver needs the separation distance of about 10 m or more to avoid the throughput degradations. In the case of the *C/N* in the minimum receiver sensitivity, the separation distance was 5.3 m.

The APD of the DS-UWB signal was conducted at each subcarrier frequency of the victim IEEE 802.11a signal. It was found that the APD of the UWB signal measured using the subchannel bandwidth of IEEE 802.11a could not be regarded as Gaussian but the total effect of the interference on the measured throughput was nearly the same as that of AWGN.

References

1. FCC CFR47 part 15, 2002.
2. ITU-R Recommendations SM.1754 – SM.1757, 2006.
3. D.Konigstein and D. Hansen, Proceedings of the Seventh International Zurich Symposium and Technical Exhibition on EMC, pp. 127–132, March 1987.
4. IEC 61000-4-20 Ed.1.0, 2005.
5. K. Gotoh, et al. 2004 International Symposium on EMC, Sendai, 1B1-2, pp. 69–72, Jun, 2004.
6. K. Wiklundh, IEEE Transactions on Electromagnetic Compatibility, vol. 48, no. 3, pp. 537–44, 2006.
7. Y. Matsumoto, IEEE Transactions on. Electromagnetic Compatibility, vol. 49, no. 4, pp. 940–41, 2007.

Simulation of the Effects of Radiation on a Satellite Memory and Improving Its Fault-Tolerant Ability, Using SIHFT

S.M. Nematollahzadeh and A.A. Jamshidifar

Abstract   This chapter describes a software environment based on VirSim tool to simulate the effect of radiation on COTS (commercial off-the-shelf) memories and shows the efficiency of the software EDAC (error detection and correction). As a case study, a sample student LEO (low Earth orbit) satellite with 8-MB (megabytes) RAM (random access memory) is considered and software EDAC for detecting and correcting the faults in the memory is implemented. The software EDAC is responsible for reliability of data in this 8-MB RAM. One separated task in VirSim tool has been developed for injection SEUs (single event upset) to the 8-MB memory of the satellite. The SEUs have been generated based on the ARGOS satellite reports. According to these reports the average of SEUs is about 5.5 SEU/MB per day, where it generates about 5 MBU (multiple bit upset) out of any 100 SEU. About four of these MBUs are double events (2-bit upset in one word) and one of them is triple. The software EDAC detects and corrects all 1-bit SEUs and detects double MBUs but it does not guarantee the detection of triple MBUs. This kind of simulation is very simple, accessible, and very close to the real environment and one can use it for checking effectiveness of the approach. The simulation results demonstrate efficacy of the approach in terms of fault detection and correction capabilities.

Keywords   Space radiation · SEU · SIHFT · Software EDAC · Simulation

1 Introduction

Transient errors and permanent faults in memory chips are well-known reliability issues in computer systems. Typically, the memory bus architecture is extended to accommodate extra bits, and encoding and checking circuitry are added to detect and correct memory errors. This additional hardware is sometimes omitted due to its cost. If a computer is designed using COTS components without EDAC hardware for memory, the reliability problem has to be addressed with another form of redundancy. Hardware redundancy techniques, such as duplication or TMR (triple modular redundancy), can be one solution, but they are very expensive. When hardware redundancy is not feasible, one must resort to software solutions. SIHFT (software-implemented hardware fault tolerance) techniques provide low-cost solutions for online detection and correction of transient errors due to the

S.M. Nematollahzadeh (✉)
Iran Telecommunication Research Center, Tehran, Iran
e-mail: nematz@itrc.ac.ir

effects of the environment like radiation, EMI (electromagnetic interference). Software EDAC is one of these techniques and is the prevailing solution to this problem [1].

This chapter discusses a software tool as a simulation environment called VirSim_RAD (Virtuoso simulator radiation) which has been implemented based on VirSim tool [2]. The tool simulates the fault injection in 8 MB of 8-bit RAM of a LEO satellite and implements an EDAC in software. It presents a technique for a system without hardware EDAC but requires protection for code and data. The goal is to protect against transient errors (soft errors) that manifest themselves as bit flips in memory. This approach is also well suited for COTS memories, which has been validated through fault injection experiments and radiation testing campaigns.

2 Harsh Environments

Engineers have traditionally handled the space radiation environment by designing computer hardware largely immune to space radiation's effects. SEUs, or single event upsets, are the major concern when computer systems are working with circuits that need to operate in certain environments, for example, in space applications [3]. SEU occurs when an energetic proton or heavy ion causes an electrical transient in a circuit, resulting in a bit flip known as a soft error. EMI can cause the same effects on electronic components.

3 COTS Products

The use of commercial off-the-shelf (COTS) products (hardware and software) and COTS-based systems in space missions is particularly attractive, as the ratio of performance to power consumption of commercial components can be an order of magnitude greater than that of radiation-hardened components, and the price differential is even higher. Figure 1 shows a comparison of the capabilities
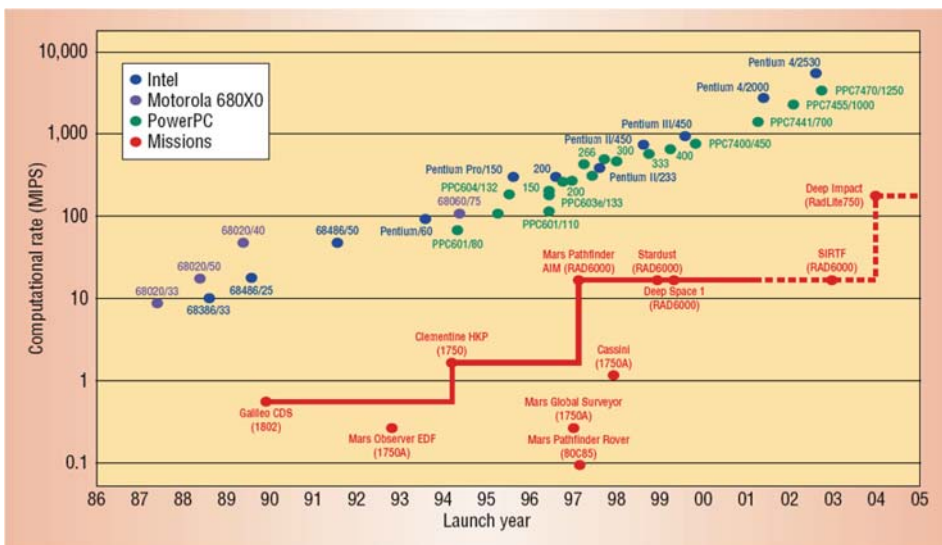
Fig. 1 Performance of commodity and RadHard processors over time

of past, present, and near-future commodity and radiation-hardened processors. Radiation-hardened processors are between one and two orders of magnitude less capable at any given time [4].

COTS are not usually designed for the stringent requirements of space applications. This means that the actual use of COTS components in space missions must be preceded by careful study of the impact of faults such as the ones caused by space radiation (e.g., single event upsets (SEUs)) in order to identify weak points that should be strengthened with specific fault tolerance techniques [5].

One proposal of using COTS-based systems in space applications is to use these systems for scientific data processing and not for spacecraft control [6,7].

4 ARGOS Experiments

The Advanced Research and Global Observations Satellite (ARGOS) was launched in February 1999. The objective of the computing test bed in ARGOS is the comparative evaluation of approaches to reliable computing in space, including radiation hardening of processors. This goal is met by flying processors and comparing performance in orbit during the ARGOS mission.

The ARGOS satellite has a Sun-synchronous, 800-km altitude orbit. A variety of radiation environments are encountered during this mission, providing a rigorous test. SEUs are the main type of errors that we are expecting to see in ARGOS. The simple memory test collected 113 errors from 1999/244 to 1999/345 in 84 days of actual run time. The test buffer was 256 KB. The overall SEU rate is 6.1×10^{-7} errors/bit-day or about 5.4 SEU/Mb per day [8].

From day 2000/130 to day 2001/243, the ARGOS COTS board detected a total of more than 2000 SEUs over 444 days of actual run time. As Fig. 2 shows, geographic locations of these errors correlate well with high particle regions such as the SAA (South Atlantic Anomaly) and the radiation belts [9].
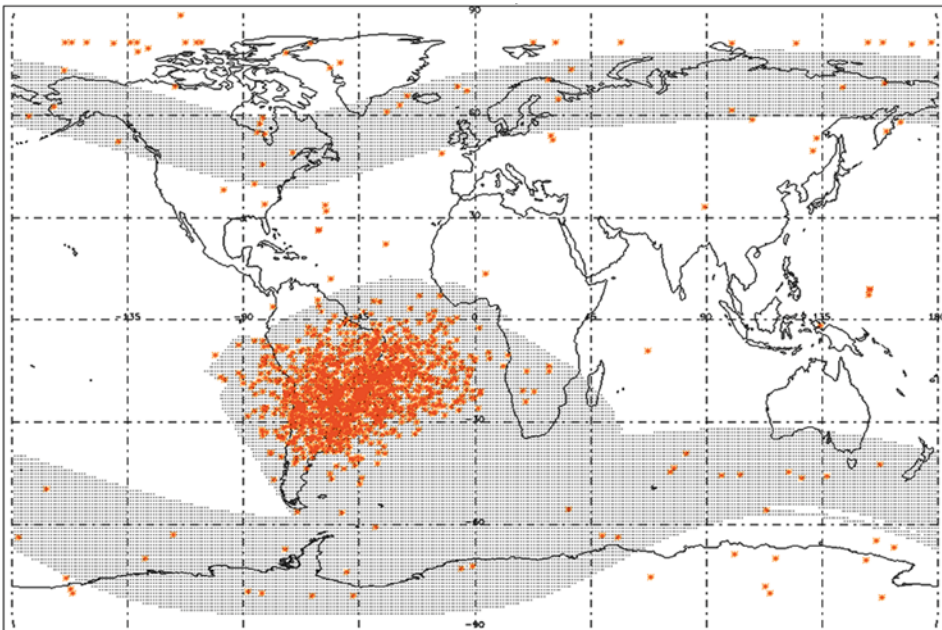
Fig. 2 Summary of SEUs in ARGOS COTS board

5 Software-Implemented Fault Injection

Fault injection can be applied either on a simulation model of the target fault-tolerant system or on a hardware-and-software implementation. Clearly, simulation-based fault injection is desirable as it can provide early checks in the design process of fault tolerance mechanisms. Initially, most studies related to the application of fault injection on a prototype of a fault-tolerant system relied on physical fault injection, i.e., the introduction of faults through the hardware layer of the target system. A trend favoring the injection of errors through the software layer for simulating physical faults, thus software-implemented fault injection (SWIFI), has emerged. Software-implemented fault injection (SWIFI) provides a low-cost and easy-to-control fault injection technique for generating faults to the target system [10]. Moreover, recent studies have shown that SWIFI was also able to emulate some types of software faults [11].

In this chapter we designed and implemented a task in the VirSim environment to simulate the fault injection in the 8-MB RAM of the satellite. This task uses the ARGOS experiments for implementing the faults in memory. For this job the task runs automatically by a predestined timer. According to the ARGOS reports the average of SEUs is about 5.5 SEU/MB per day, which generates about 5 MBU (multiple bit upset) out of any 100 SEU. About four of these MBUs are double events (2-bit upset) and one of them is triple [1].

6 SIHFT

Error detection techniques for software-based systems can be organized in three categories: software-implemented, hardware-based, and hybrid techniques. SIHFT techniques exploit the concepts of information, operation, and time redundancy to detect the occurrence of errors during program execution. SIHFT has been divided into various software techniques and software EDAC (SWEDAC) is one of them [12–14].

6.1 Software-Implemented EDAC

In many computer systems, memories are protected against SEUs by an error detection and correction (EDAC) code. This code is usually implemented in hardware using extra memory bits and encoding/decoding circuitry. EDAC protection can also be implemented in software. For example, a software implementation of a Hamming code that can do single-bit error correction to protecting RAM disks of satellite memories. This section briefly discusses our approach in this area. With hardware EDAC, the encoding is checked on each read operation and new codewords are generated on each write operation. In addition, the contents of memory are read periodically and all the correctable errors are corrected. This operation is called scrubbing and avoids accumulation of errors, thereby reducing the probability of multiple errors that may not be correctable.

If the same protection that is provided by hardware is to be provided in software, the software EDAC has been implemented. The software EDAC is given the address and size of the memory block that needs to be protected. It requests another block from the OS to be used for the check bits. Then, it calculates the check bits (encoding) and stores them in the allocated block. Upon request, it checks for errors (decoding) and corrects them if possible.

The software EDAC contains the algorithm necessary to generate check bits on 64 bits of data input according to a modified Hamming code. The EDAC can compare generated check bits against

those read with the 64-bit data to allow correction of any single bit data error and detection of all double (and some triple) bit errors. The software EDAC can also be used for 32-bit data words (7 check bits) with a few changes.

6.1.1 Check and Syndrome Bits (C_n, S_n)

The software provides either check bits or syndrome bits, SC0–7. Check bits are generated from a combination of the data input bits, while syndrome bits are an exclusive OR of the check bits generated from read data with the read check bits stored with the data. Syndrome bits can be decoded to determine the single bit in error or that a double (some triple) error was detected.

Our software EDAC is specially made for 64-bit error detection and correction. Check bits are generated and saved in the EEPROM memory of the satellite in the initial program load. Those check bits are used in the lifetime of the software and operating system can change them at the beginning of every restart or changing the memory contents. Syndrome bits are generated by an exclusive OR of the generated check bits with the read check bits. For example, S_n is the XOR of check bits C_n from those read with those generated.

Table 1 indicates the decoding of the eight syndrome bits to determine the bit in error for a single bit error or whether a double or triple bit error was detected. The SWEDAC uses the address of bit flip in the memory cell for correcting it. For multiple bit upsets (MBUs) the SWEDAC cannot

Table 1 Syndrome decode to bit-in-error (64-bit configuration)

				Hex	0	1	2	3	4	5	6	7	8	9	A	B	C	D	E	F
Syndrome Bits				S_7	0	0	0	0	0	0	0	0	1	1	1	1	1	1	1	1
				S_6	0	0	0	0	1	1	1	1	0	0	0	0	1	1	1	1
				S_5	0	0	1	1	0	0	1	1	0	0	1	1	0	0	1	1
				S_4	0	1	0	1	0	1	0	1	0	1	0	1	0	1	0	1
Hex	S_3	S_2	S_1	S_0																
0	0	0	0	0	*	C3	C5	T	C6	T	T	62	C7	T	T	46	T	M	M	T
1	0	0	0	1	C0	T	T	14	T	M	M	T	T	M	M	T	M	T	T	M
2	0	0	1	0	C1	T	T	M	T	34	56	T	T	M	40	T	M	T	T	M
3	0	0	1	1	T	18	8	T	M	T	T	50	M	T	T	M	T	2	24	T
4	0	1	0	0	C2	T	T	55	T	35	57	T	T	51	41	T	M	T	T	31
5	0	1	0	1	T	19	9	T	M	T	T	30	M	T	T	47	T	3	25	T
6	0	1	1	0	T	20	10	T	M	T	T	M	M	T	T	M	T	4	26	T
7	0	1	1	1	M	T	T	M	T	59	58	T	T	52	53	T	M	T	T	M
8	1	0	0	0	C4	T	T	M	T	37	36	T	T	42	43	T	M	T	T	M
9	1	0	0	1	T	21	11	T	M	T	T	M	M	T	T	M	T	5	27	T
A	1	0	1	0	T	22	12	T	33	T	T	M	49	T	T	M	T	6	28	T
B	1	0	1	1	17	T	T	M	T	38	60	T	T	54	44	T	1	T	T	M
C	1	1	0	0	T	23	13	T	M	T	T	M	M	T	T	M	T	7	29	T
D	1	1	0	1	M	T	T	M	T	39	61	T	T	15	45	T	M	T	T	M
E	1	1	1	0	16	T	T	M	T	M	M	T	T	M	M	T	0	T	T	63
F	1	1	1	1	T	M	M	T	32	T	T	M	48	T	T	M	T	M	M	T

NOTES:

* = No errors detected

Number = The number of the single bit-in-error

T = Two errors detected

M = Three or more errors detected

correct the errors, thus it blocks the memory address for rejecting the future uses. The all-zero case indicates no errors detected.

7 VirSim as a Simulation Tool

For executing application software on special hardware, we need an operating system, which is loaded on the hardware and provides the hardware resources for the application. Especially for real-time and multi-task software, it is better to use a multi-task and real-time operating system. Although there are many different multi-task operating systems provided for various hardwares, they have a few simulation, monitoring, and debugging capabilities. VirSim is a software tool, which runs on Windows OS platform and provides wide facilities of debugging and monitoring for developers [2]. Some of these facilities are as follows:

- A visual environment, which provides useful information about the software resources, which has been used in multitask programming, such as semaphores, queues
- Capability of step-by-step running of software and using the powerful debugging facilities of C++ Builder Compiler
- Simulation of some parts of software or hardware using visual environment
- Visualization of the memory in some tables to observing memory changes
- Capability of adding some extra tasks for simulation test procedures
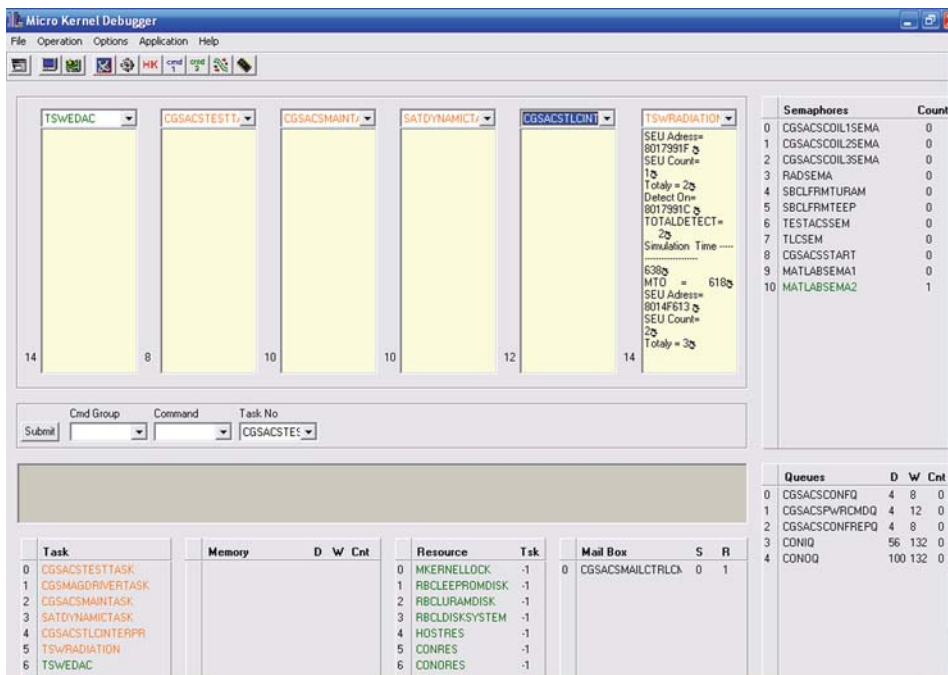
Fig. 3   User interface debugger menu
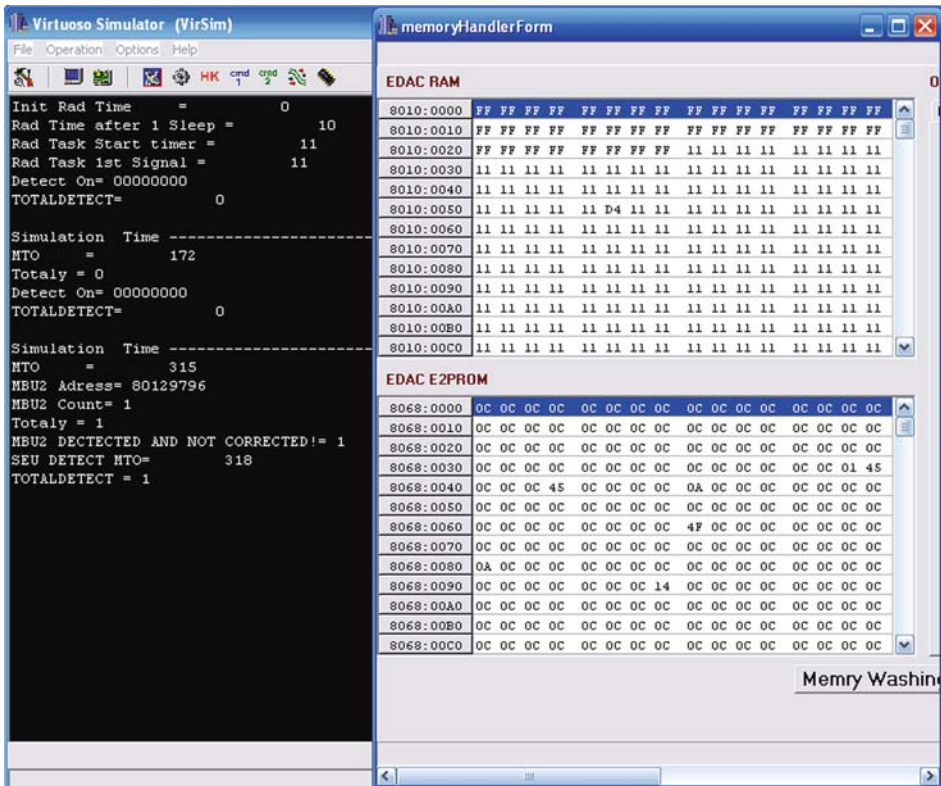
Fig. 4 User interface memory status

Figure 3 shows one of the VirSim menus, which can be used for debugging the software. In Fig. 4, user can see the memory table of satellite and the situation of SEU, MBU2, and MBU3, which have been occurred in the memory and then have been detected for possible correction by the SWEDAC. In dark menu, you can see the following information: Number of SEU, MBU2, or MBU3 and total errors, the address of error, time, number of SEU, MBU2, or MBU3 detected and corrected, address of those which have been detected and time.

The software tries to correct the errors which have been detected in memory, but for MBUs, software marked the address of the memory cell and prohibits access to them. Moreover, the software saves all these useful data in some specified datfiles.

8 Simulation Results

Two types of simulation have taken place in this work: the first one was simulating the effects of SEU in 1-MB RAM for 20 days and another one was simulating in 8 MB for 44 days approximately. The following tables show the results of two simulations which have been done in separate conditions and different times. The software with this structure is able to simulate same experiments for about 250 days. Simulations with more than 250 days need some changes in the software structure.

Table 2 shows the number of SEUs in two experiments. In the first one, 1-MB memory has been considered and the SWIFI provides 107 failures in 20 days to the memory which gives the 5.35

Table 2 SEUs have been injected to RAM

	Memory size (MB)	Radiation time (days)	Num of 1-bit SEU	Num of double MBU	Num of triple MBU	SEU/MB per day
First test	1	20	101	5	1	5.35
Second test	8	44	1457	73	11	4.37

Table 3 Error detection and correction coverage

	Memory size (MB)	Total errors	Error detected	Error corrected	Blocked cells	Undetected errors
First test	1	107	106	101	6	0
Second test	8	1541	1536	1457	79	5

SEU/MB per day. In the second simulation 8-MB memory has been impressed under SWIFI and it provides 1541 failures in about 44 days, which gives the 4.37 SEU/MB per day. As shown in Table 3 the SWEDAC could detect and correct more than 99% of faults in the satellite RAM. Only 5 MBU3 did not detected, in fact the SWEDAC detected them as a single SEU and tried to correct them but it is not accepted.

9 Conclusion

Random access memory is one of the basic parts in the computer systems which have been widely used in satellites. However, this type of devices is quite sensitive to SEUs. SIHFT techniques provide low-cost solutions for online detection and correction. Software EDAC is one of these techniques. VirSim is a software tool for developing and testing the same techniques. VirSim provides a useful environment for developing and debugging the SWIFI and SWEDAC.

In this chapter, we presented a software tool that is able to simulate the effects of SEUs in RAM memory of a LEO satellite and predict efficiency of a SWEDAC algorithm. The approach is based on VirSim as a software environment for technology characterization, on simulation-based fault injection for showing the effects of SEUs, and simulation of the effects of software EDAC for analyzing the accuracy of the proposed approach. Experimental results show that SWEDAC can detect and correct more than 99% of faults which have been accrued in memory of LEO satellites.

References

1. P. P. Shirvani et al., Software-implemented EDAC protection against SEUs, IEEE Transactions on Reliability, Special Section on Fault-Tolerant VLSI Systems, vol. 49, no. 3, pp. 273–284, 2000.
2. Sh. Jalilian, A. A. Jamshidifar, S. M. Nematollahzadeh, VirSim, a simulated environment for developing multitask software of satellite, Third International Conference on Recent Advances in Space Technology, Turkey, June 2007.
3. P. Reyes et al., New protection techniques against SEUs for moving average filters in a radiation environment, IEEE Transactions on Nuclear Science, vol. 54, no. 4, pp. 957–964, 2007.
4. D. S. Katz and R. R. Some, NASA Advances Robotic Space Exploration, Jet Propulsion Laboratory, Published by the IEEE Computer Society, 2003.
5. H. Madeira et al., Experimental evaluation of a COTS system for space applications, Proceedings of the International Conference on Dependable Systems and Networks (DSN'02) 2002, IEEE.

6. R. R. Some and D. C. Ngo, REE: A COTS-based fault tolerant parallel processing supercomputer for spacecraft onboard scientific data analysis, Proceedings of the Digital Avionics System Conference, vol. 2, pp. B3-1-7–B3-1-12, 1999.

7. K. Whisnant, R. Iyer, D. Rennels, and R. Some, An experimental evaluation of the REE SIFT environment for spaceborne applications, International Performance and Dependability Symposium, Washington, DC, June 2002.

8. P. P. Shirvani et al., Fault-Tolerant Systems in a Space Environment: The CRC ARGOS Project, Stanford University, CRC-TR 98-2, December 1998.

9. P. Shirvani et al., Strategies for Fault-Tolerant, Space-Based Computing: Lessons Learned from the ARGOS Test bed, Center for Reliable Computing, Stanford University.

10. J. Arlat et al., Comparison of physical and software-implemented fault injection techniques, IEEE Transactions on Computers, vol. 52, no. 9, pp. 1115–1133, 2003.

11. H. Madeira, D. Costa, and M. Vieira, On the emulation of software faults by software fault injection, Proceedings of the International Conference on Dependable Systems and Networks (DSN-2000), pp. 417–426, 2000.

12. P. Shirvani et. al., Software-implemented hardware fault tolerance experiments; COTS in space, International Conference on Dependable Systems and Networks, Fast Abstracts, June 25–28, 2000.

13. N. Oh, Software Implemented Hardware Fault Tolerance, PhD Thesis, Stanford University, December 2000.

14. P. P. Shirvani, Fault-Tolerant Computing for Radiation Environments, CRC-TR 01-6 (PhD Thesis), Stanford University, Stanford, CA, June 2001.

Investigations of Electromagnetic Behavior and Interaction of Motion Control Electronic Devices

J.-M. Dienot

Abstract As some actual or future prototypes for electronic motion control are designed with higher chip density and constraints for integration challenges, new electromagnetic interactions and compatibility cases have to be considered and modeled to prevent really bad electromagnetic compliance and less-of-motion risks. In consequence, the reliability and the functionalities of the embedded system itself can be affected. First this chapter deals with emission and immunity studies combined with temperature influence on electronic devices used to control power electronic motion modules. Specific Thermal-EM test setup and boards especially developed for these investigations are described. Then experimental results and first approaches of global modeling work for this issue on modern PCB technology are discussed.

Keywords Electromagnetic noise · Thermal impact · Radiated immunity · Programmable chips · Driver · PCB couplings

1 Introduction

The impacts of real physical environment, such as temperature, humidity, or reliability for conventional EMC behavior of modern hybrid electronic modules are non-negligible. It is important actually to estimate the realistic impact of external temperature on emissions and susceptibility cases of electronic devices [1,2]. An aggressive external quasi-static temperature, with high values as 150–200°C, can be inherently generated in an electronic transport architecture, either by motion thermal devices or by high power chip and radiator system [3]. Elsewhere, the most thermal-sensitive chips used in these power electronic modules are the control electronic devices including programmable driver technology [4, 5]. With actual state of the art of radiated EMC characterizations, both emission and immunity investigations can be performed over PCB and integrated circuits with near-field probe sets guided by a motorized scan table and/or TEM cells [6,7]. In these two cases, often dedicated PCBs are especially designed, inherently for TEM cell to comply with standardized cell aperture (10 cm × 10 cm) and also to separate inside/outer electromagnetic sources and victims [8]. To accede to parametric thermal characterization, some modifications of these radiated test

J.-M. Dienot (✉)
Tarbes University Institute of Technology, Tarbes, France
e-mail: jm.dienot@iut-tarbes.fr

setups, with a combination of warming plate solution, up to 250°C and spatial onboard temperature measurements are presented. We start from reference behavior of gate devices and programmable devices at ambient temperature and with failure criteria representative of the device's electronic activity [9]. Then, we focus on PWM pattern characteristics in both time domain and frequency domain, which are representative of the immunity compliance cases, with potential bad effects on motion control. Then, by combining physical and electrical modeling methodologies, some electrical parameters, models, and schematics are proposed, developed, and refined to start global modeling approach of these characteristics and help understanding of these new real multi-physics EMC behavior at device and PCB levels.

2 New Thermos-EM Experimental Method

2.1 Electromagnetic Characterizations for Devices and Circuits

Electrical E-field and magnetic H-field are the two components of global electromagnetic waves and energy, representative of high-speed and high-level switching activity in integrated and hybrid actual devices. As shown in Fig. 1, the measurement and injections of these two components of the complete electromagnetic field can be realized over different areas of the PCB and the circuit, with a dedicated probe set like H-spires and E-dipoles associated with a scan table system [10]. As actual near-field electromagnetic behavior of PCBs and integrated circuits cover a wideband of frequency, from 1 MHz to 1–3 GHz, dedicated electromagnetic probes fabricated with high-frequency semi-rigid coaxial cable, represented in Fig. 1, are suitable and necessary to accede to the upper range of
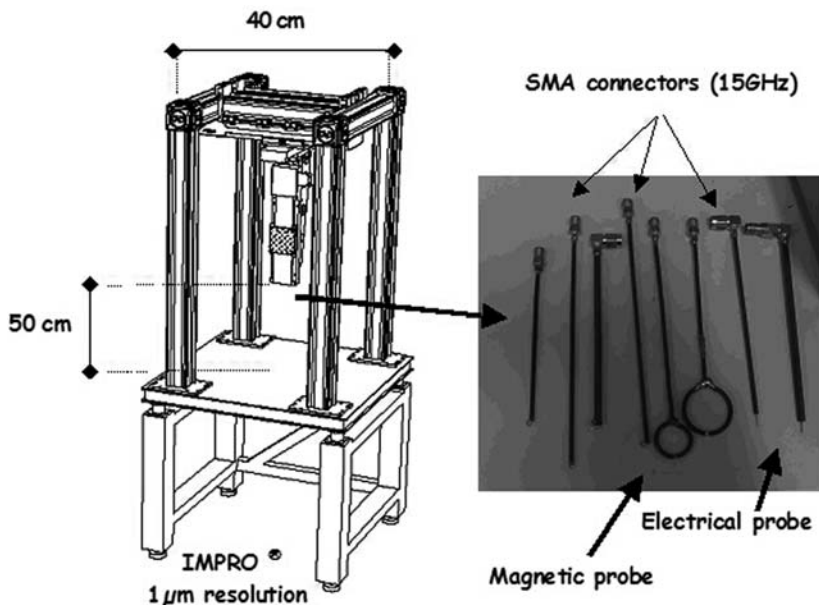
Fig. 1 Motorized scan table with its HF wideband electric and magnetic field probes dedicated for near-field EMC characterization on integrated circuit and PCBs

frequency spectrum. Characterization resolutions are driven by a 0.3 mm diameter for H-spire and 1 cm length for E-probe [11].

Complementary electromagnetic characterizations on PCBs and integrated circuits are performed with transverse electrical-magnetic mode cell, also commonly called Crawford TEM cell. It can be used from 1 MHz to 10 GHz, at PCB and integrated circuit (IC) levels [7–9], as a well-suited alternative to large size experimental equipment for conventional radiated characterization. It also allows pertinent solutions for selective electromagnetic characterization of single electronic device enclosed in the shielded cell environment. For this, specific printed circuit boards (PCB) have to be designed for TEM cell solution, with the dimension of the aperture cell, the completion of shielding quality of the system with a one-face metallic plane, and the choice of inside components to be coupled with TEM cell septum. Inside-cell electromagnetic waves, in TEM mode propagation, are collected or injected on one port of the cell with the RF generator and the other port is loaded by a 50 Ω HF impedance.

With these two types of electromagnetic equipment, both emission and immunity cases can be alternatively performed: for emission and radiated noises, high-frequency receiver or spectrum analyzer is connected to the near-field probe outputs and the TEM cell ports; for immunity cases, replacing receivers by wide-band amplifier and versatile waveform generators allow harmonics and transient aggression experiments.

2.2 EM Setup's Completed with Thermal Solutions

For the interest of temperature influence on the electromagnetic disturbance effects of an active device, new experimental techniques have been developed to complete both near-field and TEM characterizations. For near-field subject, the special design of an "XYZ" scan table has been performed in Z-direction to allow the insertion of a directive warming plate, where volume occupancy is about 22 cm × 30 cm × 12 cm, below the arm fixture. Z-position and reference can be adjusted and hold, with respect to the test PCB minimum distance (1.5 cm) to provide efficient heating avoiding destructive burning contacts. For dealing with both thermal measurements in association with near-field measurements, a thermal contact probe, with a touch end of 0.1 mm diameter and a thin body support of 8 cm length, has been coupled on the same scan table moving fixture, with a slightly different Z-axis reference than EM probe. When moving and positioning the measurement point, thermal probe stays in contact with the body of the electric element as near-field probes are just over, as shown in Fig. 2. Electromagnetic responses are collected in frequency domain, as H or E levels in decibels. Temperature responses, with a more long time constant and variation, are collected by sampling digital acquisition system and the global setup is controlled by PC [11].

For transverse electrical-magnetic mode cell configurations, some new solutions have also been developed to include the thermal experiment parameters [12]. The first modification proposed is to realize the placement of the PCB test fixed with the TEM cell fixture over the heat zones of the warming plate. To achieve this, the TEM cell with its test PCB has to be maintained over maximum 4 cm of the warming plate to keep efficient heating action, with a special fixture arm (Fig. 3). The constraints are to report electrical and thermal connections very close to the PCB and to go at the control-measurement system with a 90° angle so as to not touch the hot warming plate, as represented in Fig. 3.

The second development concerns the real acquisition of the temperature aggression value on board. The TEM cell configuration does not comply with an external contact thermal probe solution. To overtake this, we propose the integration of thermal resistors in surface-mounted device (SMD)
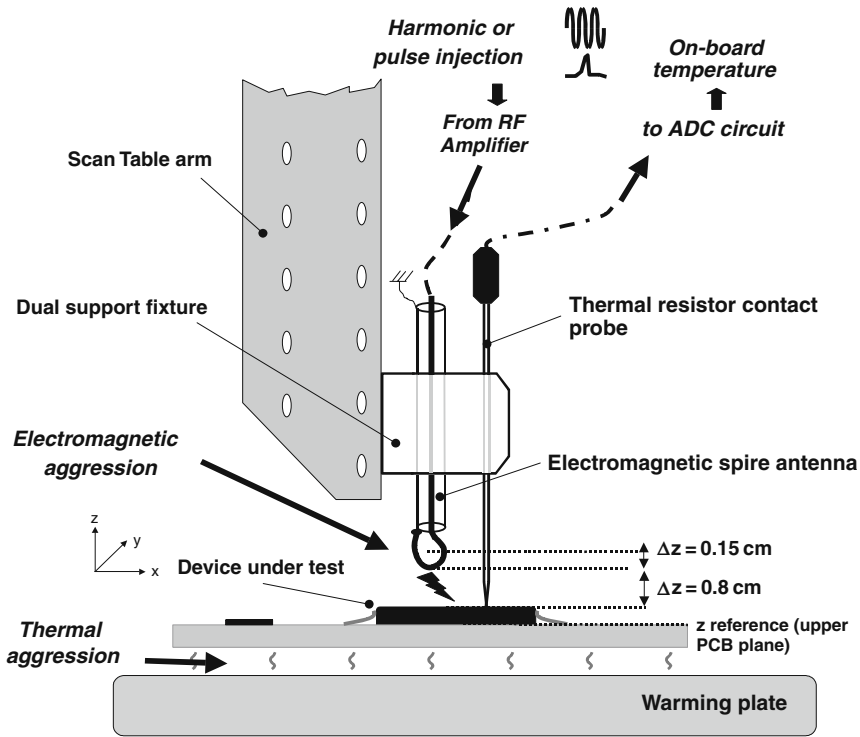
Fig. 2 Two-dimensional view of the experimental dual thermal near-field setup configuration for immunity
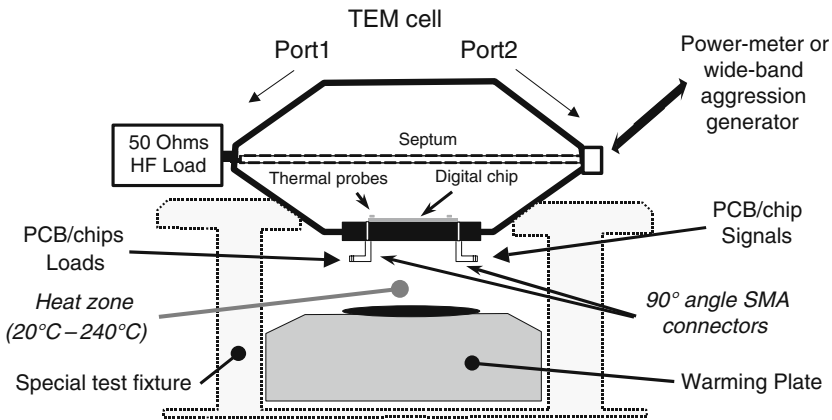
Fig. 3 Two-dimensional view of new heated TEM cell configuration for immunity/emission testing on motion control boards

or thin film technology. The four-wire connection for each probe must be "electrically length" and optimized to avoid more unwanted radiated noise or parasitic coupling, even if thermal signal is a low-frequency excited one. Inside-cell probes are connected on the outer using via-hole techniques, as visible in Fig. 4.
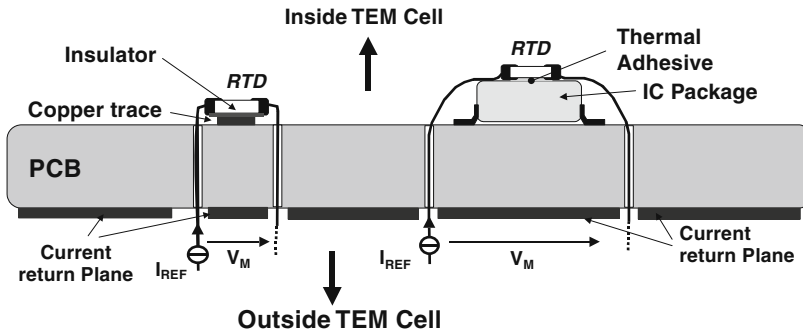
Fig. 4 Transverse view of dedicated PCB specifications with onboard thermal probes

3 Application on Control Circuit Boards

3.1 Description of the Control Test Boards

As control circuits are used to drive power converter boards designed for well-suited motion or energy supply function [4], we want to mainly focus on their real EMC behavior with non-ambient temperature environment. PCB prototypes have been designed for this, using programmable integrated circuit type for motion control-embedded applications with mainly pulse width modulation (PWM) patterns controlled by versatile cyclic rate input command. Example layout is on Fig. 5, including thermal scan. Signal output is delivered on internal capacitance load (500 fF) in parallel to the external capacitive load (1 pf). Electromagnetic disturbances issued from these boards are observed or attended in the range of 1 MHz to 1 GHz. Immunity cases can occur with a –10 dB m of aggression levels, typical values for harmonic case and low-voltage circuits [13].
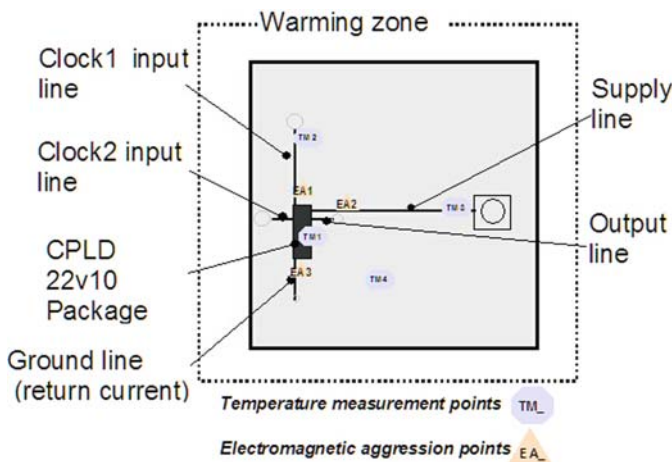
Fig. 5 Example of layer upper view of control circuit PCB and configuration for dual Thermos-EM characterization in TEM cell

3.2 Emission Case Results

For emission, experimental studies have covered different digital electronic architectures, from elementary digital chip [14] to complex integrated chips [15]. All of them show significant shifts of radiated global noise of PCB including active chips in normal activity and different noise and energy frequency repartitions than usual emission characterizations at ambient temperature (Fig. 6). To resume the most recent results, concerning the activity of a CPLD/FPGA circuit on a PCB, H-field and E-field have been collected up to 1 GHz, as a good image of radiated noise and integrity signal responses. Figure 8, with a pertinent 3D view on both frequency repartitions, fields amplitude, and steps of temperature values, shows the real impact of temperature aggression on emission behavior of this device. Starting from a maximum peak level at 90 MHz, then at 120, 178, 240, and 320 MHz with 5–25 dB lower levels, all this for the reference temperature of 20°C, main significant spectral shifts are observed when temperature is forced from 24 to 120°C. Finally, important conclusion is that H-field is quite twice or three times more temperature sensitive than E-field, especially over the active device package. This is due to the IC used for these studies, which is mainly current switching driven. With the aid of complementary modeling work [14], it has been pointed out that important contributors for the explication of temperature influence are globally the active chip for 75%, the ground-supply network for 10%, and EM coupling factors with antennas for 15%.
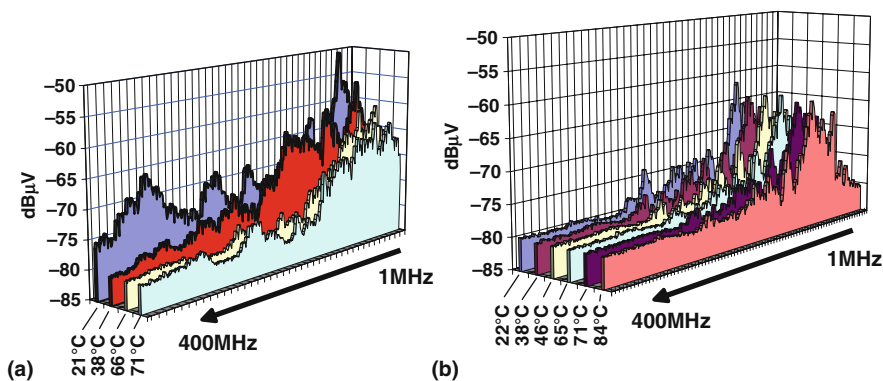
Fig. 6 The CPLD/FPGA dual near-field case: Emission levels among the frequency for different steps of temperature: (**a**) magnetic field *H* and (**b**) electric field *E*

3.3 Immunity Case Results

Main phenomena observed for susceptibility aspects are generally, for digital mode device, the modifications of threshold levels and switching times. This is due to the couplings of external parasitic signals on supply and I/O ports. For hard aggression cases, temporary or definitive loss of function can be observed [15]. In the application example, we combine the aggression of dual thermal-electromagnetic disturbances and its impact on PWM pattern output. In Fig. 7, on a control driver integrated circuit based on an FPGA (MACH4 from lattice), instable behavior among different aggression waveform characteristics can be observed, using initial threshold reset level as the default criteria. Then, to complete this, the wave aggression impact with temperature is performed. The observation criterion is now centered on the shifts in switching current spectrum and the PWM
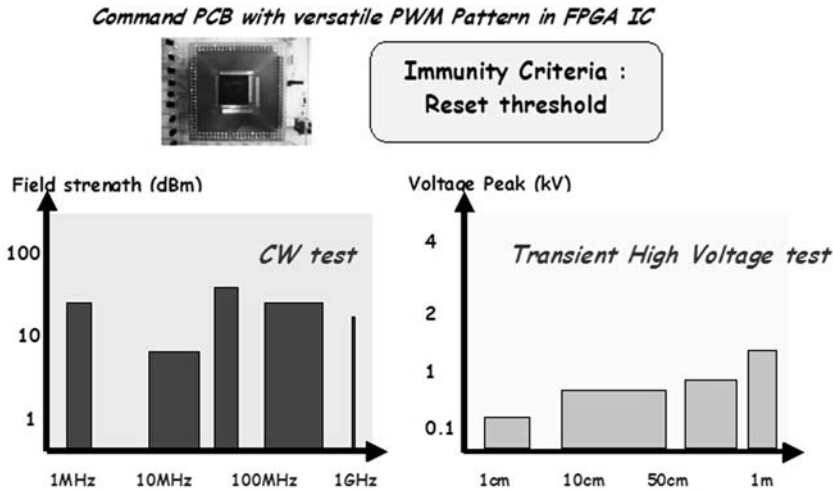
Fig. 7 Results of immunity behavior of a programmable driver in harmonic and transient modes

pattern frequency signature. A significant result is reported in Fig. 8: Relative global amplitude of waveform of current switching device, I_{VDD}, is reported with significant harmonic frequency impact couplings, at ambient temperature, in the 100—800 MHz zone. This variation is enforced when increasing, step by step, the external temperature and so the device package measured temperature. This indicates and confirms the modifications of switching current performances and, more significantly, an impact of high temperature as extra external energy conditions on electrical behavior of the programmable chip under electromagnetic pressure.

Fig. 8 Relative variation of switching current amplitude with dual thermal-harmonic wave aggressions in TEM cell
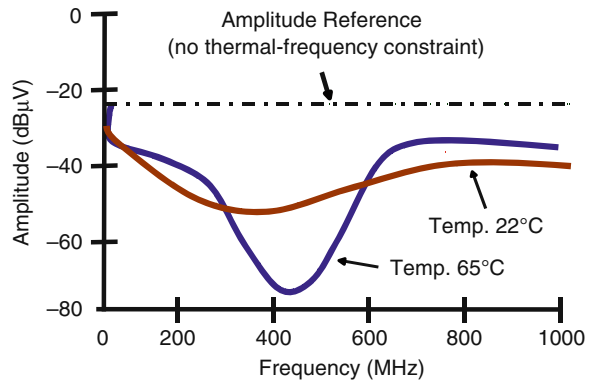
4 Conclusions

With these works, a new modified EMC characterization approach is in progress, for pertinent real-case EMC investigations. New test benches and dedicated PCBs have been developed, and dual Thermos-EM campaign has started with a focus on command circuit behavior. With some applications on this type of device, some electromagnetic interactions and responses have been reviewed to

explain the effect of external temperature on basic EMC characteristics, emission and susceptibility, of digital device. Most interesting conclusions concern the link and the influence of thermal energy on high-speed and radiated behavior of the switching current of the driver circuit [16].

References

1. S. Weber, S. Guttowski, E. Hoene, W. John, and H. Reichl, EMI couplings from automotive traction systems, Proceedings of the IEEE EMC-S, pp. 591–594, May 2003.
2. R. Hoad, N. J. Carter, D. Herke, and S. Watkins, Trends in EM susceptibility of IT equipment, IEEE Transactions on Electromagnetic Compatibility, vol. 46, no. 3, pp 390–395, 2004.
3. Power Electronics Associated Research Laboratory, Technological issues of future integrated power module for electrical traction, http://lab-pearl.com/activites.htm
4. B. Murari, F. Bertotti, and G. A. Vignola, Smart Power Ics, Technologies and Applications, 2nd edition, Springer Ed., New York, ISBN 3-54043238-8.
5. E. Hoene, A. Lissner, S. Weber, S. Guttowski, W. John, and H. Reichl, Simulating electromagnetic interactions in high power density inverters, Proceedings of IEEE 36th PESC Conference, Recife, pp. 1665–1670, 2005.
6. K. P. Slattery, J. Neal, and W. Cui, Near-field measurements of VLSI devices, IEEE Transactions on Electromagnetic Compatibility, vol. 41, no. 4, pp. 374–384, 1999.
7. SAE 175/3, Electromagnetic compatibility measurement procedures for radiated emission measurements, 150 kHz to 1 GHZ, TEM Cell, Society of Automotive Engineers, 1995.
8. J. P. Muccioli, T. M. North, and K. P. Slattery, Investigations of the theoretical basis for using a 1 GHz TEM cell to evaluate the radiated emissions from integrated circuits, Proceedings of the IEEE EMC-S, Santa-Clara, pp. 63–67, August 1996.
9. IEC 62132, Characterization of integrated circuit electromagnetic immunity, IEC Standard, 2003.
10. J. C. Bolomey, Introduction to near-field techniques for EMC applications: state of the art and prospectives, IEEE International Symposium on Electromagnetic Compatibility, Proceedings of the IEEE EMC-S, Montreal, vol. 1, pp. 356, August 2001.
11. M. Bernard, J. M. Dienot, Développement des bancs d'experimentations THERMOS EM&IMPRO, Internal Technical Report, LabCeem laboratory, Tarbes Institute of Technology, July 2007. Internal Report, Available on http://www.jmd.fr.vu
12. J. M. Dienot, Experimental thermal impacts on EMC characteristics with new near-field measurements approach, Proceedings of the 3rd International Conference on Electromagnetic Near-Field and Imaging Characterization, St Louis, pp. 302–307, June 2007.
13. L. Chahine, M. Kadi, E. Gaboriaud, C. Maziere, A. Louis, and B. Mazari, Modelling of Integrated circuit susceptibility to conducted electromagnetic disturbances using neural network theory, Electronics Letters, vol. 42, no. 18, pp. 15–16, August 2006.
14. J. M. Dienot, Characterization and simulation of digital device electromagnetic noise under non-ambient temperature conditions, Electronics Letters, vol. 43, no. 20, pp 1073–1074, September 2007.
15. S. Bendhia, E. Sicard, A. Boyer, Y. Mequignon, and J. M. Dienot, Thermal influence on 16 bits microcontroller emission, Proceedings of the IEEE EMC S, Honolulu, July 2007.
16. L. Lonzi, M. Piccoli, and F. Speroni, Failure mechanisms in Smart Power Ics, Proceedings of the 5th ESREF, Glagcow, 1994.

Wunsch–Bell Criterial Dependence for Si and GaAs Schottky-Barrier Field-Effect Transistors

G.I. Churyumov, M.P. Gribskii, V.V. Starostenko, V. Yr. Tereshenko, D.A. Unzhakov, and S.A. Zuev

Abstract In this chapter a numerical mathematical model of the Si and GaAs Schottky-barrier field-effect transistor is considered. This model permits current and thermal modes of these devices to be investigated when reaction of powerful electromagnetic pulses takes place. In this case changing characteristics of semiconducting materials with increasing temperature is taken into account. Using the mathematical model allows dynamics of electrothermal processes to be studied including an outgrowth of avalanche process, forming current "cord," thermal breakdown of the devices. The computer modeling results showed that in studies of the external reaction of the electromagnetic pulses with semiconductor devices as criterion of the resistance it is necessary to take into account the volume density of power instead of its surface density.

Keywords Electromagnetic pulse · Semiconductor device · Mathematical model · Wunsch–Bell criterial · Computer modeling

1 Introduction

The reaction of powerful pulsed electromagnetic fields with semiconductor devices affects electrical and thermal conditions their operation and, finally, can lead to a breakdown and failure of the device.

For determining the resistance of semiconductor devices affected by pulse electromagnetic fields Wunsch–Bell criterion is used [1]. The given criterion does not include a series of the factors influencing the final result of the impact. In particular, the polarization pattern of an electromagnetic wave, defining the additional voltage value and also the pulse edge bias current and high-frequency interpolation, is not considered. During imitation of the impact of an electromagnetic field upon the semiconductor devices its characteristics are not bound to the result of the impact. For some cases, for example, with the dimensional change of the active chip area of a semiconductor and the change of heat dissipation from the device, the given criterion is not held true [1].

———————————

G.I. Churyumov (✉)

Microwave & Optoelectronics Lab., Kharkov National University of Radio Electronics, 14, Lenin Ave., Kharkov, 61166, Ukraine
e-mail: g.churyumov@ieee.org

In this chapter the mathematical models of Si and GaAs Schottky-barrier field-effect transistors (FET) and the results of modeling of physical processes in these devices in intense current and thermal conditions are considered.

2 Problem Statement

Modeling of the operation of a semiconductor device under conditions of influence of an intense electromagnetic field (a nonlinear mode) requires a strict (self-consistent) target setting. In [2–4] it is shown that for the investigation of the influence of an external electromagnetic field on performances and electrical functional mode of Si and GaAs FETs with various geometries of the active chip area of the device it is necessary to take into account the thermal processes bound with the allocation of heat in various parts of the active chip area of the FET and also the processes of generation of surplus pairs of electron–hole capable to lead to the avalanche breakdown. For analyzing the processes of localization and distribution of heat, the heat conduction equation with heat release sources, the intensity of which is calculated on the basis of the processes of energy interchanging between electronic gas and crystal lattice at scattering on phonons, is solved.

As a method of the solution of a self-consistent set of equations the method of large particles is used [5]. The process of modeling of an impact of the external electromagnetic field on the semiconductor devices suggests, at the first stage, the solution of the diffraction problem bound to the estimation of allocation of an electromagnetic field near the device and the determination of the voltage value, applied to the device, and at the second stage reviewing of the electro-thermal processes which are taking place in the device.

3 The Basic Mathematical Model Equations

For modeling of physical processes in the Schottky-barrier FETs the following fundamental equations are used:

Boltzmann kinetic equation

$$\frac{\partial f}{\partial t} + \left(\vec{v} \vec{\nabla}_r f \right) + \frac{1}{\hbar} \left(\vec{F}_i \vec{\nabla}_k f \right) = \left(\frac{\partial f}{\partial t} \right)_i \tag{1}$$

Poisson equation

$$\Delta \varphi = -\frac{1}{\varepsilon} \left(\rho \left(\vec{r} \right) - \sum_i e_i \int f_i \, d\vec{v}_i \right) \tag{2}$$

Heat conduction equation

$$cd \cdot \frac{\partial T}{\partial t} = \frac{\partial}{\partial x} \left[K \left(T \right) \cdot \frac{\partial T}{\partial x} \right] + \frac{\partial}{\partial y} \left[K \left(T \right) \cdot \frac{\partial T}{\partial y} \right] + q \left(x, y, t \right), \tag{3}$$

where f is a cumulative distribution function of carriers due to their energy and impulses, $\vec{v}_i$ a velocity of charge carriers e_i, $\vec{F}_i$ the force operating on a charge on the part of an external electromagnetic field and other charge carriers, $\left(\partial f / \partial t \right)_i$ a collision integral, ρ the space-charge density, $\sum_i e_i \int f_i \, d\vec{v}_i$ the space-charge density created by the free current carriers, c a specific thermal capacity of the crystal,

d its density, $K\,(T)$ a thermal conductivity factor, and $q\,(x,y,t)$ a density of heat release sources which is bound to the scattering integrals.

The boundary conditions for a cumulative distribution function are determined by injection and reflective properties of boundaries and for a potential φ by the values of a potential or its derivative on the area boundaries.

The value $q\,(x,y,t)$ in (3) represents the amount of heat obtained or lost in a crystal sector of unit volume for a time unit, and it is proportional to the number of scattering processes of carriers on phonons. At scattering on acoustical phonons the density increment value of heat release sources is equal:

$$\pm\,\Delta q\,(x,y,t) = \frac{\varepsilon}{S_{\text{cell}} \cdot dt},$$

where $S_{\text{cell}} \cdot dt$ is the volume of the partial model mesh in the space coordinate–time. The sign in the expression for Δq determines the emanation of a phonon or its absorption by the charge carrier: in case of emanation, the lattice gains energy and in the case of absorption, gives it back.

The solution of the kinetic equation is carried out by the macroscopic particles method and is reduced to the solution of equations of motion for charge carriers in a crystal in view of operating fields and mechanisms of scattering:

$$\frac{d\vec{r}}{dt} = \frac{1}{\hbar}\frac{d\varepsilon_k}{d\vec{k}} \quad \text{and} \quad \frac{d\vec{k}}{dt} = \frac{1}{\hbar}\frac{\vec{F}}{m^*},$$

where ε_k is the energy of the carrier, $\vec{F}$ the external force operating on it, $m^* = m(q^*/q)$ the reduced mass of a charge.

The scattering integrals $\left(\partial f / \partial t\right)_i$ in the right part of Boltzmann equations are like the similar integrals for vacuum; however, they include the specific features of motion and collision of electrons in the semiconductor. The centers of scattering in this case are ions and neutral atoms of impurities (alloying and compensating), other free charge carriers, thermal crystal lattice vibrations (optical and acoustical phonons), etc. Each of the centers of scattering is characterized by its own scattering frequency.

The process of scattering of a charge carrier can be considered as a transition from one state with a quasi-impulse $\vec{k}_i$ to another allowed state with $\vec{k}_f$. The probability of a drift from the state i can be interpreted as a scattering frequency. It is given by the first-order expression of perturbation theory:

$$W = \int \frac{2\pi}{\hbar}\left|\langle f|H_s|i\rangle\right|^2 \cdot \delta\left(E_f - E_i\right)\,dS_{\text{f}},$$

where the integral is undertaken on all finite states S_{f}; the delta function expresses the law of conservation of energy; H_s the Hamiltonian of scattering, the aspect of which is determined by the scattering center; f and i are the allowed states.

Considering that the modeling area heterogeneity enters the given expression as association of the parameters of the medium (temperatures, impurities densities, imperfections, carriers, etc.) on the coordinate, it is possible to assume that

$$W_s = W_s\,(k) = \frac{1}{\tau_s(k)},$$

where τ_s is the time between one type scattering acts, the association of probability on coordinate is dropped. The probability of scattering is the function of coordinate and impulse of the carrier and it is determined by the properties of a medium.

To describe the process of avalanche breakdown it is necessary to take into account the generation of non-equilibrium carriers in the semiconductor structure [6]. The expression for probability of ionization as one of the probable mechanisms of scattering in the semiconductor structure depending on a quasi-impulse of an ionizing macroscopic particle, which can be used for solving a set of equations (1), (2), and (3), has the following aspect [2–4]:

$$\nu(k) = \frac{\sqrt{2}\pi e_q^4 N \left(1 - \left(k_i/k\right)\right)}{\sqrt{\frac{1}{2}h^2 k^2 k_0^2 E_i}}.$$

(4)

The obtained correlation (4) expands the scope of possible models of the transistor [2,3], allowing to explore the dynamics of avalanche multiplication of non-equilibrium carriers in the active chip area. As a result of the act of ionization, when an electron gets sufficient energy, there is a scattering of the primary electron with the formation of a non-equilibrium pair of electron–holes. Accordingly, while modeling the physics of avalanche formation processes it is necessary to take into account the dynamics of non-equilibrium holes ensemble.

As the velocity of holes is much smaller than the velocity of electrons, it is possible to use the drift velocity model for holes in gallium arsenide or silicon to keep record of the holes movement on the basis of association of the drift velocity with the field intensity and the crystal temperature.

The relations of the electron scattering frequencies with the quasi-impulse for the most probable mechanisms of scattering are offered in [2,4].

4 Analysis of the Obtained Results

The calculations were carried out for the n-type Schottky-barrier FET on Si, with effective lengths of gate 60 and 150 nm; doping level of layers of Si: n^- – buffer layer – 10^{21}m^{-3}, n – channel – 10^{23}m^{-3}, n^+ – a contact layer – 10^{24}m^{-3}. The substance for gate metallization was Au with an underlayer of W. For GaAs the transistor was calculated with the gate width 30 nm, concentrations $N_i = 10^{21}\text{m}^{-3}$, $N_n = 5 \times 10^{23}\text{ m}^{-3}$, and $n^+ = 10^{25}\text{ m}^{-3}$. The topology and geometrical sizes of the FET are given in Fig. 1.
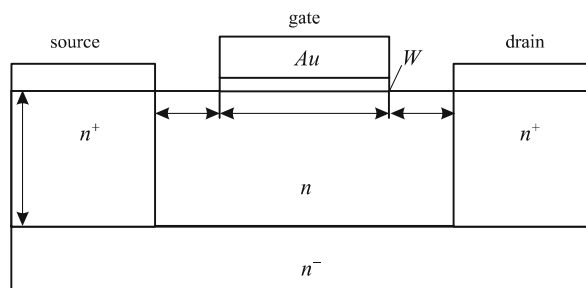
Fig. 1 Topology and geometrical sizes of the Schottky-barrier FET on silicon

Model adequacy was estimated in comparison with the experimental data for integral characteristics of discrete devices of micron sizes. The effect of electromagnetic fields on the considered devices is reduced to feeding additional voltages to two of the three contacts of the device. At modeling of the operation of the transistor in intense current and thermal conditions the additional voltage was applied, as a rule, between the drain and the source. The study of operation of the field-effect transistor as a modulator is an exception. The calculated modulation characteristics allow estimating the voltage values between the source and the gate, and also between the source and the drain, the exceeding of which leads to the distortions during the operation of the transistor as a modulator. The same values determine the values of additional voltages at the impact of the electromagnetic fields leading to the malfunctions in operation. It is necessary to note that with the overrunning of the linear sector of modulation characteristics the temperature conditions of the transistor practically do not differ from the rated condition.

During the numerical experiments parameters such as current, temperature, allocation of charge carriers density, field distribution were fixed. At reaching the temperature of melting of contact platforms (catastrophic failure), the time was fixed and the radiated power was calculated. The results of the carried out experiments are given further.

In Fig. 2 the aspect of allocation of macroscopic particles in the field-effect transistor at the initial stage (about 0.1 ps) is given and at the moment of avalanching near to the gate (0.8 ps). Apparently from Fig. 2a, and at the initial moment an area of space charge was generated, the electron flow along the channel was formed. In accordance with the effect of an external impulse of voltage, in the region of the gate the beginning of forming of a boosted density of electrons is observed. These electrons are formed as a result of ionization of impurity atoms, which is also testified by the occurrence of excess holes in this area (Fig. 2b). The given pattern corresponds to a breakdown of a gate.
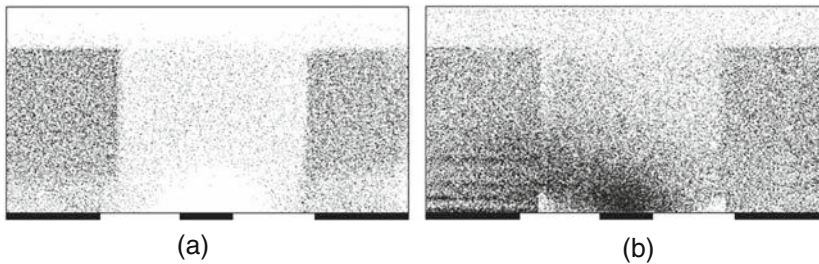
Fig. 2 Allocation of macroscopic particles in the active chip area of the FET: t = 0.1 ps (**a**) and t = 0.8 ps (**b**)

During the studies that have been carried out for transistors with a variable channel length, a set of the curves circumscribing the association of time for failure of GaAs Schottky-barrier FETs with the wattage of current at the impact of an external pulse electromagnetic field and relevant to the Wunsch–Bell criteria associations (Fig. 3) have been obtained. As a criterion of failure of the device, the moment when the temperature in local points of a crystal reached the temperature of melting of contacts has been chosen. It is visible that the time for a failure as the result of an avalanche breakdown decreases exponentially with the increment of the sent impulse voltage.

The obtained curves are well compounded with the experimental data [1]. Apparently, with the extension of the channel length, in spite of the fact that the cross section of the device remains constant, the associations drift and with the extension of the channel length, the time of failure of the device also increases (Fig. 3a). However, all the three curves constructed for the current power reduced to the unity of volume have practically coincided. Thus, it is possible to make a definite conclusion that at buildup of the criterial associations of failure of the devices it is expedient to use
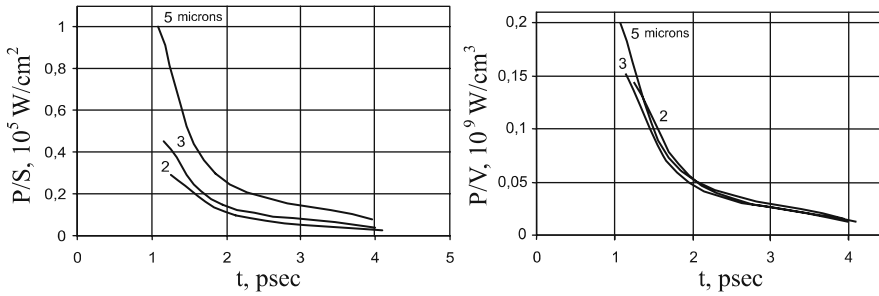
Fig. 3 Wunsch–Bell associations, for the current power referred to a cross section (**a**) and to a specific power of the current (**b**) in the transistor with a channel length of 2, 3, and 5 μm accordingly

the specific volumetric power P/V, but not P/S, as shown in [1]. The similar results are obtained for FET on silicon [3].

5 Conclusions

In this chapter the results of numerical calculations of origin and dynamics of development of avalanche breakdown in GaAs Schottky-barrier FETs are given depending on the electrical conditions and the sizes of the active chip area; their brief analysis is provided.

The carried out studies of the peculiarities of avalanche breakdown have shown that for the mentioned geometrical parameters the breakdown originates in the gate area and it has an electrostatic character. In due course, the avalanche region of carriers is spread to the entire channel; a local overheating of the crystal lattice takes place. The results obtained during the investigation are compounded with the theoretical and experimental researches given in [1]. However it is shown that as the criterion of a failure of the device it is necessary to use not the power referred to a cross section of the device but the specific power.

References

1. D. C. Wunsch, R. R.Bell, Determination of threshold failure of semiconductor diodes and transistors due to pulse voltages, IEEE Transactions of Nuclear Science, vol. 15, pp. 244–259, 1968.
2. S. A. Zuev, V. V. Starostenko, V. Y. Tereshenko, A. A. Shadrin, Influence of thermal processes on drift characteristics of semiconductor structures. Radiophysika i Elektronika, vol. 1, pp. 271–274, 2004 (in Russian).
3. S. A. Zuev, V. V. Starostenko, V. Y. Tereshenko, G. I.Churyumov, A. A. Shadrin, Silicon Schottky barrier FET with submicron scales, Radioelektronika i Informatika. Part 1. Mathematical Model, vol. 3, 47–53, 2004; .Part 2. Modeling Results, vol. 4, pp. 14–21, 2004 (in Russian).
4. S. A. Zuev, V. V. Starostenko, V. Y. Tereshenko, G. I. Churyumov, D. A. Unzhakov, E. V.Grigor'ev, Computer modeling of avalanche break-down in the GaAs Schottky barrier FET, Applied Radio Electronics, vol. 3, pp. 353–356, 2005 (in Russian).
5. R. W. Hokney, J. W. Eastwood, Computer Simulation Using Particles, Taylor & Francis, London, 1989.
6. J. Carroll, Hot electron microwave generators, Edward Arnold, London, 1970.

RF Breakdown Prediction for Microwave Passive Components in Multi-carrier Operation

S. Anza, M. Mattes, J. Armendariz, J. Gil, C. Vicente, B. Gimeno, V.E. Boria, and D. Raboso

Abstract This work addresses the multipactor problem for multi-carrier operation inside rectangular waveguide-based devices, by means of numerical simulations of the electron trajectories and multiplication inside the structure. Accurate field calculation and considering space charge effects are mandatory. For this, a PIC-FDTD method has been employed. As a result, novel software has been implemented offering the possibility of predicting multipactor in multi-carrier systems for a wide variety of situations. Simulation results show that multipactor can occur even for short pulse durations if an inter-period charge accumulation is present.

Keywords Breakdown · Multi-carrier signals · Multipactor

1 Introduction

Nowadays, the continuously increasing number of channels in multiplexers for satellite applications forces space industry to face the problem of power handling during the design process. This leads to extremely high power levels within the devices and increases the risk of RF breakdown due to corona discharge or multipactor breakdown.

The multipactor effect is an electron discharge which takes place between dielectric or metal surfaces in the presence of a high-level and high-frequency electromagnetic field and in vacuum conditions [1]. Multipactor is a matter of special importance in microwave circuits for space communications and particle accelerators.

A lot is known about multipactor breakdown for the single carrier case and parallel plate configurations (see, for example, [2]). However, the prediction of multipactor in multi-carrier operation is much more complex, due to the time variability of the RF amplitude [3,4].

This work presents a novel software for multipactor analysis in multi-carrier operation, inside rectangular waveguide-based devices, e.g. filters, combining integral equations and the method of moments (MoM), a particle in cell code (PIC) and a finite-difference time-domain (FDTD)

S. Anza (✉)
Aurora Software and Testing S. L. Universidad Politecnica de Valencia,
46022, Ed. D. Empresarial 9B, Valencia, Spain
e-mail: sergio.anza@aurorasat.es

scheme. Section 2 introduces some multipactor basics. Sections 3 and 4 present the electromagnetic field computation and electron trajectories and space charge modelling. Finally, some results and conclusions are presented in Sections 5 and 6, respectively.

2 Multipactor Basics

Multipactor takes place when the electromagnetic field and the geometry of the component are such that electrons follow a resonant trajectory, impacting consecutively from wall to wall of the device, with the adequate impact energy to ensure a secondary emission yield (SEY) higher than 1. According to the classical single carrier multipactor theory [1], in order to achieve resonance, the electron travel phases between plates must be an odd number of half-periods, i.e. $n\pi$, where $n = 1, 3, 5, 7,...$ is the multipactor order. The theory sets the value of the breakdown voltage, V_B (the minimum voltage to induce a multipactor discharge), as a function of the frequency times the device gap $f \times d$ and the SEY properties of the device material.

On the other hand, in typical communication applications, a multi-carrier signal is composed of N carriers having the same amplitude V_0, equally spaced in frequency (Δf) and with relative phases ϕ_i, where i stands for each individual carrier

$$V(t) = V_0 \sum_{i=1}^{N} \sin\left\{2\pi\left[f_\mathrm{m} + \left(i + \left(\frac{N+1}{2}\right)\Delta f\right)\right]t + \varphi_i\right\},\tag{1}$$

$V(t)$ being the voltage of the compound signal and f_m the mean frequency of all carriers. Under these circumstances, the compound signal can be treated as a single carrier signal with frequency f_m, modulated by an envelope, whose time evolution depends on the relative phases between the carriers. The absolute value of the envelope is periodic with a period of $T = 1/\Delta f$.

The single carrier case is easy to characterize because when multipactor conditions are accomplished the electron avalanche will reach its saturation level since the single carrier signal has constant amplitude [5].

On the contrary, the amplitude of a multi-carrier signal varies with time periodically and the multipactor discharge can be understood as periodic electron avalanches, which takes place whenever the signal envelope is higher than V_B ("ON" intervals), with intercalated periods of inactivity when the amplitude is too low to hold a discharge ("OFF" intervals) [4].

The European Space Agency (ESA) employs the 20-gap-crossing rule as the standard for multipactor design and test [3], which establishes that multipactor takes place if the ON interval is longer than the 20-gap-crossing time, $T_{20} = 10n/f_\mathrm{m}$.

However, the 20-gap-crossing rule only covers single-period discharges and does not offer a good understanding of the real processes that lay underneath. In this scenario, multipactor numerical simulations taking into account the electronic space charge give very valuable information and ultimately may lead to the redefinition of the criterion.

3 Field Analysis of Microwave Devices

Microwave devices such as filters and multiplexers are typically operated in a narrow frequency range. For this reason, the electromagnetic field distribution needed to simulate the RF breakdown is most efficiently computed in the frequency domain. Assuming a time-harmonic excitation, spatial

and time dependency can be separated:

$$\vec{E}(\vec{r},\omega,t) = \underline{\vec{E}}(\vec{r},\omega) \cdot e^{j\omega t} \quad \text{and} \quad \vec{H}(\vec{r},\omega,t) = \underline{\vec{H}}(\vec{r},\omega) \cdot e^{j\omega t}. \tag{2}$$

The phasors $\underline{\vec{E}}(\vec{r},\omega)$ and $\underline{\vec{H}}(\vec{r},\omega)$ are computed inside the device under test for the frequency ω of interest.

To analyse a certain structure a divide-and-conquer approach is applied [6]. For this, the device is separated into pieces of canonical shape, e.g. rectangular waveguides, as in Fig. 1. Then the response of each transition between two different waveguides is computed and characterized by means of an impedance matrix. The individual impedance matrices are then connected using microwave network theory [7] to obtain the overall response of the device.
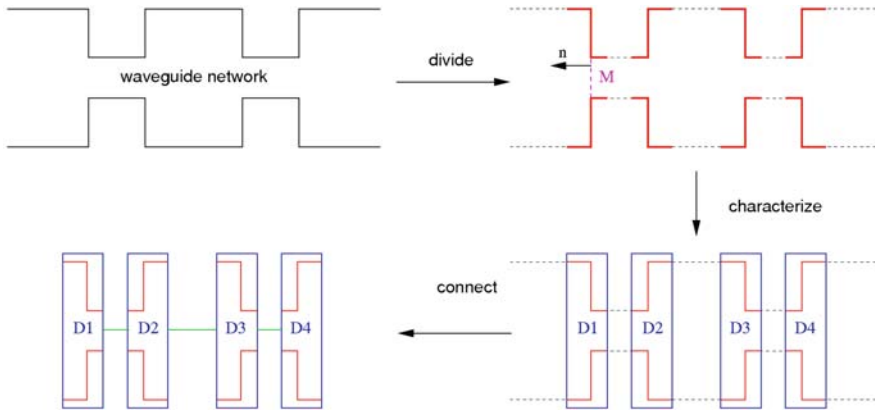
Fig. 1 Divide-and-conquer approach to model complex devices based on waveguides. D1–D4 are the four disconti-nuities between the five waveguides. $\underline{\vec{M}} = \vec{n} \times \underline{\vec{E}}$ denotes the tangential electric field in the aperture and is used to set up an integral equation to characterize the discontinuity

In order to obtain an impedance matrix representation, an integral equation is settled. This is done by imposing the continuity of the magnetic field in the aperture (see, for instance, the first discontinuity in the upper right picture in Fig. 1)

$$\vec{n} \times \left(\underline{\vec{H}}^{(1)} - \underline{\vec{H}}^{(2)} \right) = 0. \tag{3}$$

Then, incident and scattered fields are separated and the latter is expressed by means of the waveguide Green's function

$$\vec{n} \times \left(\underline{\vec{H}}_i^{(1)} - \underline{\vec{H}}_i^{(2)} \right) = -\vec{n} \times \int\limits_{\text{aperture}} \left(G_{\text{HM}}^{(1)} + G_{\text{HM}}^{(2)} \right) \cdot \underline{\vec{M}} \, dS, \tag{4}$$

where $G_{\text{HM}}^{(k)}$ is Green's function of waveguide k relating a magnetic source (tangential electric field) with the magnetic field. $\underline{\vec{M}} = \vec{n} \times \underline{\vec{E}}$ is the tangential electric field in the aperture (see Fig. 1 upper right picture).

The integral equation (4) is solved by means of the method of moments expanding $\underline{\vec{M}}$ with an appropriate basis and testing (4) with suitable test functions.

The impedance matrix of each discontinuity is then connected by transmission lines representing the waveguide between two transitions, to obtain the frequency response of the device.

To compute the electromagnetic field, it is expressed using the eigensolutions (modes) associated with the waveguides. For example, the electric field can be written as (see, e.g. [8])

$$\underline{E}\,(\vec{r},\omega) = \sum_{k=1}^{\infty} V_k(\omega) \cdot \vec{e}_k(\vec{r}), \tag{5}$$

where $\vec{e}_k(\vec{r})$ is the kth mode of the electric field of the waveguide and $V_k(\omega)$ its amplitude, available after having simulated the response of the device. Similar expression holds for the magnetic field.

Equation (5) is the field distribution for a harmonic excitation of angular frequency ω. For a multi-carrier signal, the field distribution is obtained by the superposition principle, i.e. summing the field distribution associated with the individual carriers

$$\underline{E}\,(\vec{r},\omega_1,\ldots,\omega_n) = \sum_{l=1}^{n} \underline{E}\,(\vec{r},\omega_l), \tag{6}$$

n being the number of carriers.

Figure 2 shows an example of a multi-carrier signal inside a band-pass filter obtained with the method outline here above.
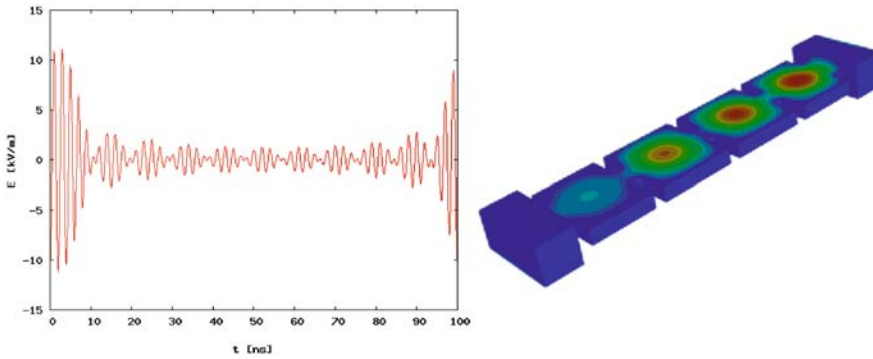
Fig. 2 Multi-carrier signal: The *left picture* shows the electric field strength in the centre of one of the cavities and the *right figure* visualizes the normal component of the electric field on the walls of the band-pass filter

4 Electron Motion and Space Charge Computation

The diagram of the implemented PIC method is depicted in Fig. 3.

Assuming that the initial position and velocity of each electron is known, as well as the initial electric and magnetic fields, the PIC procedure can be summarized as follows (more details on PIC codes can be found, e.g. in [9]):

- **Particle-to-grid weighting**: The charge, position and velocity of each particle are used to interpolate the charge and current densities at the mesh nodes.
- **Integration of field equations**: The values of the electric and magnetic fields are computed for the next time step using FDTD of the Maxwell equations.

Fig. 3 PIC general scheme
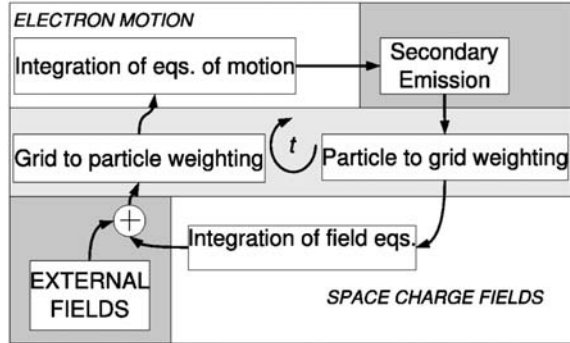
- **External fields**: Calculated with the method of Section 3 are added to the space charge fields in order to calculate the total force on the particles.
- **Grid-to-particle weighting**: The fields at the mesh nodes' locations are interpolated to each one of the particle locations.
- **Integration of the equations of motion**: The next time step position and velocity are computed employing a leap frog algorithm.
- **Secondary Electron Emission (SEE):** The SEY is modelled by a modification of the Vaughan′s model [5].

5 Results

The presented method outlined above has been implemented in a software [10,11]. In a first step, simple rectangular waveguides have been used to asses the tool, since, only for these structures, results can be found in literature. Moreover, comparisons with the traditional parallel plate case are possible for which a lot of data are also available.

Two kinds of simulation have been carried out: First, the results of a single-event multipactor discharge are presented and, next, an inter-period charge accumulation process simulation, which ends up in a long-term multipactor discharge [4], is shown.

For the single event simulations, a multi-carrier signal composed of 10 carriers of equal amplitude (12 V or 16.5 W) was used with the frequencies and phases of Table 1, where the voltage is defined as the value of the vertical electric field at the centre plane of the waveguide multiplied by the waveguide height d. The resulting signal has a multipactor ON time, $T_{on} = 1$ ns. The test has been run on a silver-plated waveguide of dimensions $a = 22.86$ mm, $d = 0.1$ mm, with $f \times d = 1$ GHz mm.

Table 1 Frequency and phases of carriers

Frequency (GHz)	9.46	9.58	9.70	9.82	9.94	10.06	10.18	10.30	10.42	10.54
Phase (°)	0	0	0	0	0	0	0	0	0	0

The RF applied signal and the evolution of the number of electrons can be seen in Fig. 4. As expected, two different behaviours are observed. First, when the envelope is higher than the multipactor threshold V_B (47 V from standard susceptibility charts), the number of electrons grows exponentially; next, when the amplitude of the envelope goes below V_B, the avalanche stops and
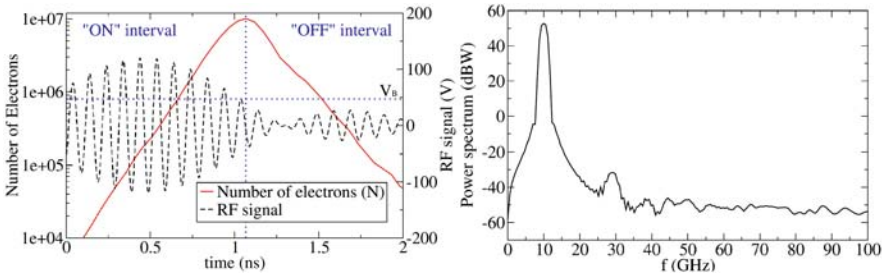
Fig. 4 RF signal and the number of electrons evolution in time (*left*) and power spectrum of the fields at output port (*right*)

the electrons start to be absorbed decreasing its population. If the maximum electron density during this period is high enough in order to be detected, we say that a single-event multipactor discharge occurs. In order to determine if such number of electrons are significant, the power spectrum of the signal was computed, which is shown in Fig. 4. It can be seen, in fact, the presence of the third harmonic generated by the discharge [12], located to the right of the RF carrier at a frequency of 30 GHz having an amplitude of about –30 dB m. Considering a typical sensitivity of –60 dB m for a multipactor experimental set-up [2], this discharge would be quite well detected in the laboratory.

Table 2 shows the phase distribution for the long-term discharge simulation. In this case, a waveguide of dimensions $a = 22.86$ mm, $d = 2$ mm, with $f \times d = 20$ GHz mm and $n = 15$, has been chosen. The carriers have equal amplitude of 600 V each (2 kW) and follow a triangular distribution which assures enough width and flatness of the main lobe of the multi-carrier envelope to ensure accumulation [4].

Table 2 Frequency and phases of carriers

Frequency (GHz)	9.46	9.58	9.70	9.82	9.94	10.06	10.18	10.30	10.42	10.54
Phase (°)	0	41.02	82.04	123.06	164.08	164.08	123.06	82.04	41.02	0

It is important to remark that this specific case ensures a T_{on} time lower than the time T_{20} ($T_{on} = 12$ ns against $T_{20} = 15$ ns) and that, according to the standards, there should not be a multipactor discharge. However, as shown in Fig. 5, in this case inter-period accumulation makes the electron population rise to the saturation level producing a multipactor discharge.
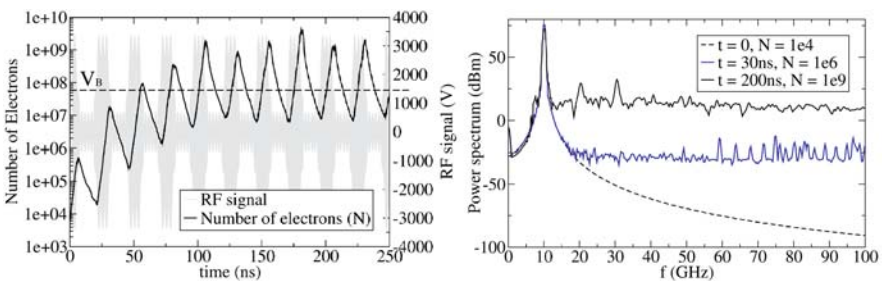
Fig. 5 RF signal and the number of electrons evolution in time (*left*) and power spectrum of the signal for three different stages of the discharge (*right*)

The power spectrum of the signal at three different time instants of the discharge is also presented in Fig. 5. At initial stages of the discharge, the number of electrons is so low that the harmonics, if present, are not noticeable. But for longer times and higher number of electrons the noise level increases until the third harmonic appears once after reaching saturation.

6 Conclusions

A novel tool for multipactor analysis in passive microwave structures using multi-carrier signals has been presented. It implements a fast and accurate electromagnetic field using a divide-and-conquer strategy. The electron avalanche for multipactor simulations is modelled with a PIC-FDTD code allowing for monitoring the electronic charge density time evolution and the transmitted power spectrum of a multipactor discharge. The simulation results show that discharges also can occur when inter-period discharges are present.

Future enhancements of such a tool, combined with experimental evidences, may help to define a multipactor criterion for multi-carrier signals in order to cover a wide range of cases.

References

1. J. Vaughan, Multipactor, IEEE Transactions on Electron Devices, vol. 35, pp. 1172–1180, 1988.
2. A. Woode and J. Petit, Diagnostic investigations into the multipactor effect, susceptibility zone measurements and parameters affecting a discharge, ESA Working Paper No. 1556, November 1989.
3. Space Engineering: Multipacting Design and Test, vol. ECSS-20-01A, edited by ESA-ESTEC. ESA Publication Division, The Netherlands, May 2003.
4. S. Anza, C. Vicente, B. Gimeno, V. E. Boria, and J. Armendariz, Long-term multipactor discharge in multicarrier systems, Physics of Plasmas, vol. 14, pp. 082112–082112–8, 2007.
5. C. Vicente, M. Mattes, D. Wolk, H. L. Hartnagel, J. R. Mosig, and D. Raboso, Multipactor breakdown prediction in rectangular waveguide based components, Microwave Symposium Digest, 2005 IEEE MTT-S, Long Beach, CA, USA, vol. 2, pp. 1055–1058.
6. M. Mattes, Contribution to the electromagnetic modeling and simulation of waveguide networks using integral equations and adaptive sampling, PhD Dissertation, Ecole Polytechnique Fédérale de Lausanne, CH-1015 Lausanne, Switzerland, 2003, Thesis No. 2693.
7. A. A. Oliner, Historical perspectives on microwave field theory, IEEE Transactions on Microwave Theory and Techniques, vol. 32, no. 9, pp. 1022–1045.
8. N. Marcuvitz, Waveguide Handbook, M. I. T. Radiation Laboratory Series, vol. 10, McGraw-Hill, New York, 1951.
9. C. Birdsall and A. Langdon, Plasma Physics via Computer Simulation. Taylor & Francis Group, London, UK, 2005.
10. S. Anza, C. Vicente, D. Raboso, J. Gil, B. Gimeno, V. E. Boria, Enhanced prediction of multipaction breakdown in passive waveguide components including space charge effects, IEEE 2008 International Microwave Symposium, June 2008, Atlanta, GA, USA.
11. www.aurorasat.es/fest3d.php, July 2008.
12. E. Sorolla, S. Anza, B. Gimeno, A. M. Perez, C. Vicente, J. Gil, F. J. Perez-Soler, F. D. Quesada, A. Alvarez, and V. Boria, An analytical model to evaluate the radiated power spectrum of a multipactor discharge in a parallel-plate region, IEEE Transactions on Electron Device Letters, vol. 55, no. 8, pp. 2252–2258, 2008.

UWB Radar: Mechanical Scanning and Signal Processing for Through-the-Wall Imaging

C. Liebe, A. Gaugue, J. Khamlichi, M. Menard, and J.-M. Ogier

Abstract This chapter presents a state of the art of the UWB (ultra-wideband) radar for through-the-wall imaging, followed by a description of different methods to scan a scene situated through a wall using a UWB system. Principal attention of this chapter focuses on a mechanical scanning radar system and associated image processing to detect a human body through a wall and also the environment of a target.

Keywords UWB · Radar · Through-the-wall surveillance · Bistatic radar · Imaging system · Imaging processing · Mechanical scanning

1 Introduction

The detection of a target behind an obstruction is very interesting for a wide range of industries. For example, seeing through a wall could be utilized by rescue services, searching for people in rubble and in buildings on fire. The military industry could use this technology for bomb disposal, neutralization of aggressors, hostage rescue, etc. A lot of methods exist to see through an opaque medium [1]. There are two different types: passive systems, imaging system running in millimetre and submillimetre wavelengths, and active systems, imaging system based on radar technology, running in centimetre and millimetre wavelengths and even X-rays. In a lot of situations, a clear picture of the watched scene is not necessary, because the relevant information, i.e. number of people, positions, speed of movement, etc. is sufficient. UWB radar is a very good solution for obtaining this information, because it presents many advantages compared to other systems [2]. At present the technology UWB is suitable for detection and localization of a human body through a wall.

We have developed UWB radar with a mechanical scanning system and specific image processing tools to extract the objects of interest. Under strong noise environments, the image segmentation often performs badly. In order to make some improvements, an image decomposition model is used. Experiments show decomposition algorithm is helpful to extract the characteristic parameters of the signals and is also capable to improve the performance of extracting the objects of interest.

———————————————

C. Liebe (✉)

Laboratoire Informatique Image Interaction (L3i), Université de La Rochelle, Avenue Michel Crépeau, 17042 La Rochelle Cedex 1, France

e-mail: christophe.liebe@univ-lr.fr

2 Specificity and State of the Art of UWB Radar

UWB radar uses very short duration pulses that result in very large wideband. The Federal Communication Commission (FCC) [3] adopted a report on using this technology with imaging systems, but with certain frequency and power limitations: systems must be operated below 960 MHz or within the frequency band 1.99–10.6 GHz.

An important specificity of these UWB radars is the wide bandwidth: The low frequencies can easily penetrate the materials of walls (concrete blocks, wood, and all non-metallic materials) and high frequencies give a good spatial resolution, but with difficulty through a wall. Nevertheless, this system presents other advantages compared to classical radar:

- A good picture spatial resolution (approximately 10 cm). The wider the bandwidth the radar uses, the finer the resolution it obtains:

$$\Delta R = \frac{V}{2\Delta F} \, ,$$

(1)

where ΔR is the spatial resolution, V is the propagation speed of impulse, and ΔF is the bandwidth

- A possibility to identify targets due to the great number of emitting frequencies
- Noise robustness due to large bandwidth

For less than a decade, there have been fewer than 10 laboratories and companies throughout the world, working on the UWB radar application "detection/vision through the walls". The Company Time Domain (USA) is the first producer of this system. Camero has created two types of systems Xaver 400 and 800, which have actually the best performances. Lawrence Livermore National Laboratory (LLNL) with radar MIR (micropower impulse radar) is able to detect a man through a concrete wall of 40 cm. The Moscow Aviation Institute (Russia) produced some UWB radar prototypes that operate in different frequencies (from 800 MHz to 1.5 GHz). The technical characteristics of these systems are mentioned in Table 1.

Other companies or laboratories also work on the subject, but information about their prototypes is unavailable. Examples are Satimo (France), Akela (USA), University of Rome (Italy) and Defence R&D Canada which works on UWB radar simulation [10].

3 Description of the Prototype

There are two different approaches to through-the-wall radar imaging.

The first approach is coherent imaging that requires wideband beam forming to be applied, using multiple antenna transmitter and receiver arrays. Measurements must include the data magnitude and phase to be used in post-data processing for imaging each pixel behind the wall.

The non-coherent approach involves several, more simplified, and stand-alone radar units. In this case, imaging is performed based on the triangulation technique [10], which is a method used to determine the position of an object based on range measurements (obtained from time-of-arrival information) from three antenna units located at a known site.

Table 1 State of the art of the available UWB radar technology

Authors, laboratory/company	Prototype/centre frequency (GHz)	Bandwidth/spatial resolution	Range	Field of view/power
L. Fullerton Time Domain [4]	RadarVision 3.85	3.5 GHz 5 cm	10 m	Hor.: ±60° Ver.: ±45° 50 μW
D. Gazelle Camero Tech [5]	Xaver 800 –	7.5 GHz 2 cm	20 m	Hor.: ±40° Ver. : ±40° –
Mc Ewan LLNL [6]	MIR 2.5	1 GHz 15 cm	50 m	–
Cambridge Consultants [7]	PRISM 200 2	0.5 GHz 30 cm	20 m	Hor.: ±70° Ver.: ±60°
I. Immoreev MAI [8]	1	0.8 GHz 0.5 m	3 m	240 μW
J. Tatoian [9] Eureka Aero	ImpSAR 2	3.5 GHz 5 cm	100 m	–

Our approach consists in using a bistatic radar: An omnidirectional emitter for lighting the scene, associated with a mechanical system for the directional receiver.

The radar core is based on sinusoid modulated by Gaussian impulse transmitter/receiver modules which allow the evaluation of the features of UWB technology. The first module can be configured as the impulse transmitter and the second as an impulse receiver. The centre emitting frequency is 4.7 GHz and its bandwidth is 3.2 GHz. These modules (initially designed for communication in UWB) have reconfigured hardware (antennas) and software, in order to be able to use these as the radar UWB. An omnidirectional antenna is mounted on the output of the transmitter and a directional antenna on the receiver input. Then it follows ADC (analog-to-digital converters), correlators, and the directional antenna (gain 7 dB, field of view ±45°) [11]. This disposition allows a spatial resolution of 5 cm (formula (1) with $V = 3 \times 10^8$ m/s).

To scan a complete scene behind a wall, the system must acquire echoes in different positions. The principle is based on the association receiver/directional antenna, fixed to a mobile arm which moves degree by degree has an opening of 60°. The emitter is fixed, situated above the mobile arm (cf. Fig. 1). An acquisition has to be done for each position of the association receiver/directional antenna.

The mechanical system must be synchronous with the emitter and the receiver, because the position of the receiver is an important parameter. So a program has been developed to synchronize the movement of the arm with the receiver.

Figure 2a corresponds to the test scene, which contains a human body with an open door behind. Figure 2b is an acquisition obtained in one direction (highlighted by the white line in Fig. 2c). The echo "E1" corresponds to direct field between the emitter and the receiver. The echo "E2" is due to the reflection on the wall. The echo "E3" corresponds to the presence of the human body. The echo "E4" is due to the wall behind the human body. Figure 2c is obtained using 60 acquisitions done with the system and saved in files (one acquisition by angle). These files are assembled to create a matrix in rectangular coordinates (time, angle) (an example can be seen in Fig. 4a). We changed these coordinates to polar coordinates (ρ, θ). The result obtained, Fig. 2c, was realized without treatment (e.g. filtering, correlation).
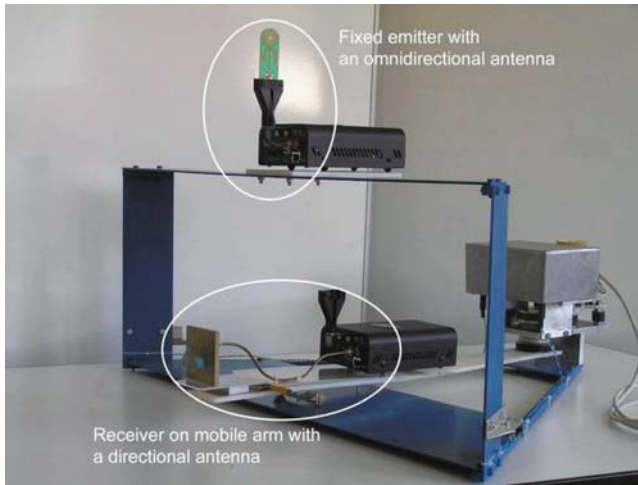
Fig. 1 Photography of the UWB radar prototype: The emitter is fixed above the mobile arm (equipped with the receiver)

(a)

(b)

(c)
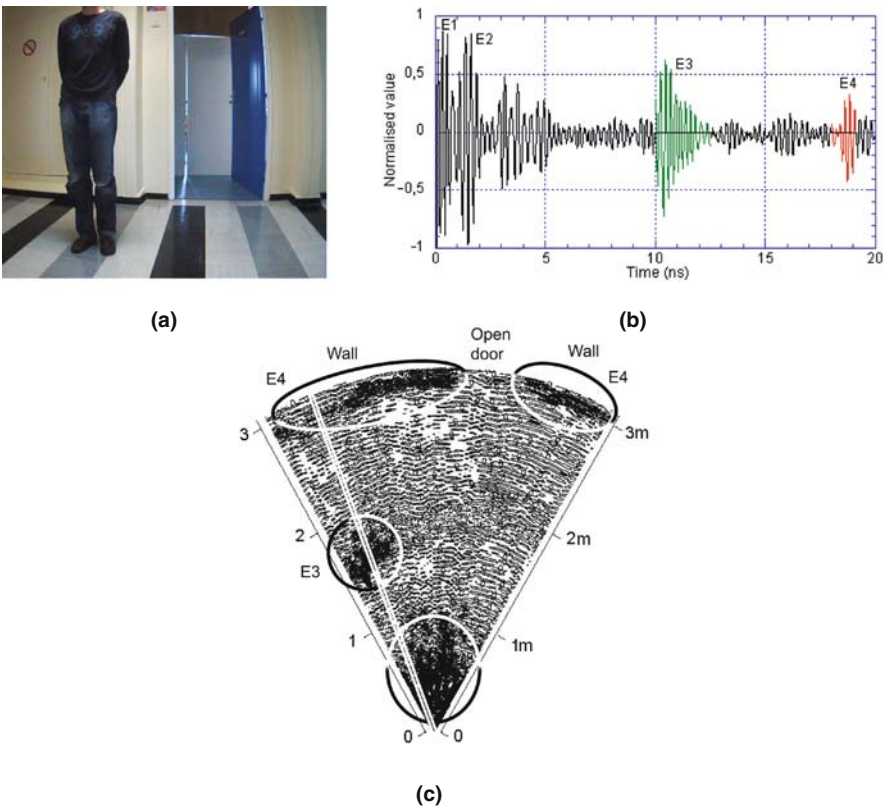
Fig. 2 A result of an acquisition with the UWB radar: (**a**) A photography of the scene acquired through a 15-cm-thick concrete wall; (**b**) the cross section follows the white line; and (**c**) the result of 60 acquisitions obtained by mechanical scanning

4 Image Processing

Signals measured by a UWB radar through a wall have the characteristics of being noisy and oscillating. Therefore, we propose a new approach to de-noise the received signals and to enhance the segmentation step. After having applied a Hilbert transform to demodulate the signals and in order to suppress the residual oscillation of the envelope, we describe a norm introduced by Meyer to identify oscillating components [12]. Then, we present the Aujol–Chambolle decomposition model in order to obtain three components.

4.1 Adapted Norm and Decomposition Model

Another way of looking at de-noising problems is by separating a given noisy image x into components: a geometrical component u, a texture component (oscillating component) v, and a noise component w. Decomposing an image into meaningful components is an important and challenging inverse problem in image processing. The space $G\left(\Re^2\right)$, more adapted to capturing oscillating signals in a minimization process, was introduced by Meyer. It consists of the following set of distributions:

$$G\left(\Re^2\right) := \operatorname{div}\left(\left[L^\infty\left(\Re^2\right)\right]^2\right).$$ (2)

Endowed with the norm

$$\|v\|_{G(\Re^2)} := \inf\left\{\|\xi\|_\infty : \xi \in \left(\left[L^\infty\left(\Re^2\right)\right]^2\right), v = \operatorname{div}(\xi)\right\},$$ (3)

the space $G\left(\Re^2\right)$ is a Banach space.

In order to decompose an image into suitable components we use the Aujol–Chambolle decomposition model [13]. It relies on dual norms derived from $BV,$[1] $G,$[2] and E[3] spaces. The authors propose minimizing the following discretized functional:

---

[1] $BV(\Omega)$ is the subspace functions $u \in L^1(\Omega)$ such that the following quantity, called the total variation of u, is finite:

$$J(u) = \sup\left\{\int_\Omega u(x)\operatorname{div}(\xi(x))\,dx\right\},$$

such that $\xi \in C_c^1\left(\Omega, \Re^2\right), \|\xi\|_{L^\infty(\Omega)} \leq 1$.

[2] G the subspace introduced by Meyer; oscillating patterns have a small G-norm.

[3] E is a dual space to model the noise: $E = B_{-1,\infty}^\infty$ dual space of $B_{1,1}^1$.

$$\inf_{(u,v,w)\in x^3} F(u,v,w) = \underbrace{J(u)}_{\text{RegularizationTV}} + \underbrace{J^*\left(\frac{v}{\mu}\right)}_{\substack{\text{Texture/ oscillating\_comp.} \\ \text{extraction}}} + \underbrace{B^*\left(\frac{w}{\delta}\right)}_{\substack{\text{Noise\_extraction\_by} \\ \text{Shrinkage}}}$$

$$+ \underbrace{\frac{1}{2\lambda}\|f - u - v - w\|_X^2}_{\text{Residual\_part}},$$ (4)

where X is the Euclidian space $\Re^{n\times n}$ for image size $n \times n$. For minimizing (2), Chambolle's projection [14] is used. Using the space $BV(\Omega)$ to obtain the component u allows edges to be preserved. The decomposition algorithm is used as a filter to remove the residual oscillating and noise components ($v + w$). Only the structure component u is thresholded by using optimal thresholding. Level sets are then detected and traced. The segmented image can be ANDed with the original image in order to extract the objects of interest. Figure 4d shows the thresholded image and traced target contours. Figure 3b shows the extracted oscillating component v.

4.2 Image Processing

Necessary image processing is as follows:

- Envelop detection: In order to extract the information from the modulated signal, the associated analytical signal is computed. The existence of a signal with the same frequency and phase of the carriers is not required. So the demodulation process is much easier. The analytical signal $z(t)$ associated with the received continuous-time real signal $x(t)$ is obtained by filtering $x(t)$ using the filter with $H(f) = 2U(f)$ as its complex gain, where $U(f)$ is the unit-step function, equal to 1 if $f > 0$ and 0 if $f < 0$. By definition, the modulus of $z(t)$ is the envelop of the signal $x(t)$. Figure 3a shows the graph of the signal $x(t)$ and its envelop, $|z(t)|$.
- Decomposition: In order to suppress oscillating and noise components from the demodulated signal envelop, the decomposition model is used. Figure 3b shows the oscillating component of the envelop of $x(t)$ for one signal. Figure 4b represents the enhanced image built with signals u.
- Segmentation: In order to detect a target, the structure component u is thresholded by using optimal thresholding. Level sets are then detected and traced. The segmented image can be ANDed with the original image in order to extract the objects of interest. Figure 4d shows an image obtained after segmentation.

By looking at the graph of the image resulting from the decomposition (cf. Fig. 4b), desynchronization artefacts can be noticed. These errors are corrected by using the correlation between different signals. Results are shown in Fig. 4c. Figure 4d shows the thresholded image and traced target contours.

5 Conclusion and Future Implications

We have developed a UWB radar with mechanical scan. This system provides a radar image behind a wall. It can detect and localize targets such as human beings and objects. Unfortunately this system is slow (a scene scan takes 30 s). But it permits the testing of new signal algorithms and image
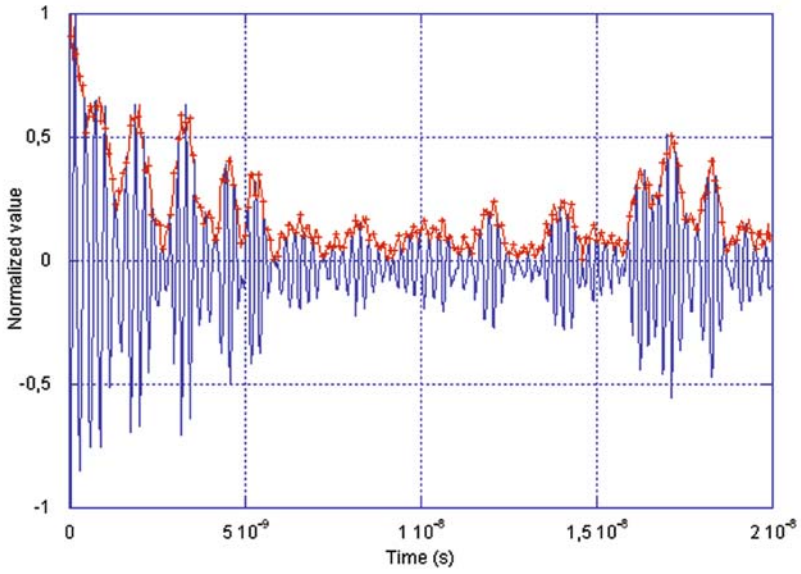
(a)
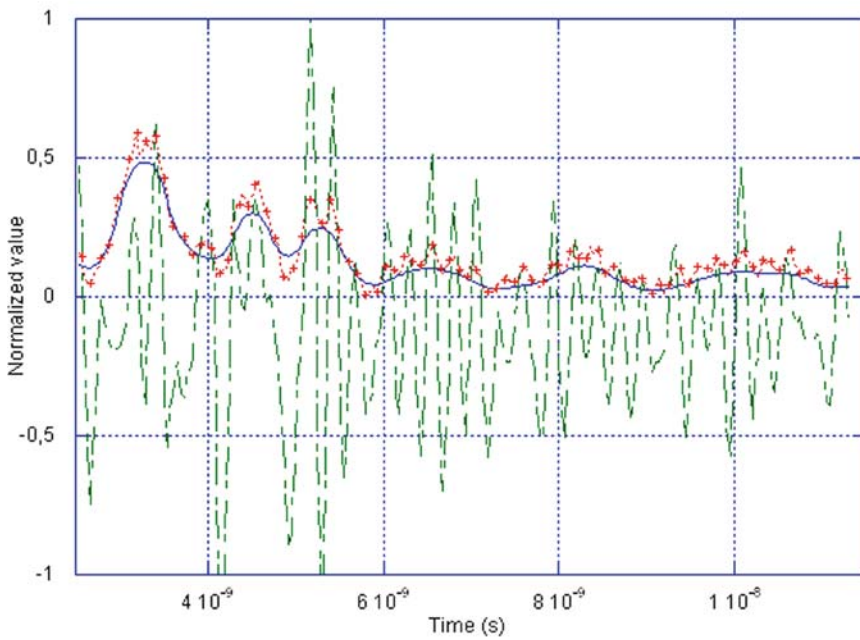
(b)

Fig. 3 Envelop detection and signal decomposition. (**a**) Signal x and its envelop $|z|$ and (**b**) example of envelop decompositions. *Continuous signal*: normalized oscillating component v; *signal with cross*: normalized envelop $|z|$; *dotted signal*: normalized structure component u ($u = |z| - (v + w)$)
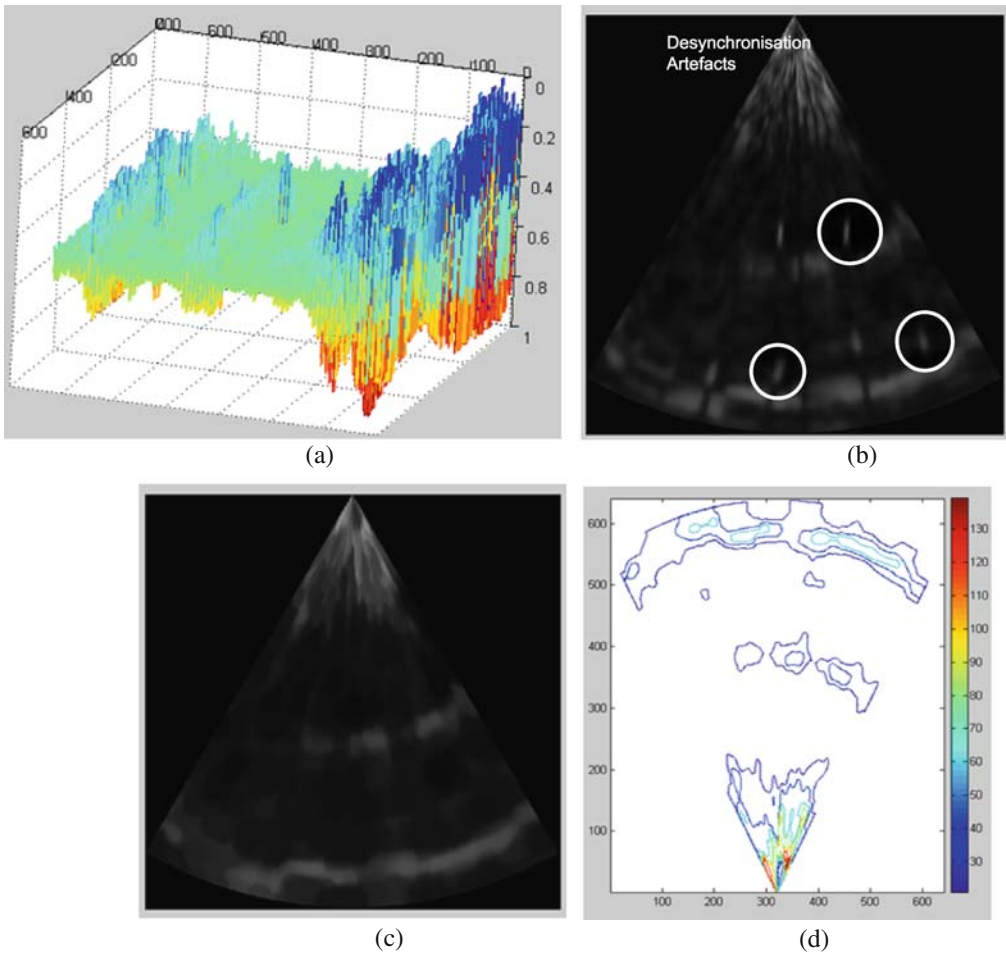
Fig. 4 Image processing (the scene is the same as precedent part with the door closed and a metallic object replaces the human body): decomposition and segmentation. (**a**) Modulated original image *x* (time and angle coordinates); (**b**) normalized structure component *u* (polar coordinates) obtained by envelop detection and decomposition; (**c**) desynchronization artefacts corrected by using correlation; and (**d**) segmented image *u* by using optimal thresholding

processing for through-the-wall imaging. The next step of this work will be to accelerate the scanning system.

References

1. A. Gaugue, J. L. Politano, Overview of current technologies for through-the-wall-surveillance. Proceedings of SPIE Passive Millimetre-Wave and Terahertz Imaging II, vol. 5989, pp. 1H-1–1H-11, 2005.
2. J. D. Taylor, Ultra-wideband Radar Technology, CRC Press, New York, 2001.
3. http://www.fcc.gov/Bureaus/Engineering_Technology/Orders/2002/fcc02048.pdf

4. K. Siwiak, Time Domain Corp.: an introduction to ultra-wideband wireless technology, IEEE VTC (Vehicular Technology Conference), Rhodes, Greece, 2001.
5. www.camero-tech.com
6. F. Nekoogar, F. Dowla, A. Spiridon, Rapid synchronisation of ultra wide band transmitted reference receivers. Wireless, 2004.
7. G. Oswald, Cambridge Consultants: UWB radar applications. Ultra-wideBand Conference, Downtown, Washington, 1999.
8. I. Y. Immoreev, P. G. Sergey, V. Samkov, T. The-Ho, Short-distance ultra-wideband radars. Theory and designing. Radar 2004: International Conference on Radar Systems, pp. 211–213, 2004.
9. http://eurekaaerospace.com/impsar.php
10. S. Gauthier, E. Hung, W. Chamma, Surveillance through concrete walls. Proceedings of SPIE Defense and Security Symposium, vol. 5403, pp. 597–608, 2004.
11. A. C. Lepage, X. Begaud, A compact ultrawideband triangular patch antenna. Microwave and Optical Technology Letters, vol. 40, no. 4, pp. 287–289, 2004.
12. Y. Meyer, Oscillating patterns in image processing and non-linear evolution equations. The Fifteenth Dean Jacqueline B. Lewis Memorial Lectures, vol. 22, 2001.
13. J. F. Aujol, A. Chambolle, Dual norms and image decomposition models. International Journal of Computer Vision, vol. 63, no. 1, pp. 85–104, 2005.
14. A. Chambolle, An algorithm for total variation minimization and applications. Journal of Mathematical Imaging and Vision, vol. 20, pp. 89–97, 2004.

Radar Observation of Objects, Which Fulfill Back-and-Forth Motion

I. Immoreev

Abstract Consideration is given to the specific features of radars used for observation of biological objects (people and animals) to define their physiological parameters, such as respiration rate and heart rhythm. Also demonstrated are variations in the form and spectrum of radar signals emerging when signals are reflected from a person's thorax and heart during his back-and-forth motion. Methods of signal processing, which provide restoration of the real form of object motion, are proposed.

Keywords Ultra-wideband radar · Back-and-forth motion · Respiratory rate and heart rate · Hospital

1 Introduction

Emergence and development of ultra-wideband (UWB) technologies, which operate with pulses of nanosecond and picosecond durations, made possible the production of radars with high space resolution of objects observed.

Such radars can have various applications: in medicine for monitoring of the patients in rehabilitation chambers in hospitals (Fig. 1); in psychophysiology to provide the control over the condition of people engaged in high danger work, as well as in biology to observe the behavior of test animals. In all these cases, the biological objects (thorax and heart) make back-and-forth motion. This creates the specific conditions for radar observation of these objects.

2 Modeling

The regular features, which appear with back-and-forth motion of the object, will be examined by using a simple model as an example (Fig. 2).

The object located at a distance R from the radar makes back-and-forth motions in the direction of the normal to the radar, approaching to the radar at the minimal distance $R_{\min}$ and moving away at the maximal distance $R_{\max}$. Let us consider the simple case when the object motion corresponds to

I. Immoreev (✉)
Moscow Aviation Institute, Gospitalny val, Home 5, Block 18, Apt. 314, Moscow 105094, Russia
e-mail: immoreev@aha.ru
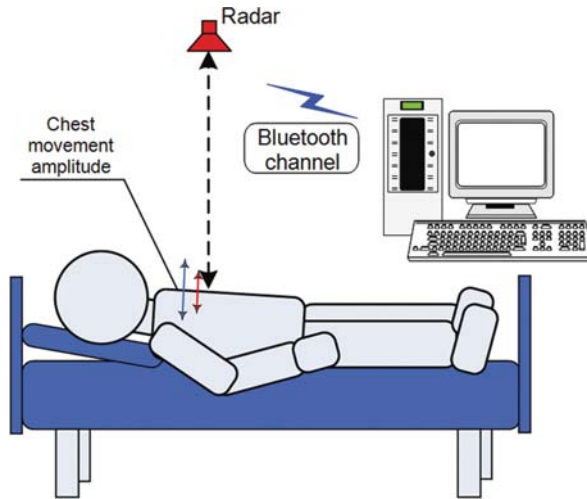
Fig. 1 The scheme of the patient's monitoring in hospital with help of the radar
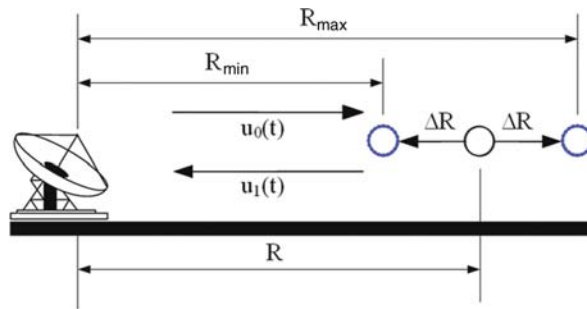
Fig. 2 Model of back-and-forth motion of the object

the harmonic law with frequency F. In this case, the distance $R(t)$ between the radar and the object is varied in time according to the following law:

$$R(t) = R + \Delta R \sin (\Omega t + \theta), \tag{1}$$

where ΔR is the amplitude of the object motion;

$\Omega = 2\pi F$ is the circular frequency of the object motion;

θ is the initial phase on the object motion.

The radiated signal is a harmonic wave with amplitude E_0 and frequency ω_0: $u_0(t) = E_0 \sin \omega_0 t$.

At the receiving position, we use a correlator (Fig. 3). In the correlator, signal $u_1(t)$ reflected by the object and received with delay t_R is multiplied with the reference (radiated) signal $u_0(t)$. The resultant product is integrated during time $n T_0$ ($T_0 = 2\pi/\omega_0$).

If the object is motionless, the reflected signal $u_1(t)$ will return to the radar with amplitude E_1 in time $t_R = 2R/c$ (c – the velocity of light); it will be equal to

$$u_1(t) = E_1 \sin \omega_0(t - tR) = E_1 \sin \omega_0(\text{t} - 2R/c). \tag{2}$$
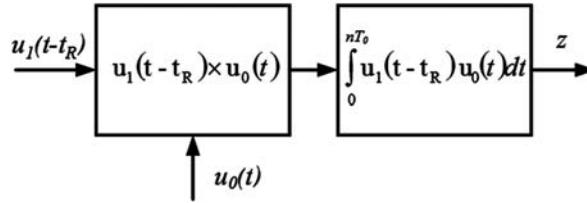
Fig. 3 Correlator (phase detector and integrating filter)

The phase difference between radiated and reflected signal oscillations will be

$$\Delta\phi = \omega_0 t - \omega_0 (t - 2R/c) = 2\omega_0 R/c = 4\pi R/\lambda_0,$$

where λ_0 is the wavelength of the radiated signal.

Then, the output correlator's signal is equal to

$$z = E_0 E_1 \int_0^{nT_0} \sin \omega_0 t \times \sin \omega_0 (t - 2R/c) \, dt = \frac{E_0 E_1}{2} nT_0 \cos \Delta\phi. \tag{3}$$

It is clear that the output correlator's signal is equal to zero at distances $R_k = k\lambda_0/4\pi$ ($k = 1, 2, 3, \ldots$). To prevent the losses of information on the object at these distances, we use two correlators operating in parallel with the reference signals shifted by 90^0 relative to each other applied to them (in-phase and quadrature channels, Fig. 4).

Fig. 4 In-phase and
quadrature channels
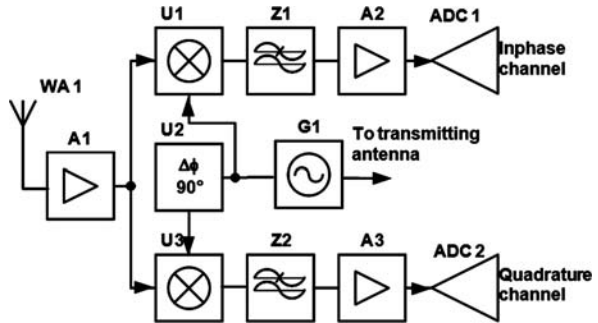
The reflected signal corresponding to the back-and-forth motion of the object can be obtained by substituting in (2) instead of constant value R variable value $R(t)$ from (1):

$$u_1(t) = E_1 \sin \omega_0 \left[t - \frac{2R(t)}{c} \right] = E_1 \sin \left[\omega_0 \left(t - 2 \left(\frac{R + \Delta R \sin(\Omega t + \theta)}{c} \right) \right) \right].$$

The frequency of the object's motion is many times less than the oscillation frequency of the radiated signal $\Omega \ll \omega_0$; the correlator's integration time is much less than the period of the object motion $nT_0 \ll T = 1/F$. So, we can assume the object as motionless during the integration time. So, we can use the solution for a motionless object (3) and obtain the value of the correlator's output signal for the case of back-and-forth motion:

$$z_c(t) = \frac{E_0 E_1}{2} n T_0 \, \cos\left[2\omega_0\left(\frac{R + \Delta R \, \sin(\Omega t + \theta)}{c}\right)\right]. \tag{4}$$

The signals from the correlator's output are video pulses with duration equal to twice the integration time. Expression (4) determines the amplitude and polarity of these pulses.

Let us analyze this expression. To provide an analysis, we transform the expression by the formula of cosine of the sum of two arguments with regard to $\omega_0/c = 2\pi/\lambda_0$:

$$\begin{aligned}
z_c(t) = {} & \frac{E_0 E_1}{2} n T_0 \cos\left(\frac{4\pi R}{\lambda_0}\right) \, \cos\left[\frac{4\pi \Delta R}{\lambda_0} \sin(\Omega t + \theta)\right] \\
& - \frac{E_0 E_1}{2} n T_0 \, \sin\left(\frac{4\pi R}{\lambda_0}\right) \, \sin\left[\frac{4\pi \Delta R}{\lambda_0} \sin(\Omega t + \theta)\right].
\end{aligned} \tag{5}$$

The amplitudes of cosine and sine components of the output signal equal to (5)

$$Z_{\cos} = \frac{E_0 E_1}{2} n T_0 \, \cos\left(\frac{4\pi R}{\lambda_0}\right)$$

$$\text{and } \; Z_{\sin} = \frac{E_0 E_1}{2} n T_0 \, \sin\left(\frac{4\pi R}{\lambda_0}\right)$$

depend on the ratio of R to λ_0. At distances $R_k = (\lambda_0/8)k$ (where $k = 1, 2, 3, \ldots$), amplitude $Z_{\cos} = 0$. But at the same distances amplitude $Z_{\sin} = ((E_0 E_1)/2)n T_0$. In its turn, at distances $R_{2k+1} = \frac{\lambda_0}{8}(2k+1)$ amplitude $Z_{\sin} = 0$, while at these distances amplitude $Z_{\cos} = ((E_0 E_1)/2)n T_0$. The time depending factors of the cosine and sine components in the correlator's output signal

$$\cos\left[\frac{4\pi \Delta R}{\lambda_0} \sin(\Omega t + \theta)\right] \text{ and } \sin\left[\frac{4\pi \Delta R}{\lambda_0} \sin(\Omega t + \theta)\right]$$

are not harmonic functions; their character largely depends on the ratio of ΔR to λ_0.

Each of these factors can be expanded into the Fourier series using the formulas

$$\begin{aligned}
\cos(m \cdot \sin x) &= J_0(m) + 2 \sum_{n=1}^{\infty} J_{2n}(m) \, \cos 2nx, \\
\sin(m \cdot \sin x) &= 2 \sum_{n=1}^{\infty} J_{2n-1}(m) \, \sin(2n-1)x
\end{aligned} \tag{6}$$

Amplitudes of the harmonic functions of this series can be expressed with Bessel's functions of the first-type m-order $J_n(m)$. Figure 5 demonstrates the plots of Bessel's functions of the first type and orders from zero to the fourth.

In the case discussed, it is indispensable to substitute $m = (4\pi \Delta R)/\lambda_0$ in (6). Let us also assume that $x = \Omega t$, with neglect to phase θ, which we consider as not essential.

From plots of Fig. 5, it is clear that for low values of $m = 1$, that is for $\Delta R \ll \lambda_0$, function $\cos(m \cdot \sin x)$ is comprised of basically constant value J_0 and the second harmonic of amplitude J_2; while function $\sin(m \cdot \sin x)$ is comprised of the first harmonic of amplitude J_1. Other harmonics of the series for values $m = 1$ can be ignored. With a growth of m, that is, an increase in amplitude of back-and-forth motion of the object ΔR and while it is approaching the radiated signal wave λ_0, an increasing number of functions $J_n(m)$, amplitudes of the Fourier series harmonic, will play a role in formation of functions $\cos(m \cdot \sin x)$ and $\sin(m \cdot \sin x)$; the functions themselves and their spectrums will take more and more complicated form.
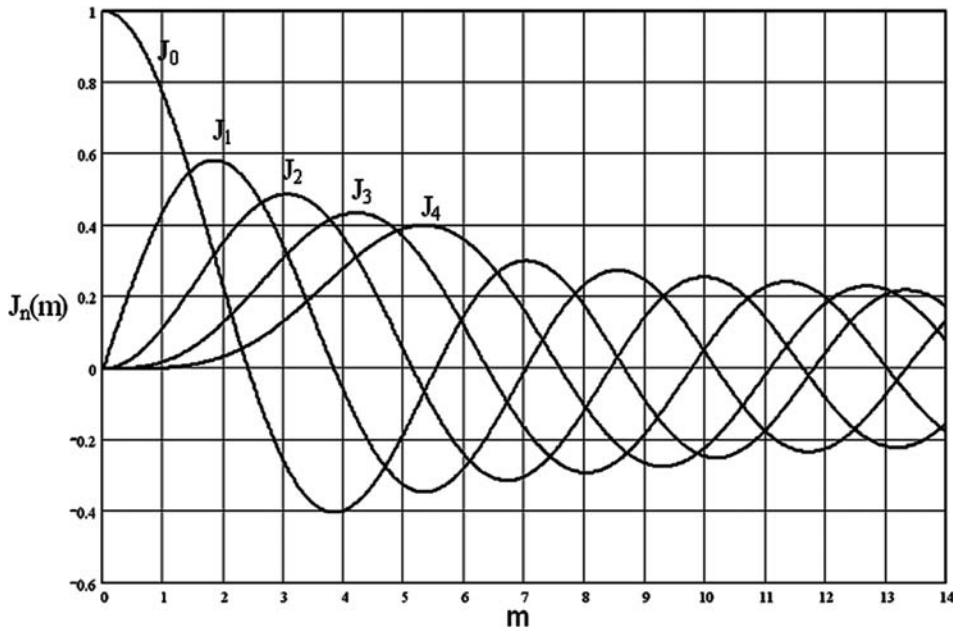
Fig. 5 Bessel's functions of the first type

In Figs. 6, 7, 8, and 9 the plots of cosine and sine components of the correlator's output signal $z_c(t)$ and their spectrums are given. To present each of the parts in its "clear" view, the plot for each of the parts is constructed for the range R_k and R_{2k+1} correspondingly where the amplitude of another part is equal to zero.

Figures 6, 7, 8, and 9 illustrate the variations in the form and spectrum of the output signal when the amplitude of the object's motion is increasing. With $m > 1$, a direct determination of the true law of the object's motion and a motion frequency becomes rather difficult and even impossible in some cases.

Formula (4) describes a cosine signal at the correlator's output for back-and-forth motion of an object. To restore the signal form corresponding to the real motion of an object, it is necessary to introduce into the receiver's scheme the second (sine) receiving channel, in which the reference signal is phase shifted by 90° relative to the reference signal in the first (cosine) channel (i.e., in-phase and quadrature channels). The output signal of the sine channel can be described by formulas, which are symmetrical to formulas (4) and (5):
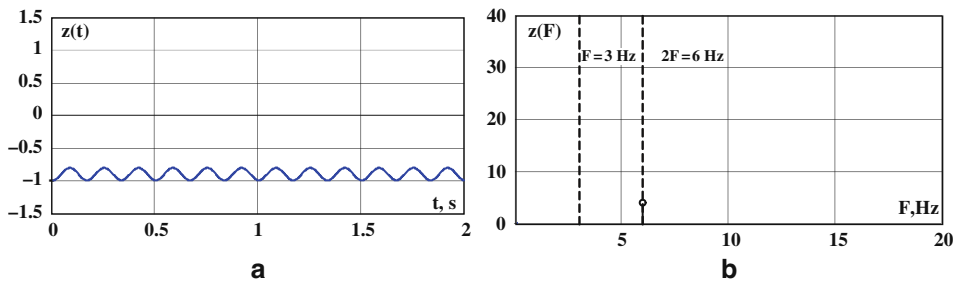
Fig. 6 Cosine part of the correlator's output signal (**a**) and amplitude–frequency spectrum of the cosine part of the correlator's output signal (**b**) for $m = 0.6$

$$z_s(t) = \frac{E_0 E_1}{2} n T_0 \, \sin\left[2\omega_0\left(\frac{R + \Delta R \, \sin\left(\Omega t + \theta\right)}{c}\right)\right],$$

$$z_s(t) = \frac{E_0 E_1}{2} n T_0 \, \sin\left(\frac{4\pi R}{\lambda_0}\right) \, \cos\left[\frac{4\pi \Delta R}{\lambda_0} \sin\left(\Omega t + \theta\right)\right]$$

$$-\frac{E_0 E_1}{2} n T_0 \, \cos\left(\frac{4\pi R}{\lambda_0}\right) \, \sin\left[\frac{4\pi \Delta R}{\lambda_0} \sin\left(\Omega t + \theta\right)\right]$$

The signals $z_c(t)$ and $z_s(t)$ are in fact two vectors of the trajectory of object's motion on a complex plane. To restore the trajectory of object's motion, it is indispensable to determine the argument of their sum:

$$R(t) = \frac{\lambda_0}{4\pi} \, \arg\left[z_c(t) + j z_s(t)\right].$$

To determine this argument, it is needed to calculate the arc tangent function:

$$\arg\left[z_c(t) + j z_s(t)\right] = \text{arctg}\left(\frac{\sin\left(4\pi \frac{R}{\lambda_0} + 4\pi \frac{\Delta R}{\lambda_0} \sin\left(\Omega t + \theta\right)\right)}{\cos\left(4\pi \frac{R}{\lambda_0} + 4\pi \frac{\Delta R}{\lambda_0} \sin\left(\Omega t + \theta\right)\right)}\right) = \frac{4\pi}{\lambda_0}\left[R + \Delta R \, \sin\left(\Omega t + \theta\right)\right]$$

(7)

Then, the law of the object's motion $R(t)$ will be as follows:

$$R(t) = R + \Delta R \sin\left(\Omega t + \theta\right).$$

(8)

If the radar equipment is capable to determine the distance to the object R, then subtracting it from $R(t)$, we can determine correctly the law of object motion: $\Delta R \sin(\Omega t + \theta)$.

In the general case, the law of object motion can be not a harmonic one, as we assumed before, but an arbitrary $f(\Omega t)$. In this case $R(t) = \Delta R f(\Omega t)$.

3 General Signal Processing Scheme

The general scheme of radar signal processing designed to measure the parameters of the object making back-and-forth motion is given in Fig. 10. Figure 11 demonstrates the results of modeling the processing of in-phase and quadrature channel signals from the scheme Fig. 10 for the object
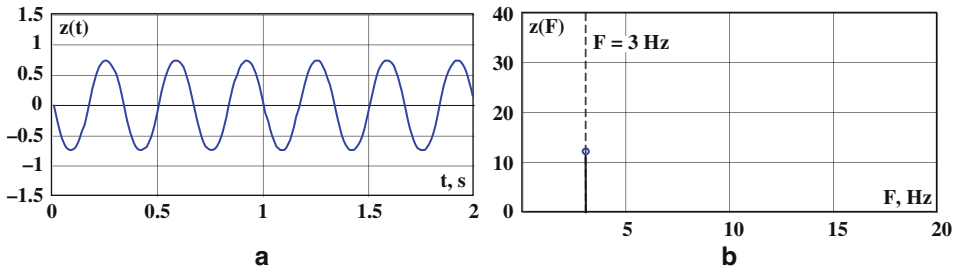
Fig. 7 Sine part of the correlator's output signal (**a**) and amplitude–frequency spectrum of the sine part of the correlator's output signal (**b**) for $m = 0.8$
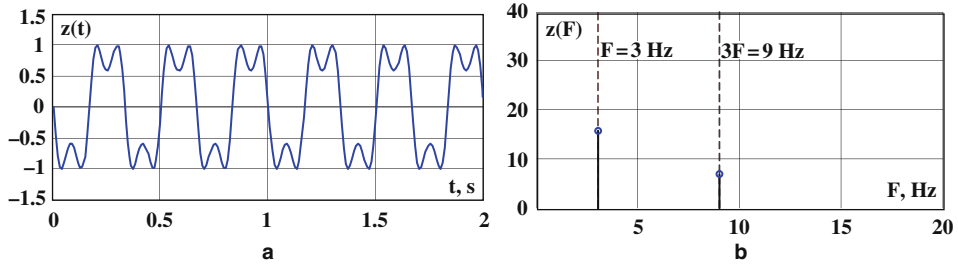
Fig. 8 Sine part of the correlator's output signal (**a**) and amplitude–frequency spectrum of the sine part of the correlator's output signal (**b**) for $m = 2.5$
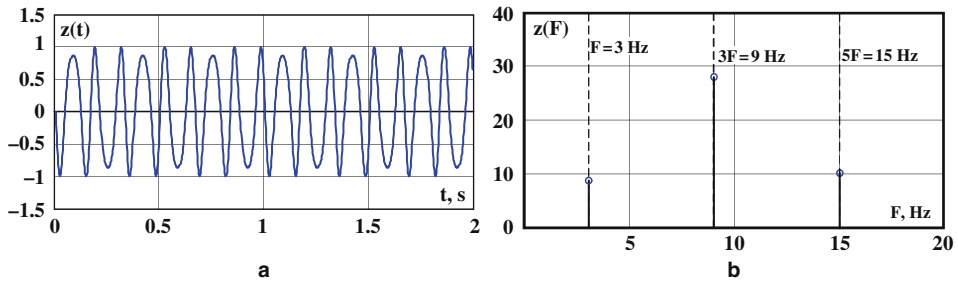
Fig. 9 Sine part of the correlator's output signal (**a**) and amplitude–frequency spectrum of the sine part of the correlator's output signal (**b**) for $m = 4.0$

moving by a harmonic law and for $m = 10$. Figure 11a shows the received signal (trajectory of object), Fig. 11b demonstrates the signals at the correlators' outputs for both channels, Fig. 11c demonstrates the output signal after performing the arc tangent operation. From the figure, it is evident that the output signal after processing is fully correlated with the received signal.
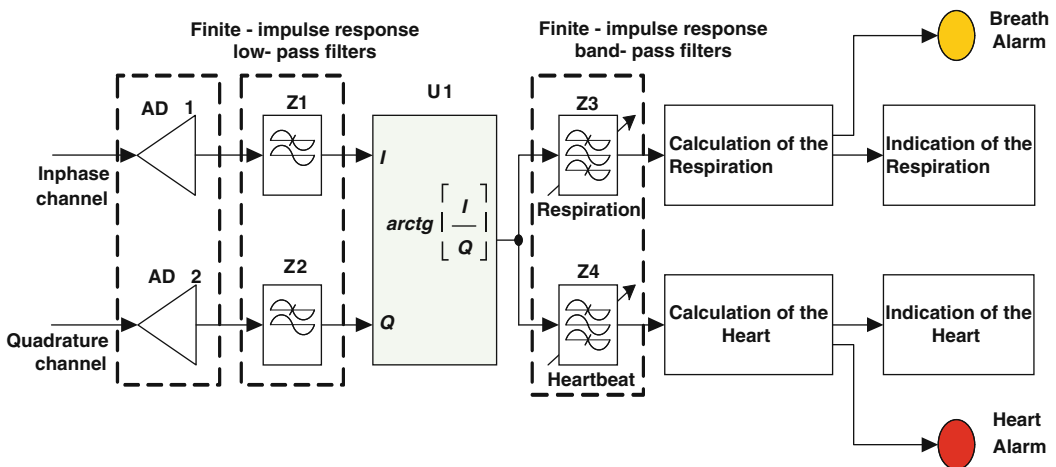
Fig. 10 Signal processing scheme
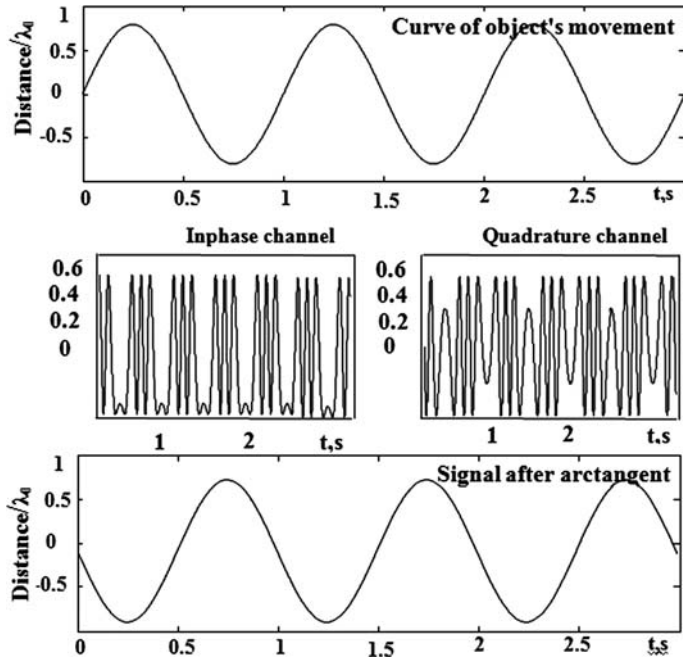
Fig. 11 Signals for the case $m = 10$ (model)

Fig. 12 Real medical UWB radar for remote measurements of the respiratory rate and the heart rate in the hospital
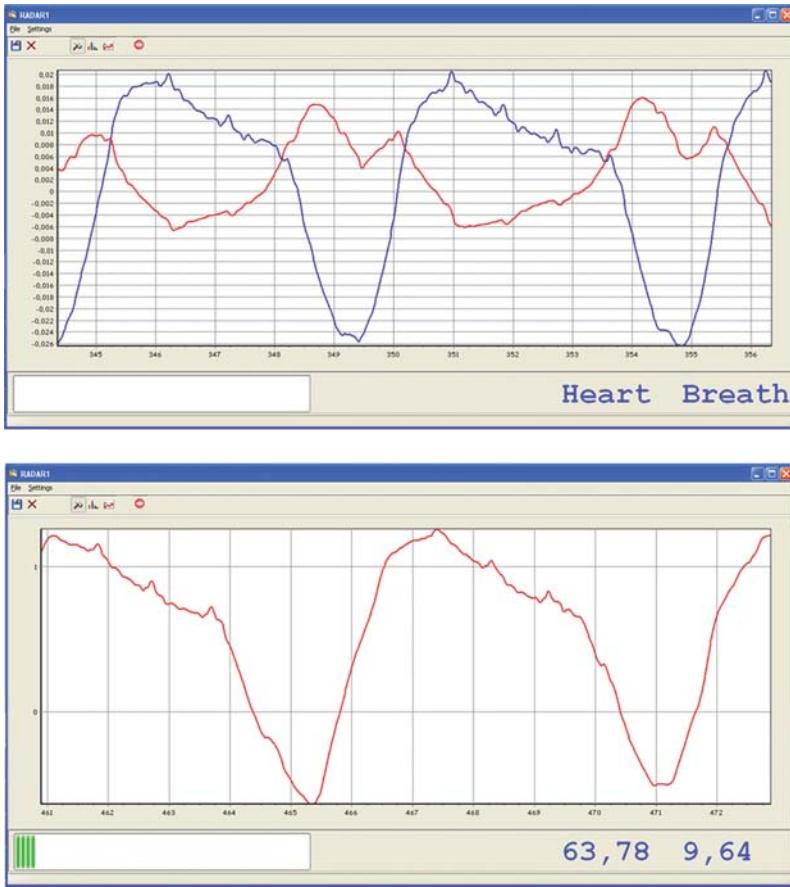
Fig. 13 Real signals, reflected from a patient's heart and thorax, obtained using UWB radar. On the *top* are correlators' outputs in in-phase and quadrature channels; at the *bottom* is output signal after arc tangent operation

In Fig. 12 real medical UWB radar for remote measurements of the respiratory rate and the heart rate in one of Russian hospital is shown.

In Fig. 13, the results of application of this processing scheme to real signals reflected from a patient's heart and thorax obtained using UWB radar are given. On top of Fig. 13 the signals at correlators' outputs in in-phase and quadrature channels are demonstrated and at the bottom of Fig. 13 the output signal after arc tangent operation is shown.

4 Conclusions

As it was demonstrated above, with low amplitudes of the object motion a constant component appears in the correlator's output signal (cosine channel) (Fig. 6). The radar usually receives a signal reflected from a moving object against a background of a large number of signals reflected by stationary objects. These signals produce another constant component at the correlator's output; it is usually rejected by a low-frequency filter. While performing this filtration, the desired constant

component of the cosine channel signal will be deleted as well; without this component, the argument in formula (7) and the law of the object motion (8) will be determined incorrectly. It is possible to restore this constant component using the mathematical method of sum-and-difference equations. But this constant component in cosine channel's output signal can also be rejected (or essentially reduced) by appropriate selection of parameter m. From plots in Fig. 5, it is clear that Bessel's function $J_0(m)$, which determines the value of this constant component, has the first zero at $m \approx 2$. If the amplitude of object's motion ΔR is known or given from the practice experience, then it is possible to select the medium frequency of a radiated signal spectrum, at which value λ_0 provides $m \approx 2$. So for an example, with amplitude of thorax motion about 1 cm (full oscillation – 2 cm), to obtain $m \approx 2$ the radar wavelength should be taken about 6 cm (5 GHz).

So, the usage in the receiver of UWB medical radar of in-phase and quadrature channels and digital processing, which performs arc tangent operation, makes possible the restoration of all parameters of object's back-and-forth motion. After restoration of the law of the object's motion, the amplitudes of thorax and heart motions and their oscillation frequency are determined.

Human Being Imaging with cm-Wave UWB Radar

A. Yarovoy, X. Zhuge, T. Savelyev, J. Matuzas, and B. Levitas

Abstract Possibilities of high-resolution human body imaging and concealed weapon detection using centimeter-wave microwave frequencies are investigated. Dependencies of the cross-range resolution of different imaging techniques on operational bandwidth, center frequency, imaging aperture size, and imaging topology have been studied. It has been demonstrated that the cross-range resolution of 2 cm can be achieved using frequencies below 10 GHz. These findings have been verified experimentally by producing high-resolution images of a foil-covered doll and some weapons.

Keywords UWB radar, Imaging, Near-field imaging, Image resolution, Medical imaging, Concealed weapon detection

1 Introduction

Recently, human being imaging by means of active and passive radars became a hot research and development topic due to concealed weapon detection and search for victims/survivals in buildings on fire or after earthquake. It has been demonstrated that mm-wave radars and radiometers can produce high-quality images [1–3]. However, both require several seconds of time for data acquisition, during which the scene and objects under investigation should be completely still. Furthermore, both system types require expensive mm-wave multi-channel receivers and large antenna arrays (combined with mechanical scanners). UWB radars operating at the frequencies below 10 GHz (in this chapter we refer to these frequencies as low microwave frequencies to distinguish them from mm-wave frequencies) might be a faster and cost-efficient technological solution for this application. Use of low frequencies has an additional advantage over mm-waves, i.e., possibility to penetrate through skin and human tissues, walls, and natural materials which makes it possible to use these radars for medical imaging, victim search after earthquake, or for security applications [4]. Furthermore, the frequency band from 1.99 to 10.6 GHz is also allocated by FCC to license-free operation of UWB surveillance systems. The major challenge associated with low-frequency use is the cross-range resolution of the radar, which believed to be inversely proportional to the central operational frequency of

A. Yarovoy (✉)
Delft University of Technology, International Research Centre for Telecommunications and Radar, Delft, The Netherlands
e-mail: a.yarovoy@ewi.tudelft.nl

the imaging radar [3]. This chapter describes theoretical and experimental study on cross-range resolution of short-range UWB radars and demonstrates principal possibility of high-resolution images (sufficient for human being imaging and concealed weapon detection) produced by low-frequency UWB radar.

2 Imaging Techniques

In order to produce a radar image of a target from data acquired over 2D aperture different techniques can be used. In all cases it is important that both amplitude and phase of the scattered field are recorded. The simplest approach is called microwave holography and is based on Fourier optics [5]. In this case the inverse Fourier transform of the scattered field measured in target far-field produces 2D image of a target. In its essence this approach is narrowband (single frequency) method and thus does not provide any depth (range) resolution in the target image.

Reconstruction of 3D target images typically requires scattered field measurements over large frequency band. Bandwidth of the measured data determines depth resolution of the image ΔR, which is of the order of (see, e.g., [3])

$$\Delta R \approx \frac{c}{2B},\tag{1}$$

where c is the speed of light and B is the operational bandwidth.

The most widely used methods for 3D image reconstruction are diffraction stack algorithm [6], Kirchhoff migration [7], and Stolt migration [3,8]. All these methods use back-propagation of the measured signals from an acquisition aperture to a target area. This back-propagation is done either in spatial domain (diffraction stack algorithm) or in spectral domain (Kirchhoff and Stolt algorithms). Despite different starting points these algorithms in free space differ from each other only by a weight coefficient (which depends on frequency and geometry) in the integral (see (2) and (3)) and thus deliver similar performance. These methods do not take into account possible multiple scattering at a target and this determines area of their validity.

Below we briefly discuss formulations of the diffraction stack and Kirchhoff algorithms and illustrate resolution capabilities of these two methods. Both imaging techniques are used later for low-frequency object imaging.

2.1 Diffraction Stack

In the classical diffraction stack migration, which is also called back projection algorithm the observed events are moved from the data acquisition position back to their true spatial location by propagating each collected time-domain range profile backward in reverse time. In a constant velocity medium, the unfocused data of a point-like reflector is characterized by a diffraction hyperbola. Thus for each point of the object plane, we construct a diffraction hyperbola in the image plane and determine where the hyperbola intersects with each trace. Then we take the value of each trace at the point of intersection and sum all these values together. The result of this summation is taken as the value of the pixel, and this value is placed in the object plane at that point. Suppose we collected the field $u(\mathbf{r},t)$ on a plane, the radar reflectivity at a point with coordinates $\mathbf{r}'$ can be expressed as

$$u(\mathbf{r}',t) = \iint w(\mathbf{r}) \cdot u\left(\mathbf{r},t + \frac{R_1 + R_2}{v}\right) dx\,dy\,|_{t=0},\tag{2}$$

where R_1 and R_2 represent the propagation distances between the point to be migrated $\mathbf{r}'$ and the positions of transmit and receive antennas, respectively, $w(\mathbf{r})$ is the weight coefficient designed to compensate the possible non-uniform illumination of transmitted waves over the field, and v denotes the propagation velocity in the medium.

To illustrate the algorithm performance an image of a point-like scatterer placed in front of the data acquisition aperture and at the half-meter range from it is computed (Fig. 1). The scatterer has been illuminated by EM spherical wave with a source in the middle of the aperture and with a bandwidth from 3 to 10 GHz. The scattered field has been acquired at 101 equidistant spaced points over the aperture of 1 m. It can be seen that the cross-range resolution is finer than the down-range resolution. The cross-range resolution is about 2.2 cm. The artifacts of the image are mainly determined by finite size of the aperture.
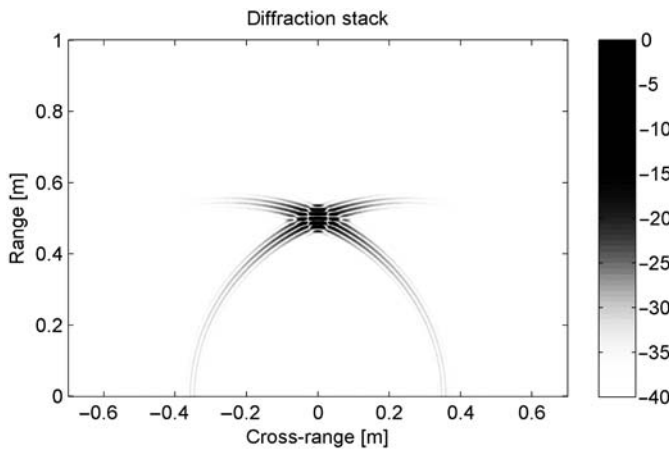
Fig. 1 Image of a point-like scatterer produced by diffraction stack algorithm

As the cross-range resolution is a crucial parameter for getting high-quality radar images, it has been further evaluated using numerical simulations. For this analysis imaging aperture of 1 m with 51 receive antennas has been used. The numerical simulations have confirmed that the cross-range resolution is inversely proportional to the central frequency (Fig. 2). However, increase of the central frequency above 20–25 GHz does not result in improvement of the cross-range resolution essential for human body imaging. On the other hand, use of an array of transmitters (whose positions coincide with receivers) results in an essential improvement of the cross-range resolution. So improvement of the data acquisition topology is more essential than an increase of the central frequency above 20 GHz.

Due to its straightforward implementation, diffraction stack migration is quite flexible and can be easily applied to different array configurations, therefore gaining notable popularity among different systems. However, it also has an undesirable characteristic. Assuming a single spike on the unmigrated signal, diffraction stack has no choice but to spread out the spike over the locus of all possible reflection points, which will bring up the sidelobes that will decrease the dynamic range of
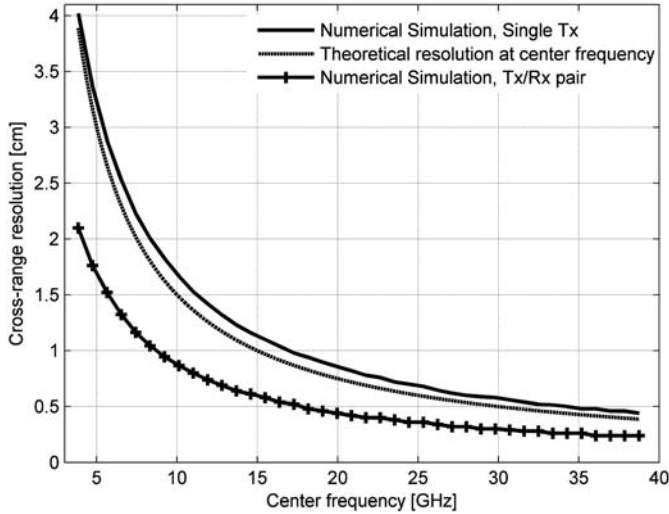
Fig. 2 Cross-range resolution as the function of the center frequency for different data acquisition scenarios

the system. The reason of this shortcoming is rooted in the fact that while diffraction stack procedure makes good sense and is intuitively obvious, it is not based on a rigorous wave theory.

2.2 Kirchhoff Migration

As a wave-equation-based successor to the classical diffraction stack, Kirchhoff migration finds its origin in the field of geophysics. The firm wave-equation basis for Kirchhoff migration is provided in [7]. By expressing the value of the wavefield at an arbitrary point according to the Kirchhoff integral theorem using the value of wavefield and its normal derivative, Kirchhoff migration delivers significantly higher quality image and lower sidelobe level than diffraction stack.

The idea of Kirchhoff migration is to back-propagate the scalar wave front, measured in the data acquisition plane, to the object plane at time zero, using an integral solution to the scalar wave equation. The feasibility of applying Kirchhoff migration to electromagnetic waves lies on the fact that vector wave equations reduce to scalar wave equation in a homogeneous, isotropic medium. Based on exploding reflector model (ERM) which assumes that the wave field starts from the target at time zero with half actual propagation speed, the migrated wave field can be obtained from the following equation:

$$u(\mathbf{r}',t) = \frac{1}{2\pi} \iint \frac{\cos\phi}{vR} \frac{\partial}{\partial t} u\left(\mathbf{r},t + \frac{2R}{v}\right) dx\,dy|_{t=0}, \tag{3}$$

where ϕ denotes the angle between the range axis and the line joining the migrated point $\mathbf{r}'$ and data acquisition point r. The use of ERM model limits the application of Kirchhoff migration to array-based configurations where transmit and receive antennas are collocated.

To illustrate the algorithm performance an image of the same scatterer and in the same conditions as in Fig. 1 is computed. The result is shown in Fig. 3. It can be seen from the figure that Kirchhoff migration provides slightly better cross-range resolution than the diffraction stack
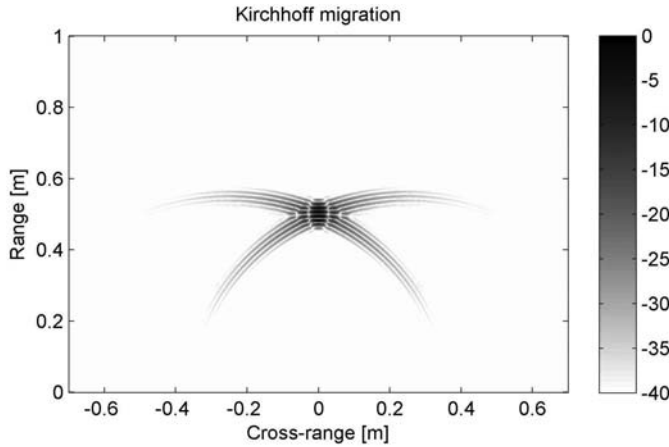
Fig. 3 Image of a point-like scatterer produced by Kirchhoff migration

algorithm. However the main advantage of the Kirchhoff migration is much lower level of sidelobes in the image.

3 Examples of Low-Frequency UWB Imaging

Simulation results above suggest that 3D radar imaging with a 2 cm resolution in both down- and cross-ranges can be achieved using the bandwidth from 3 to 10 GHz and the data acquisition of a meter wide aperture. The distance from the aperture to a target is assumed to be of about half a meter. These results are verified experimentally by imaging a number of objects including foil-covered doll, knife, and hand gun. The data have been collected in time domain. The pulse generator fires a pulse with 30 ps duration, which is transmitted by an antenna with operational bandwidth from 3 to 10 GHz. The scattered field is received by a similar antenna and is sampled by a 26 GHz stroboscopic receiver. The antenna pair is mounted on a 2D scanner with a maximal scanning area of 1 m × 1 m. The system has been calibrated by measuring reflection from a metal plate. The waveform of the received signal is shown in Fig. 4a while the spectrum of the reflected from the
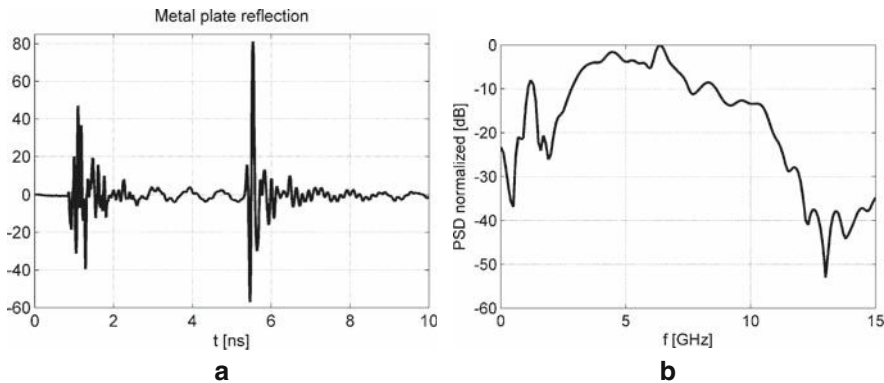
Fig. 4 Waveform of the received signal (**a**) and normalized spectrum of the probing pulse (**b**)
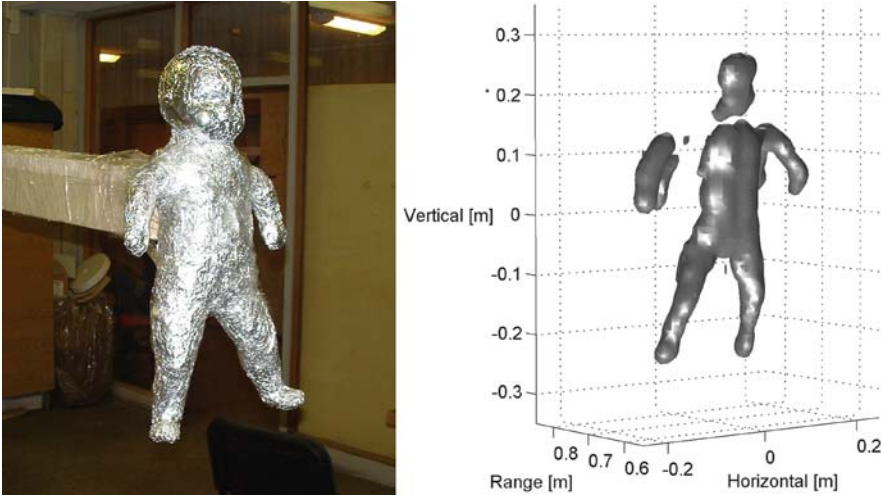
Fig. 5 Photo of a doll covered with metal foil (*left*) and its 3D radar image (*right*). Image dynamic range equals 15 dB

metal plate signal is shown in Fig. 4b. The part of the measured signal between 1 and 4 ns is due to transmit–receive antenna coupling.

Radar image of 60 cm high aluminum foil-covered doll (Fig. 5) has been obtained using an imaging aperture of 1 m × 1 m in a common offset mode with 1 cm step size. Measurements have been performed using vertically polarized EM fields. Kirchhoff migration algorithm has been used for imaging. Despite uneven surface of the foil and lack of electric contact between different layers of folded foil, the doll is relatively good imaged. Dimensions of the doll are properly recovered. Almost all parts of the doll and their relative position can be clearly seen.

Image of smaller objects such as knife and gun is shown in Fig. 6. Both objects can be easily recognized by their shapes.
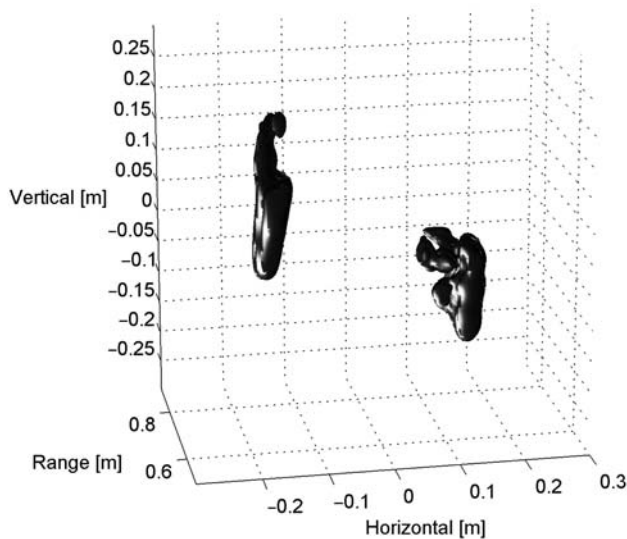
Fig. 6 Three-dimensional radar image of knife and gun. Image dynamic range equals 15 dB

Simulating scenario of concealed weapons detection, imaging of knife and gun placed on a foil-covered doll has been one as well. It has been found that both weapons can be detected by body shape change, while the radar contrast between the foil and weapons is very small.

4 Conclusions

In a number of emerging applications 3D high-resolution radar imaging at low microwave frequencies seems to be an interesting option. To investigate capabilities of such imaging we have theoretically studied cross-range resolution of different imaging techniques as a function of operational bandwidth, center frequency, imaging aperture size, and imaging topology. We have demonstrated that by using bandwidth of 7.5 GHz and an imaging aperture size of 1 m the cross-range resolution of 2 cm at the range of 50 cm can be achieved either by using an electromagnetic pulse with a center frequency of 4 GHz and coinciding positions of transmit and receive antennas or by using an electromagnetic pulse with a center frequency of 8 GHz and a single position of the transmit antenna. These findings have been verified experimentally by producing high-resolution images of a foil-covered doll and some weapons (such as knife and gun). The results achieved prove principal possibility of concealed weapon detection using microwave frequencies below 10 GHz.

References

1. G. N. Sinclair, R. N. Anderton, and R. Appleby, Outdoor passive millimetre wave security screening, IEEE 35th International Carnahan Conference Security Technology, pp. 172–179, 2001.
2. M. Peichl, H. Still, S. Dill, M. Greiner, and M. Jirousek, Imaging technologies and applications of microwave radiometry, First European Radar Conference, pp. 269–273, 2004.
3. D. M. Sheen, D. L. McMakin, and Th. E. Hall, Three-dimensional millimeter-wave imaging for concealed weapon detection, IEEE Transactions on Microwave Theory and Techniques, vol. 49, pp. 1581–1592, 2001.
4. T. Dogaru and L. Nguyen, FDTD models of electromagnetic scattering by the human body, IEEE Antennas Propagation Society and International Symposium, pp. 1995–1998, 2006.
5. J. W. Goodman, Introduction to Fourier Optics, McGraw-Hill, New York, 1968.
6. E. M. Johansson and J. E. Mast, Three-dimensional ground penetrating radar imaging using synthetic aperture time-domain focusing, Proceedings of SPIE, vol. 2275, pp. 205–214, 1994.
7. W. A. Schneider, Integral formulation for migration in two and three dimensions, Geophysics, vol. 43, pp. 49–76, 1978.
8. R. H. Stolt, Migration by Fourier transform, Geophysics, vol. 43, pp. 23–48, 1978.

A Metallic Wire Electromagnetic Crystal Structure for Radar Applications

F. Ghanem, G.Y. Delisle, T.A. Denidni, and K. Ghanem

Abstract In this chapter, an electromagnetic crystal (EC) composed of one radiating element enclosed inside a metallic wire structure is presented for radar applications. The new radar does not contain any mechanically rotating element and the space scanning is performed by exploiting the frequency dispersion of the radiation patterns of this type of EC. Indeed, their radiation patterns consist of narrow beams whose steering angles vary with the frequency; the target direction is determined by the frequency of the signal reflected on the radar system. Since the target direction is discriminated in frequency, the different radiation patterns needed for the radiolocation are deployed simultaneously in time, which makes the proposed radar capable of tracking targets moving, in theory, at the order of light speeds. To present the developed approach, both theoretical study and numerical simulations using finite difference time domain (FDTD) method are given. To validate the developed approach, experimental measurements are also presented and discussed.

Keywords Electromagnetic crystals · Periodic structures · Radar · Radiolocation · Directive antennas

1 Introduction

Electromagnetic crystals are being deeply investigated by researchers. Composed of periodic alternation of dielectric media (e.g., air and dielectric) or dielectric and conductor media (e.g., air and metal), these structures can exhibit interesting properties that can be used for surface wave suppression [1–3], size reduction [4,5], high directivity antennas [6–9], beam reconfiguration [10,11], and ultrafast radiolocation [12]. Research efforts in electromagnetic crystal fields are being deployed to try to discover all the potential of these structures. This chapter falls within this scope and proposes the use of EC for radar applications.

From the information theory perspective, the determination of the target direction necessitates the modulation of the different steering angles in space by one of the three information supports which are the amplitude, the frequency, and the phase (or time delay) of a signal. In other words, the antenna used in the radar must have different amplitudes or phases or frequencies for each direction in space.

F. Ghanem (✉)
Prince Mohammad Bin Fahd University, Al-Khobar, Saudi Arabia
e-mail: f.ghanem@bham.ac.uk

To the best of knowledge of the authors, there is no antenna that modules the space by the phase or the amplitude. Also, the radiation patterns of the antennas usually used in wireless communications have very low variations with frequency. Failing to have antennas that module the space with one of the three supports, the usual radar systems have adopted to combine two of the supports, namely, time delay and amplitude. So at each time delay, the antenna amplitude is deployed in one steering angle. The entire space is scanned sequentially, one angle at each time step, which is made either by mechanically rotating the antenna or electronically swiping the antenna beam of a smart antenna. One evident drawback of this approach is the difficulty to track targets moving at speeds of the order or greater than the scanning speed.

In this chapter, a new radar that modulates the space with frequency is proposed. It is composed of metallic wire EC that has high-frequency dispersion radiation patterns. Their radiated power consists of narrow beams whose steering angles vary with the frequency, which allows scrutinizing the space by using the frequency. Figure 1 shows the principle of the proposed radar.

Fig. 1 Principle of the proposed radar
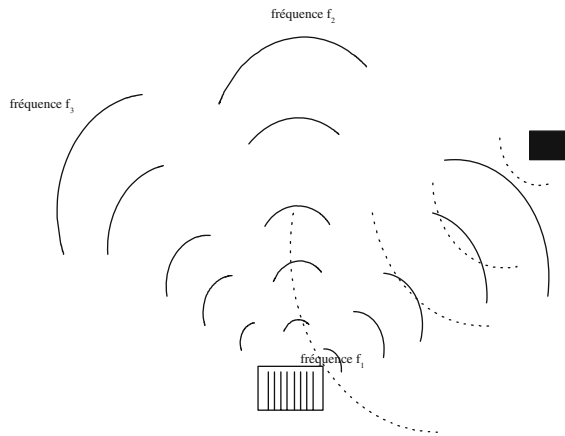
The radar starts by transmitting a UWB signal that contains all frequencies needed to scan the entire desired space region. Due to the frequency dispersion of the radiation patterns, the different signal frequencies will be transmitted in different directions as shown in Fig. 1. If any target is present, then only the signal having the frequency that goes in its direction (frequency 1) is reflected. The other components (frequencies 2 and 3) propagate in different directions and will not be reflected to the radar. The detected frequency determines the angle of the target and the time propagation determines its distance.

The proposed radar is able to modulate the space with the frequency only and has the advantage of being able to scan it instantaneously.

2 Frequency Beam Sweeping Principle and Antenna Design

Figure 2 shows the schematic of the antenna used in the proposed radar system. It is quite similar to that used in [12] and is composed of six rows of metallic wires disposed symmetrically to a monopole. The inner and outer rows have the same period $P_1 = P_3 = 20$ mm, while the period of the middle one is $P_2 = 40$ mm. The cavities are equally spaced between them by a distance,
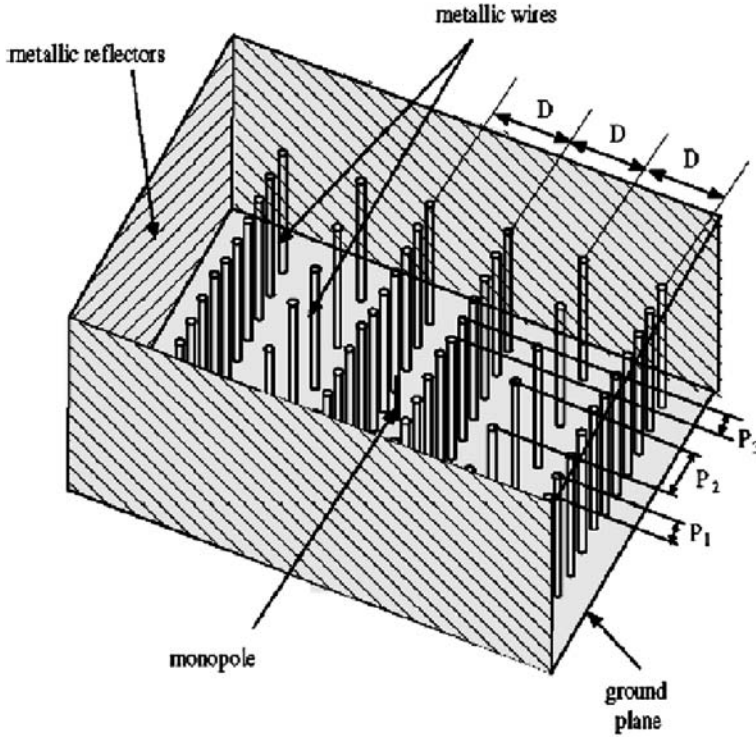
Fig. 2 Schematic of the proposed EC antenna

$D = 20$ mm. The wires have a length of 260 mm and a diameter of 0.86 mm. To make the antenna radiating from one side only, metallic reflectors are put on the three remaining sides.

The design of the proposed antenna is based on the transmission factor parameter given by [12]

$$T_n = \frac{t_n \exp\left(-jkD\cos(\theta)/2\right)}{1 - r_n \exp\left(-jkD\cos\theta\right)},$$
(1)

where the transmission coefficient (t_n) and reflection coefficient (r_n) are, respectively, given by

$$t_n = \frac{t_{n-1} \cdot t \cdot \exp\left(-jkD\cos(\theta)/2\right)}{1 - r_{n-1} \cdot r \cdot \exp\left(-jkD\cos\theta\right)}$$
(2)

and

$$r_n = r_{n-1} + \frac{t_{n-1}^2 \cdot r \cdot \exp\left(-jkD\cos(\theta)/2\right)}{1 - r_{n-1} \cdot r \cdot \exp\left(-jkD\cos\theta\right)}.$$
(3)

The terms t_{n-1} and r_{n-1} are the transmission and reflection coefficients of the structure composed by $n - 1$ cavities (internal rows); t and r are the coefficients of the new added rows (external rows), and D is the distance between them. The transmission and reflection coefficients of a single metallic wire row, t and r, are determined numerically by using the incident, reflected, and transmitted waves.

The transmission factor T_3 of this structure is shown in Fig. 3.
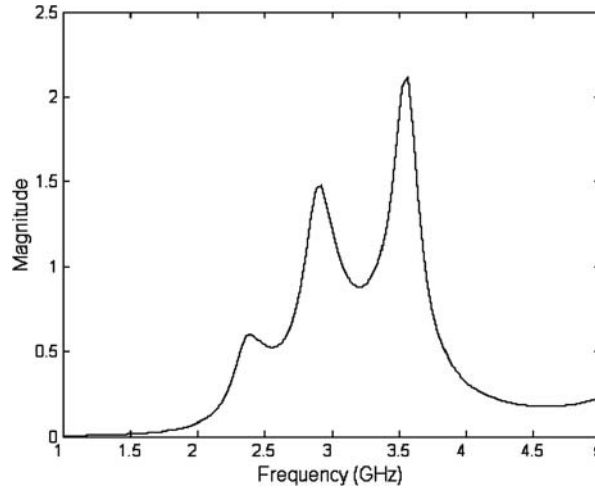
Fig. 3 Transmission factor of the structure as a function of frequency

The transmission factor of Fig. 3 can be assimilated to a graphical curve used in array antennas, except that the abscissa is frequency and not phase [6]. The visible region extends from the considered frequency, *f*, to its image –*f*. The negative frequencies correspond to the curve of the transmission factor mirrored about the coordinate axis. At a resonance, the antenna exhibits a single narrow beam and when the frequency increases, the main beam is transformed to two main beams symmetrical to the broadside position. The more the frequency increases, the more the beam deviation increases. Figure 4 shows the radiation patterns of this structure when excited by a 25 mm monopole disposed in its center. The curves have been obtained using the FDTD method.

As it can be seen, from Fig. 4, the proposed antenna is able to instantly scan the space between –50° and 50° by exciting the monopole at frequencies going from 2.95 to 4.26 GHz. By transmitting a UWB signal, the different frequencies that may be of infinite number will propagate in different directions. At reception, the radar detects a finite number of desired frequencies, which may be, for example, 2.95, 3.04, 3.20, 3.41, 3.69, and 4.26 GHz as shown in Fig. 4. When the target moves, the radar will detect it at different frequencies.

It can be noted in Fig. 4 that some diagrams present sidelobes. This is not a problem and it is shown in [12] how they can be used to perform robust radiolocation.

The frequency of the reflected signal determines the angle of the target and the propagation time determines its distance. The direction finding processing unit of the radar system is composed of frequency detectors only and the target position is determined by reading their outputs and calculating the propagation time.

Finally, it is important to note that the radiation patterns remain in an angle over an appreciable frequency bandwidth which is of the order of 70 MHz as shown in [7]. The maximum speed for the worst case (for $\theta = 0$) for which the radar can perform well is given by

$$v_{max} = \frac{f_D}{2} \frac{c}{f_{transmitted}} = 35 \times 10^6 \frac{c}{f_{transmitted}} \ . \tag{4}$$

So even if the radar is used at 100 GHz, it will be possible to track targets moving transversally at 105 km/s.
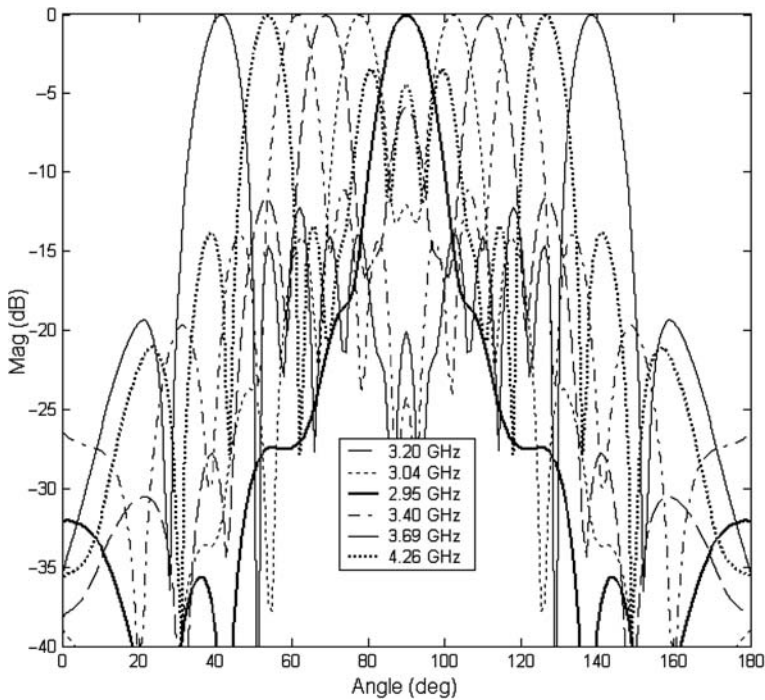
Fig. 4 Normalized antenna radiation patterns at frequencies 2.95, 3.04, 3.20, 3.41, 3.69, and 4.26 GHz

3 Experimentation

A prototype of the designed system was fabricated using a wood structure that holds the metallic wires as shown in Fig. 5a. Figure 5b illustrates the back of the ground plane on which the monopole and metallic stems are soldered.

The return loss of the fabricated prototype was measured and the results are shown in Fig. 6. From this curve, it can be seen that the antenna is impedance matched from 2.86 to 4.31 GHz, which covers the entire bandwidth needed to scan the space between –50° and 50°.
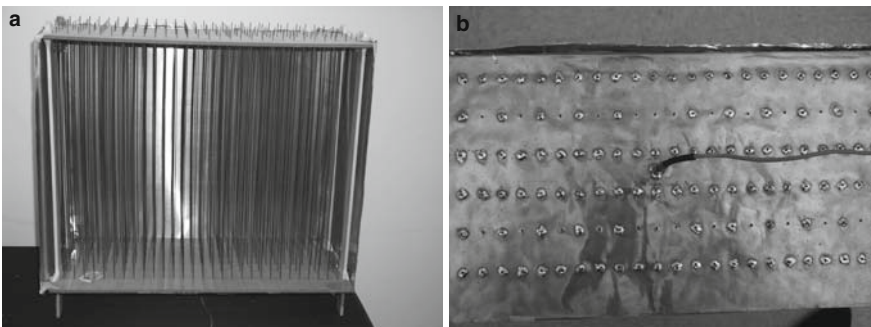
Fig. 5 Photography of the antenna prototype: (**a**) front view and (**b**) bottom view
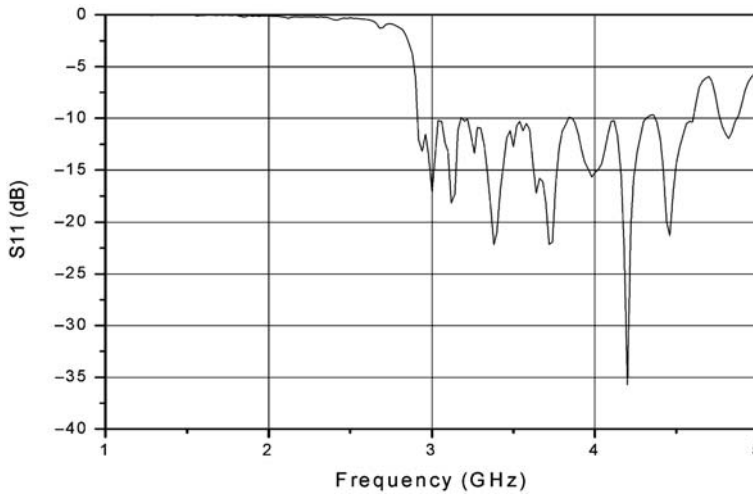
Fig. 6 Measurement results of S_{11} parameter

The radiation patterns of the prototype were measured at different frequencies. Figure 7 shows the measured radiation patterns at 2.95 and 4.26 GHz corresponding to 0° and 50° deviation.

The obtained results have validated the concept of scanning the space by varying the operating frequency, despite an asymmetry in the radiation patterns due to a physical flaw in the fabrication of the prototype.

Indeed, this type of antennas is sensitive to the position and the fixation of the wires, a detail that should be taken into account in their fabrication. Finally, it is important to note that efficiency of these antennas is appreciable since the electromagnetic waves propagate in the air between the wires.

4 Target Side Discrimination

With the proposed antenna it is possible to determine the direction of a target. However, since the radiation patterns are composed of two main beams symmetrical to the broadside direction, it is not possible to know whether the target is on the left or right. To mitigate the target side, it is worth to note that the symmetry of the radiation pattern beams is a direct consequence of the antenna structure symmetry. Thus, a straightforward approach to address this drawback is to create a dissymmetry in the structure that would propagate to the radiation pattern beams. The dissymmetry consists in disconnecting wires by using switches. After a parametrical study, it was found that the radiation patterns are more sensitive to the outer wire row. To minimize the drop in the power efficiency of the system due to DC supplying the switches, an optimization has been carried out to minimize the number of switches to use. Figure 8 shows the radiation patterns obtained by disconnecting the first wire above the symmetry plane of the structure.
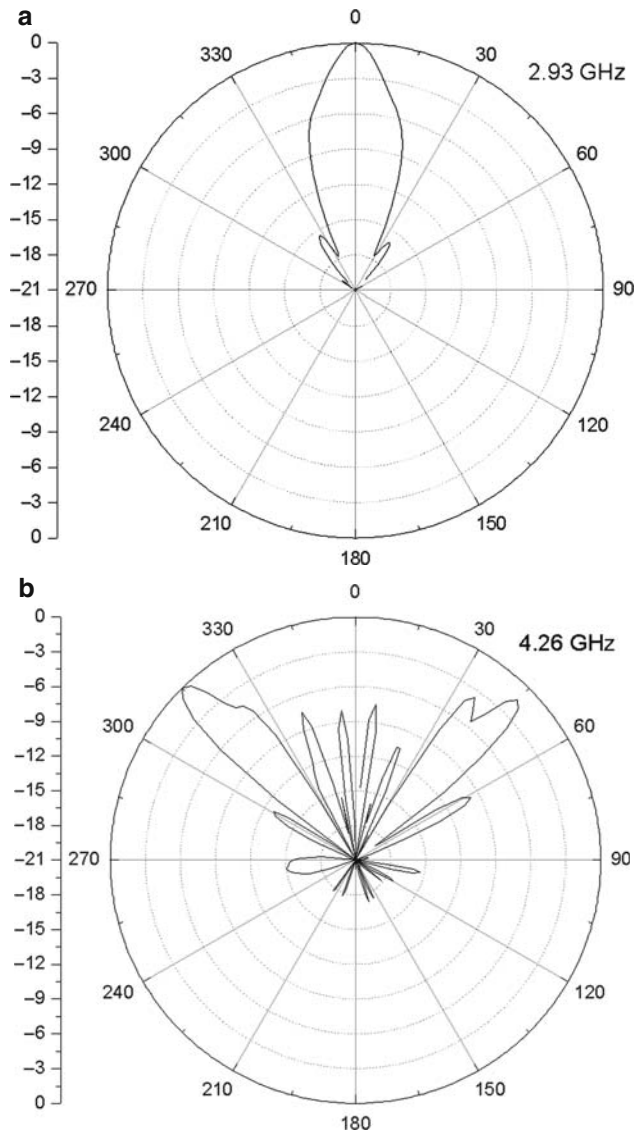
Fig. 7 Normalized measured radiation patterns at (**a**) 2.95 GHz and (**b**) 4.26 GHz

As it can be seen from Fig. 8, when disconnecting the wire, one side of the radiation patterns is attenuated without affecting the steering angles. Thus, to discriminate the target side, the wire is disconnected and if the amplitude of the signal diminishes then the target is on the left and if not, then the target is on the right. It is important to note that the disconnection of the wires does not disturb the radiolocation process since the radar will still able to determine the target position, irrespective of the switch state.
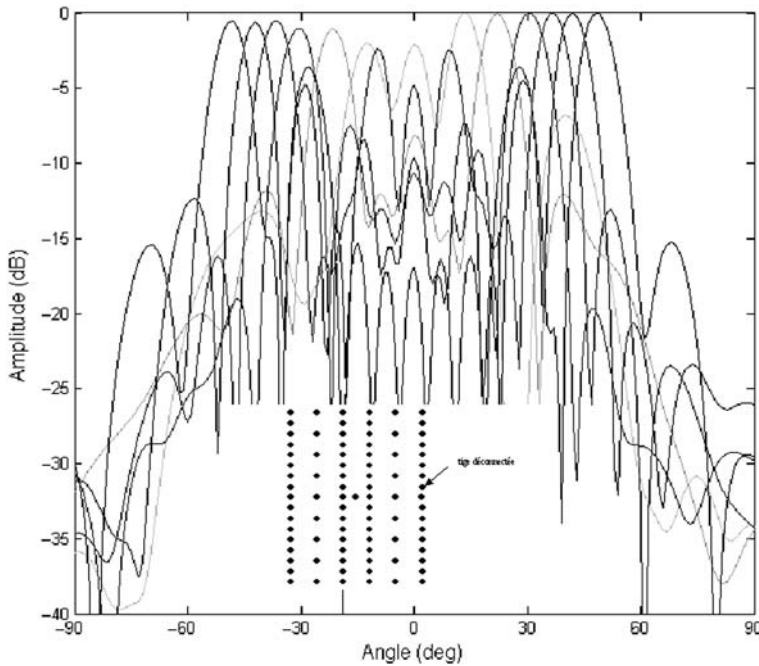
Fig. 8 Superposition of simulated radiation patterns when disconnecting one stem

5 Conclusion

A new radar based on electromagnetic crystal material has been presented. The proposed radar is proved to have the capability of instantaneously scanning a given region by varying the frequency. Unlike traditional radars, no sequential scanning is needed and the direction finding processing unit is very simple and consists of frequency detectors and a switch controller. Both simulated and measured results presented here validate the principle of beam scanning by varying the frequency.

References

1. F. Yang and Y. Rahmat-Samii, Microstrip antennas integrated with electromagnetic band-gap (EBG) structures: a low mutual coupling design for array applications, IEEE Transactions on Antennas and Propagation, vol. 51, no. 10, pp. 2936–2946, 2003.
2. R. Coccioli, F. R. Yang, K. P. Ma, and T. Itoh, Aperture-coupled patch antenna on UC-PBG substrate, IEEE Transactions on Microwave Theory and Techniques, vol. 47, no. 11, pp. 2123–2130, 1999.
3. R. Gonzalo, P. de Maagt, and M. Sorrolla, Enhanced patch-antenna performance by suppressing surface waves using photonic-bandgap substrates, IEEE Transactions on Microwave Theory and Techniques, vol. 47, no. 11, pp. 2131–2138, 1999.
4. H. Mosallaei and K. Sarabandi, Antenna miniaturization and bandwidth enhancement using a reactive impedance substrate, IEEE Transactions on Antennas and Propagation, vol. 52, no. 9, pp. 2403–2414, 2004.
5. T. H. Liu, W. X. Zhang, M. Zhang, and K. F. Tsang, Low profile spiral antenna with EBG substrate, Electronics Letters, vol. 36, no. 9, pp. 779–780, 2000.
6. H. Boutayeb, K. Mahdjoubi, A. C. Tarot, and T. A. Denidni, Directivity of an antenna embedded inside a Fabry–Perot cavity: analysis and design, Microwave and Optical Technology Letters, vol. 48, no. 1, pp. 12–17, 2006.

7. F. Ghanem, G. Y. Delisle, T. A. Denidni, and K. Ghanem, A directive dual-band antenna based on metallic electromagnetic crystals, IEEE Antennas and Wireless Propagation Letters, vol. 5, pp. 384–387, 2006.
8. M. Thevenot, C. Cheype, A. Reineix, and B. Jecko, Directive photonic bandgap antennas, IEEE Transactions on Microwave Theory and Techniques, vol. 47, no. 11, pp. 2115–2122, 1999.
9. G. Von Trentini, Partially reflecting sheet arrays, IEEE Transactions on Antennas and Propagation, vol. AP-4, no. 4, pp. 666–671, 1956.
10. D. F. Sievenpiper, J. H. Schaffner, H. J. Song, R. Y. Loo, and G. Tangonan, Two-dimensional beam steering using an electrically tunable impedance surface, IEEE Transactions on Antennas and Propagation, vol. 51, no. 10, pp. 2713–2722, 2003.
11. G. Poilsaneal et al., Active metallic photonic bandgap material MPBG: experimental results on beam shaper, IEEE Transactions on Antennas and Propagation, vol. 48, no. 1, pp. 117–119, 2000.
12. F. Ghanem, G. Y. Delisle, and T. A. Denidni, A new electromagnetic crystal-based antenna for ultrafast radiolocation applications, IEEE Antennas and Wireless Propagation Letters, vol. 5, pp. 199–203, 2006.

Small Printed Ultra-Wideband Antennas Combining Electric- and Magnetic-Type Radiators

D.-H. Kwon, E.V. Balzovsky, Y.I. Buyanov, Y. Kim, and V.I. Koshelev

Abstract Small printed ultra-wideband (UWB) antennas that combine electric-type and magnetic-type radiators are presented. Combining the two types of radiators can extend the passband in the lower frequency direction compared with antennas of either individual type. Moreover, combined antennas can be designed to feature increased gain by allowing the electric fields radiated by the electric and magnetic sources combine in-phase in the desired direction. Two designs of the size 20 mm × 30 mm are presented together with measured impedance and radiation characteristics.

Keywords Directive antenna · Impulse-radiating antenna · Printed antenna · Small antenna   · Ultra-wideband antenna

1 Introduction

With the ever-decreasing sizes of modern personal wireless devices, designing physically/electrically smallest antennas that satisfy a given set of electrical performance requirements has become an important practical target for antenna designers. Considering that mobile devices increasingly support multiple wireless communication protocols, small antennas for ultra-wideband or multiband operations are desired. In addition, possibility of fabrication at low cost constitutes an important factor for communication antennas.

Ultra-wideband (UWB) communication antennas need to operate over the frequency band of 3.1–10.6 GHz. Traditionally, research on UWB antennas has been focused on impulse radiating antennas [1–3] having large dimensions, mainly targeted at high-power applications. However, small planar structures that are amenable to printed circuit technology are better suited for low-cost communication purposes. Depending on the radiation pattern requirements, planar or printed UWB communication antennas can be categorized into two classes – planar monopoles/dipoles and tapered slot antennas. For omnidirectional radiation patterns, planar monopoles [4,5] or planar dipoles [6,7] can be used to satisfy both impedance and pattern requirements. If directive radiation patterns are needed, a tapered slot antenna, such as the Vivaldi antenna [8], can satisfy the UWB bandwidth requirement.

D.-H. Kwon (✉)

Department of Electrical and Computer Engineering, University of Massachusetts Amherst, Amherst, Massachusetts 01003, USA

e-mail: dhkwon@ecs.umass.edu

Combining electric-type and magnetic-type dipole antennas can extend the operation bandwidth in the lower frequency direction [9]. In terms of the spherical vector wave theory, this corresponds to a reduced antenna radiation quality factor for a combined radiation of TM and TE spherical modes compared with a source radiating either the TM or TE modes only [10,11]. At the same time of enhanced bandwidth, this combination of spherical modes can lead to a gain enhancement of up to 3 dB as well in principle. Combining electric and magnetic dipole radiations to obtain a wide operation bandwidth and an enhanced gain has been reported in three-dimensional (3D) antenna designs [12–14].

This chapter presents printed UWB antenna designs that simultaneously excite electric- and magnetic-type radiators with the goal of achieving smaller antenna dimensions and enhanced gain properties. The printed antennas may be considered two-dimensional versions of the 3D antenna presented in [13]. Two antennas of size 20 mm × 30 mm are designed and fabricated. They are edge-fed with one from the bottom edge and the other from the back edge. Measured performance parameters are provided.

2 Design and Operation Principle

Figure 1 illustrates the fundamental structure of the printed UWB antenna design. In essence, it is a hybrid of an electrical radiator (ER) formed by arms 1 and 2 and a magnetic radiator (MR) realized by an electric loop formed within arm 1. The radiators are formed on one side of a dielectric substrate by selectively etching the conductor cladding using the printed circuit technology in this planar design. They are simultaneously excited by a single feed realized by an asymmetric coplanar waveguide (CPW) located at either the back or the bottom edge of the antenna. An end-launch SMA connector can be used to excite the antenna via a coaxial cable. Denoting the wavelength at the lower edge of the UWB passband by λ_l, the overall dimension $W \times L$ of the antenna is approximately given by $W \approx 0.2\lambda_l$ and $L \approx 0.3\lambda_l$. The electric radiator has the form of a tapered slot antenna (TSA) of dimensions $w \times l$. However, it should be noted that it operates as a TSA only in the higher frequency range of the UWB band. In the lower frequency range, its operation is closer to that of a straight planar dipole due to the small electrical dimensions.

The purpose of combining an ER and an MR to form one antenna is to reduce the size of the overall antenna for a given bandwidth compared with antennas that operate either as an ER or as
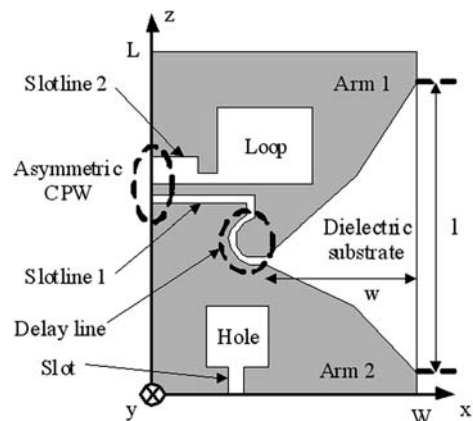
Fig. 1 The basic structure of a printed combined antenna. The *shaded region* represents conductor cladding on the top side of a dielectric substrate after selective etching process

an MR only. The ER is in itself a wideband radiator composed of wide conducting radiating arms. Below the first resonance frequency of the ER, its input impedance is capacitive, i.e., a larger amount of electric energy is stored around the ER than magnetic energy. In contrast, the MR has inductive input impedance before it becomes an efficient radiator with respect to frequency. Therefore, if the resonance frequencies of the ER and MR are matched, the excess electrical energy and the excess magnetic energy of the two radiators will balance out to make the whole structure self-resonate before each of the individual radiators becomes an efficient radiator. In terms of the simple lowest order spherical vector waves, this observation corresponds to a reduced quality factor for a point Huygens' source radiating simultaneous TM and TE modes compared with individual infinitesimal electric or magnetic dipoles [10]. To this end, the individual resonance frequencies of the radiators should match, and this may be achieved by properly adjusting the shapes and the dimensions of the loop and the ER given by w and l. In addition, the excitation strengths of the TM and TE modes should be equal. The relative strengths of the ER and MR excitations can be adjusted by changing the widths of the slotlines 1 and 2 in Fig. 1 while keeping the characteristic impedance of the resulting asymmetric CPW feed line equal to 50 Ω.

As long as the strengths of the ER and MR excitations are equal, the phase difference between the two sources has little impact on the bandwidth enhancement of the combined antenna. However, the maximum gain of the antenna is a strong function of the phase difference, and a gain enhancement by up to 3 dB is possible compared with the gain of either individual radiator [10]. It is desired that the fields radiated by the ER and MR interfere in-phase in the +x-direction and out-of-phase in the –x-direction. The right amount of phase difference between the two radiators is obtained using the delay line shown in Fig. 1. The length of the delay line is approximately equal to $0.2\lambda_l / \sqrt{\varepsilon_r - 1}$, where ε_r is the relative permittivity of the dielectric substrate.

Finally, the hole and slot formed within arm 2 of the ER prevents the current from reaching the edge having the connector attachment and becoming leakage current. Its exact shape can be adjusted to control the input impedance characteristic primarily in the lower frequency range of the UWB band.

3 Antenna with a Horizontal Feed

The geometry of the antenna design A with a horizontal feed from the back edge is shown in Fig. 2a. The detailed geometry of antenna A was reported in [15]. The dimension of A is given by 20 mm × 30 mm, which amounts to the electrical size of 0.21λ × 0.31λ at 3.1 GHz. A low-loss dielectric substrate RO3210 (tan $\delta = 0.0027$) with the relative dielectric constant $\varepsilon_r = 10.2$ from Rogers Corporation has been used with the substrate of thickness 1.27 mm. The size of the ER is given by $w = 13.4$ mm and $l = 24.9$ mm. It was found out that the necessary width of slotline 2 exceeded the distance between the center pin and the ground leg of the SMA connector for the given substrate. Since a lower permittivity of the substrate leads to a higher slotline impedance [16], two circular air holes of diameter 1.3 and 1.0 mm were created to effectively lower the permittivity of the substrate.

A prototype was fabricated and the input VSWR was measured using an Agilent 8722ES vector network analyzer. A full-wave simulation was performed using the commercial software Ansoft HFSS. The measurement and simulation results are compared in Fig. 2b. The measurement result indicates that the antenna satisfies VSWR < 2 over 2.56–10.83 GHz, making it suitable for entire UWB band operations.
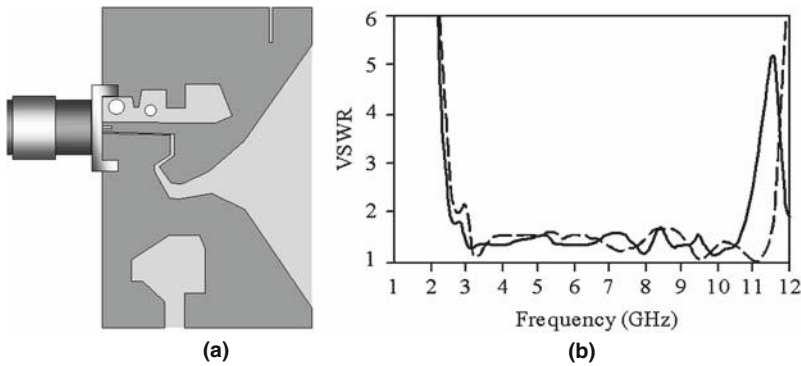
Fig. 2 The antenna A with a horizontal feed. (**a**) The geometry. (**b**) The VSWR performance comparison between measurement (*solid line*) and simulation results (*dashed line*)
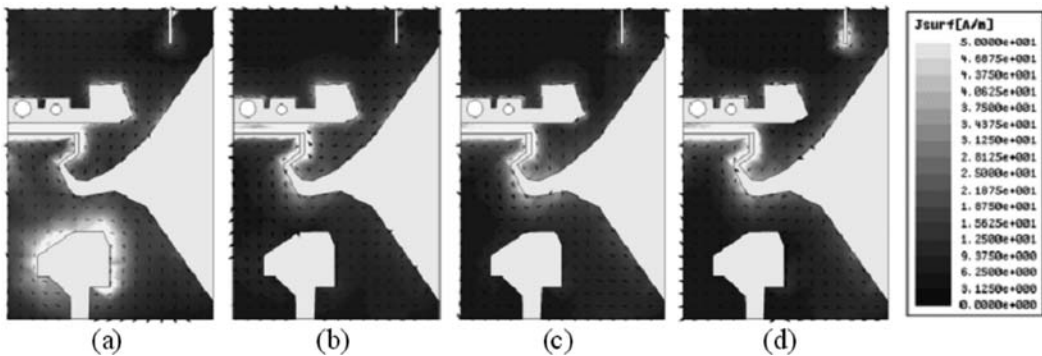
Fig. 3 Simulated surface current distribution of antenna A: (**a**) 3.1 GHz, (**b**) 5.1 GHz, (**c**) 7.1 GHz, and (**d**) 9.1 GHz. All four plots use the same legend shown at the far right. The maximum surface current density has been clipped at 50 A/m for visualization

Figure 3 shows the surface current flow at four frequency points within the UWB band. It can be observed that the current distributions close to the inner boundary of the loop and along the tapered slot portion of the ER do not change significantly with respect to frequency. This signifies that the radiation patterns will not be a strong function of frequency. The E-plane and H-plane radiations gain patterns at these frequency points are found to have the maximum radiation direction fixed in the +x-direction and the directive patterns stay relatively unchanged [15]. One can also note from Fig. 3a that the hole and slot resonate strongly at 3.1 GHz. The corresponding simulated gain patterns revealed that this hole resonance contributes to a gain increase in the ±z-directions more than it does in the +x-direction.

The measured forward gain in the +x-direction is plotted with respect to frequency in Fig. 4a, where the impedance mismatch factor relative to a 50 Ω reference impedance is included. The most notable feature is high gain values realized in the lower 3–6 GHz range. They are significantly higher than those of UWB antennas that utilize only the electric-type radiators of similar dimensions. The geometrical average of the forward gain over the UWB band is equal to 4.13 dBi. In Fig. 4b are shown time-domain radiation patterns in the two principal planes in terms of peak power. The prototype of antenna A was used as the transmitting antenna and a TEM horn antenna was used as
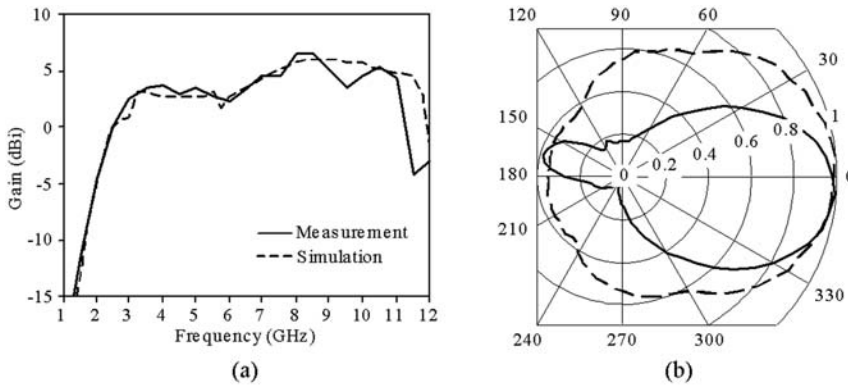
Fig. 4 Radiation characteristics of the antenna A. (**a**) Forward gain in the +*x*-direction. (**b**) The E-plane (*solid line*) and the H-plane (*dashed line*) radiation patterns in the time domain by peak power

the receiving antenna with a 1.2 m separation. The transmitting antenna was excited by 0.2 ns long bipolar pulses. Both E-plane and H-plane patterns clearly show directive radiation characteristics.

4 Antenna with a Vertical Feed

An antenna design having a vertical feed on the bottom edge is shown in Fig. 5a. This antenna is denoted antenna B and it has the same overall dimensions as antenna A, which also utilizes the same high-frequency laminate as the substrate. The size of the ER for antenna B is given by 11.7 mm × 24.9 mm. In order to increase the impedance of slotline 2, part of the dielectric substrate was removed in a rectangular form. Two narrow slots 1 and 2 that are bent at right angles were incorporated into arm 1 of the ER to prevent current from flowing over the connector and the feeding cable. The hole and slots 3 and 4 in arm 2 of the ER control the current flow and affect the input impedance, most significantly in the lower frequency range.

The simulation and measurement results for the input VSWR are shown in Fig. 5b, where the measurement result indicates that the antenna B satisfies VSWR < 2 over 2.93–10.67 GHz.
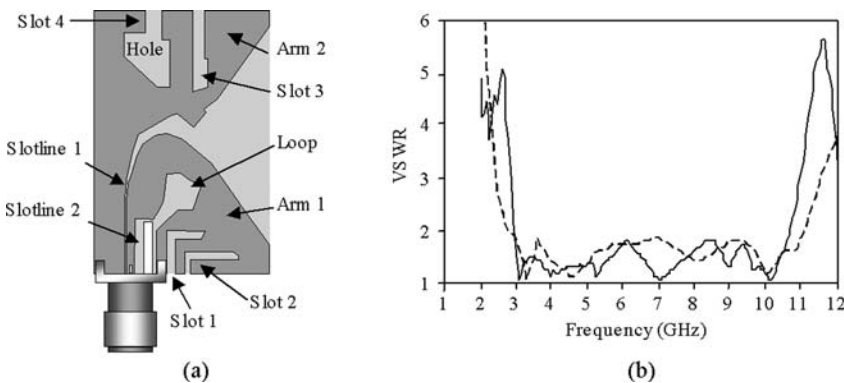
Fig. 5 The antenna B with a vertical feed. (**a**) The antenna geometry and (**b**) the comparison of measured (*solid line*) and simulated (*dashed line*) VSWR responses
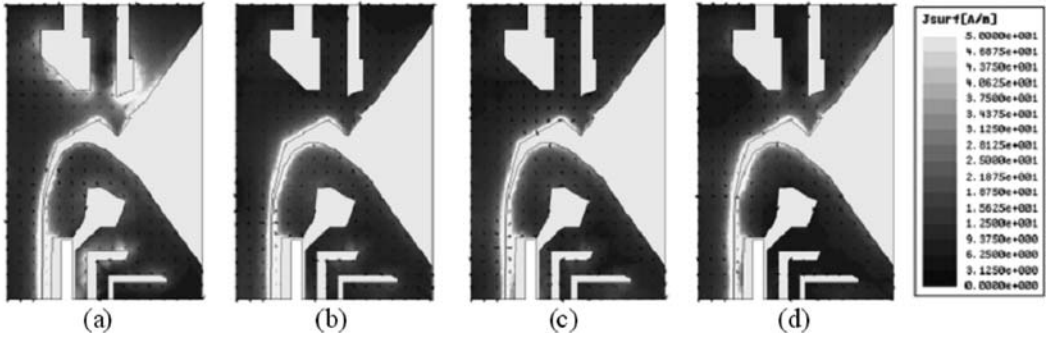
Fig. 6 Simulated surface current distribution of antenna B: (**a**) 3.1 GHz, (**b**) 5.1 GHz, (**c**) 7.1 GHz, and (**d**) 9.1 GHz

Simulated surface current distributions are shown at four discrete frequencies in Fig. 6. Similar to the case of antenna A, the current distributions along the loop and the tapered slot do not change significantly as a function of frequency. The hole and slots 3 and 4 in arm 2 resonate at 3.1 GHz and this contributes to better impedance matching at low frequencies.

The measured and simulated forward gain results are shown in Fig. 7a with respect to frequency. In the low-frequency range 3.5–5.5 GHz, the measured gain values are lower than the simulated values. These differences are attributed to the leakage current that flows over the connector and the outer shield of the feeding coaxial cable. They tend to tilt the main beam of the radiation pattern toward the direction of the cable and this adverse effect is most significant in the low-frequency range, where the antenna is electrically small. The average forward gain taken over the UWB frequency range is found to be 3.9 dBi and its variation within the range is equal to 5.6 dB. The E-plane and the H-plane radiation patterns measured in time domain by peak power are plotted in Fig. 7b. Distinctive directive patterns due to constructive interference in the +x-direction and destructive interference in the –x-direction by the ER and MR are evident.
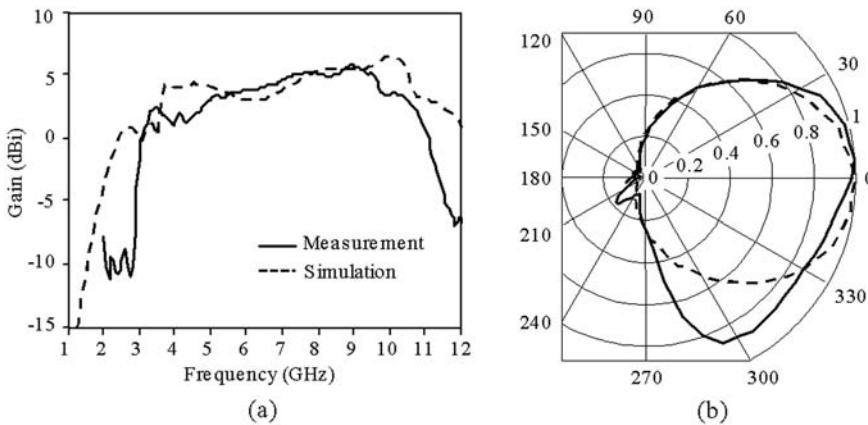
Fig. 7 Radiation characteristics of the antenna B. (a) Forward gain in the +x-direction. (b) The E-plane (*solid line*) and the H-plane (*dashed line*) radiation patterns in the time domain by peak power

5 Conclusion

Printed UWB antennas that combine electric- and magnetic-type radiators to simultaneously achieve smaller antenna dimensions and an enhanced gain were presented. The radiators were realized by copper cladding on one side of a dielectric substrate using the printed circuit technology. Two prototype antennas of size 20 mm × 30 mm × 1.27 mm were fabricated and their measured performance parameters were presented.

References

1. C. E. Baum, E. G. Farr, Impulse radiating antennas, In H. L. Bertoni, L. Carin, L. B. Felsen (eds), Ultra-wideband Short-Pulse Electromagnetics, Plenum Press, New York, pp. 139–147, 1993.
2. E. G. Farr, C. E. Baum, C. J. Buchenauer, Impulse radiating antennas, part II, In Carin L, Felsen L B (eds), Ultra-wideband Short-Pulse Electromagnetics 2, Plenum Press, New York, pp. 159–170, 1995.
3. E. G. Farr, C. E. Baum, Impulse radiating antennas, part III, In C. E. Baum, L. Carin, A. P. Stone (eds), Ultra-wideband Short-Pulse Electromagnetics 3, Plenum Press, New York, pp. 43–56, 1997.
4. N. P. Agrawall, G. Kumar, and K. P. Ray, Wide-band planar monopole antennas, IEEE Transactions on Antennas and Propagation, vol. 46, pp. 294–295, 1998.
5. J. A. Evans, M. J. Ammann, Planar trapezoidal and pentagonal monopoles with impedance bandwidths in excess of 10:1, Proceedings of the IEEE Antennas and Propagation Society International Symposium, vol. 3, pp. 1558–1561, 1999.
6. H. G. Schantz, Planar elliptical element ultra-wideband dipole antennas, Proceedings of the IEEE Antennas and Propagation Society International Symposium, vol. 3, pp. 44–47, 2002.
7. H. G. Schantz, Bottom fed planar elliptical UWB antennas, Proceedings of the IEEE Conference on Ultra Wideband Systems and Technologies, pp. 219–223, 2003.
8. P. J. Gibson, The Vivaldi areal, Proceedings of the 9th European Microwave Conference, pp. 101–105, 1979.
9. V. P. Belichenko, Y. I. Buyanov, V. I. Koshelev, V. V. Plisko, On the possibility of extending the passband of small-size radiator, Journal of Communications Technology and Electronics, vol. 44, pp. 167–172, 1999.
10. D.-H. Kwon, On the radiation Q and the gain of crossed electric and magnetic dipole moments, IEEE Transactions on Antennas and Propagation, vol. 53, pp. 1681–1687, 2005.
11. D.-H. Kwon, Radiation Q and gain of TM and TE sources in phase-delayed rotated configurations, IEEE Transactions on Antennas and Propagation, vol. 56, pp. 2783–2786, 2008.
12. C. E. Baum, E. G. Farr, D. V. Giri, Review of impulse-radiating antennas, In W. R. Stone (ed.), Review of Radio Science 1996–1999, Wiley, New York, 1999.
13. V. I. Koshelev, Y. I. Buyanov, Y. A. Andreev, V. V. Plisko, K. N. Sukhushin, Ultrawideband radiators of high-power pulses, Proceedings of the Pulsed Power Plasma Science, pp. 1661–1664, 2001.
14. X. Liu, G. Wang, W. Wang, Design and performance of TEM horn antenna with low-frequency compensation, Proceedings of the Asia-Pacific Conference on Environmental Electromagnetics, pp. 306–309, 2003.
15. D.-H. Kwon, E. V. Balzovsky, Y. I. Buyanov, Y. Kim, V. I. Koshelev, Small printed combined electric-magnetic type ultrawideband antenna with directive radiation characteristics, IEEE Transactions on Antennas and Propagation, vol. 56, pp. 237–241, 2008.
16. K. C. Gupta, R. Garg, I. Bahl, P. Bhartia, Microstrip Lines and Slotlines, 2nd edn., Artech House, Norwood, MA, 1996.

A Bandwidth Reconfigurable Antenna for Cognitive Radios

F. Ghanem and P.S. Hall

Abstract Cognitive radios have two operating modes, the searching mode where the system looks for the bandwidth to operate in and the operating mode where users transmit and receive information data through this bandwidth. In the first mode, one may have a very wide bandwidth antenna to be able to scan all the spectrum and in the operating mode one may have a narrow bandwidth antenna to filter out unwanted signals. In this chapter, we present a new antenna capable of operating in both UWB and narrowband modes, which is also tunable in the operating (narrowband) mode. It is composed of a microstrip disc monopole with defect slots in its ground plane. When the slots are deactivated, the antenna exhibits UWB behaviour from 2 to 10 GHz. To narrow the frequency bandwidth, defect slots are activated to act as a band-pass filter that narrows the antenna response. The activation and deactivation of the slots can be achieved by using switches located under the antenna feed line. In this case, the antenna response can be tuned by varying the slots' length. To examine the presented approach, both simulated and measured results are presented and discussed.

1 Introduction

With the growth of wireless communication systems, researchers have been able to overcome the saturation of the available frequency spectrum by proposing processing techniques that enhanced the spectral efficiency [1–3] and increased the channel capacity [4,5]. However, the more the processing techniques achieve advances the more the wireless media becomes attractive and the more the number of users increases. To anticipate further saturation of the spectrum, researchers are considering systems that would not be restricted to a specific bandwidth but could use any desired frequency band. An example of such is cognitive radio [6–8]. These systems have the ability to search through a very wide frequency range for a suitable bandwidth to operate in, and then start to use it to transmit and receive information data. In these systems, there is a need for both very wideband and narrow band antennas. The wideband antenna allows for the available frequency range to

F. Ghanem (✉)
Prince Mohammad Bin Fahd University, Al-Khobar, Saudi Arabia
e-mail: f.ghanem@bham.ac.uk

be sensed or searched and the narrowband to transmit and receive in the desired bandwidth and filter out other signals.

In this chapter, we present an antenna that is capable of exhibiting both very wideband and narrow bandwidth behaviours. It is composed of a disc monopole with defect slots in its ground plane. When the slot effect is deactivated, the antenna exhibits wideband behaviour from 2 to 10 GHz. To narrow the frequency bandwidth, the defect slots are activated to act as a band-pass filter that responses. The activation and deactivation of the slots can be achieved by using switches located under the antenna feed line. In this case, the antenna response can be tuned by varying the slots' length.

The approach to introduce and control filtering in the antenna is explained in Section 2 and validated by presenting both simulated and measured results.

2 Design Approach

The proposed approach to achieve switchable wideband–narrowband antennas consists in using a wideband disc monopole antenna and using switches to activate and deactivate a band-pass filter that passes desired frequencies and suppressing unwanted ones. The band-pass filter is composed of defect slots printed on the ground plane of the antenna.

By printing a slot under a microstrip line, a notch is created at a frequency proportional to the length of the slot length, as shown in Fig. 1, that illustrates the S_{21} parameter for two different lengths L of the slot.
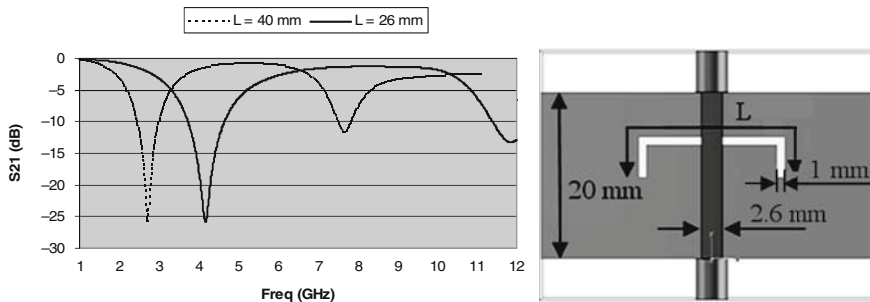
Fig. 1 S_{21} parameter for a microstrip line with a defect slot in the ground plane for two different lengths of the slot

The substrate used is the FR-4 having 4.7 permittivity and 1.6 mm height. The feed line width is 2.6 mm and its length is 20 mm. The slot path is of 1 mm width.

The behaviour of defect slots is similar to that of strip resonators except that the latter introduce conductive resonances while the former gives blocking resonances. In the same way as for strip resonators, it is also possible to couple different slots. To study the coupling, a slot resonator was put under the feed line and another one was put next to the first at various distances. Figure 2a shows the schematic for the coupling and Fig. 2b shows the S_{21} curves corresponding to different distances g between the slots.

As it can be seen from Fig. 2, the two slots generate two different blocking resonances. When the distance between slots increases, the resonances move inward and when it decreases, the resonances move outward. It is important to note that when the gap between resonances is big enough,

(a)   (b)
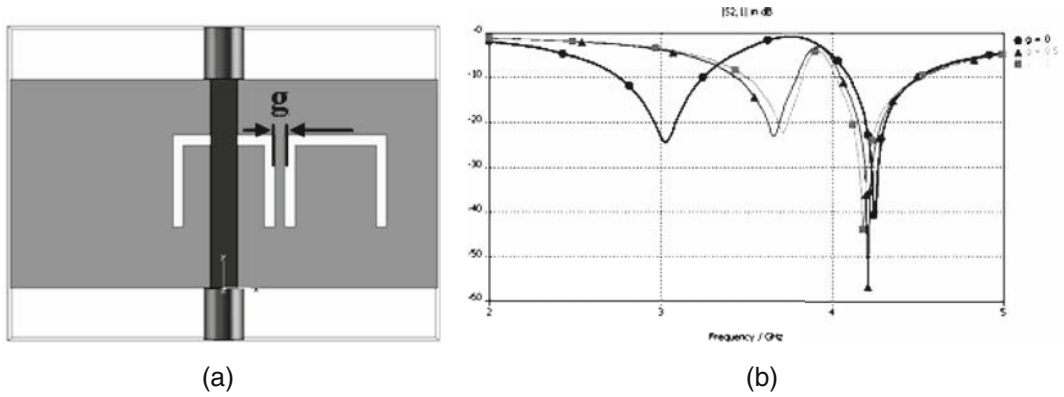
Fig. 2 S_{21} parameter for a microstrip line with two defect slots in the ground plane for different distances between them (details are as in Fig. 1). Gap between the slots is ● = 0 mm, ▲ = 0.5 mm, ■ = 1 mm

a frequency passband is created, where all the energy entering from one side of the feeding line is transmitted to the other side.

Based on this study, an antenna with slots in its ground plane has been designed to pass frequencies in the band 5–6 GHz and suppressing frequencies around. Figure 3 shows both the schematic of the antenna and its simulated response.

The filter schematic and its S parameters are shown in Fig. 4.

As it can be seen from Fig. 3, the S_{11} curve has been shaped by the slot filter printed on the ground plane of the antenna as the Q is much higher than the antenna alone. The antenna response is impedance matched better than –10 dB return loss around the desired frequency band and the frequencies outside are suppressed. This performance has been achieved without any increase in the antenna dimensions and in the antenna realization cost.

The disc monopole alone is impedance matched from 2.4 to 12 GHz and the designed filter suppresses frequencies outside the 5–6 GHz band from 2.4 and 8 GHz. The combination of disc monopole and the filter is responsible for the resonances shown in Fig. 3 at 2.4 and 9.3 GHz.
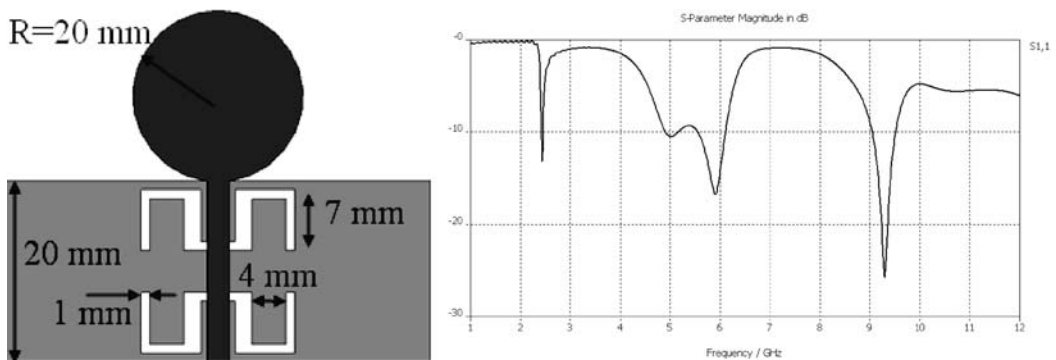
Fig. 3 Schematic of the antenna with ground plane slots and S_{11} simulated results
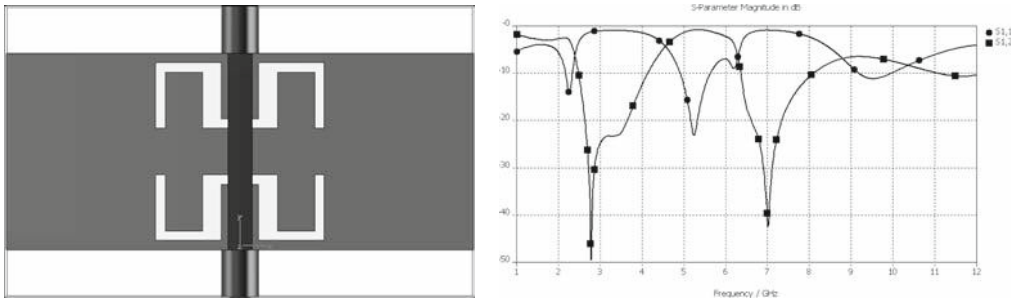
Fig. 4 Schematic of the designed ground plane slots filter and its simulated S_{11} results

3 Experimental Results

A prototype of the designed antenna has been realized and tested. Figure 5 shows both the photograph of the antenna and its simulated and measured responses.

As it can be noted from Fig. 5, there is a good agreement between simulated and measured results, which validates the proposed approach of integrating a filter to the ground plane of the antenna. The S_{11} out-band suppression achieved is around 0.6 dB, which results in significant interference suppression.
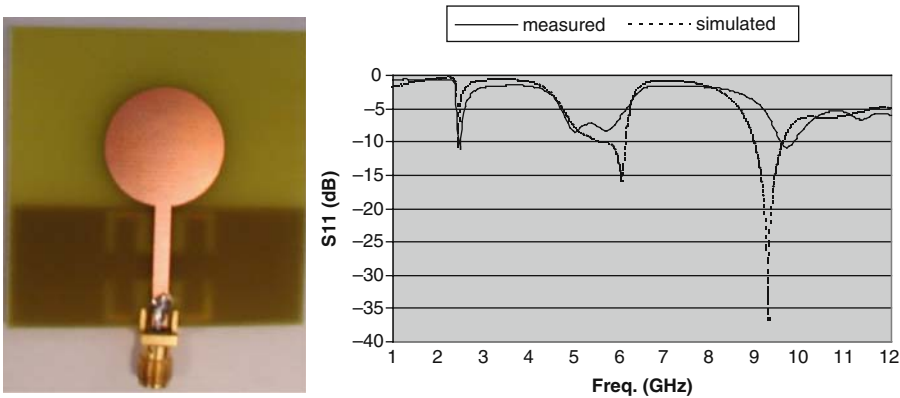
Fig. 5 Photograph with simulated and measured responses

4 Narrowband–Wideband Switching

The proposed antenna offers the possibility of deactivating the effect of the filter printed on the ground plane to recover the wideband property of the disc monopole. This can be done by disrupting the slots by means of switches. Figure 6 shows both the schematic of the antenna with disrupted slots and simulated and measured results. The switching is modelled by putting and removing a strip through the slot.
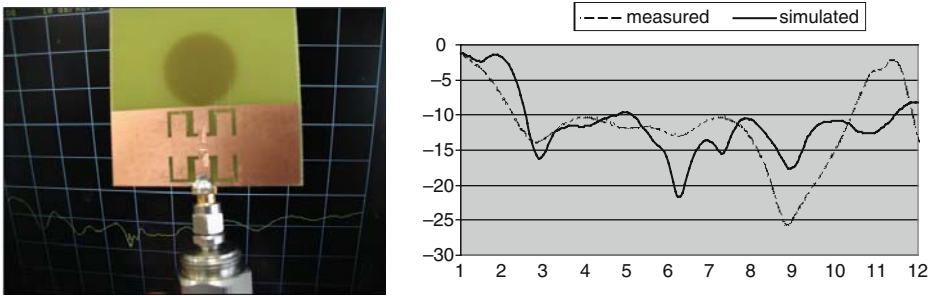
Fig. 6 Photograph of the antenna with simulated and measured responses with disrupted slots

As it can be seen from the figure, the antenna can be easily switched between narrowband and wideband modes, which make it a good candidate for cognitive radios.

5 Tuning the Antenna in Narrowband Mode

For the operation of cognitive radios, it is necessary to have the possibility of operating in both narrowband and wideband modes but it is also necessary to tune the antenna in the narrowband mode. The proposed antenna has this capability and the operation band of the antenna can be shifted by varying the slot's length. This can also be realized by using switches.

6 Conclusion

A new antenna for cognitive radios has been presented. The antenna can be operated in both wideband and narrowband modes by means of switches, which allows using it in both the operating and searching modes of the cognitive radio. It has also the possibility to be tuned when operated in the narrowband mode, a characteristic that is also needed in cognitive radios in order to adapt the operation frequency to any suitable frequency band.

References

1. F. R. Farrokhi, A. Lozano, G. J. Foschini, and R. A. Valenzuela, Spectral efficiency of FDMA/TDMA wireless systems with transmit and receive antenna arrays, IEEE Transactions on Wireless Communications, vol. 1, no. 4, pp. 591–599, 2002.
2. A. G. Burr, Bounds on spectral efficiency of CDMA and FDMA/TDMA in a cellular system, IEE Colloquium on Spread Spectrum Techniques for Radio Communication Systems, pp. 12/1–12/6, 1993.
3. A. M. Tulino, L. Li, and S. Verdú, Spectral efficiency of multicarrier CDMA, IEEE Transactions on Information Theory, vol. 51, no. 2, pp. 479–505, 2005.
4. M. Sánchez-Fernández, E. Rajo-Iglesias, Ó. Quevedo-Teruel, and M. L. Pablo-González, Spectral efficiency in MIMO systems using space and pattern diversities under compactness constraints, IEEE Transactions on Vehicular Technology, vol. 57, no. 3, pp. 1637–1645, 2008.
5. A. Goldsmith, S. A. Jafar, N. Jindal, and S. Vishwanath, Capacity limits of MIMO channels, IEEE Journal on Selected Areas in Communications, vol. 21, no. 5, pp. 684–702, 2003.
6. W. Q. Malik and D. J. Edwards, Cognitive techniques for ultra wideband communications, The IET Seminar on Ultra Wideband Systems, Technologies and Applications, London, UK, 2006.

7. D. Čabrić, S. M. Mishra, D. Willkomm, R. Brodersen, and A. Wolisz, A cognitive radio approach for usage of virtual unlicensed spectrum, Fourteenth IST Mobile Wireless Communications Summit, Dresden, Germany, 2005.
8. J. T. Aberle et al., Automatically tuning antenna for software-defined and cognitive radio, SDR Technical Conference, 2005.

A Long-Range UWB Channel Sounding System Exploiting UWB over Fibre Technology

A. Kavatjikidis, D.J. Edwards, and C.J. Stevens

Abstract This study presents the design and realisation of an innovative ultra-wideband over fibre vector network analyser channel sounder for channel measurements. This technique exploits the low insertion loss and low dispersion penalty of an electro-absorption modulator and achieves good performance in terms of UWB transmission with very low power. Experimental results demonstrate that this technique achieves high-quality UWB signal distribution up to 20 GHz with the current equipment. A link budget for long distance channel measurements is analysed to investigate the expected received power levels, in order to identify a suitable power amplifier for the distance of 100 m. The system performance confirmed by conducting an indoor line-of-sight UWB measurement in a dense multipath environment. Channel parameters are reported and the system is shown to be suitable for point-to-point characterisation, synthetic aperture and multiple antenna measurements.

1 Introduction

Ultra-wideband (UWB) technology has been the subject of extensive research in recent years due to its unique capabilities and potential applications, particularly in short-range applications. In principle a UWB system uses short pulses instead of continuous waves to transmit information, where the occupied bandwidth is greater than 25% of the centre frequency or at least 500 MHz [1]. The US Federal Communications Commission (FCC) has regulated UWB systems to operate in the frequency range from 3.1 to 10.6 GHz with an effective isotropic-radiated power level of a maximum −41 dB m/MHz for indoor environments [1].

UWB transmission is one of the promising approaches that can provide high-quality broadband access personal area networks. UWB systems offer a technology that can achieve good performance for indoor and outdoor channel measurements thanks to its intrinsic properties, such as the immunity to multipath fading (due to its fine delay resolution), extremely short time duration, wide bandwidth 7.5 GHz and low power spectral density [1,2]. However, the combination of very low transmitted power and the poor performance of long RF cables at high frequencies limits the performance to

C.J. Stevens (✉)

Department of Engineering Science, University of Oxford, Parks Road, Oxford, OX1 3PJ, UK
e-mail: christopher.stevens@eng.ox.ac.uk

short distances of a few meters in indoor environments [1,2]. A typical UWB cable with 0.5 m length has a loss that reaches 2 dB at the UWB bandwidth. In a typical indoor scenario with an antenna separation of 2–3 m a total length of 5 m UWB cables is needed for a channel sounding system. With this length of cables a loss of 20 dB will be introduced and the system's performance will be reduced substantially.

UWB networks that use conventional RF cables can operate mainly in indoor short-range channel sounding applications without having the ability to be integrated for long-range and outdoor channel measurements. Furthermore, UWB networks with RF cables cannot be used in wide-wired networks that can distribute UWB signals for longer range high data rate consumer applications. An efficient solution can be given using UWB over optical fibre technology. The combination of very low loss of optical fibres 0.5 dB/km at frequencies up to 100 GHz with the immunity to electrical interference, which prevents cross-talk between signals in different cables and pickup of environmental noise, makes the UWB over fibre a reliable technology for UWB transmissions even for medium-range high-throughput applications. With the optical fibre system an effective approach is proposed and eventually high data rate transmissions in longer distances can be achieved. Thus, UWB over fibre technology can achieve not only longer range channel measurements but also real-time indoor environment applications such as audio and video streaming among networked consumer electronics can be realised with undisrupted transmissions [1–4].

In this work, we present a UWB over fibre remote antenna system, which can be used with a vector network analyser-based channel sounder for wideband channel measurements. The concept of the measurement system is based upon the classic vector network analyser technique [5]. The vector network analyser can measure both the magnitude and the phase of components and is used to analyse the properties associated with the reflection and transmission of electrical signals known as scattering parameters (S-parameters). A point-to-point UWB over fibre connection has been experimentally implemented with a tunable laser source to emit through a single mode fibre between 1530 and 1615 nm. The signal is then transmitted to the wireless channel through broadband discone antennas for a test indoor UWB channel measurement.

2 Experimental Set-Up

The transmission procedure starts with the light emission at 1580 nm from the CW tunable laser. A swept RF signal from port 1 of the vector network analyser is fed to the electro-absorption modulator to modulate the optical signal and to drive the fibre optical link. A wideband signal is passed through a single mode fibre, which can be hundreds of meters in length, with the advantages of light weight, low-loss and near-zero electromagnetic interference. The signal is received by the ultra-fast photodetector, which converts optical modulation to electrical signals. After photodetection the signal is transmitted through an RF cable via a broadband discone antenna straight to the wireless channel. At the receiver side the signal is fed from the antenna to a 30 dB gain low-noise amplifier to optimise the output performance. The vector network analyser is used to measure the forward transmission scattering coefficient S_{21} (which is the complex channel frequency response) and data are recorded on the PC. Figure 1 shows the configuration of the proposed UWB over fibre system. Such a measurement technique is extremely useful in identifying the propagation mechanisms and supporting the validation of propagation modelling. The data are processed by producing a 3D matrix of $X \times Y \times$ no. of frequency points. This is achieved by means of constructing a synthetic volume aperture, which in this case consists of a large X–Y positioner (1 m $\times$ 1 m) under stepper motor control. Channel complex impulse responses are obtained from the rectangular grid. Further, the
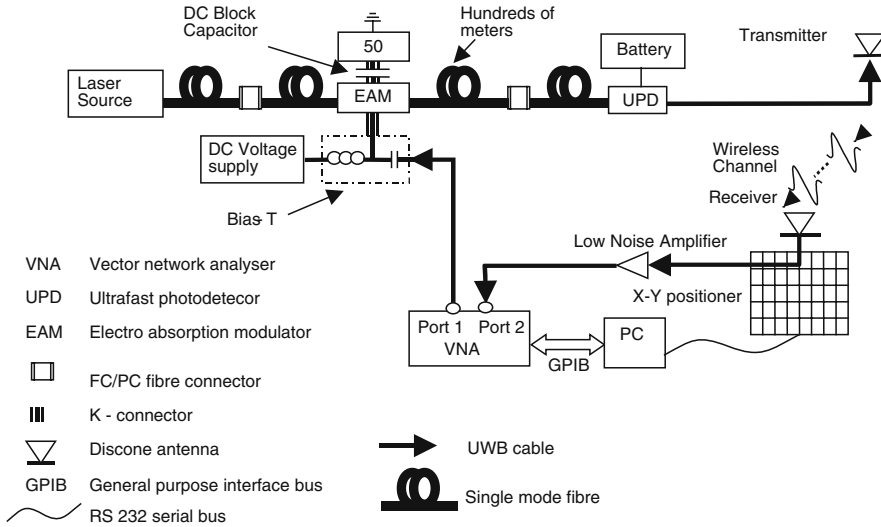
Fig. 1 Schematic diagram of the UWB fibre system

inherent vector error correction facility in the vector network analyser allows tracking error of the entire system [5]. Therefore, the effects of the cables and amplifiers can be removed from measured channel data.

The laser used in this study was a tunable Fabry–Perot (FP) InGaAsP source (Agilent 81642A) that covers the wavelength range 1530–1615 nm. The maximum output power was 3 mW [6]. The modulator chosen for this instrument was the CIP 40G-SR-EAM-1550 that operates across the 1550 nm band, because of the low insertion loss (typical value 4.8 dB) and dispersion penalty (typical value 1–2 dB) [7]. In the electro-absorption modulator an applied electric field affects the output intensity by shifting the optical absorption band edge in a semiconductor [8]. The modulation in the electro-absorption modulator arises from a combination of Franz–Keldysh effect and the quantum-confined Stark effect [8]. The modulator can operate at very high speeds and can achieve a modulation bandwidth of tens of gigahertz [9]. The modulator is driven via a bias-T and is terminated via a blocking capacitor with a 50 Ω broadband load. A negative DC bias is used to tune the electro-absorption modulator's performance. The conversion from optical back to electrical signals is achieved by the InGaAs ultrafast p–i–n photodiode (u^2t Photonics XPDV2040R) [10]. This device has a typical responsivity of 0.7 A/W and a reflection loss of 2 dB up to 50 GHz [10]. Conventional RF coaxial cables of a total length of 1 m are used to connect the receiving antenna to the vector network analyser port 2 and the ultrafast photodetector to the transmitting antenna.

3 System Characterisation

The system characterisation begins by identifying the optimum operating characteristics of the electro-absorption modulator. This characterisation plays a major role for the overall system performance. To determine the modulator insertion loss, the laser source is connected through the single mode fibre to the FC/PC connector and then the power loss is measured with an optical power metre. This configuration was used to calibrate the optical fibre vs FC/PC connector losses. A power of 1 mW is applied at 1550 nm. The total optical power loss was –0.8619 dB.

The modulator was then inserted in between the power meter and the laser source, resulting in an overall loss measurement with the wavelength λ. The measurement is conducted by applying an optical power of 1 mW and an initial reverse bias voltage of 1 V [7], while varying the wavelength from 1530 to 1600 nm. The insertion loss L in decibels is evaluated according to (1) and the results are presented in Fig. 2:

$$L_{\mathrm{dB}} = 10 \, \log \left({}^{P_{\mathrm{out}}}\!/\!{}_{P_{\mathrm{in}}} \right). \tag{1}$$

Fig. 2 Measured electro-absorption modulator insertion loss spectrum. *A, B* and *C* are points chosen for modulation tests
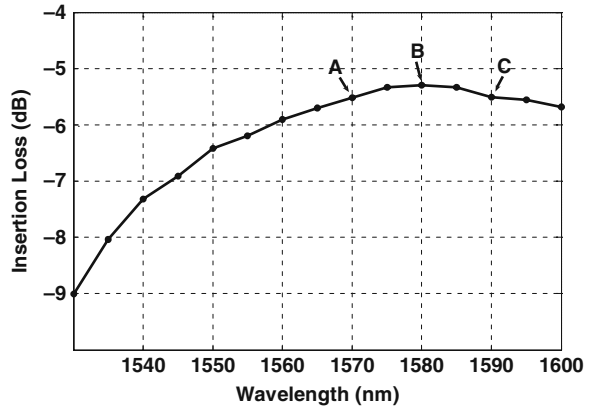
As illustrated in Fig. 2 the modulator has the lowest insertion loss at the longer wavelengths. The minimum insertion loss is point *B* at 1580 nm. A key feature in our system is to achieve high modulation efficiency which requires the largest rate of change in optical transmission with varying the electrical bias level. Three different wavelengths for performance evaluation are chosen: *A* (1570 nm), *B* (1580 nm) and *C* (1590 nm) to find the insertion loss as a function of reverse bias voltage. The reverse bias voltage range was from 0 to 3.5 V (4 V is the maximum-rated DC reverse bias of the device) with an increment of 0.25 V. The optical power was 1 mW, although identical results were found up to the maximum available optical power of 3 mW. As it can be seen from Fig. 3 all three wavelengths follow a sigmoid curve variation of insertion loss with bias voltage. The wavelength 1580 nm (*B*) has the lowest overall loss with greater variation at higher reverse bias voltages. While the 1580 nm wavelength has lowest overall insertion loss, the slope of increasing loss with voltage is in fact greatest for 1570 nm (at 2 V of bias) which suggests that the modulation performance may be best at shorter wavelengths.

The response of the whole system with the applied UWB signal is measured following the configuration in Fig. 1 with antennas replaced by a short cable link. The measurement was conducted with and without the low noise amplifier at the receiver side of the vector network analyser. The low noise amplifier used had an approximately flat 30 dB gain up to 12 GHz, beyond which its performance fell by 10 dB/decade. The optimum reverse bias operating points for the range of wavelengths between 1530 and 1600 nm are experimentally evaluated with the maximum available optical power of 3 mW within the bandwidth of 1–12 GHz. The results showed a linear relationship of the optimum reverse bias point of the modulator with the wavelength λ and presented in Table 1.

The data of S_{21} (which is the complex transfer functions) are recorded and the frequency response is calculated by plotting the power gain against the UWB bandwidth.
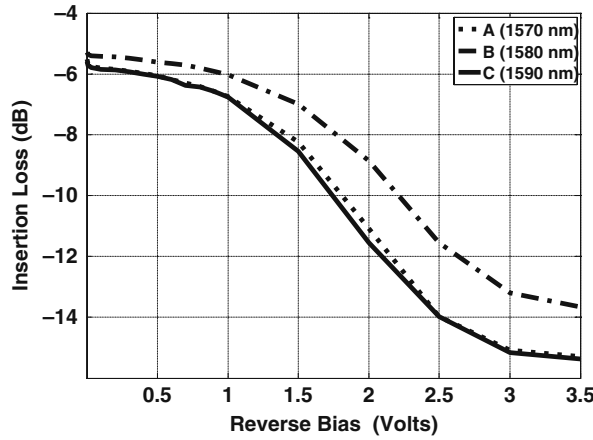
Fig. 3 Measured electro-absorption modulator insertion loss with reverse bias voltage variation

The system was tested using the experimentally determined optimum operating characteristics for the maximum frequency range. In the case where the low noise amplifier is used the frequency is limited to 12 GHz due to the poor performance of the low noise amplifier above that point. In Fig. 4 the frequency response of a 2 m optical fibre is compared with a 0.5 m UWB cable.
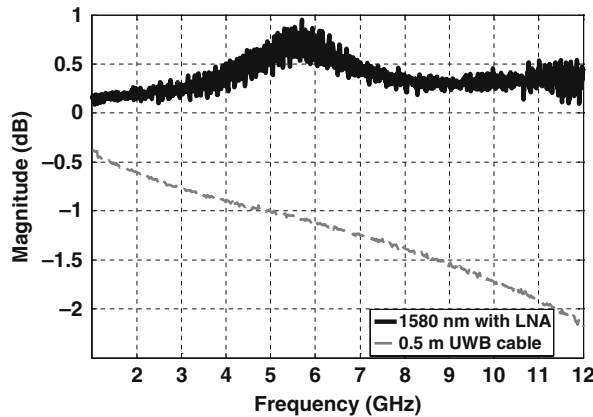
Fig. 4 A frequency response comparison of the proposed system performance with a 0.5 m UWB

As it can be seen from Fig. 4, UWB over fibre system is better than the cable by 0.5 dB at 1 GHz and 2.5 dB at 12 GHz (in comparison with a 0.5 m UWB cable). This improvement is significant if we take into account that in a real measurement scenario a total length of UWB cable that is needed is approximately 5 m. Thus, a total improvement of 20 dB can be achieved with the proposed UWB over fibre system.

The frequency range of the system is extended to 20 GHz without the low noise amplifier as shown in Fig. 5. The frequency of this measurement is limited to 20 GHz due to the poor UWB cable performance. It can be observed that the system has an overall drop of 5 dB between 1 and 20 GHz.

Fig. 5 Maximum frequency
response of the UWB over
fibre system without low
noise amplifier
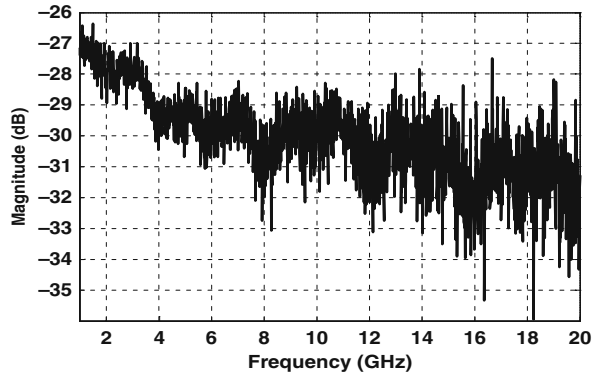
Despite this degradation in performance the system can still achieve transmission at 20 GHz. Large fluctuations are observed at high frequencies. This is caused predominantly by the very poor cable performance at high frequencies.

From comparison of Figs. 4 and 5 the performance improvement of the system with the use of the LNA is clearly illustrated. An increase in the range of 27–29 dB is observed to the whole bandwidth of the tested UWB bandwidth of 1–12 GHz. The noisy frequency response that is observed above 12 GHz makes the use of an appropriate LNA unavoidable with the designed UWB over fibre system in higher frequencies.

A very useful measurement for the wideband channel sounding system is the noise frequency response of the optical link. The noise frequency response will identify the noise level that will be added to the measurement and it will play an important role for the use of an amplifier in longer distance channel measurements. The noise of the optical link can be measured using the configuration for the response of the whole system and disconnecting port 1 of the vector network analyser, thus disconnecting the transmitted UWB signal from the electro-absorption modulator. In this measurement only the optical signal is applied to the link. The vector network analyser at port 2 is receiving only the noise which is introduced from the optical link, while the optical signal passing through it. This recorded noise originates from the laser and the nonlinear behaviour of the electro-absorption modulator.

The noise response is measured to be flat at −15 dB. This suggests that the use of the low-noise amplifier is inevitable, especially in dense multipath indoor environments and long-range (more than 10 m) outdoor environments where severe environmental losses will occur.

4 Indoor UWB Channel Measurement

A measurement was conducted in line of sight (LOS) using the configuration shown in Fig. 1 to confirm that a real UWB radio transmission can be achieved. The two antennas are set at a height of 1.18 m in antenna separation of 2 m. The room was 5.2 m long, 3 m wide and 3 m in height. The measurement environment was a dense multipath environment due to the metallic surfaces inside the room. The frequency range of 1–12 GHz was used, which is the maximum frequency range measured with the low noise amplifier. The overall system without the two antennas was calibrated prior the measurement to remove frequency-dependent attenuation, phase distortions and the delay that is introduced by the optical fibres. The transmit port of the vector network analyser is set up to transmit

a swept frequency signal of –10 dB mW. The complex transfer functions (S_{21}) are recorded with the vector network analyser. The channel is mathematically represented as in [5]. The bandwidth B of the channel is divided at $n_f = 1601$ discrete frequencies.

Figure 6 shows the frequency response of the LOS UWB channel extracted from the measured $H(f)$ indoor channel. A number of magnitude nulls can be observed in the frequency response, so that the channel exhibits frequency-selective fading behaviour. This is one of the dominant characteristics of indoor UWB channels with a large number of incident multipaths.

Figure 7 shows a comparison of the complex impulse response for this LOS UWB channel using the designed UWB over fibre system and the complex impulse response on the same channel using conventional RF cables with total length of 5 m. A number of clustered multipaths are apparent. The direct path is not the strongest path. Thus, multipath overlapping in some time-delay bins has occurred. With a noise floor threshold of 32 dB, at least 75 ns of transmission can be observed before the noise floor is reached. The direct path was arrived at 6.6 ns and confirms the antenna separation of 2 m. From these results we can analyse the behaviour of a real UWB channel by measurement. Even though the measurement was conducted in an extremely dense multipath environment, it is very clear from Fig. 7 that with the designed UWB over fibre system, an improvement of 20 dB can be achieved in contrast to conventional RF cables.
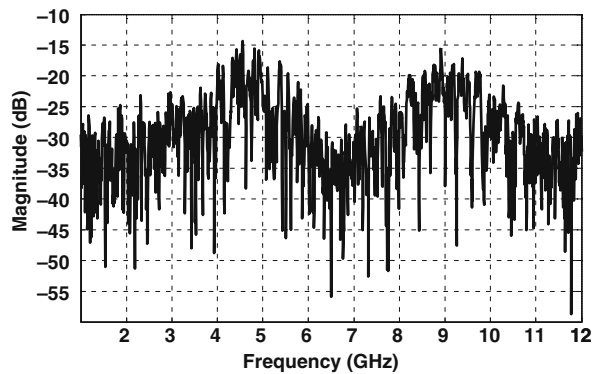
Fig. 6 The complex channel transfer function of the measured channel using the UWB over fibre system
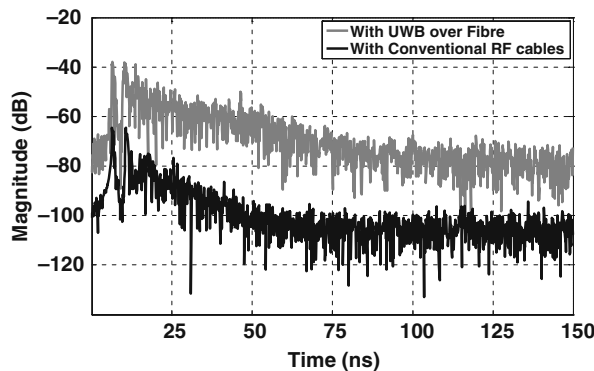
Fig. 7 The power delay profile of the measured channel

5 Long-Range Measurement Link Budget

The proposed system can also be used to distribute UWB signals not only over short-range indoor environments but also for long-range indoor and outdoor environments utilising the low loss of UWB over fibre. As is well known, the received power decreases as $1/d^2$ (in free space) [11]. Thus, a link budget was calculated for a distance of 100 m and at 1 mW of optical power, to investigate the total received power at the vector network analyser. This will enable the selection of an appropriate power amplifier at the transmitter for this distance.

The minimum insertion loss from the electro-absorption modulator is -5.2 dB (302 mW) from Fig. 2 point B. The dynamic extinction ratio under non-return-to-zero modulation for the modulator is typically 9 dB [7]. The modulation depth is

$$-5.2 - 9 = -14.2 \text{dB (38 mW)}. \tag{2}$$

The DC signal is

$$\text{DC}_{\text{signal}} = {}^{(302+38)}/2 = 170 \text{ mW}. \tag{3}$$

The AC signal is

$$\text{AC}_{\text{signal}} = 170 - 38 = 132 \text{ mW}. \tag{4}$$

Now due to DC responsivity from the photodetector of 0.7 A/W [10], the AC signal is

$$0.132 \times 0.7 = 92.4 \text{ mA}, \tag{5}$$

$$P_{\text{out}} = I^2 R = 4.6 \text{ mW}. \tag{6}$$

So the output power that will be sent to the transmitting antenna is 4.6 mW. This is the total RF power to be transmitted. Using the Friis equation [11] for 100 m distance, the power is calculated at the receiving end as

$$P_{\text{r}} = G_{tx} \times G_{rx} \times \left(\frac{\lambda}{4\pi R}\right)^2 \times P_{\text{out}} = -113.3154 \text{ dB}, \tag{7}$$

where G_{tx}, G_{rx} are the antenna gains (in our case the discone antennas have a gain of 0 dBi), P_{r} is the received power and P_{out} is the total RF power to be transmitted. λ is the wavelength at the centre frequency of the UWB band. This signal will be inserted to the 30 dB gain low-noise amplifier and then straight to the vector network analyser. The vector network analyser can detect a signal of no less than -80 dB and this suggests that a 15 dB gain RF power amplifier, in addition to the low noise amplifier, must be used before the transmitting antenna to improve the received signal for reliable channel data. The ultrafast photodetector parameters [10] allow the use of an optical power amplifier after the electro-absorption modulator instead of an RF power amplifier. The optical power amplifier will avoid the nonlinear effects from the RF power amplifier and will improve the received signal calculated in (7) by 17 dB.

6 Conclusion

This study has presented a new UWB over fibre system using single mode fibres which can be used as vector network analyser-based wideband channel sounder. The performance of UWB radio through the UWB over fibre network is evaluated. Results from an indoor LOS UWB channel measurement confirmed that an improvement of 20 dB can be achieved with the proposed system in comparison with indoor LOS UWB channel measurements conducted with conventional 5 m UWB cables. The very low attenuation of single mode fibres, which is only 0.5 dB/km, allows the distribution of UWB signals of up to 30 km of fibre with our system before the noise floor is reached. This enables longer range UWB systems than has hitherto been explored. This is not possible with conventional UWB cables due to severe losses at high frequencies. A maximum frequency range of 20 GHz was achieved, with 5 dB degradation in performance. Quality UWB radio transmissions are confirmed by identifying the dominant characteristics of indoor UWB channels such as frequency-selective fading behaviour and large number of incident multipaths. With a noise threshold of 30 dB below the maximum received peak, at least 75 ns of transmission can be observed before the noise floor is reached. A link budget for the use of the system at antenna separation of 100 m showed that an RF power amplifier of 15 dB of gain or an optical power amplifier is needed at the transmitter for that distance. This technology can also be used to distribute UWB signals around buildings or medium-range networks. Thus, this technology can provide UWB signal distribution for high-throughput wireless communication and sensor network services.

References

1. Federal Communications Commission, Revision of Part 15 of the Commission′s Rules Regarding Ultra-wideband Transmission Systems, First Report and Order, Federal Communications Commission, ET Docket 98–153, FCC–2–48, April 2002.
2. D. Porcino, W. Hirt, Ultra-wideband radio technology: potential and challenges ahead, Communications Magazine, IEEE, vol. 41, no. 7, pp. 66–74, 2003.
3. F. Zeng, J. P. Yao, An approach to ultrawideband pulse generation and distribution over optical fiber, IEEE Photonics Technology Letters, vol. 18, no. 7, pp. 823–825, 2006.
4. L. Wen-Piao, C. Jun-Yu, Implementation of a new ultrawide-band impulse system, IEEE Photonics Technology Letters, vol. 17, no. 11, 2005.
5. A. M. Street, L. Lukama, D. J. Edwards, Use of VNAs for wideband propagation measurements, IEE Proceedings – Communications, vol. 148, no. 6, pp. 411–415, 2001.
6. Agilent, Agilent 81642A Tunable Laser User's Guide.
7. CIP Preliminary Data Sheet of 40G-SR-EAM-1550.
8. M. T. Abuelma′atti, Large signal analysis of the electroabsorption modulator, International Conference on Information and Communication Technologies Proceedings, 2004.
9. J. M. Longras-Figueiredo et al., Electric field switching in a resonant tunneling diode electroabsorption modulator, IEEE Journal of Quantum Electronics, vol. 37, no. 12, pp. 1547–1552, 2001.
10. u2t Ultrafast Photodetector XPDV2040R Manual.
11. I. Glover, P. Grant, Digital Communications, Prentice-Hall, London, 1998.

UWB Antennas Integration Effects for Wireless Communication Applications

M.-A. Mellah, C. Roblin, and A. Sibille

Abstract In this chapter, a return loss measurement campaign was achieved to study the effect of the close environment on antenna's behavior in wireless application scenarios. Five different planar ultra-wideband antennas were measured on different devices (keyboard, screen, Internet box, and two laptops). General similarities in the bandwidth and matching efficiency behaviors were noticed for the antennas when mounted on the same devices in the same positions. In a purpose of modeling, the results can be used to classify the antennas and describe general behaviors on common used devices in wireless applications.

Keywords Antennas · UWB · Measurement · Statistical models

1 Introduction

In a context of cognitive radio and terminal awareness, the interconnection and communication between different devices in a given environment is becoming an important aspect of the wireless communication applications. The UWB technology is one of the best candidates for such applications since it allows high data transmission rates. The recent success of the wireless communication technologies has increased the interest of the researchers in studying antennas. Thus, different types of antennas were designed for many wireless applications these last years. As a first step, the antenna's characteristics were always presented for ideal conditions [1,2], then many studies started to include the close environment of the antenna in a defined scenario [3]. All the results show that the antenna's characteristics can be strongly affected by the close environment. However, considering the huge number of antennas and possible scenarios, it might be interesting to approach the problem statistically and try to extract common aspects and behaviors.

2 Measurement Campaign

Figure 1 shows the five planar ultra-wideband antennas used for this campaign. Three were designed and fabricated in ENSTA's laboratory: a monopole disc antenna (MDIS) [4], a monopole stripline

---

M.-A. Mellah (✉)
ENSTA (Ecole Nationale Supérieure de Techniques Avancées), ParisTech. 32, Boulevard Victor, 75738 Paris, France
e-mail: mohammed-amine.mellah@ensta.fr
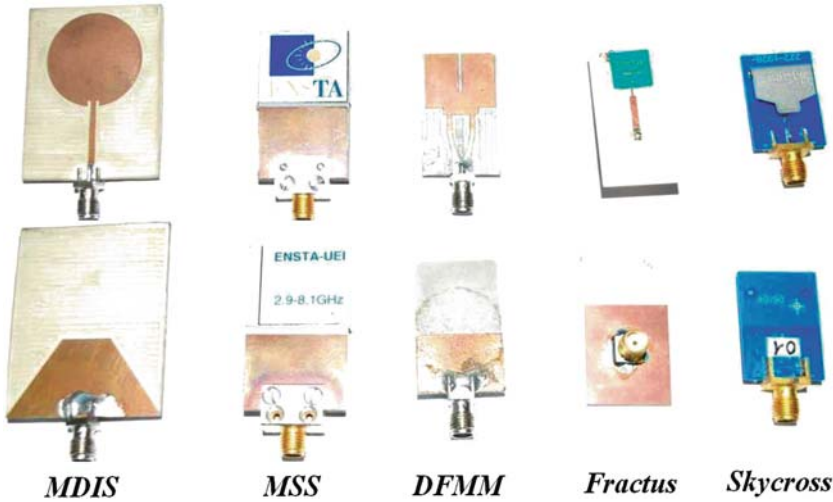
Fig. 1 UWB antennas used for the measurements

antenna (MSS) [5], and a dual-fed monopole antenna (DFMM) [6]. The last two are commercial antennas: Fractus UM_FR05-S1-P-0-107 [7] and Skycross SMT-3TO10M-A [7]. The antennas were first measured in free space (Fig. 2 isolated cases), and then in close proximity of different commonly used devices: screen, keyboard, Internet box, and two different laptops (Fig. 3 shows some examples of measured configurations). For each device, the antenna's return loss was measured in several positions as summarized in Table 1.

The investigation methodology followed in this campaign was to study first one antenna (MDIS) on all the devices and then proceed to comparisons between different antennas when mounted on the same device in the same positions.
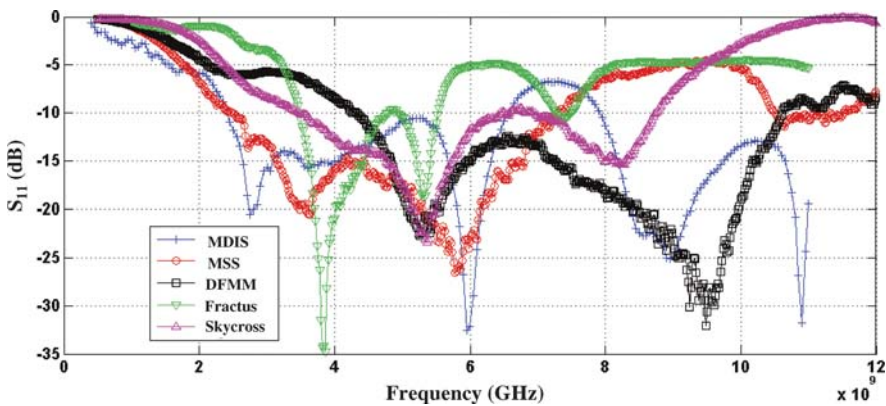
Fig. 2 Measured antennas return loss in free space (isolated case)

Fig. 3 Examples of scenarios (MSS on screen, keyboard/MDIS on laptop (zoom))

Table 1 Number of positions measured for each antenna and device

	Screen	Keyboard	Laptop 1	Laptop 2	Box	Total
MDIS	10	12	8	8	4	42
MSS	6	4	–	8	4	22
DFMM	6	4	–	8	4	22
Fractus	–	–	8	–	–	8
Skycross	6	4	–	–	4	14
Total	28	24	16	24	16	108

The positions on devices were chosen depending on the shape and the configuration of the devices. Only realistic positions were considered.

3 Results

3.1 MDIS Antenna on All Devices

The close environment disturbs the antenna's performances through the losses introduced by the devices leading to variations in the antenna's characteristics.

Figure 4 presents the variations for the reflection coefficient of the MDIS's antenna placed on a laptop in different positions.

For a better illustration, the matching bandwidth (defined for $S_{11} < -10$ dB) was extracted for each in situ measurement and compared with the isolated case as shown in Fig. 5.

Referring to the results, a bandwidth shift toward lower frequencies is noticed for the majority of the cases which can be explained by the higher permittivity presented by the devices comparing with the free space. Also, in some positions, mainly for the laptops, the bandwidth was divided into several separated parts reflecting a greater disturbance of the reflection coefficient. This is due to
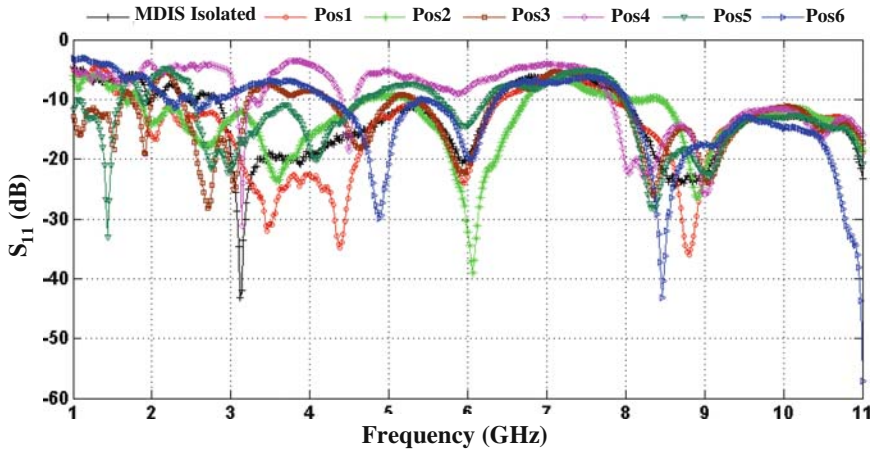
Fig. 4 MDIS return loss isolated and on laptop 2
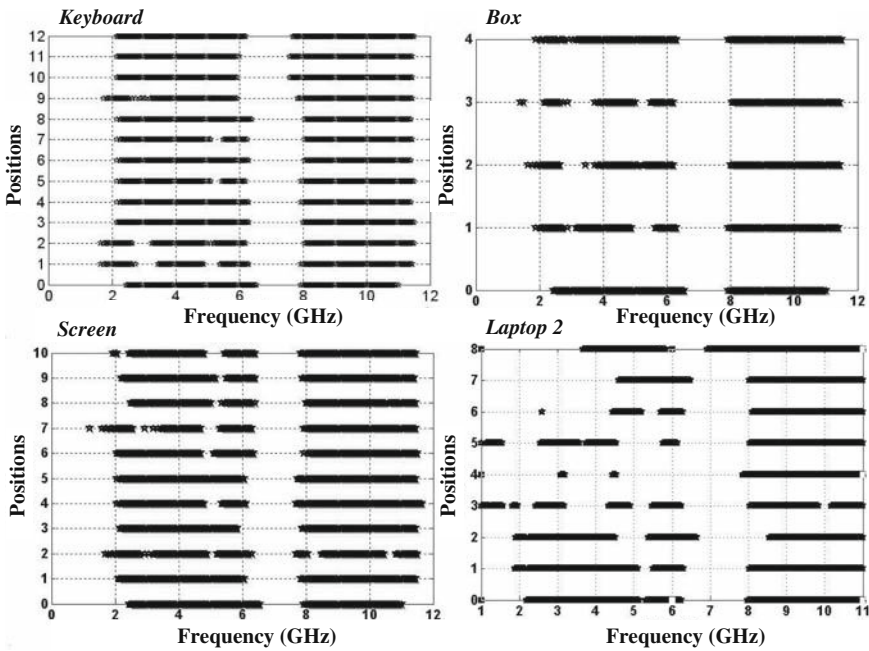
Fig. 5 Matching bandwidth for MDIS on devices (position 0 = isolated case)

the material composition of the laptops which includes metallic components like USB connections or printed circuits that affect furthermore the antenna's current distribution in comparison with the plastic cover of a screen or a keyboard. Consequently, the same behavior is noticed for the matching efficiency (Fig. 6) with values decreasing down to 60% for the laptops and only to 90% for the screen and keyboard considering mean values on 100 MHz of bandwidth around 3.5 GHz.
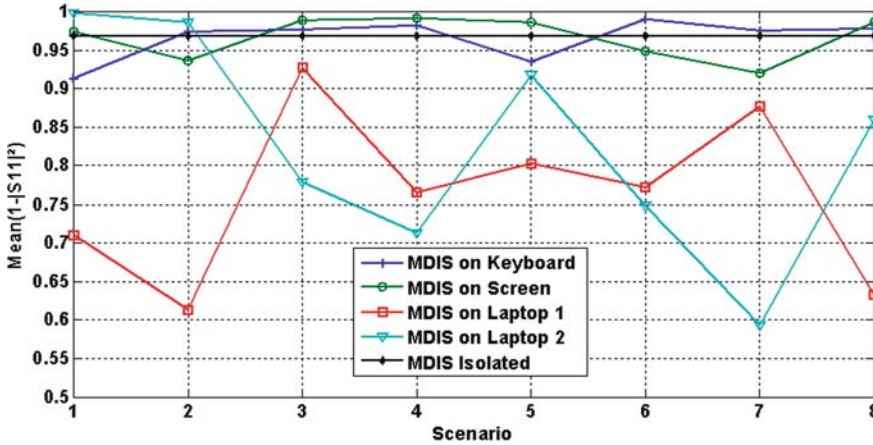
Fig. 6 Matching efficiency for MDIS antenna on devices

3.2 Statistics and Comparisons

To illustrate the comparison, we introduce the relative indicator Bandwidth Ratio (BR) defined as

$$\text{BR}(A,D,I) = \frac{\{\text{Cumulated bandwidth of antenna } A \text{ on device } D \text{ inposition } I\}}{\{\text{Cumulated bandwidth of antenna } A \text{ isolated}\}} . \tag{1}$$

Depending on the device and the position, the bandwidth can be enhanced (BR > 1) or reduced (BR < 1) referring to the bandwidth in free space. The distribution of all the BRs obtained for the CIR antenna is presented in Fig. 7. We can see that the range of values starts from 0.3 to 1.1 with an increasing concentration of values toward the upper ratio limit. Such distributions presenting a pick value remind us of the extreme value and generalized extreme value distributions. These two in addition to three other distributions (normal, lognormal, and Rayleigh) were tested before concluding that the probability law that best fits our data regarding the maximum likelihood criterion is the generalized extreme value (GEV[1]) with the parameters $(k, \mu, \sigma) = (-0.95, 0.87, 0.2)$ where k, μ, σ are, respectively, the estimated parameters: shape, scale (standard deviation), and location (average).

---

[1]The probability density function for the generalized extreme value distribution with location parameter μ, scale parameter σ, and shape parameter $k \neq 0$ is

$$y = f(x; k, \mu, \sigma) = \left(\frac{1}{\sigma}\right) \exp\left\{-\left(1 + k\frac{(x - \mu)}{\sigma}\right)^{-1/k}\right\} \left(1 + k\frac{(x - \mu)}{\sigma}\right)^{-1-(1/K)}$$

for $1 + k\frac{(x-\mu)}{\sigma} > 0$. $k > 0$ corresponds to type II case, while $k < 0$ corresponds to type III case. In the limit for $k = 0$, corresponding to type I case, the density is

$$y = f(x; k, \mu, \sigma) = \left(\frac{1}{\sigma}\right) \exp\left\{-\exp\left(-\frac{(x - \mu)}{\sigma}\right) - \frac{(x - \mu)}{\sigma}\right\} .$$
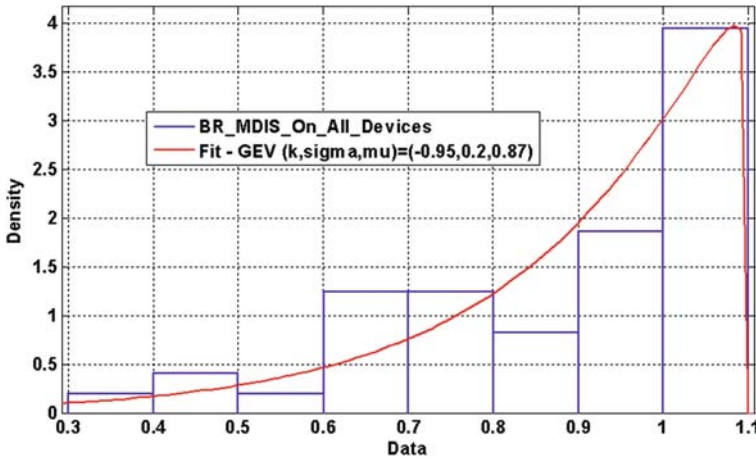
Fig. 7 Bandwidth ratio for MDIS antenna on all devices
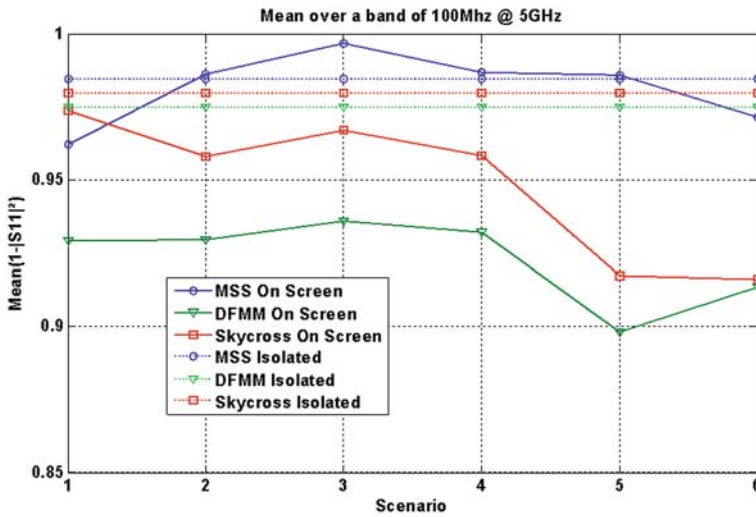
Fig. 8 Matching efficiency for MSS, DFMM, and Skycross on screen (mean over a band of 100 MHz at 5 GHz)

Finally, Figs. 8 and 9 compare, respectively, the matching efficiency and the BR for different UWB antennas on same devices in same positions. Despite the differences between the antennas (size, material, etc.), similarities in the behaviors are noticed which reinforce the idea of classifying the antennas and applying general models of behaviors. Indeed, considering that these small planar UWB antennas belong to the same class of antennas – called, for example, "UWB antennas for wireless applications" – models describing the general behaviors of the antennas performances (BR, efficiencies) could be defined based on mean values. Obviously, the models' accuracy can be enhanced by increasing the measurement campaign samples (more antennas and more devices).
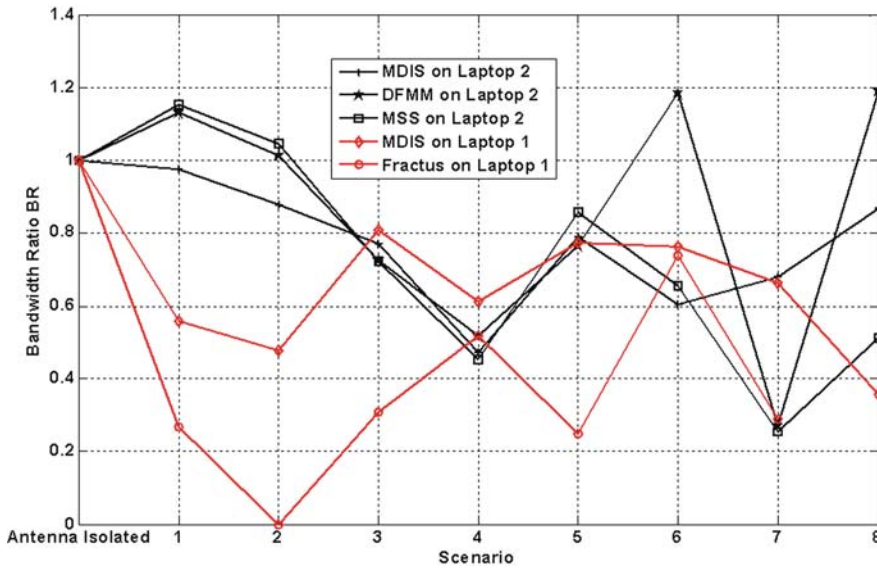
Fig. 9 Bandwidth ratio of antennas on laptops

4 Conclusions

A measurement campaign was carried out to study the effect of UWB antennas integration on commonly used devices in wireless communication applications. The close environment disturbs the antenna's characteristics introducing variations of the matching bandwidth and efficiency. The behavior of bandwidth ratio of a planar UWB antenna mounted on devices can be estimated by a generalized extreme value distribution of parameters $(k, \mu, \sigma) = (-0.95, 0.87, 0.2)$. Similarities were noticed in the general behavior of the different planar UWB antennas which is promising in a purpose of antenna classification and modeling.

References

1. T. Wei, Z. R. Hu A CWP fed circular monopole antenna for ultra wideband wireless communications, Antennas and Propagation Society International Symposium, 2005 IEEE vol. 3A, July 3–8, 2005, pp. 528–531.
2. T. A. Denidni, H. Lee, Y. Lim, Q. Rao, Wide-band high-efficiency printed loop antenna design for wireless communication systems, IEEE Transactions on Vehicular Technology, vol. 54, no. 3, pp. 873–878, 2005.
3. G. H. Huff, J. Feng, S. Zhang, G. Cung, J. T. Bernhard, Directional reconfigurable antennas on laptop computers: simulation, measurement and evaluation of candidate integration positions, IEEE Transactions on Antennas and Propagation, vol. 52, no. 12, pp. 3220–3227, 2004.
4. M. A. Mellah, Ch. Roblin, A. Sibille, 2007 IET Seminar on Body Loss Modeling for Wireless Communications Standards Bands Antennas and Propagation for Body-Centric Wireless Communications, April 24, 2007, p. 75.
5. S. Bories, H. Ghannoum, C. Roblin, Robust planar stripline monopole for UWB terminal applications; IEEE International Conference on ultra-wideband, ICU 2005, September 5–8, 2005, pp. 80–84.
6. H. Ghannoum, S. Bories, R. D'Errico, The Institution of Engineering and Technology Seminar on Small-Size UWB Planar Antenna and Its Behaviour in WBAN/WPAN Applications Ultra Wideband Systems, Technologies and Applications, April 2006, pp. 221–225.
7. http://ww.fractus.com; http://ww.skycross.com

Bit Error Rate of a Non-ideal Impulse Radio System

J. Timmermann, E. Pancera, P. Walk, W. Wiesbeck, and T. Zwick

Abstract The development of a UWB impulse radio front end for commercial indoor applications is a challenging task, since its components must have constant characteristics over an ultra-wide bandwidth to achieve high performance. In reality, non-ideal behavior cannot completely be cancelled out. For the estimation of the performance of such a non-ideal system by a system simulation, dedicated modeling of the components is important. This contribution shows the modeling of non-ideal components like oscillator, UWB antennas, indoor channel, and low noise amplifier, based on rigid assumptions. A system simulation of the (simplified) non-ideal impulse radio system is performed with the advanced design system (ADS) showing the achievable bit error rate. To improve the performance, optimal pulse shaping in the presence of non-ideal components is discussed.

Keywords UWB · Non-ideal front end · Impulse radio · Component modeling · System simulation · Pulse shaping

1 Introduction

Classical narrowband systems are tuned to work around the design frequency of the system. The problem arises with ultra-wideband impulse radio transmission, where the performance of the front-end components is required in a range of several gigahertz. In reality, the system performance can degrade because of the non-ideal "Dirty RF" [1] behavior of the integrated components. For the estimation of the system behavior without the need of an expensive hardware prototype, a simulation-based approach makes sense, whereas dedicated component modeling is a basic prerequisite. This contribution is organized as follows: In Section 2, we investigate non-ideal components and effects which are critical in an impulse radio transmission system using a correlation receiver. Section 2 also shows how these elements can be modeled, based on simplified assumptions. In Section 3, the impact of non-ideal components on the signal is studied as well as the resulting performance. To our knowledge, there is no publication that studies and links all mentioned non-ideal elements for impulse radio. The results shown in Section 3 are based on the developed system model in ADS as an extension of [2] and include the achievable bit error rates. They serve as performance measure

J. Timmermann (✉)

Institut fuer Hoechstfrequenztechnik und Elektronik, Universitaet Karlsruhe, Kaiserstr. 12, 76131 Karlsruhe, Germany

e-mail: jens.timmermann@ihe.uka.de

to characterize non-ideal impulse radio transmission. To improve the system performance, Section 4 discusses optimal pulse shaping at the transmitter side. Finally, Section 5 gives a conclusion and an outlook.

2 Critical Components and Component Modeling

Since the indoor propagation channel is characterized by frequency-dependent multipath propagation, the channel is a critical element. Furthermore, the antennas, both at the transmitter (Tx) and at the receiver (Rx) sides, are critical because of their frequency-dependent radiation patterns. Another non-ideal component is the low noise amplifier at the Rx side, due to its non-linear behavior versus frequency [3]. Oscillators are also critical because of a possible jitter. Also the design parameter pulse repetition time T is critical because it must be longer than the channel delay spread to avoid intersymbol interference [4]. Finally, interference is critical, especially in the case of UWB interference, which may result from other users.

2.1 Oscillator

The oscillator in the UWB system generates the pulse repetition frequency (PRF $= 1/T$). It is a critical component due to the oscillator jitter, which means that the clock is not ideal. Both, at the Tx and at the Rx sides, an oscillator is implemented and modeled as an ideal oscillator corrupted by random jitter. The jitter is described by a mean value of zero and a variance σ_{Jitter} as suggested in [5].

2.2 Ultra-Wideband Indoor Channel Including Antennas

Since antennas radiate and receive differently in different directions, the influence of antennas on a channel can entirely be studied if the channel model is three dimensional (3D). A suited channel model is 3D ray tracing where propagation paths between Tx and Rx are found in a given environment at a given frequency. The ray tracer used in this contribution has been developed at the "Institut fuer Hoechstfrequenztechnik und Elektronik, Universitaet Karlsruhe (TH)." Detailed information can be found in [2,6]. The main idea is to divide the bandwidth into a set of frequencies and to run a simulation for each frequency. Here, 1601 equidistant frequencies are chosen from 2.5 to 12.5 GHz with frequency steps of 6.25 MHz. At a given frequency f, the relationship between transmit voltage $U_{\text{Tx}}(f)$ and receive voltage $U_{\text{Rx}}(f)$ can be described as

$$
\begin{aligned}
S_{21}(f) = H_{\text{channel\_ant}}(f) &= \frac{U_{\text{Rx}}(f)}{U_{\text{Tx}}(f)} \\
&\propto \sum_{i=1}^{N} \begin{pmatrix} C_{\theta}^{\text{Rx}}(\theta_i^{\text{Rx}}, \ \psi_i^{\text{Rx}}) \\ C_{\psi}^{\text{Rx}}(\theta_i^{\text{Rx}}, \ \psi_i^{\text{Rx}}) \end{pmatrix}^{\text{T}} \begin{bmatrix} T_{\theta\theta,i}^{\text{Rx}} & T_{\Theta\psi,i}^{\text{Rx}} \\ T_{\psi\theta,i}^{\text{Rx}} & T_{\psi\psi,i}^{\text{Rx}} \end{bmatrix} \begin{pmatrix} C_{\theta}^{\text{Tx}}(\theta_i^{\text{Tx}}, \ \psi_i^{\text{Tx}}) \\ C_{\psi}^{\text{Tx}}(\theta_i^{\text{Tx}}, \ \psi_i^{\text{Tx}}) \end{pmatrix},
\end{aligned} \tag{1}
$$

where the index i describes the ith path of altogether N paths, ψ the azimuth and θ the elevation angle, $(C(q, y))$ the frequency-dependent, complex, polarimetric antenna pattern, and $[T_i]$ the frequency-dependent polarimetric path transfer matrix of path i. Taking into account antennas

require a measured complex Tx pattern to be included in the ray tracer that determines the path transfer matrices $[T_i]$. After weighting the transfer matrices with the Tx and Rx antenna patterns, the contributions are summed up coherently for the complex receive voltage strength $U_{Rx}(f)$ at a given frequency f. This procedure is done for all frequencies to generate the complex transfer function $H_{channel\_ant}(f) = U_{Rx}(f)/U_{Tx}(f)$. To summarize, channel and antenna influences are modeled by determining $S_{21}(f)$, and ideal matching ($S_{11} = S_{22} = 0$) and reciprocity $S_{12} = S_{21}$ are assumed. In the literature, the modeling of antennas and channel is often described by more simplified models. They describe only the effect of the antennas by a derivation of the time signal [7] or only the UWB multipath channel, modeled as a Saleh–Valenzuela model, such as the IEEE 802.15.4a channel model [8,9], excluding the antennas.

2.3 Noise

Noise is modeled in terms of noise figure and noise temperature. Since indoor channels are considered, it is supposed that the receive antenna has a noise temperature of $T_{system} = 300$ K. As a consequence, the resulting noise power is

$$P_{noise} = k T_{system} B , \tag{2}$$

where k is Boltzmann's constant and B the bandwidth of the system. With $B = (10.6-3.1)$ GHz $= 7.5$ GHz, the noise power is -75.2 dB m. This contribution is modeled as additive white Gaussian noise (AWGN).

2.4 Interference

In general, interference can be divided into narrowband interference and (ultra)-wideband interference. In this contribution, interference is modeled as AWGN with a flat PSD inside the considered ultra-wideband frequency range.

2.5 Low Noise Amplifier (LNA)

The model of a non-ideal UWB LNA is derived from measurement data. Figure 1 shows the frequency behavior of the Hittite amplifier HMC-C022. The transmission S_{21} varies only slightly inside the relevant frequency range and a nearly linear phase behavior can be seen. The amplifier model used here consists of all measured S parameters versus frequency. Noise figure (2.5 dB), 1 dB compression output power, third-order intercept output, and saturation power are also considered, but only for the center frequency of 8 GHz. Other modeling methods of an LNA use, for example, Taylor series [10] or Volterra series representations [11].

3 System Simulation

All component models are linked in ADS to form a system simulator. It can visualize the signal in time and frequency domains and determine the bit error rate. As an example, this chapter presents
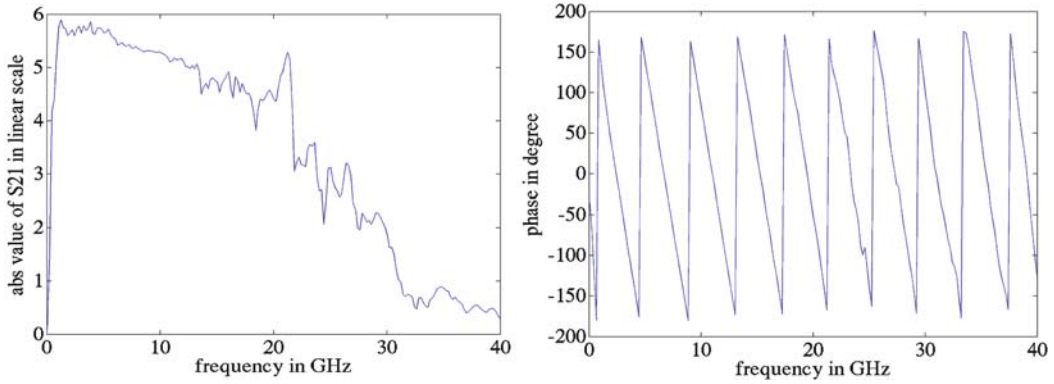
Fig. 1 Amplification and phase behavior of non-ideal LNA

the influence of oscillator jitter on the power spectral density (PSD) in the presence of a series of non-ideal components. Furthermore, the BER is investigated as a function of distance, SNR, and data rate.

3.1 Effect of Oscillator Jitter in Frequency Domain

According to Wiesbeck and Jondral [12], any UWB signal with random data can be expressed as

$$x(t) = \sum_{n=-\infty}^{n=\infty} \{A(0,n)\,p_0(t - nT - \Theta_n) + A(1,n)\,p_1(t - nT - \Theta_n)\}, \tag{3}$$

where $p_0(t)$ and $p_1(t)$ are the transmitted pulse shapes in case of bit 0 or 1. $A(j,n)$ represents the appearance of symbol j inside the nth frame and T is the pulse repetition time. Oscillator jitter can be represented by additive random delays θ_n. Assuming that the bits are uncorrelated and have an uniform distribution, and that the θ_n are uncorrelated for different n and have the same probability density function $q(t)$, the PSD of the signal is determined by

$$
\begin{aligned}
\text{PSD}(f) = {} & \tfrac{1}{4T^2} \sum_{k,l=0}^{1} \sum_{m=-\infty}^{\infty} P_k\left(\tfrac{m}{T}\right) P_l^*\left(\tfrac{m}{T}\right) \left|Q\left(\tfrac{m}{T}\right)\right|^2 \delta\left(f - \tfrac{m}{T}\right) \\
& + \tfrac{1}{2T} \sum_{k=0}^{1} |P_k(f)|^2 - \tfrac{1}{4T} \sum_{k,l=0}^{1} P_k(f)P_l^*(f) |Q(f)|^2 \quad .
\end{aligned}
\tag{4}
$$

In (4), capital letters signify Fourier transforms of the corresponding time signals. The first term in (4) represents discrete spectral lines with $\Delta f = 1/T = \text{PRF}$ that are an unwanted effect in pulsed UWB transmission because they can hurt the FCC mask.

Since this term is maximal if $Q(f)=1$ ($q(t)=\delta(t)$) which means no jitter, applying jitter to a UWB signal reduces discrete spectral lines. This effect can also be seen in the results of the system simulator. Figure 2 plots the PSD (without and with jitter) of an OOK-modulated transmit signal with PRF = 333 MHz and a Gaussian monocycle as pulse shape. The jitter variance was chosen as σ_{Jitter} = (0.1/PRF).
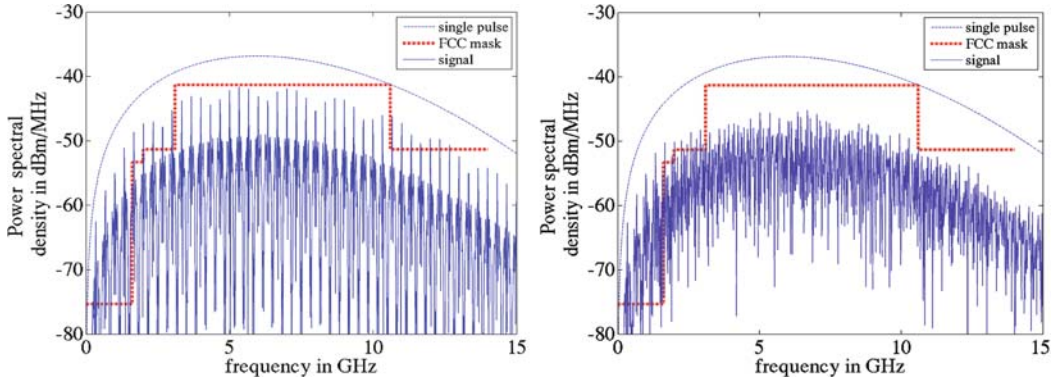
Fig. 2 L*eft*: *PSD* of a OOK-modulated signal without jitter together with *PSD* of single pulse and FCC regulation; *right*: signal including jitter

3.2 Performance in Terms of Bit Error Rate

For further simulation, the input signal is a PPM-modulated pulse train with binary random data. The reference signal has the identical pulse shape like the transmit signal (Gaussian second derivative, pulse width = 100 ps). The power of the transmit signal inside [3.1–10.6 GHz] is −16 dB m. A time hopping (TH) code is used to avoid discrete spectral lines. The PRF is 333 MHz and a bit is represented by two pulses. The modulated sequence is radiated via a non-ideal monocone Tx antenna, an indoor channel, and a non-ideal monopole Rx antenna. AWGN noise, interference, and LNA are modeled according to Section 2. The correlation receiver is perfectly synchronized and uses the same TH code. For a fixed distance, the interference power is varied (−77.125 dB m $< P_{\text{PSD}} < -52.125$ dB m) which leads to different receiver signal-to-noise interference ratios (SNR). The theoretically available SNR can be approximated by the SNR before the LNA:

$$P_{\text{signal}} = \int\limits_{3.1\,\text{GHz}}^{10.6\,\text{GHz}} \text{PSD}_{\text{signal}}(f)\, df \ , \tag{5}$$

$$P_{\text{noise\_interf}} = \int\limits_{3.1\,\text{GHz}}^{10.6\,\text{GHz}} \text{PSD}_{\text{noise}}(f) + \text{PSD}_{\text{interfer}}(f)\, df \ , \tag{6}$$

$$\text{SNR} = \frac{P_{\text{signal}}}{P_{\text{noise\_interf}}} \ . \tag{7}$$

The bit rate can be determined by

$$R = \frac{1\ \text{bit}}{N \cdot 1/\text{PRF}} = \frac{1\ \text{bit}}{N} \cdot \text{PRF} \ . \tag{8}$$

For the chosen parameters, (8) results in a bit rate of 166.67 Mbit/s. The BER for five different distances are simulated. The left figure in Fig. 3 shows the simulated bit error rate BER as a function
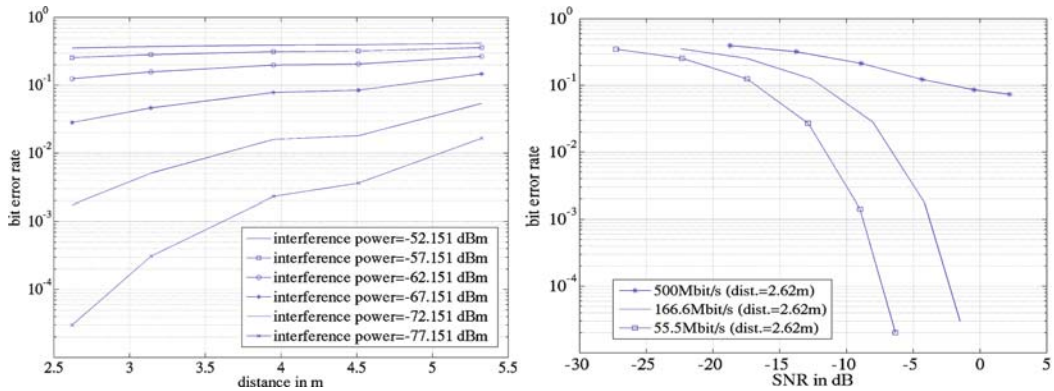
Fig. 3 *Left*: BER versus distance for data rate of 166.6 Mbit/s and several levels of interference power; *right*: BER versus SNR for three data rates and fixed distance.

of distance for different levels of interference power. The right figure visualizes the data versus the SNR for three different data rates: Decreasing the PRF by factor 3 (data rate=55.5 Mbit/s), the transmit power and consequently the SNR decreases by factor 3 (4.77 dB). The BER curve is shifted 4.77 dB to the left due to the processing gain. Increasing the PRF by factor 3 (500 Mbit/s) leads to a saturated curve, since 1/PRF gets smaller than the channel delay spread resulting in strong inter-symbol interference.

4 Improvement of Performance by Optimal Pulse Shaping

The results shown in Section 3 are based on a pulse shape that does not fully exploit the FCC mask. To maximize the SNR and – as a consequence – to improve the system performance, the radiated signal must optimally exploit the mask. First, the effect of the Tx antenna is neglected. To improve the system performance, the pulse shape must be optimized: This can be done by a pulse shaping FIR filter (FIR = finite impulse response) where a desired normalized mask and the filter order N is chosen. Applying Parks McClellan algorithm [13], optimal FIR coefficients are determined. When the time signal at the input of the filter is a Dirac, the output is a pulse that optimally exploits the desired mask. In this contribution, the normalized desired mask has infinite attenuation outside the frequency range [3.1–10.6 GHz] which is a stronger requirement than the FCC regulation. The maximal frequency of the mask is defined as 14 GHz. This results in three sub-bands [0–3.1 GHz], [3.1–10.6 GHz], and [10.6–14 GHz]. For each sub-band, the tolerances for the optimization can be defined. Here, the value is ±1% in each sub-band. Figure 4 (left) shows the resulting normalized pulse spectrum for different filter orders ($N = 40,\ldots, 200$) together with the normalized FCC mask whereas an increasing filter order leads to a higher sharpness and consequently to a stronger attenuation outside the frequency range [3.1–10.6 GHz]. Convoluting the optimal FIR coefficients for $N = 200$ and the Dirac function leads to the optimal pulse shape shown in Fig. 4 (right). In reality, the Tx antenna is non-ideal versus frequency, since the transfer function decreases with frequency.

Furthermore it is a function of angle. If at transmitter side, the transfer function of the transmit antenna is known together with the angle of the main path, it is possible to compensate the main contribution of the degrading antenna influence by inverse filtering with the antenna's transfer function.
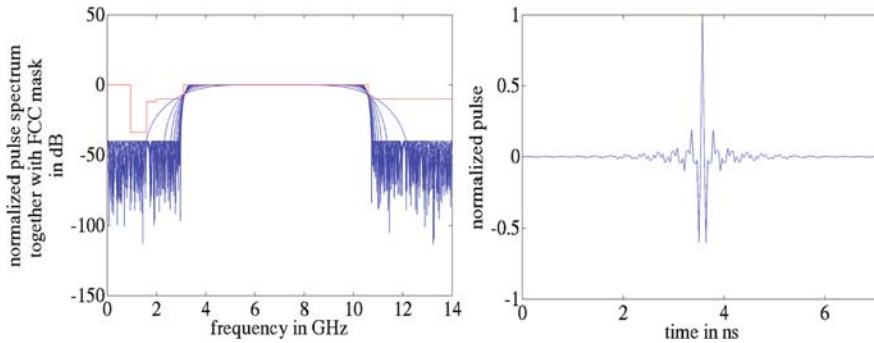
Fig. 4 *Left*: PSD for filter order $N = 40, \ldots, 200$; *right*: optimal pulse shape for $N = 200$

5 Conclusions

This contribution showed the modeling of non-ideal front-end components for impulse radio systems. To be close to reality, measurement data have been used for some models. To analyze the system behavior, the BER was investigated as a function of distance, SNR, and data rate and compared with theory. The results show the achievable performance using non-ideal front ends. Finally, it was discussed how the transmit SNR can be improved to get a better system performance. Future research will investigate the performance based on parameter studies. Second, compensation strategies will be further developed to get an ultra-efficient system.

References

1. G. Fettweis, M. Löhning, D. Petrovic, M. Windisch, P. Zillmann, and W. Rave, Dirty RF – a new paradigm, International Journal of Wireless Information Networks, vol. 14, no. 2, pp. 133–148, 2007.
2. J. Timmermann, D. Manteuffel, and W. Wiesbeck, Simulation of the impact of antennas and indoor channels on UWB transmission by ray tracing and measured antenna patterns, IEEE International Conference on Ultra-Wideband, Singapore, 2007, pp. 194–197.
3. A. Reisenzahn, Hardwarekomponenten für Ultra-Wideband Radio, M.S. Thesis, ICIE, Universität Linz, Linz, Austria, 2003.
4. S. Zhao, Pulsed Ultra-Wideband: Transmission, Detection, and Performance, Ph.D. Dissertation, EECS, Oregon State University, Corvallis, OR, USA, 2007.
5. U. Onunkwo, Timing Jitter in Ultra-Wideband (UWB) Systems, Ph.D. Dissertation, ECE, Georgia Institute of Technology, Atlanta, GA, USA, 2006.
6. C. Sturm, W. Sörgel, T. Kayser, and W. Wiesbeck, Deterministic UWB wave propagation modeling for localization applications based on 3D ray tracing, IEEE International Microwave Symposium, San Francisco, CA, USA, 2006, pp. 2003–2006.
7. A. Kanchev and U. Baumgarten, Ultra Wide Band, Thesis, Forschungs- und Lehreinheit XIII, Technical University of Munich, Munich, Germany, 2006.
8. A. F. Molisch, K. Balakrishnan, D. Cassioli, C. Chong, S. Emami, A. Fort, J. Karedal,. J. Kunisch, H. Schantz, U. Schuster, and K. Siwiak, IEEE 802.15.4a Channel Model – Final Report, IEEE 802.15.4a, 2005.
9. M. Hämäläinen, Singleband UWB Systems – Analysis and Measurements of Coexistence with Selected Existing Radio Systems, Ph.D. Thesis, Department of Electrical and Computer Engineering, University of Oulu, Finland, 2006.
10. C. Hung, W. Wuen, M. Chou, K. Wen, A unified behavior model of low noise amplifier for system-level simulation, Ninth European Conference on Wireless Technology, Manchester, UK, 2006, pp. 139–142.

11. Y. Park, C. Lee, J. Cressler, J. Laskar, The analysis of UWB SiGe HBT LNA for its noise, linearity, and minimum group delay variation, IEEE Transactions on Microwave Theory and Techniques, vol. 54, no. 4, pp. 1687–1697, 2006.
12. W. Wiesbeck, F. Jondral, Ultra-Wide-Band Kommunikationssysteme - Skriptum zum CCG Seminar DK 2.15, IHE, Universität Karlsruhe, Karlsruhe, Germany, 2006.
13. R. Hao, Z. Zhang, and H. Wang, UWB pulse design method based on Chebyshev function approximation, International Conference on Wireless Communications, Networking and Mobile Computing, 2007, pp. 546–549.

Integrated cm- and mm-Wave UWB Transceiver for M-Sequence-Based Sensors

M. Kmec, J. Müller, P. Rauschenbach, S. Rentsch, J. Sachs, and B. Yang

Abstract An integrated, completely balanced broadband transceiver front end for operation in the cm- and mm-wave range is presented. It is compatible with our ultra-wideband M-sequence base-band system. The transceiver front end is based on the application of specific integrated circuits (ASICs) designed for a 0.25 μm SiGe process with $f_T/f_{max} = 180/220$ GHz. To achieve an optimum reasonable compromise between flexibility, complexity, and the system performance, we decided to design three different front-end ASICs – an up-converter, a down-converter, and a LO unit. All of them are mounted on an RF-LTCC (low-temperature co-fired ceramics) test board for optimal RF wiring. The final goal is to provide an integrated transceiver module which covers the whole RF part from the antennas to the IF stage. First measurement results will be shown.

Keywords M-sequence sensors · UWB front end · UWB ASICs · Up- and down-converters · LTCC antenna

1 Introduction

By some modifications and in connection with suitable up–down-converters, the operational frequency band of an ultra-wideband M-sequence device [1] can be extended to the mm-wave range [2–4]. Up to now, III/V semiconductor technologies offer one of the fastest transistors with good noise performance to build corresponding mm-wave front ends. However, the possible integration level is moderate and the manufacturing costs are relatively high. An alternative solution for our purposes is offered by the standard SiGe BiCMOS process which will finally permit a complete monolithic integration of the whole M-sequence device.

The operational frequency bands of interest for our sensor applications cover the baseband (DC to ∼20 GHz) as well as the cm- and mm-frequencies. In order to meet these requirements an ASIC design program for integrated UWB SiGe components has been initiated at our university. Several SiGe ASICs (diverse pn-generators with up to 22 GHz of toggle frequency, track and hold circuits with an analog bandwidth of up to 19 GHz, programmable dividers operating up to 20 GHz)

M. Kmec (✉)
Technische Universität Ilmenau, Ilmenau, Germany
e-mail: martin.kmec@tu-ilmenau.de

have been designed and used in various research applications [5,6]. This leads to UWB system implementations which can operate up to 19 GHz of bandwidth.

The chapter deals with an integrated SiGe up–down-converter which extends the operational band of the aforementioned UWB system to the mm-wave range. It is known that the breakdown voltage of SiGe transistors is restricted to a relative low voltage particularly if they are designed for very high cutoff frequencies. Therefore the amplitude of signals in higher gigahertz bands is restricted to a few hundred millivolts. In order to gain sufficient transmit power it is recommended to spread the wideband stimulus over a large time which is met by modulating the carrier frequency with an M-sequence. This approach enables the combination of the proven baseband M-sequence concept with broadband heterodyne or homodyne converters in order to shift the operation frequency in the application-specific frequency band. Figure 1 depicts the device structure indicating the two main parts – the M-sequence system and the mm-wave up–down-converter. The shift register (extended by a xor-gate at the output) provides a wideband stimulus in the IF band $f_c/2...3f_c/2$, which the up-converter shifts to the band of interest. The down-converter shifts back the receive signal into the IF band where it is captured in a sub-sampling approach by a wideband track and hold.

The RF front end is designed for flexible operation within the cm- and mm-wave range. It is based on a balanced circuit layout matching the feeding of the antenna [7] as well as the M-sequence electronics. The design of such front-end ASICs is a challenging task due to the high and selectable carrier frequency in combination with the large bandwidth. For example, every transition between the chip and its carrier or between different types of RF lines causes discontinuities which disturb the broadband signal. With a system-on-chip (SoC) solution, one could avoid many interface problems of such kind, but parasitic signal coupling on the chip would provoke other difficulties.

Thus, we decided to design three different ASICs (up-converter, down-converter, and LO unit) in order to achieve a compromise between complexity and flexibility of the layout and the device performance. In a final version, they are mounted jointly with the antennas on low-temperature co-fired ceramics (LTCC) [8]. For that purpose, the mm-wave dies are flip-chipped directly in the feed-point of the radiators. The ASICs were designed for a 0.25 μm SiGe process with $f_T/f_{max} = 190/220$ GHz using a standard Cadence-based methodology, with SpectreRF and ADS as the simulators.
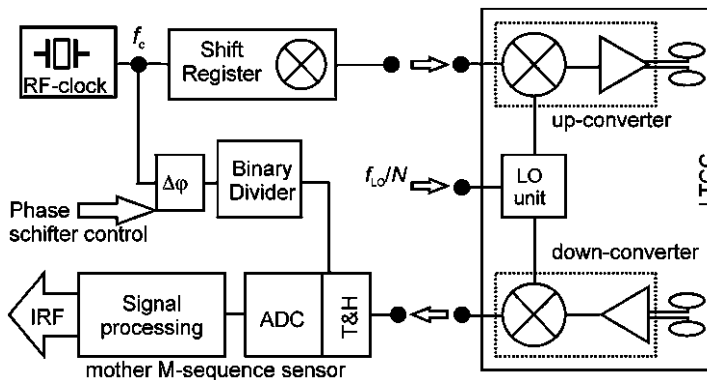
Fig. 1 Modified M-sequence baseband system (*left*) connected with a wideband up–down-converter

In what follows, the main components of the up–down-converter front end will be explained and first results will be shown.

2 Transmitter (Up-Converter)

The circuit on the transmitter side consists of a double-balanced Gilbert-cell mixer and the output buffer. The simplified schematics are shown in Fig. 2. The mixer is designed to handle the broadband sensor stimulus signal with a conversion loss of about 0 dB in the frequency range from 15 to 67 GHz (RF port). The differential LO signal with nominally –3 dB m power may be arbitrary selected within the frequency range of 10–57 GHz.
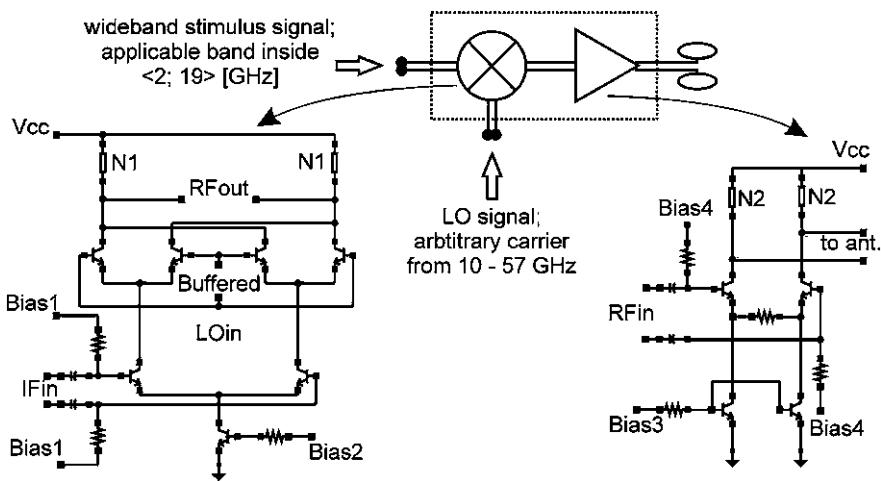
Fig. 2 Transmitter architecture and the simplified schematics of the particularly building blocks

The output buffer serves as a differential interface to the radiator. It is based on the differential pair structure having collector loads optimized for broadband operation. These loads consist of a network of short lines with minimized parasitic capacitances in order to emphasize higher frequencies (to provide the desired level peaking). The simulations result in a gain of 5 dB within the passband from 15 up to 67 GHz (3 dB cutoff) and the 1 dB (output) compressions were calculated to be 5 dB m. Figure 3 shows the first results of on-wafer network analyzer measurements (R&S ZVK) of the conversion gain. For this purpose, the up-converter was excited with IF and LO signals as follows: $f_{IF} \in \langle 5; 13 \rangle$ (GHz), $f_{LO} = 15$ GHz and $f_{IF} \in \langle 0,2; 19 \rangle$ (GHz), $f_{LO} = 20$ GHz. The upper sideband was observed. The measurements are in good agreement with the expectations.

The designed circuit cores are optimized for minimum wire length and maximum symmetry. The chip dimensions are $800 \times 800 \ \mu m^2$. Figure 3 (left) shows the up-converter chip die. The octagon-shaped pads are used at the input and output to reduce the parasitic capacitance of the pad. The DC power consumption of the transmitter is 200 mW at 4 V supply voltage.

A very important point is that the whole circuit topology is implemented by balanced structures. On the one hand, it permits direct feeding of symmetric broadband radiators and on the other hand it avoids the so-called via holes problem. The wiring of unbalanced integrated circuits needs a ground
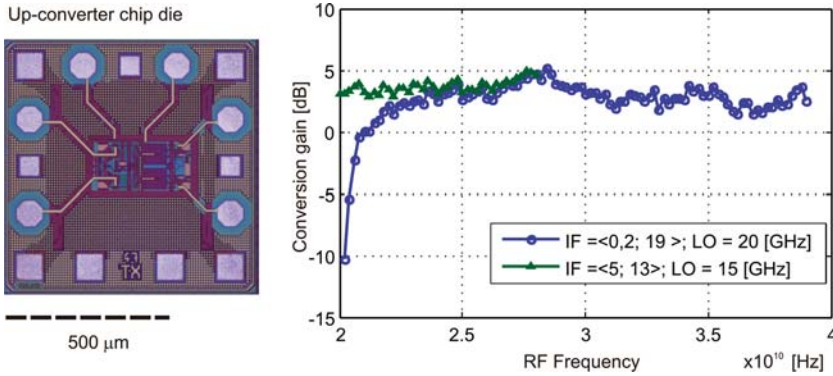
Fig. 3 The die photograph of the transmitter and measured conversion gain

plane that usually lies opposite to the mounting side. Therefore, in order to obtain a ground reference for such circuits, many via holes must be inserted to guarantee a proper connection between the top and bottom layers. However, vias cause additional inductances which lead to problems at high operational frequencies. Furthermore, extra costs and complexity arise.

In addition to the on-wafer testing, an LTCC test board is designed for characterization purposes. It is shown in Fig. 4. The board represents the whole transmitter chain covering the M-sequence generation and a first up-conversion (within the M-sequence chip) as well as the mm-wave up-conversion. The chip interconnection is made as intended by symmetrical lines while the connections to the measurement ports are made by unbalanced lines for simplicity of device connection and measurement purposes only. This device can be operated with the full bandwidth of about 19 GHz.
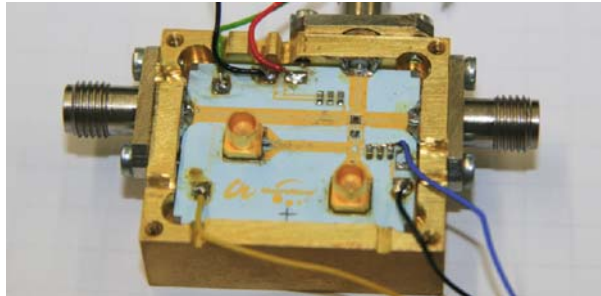
Fig. 4 The first prototype version of the transmitter module

3 The Radiators

It is intended to join RF electronics and antennas onto the same LTCC substrate. The antenna is built from elliptically shaped radiators and a back-shielded cavity (see [7] for details). Figure 5 depicts a test example of an individually integrated antenna.
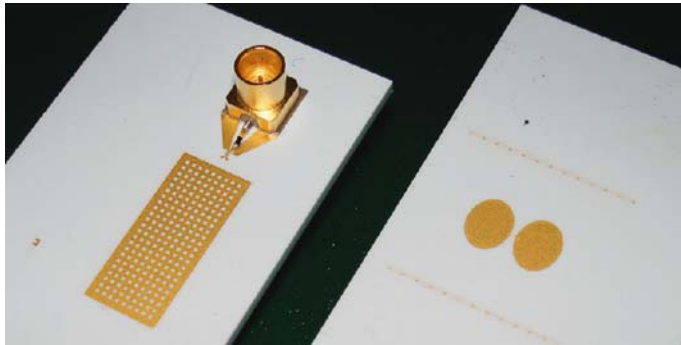
Fig. 5 LTCC antenna designed for the operation from 25.5 to 29.5 GHz

4 Receiver (Down-Converter)

The front end on the receiver side is constructed by two building blocks, an ultra broadband input preamplifier and the down-converting mixer. The circuits are designed to handle the broadband signals in the same frequency range as the transmitter.

The preamplifier is a two-stage device with common emitter differential topology. Figure 6 shows the simplified schematic. The first stage consists of a differential pair with inductive loads. The second stage is based on a differential amplifier with inductive loads and emitter degeneration to improve the receiver linearity. The simulated gain of the preamplifier chain in the frequency range of interest is about 8 dB and noise figure less than 12 dB. The poor noise figure of the circuit was accepted in favor of the ultra-broadband operation capability.

The mixer is a conventional emitter-degenerated double-balanced Gilbert cell, as shown in Fig. 6. It is designed for a conversion gain of about 3 dB in the frequency range of interest.
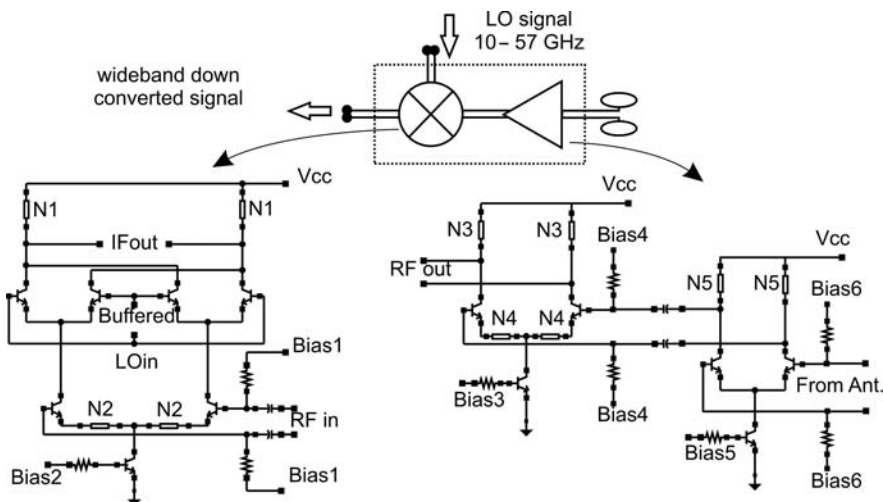
Fig. 6 Receiver architecture and the simplified schematics of the particular building blocks

The simulated 1 dB compression point of the receiver ASIC is about –16 dB m at the RF input. This results in a power of about −6 dB m at its output, which is the maximum level to be handled with the current T&H ASICs. Figure 7 depicts two measurement examples which are complementary to the measurements discussed above in the case of the up-converter. The down-converter were excited with RF and LO signals as follows: $f_{RF} \in \langle 20; 28 \rangle$ (GHz), $f_{LO} = 15$ GHz and $f_{IF} \in \langle 20,02; 39 \rangle$ (GHz), $f_{LO} = 20$ GHz. The RF signal level was adjusted to −20 dB m.
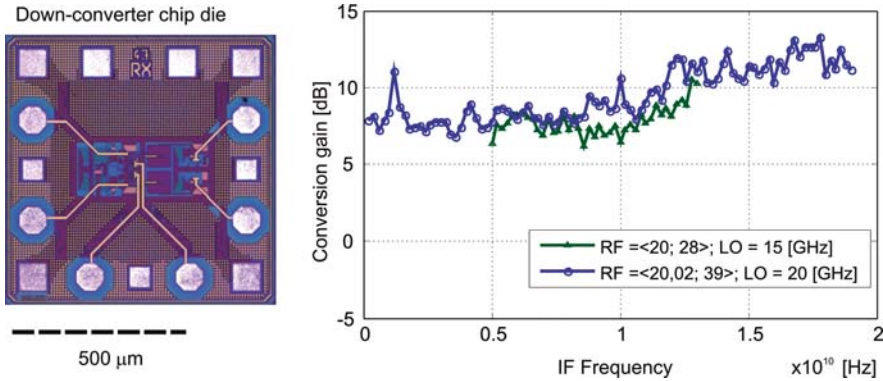
Fig. 7 The die photograph of the transmitter and the measured conversion gain (example)

The preamplifier, mixer, and associated LO buffer drive 38 mA from 4 V supply. A die photograph of the receiver chip is shown on Fig. 7. The die size is $800 \times 800 \ \mu m^2$.

5 LO Unit

Since it is extremely difficult and costly to externally generate and distribute differential LO signals for mm-wave converters, a frequency multiplier jointly integrated with the mixers on LTCC was preferred. Its mixer feeding is designed for differential operation while the input is unbalanced in order to be flexible with respect to usual sine-wave sources. The first LO unit version is designed to supply the above-discussed up- and down-converter ASICs with the differential LO signal at about 56 GHz.

The circuit consists of a cascaded tripler and doubler, whereas the doubler can also operate separately. The tripler schematic is depicted in Fig. 8 (left). The circuit is based on a differential pair with the load resonant at $3f_{in}$. This method provides better suppression of unwanted harmonic than a simple non-linear device. In the shown example, the load resonance is matched to 28 GHz.

The frequency doubler is based on a Gilbert cell with both inputs connected together as shown in Fig. 8. The doubler output is matched at 56 GHz to the input of the active output power splitter. The interstage matching is realized with microstrip stubs and capacitors resulting in undesirable harmonics rejection better than 35 dB. The output splitter is equipped with the differential buffers optimized for operation at 56 GHz. By doing so, the LO unit can be driven from nominally +4 dB m clock, which lies at about 9 or 28 GHz (at the doubler) input that are the regions of the best conversion gain and correspond to 6 dB m of output power at 56 GHz. The chip die and the simulation example of the output power spectrum are depicted in Fig. 9. The LO unit draws 60 mA from 4 V supply.
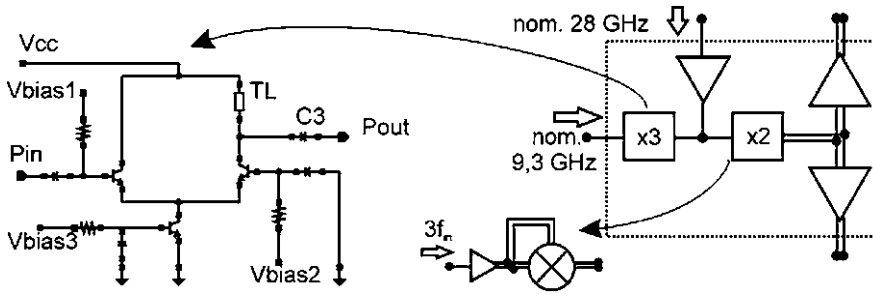
Fig. 8 LO unit architecture and the simplified schematic of the tripler block (*left*)
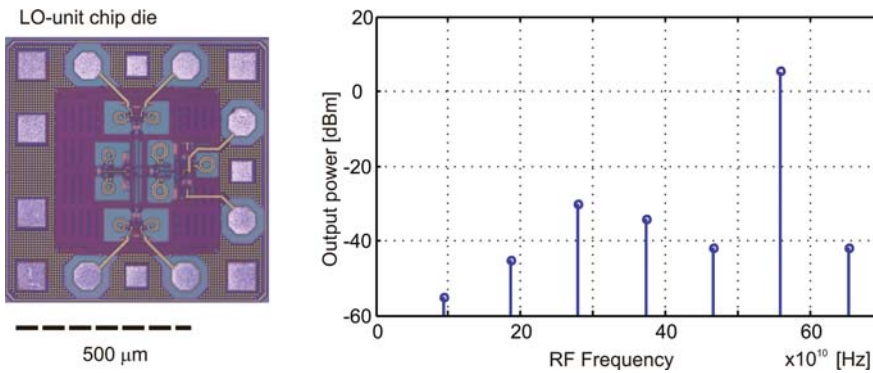
Fig. 9 The die photograph of the LO-unit chip and the simulated output spectrum at +4 dB m, $f_{in} = 9.3$ GHz

6 Conclusion

We have presented the front-end topology for M-sequence-based sensors. The key components are ASICs realized in 0.25 μm SiGe process, designed to operate with the broadband signal in the cm- and mm-wave range. The proposed hardware, mounted on LTCC, is the first step toward the M-sequence-based sensor which is intended to operate in an arbitrary frequency band up to 67 GHz, using proper radiators. The first measurement results up to 40 GHz are shown.

References

1. J. Sachs and P. Peyerl, A new principle for sensor-array-application, Proceedings of 16th IEEE Instrumentation and Measurement Technology Conference, IMTC/99, Venice, Italy, May 24–26, 1999, pp. 1390–1395.
2. M. Kmec, R. Herrmann, J. Sachs, P. Peyerl, and P. Rauschenbach, Extended Approaches for M-Sequence based UWB Systems, In J. S. Tyo, C. E. Baum, and A. P. Stone (eds.), Ultra-Wideband Short-Pulse Electromagnetics 8, pp. 135–142, 2007.
3. M. Kmec, J. Sachs, P. Peyerl, P. Rauschenbach, R. Thomä, and R. Zetik, A novel ultra-wideband real-time MIMO channel sounder architecture, XXVIIIth URSI General Assembly 2005, October 23–29, 2005, New Delhi.

4. S. Ranvier, J. Kivinen, S. Geng, P. Vainikainen, R. Zetik, M. Kmec, R. S. Thoma, and J. Sachs, Mm-wave wideband MIMO channel sounding, XXVIIIth URSI General Assembly 2005, October 23–29, 2005, New Delhi.
5. J. Sachs, R. Herrmann, M. Kmec, M. Helbig, and K. Schilling, Recent advances and applications of M-sequence based ultra-wideband sensors, ICUWB 2007, Singapore, September 24–26, 2007
6. R. Herrmann, J. Sachs, K. Schilling, and F. Bonitz, New extended M-sequence ultra wideband radar and its application to the disaggregation zone in salt rock, GPR 2008 12th International Conference on Ground Penetrating Radar, June 15–19, 2008, Birmingham, UK.
7. B. Yang, A. Vorobyov, A. G. Yarovoy, L. P. Ligthart, S. Rentsch, and J. Müller, A novel shielded UWB antenna in LTCC for radar and Communications applications, ICUWB 2008, Hannover.
8. S. Rentsch and J. Müller, Design and implementation of baluns at 60 GHz on LTCC, Invited Paper, Journal of Microelectronics and Electronic Packaging, vol. 4, no. 4, pp. 181–185, 2007.
9. B. A. Floyd, S. K. Reynolds, U. R. Pfeiffer, T. Zwick, T. Beukema, and B. Gaucher, SiGe bipolar transceiver circuits operating at 60 GHz, IEEE Journal of Solid-State Circuits,vol. 40, no. 1, pp. 156–167, 2005.

Experimental Focal Waveforms of a Prolate-Spheroidal Impulse-Radiating Antenna

S. Altunc, C.E. Baum, C.G. Christodoulou, and E. Schamiloglu

Abstract Impulse-radiating antennas (IRAs) have been used for different applications and the basic motivation for developing IRA systems is to radiate large amplitude, large band ratio, undispersed pulses. This chapter discusses applying fast, high-electric-field pulses without direct contact for killing skin cancer, i.e., to irradiate them using a prolate-spheroidal IRA. This technique is less invasive than inserting electrodes near the tumor. Even though this chapter is devoted to discussion of the experimental aspect of this problem, analytical and numerical behaviors for the focal waveforms and spot sizes of two- and four-feed arm prolate-spheroidal IRAs are also explored for comparison.

Keywords Impulse-radiating antenna · Prolate spheroid · Focal waveform · Electromagnetic implosion · Focusing

1 Introduction

Experimental setups using two-arm and 60° four-arm prolate-spheroidal IRAs are used to obtain better focusing at the second focus of a prolate-spheroidal IRA and these results are compared with analytical and numerical results for verification. The dimensions of these experiments are based on [1–3] and these setups are motivated by a biological application [4]. Figure 1 presents the prolate-spheroidal IRA geometry and the parameters for this geometry are as follows:

$$z_p = 0, \ a = 0.625 \text{ m}, \ b = \Psi_0 = 0.5 \text{ m}, \ z_0 = 0.375 \text{ m}, \ \ell = 1 \text{ m}, \tag{1}$$

where z_p is the z-coordinate of the truncation plane, a and b are the two radii for the prolate spheroid, z_0 is the focal distance, and l is the distance that can be used for normalization.

2 Experimental Setups and Data Analysis

Our design has two TEM feed arms and the dimensions of these arms are determined by a 400 Ω pulse impedance [2]. In our design, we also used 60° four arm because of the nearly maximum

S. Altunc (✉)
Department of Electrical and Computer Engineering, University of New Mexico, Albuquerque, NM 87131, USA
e-mail: saltunc@ece.unm.edu
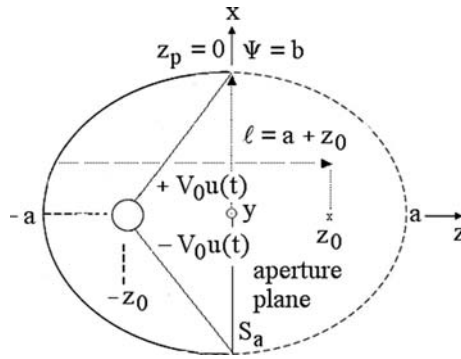
Fig. 1 Prolate-spheroidal IRA geometry

voltage gain and easy geometrical construction. An increase of 1.606 in the fields can be obtained by using the 60° TEM feed-arm case as compared with the two-arm case [2]. The experimental setups for two-feed arm and 60° four-feed arm prolate-spheroidal IRA are presented in Fig. 2.

Figure 3 shows the three types of probes to measure the field and the spot size grids in the *xz*-coordinate and these probes are B-dot probe (rise time < 150 ps), D-dot (rise time < 150 ps), and fast D-dot (rise time < 15 ps) probes.

The experimental setup includes three components. These are a prolate-spheroidal reflector with feed arms, a sampling oscilloscope, and a pulse generator. The step generator has a 22-ps rise time

Fig. 2 Experimental setups for two-feed arm and 60° four-feed arm prolate-spheroidal IRA
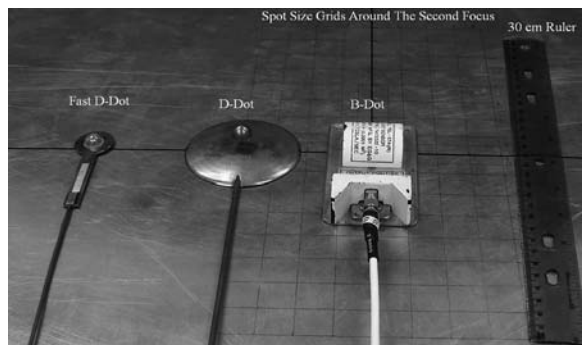
Fig. 3 Fast D-dot, D-dot, and B-dot probes and spot size grids

(t_{mr}, introduced later) and 10 V amplitude output. Cables of 2 and 3 ns length are used to connect the pulser to the feed arms and sensors to the sampling oscilloscope. We use foam with a relative dielectric constant $\varepsilon_r = 1.013$ to maintain the feed arms angle at $60°$.

2.1 Data Analysis Technique

We use the B-dot probe to obtain the magnetic field and also use the prepulse data of the B-dot probe to calibrate the D-dot probe data. We use the data from the B-dot probe which has an equivalent area $A_{eq} = 1 \text{ cm}^2$ and analyze the data as follows:

$$V = A_{eq} \frac{dB}{dt} \quad \text{and} \quad B = \frac{1}{A_{eq}} \int_{-\infty}^{t} V(t') \, dt' . \tag{2}$$

We can find the equivalent electric field as

$$E_{eq} = cB = \frac{c}{A_{eq}} \int_{-\infty}^{t} V(t') \, dt'. \tag{3}$$

This equivalent electric field, E_{eq}, gives the exact result for the prepulse because we have a TEM wave and $E/H = \eta_0 \approx 377 \ \Omega$ for free space. We calibrate our D-dot data by comparison to the prepulse term. We obtain the data from the D-dot probe and analyze it as follows:

$$I = \frac{V}{Z_0} = A_{eq} \frac{dD}{dt} \quad \text{and} \quad E = \frac{1}{\varepsilon_0 Z_0 A_{eq}} \int_{-\infty}^{t} V(t') \, dt' . \tag{4}$$

Our pulse generator has a $V_0 = 10$ V excitation and we feed our IRA with

$$V = T \, V_0 , \tag{5}$$

where T is the transmission coefficient

$$T = 2Z_L / (Z_L + Z_0) . \tag{6}$$

In our analytical calculation we use $V_0 = 0.5$ V and then normalize the data to obtain the electric field as

$$E_N = \frac{1}{20 \, T \, \varepsilon_0 \, Z_0 \, A_{eq}} \int_{-\infty}^{t} V(t') \, dt. \tag{7}$$

2.2 Experimental Results

The analytical focal waveforms for a ramp-rising step excitation are from [2]. The excitation is a 1 V ($V_0 = 0.5$ V) step, rising as a ramp function lasting $t_\delta = 100$ ps. Figure 4 presents the ramp-rising step excitation, step response, and analytical ramp-rising step response.
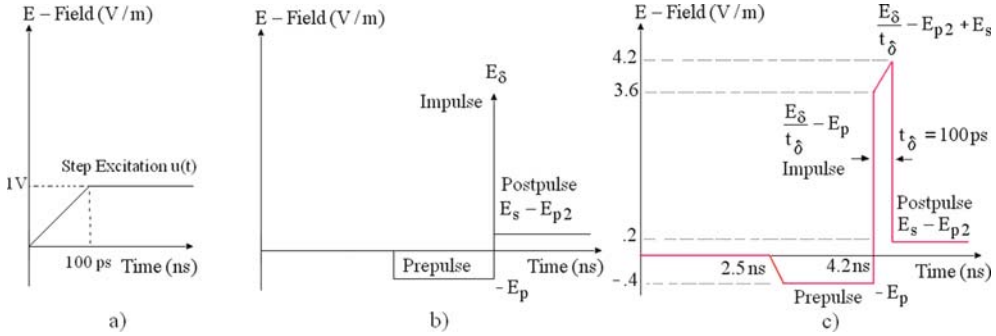
Fig. 4 (**a**) Ramp-rising step excitation; (**b**) step response; and (**c**) analytical ramp-rising step response

E_δ and E_s are the impulse and step terms from the reflection from the prolate sphere, respectively. E_p is the magnitude of the prepulse wave from the first focus and E_{p2} is the prepulse term after the impulse.

The experimental results are normalized to 1 V differential input and t_{mr} (maximum rate of rise) is used as t_δ to compare our experimental results with analytical and numerical results. For a step like $f(t)$, the t_{mr} is

$$t_{mr} = \frac{f_{max}}{df/dt|_{max}} .$$
(8)

In Fig. 5a, the analytical, experimental, and numerical focal waveforms are presented for two-arm prolate-spheroidal IRA and Fig. 5b shows the fast D-dot probe analytical and experimental focal waveforms, for 60° four-feed arm prolate-spheroidal IRA. The analytical peak is calculated based on the t_{mr} values from the experiment. Even though the B-dot sensor is more sensitive than the fast D-dot sensor, it is not fast enough to obtain the actual minimal t_{mr} values. This leads to a decrease in the amplitude of the impulse part of the experimental focal waveform in Fig. 5a for $t_{mr} = 119$ ps. The fast D-dot sensor is less sensitive; therefore, we observe lower amplitude of the impulse part of the experimental focal waveform in Fig. 5b for $t_{mr} = 119$ ps.

We are at the limit of our measurement instrumentation. One can see from Fig. 5a that the prepulses for analytical, numerical, and experimental focal waveforms agree very well. Although the analytical and numerical impulses' amplitudes agree, the experimental impulse amplitude is less than the others. Any misshape of the reflector, experimental, and numerical errors and the limitations of the idealized analytical assumptions may lead to the differences between analytical, experimental, and numerical results.
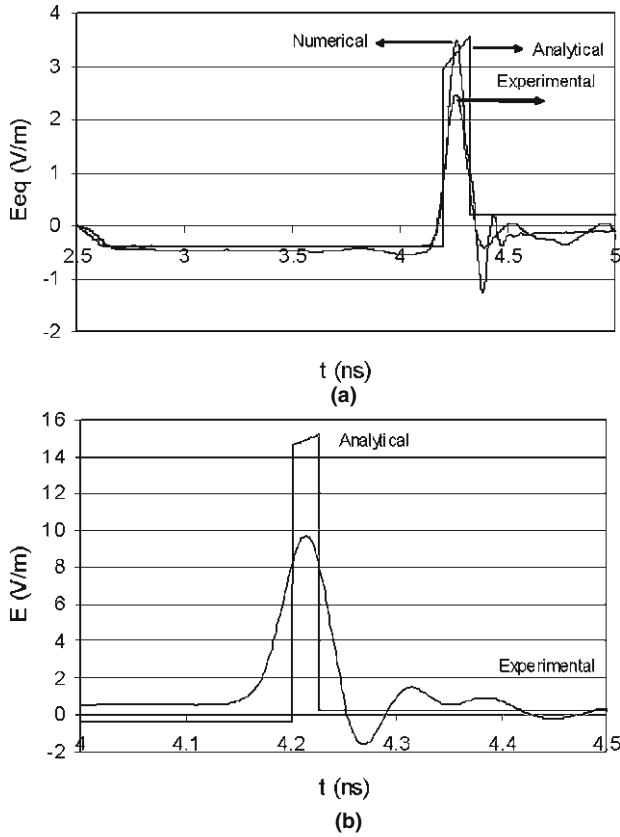
Fig. 5 (**a**) B-dot probe analytical, numerical, and experimental focal waveforms, for two arm (t_{mr} =119 ps). (**b**) Fast D-dot probe analytical and experimental focal waveforms, for 60° four-feed arm (t_{mr} =22 ps) prolate-spheroidal IRA

2.3 Spot Size Analysis

Given that the impulse has some small width $t_\delta = 100$ ps, the maximum fields will exist in some small region around Z_0. We can make a rough estimate of spot sizes [1]. Pulse width to define boundary spot with respect to Ψ and z

$$t_\Psi = t_z = 2t_\delta = 200 \text{ ps.} \tag{9}$$

Spot sizes are calculated analytically in [1] as

$$|\Delta z| = 2 \left[1 - z_0/a\right]^{-1} ct_\delta = 15 \text{ cm}, \quad \Delta\Psi = \frac{a}{b} ct_\delta = 3.75 \text{ cm.} \tag{10}$$

These calculations are based on the two-arm case and do not apply to the 60° four-arm case. The spot sizes for the 60° case can be discussed numerically and experimentally. Table 1 presents the electric field peak amplitude values at the analytical spot size locations.

Although the amplitudes of the electric fields should be symmetric along the *y*-axis with respect to $y = 0$, they are different. This is because of errors in the geometric shape or alignment of the

Table 1 The electric field peak amplitude values at the analytical spot size locations for two- and four-arm prolate-spheroidal IRA ($t_{mr} = 119$ ps)

	E-field peak value (V/m)	$y = -3.75$ cm	$y = +3.75$ cm	$z - z_0 = -15$ cm	$z - z_0 = +15$ cm	Focal waveform peak value (V/m)
Two arm	Numerical	1.80	1.80	1.80	2.00	3.50
	Experimental	2.27	1.44	1.20	1,43	2.45
Four arm	Numerical	2.20	2.20	2.00	2.70	5.20
	Experimental	2.94	1.50	2.05	2.17	3.36

prolate-spheroidal reflector. Table 1 shows that the waveforms are not symmetrical with respect to the $z = z_0$ plane (which is not a symmetry plane). We have competing factors. As we move away from S_a (aperture plane) this gives lower fields, due to inverse distance in the integrals. However the wave from S_a is not oriented in the x-direction, but is tilted, this being more severe closer to S_a. Therefore, the electric field peak amplitude values at $z - z_0 = -15$ cm are always lower then the values at $z + z_0 = -15$ cm. One can conclude from Table 1 that both our numerical and experimental results at the spot size locations are almost half of the results at the focal point. This gives us confidence about our rough analytical calculations on the spot size analysis.

3 Conclusions

This chapter proposes a new type of prolate-spheroidal IRA which can be used to kill skin cancer in the near-field region. We used analytical calculations, numerical simulations, and experiments to find the focal waveform characteristics and spot sizes. Analytical, numerical, and experimental prepulses' amplitude agree very well. The analytical and numerical impulses' amplitudes agree. However, the experimental impulse amplitude was smaller than the others. For all cases the postpulse behaviors were different. This part of the pulse was less important for our biological application. Our concern was to obtain the largest possible impulse amplitudes at the focal point. The analytical waveform, while simple, is still good, albeit not perfect.

References

1. C. E. Baum, Focal waveform of a prolate-spheroidal impulse-radiating antenna (IRA), Radio Science, vol. 42, RS6S27, 2007.
2. S. Altunc, C. E. Baum, C. G. Christodoulou et al. Focal waveforms for various source driving a prolate-spheroidal impulse-radiating antenna (IRA), Radio Science, RS003775, 2008.
3. C. E. Baum, S. Altunc, C. G. Christodoulou et al. Electromagnetic implosion using an array, IEEE Transactions on Plasma Science, vol. 36, pp. 757–763, 2008.
4. K. H. Schoenbach, R. Nuccitelli, and S. J. Beebe, ZAP, IEEE Spectrum, vol. 43, p. 20, 2006.

Development of a Resonant Chamber Microwave Tomography System

C. Kaye, C. Gilmore, P. Mojabi, D. Firsov, and J. LoVetri

Abstract This chapter documents the hardware specifications of a prototype resonant chamber microwave tomography system that is currently under development for biomedical applications. The electromagnetic fields are generated and measured using a vector network analyzer. Details of the calibration procedure necessary to provide accurate information on the incident fields inside the imaging region and the scattered fields at observation points within the chamber are presented. The calibration procedure is based on an electromagnetic analysis of a detailed numerical model using the finite-volume time-domain (FVTD) technique. Images of dielectric profiles of simple objects using synthetic data obtained using idealized 2-D and 3-D FVTD models are provided using two inversion algorithms: DBIM and MR-CSI.

Keywords Microwave tomography · Resonant chamber · FVTD · Distorted Born iterative method · Contrast source inversion

1 Introduction

Microwave tomography (MWT) is emerging as a promising alternative or complementary diagnostic technique for conventional soft-tissue imaging modalities. The appeal of MWT arises from its use of safe, non-ionizing radiation (consisting of low-power microwaves in the frequency range of 500 MHz to 8 GHz), its relatively low system costs, and its ability to provide an image based on a unique contrast property: the dielectric permittivity of tissue. The values of dielectric permittivity in the human body are known to vary significantly between a number of tissue types (fat, bone, muscle) and more importantly, between healthy and malignant tissues [1], highlighting MWT's great potential as a cancer diagnostic tool.

Despite these advantages, there have been surprisingly few clinical MWT prototypes developed in the past for biomedical applications, largely due to relatively poor imaging results obtained with existing algorithms. Inverse scattering algorithms applicable to MWT must take into account the complex wave-like interactions that occur at microwave frequencies. The recent development of algorithms that solve the nonlinear inverse scattering problem has spurred a renewed interest in

C. Kaye (✉)
Department of Electrical and Computer Engineering, University of Manitoba, Winnipeg, Canada
e-mail: umkayecj@cc.umanitoba.ca

MWT for biomedical applications [2–5]. Two successfully applied methods, which we use in this work, are the contrast source inversion (CSI) and distorted Born iterative (DBIM) methods [6,7].

Previously reported MWT systems have assumed that imaging is performed in open boundary region and the applied imaging algorithms have made such an assumption whether or not such an approximation was valid. An exception has been the work reported by Franchois and Tijhuis [8] wherein the measurements were taken in their semi-metallic enclosure and their reconstruction algorithm attempted to remove the effects of multiple reflections from the metallic walls. By contrast, our imaging algorithm makes full use of the resonant nature of the fields inside the metallic chamber. Algorithmically, inversion of resonant chamber MWT data using an integral equation technique requires the use of a modified Green's function applicable to the PEC chamber. This extension of MWT to resonant chamber imaging provides some advantages over more traditional open-region MWT systems, as shown by Gilmore and LoVetri [9] based on synthetically generated scattering data.

The purpose of the research reported herein is to develop an experimental prototype of a novel resonant chamber MWT system employing a metallic cylindrical enclosure with an array of antennas lining its internal periphery, which are used to transmit and receive microwave energy. Photos of the current prototype are shown in Fig. 1.

The physical details of our MWT system are given in the first section below while the complex calibration procedure necessary to properly determine incident electric fields for different transmitter antennas and locations inside the chamber are described in the second section. The final section of the chapter is dedicated to preliminary imaging results of the inversion algorithms using an ideal analytic line source and an FVTD model of the constructed prototype in two different cases.
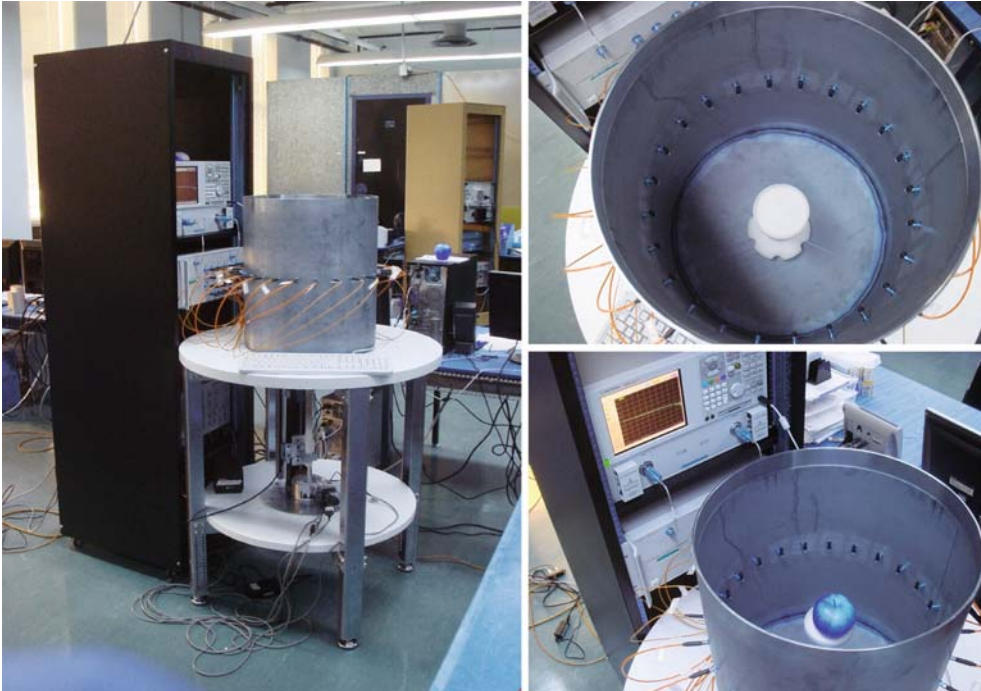
Fig. 1 Photo of prototype resonant chamber MWT system (*left*), top view of chamber with array of antennas visible (*top right*), another top view of system (*bottom right*)

2 Physical Description

Photos of the current prototype and a schematic of the complete system are shown in Figs. 1 and 2, respectively. We have employed a two-port Agilent 8363B PNA-Series Network Analyzer as our microwave source and receiver, capable of producing discrete frequencies or sweeps within our chosen range of 0.5–8 GHz at an approximate system dynamic range of 120 dB (an additional 15 dB of dynamic range is available using the configurable test set). The 24 antennas are arranged at even intervals of 15 in a circular array at the midpoint height along the inside of a stainless steel cylinder. Various antennas, including commercially available 2.45 GHz monopoles meant for wireless applications, can be used. The monopoles are designed with SMA right angle connectors such that the arm of the monopole is parallel to the wall of the cylinder, oriented in the vertical direction. Positioning the antennas inside the resonant chamber affects the operating frequency of the antenna as well as the input impedance. The system has been designed in a modular way with removable cylindrical chambers for testing purposes. The current prototype includes cylinders with varying parameters: two materials (stainless steel and acrylic), two different diameters (45.7 and 30.5 cm), and two types of sealed bottom boundaries (welded stainless steel and Teflon). Each cylinder is 50.8 cm tall and is watertight, allowing it to be filled with a matching liquid. The motor assembly located underneath the cylinder support structure consists of two precision stepper motors arranged to provide extremely accurate positioning of the OI within the chamber. The object is placed on a plastic platform mounted on a central Teflon pillar protruding from a watertight, sealed hole in the center of the cylinder's bottom boundary and can be rotated 360° (at increments smaller than 1° if needed). A vertical movement range for the pillar of roughly 15 cm is also accommodated by the motor assembly to provide full 3-D positioning of the OI through the 2-D plane of the monopole array.
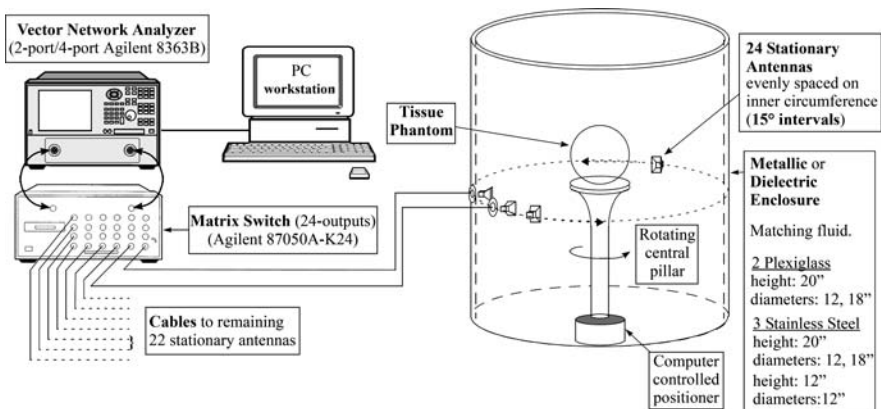
Fig. 2 Schematic of resonant chamber MWT system

3 Inversion Algorithms

A schematic representation of the data collection setup is shown in Fig. 3, where D denotes the imaging domain and S is the measurement surface which is outside D. The term *contrast* is typically used to refer to the bulk-electrical properties being imaged and is denoted by the symbol χ in the

Fig. 3 Schematic of imaging problem
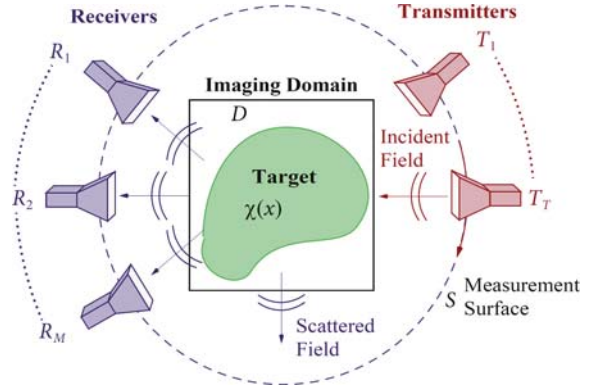
figure. The contrast at a point $\mathbf{q}$ in D is defined as $\chi\,(\mathbf{q}) = (\varepsilon\,(\mathbf{q}) - \varepsilon_{\mathrm{b}})/\varepsilon_{\mathrm{b}}$, where $\varepsilon(\mathbf{q})$ and ε_{b} are the complex permittivities of the imaging domain and the background medium, respectively. Assume that a particular component of the electric field is represented as u, and the corresponding scattered field as $u^{\mathrm{s}} = u - u^{\mathrm{i}}$ where u^{i} denotes the incident field. The so-called data integral equation can be written as $u^{\mathrm{s}}\,(\mathbf{q} \in S) = G_S\,\{\chi u\}$, and the domain integral equation can be written as $u^{\mathrm{i}}\,(\mathbf{p} \in D) = u\,(\mathbf{p} \in D) - G_D\,\{\chi u\}$ where the data operators $G_s\{\cdot\}$ and $G_D\{\cdot\}$ are defined as

$$G_{\{S,D\}}\,\{\psi\} = k_{\mathrm{b}}^2 \int\limits_{q \in D} g\,(\mathbf{p}, \mathbf{q})\,\psi\,(\mathbf{q})\,dv\,(\mathbf{q}), \quad \mathbf{p} \in \{S, D\} \tag{1}$$

where g is the appropriate Green's function for the problem. Assuming that for each set of $m = 1 \ldots M$ measurements the object is illuminated by some known incident fields u_m^{i}, the microwave imaging problem can be formulated as the following minimization:

$$\chi = \underset{\chi, u_m}{\arg\min} \quad \left\{ \sum_{m=1}^{M} \left\| \tilde{u}_m^s - G_S\,\{\chi u_m\} \right\|_S^2 \right\} \tag{2}$$
$$\text{subject to } u_m^{\mathrm{i}}\,(\mathbf{p} \in D) = u_m\,(\mathbf{p} \in D) - G_D\,\{\chi u_m\}$$

where $\tilde{u}_m^s$ represents the measured data and $\|\cdot\|_s$ denotes the L_2-norm on the measurement surface S. This minimization is ill-posed and needs regularization.

In recent years, techniques have been developed to solve the full nonlinear microwave imaging problem. In this work we present reconstructions based on the distorted Born iterative method (DBIM) as well as the multiplicative regularized contrast source inversion (MR-CSI) method. Details of these methods can be found in [6,7].

In both these methods, the incident field inside the imaging domain, $u_m^{\mathrm{i}}\,(\mathbf{p} \in D)$, needs to be known to a very good approximation. For the DBIM, the Jacobian matrix containing the first-order derivatives of the scattered field components with respect to the contrast is calculated using a forward solver which requires the incident field inside the imaging domain for an estimated inhomogeneous contrast at a particular iteration. In the MR-CSI method, the functional is dependent on the incident field in D, and therefore, an accurate approximation to the incident field inside the imaging domain is required for a good reconstruction with an acceptable convergence rate. For the resonant chamber MWT system, calculating an accurate description of the incident field is part of the calibration procedure which will now be described.

4 Calibration Procedure

The incident field values inside the imaging region, together with the measured *scattered* field values at the receiver points (determined through the measurement of the induced voltage at the receiving antenna terminals), constitute the information required for the inversion algorithms.

Traditionally, the incident field distribution of the transmitting antenna is approximated with a mathematical analytic model of a simplified source, such as a point or line source, scaled by a correction factor obtained as the ratio of the measured field to the analytic field at some measurement point. In some cases, such a crude approximation may not sufficiently match the true incident field of the actual physical setup, and this is especially true for the resonant chamber MWT systems under consideration. For our experimental setup, we propose using a new calibration technique: FVTD will be employed to simulate the incident field distribution inside an actual 3-D model of the system, including transmitting and receiving antennas.

As a comparative example, Fig. 4 shows the analytically derived electric field of a line source inside a 2-D circular cylindrical PEC chamber having a radius of 10 cm, as well as the field of a Wu–King resistively loaded dipole analyzed using FVTD [10] for a more accurate 3-D model of the setup. The 3-D model has a height of 21 cm capped by absorbing boundary conditions and the source is located at $x = 8.47$ cm, $y = z = 0$ (outside the shown imaging region).

It should be noted that since the experimental field cannot be directly measured, it must also be calculated based on the *antenna factor* of the radiating element. The antenna factor, usually a documented characteristic of the physical antenna in *free space*, multiplies the antenna terminal voltage to give the received electric field. This factor is also a source of inaccuracy if the free-space value is used, because it may be affected by the environment of the antenna (notably the PEC chamber of our MWT system). Thus, antenna factors for a given antenna placed inside the chamber need to be determined. In our work, these antenna factors are also obtained by accurately modeling the system in FVTD.
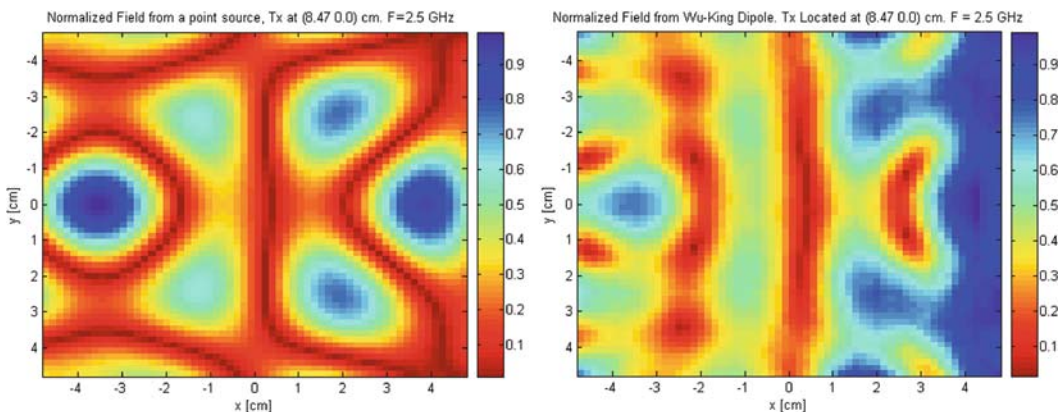
Fig. 4 Comparison of incident electric field in the imaging region for the analytic field of a line source inside a 2-D circular cylinder (*left*), and the FVTD 3-D simulated field due to a Wu–King resistively loaded dipole (*right*)

5 Results

Results of inversions using experimental data were not available at the time of writing and thus we present two examples of imaging using resonant chamber MWT: a synthetic 2-D transverse magnetic (TM) idealized model and a 3-D model wherein the FVTD technique is used to accurately model the MWT system. In all cases, additive white noise was added to all the synthetically derived scattered field at the observation points. The noise level was set to 10% of the maximum scattered field (real and imaginary parts of the phasor).

The first 2-D idealized reconstruction, performed using the DBIM, is of two concentric square cylinders placed inside the circular PEC of radius 20 cm. The larger cylinder is 10 cm^2 with a contrast of $\chi = 1 + j0.5$ and the inner smaller cylinder is 5 cm^2 with a contrast of $\chi = 2 + j$. The background permittivity is 3. The Tikhonov regularizer in the DBIM is the additive L_1-norm total variation [11] and the weight of the regularizer is chosen using the L-curve method [12]. Synthetic scattering data were obtained using a 2-D finite element code for solving the Helmholtz equation. The same FEM code was used in the DBIM inversion algorithm with a different mesh. There are 40 transmitters (line sources) and receivers equally spaced on a circle of radius 17 cm, giving 1600 scattered field data points for every frequency. Reconstruction results for a single frequency (1 GHz) are shown in Fig. 5.
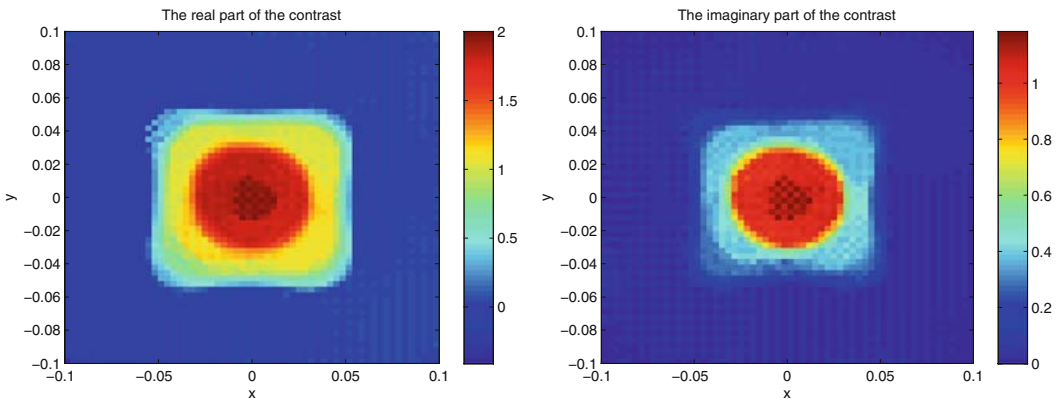
Fig. 5 Real (*left*) and imaginary (*right*) parts of the contrast for 2-D TM DBIM reconstruction of concentric square cylinders inside a PEC circular cylinder of radius 20 cm

The second test case is the MR-CSI reconstruction of two concentric circular dielectric cylinders embedded inside a circular cylinder 3-D resonant chamber MWT having a radius of 10 cm. Both dielectric cylinders are lossless and the outer cylinder has a radius of 4.5 cm and a contrast of $\chi = 0.33$ whereas the inner cylinder has a radius of 1.5 cm and a contrast of $\chi = 1.0$. The background medium has a dielectric constant of 6.0. The height of the resonant chamber and both dielectric cylinders is 21 cm. Dipole antennas that are resistively loaded according to the traditional Wu–King profile are located at a height of 10.5 and 1.5 cm away from the enclosure wall. Data for three frequencies (0.5, 1.5, and 2.5 GHz) were chosen and the scattered field was received at 40 equally spaced planar points on a circle of 8 cm centered inside the enclosure. A schematic of the configuration, as well as the reconstruction, is shown in Fig. 6. The FVTD technique was used to model the incident field inside the imaging region and generate the scattered data, with the enclosure capped using absorbing boundary conditions.
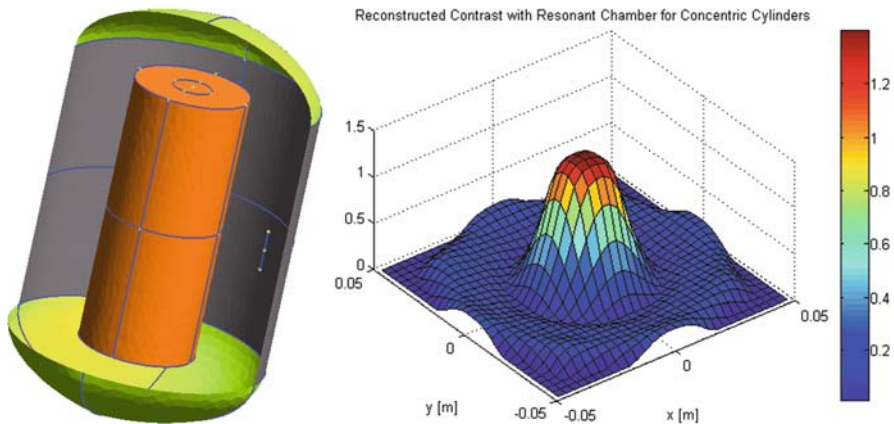
Fig. 6 Configuration of 3-D FVTD model for generation of synthetic data for the second test case (*left*) and subsequent reconstruction of contrast using MR-CSI method (*right*)

6 Conclusion

A new resonant chamber MWT prototype consisting of a circular cylindrical PEC chamber with a planar circular array of antennas mounted on the inside periphery has been developed. Although actual dielectric contrast reconstructions from experimental data have not yet been achieved, inversions of two separate synthetic data sets using the DBIM and MR-CSI techniques have been presented. These data sets were generated using a 2-D TM idealized model for the DBIM case and a more accurate 3-D FVTD model for the MR-CSI case. The next phase of the development will include inversions from experimental data using the FVTD calibration technique that has been outlined herein.

References

1. M. Lazebnik et al., A large-scale study of the ultrawideband microwave dielectric properties of normal breast tissue obtained from reduction surgeries, Physics in Medicine and Biology, vol. 52, pp. 2637–2656, 2007.
2. R. Rubaek et al., Nonlinear microwave imaging for breast-cancer screening using Gauss–Newton's method and the CGLS inversion algorithm, IEEE Transactions on Antennas and Propagation, vol. 55, no. 8, pp. 2320–2331, 2007.
3. S. Y. Semenov et al., Microwave-tomographic imaging of the high-dielectric-contrast objects using different image-reconstruction approaches, IEEE Transactions on Microwave Theory and Techniques, vol. 53, no. 7, pp. 2284–2294, 2005.
4. E. Bond et al., Microwave imaging via space–time beamforming for early detection of breast cancer, IEEE Transactions on Antennas and Propagation, vol. 51, no. 8, pp. 1690–1705, 2003.
5. J. De Zaeytijd et al., Full-wave 3D microwave imaging with a regularized Gauss–Newton method—theory and experiment, IEEE Transactions on Antennas and Propagation, vol. 55, no. 11, pp. 3279–3292, 2007.
6. A. Abubakar et al., Imaging of biomedical data using a multiplicative regularized contrast source inversion method, IEEE Transactions on Microwave Theory and Techniques, vol. 50, no. 7, pp. 1761–1771, 2001.
7. W. C. Chew, Y. M. Wang, Reconstruction of two-dimensional permittivity distribution using the distorted born iterative method, IEEE Transactions on Medical Imaging, vol. 9, no. 2, pp. 218–225, 1990.

8. A. Franchois, A. Tijhuis, A quasi-Newton reconstruction algorithm for a complex microwave imaging scanner environment, Radio Science, vol. 38, no. 2, p. 8011, 2003.
9. C. Gilmore, J. LoVetri, Enhancement of microwave tomography through the use of electrically conducting enclosures, Inverse Problems, vol. 24, pp. 1–21, 2008.
10. D. Firsov et al., High-order FVTD on unstructured grids using an object-oriented computational engine, ACES Journal, vol. 22, no. 1, pp. 71–80, 2007.
11. C. R. Vogel and M. E. Oman, Fast, robust total variation-based reconstruction of noisy, blurred images, IEEE Transactions on Image Processing, vol. 7, pp. 813–824, 1998.
12. P. C. Hansen, Analysis of discrete ill-posed problems by means of the *L*-curve, SIAM Review, vol. 34, pp. 561–580, 1992.

Index